Genomics spawns bigger, hardier farmed fish p. 902

Maternal IgE transfer drives postnatal allergy pp. 907 & 941

Single-cell development tracking wins *Science* & SciLifeLab Prize p. 924

Science

$15
20 NOVEMBER 2020
sciencemag.org

AAAS

MOLECULAR TELEGRAPHY

Organic molecules transit between charged probe tips on a silver surface pp. 912 & 957

CONTENTS

20 NOVEMBER 2020 • VOLUME 370 • ISSUE 6519

902

PHOTO: HENDRIX GENETICS

NEWS

IN BRIEF

892 News at a glance

IN DEPTH

894 Vaccine wagers on coronavirus surface protein pay off
Moderna reports early evidence of excellent efficacy, moving its mRNA candidate closer to widespread use *By J. Cohen*

895 Reinfections, still rare, provide clues on immunity
The growing group of people who get sick twice suggests protection can wane relatively quickly *By J. de Vrieze*

897 'Magic angle' graphene's next trick: superconducting devices
Twisted carbon sheets turned into switches that could make quantum computers smaller and more controllable *By C. Wood*

898 Like CRISPR, mystery gene editor began as a virus fighter
The genetic elements called retrons can only edit single-cell organisms, so far *By E. Pennisi*

900 China set to bring back rocks from the Moon
Chang'e-5's lunar samples could firm up shaky crater count dating system for the rocky planets *By D. Normile*

901 Seas are rising faster than ever
A new satellite will monitor coastal hot spots, where currents amplify global trends
By P. Voosen

FEATURES

902 Tomorrow's catch
Genomic technologies promise dramatic gains for aquaculture by accelerating the breeding of better strains *By E. Stokstad*
PODCAST

INSIGHTS

PERSPECTIVES

906 Drugs from bugs in creatures of the sea
A bacterium from the sea squirt microbiome makes a natural product with antifungal activity
By L. E. Cowen
REPORT P. 974

907 Transferring allergies in the womb
Maternal antibodies prime fetal mast cells in utero for subsequent postnatal allergy responses *By M. E. Rothenberg*
RESEARCH ARTICLE p. 941

909 The origin of diarrhea in rotavirus infection
Messengers from rotavirus-infected cells induce pathogenic signaling in neighboring cells *By M. Stanifer and S. Boulant*
RESEARCH ARTICLE P. 930

910 The more and less of electronic-skin sensors
Sensors can measure both strain and temperature or measure force without affecting touch *By X. Liu*
REPORTS pp. 961 & 966

912 The molecular wagon that stays on track
Single molecules are sent and received accurately over long distances across a surface *By F. Esch and B. A. J. Lechner*
REPORT p. 957

913 Advancing new tools for infectious diseases
Therapeutics and vaccine development for infectious diseases could be transformed
By R. Gupta

915 Georgina Mace (1953–2020)
Pioneering conservation biologist and sustainability scientist *By A. Purvis and K. E. Jones*

POLICY FORUM

916 Community-led governance for gene-edited crops
A post–market certification process could promote transparency and trust
By J. Kuzma and K. Grieger

BOOKS *ET AL.*

919 Alphabets and their origins
A new documentary series surveys the inception and evolution of the written word
By A. Robinson

Published by AAAS

920 Probing COVID's complexity in real time
The pandemic is as much about society, leaders, and values as it is about a pathogen
By S. V. Scarpino

LETTERS

921 Retraction
By T. Sijen et al.

921 Eroded protections threaten U.S. forests
By K.-V. Pérez-Hämmerle et al.

922 Space debris puts exploration at risk
By D. Greenbaum

922 Technical Comment abstracts

922 Errata

PRIZE ESSAY

924 Tracking development at the cellular level
Single-cell genomic methods enable developmental mapping of entire organisms
By J. Cao

RESEARCH

IN BRIEF

926 From *Science* and other journals

REVIEW

929 Fire ecology
Fire and biodiversity in the Anthropocene
L. T. Kelly et al.
REVIEW SUMMARY; FOR FULL TEXT: DX.DOI.ORG/10.1126/SCIENCE.ABB0355

RESEARCH ARTICLES

930 Virology
Rotavirus induces intercellular calcium waves through ADP signaling *A. L. Chang-Graham* et al.
RESEARCH ARTICLE SUMMARY; FOR FULL TEXT: DX.DOI.ORG/10.1126/SCIENCE.ABC3621
PERSPECTIVE p. 909

931 Photosynthesis
Architecture of the photosynthetic complex from a green sulfur bacterium *J.-H. Chen* et al.
RESEARCH ARTICLE SUMMARY; FOR FULL TEXT: DX.DOI.ORG/10.1126/SCIENCE.ABB6350

932 Neurodegeneration
Autosomal dominant VCP hypomorph mutation impairs disaggregation of PHF-tau
N. F. Darwich et al.
RESEARCH ARTICLE SUMMARY; FOR FULL TEXT: DX.DOI.ORG/10.1126/SCIENCE.AAY8826

933 Wildlife disease
Divergent impacts of warming weather on wildlife disease risk across climates
J. M. Cohen et al.
RESEARCH ARTICLE SUMMARY; FOR FULL TEXT: DX.DOI.ORG/10.1126/SCIENCE.ABB1702

934 Neurodevelopment
Gene regulatory networks controlling vertebrate retinal regeneration *T. Hoang* et al.
RESEARCH ARTICLE SUMMARY; FOR FULL TEXT: DX.DOI.ORG/10.1126/SCIENCE.ABB8598

935 Developmental biology
A human tissue screen identifies a regulator of ER secretion as a brain-size determinant
C. Esk et al.

941 Immunology
Fetal mast cells mediate postnatal allergic responses dependent on maternal IgE
R. Msallam et al.
PERSPECTIVE p. 907

950 Coronavirus
Ultrapotent human antibodies protect against SARS-CoV-2 challenge via multiple mechanisms *M. A. Tortorici* et al.

REPORTS

957 Surface science
Control of long-distance motion of single molecules on a surface *D. Civita* et al.
PERSPECTIVE p. 912

Materials science
961 Artificial multimodal receptors based on ion relaxation dynamics *I. You* et al.

966 Nanomesh pressure sensor for monitoring finger manipulation without sensory interference *S. Lee* et al.
PERSPECTIVE p. 910

970 Stellar astrophysics
An extremely metal-deficient globular cluster in the Andromeda Galaxy *S. S. Larsen* et al.

974 Antifungal discovery
A marine microbiome antifungal targets urgent-threat drug-resistant fungi *F. Zhang* et al.
PERSPECTIVE p. 906

978 Water phases
Experimental observation of the liquid-liquid transition in bulk supercooled water under pressure *K. H. Kim* et al.

983 Geophysics
Oceanic plateau of the Hawaiian mantle plume head subducted to the uppermost lower mantle *S. S. Wei* et al.

987 Developmental biology
Tissue topography steers migrating *Drosophila* border cells *W. Dai* et al.

991 Zika virus
Enhanced Zika virus susceptibility of globally invasive *Aedes aegypti* populations *F. Aubry* et al.

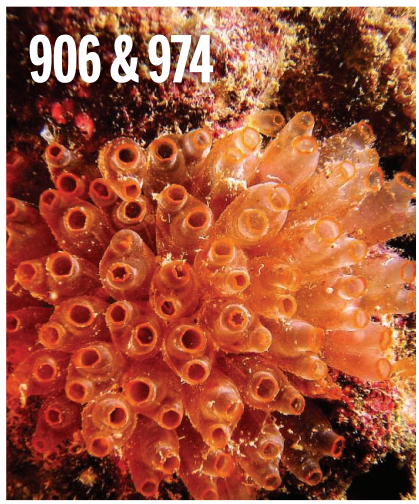

DEPARTMENTS

886 Editorial
The excellence question *By Ottoline Leyser*

887 Editorial
Let's not overthink this *By H. Holden Thorp*

1006 Working Life
Should I stay or should I go? *By Jessica Toothaker*

ON THE COVER

Spatial control over molecular movement is typically limited because motion at the atomic scale follows stochastic processes. When single dibromoterfluorene molecules are aligned along a specific direction on a silver surface, they become highly mobile and can be controllably transferred between two sharp probes, as illustrated here. Such a sender-receiver experiment enables transport of information, encoded in individual molecular entities, between precisely defined locations. See pages 912 and 957. *Illustration: C. Bickel/*Science

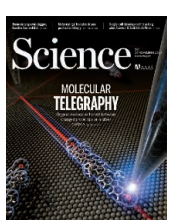

New Products 1000
Science Careers 1001

SCIENCE (ISSN 0036-8075) is published weekly on Friday, except last week in December, by the American Association for the Advancement of Science, 1200 New York Avenue, NW, Washington, DC 20005. Periodicals mail postage (publication No. 484460) paid at Washington, DC, and additional mailing offices. Copyright © 2020 by the American Association for the Advancement of Science. The title SCIENCE is a registered trademark of the AAAS. Domestic individual membership, including subscription (12 months): $165 ($74 allocated to subscription). Domestic institutional subscription (51 issues): $2148; Foreign postage extra: Air assist delivery: $98. First class, airmail, student, and emeritus rates on request. Canadian rates with GST available upon request, GST #125488122. Publications Mail Agreement Number 1069624. **Printed in the U.S.A.**
Change of address: Allow 4 weeks, giving old and new addresses and 8-digit account number. **Postmaster:** Send change of address to AAAS, P.O. Box 96178, Washington, DC 20090–6178. **Single-copy sales:** $15 each plus shipping and handling available from backissues.sciencemag.org; bulk rate on request. **Authorization to reproduce** material for internal or personal use under circumstances not falling within the fair use provisions of the Copyright Act can be obtained through the Copyright Clearance Center (CCC), www.copyright.com. The identification code for *Science* is 0036-8075. *Science* is indexed in the *Reader's Guide to Periodical Literature* and in several specialized indexes.

PHOTO: JOSE B. RUIZ/MINDEN PICTURES

Published by AAAS

EDITORIAL

The excellence question

Ottoline Leyser
is the chief executive officer of UK Research and Innovation, Swindon, UK.
Email: ceo@ukri.org

Five months ago, when I stepped into my new role as the chief executive officer of the UK Research and Innovation (UKRI) organization, a question loomed large for me: What is excellence? After all, UKRI is the major public funder of science in the United Kingdom, spending billions of taxpayer money every year. To spend this money well, UKRI must support a portfolio of truly excellent work. So, what then is excellence?

Some years ago, I was contacted about a plan to establish a new research journal. I was asked, "Where do you submit your best work for publication?" To answer this, I had to define my best work. I ought to know how to do that, having served on the Board of Reviewing Editors for *Science*, which aims to publish the very best research across the sciences. In that role, I considered whether the work constituted a major advance and if it was of interest to a wide audience. In a similar vein, the European Research Council, which has had an extraordinary impact on research funding in Europe, uses "excellence" as the sole criterion for funding. Instructions for panel members who evaluate proposals define such excellence as ground-breaking and high-risk, high-gain.

"The systems in place for defining excellence are not sufficiently open-minded..."

There is no doubt that truly excellent and ground-breaking work is published in *Science* and funded by the European Research Council, but are those the only definitions of excellence?

It is worth remembering that the term "ground-breaking" comes from construction. There is often a ground-breaking ceremony, but then the building must be erected. This comes only after much preparation, from determining the ideal location to securing all the planning permissions. Likewise, for every ground-breaking discovery, a huge amount of work has paved the way, and follow-up work to solidify the evidence and demonstrate reproducibility and generality is essential. High-quality work of this sort is rarely recognized as excellent by the scientific enterprise but is excellent nonetheless, and without it, there would be no progress.

Even at the cutting edge, work that looks at things in a new or different way can be harder to recognize as valuable. It is less obviously ground-breaking in the short term, not least because it might be wrong, but it is arguably more transformative in the long term. The systems in place for defining excellence are not sufficiently open-minded to alternative ways of looking at things.

And the desire for excellence as the only criterion for selection is often understood to mean research unrestricted by a requirement for utility—in other words, blue skies research for which applications are not immediately apparent. This contributes to the view that there is a compromise between excellence and applied research. Although there is a continuous need to emphasize the value of blue skies research, the implication that it is better than applied research is insidious.

In the United Kingdom, the question of what constitutes excellence in research is particularly pertinent with the announcement of a review of the Research Excellence Framework. This system allocates block grant funding to U.K. universities based on the excellence of their research, with assessment of a selected sample of research outputs as an important component. A high-quality portfolio should surely include a range of types of output, but universities are extremely conservative in their selection and typically focus on high-impact papers that their faculty has published, embedding a culture of narrowly defined excellence.

It is time for assessment systems to support and value a robust portfolio of work of different sorts, and by association, a diverse range of people to do this work. Organizations such as UKRI, which supports research across sectors, have a major responsibility in this regard. UKRI was created by bringing together nine different research funders. Some argued that a "monolithic" funder would reduce diversity in funding. My view is quite the opposite. Organizations with a broad funding mandate must address the portfolio challenge by recognizing and supporting excellence in all its forms.

The world is wrestling with crises such as climate change and the coronavirus disease 2019 (COVID-19) pandemic. Let's redefine excellence in ways that open up opportunities for projects and talent to break through the problems of today and tomorrow.

–Ottoline Leyser

PHOTO: SAINSBURY LABORATORY, UNIVERSITY OF CAMBRIDGE

10.1126/science.abf7125

Published by AAAS

Let's not overthink this

H. Holden Thorp
Editor-in-Chief,
Science journals.
hthorp@aaas.org;
@hholdenthorp

For some observers, the U.S. presidential election of 2020 appeared to be about science. Outgoing President Donald Trump consistently and dishonestly played down the threats from coronavirus disease 2019 (COVID-19) and climate change. President-elect Joe Biden said he would listen to scientists, a position that was mocked by Trump. Some might take Biden's victory—decisive but hardly a landslide—as feeble support for science. But was science actually on the ballot? Maybe it's best not to overthink this.

Science and political communication scholar Kathleen Hall Jamieson of the University of Pennsylvania believes that it is wrong to construe the election in such simple terms. "Science was not on the ballot," she said in a recent conversation. When viewed in the heat of the battle, she says, the 73 million people who voted for Trump may seem to have been rejecting science, but many of them live in areas of the country that had, until recently, barely experienced the COVID-19 outbreak. Now they are getting it full blast. Others simply believed that the health of the economy should not be jeopardized by what they saw as a draconian pandemic response. As for the fight against climate change, many people feared that their livelihoods would be threatened by calls for a major move away from fossil fuels. Add to that the millions of people whose religious beliefs enjoin them from appreciating the beauty and power of the theory of evolution. There is not one great horde of Americans (many of whom happen to be Trump supporters) who are anti-science. It is a mixture of people who, for personal reasons, resist facts that challenge their thinking.

If you stand back and look at the big picture, science seems to be in no different a place now than it has been in the past. Except for the scientists themselves and members of the public who avidly consume science documentaries, books, and magazines, most Americans care only about the products of science that directly affect their personal lives. And this caring doesn't usually cut very deep. Most people don't think about the biology of the promised coronavirus vaccine any more than they marvel at how the theory of general relativity is used by satellites to guide them as they navigate with Google Maps.

The periods of high American enthusiasm for science have all coincided with great triumphs for science such as the Moon landing or the polio vaccine. But after all this excitement, science moved off center stage, and the scientists could quietly go back to work. We're on the cusp of a similar cycle. The putative vaccines will hopefully end the pandemic in the late spring, and although there will be a round of celebration for the scientific quest, it's unlikely that there will be an enduring appreciation for the people and processes that got us there.

> **"With the election behind us all, it's time... to do the best science imaginable."**

The scientific community in the United States should do as much as it can to improve science education and science communication, but not to suddenly get all Americans to wake up to scientists' ideas about climate change or evolution. There are plenty of students—potential scientists—who don't have equitable access to high-quality science teaching, and the focus should be on bringing in as many scientists as possible. The scientific community shouldn't beat itself up over the fact that there is probably little it can do to induce many of the 73 million people who voted for Donald Trump to abruptly decide that they were wrong about climate change and COVID-19.

With the election behind us all, it's time for science to do what it has always done. Double down on its best practices of inductive reasoning and quantitative analysis. Question everything. Do things no one has done before. In other words, to do the best science imaginable.

And about that ubiquitous climate-denying uncle that apparently nearly every scientist has to interact with on the Thanksgiving holiday in the United States—this year, the gathering will hopefully take place virtually, so, maybe just sit back and smile, knowing that science will produce the vaccine that will let his life get back to normal. And let him enjoy his turkey.

–H. Holden Thorp

PHOTO: CAMERON DAVIDSON

10.1126/science.abf7407

Published by AAAS

NEWS

> "I'm an engineer. ... We look at hard data."
>
> **Brad Raffensperger,** Georgia's secretary of state, in *The Washington Post*, about being pressured by fellow Republicans to question the validity of legally cast absentee ballots and reverse President Donald Trump's narrow loss in the state. He said he has received death threats.

IN BRIEF

Edited by **Jeffrey Brainard**

Hospital workers in Houston, checking on a COVID-19 patient, wear photos showing themselves without protective gear.

PHOTO: GO NAKAMURA/BLOOMBERG VIA GETTY IMAGES

INFECTIOUS DISEASES

Pandemic reaches record highs across the United States

The United States posted record numbers of COVID-19 diagnoses and hospitalizations this week, grim new milestones for the country, which leads the globe in deaths. Hospitals were treating more than 73,000 patients on 16 November, nearly double the number only 1 month ago, according to the COVID Tracking Project. New confirmed cases reached more than 1 million for the 7 days ending 15 November, another first. The highest case growth rates were in South Dakota and other Midwest states, but cases increased in 46 of 50 states during the previous 2 weeks, according to trackers at Johns Hopkins University. Iowa's and North Dakota's governors ordered residents to wear masks in public spaces, dropping earlier resistance to the measure, while Michigan, Washington state, and other jurisdictions suspended indoor restaurant dining and took other steps that public health specialists hope will prevent the need for more extensive lockdowns, as hospitals in several areas neared capacity.

Amazon CEO gives climate grants

PHILANTHROPY | A methane-sniffing satellite and climate-friendly crops are among the projects supported by the first $791 million in grants announced this week from the $10 billion Bezos Earth Fund, financed by Amazon CEO Jeff Bezos. The nonprofit Environmental Defense Fund, which received $100 million, said the money would help it complete MethaneSAT, its high-resolution tracker of the potent greenhouse gas, for launch in 2022. A $30 million grant to the Salk Institute for Biological Studies, meanwhile, will go to a project seeking to increase carbon sequestration by the world's six leading crop species. Other grants support advocacy to upgrade the electrical grid for renewable energy, developing seaweed as a climate-friendly protein source, and planting 35 million trees in Kenya, Madagascar, and Mozambique. The fund also supported several nonprofits focused on environmental justice, including through a $43 million grant to the Solutions Project, which funds nonprofits on the front lines of climate change and racial equity.

Published by AAAS

European budget edges up

FUNDING | The European Parliament last week negotiated an unexpected €4 billion boost to Horizon Europe, the European Union's next research funding program, but research advocates aren't cheering: Basic science may still see a funding squeeze in 2021. Within the final €85 billion, 7-year budget, €5 billion is reserved for applied research and support for small tech firms under a postpandemic recovery fund—which leaves the remaining budget only a little larger than the current program, Horizon 2020. European agencies receive less in the early years of a 7-year budget, so the final figure means the European Research Council and other bodies that support basic science could receive less money in 2021 than in 2020. The extra €4 billion will come from antitrust fines and unspent budget commitments that would normally be deducted from national contributions; some observers view those sources as unreliable.

Newton's *Principia* abounds

HISTORY OF SCIENCE | Isaac Newton's masterpiece, *Philosophiae Naturalis Principia Mathematica*, also known as the *Principia*, lays out the foundations of physics, including the laws of motion and gravity. It was a hit even in its day, suggests a tally of first edition copies of this book, printed in 1687 in London and worth millions of dollars today. The new census has uncovered 386 copies, more than double the number tallied in the 1950s. Two researchers spent more than a decade searching worldwide through collections held by museums, universities, libraries, and private individuals. The higher number of copies suggests the *Principia* enjoyed a wider readership than previously believed, the team reported recently in the *Annals of Science*. The researchers plan to analyze the handwritten annotations that pepper many of the books for clues to the influence of Newton's ideas.

COVID-19 maverick in hot seat

PUBLIC HEALTH | Prominent French microbiologist Didier Raoult will face a disciplinary hearing next year for promoting the antimalarial drug hydroxychloroquine as a COVID-19 treatment despite a lack of evidence that it works. Members of France's Infectious Diseases Society filed a complaint in July with the regional arm of a national medical regulatory body alleging that Raoult's promotion of the drug violated a code of medical ethics. Raoult led four controversial studies that purported to show the drug's benefits for treating COVID-19, but more robust studies have found no benefit. The regional board held an initial hearing in October with Raoult, who heads the Mediterranean Infection University Hospital Institute, and confirmed last week it will proceed with the complaint. The charges may result in Raoult being fined, warned, or barred from practicing medicine. Raoult continues to tout hydroxychloroquine and plans to contest the National Agency for Medicines and Health Products Safety's refusal to temporarily authorize it to treat COVID-19, saying the agency is endangering lives by preventing its use.

PHOTO: AUSCAPE/UNIVERSAL IMAGES GROUP VIA GETTY IMAGES

CONSERVATION

Atlantic gets its largest marine reserve

A United Kingdom overseas territory announced a marine reserve last week that will be the Atlantic Ocean's largest and accomplishes a U.K. goal to protect 4 million square kilometers (km^2), or about 1%, of the global ocean. The territory of Tristan da Cunha banned fishing and underwater mining in 90% of its territorial waters—687,000 km^2—making this marine protected area the world's fourth largest. Tristan da Cunha is Earth's most remote archipelago, located about 2400 kilometers west of South Africa, and boasts 25 endemic species of seabird, including the endangered spectacled petrel of Inaccessible Island. About 90% of all northern rockhopper penguins (above, on Gough Island) breed in the archipelago. Fishing for the Tristan rock lobster, a mainstay of the local economy, will continue. But enforcement of the fishing ban in the open ocean, even with help from remote sensing, remains a challenge.

Dino pair heads for museum home

PALEONTOLOGY | After years of controversy befitting their name, the Dueling Dinosaurs have found a resting place at the North Carolina Museum of Natural Sciences. The acquisition, announced on 17 November, is good news for researchers, who feared a private collector might buy the intertwined fossils of what appear to be a juvenile *Tyrannosaurus rex* and a *Triceratops horridus*. The deal will "ensure that this extraordinary specimen can be enjoyed not just by one person, but by everyone," says Lindsay Zanno, the museum's head of paleontology. The creatures' unusual remains have made them celebrities in the fossil world, and the subject of years of legal fights over who owned them. In May, the Montana Supreme Court sided with the owners of the eastern Montana land where the dinosaurs were found, rather than others who owned the partial rights to minerals under the land. The museum's charitable arm, the Friends of the North Carolina Museum of Natural Sciences, bought the dinosaurs from the landowners, Mary Anne and Lige Murray, for $6 million. For comparison, a private collector paid a record-setting $31.8 million this year for an adult *T. rex* fossil skeleton.

Published by AAAS

New York Times reporter Helene Cooper (right) participates in Moderna's vaccine efficacy trial in Washington, D.C.

PHOTO: ERIN SCHAFF/*THE NEW YORK TIMES*/REDUX

IN DEPTH

COVID-19

Vaccine wagers on coronavirus surface protein pay off

Moderna reports early evidence of excellent efficacy, moving its mRNA candidate closer to widespread use

By **Jon Cohen**

Designers of COVID-19 vaccines appear to have made a spectacularly successful bet. When devising a vaccine against a virus, scientists choose ways to mimic it that they hope will safely teach the immune system how to defeat the foreign invader. For COVID-19, most developers gambled on spike, the protein that allows SARS-CoV-2 to dock onto and infect cells. This week's announcement by the biotech Moderna that its COVID-19 vaccine powerfully protected people from the disease in an efficacy trial was the strongest sign yet that spike is a winning hand.

Since 9 November, Moderna, the pharma giant Pfizer and its German collaborator BioNTech, and a Russian institute have all offered preliminary evidence that spike-based vaccines can achieve greater than 90% efficacy. Because the vast majority of remaining COVID-19 vaccine candidates are also designed to deliver spike—either via its genetic code or the protein itself—the good news may keep arriving. Anthony Fauci, head of the U.S. National Institute of Allergy and Infectious Diseases (NIAID), says he's "optimistic that all the vaccines are going to have very favorable results." He adds that the strong early reports suggest SARS-CoV-2 is not a particularly formidable foe for a vaccine.

No COVID-19 vaccine efficacy trial has yet to cross the finish line, but the details Moderna provided in a press release impressed many scientists. An independent board monitoring its 30,000-person vaccine trial met on 8 November and reported to the company and U.S. government health officials that only five people in the vaccinated group had developed confirmed cases of COVID-19, whereas 90 people who received placebo shots became ill with the disease. That 94.5% efficacy matched the "greater than 90%" interim figure reported by Pfizer and BioNTech and the 92% claimed for a Russian candidate. (That vaccine uses viral vectors to deliver the spike gene but its announced success was based on only 20 COVID-19 cases and drew skepticism in many quarters.) If those numbers translate into equally high levels of real-world protection, then COVID-19 vaccines could rapidly stop the pandemic when widely distributed.

Moderna's "efficacy is just beautiful, and there's no question about the veracity of it either," says Lawrence Corey, a virologist at the Fred Hutchinson Cancer Research Center who co-led the clinical trials network that is testing the candidate.

Moderna offered compelling evidence that its candidate did more than just prevent symptomatic disease, the main endpoint for its trial. The company reported that 11 people in the trial's placebo arm developed severe cases of COVID-19, whereas no one in the vaccinated group did. The vaccine, which like the Pfizer/BioNTech candidate uses messenger RNA (mRNA) to produce spike inside cells, appears to work equally well in all populations studied, Moderna said, including the elderly and ethnic minorities, and people with conditions such as diabetes and heart disease that make them vulnerable to severe COVID-19.

"Obviously, the data speak for themselves," says Fauci, whose institute helped support the study. He suspects that by late next month doses of one or both mRNA vaccines could start to be offered to people at highest risk from the coronavirus.

Many questions remain—about how long the protection offered by the vaccines will last, how safe they are, what regulators will demand to approve them, and how to meet the challenge of rapidly producing and distributing hundreds of millions, if not billions, of doses. Because warm temperatures cause the RNA and the lipid particles in which it is encapsulated to degrade, the vaccines must be kept frozen until days before use, requiring a cold chain to move them from manufacturing plants to pharmacies and clinics. In the short term, Moderna's vaccine may have an advantage for storage and transport as it proved to stay stable for long periods at –20°C, a normal pharmacy freezer tempera-

Published by AAAS

ture, whereas the Pfizer/BioNTech candidate appears to require ultracold freezers or dry ice to keep the product below –70°C.

Even –20°C is a challenge, and high-tech thermoses that were used to transport Ebola vaccines in sub-Saharan African countries at ultracold temperatures may be called into action. Longer term, Pfizer and BioNTech have said they intend to create a more stable freeze-dried powder formulation; another company, CureVac, said last week its COVID-19 mRNA vaccine remains stable at normal refrigeration and will soon start an efficacy trial.

Ruth Karron, who heads the Center for Immunization Research at the Johns Hopkins Bloomberg School of Public Health, notes another uncertainty: whether the mRNA vaccines prevent people from becoming infected in the first place, which is key to controlling the spread of the virus. "The data we have are that these vaccines protect you against severe illness, but it doesn't mean that you can't get infected and give it to your patient, your neighbor, your customer, or whomever." But Karron also says of the Moderna result: "Wow, fantastic, amazing."

Science's COVID-19 reporting is supported by the Pulitzer Center and the Heising-Simons Foundation.

Operation Warp Speed, the U.S. government effort to develop COVID-19 vaccines and rapidly move them into efficacy trials, has invested $1 billion in Moderna's COVID-19 vaccine R&D. (Pfizer did not take Warp Speed money for development.) This summer, Warp Speed committed another $1.5 billion to Moderna to purchase 100 million doses of its candidate and $1.9 billion to Pfizer for the same amount of its product, which was developed at BioNTech, a company that has focused on treating cancer with mRNA.

Small studies have shown mRNA vaccines can trigger immune responses and don't have obvious, significant safety issues, but the two efficacy trials are the first to report that they can actually protect people from a pathogen. The snippet of mRNA at the heart of both vaccines was initially designed by a team led by Barney Graham of NIAID's Vaccine Research Center. When he learned that the strategy worked, Graham says, "I had my moment of relief and sobbing tears."

Both mRNA vaccines have yet to complete their trials, which aim to accrue about 150 to 165 cases of COVID-19 to provide greater statistical certainty about efficacy. They should hit those targets by December, when the U.S. Food and Drug Administration plans to convene an advisory panel to review the data. Cases are accumulating fast because most trial sites are in the United States, where the epidemic has exploded. If the advisers recommend emergency use authorizations for the vaccines, Warp Speed plans to start to deliver them to U.S. pharmacies and clinics the next day.

Moderna projects it can have about 20 million doses for the United States by the end of the year. Pfizer, which has made sales agreements with several countries in addition to the one it negotiated with Warp Speed, projects it can supply a total of 50 million doses by the end of this year, with an unspecified number going to Warp Speed. The U.S. Centers for Disease Control and Prevention will prioritize who should receive the vaccine first, but the companies say there should be enough to vaccinate the entire United States by the spring.

Both vaccines require two doses separated by weeks. Pfizer says it will have 1.3 billion doses next year. Moderna's vaccine delivers more mRNA—100 micrograms of mRNA per dose, versus Pfizer's 30 micrograms—and it does not see a way to produce more than about 1 billion doses in 2021. "We don't have a billion-dose manufacturing capacity sitting idle somewhere. We are increasing our output more and more and all our key engineers are working to make that happen," says Stéphane Bancel, Moderna's CEO.

The cost of the vaccine—Warp Speed paid about $25 per dose, all told—may also be far too high for many countries. Bancel says his company is in discussions with the COVID-19 Vaccines Global Access Facility, a nonprofit set up to help resource-limited countries purchase the vaccine at discounted prices.

Once supplies are available, the question will become whether people who are hesitant about a COVID-19 vaccine—especially a novel type that has no long-term safety record—will roll up their sleeves. Still, Karron suspects hesitancy will drop if people see the vaccine works and no serious side effects surface. She also imagines pressure will build to contribute to the social good. "There's going to come a moment where you're going to be able to say, you know, we could open up our community, except for people like you," Karron says. "If you would get vaccinated, we could get back to some semblance of life as we knew it."

Fauci says a COVID-19 vaccine always looked like a solid bet. The fact that many infected people clear the virus without developing serious, if any, symptoms, shows that the immune system can beat it back. "I've been saying all along that when the body tells you that it's capable of making an adequate immune response against natural infection, that tells you you have a pretty good chance to get a vaccine." ■

With reporting by Jocelyn Kaiser.

COVID-19

Reinfections, still rare, provide clues on immunity

The growing group of people who get sick twice suggests protection can wane relatively quickly

By **Jop de Vrieze**

In late June, Sanne de Jong developed nausea, shortness of breath, sore muscles, and a runny nose. At first, she thought it might be lingering effects from her COVID-19 infection in the spring. De Jong, 22, had tested positive on 17 April and suffered mild symptoms for about 2 weeks. She tested negative on 2 May—just in time to say farewell to her dying grandmother—and returned to work as a nursing intern in a hospital in Rotterdam, the Netherlands.

But when her symptoms re-emerged, her doctor suggested she get tested again. "A reinfection this soon would be peculiar, but not impossible," she told De Jong, who by then had again lost her sense of smell and had abdominal pains and diarrhea.

The call from her municipal health service came on 3 July. De Jong had tested positive again. "You're kidding me!" she recalls saying.

Scientists are keenly interested in cases like hers, which are still rare but on the rise. Reinfections hint that immunity against COVID-19 may be fragile and wane relatively quickly, with implications not just for the risks facing recovered patients, but also for how long future vaccines might protect people. "The question everybody wants to answer is: Is that second one going to be less severe most of the time or not?" says Derek Cummings, who studies infectious disease dynamics at the University of Florida. "And what do reinfections teach us about SARS-CoV-2 immunity in general?"

South Korean scientists reported the first suspected reinfections in May, but it took until 24 August before a case was officially confirmed: a 33-year-old man who was treated at a Hong Kong hospital for a

Published by AAAS

mild case in March and who tested positive again at the Hong Kong airport on 15 August after returning from a trip to Spain. Since then, at least 24 other reinfections have been officially confirmed—but scientists say that is definitely an underestimate.

To count as a case of reinfection, a patient must have had a positive polymerase chain reaction (PCR) test twice with at least one symptom-free month in between. But virologist Chantal Reusken of the Dutch National Institute for Public Health and the Environment (RIVM) explains that a second test can also be positive because the patient has a residue of nonreplicating viral RNA from their original infection in their respiratory tract, or because they had suppressed but never fully cleared the virus. So most journals want to see two full virus sequences, from the first and second illnesses, that are sufficiently different, says Paul Moss, a hematologist at the University of Birmingham. "The bar is very high," Moss says. "In many cases, the genetic material just isn't there."

Even if it is, many labs don't have the time or money to clinch the case. As a result, the number of genetically proven reinfections is orders of magnitude lower than that of suspected reinfections. The Netherlands alone has 50 such cases, Brazil 95, Sweden 150, Mexico 285, and Qatar at least 243.

The Hong Kong patient's second infection was milder than the first, which is what immunologists would expect, because the first infection typically generates some immunity. That may explain why reinfections are still relatively rare, says Maria Elena Bottazzi, a molecular virologist at Baylor College of Medicine and Texas Children's Hospital.

They could become more common over the next couple of months if early cases begin to lose their immunity. Reinfections with the four coronaviruses that cause the common cold occur after an average of 12 months, a team led by virologist Lia van der Hoek at Amsterdam University Medical Center recently showed. Van der Hoek thinks COVID-19 may follow that pattern: "I think we'd better prepare for a wave of reinfections over the coming months." That's "bad news for those who still believe in herd immunity through natural infections," she adds, and a worrisome sign for vaccines.

Others are less pessimistic. Although antibodies can wane within months—particularly in mild cases—they sometimes persist. Neutralizing antibodies, the most important kind, as well as memory B cells and T cells seem to be relatively stable over at least 6 months.

And there are hints that people who have serious COVID-19 mount the strongest responses, just as in the two other serious human diseases caused by coronaviruses, severe acute respiratory syndrome (SARS) and Middle East respiratory syndrome. Both trigger high antibody levels that last up to 2 years, and T cell responses to SARS can be detected even longer. Because of these persistent immune defenses, "I expect that most reinfections will be asymptomatic," says Antonio Bertoletti, an infectious disease specialist at the National University of Singapore. He says being reinfected might even be a good thing, "since you will continue to boost and train your immune system."

Not all reinfections seen so far are milder. "We see all different combinations," Reusken says. The second time Luciana Ribeiro, a surgeon in Rio de Janeiro, got sick, it was much worse. She was first infected by a colleague in March, developed mild symptoms, and tested negative afterward. Three months later, Ribeiro had symptoms again—she could no longer smell her breakfast, she says—but she didn't immediately get a test because she thought she was immune. When she grew more and more tired, she requested a computerized tomography scan. "It showed that half of my lungs were affected," Ribeiro says. "'This clearly is COVID,' the radiologist told me. I didn't believe it, but I tested positive."

Ribeiro thinks she was reinfected by a patient in the intensive care unit where she works, and that her second episode may have been worse because virus-laden aerosols produced during a medical procedure entered her lungs. But some scientists worry about another scenario that could make the second episode worse: enhanced disease, in which a misfiring immune response to the first infection exacerbates the second one. In dengue fever, for example, antibodies to an initial infection can actually help dengue viruses of another serotype enter cells, leading to a more severe and sometimes fatal second infection. In some other diseases, the first infection elicits ineffective, nonneutralizing antibodies and T cells, hampering a more effective response the second time around.

A recent preprint published by Chinese researchers suggested patients whose first COVID-19 infection is very severe may

"You're kidding me!" Sanne de Jong, a nursing assistant, said when she was told she had COVID-19 again in July.

PHOTO: MIRANDA DE JONG

Published by AAAS

have ineffective antibodies, which might make them more prone to severe reinfections. But so far there's no evidence from reinfected patients to suggest enhanced disease is at work in COVID-19—although scientists haven't ruled it out either. Vaccination against some diseases can also trigger enhancement later—a known or suspected complication of vaccines against dengue and respiratory syncytial virus in humans and a coronavirus disease in cats. But there is no evidence that candidate COVID-19 vaccines do so, Cummings says. "Having worked with dengue I can say the empirical basis for enhanced disease is just not there, while it was very strong in dengue."

De Jong's virus samples were both sequenced in Reusken's lab, with a surprising outcome: The sequences were not identical, but showed so much similarity that RIVM virologist Harry Vennema says she probably she did not clear the virus in April and that it started to replicate again in June. "I did have a lot of stress after that first episode because my grandmother died," De Jong says. "Maybe that had an impact on my immune system."

That makes her case different from a true reinfection—although Vennema says perhaps they should be considered similar, because in both cases the immune system failed to mount a protective response. His lab has found at least one similar case, he says, suggesting some unconfirmed reinfections might actually be a resurgence of the original virus.

Other coronaviruses can also cause persistent infections, says Stanley Perlman of the University of Iowa. In 2009, his team showed that an encephalitis-causing mouse coronavirus can linger in the body and continuously trigger immune responses, even if it doesn't replicate. And in a preprint posted on 5 November, a team of U.S. scientists shows SARS-CoV-2 can persist for months inside the gut. Persistent infections, they suggest, may help explain the extraordinarily long-lasting symptoms that afflict some COVID-19 survivors.

De Jong is experiencing some of those symptoms. Although she tested negative in September and has high levels of neutralizing antibodies, suggesting she is protected for at least a couple of months, she still suffers from gastrointestinal complaints, fatigue, and cognitive impairment. De Jong says her story is a warning to people who had the virus and think they're now invulnerable: "Please be cautious. You can get it again." ■

Jop de Vrieze is a science journalist in Amsterdam.

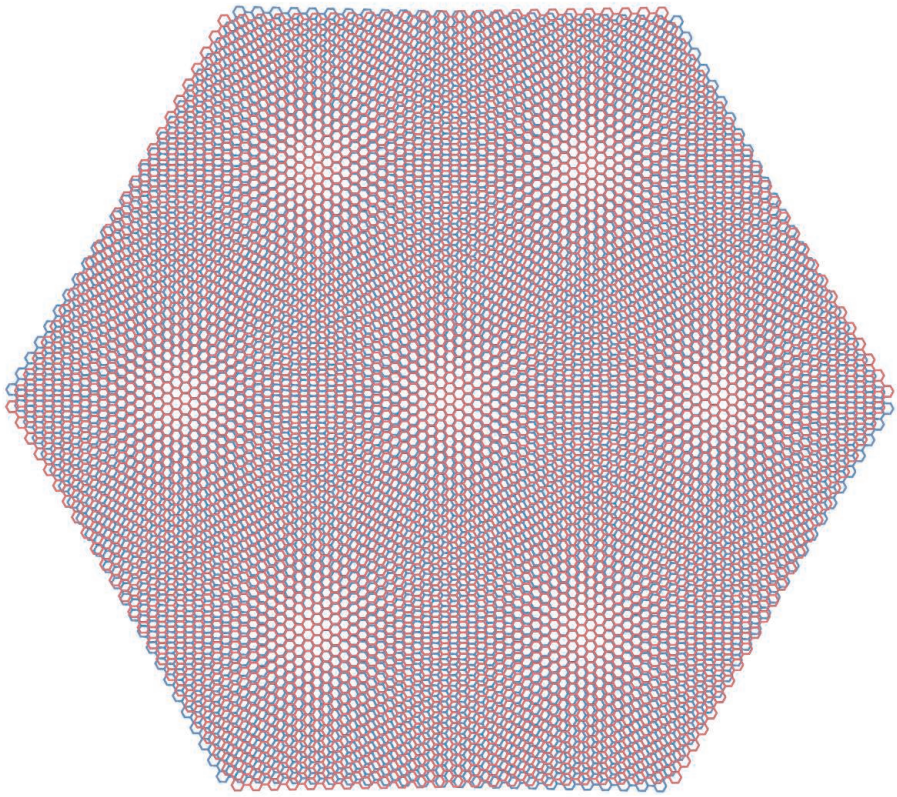

IMAGE: © 2018 BY YUAN CAO

MATERIALS SCIENCE

'Magic angle' graphene's next trick: superconducting devices

Twisted carbon sheets turned into switches that could make quantum computers smaller and more controllable

By **Charlie Wood**

In 2018, a group of researchers at the Massachusetts Institute of Technology (MIT) pulled off a dazzling materials science magic trick. They stacked two microscopic cards of graphene—sheets of carbon one atom thick—and twisted one ever so slightly. Applying an electric field transformed the stack from a conductor to an insulator and then, suddenly, into a superconductor: a material that frictionlessly conducts electricity. Dozens of labs leapt into the newly born field of "twistronics," hoping to conjure up novel electronic devices without the hassles of fusing together chemically different materials.

Two groups—including the pioneering MIT group—are now delivering on that promise by turning twisted graphene into working devices, including superconducting switches like those used in many quantum computers. The studies mark a crucial step for the material, which is already maturing into a basic science tool able to capture and control individual electrons and photons. Now, it's showing promise as the basis of new electronic devices, says Cory Dean, a condensed matter physicist at Columbia University whose lab was one of the first to confirm the material's superconducting properties after the 2018 announcement. "The idea that this platform can be used as a universal material is not fantasy," he says. "It's becoming fact."

The secret behind twisted graphene's chameleonlike nature lies with the so-called "magic angle." When researchers rotate the sheets by precisely 1.1°, the twist creates a large-scale "moiré" pattern—the atom-scale equivalent of the darker bands seen when two grids are juxtaposed. By bringing thousands of atoms together, the moiré allows them to act in unison, like super-

Published by AAAS

atoms. That collective behavior enables a modest number of electrons, shepherded to the right place by an electric field, to radically change the material's behavior, from insulator to conductor to superconductor. Interactions with the supercells also force electrons to slow down and feel each other's presence, which makes it easier for them to pair off, a requirement for superconductivity.

Now, researchers have shown they can dial desired properties into small regions of the sheet by slapping on a pattern of metallic "gates" that subject different areas to varying electric fields. Both groups built devices known as Josephson junctions, in which two superconductors flank a thin layer of nonsuperconducting material, creating a valve for controlling the flow of superconductivity. "Once you have demonstrated that then the world is open," says Klaus Ensslin, a physicist at ETH Zurich, and a co-author on one of the studies, posted to the preprint server arXiv on 30 October. Conventional Josephson junctions serve as the workhorse of superconducting electronics, found in magnetic devices for monitoring electrical activity in the brain, and ultrasensitive magnetometers.

"It's a totally new way of making materials without chemistry."
Eva Andrei, Rutgers University, New Brunswick

The MIT group went further, electrically transforming their Josephson junctions into other submicroscopic gadgets, "just as proof of concept, to show how versatile this is," says lab leader Pablo Jarillo-Herrero, whose group posted its results to arXiv on 4 November. By tuning the carbon into a conductor-insulator-superconductor configuration, they were able to measure how tightly the electron pairs were yoked together—an early clue to the nature of its superconductivity and how it compares with other materials. The team also built a transistor that can control the movement of single electrons; researchers have studied such single-electron switches as a way to shrink circuits and diminish their thirst for energy.

Magic angle graphene devices are unlikely to challenge consumer silicon electronics anytime soon. Graphene itself is easy to make: Sheets of it can be stripped off blocks of graphite with nothing more than Scotch tape. But the devices must be chilled nearly to absolute zero before they can superconduct. And maintaining the precise twist is awkward, as the sheets tend to wrinkle, disrupting the magic angle. Reliably creating smoothly twisted sheets even just 1 micron or two across is still a challenge, and researchers don't yet see a clear path toward mass production. "If you wanted to do a real complex device," Jarillo-Herrero says, "you'd need to create hundreds of thousands of [graphene substrates] and that technology doesn't exist."

Nevertheless, many researchers are excited by the promise of exploring electronic devices without worrying about the constraints of chemistry. Materials scientists typically have to find substances with the right atomic properties and fuse them together. And when the concoction is finished, the different elements may not mesh in the desired way.

In magic angle graphene, in contrast, all the atoms are carbon, eliminating messy boundaries between different materials. And scientists can change the electronic behavior of any given patch at the press of a button. These advantages grant unprecedented control over the material, Ensslin says. "Now, you can play like on a piano."

That control could simplify quantum computers. Those being developed by Google and IBM rely on Josephson junctions with properties that are fixed during fabrication. To operate the finicky qubits, the junctions must be manipulated jointly in cumbersome ways. With twisted graphene, however, qubits could come from single junctions that are smaller and easier to control.

Kin Chung Fong, a Harvard University physicist and member of Raytheon BBN Technologies's quantum computing team, is enthusiastic about another potential use for the material. In April, he and his colleagues proposed a twisted graphene device that could detect a single photon of far infrared light. That could be useful for astronomers probing the faint light of the early universe; their current sensors can spot lone photons only in the visible or nearly visible parts of the spectrum.

The field of twistronics remains in its infancy, and the fussy process of twisting microscopic specks of graphene to the magic position still requires sleight of hand, or at least deft lab work. But regardless of whether twisted graphene finds its way into industrial electronics, it's already profoundly changing the world of materials science, says Eva Andrei, a condensed matter physicist at Rutgers University, New Brunswick, whose lab was one of the earliest to notice twisted graphene's peculiar properties.

"It's a really new era," she says. "It's a totally new way of making materials without chemistry." ■

Charlie Wood is a journalist in New York City.

MICROBIOLOGY

Like CRISPR, mystery gene editor began as a virus fighter

The genetic elements called retrons can only edit single-cell organisms, so far

By **Elizabeth Pennisi**

Seven years ago, an understanding of nature inspired a revolutionary new technology, when researchers turned a defense system used by bacteria to thwart viruses into the gene-editing tool now known as CRISPR. But for another emerging gene editor the understanding has lagged the applications. For several years, researchers have been adapting retrons—mysterious complexes of DNA, RNA, and protein found in some bacteria—into a potentially powerful way to alter genomes of single-cell organisms. Now, biology is catching up, as two groups report evidence that, like CRISPR, retrons are part of the bacterial immune arsenal, protecting the microbes from viruses called phages.

On 5 November in *Cell*, one team described how a specific retron defends bacteria, triggering newly infected cells to self-destruct so the virus can't replicate and spread to others. The *Cell* paper "is the first to concretely determine a natural function for retrons," says Anna Simon, a synthetic biologist at Strand Therapeutics who has studied the bacterial oddities. Another paper, which so far has appeared only as a preprint, reports a similar finding.

The new understanding of retrons' natural function could boost efforts to put them to work. Retrons are "quite efficient tools for accurate and efficient genome editing," says Rotem Sorek, a microbial genomicist at the Weizmann Institute of Science and an author of the *Cell* study. But they don't rival CRISPR yet, in part because the technology hasn't been made to work in mammalian cells.

In the 1980s, researchers studying a soil bacterium were puzzled to find many copies of short sequences of single-stranded DNA littering the cells. The mystery deep-

Published by AAAS

ened when they learned each bit of DNA was attached to an RNA with a complementary sequence. Eventually they realized an enzyme called reverse transcriptase had made that DNA from the attached RNA, and that all three molecules—RNA, DNA, and enzyme—form a complex.

Similar constructs, dubbed retrons for the reverse transcriptase, were found in many bacteria. "They really are a remarkable biological entity, yet nobody knew what they were for," says Ilya Finkelstein, a biophysicist at the University of Texas, Austin.

Sorek came upon an early hint of their function when he and his colleagues searched through 38,000 bacterial genomes for genes used to fight off phages. Such genes tend to be close to one another, and his team developed a computer program that searched for new defense systems next to the genes for the CRISPR and other known antiviral constructs. One stretch of DNA stood out to Weizmann graduate student Adi Millman because it included a gene for a reverse transcriptase flanked by stretches of DNA that didn't code for any known bacterial proteins. By chance, she came across a paper about retrons and realized that the mysterious sequences encoded one of their RNA components. "That was a nontrivial leap," Sorek says.

The team then noticed that the DNA encoding retron components often accompanied a protein-coding gene, and the protein varied from retron to retron. The team decided to test a hunch that the cluster of sequences represented a new phage defense. They went on to show that bacteria needed all three components— the DNA-RNA hybrid, reverse transcriptase, and the second protein—to defeat a variety of viruses.

For a retron called Ec48, Sorek and colleagues showed the associated protein delivers the coup de grâce by homing in on a bacterium's outer membrane and altering its permeability. The researchers concluded in the *Cell* report that the retron somehow "guards" another molecular complex called RecBCD that is the bacterium's first line of antiviral defense. Some phages deactivate the complex, which triggers the retron to unleash the membrane-destroying protein and kill the infected cell, the team found.

A second group has reached similar conclusions. Led by Athanasios Typas, a microbiologist at the European Molecular Biology Laboratory (EMBL), Heidelberg, the group realized that next to the genes coding for a retron in a *Salmonella* bacterium was a gene for a protein toxic to *Salmonella*. The team discovered the retron normally keeps the toxin under wraps, but activates it in the presence of phage proteins.

The two groups met at an EMBL meeting in the summer of 2019. "It was refreshing to see how complementary and converging our work was," Typas says. The teams simultaneously posted preprints on their work in June on bioRxiv. (The second group's paper is under review.)

Even before these discoveries, other researchers had taken advantage of retrons' then-mysterious features to devise new gene editors. CRISPR easily targets and binds to or cuts desired regions of the genome, but so far it isn't very adept at introducing new code in the target DNA. Retrons, combined with elements of CRISPR, seem able to do better thanks to their reverse transcriptases: They can manufacture lots of copies of a desired sequence, which can be spliced efficiently into the host genome. "Because CRISPR-based systems and retrons have different strengths, combining them is a highly promising strategy," Simon says.

In 2018, researchers in Hunter Fraser's Stanford University lab introduced a retron-derived base editor, dubbed CRISPEY (Cas9 retron precise parallel editing via homology). First, they made retrons whose RNA matched yeast genes, but with one base mutated. They combined them with CRISPR's "guide RNA," which homes in on the targeted DNA, and the Cas9 enzyme that acts as CRISPR's molecular scissors. Once Cas9 cut the DNA, the cell's DNA repair mechanisms replaced the yeast gene with the DNA generated by the retron's reverse transcriptase.

CRISPEY enabled Stanford graduate student Shi-An Anderson Chen and his colleagues to efficiently make tens of thousands of yeast mutants, each different by just one base. That let them determine, for example, which bases were essential for yeast to thrive in glucose. "CRISPEY is very cool and extremely powerful," says Harmit Malik, an evolutionary biologist at the Fred Hutchinson Cancer Research Center. This year, two other teams—led by geneticist George Church at Harvard University and Massachusetts Institute of Technology synthetic biologist Timothy Lu—described similar feats in bacteria in bioRxiv preprints.

Researchers are excited about retrons, but caution they have a lot more to learn about how to turn these bacterial swords into plowshares. "It could be that retrons will be as revolutionary as CRISPR has been," Simon says. "But until we understand more about the natural biology and synthetic behavior of retrons, it is difficult to say." ■

How bacteria fight back

Genetic elements called retrons defend bacteria against viruses called bacteriophages (bottom). Retrons work by sensing viral invasion, then triggering the infected cell to self-destruct (graphic).

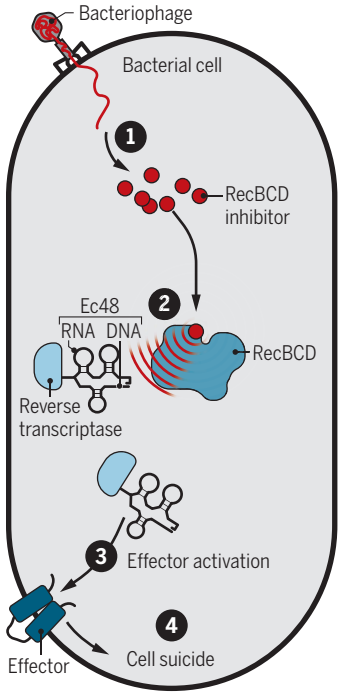

1 Many invading bacteriophages carry genes for proteins that inhibit RecBCD, the bacterium's first line of defense against viruses.

2 The Ec48 retron guards RecBCD. When it senses this defense system has been disarmed, the retron mounts a backup response.

3 Each retron is associated with a protein—called an effector—that can be toxic to the cell. When backup is needed, the retron activates this toxin.

4 Ec48's activated effector digs into and disrupts the cell membrane, so the cell dies before the virus has a chance to replicate.

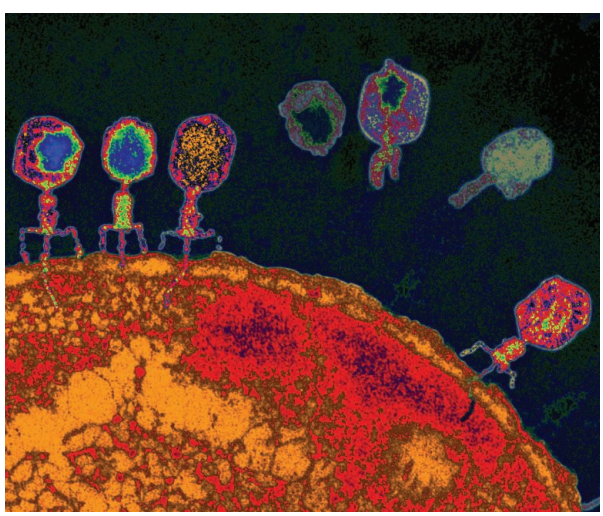

CREDITS: (GRAPHIC) V. ALTOUNIAN/*SCIENCE*; (IMAGE) EYE OF SCIENCE/SCIENCE SOURCE

Published by AAAS

Chang'e-5 is targeting Mons Rümker, a volcanic mound that may contain 1.3-billion-year-old lava.

PHOTO: NASA

PLANETARY SCIENCE

China set to bring back rocks from the Moon

Chang'e-5's lunar samples could firm up shaky crater count dating system for the rocky planets

By **Dennis Normile**

On Earth, deep time is an open book. By measuring trace radioactive compounds in rocks that decay with metronomic regularity, dating experts have learned when oceans opened, volcanoes erupted, and mass extinctions struck. But the story is muddled elsewhere in the Solar System because records are sparse. Scientists estimate ages on the Moon and the rocky planets from the number of craters that pock their surfaces. They have fixed dates from just nine places, all on the Moon: the six Apollo and three Soviet Luna sites from which samples were returned to laboratories on Earth.

China's Chang'e-5 mission, set to launch on 24 November, aims to make it 10, by returning the first Moon rocks since the last Luna mission in 1976. Getting a firm date from another location will improve the shaky crater counting scheme, says Kentaro Terada, a cosmochemist at Osaka University. It will also sharpen the picture of the Moon's history. A fresh sample date "is the most important and exciting new finding [that will come] from the Chang'e-5 samples," Terada says. Getting it will require a tour-de-force, round-trip space flight that has not been attempted for more than 40 years.

Chang'e-5's target is Mons Rümker, a 70-kilometer-wide volcanic mound on the Moon's near side, which may have erupted as recently as about 1.3 billion years ago. It is "the youngest mare basalt on the Moon," says Xiao Long, a planetary geoscientist at the China University of Geosciences, referring to the dark lava also seen in the Moon's maria, or seas. Brett Denevi, a planetary geologist at Johns Hopkins University's Applied Physics Laboratory and science chair of a NASA lunar analysis group, says China has picked a spot where it can have a big scientific impact. "Understanding the age of those samples and all of the Solar System–wide implications that flow from that result will be a big leap forward for planetary science," she says.

The crater counting method for determining age relies on the notion that surfaces scarred with fewer craters are younger than those that have accumulated more. Regions dated with Apollo and Luna samples have helped calibrate the method. But except for one young outlier, all of those dates cluster between 3.2 billion and 3.9 billion years, leaving the method unanchored, and highly uncertain, for surfaces younger than 3 billion years old, Terada says. "Chang'e-5 samples will provide another data point," he says.

Getting a firm date for Mons Rümker will also shed light on how lunar volcanism changed over time. Evidence suggests numerous eruptions in the first billion years of the Moon's existence blanketed the surface with volcanic basalts, forming the dark maria, before tapering off about 3 billion years ago. If Mons Rümker material proves to be just 1.3 billion years old, it will raise questions about how the interior of a small planetary body remained hot enough to erupt so long after formation, says Romain Tartese, a planetary scientist at the University of Manchester.

Retrieving the samples will require a complex deep-space ballet. After launch from the Wenchang launch center in southern China, Chang'e-5 will arrive at the Moon about 3 days later, where an orbiter will release a lander. Over the course of 14 days, the lander's robotic arm will scoop up surface samples and a drill will retrieve cores down to 2 meters. Scientists are hoping for 2 kilograms of material. (NASA's Apollo program brought back more than 380 kilograms; three Soviet robotic Luna missions returned 301 grams.) An ascent vehicle will ferry the samples to the orbiter, where they will be packed into a re-entry capsule for return to Earth and a touchdown in the grasslands of Inner Mongolia. Xiao says international investigators will have access to the samples, but U.S. scientists may not because of limits on cooperation with China set by the U.S. Congress.

Chang'e-5 is the latest in a set of increasingly ambitious Moon missions from the China National Space Administration, all named after Chang'e, a Chinese Moon goddess. A pair of orbiters, launched in 2007 and 2010, focused on mapping and remote observations. The lander-rover Chang'e-3 mission, in 2013, carried the first ground-penetrating radar to the lunar surface. In 2019, Chang'e-4, another lander-rover, was the first spacecraft to soft-land on the far side of the Moon. Three more Chang'e missions and a robotic scientific research station are planned by 2035.

Results from Chang'e-4, still trundling along after having traveled nearly 600 meters, are raising questions for later missions. The craft landed in the South Pole–Aitken basin, the Moon's largest, deepest, and oldest impact crater, at perhaps 4 billion years. Scientists have calculated that the impacting body likely burrowed 70 kilometers into the Moon and churned material from the mantle up to the surface. In a study published in 2019 in *Nature*, one group of Chinese scientists said the rover's instruments had detected mantle minerals, but other groups, including Xiao's, have challenged that interpretation. Patrick Pinet, a planetary geophysicist at France's Astrophysics and Planetology Research Institute, says researchers are debating why such an enormous impact apparently did not exhume mantle material—or whether the mantle composition is somehow unexpected.

Zou Yongliao, a geochemist at the Chinese Academy of Sciences's National Space Science Center, says China is making the South Pole the focus of its near-term lunar plans. And although the target site has not been revealed for Chang'e-6, another sample return mission, planetary scientists are rooting for South Pole–Aitken. A basin sample would provide clues to the mantle puzzle. It would also anchor the older end of the crater-counting curve, says Carolyn van der Bogert, a planetary geologist at the University of Münster, and "illuminate the early history of the Moon." ■

Published by AAAS

OCEANOGRAPHY

Seas are rising faster than ever

A new satellite will monitor coastal hot spots, where currents amplify global trends

By **Paul Voosen**

Ask climate scientists how fast the world's oceans are creeping upward, and many will say 3.2 millimeters per year—a figure enshrined in the last Intergovernmental Panel on Climate Change report, from 2014. But the number, based on satellite measurements taken since the early 1990s, is a long-term average. In fact, the global rate varied so much over that period that it was hard to say whether it was holding steady or accelerating.

It was accelerating, big time. Faster melting of Greenland's ice has pushed the rate to 4.8 millimeters per year, according to a 10-year average compiled for *Science* by Benjamin Hamlington, an ocean scientist at NASA's Jet Propulsion Laboratory (JPL) and head of the agency's sea level change team. "The [Greenland] mass loss has clearly kicked into higher gear," agrees Felix Landerer, a JPL sea level scientist. With the help of new data, new models of vertical land motion, and—this month—a new radar satellite, oceanographers are sharpening their picture of how fast, and where, the seas are gobbling up the land.

Hamlington and colleagues first reported signs of the speedup in 2018 in the *Proceedings of the National Academy of Sciences*. Since then, they and others have become more confident about the trends. In a 2019 study in *Nature Climate Change*, a group led by Sönke Dangendorf, a physical oceanographer at Old Dominion University, used tide gauge readings that predate satellite records to show seas have risen 20 centimeters since 1900. The team's data show that, after a period of global dam building in the 1950s that held back surface water and slowed sea level rise, it began to accelerate in the late 1960s—not the late 1980s, as many climate scientists assumed, Dangendorf says. "That was surprising," because the main drivers of sea level rise—the thermal expansion of ocean water from global warming, together with melting glaciers and ice sheets—were thought to have kicked in later.

Oceanographers are about to get a sharper view of the trends thanks to the Sentinel-6 Michael Freilich satellite, which NASA and the European Space Agency plan to launch on 21 November from Vandenberg Air Force Base in California. Named after the former head of NASA's earth science program, who died this year, the satellite will work much like its predecessors, using pulses of reflected radar to measure the ocean's height. But its higher resolution measurements will allow it to gauge ocean height within 300 meters of the coastline, far closer than before.

The coasts are where sea level rise hits home—and where large local variations can mask the global average. In work published last month in *Scientific Data*, Anny Cazenave, an ocean geophysicist at the International Space Science Institute, and colleagues reanalyzed the satellite record and showed sea level rise at 20% of the coastal sites they surveyed across Europe, Asia, and Africa was significantly different from that of the open ocean. "We have to explain that," she says.

Some of the variation reflects the vertical motion of the land itself, due to the slow bobbing of continental plates that "float" on a viscous mantle. Coastal ocean currents, freshwater from nearby rivers, and weather patterns can also inject variability by causing water to pile up or retreat from the continents, Cazenave says.

But Dangendorf believes currents in the open ocean drive much of this variable sloshing, routing rising water from the open ocean—where there is more water to warm and expand—to the coastlines. One reconstruction of Norwegian sea levels from 1960 to 2015, for example, showed shifting currents were the best explanation for mysterious, and frequent, 20-millimeter swings in height. Dangendorf is now tracing sea level rise in nine coastal regions to their ocean sources, and has found them to be typically 500 to 1000 kilometers away; much of the sea level rise in the northern half of the U.S. east coast, for example, comes from waters swept out of the Labrador Sea.

The trends are worrisome. Aimée Slangen, a climate scientist at the Royal Netherlands Institute for Sea Research, and colleagues are integrating recent projections from climate models to predict when sea levels will rise 25 centimeters above 2000 levels, a point when 100-year floods on some coastlines could be a near annual occurrence. In unpublished work, Slangen finds that the threshold will be reached sometime between 2040 and 2060. Efforts to slow climate change won't do much to postpone it given the inertia of ocean warming and ice melt, though they could forestall much greater increases later in the century. And that near-term certainty, though dire, is "quite good for decision-making," Slangen says.

Dangendorf, who joined Old Dominion late last year, is getting a front row seat to the action. The university is in Norfolk, Virginia, a part of the U.S. coast where the crust is sinking about as fast as the oceans are rising. "I watch coastal flooding every week," he says. "I see it from my balcony." ■

High water marks

Sea level rise has been accelerating since the late 1960s. Fueled by meltwater from Greenland, seas are now rising 4.8 millimeters per year and show few signs of slowing down.

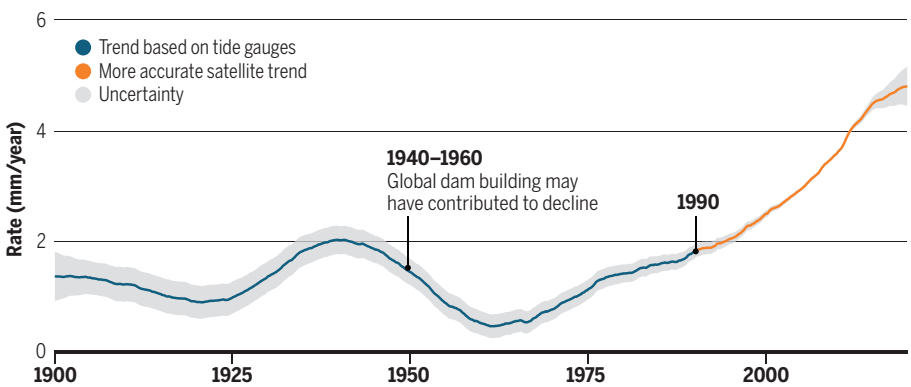

CREDITS: (GRAPHIC) SÖNKE DANGENDORF ADAPTED BY N. DESAI/*SCIENCE*; (DATA) DANGENDORF *ET AL*., *NATURE CLIMATE CHANGE*, 9, 705 (2019); LEGEAIS *ET AL*., *EARTH SYSTEM SCIENCE DATA*, 10, 281 (2018); (EDITED)

Published by AAAS

TOMORROW'S CATCH

Genomic technologies promise dramatic gains for aquaculture by accelerating the breeding of better strains

By **Erik Stokstad**

Two years ago, off the coast of Norway, the blue-hulled *Ro Fjell* pulled alongside Ocean Farm 1, a steel-netted pen the size of a city block. Attaching a heavy vacuum hose to the pen, the ship's crew began to pump brawny adult salmon out of the water and into a tank below deck. Later, they offloaded the fish at a shore-based processing facility owned by SalMar, a major salmon aquaculture company.

The 2018 harvest marked the debut of the world's largest offshore fish pen, 110 meters wide. SalMar's landmark facility, which dwarfs the typical pens kept in calmer, coastal waters, can hold 1.5 million fish—with 22,000 sensors monitoring their environment and behavior—that are ultimately shipped all over the world. The fish from Ocean Farm 1 were 10% larger than average, thanks to stable, favorable temperatures. And the deep water and strong currents meant they were free of parasitic sea lice.

Just a half-century ago, the trade in Atlantic salmon was a largely regional affair that relied solely on fish caught in the wild. Now, salmon farming has become a global business that generates $18 billion in annual sales. Breeding has been key to the aquaculture boom. Ocean Farm 1's silvery inhabitants grow roughly twice as fast as their wild ancestors and have been bred for disease resistance and other traits that make them well suited for farm life. Those improvements in salmon are just a start: Advances in genomics are poised to dramatically reshape aquaculture by helping improve a multitude of species and traits.

Genetic engineering has been slow to take hold in aquaculture; only one genetically modified species, a transgenic salmon, has been commercialized. But companies and research institutions are bolstering traditional breeding with genomic insights and tools such as gene chips, which speed the identification of fish and shellfish carrying desired traits. Top targets include increasing growth rates and resistance to disease and parasites. Breeders are also improving the hardiness of some species, which could help farmers adapt to a shifting climate. And many hope to enhance traits that please consumers, by breeding fish for higher quality fillets, eye-catching colors, or increased levels of nutrients. "There is a paradigm shift in taking up new technologies that can more effectively improve complex traits," says Morten Rye, director of genetics at Benchmark Genetics, an aquaculture breeding company.

PHOTO: HENDRIX GENETICS

Published by AAAS

At research pens in Chile (left) researchers develop strains of farmed Atlantic salmon (right) that grow faster and stay healthier.

PHOTO: HENDRIX GENETICS

Aquaculture breeders can tap a rich trove of genetic material; most fish and shellfish have seen little systematic genetic improvement for farming, compared with the selective breeding that chickens, cattle, and other domesticated animals have undergone. "There's a huge amount of genetic potential out there in aquaculture species that's yet to be realized," says geneticist Ross Houston of the Roslin Institute.

Amid the enthusiasm about aquaculture's future, however, there are concerns. It's not clear, for example, whether consumers will accept fish and shellfish that have been altered using technologies that rewrite genes or move them between species. And some observers worry genomic breeding efforts are neglecting species important to feeding people in the developing world. Still, expectations are high. "The technology is amazing, it's advancing very quickly, the costs are coming down," says Ximing Guo, a geneticist at Rutgers University, New Brunswick. "Everybody in the field is excited."

FISH FARMING may not have roots as old as agriculture, but it dates back millennia. By about 3500 years ago, Egyptians were raising gilt-head sea bream in a large lagoon. The Romans cultivated oysters. And carp have been grown and selectively bred in China for thousands of years. Few aquaculture species, however, saw systematic, scientific improvement until the 20th century.

One species that has received ample attention from breeders is Atlantic salmon, which commands relatively high prices. Farming began in the late 1960s, in Norway. Within 10 years, breeding had helped boost growth rates and harvest weight. Each new generation of fish—it takes salmon 3 to 4 years to mature—grows 10% to 15% faster than its forebears. "My colleagues in poultry can only dream of these kinds of percentages," says Robbert Blonk, director of aquaculture R&D at Hendrix Genetics, an animal breeding firm. During the 1990s, breeders also began to select for improved disease resistance, fillet quality, delayed sexual maturation (which boosts yields), and other traits.

Another success story involves tilapia, a large group of freshwater species that doesn't typically bring high prices but plays a key role in the developing world. An international research center in Malaysia, now known as WorldFish, began a breeding program in the 1980s that quickly doubled the growth rate of one commonly raised species, Nile tilapia. Breeders also improved its disease resistance, a task that continues because of the emergence of new pathogens, such as tilapia lake virus (*Science*, 6 March, p. 1064).

Genetically improved farmed tilapia "was a revolution in terms of tilapia production," says Alexandre Hilsdorf, a fish geneticist at the University of Mogi das Cruzes in Brazil. China, a global leader in aquaculture production, has capitalized on the strain, building the world's largest tilapia hatchery. It raises billions of young fish annually.

Now, aquaculture supplies nearly half of the fish and shellfish eaten worldwide (see chart, p. 904), and production has been growing by nearly 4.5% annually over the past decade—faster than most sectors of the farmed food sector. That expansion has come with some collateral damage, including pollution from farm waste, heavy catches of wild fish to feed to penned salmon and other species, and the destruction of coastal wetlands to build shrimp ponds. Nevertheless, aquaculture is now poised for further acceleration, thanks in large part to genomics.

Breeders are most excited about a technique called genomic selection. To grasp why, it helps to understand how breeders normally improve aquaculture species. They start by crossing two parents and then, out of hundreds or thousands of their offspring, select individuals to test for desired traits. Advanced programs make hundreds of crosses in each generation and choose from the best performing families for breeding. But some tests mean the animal can't later be used for breeding; measuring fillet quality is lethal, for instance, and screening for disease resistance requires quarantining the infected individual. As a result, when researchers identify a promising animal, they must pick a sibling to use for breeding—and hope that it performs just as well.

With genomic selection, researchers can identify siblings with high-performance traits based on genetic markers. All they need is a small tissue sample—such a clipping from a fin—that can be pureed and analyzed. DNA arrays, which detect base-pair changes called single nucleotide polymorphisms (SNPs), allow breeders to thoroughly evaluate many siblings for multiple traits. If the pattern of SNPs indicates that an individual carries optimal alleles, it can be selected for further breeding even if it hasn't been tested. Genomic analyses also allow breeders to minimize inbreeding.

Cattle breeders pioneered genomic selection. Salmon breeders adopted it a few years ago, followed by those working with shrimp and tilapia. As a rough average, the technique increases selection accuracy and the amount of genetic improvement by about 25%, Houston says. It and other tools are helping researchers pursue goals such as:

FASTER GROWTH

This trait improves the bottom line, allowing growers to produce more frequent and

Published by AAAS

bigger hauls. Growth is highly heritable and easy to measure, so traditional breeding works well. But breeders have other tactics for boosting growth, including providing farmers with fish of a single sex. Male tilapia, for example, can grow significantly faster than females. Another strategy is to hybridize species. The dominant farmed catfish in the United States, a hybrid of a female channel catfish and a male blue catfish, grows faster and is hardier.

Inducing sterility stimulates growth, too, and has helped raise yields in shellfish, particularly oysters. In the 1990s, Guo and Standish Allen, now at the Virginia Institute of Marine Science, figured out a new way to create triploid oysters, which are infertile because they have an extra copy of each chromosome. These oysters don't devote much energy to reproduction, so they reach harvest size sooner, reducing exposure to disease. (When oysters reproduce, more than half their body consists of sperm or eggs, which no one wants to eat.)

Looking ahead, researchers are exploring gene transfer or gene editing to further enhance gains. And one U.S. company, AquaBounty, is just beginning to sell the world's first transgenic food animal, an Atlantic salmon, that it claims is 70% more productive than standard farmed salmon. But the fish is controversial and has faced consumer resistance and regulatory hurdles.

HEALTHIER FISH

Disease is often the biggest worry and expense for aquaculture operations. In shrimp, outbreaks can slash overall yield by up to 40% annually and can wipe out entire operations. Vaccines can prevent some diseases in fish, but not invertebrates, because their adaptive immune systems are less developed. So, for all species, resistant strains are highly desirable.

To improve disease resistance, researchers need a rigorous way to test animals. Thanks to a collaboration with fish pathologists at the U.S. Department of Agriculture (USDA), Benchmark Genetics was able to screen tilapia for susceptibility to two major bacterial diseases by delivering a precise dose of the pathogen and then measuring the response. They identified genetic markers correlated with infection and used genomic selection to help develop a more resistant strain. USDA scientists have also worked with Hendrix Genetics to increase the survival of trout exposed to a different bacterial pathogen from 30% to 80% in just three generations.

Perhaps the most celebrated success has been in salmon. After researchers discovered a genetic marker for resistance to infectious pancreatic necrosis, companies quickly bred strains that can survive this deadly disease. Oyster breeders, meanwhile, have had success in developing strains resistant to a strain of herpes that devastated the industry in France, Australia, and New Zealand.

PARASITE-RESISTANT SALMON

A big problem for Atlantic salmon growers is the sea louse. The tiny parasite clings to the salmon's skin, inflicting wounds that damage or kill fish and make their flesh worthless. Between fish losses and the expense of controlling the parasites, lice cost growers more than $500 million a year in Norway alone. Lice are attracted to fish pens and can jump to wild salmon that pass by.

For years farmers have relied on pesticides to fight lice, but the parasite has become resistant to many chemicals. Other techniques, such as pumping salmon into heated water, which causes the lice to drop off, can stress the fish.

Researchers have found that some Atlantic salmon are better than others at resisting lice, and breeders have been trying to improve this trait. So far, they've had modest success. Better understanding why several species of Pacific salmon are immune to certain lice could lead to progress. Scientists are exploring whether sea lice are attracted to certain chemicals released by Atlantic salmon; if so, it's possible these could be modified with gene editing.

STERILE STOCK

No sex on the farm. That's a goal with many aquaculture species, because reproduction diverts energy from growth. Moreover, fertile fish that escape from aquaculture operations can cause problems for wild relatives. When wild fish breed with their domesticated cousins, for instance, the offspring are often less successful at reproducing.

Salmon can be sterilized by making them triploid, typically by pressurizing newly fertilized embryos in a steel tank when the chromosomes are replicating. But this can have side effects, such as greater susceptibility to disease. Anna Wargelius, a molecular physiologist at Norway's Institute of Marine Research, and colleagues have instead

A rising tide

Aquaculture is rivaling catches from wild fisheries and is projected to increase. Much of the growth comes from freshwater fish in Asia, such as grass carp, yet most research has focused on Atlantic salmon and other high-value species. Genomic technology is now spreading to shrimp and tilapia.

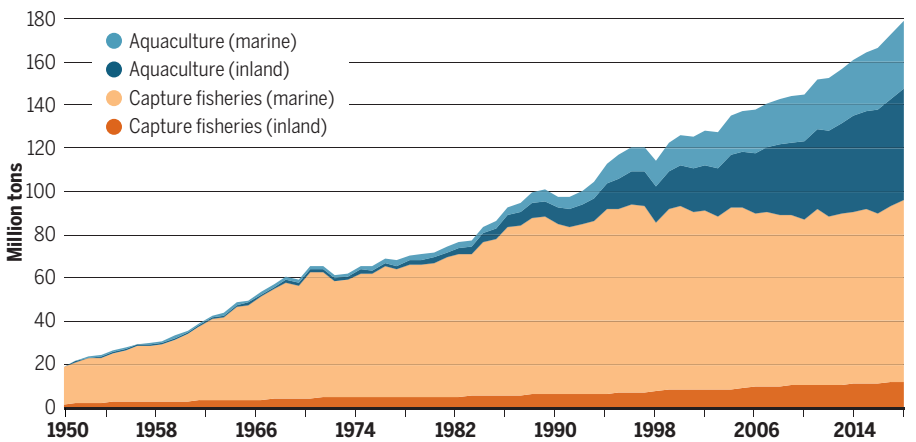

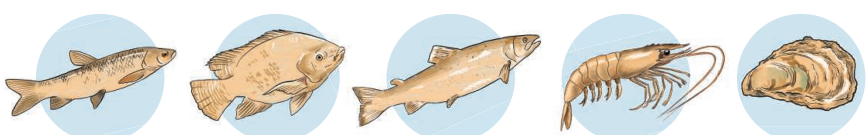

	Grass carp	Nile tilapia	Atlantic salmon	Whiteleg shrimp	Pacific cupped oyster
Value ($ billions)	12.6	7.6	16.7	26.7	1.2
Harvest (thousand tons, annually)	5704	4525	2436	4966	644
***First research on breeding**	2010	1989	1971	1995	1984

*First scientific report of breeding for a specific trait

CREDITS: (GRAPHIC) N. DESAI/*SCIENCE*; (DATA, TOP TO BOTTOM) FOOD AND AGRICULTURE ORGANIZATION OF HE UNITED NATIONS; HOUSTON *ET AL.*, *NATURE REVIEWS GENETICS* **21**, 389 (2020)

Published by AAAS

The fecundity of most aquatic species, like this trout (left), helps breeding efforts. Salmon eggs, 0.7 millimeters wide, are robust and easy for molecular biologists to work with.

altered the genes of Atlantic salmon to make them sterile, using the genome editor CRISPR to knock out a gene called *deadend*. In 2016, they showed that these fish, though healthy, lack germ cells and don't sexually mature. Now, they're working on developing fertile broodstock that produce these sterile offspring for hatcheries. Embryos with the knocked-out genes should develop into fertile adults if injected with messenger RNA, according to a paper the group published last month in *Scientific Reports*. When these fish mature later in December, they will try to breed them. "It looks very promising," Wargelius says.

Another approach would not involve genetic modifications. Fish reproductive physiologists Yonathan Zohar and Ten-Tsao Wong of the University of Maryland, Baltimore County, are using small molecule drugs to disrupt early reproductive development so that fish mature without sperm or eggs.

BONE-FREE FILLETS

Cooks and diners hate bones. Nearly half of the top species in aquaculture are species of carp or their relatives, which are notorious for the small bones that pack their flesh. These bones can't be easily removed during processing, so "you can't just get a nice, clean fillet," says Benjamin Reading, a reproductive physiologist at North Carolina State University.

Researchers are studying the biology of these fillet bones to see whether they might one day be removed through breeding or genetic engineering. A few years ago, Hilsdorf heard that a Brazilian hatchery had discovered mutant brood stock of a giant Amazonian fish, the widely farmed tambaqui, that lacked these fillet bones. After trying and failing to breed a boneless strain, he's studying tissue samples from the mutants for clues to their genetics.

Geneticist Ze-Xia Gao of Huazhong Agricultural University is focusing on blunt snout bream, a carp that is farmed in China. Guided by five genetic markers, she and colleagues are breeding the bream to have few fillet bones. It could take 8 to 10 years to achieve, she says. They have also had some success with gene editing—they've identified and knocked out two genes that control the presence of fillet bones—and they plan to try the approach in other carp species. "I think it will be feasible," Gao says.

NEW ITEMS FOR THE MENU

Aquaculture projects worldwide are hustling to domesticate new species—a kind of gold rush rare in terrestrial farming. In New Zealand, researchers are domesticating native species because they are already adapted to local conditions. The New Zealand Institute for Plant and Food Research began to breed the Australasian snapper in 2004. Early work concentrated on simply getting the fish to survive and reproduce in a tank. One decade later, researchers started to breed for improved growth, and they've since increased juvenile growth rates by 20% to 40%.

Genomic techniques have proved critical. Snapper are mass spawners, so it was hard for breeders to identify the parents of promising offspring, which is crucial for optimizing selection and avoiding inbreeding. DNA screening solved that problem, because the markers reveal ancestry. The institute is also breeding another local fish, the silver trevally, aiming for a strain that will reproduce in captivity without hormone implants. "It's a long-term effort to breed a wild species to make it suitable for aquaculture," says Maren Wellenreuther, an evolutionary geneticist at the New Zealand institute and the University of Auckland.

THESE BREEDING EFFORTS require money. Despite the growth of aquaculture, the field's research funding lags the amounts invested in livestock, although some governments are boosting investments.

Looking globally, geneticist Dennis Hedgecock of Pacific Hybreed, a small U.S. company that is developing hybrid oysters, sees a "huge disparity" between breeding investment in developed countries—which produce a fraction of total harvests but have the biggest research budgets—and the rest of the world. Simply applying classical breeding techniques could rapidly improve production, especially in the developing world, he says. Yet the hundreds of species now farmed could overwhelm breeding programs, especially those aimed at enhancing disease resistance, Hedgecock adds. "The growth and the production is outstripping the scientific capability of dealing with the diseases," he says, adding that a focus on fewer species would be beneficial.

For genomics to help, experts say costs must continue to come down. One promising development in SNP arrays, they note, is a technique called imputation, in which cheaper arrays that search for fewer genetic changes are combined with a handful of higher cost chips that probe the genome in more detail. Such developments suggest genomic technology is "at a pivot point where you're going to see it used broadly in aquaculture," says John Buchanan, president of the Center for Aquaculture Technologies, a contract research organization.

Many companies are already planning for larger harvests. SalMar will decide next year whether it will order a companion to Ocean Farm 1. It has already drawn up plans for a successor that can operate in the open ocean and would be more than twice the size, big enough to hold 3 million to 5 million salmon at a time. ■

PHOTOS: HENDRIX GENETICS

Published by AAAS

DRUG DISCOVERY

Drugs from bugs in creatures of the sea

A bacterium from the sea squirt microbiome makes a natural product with antifungal activity

By **Leah E. Cowen**

Infectious diseases can pose a devastating threat to human health around the globe. As the risk rises, the world is running out of effective drugs to treat infections caused by deadly microbes. Many existing drugs have been rendered obsolete by the rapid emergence and spread of drug resistance. Thus, there is a dire need for new medicines with which to treat infectious disease. This is especially pressing for fungal killers. There are only three major classes of antifungal drugs, and resistance is rampant, leading to the death of ~1.5 million people each year (*1*, *2*). Success in developing effective new treatments depends on creative approaches, including those that harness the chemical diversity in nature, tuned over millions of years of evolution. In this spirit, on page 974 of this issue, Zhang *et al.* (*3*) embarked on a mission to discover new antifungals produced by bacteria that inhabit marine animals.

Natural products have saved countless human lives. The majority of drugs to treat bacterial infections arose from studies of molecules produced by microbes, as seen with the discovery of the fungal product penicillin. This antibiotic helped to avert a devastating death toll from bacterial infection during the Second World War (*4*).

Microbial products underpin not only the treatment of bacterial infections but also of infections caused by fungi and protozoan parasites, as well as medicines that inhibit transplant rejection, reduce the risk of heart disease, and cure cancers. There is fascinating ecological context for the elaboration of diverse molecules by microbes, with many producers thriving in soil environments or as members of the microbiota of plants or animals (*5*). These molecules might be produced for communication or defense in competitive environments and also might serve in a symbiotic context to benefit the host of the natural product-producing microbe by modulating developmental transitions, transcriptional programs, environmental resilience, or vulnerability to infection (*6*). Unlike synthetic molecules, natural products are typically selected over evolutionary time to have properties that favor the ability to penetrate cells and engage cellular targets with high efficiency and selectivity.

Zhang *et al.* were motivated by a renaissance in natural product discovery, which was enabled by new sources of molecules and screening strategies. Exploring the chemical diversity produced by microbial inhabitants

Department of Molecular Genetics, University of Toronto, Toronto, ON M5G 1M1, Canada. Email: leah.cowen@utoronto.ca

PHOTO: JOSE B. RUIZ/MINDEN PICTURES

Published by AAAS

The sea squirt, a marine invertebrate, houses a treasure trove of natural products made by its microbiome.

of the sea squirt revealed a bacterium that produces turbinmicin, a molecule that effectively kills drug-resistant fungi by blocking vesicle trafficking, a core cellular process.

Interrogation of a chemically diverse library of small molecules is fundamental to any effort designed to discover new, bioactive natural products. To achieve this goal, Zhang *et al.* leveraged liquid chromatography–mass spectrometry profiling of 1482 strains of actinobacteria from marine invertebrates (*3*). One strain was prioritized on the basis of its chemical diversity, as deduced with metabolomic analysis; its array of fermentation products was then fractionated by using a two-step chromatographic approach. Turbinmicin was identified and prioritized on the basis of its antifungal potency and structural characteristics. Purified turbinmicin demonstrated broad-spectrum activity against diverse clinical isolates of human fungal pathogens, including those resistant to each of the three established antifungal classes. Judging from this activity profile, turbinmicin likely kills fungi through a mechanism that is distinct from azoles (inhibition of the biosynthesis of the membrane sterol ergosterol), polyenes (ergosterol depletion), or echinocandins (inhibition of the biosynthesis of the cell wall 1,3-β-D-glucan). Turbinmicin reduced fungal burden in mouse models of drug-resistant fungal infection caused by *Candida auris* and *Aspergillus fumigatus* and was well tolerated in mice. The benefit of turbinmicin production to the *Micromonospora* sp. producer or to the ascidian host remains unknown because this marine environment is not an established reservoir for these human fungal pathogens.

With 20 years having elapsed since the last antifungal class was approved for treatment of invasive infections, scientists are encouraged by recent progress with the clinical development of multiple new drugs (*7*, *8*). Improvements have been made for existing antifungal classes, as exemplified by rezafungin, a more stable next-generation echinocandin that enables intravenous administration once a week rather than every day. Ibrexafungerp exemplifies a different chemical class of compounds that engages with an established drug target by binding to an overlapping but distinct region of the echinocandin target. Compounds with new targets are also advancing rapidly in clinical development, as with olorofim, which inhibits the synthesis of DNA building blocks, and fosmanogepix, which inhibits localization of key cell wall-anchored proteins. Each of the established and emerging antifungal drugs targets essential proteins or components of the fungal cell, as is likely the case with turbinmicin. A central challenge in the development of effective antifungals is ensuring sufficient fungal selectivity to avoid deleterious effects to the human host, which shares many conserved essential cellular processes.

Leveraging a genetically tractable yeast model system, Zhang *et al.* profiled a library of mutants with reduced dosages of individual essential genes and deletion of specific nonessential genes (*9*–*11*). A reduced dosage of the essential vesicle-mediated trafficking gene *SEC14* conferred profound hypersensitivity to turbinmicin, as did deletion of nonessential regulators of this process. Consistent with the hypothesis that turbinmicin blocks vesicle-mediated trafficking by inhibiting Sec14, the compound impaired localization of a cargo protein to the plasma membrane. Turbinmicin could be docked into a specific Sec14 binding pocket, which is also consistent with Sec14 being a proximal target of the natural product. Further analysis of the binding mode, biochemical consequences and fungal selectivity of target engagement, and pharmacological properties will enable future development efforts.

There is also great opportunity in developing drug combinations that enhance potency and evade resistance, as well as in exploring the therapeutic potential of compounds that inhibit microbial virulence (*12*). Exploring the complex chemical communication that transpires between kingdoms in diverse environments is poised to catalyze the discovery and development of resistance-evasive therapeutic strategies for life-threatening infectious diseases. ■

REFERENCES AND NOTES

1. M. C. Fisher *et al.*, *Science* **360**, 739 (2018).
2. G. D. Brown *et al.*, *Sci. Transl. Med.* **4**, 165rv13 (2012).
3. F. Zhang *et al.*, *Science* **370**, 974 (2020).
4. G. D. Wright, *Nat. Prod. Rep.* **34**, 694 (2017).
5. J. O'Brien, G. D. Wright, *Curr. Opin. Biotechnol.* **22**, 552 (2011).
6. J. Davies, *J. Antibiot. (Tokyo)* **66**, 361 (2013).
7. K. Kupferschmidt, *Science* 10.1126/science.aaz9475 (2019).
8. J. R. Perfect, *Nat. Rev. Drug Discov.* **16**, 603 (2017).
9. J. S. Piotrowski *et al.*, *Nat. Chem. Biol.* **13**, 982 (2017).
10. T. Roemer, C. Boone, *Nat. Chem. Biol.* **9**, 222 (2013).
11. A. Xue, N. Robbins, L. E. Cowen, *Ann. N. Y. Acad. Sci.* 10.1111/nyas.14484 (2020).
12. N. Robbins, G. D. Wright, L. E. Cowen, *Microbiol. Spectr.* 10.1128/microbiolspec.funk-0002-2016 (2016).

ACKNOWLEDGMENTS

L.E.C. is supported by the Canadian Institutes of Health Research Foundation Grant (FDN-154288) and U.S. National Institutes of Health National Institute of Allergy and Infectious Diseases R01 grants (1R01AI127375-01, 1R01AI120958-01A1) and R21 grant 1R21AI141080-01. L.E.C. is a Canada Research Chair in Microbial Genomics and Infectious Disease and codirector of the Canadian Institute for Advanced Research Fungal Kingdom: Threats and Opportunities program. L.E.C. is a cofounder and shareholder in Bright Angel Therapeutics and a consultant for Boragen.

10.1126/science.abf1675

IMMUNOLOGY

Transferring allergies in the womb

Maternal antibodies prime fetal mast cells in utero for subsequent postnatal allergy responses

By **Marc E. Rothenberg**

Allergic diseases, which affect 10 to 30% of the global population, have a high degree of heritability contributed by a combination of parental factors (*1*). In addition to genetics, such parental factors include the amount of maternal immunoglobulin E (IgE), the antibody type that binds to allergens, which directly correlates with the risk of allergy in offspring (*2*). On page 941 of this issue, Msallam *et al.* (*3*) delve into the relationship of maternal IgE and fetal mast cells in mice and humans, demonstrating that IgE crosses the placenta and binds to fetal mast cells, and relate this to the subsequent development of allergic responses in offspring.

Mast cells reside in various tissues near mucosal interfaces, blood vessels, and nerve fibers. They serve as cellular guards, sensing a variety of chemical, pathogenic, and biophysical triggers, and subsequently release pleiotropic molecules that contribute to diverse responses ranging from protective immunity to exacerbation of inflammation. Mast cells are traditionally considered the primary cells responsible for allergies because they express the high-affinity IgE receptor FcεR1. Upon cross-linking with IgE, FcεR1 induces cellular activation, including degranulation and release of preformed and de novo immune mediators such as histamine, leukotrienes, proteases, and cytokines. The formation of IgE and its specificity for distinct antigens (allergens) is an essential pathogenic process in diseases such as atopic eczema, food allergies, asthma, and hay fever.

During embryonic development, mouse mast cells and macrophages develop from the yolk sac at an earlier stage than other

Cincinnati Children's Hospital Medical Center and University of Cincinnati, Cincinnati, OH, USA.
Email: rothenberg@cchmc.org

Published by AAAS

leukocytes (*4*). Why mast cells are present so early in development may be related to their role in organ development, but their functional competence has been unclear. Msallam *et al.* show that mouse fetal mast cells are functional and that mast cells, particularly those readily detectable and abundant in fetal skin, become loaded with surface-bound maternal IgE. These IgE$^+$ mast cells could respond to and degranulate upon exposure to an experimental allergen recognized by the IgE intravenously given to the mother, and this occurred even before birth. Furthermore, pups born to allergic mothers developed allergic responses, including airway hyperreactivity, upon their first postnatal exposure to the experimental allergen originally given to the mother (see the figure).

Fetal allergic responses

Maternal immunoglobulin E (IgE) is transported across the placenta by the neonatal Fc receptor (FcRN). Fetal mast cells bear the IgE receptor (FcεR1) and bind maternal IgE. In mice, these IgE-loaded fetal mast cells are functionally competent, degranulate upon exposure to allergen, and persist in neonates, in whom they may mediate allergic disease in early life.

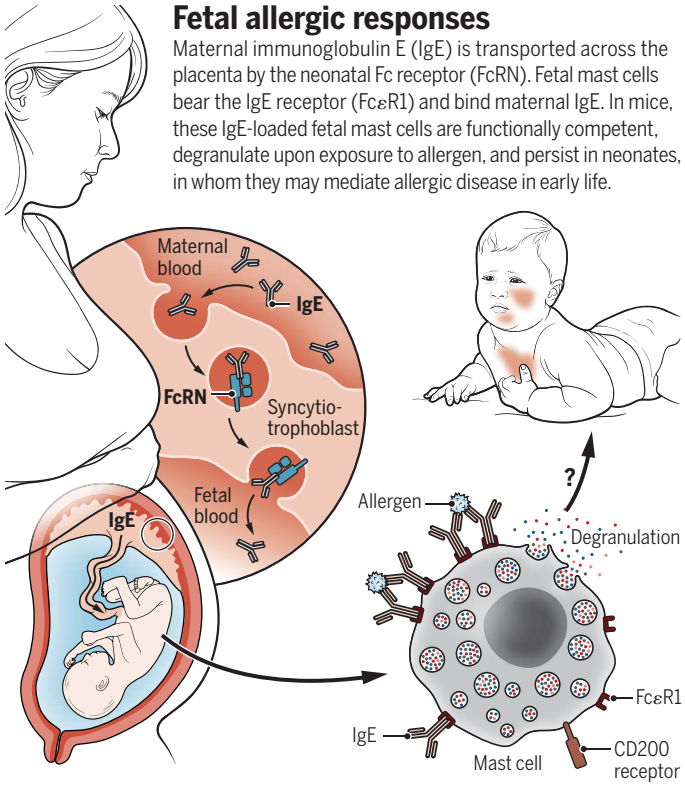

Fetal IgE has not been deeply studied, and whether it is produced by the fetus or derived from the mother (similar to most IgG in the fetus) is not agreed upon. However, emerging studies have provided evidence that human IgE in umbilical cord blood is maternally derived (*5*). Thus, the findings by Msallam *et al.* fit well with these data. The authors also identify the neonatal Fc receptor (FcRN) as the key IgE transporter, expressed by fetal endothelial cells and syncytiotrophoblast cells in the placenta. Previously, FcRN was shown to transfer IgG across the placenta (*6*).

Although fetal mast cells are capable of mediating classical allergic responses, it is important to note that the models used by Msallam *et al.* rely on artificial experimental systems that involve unnaturally high doses of passive IgE administration and allergen sensitization schemes that are likely stronger than those that occur naturally in humans (*7*). Additionally, the presence of allergen-specific IgE and the ability of allergens to degranulate mast cells are not sufficient for the development of allergies, as many individuals elicit these responses in the absence of clinical symptoms. Indeed, the development of allergic diseases involves other key immunocytes, including basophils, eosinophils, innate lymphoid cells, T helper type 2 cells, and regulatory T cells. Even when focusing on mast cells, their activation status is influenced by a variety of inhibitory signals including expression of the inhibitory receptor CD200R (*8*), which was present on fetal mast cells (*3*). Furthermore, IgG can neutralize antigens and directly inhibit mast cells (*9*); the roles of CD200R and IgG were not assessed by Msallam *et al.* Additionally, the degree of allergic inflammation seen in newborn mice could be considered modest: Lung eosinophils increased by a factor of ~2, whereas a factor of >10 increase in eosinophils is typically seen in human asthma and experimental asthma models in adult mice.

Msallam *et al.* found that human fetal lung and skin mast cells were IgE$^+$ and appeared to be functionally mature. Notably, by 14 weeks of gestation, human fetal mast cells were already present in the skin at numbers comparable to those of adults. IgE may not only equip these mast cells to respond to allergens, but also promote their functional maturation and activation potential, creating a skin environment with primed mast cells, perhaps contributing to the "sensitive" skin of newborns. Indeed, a variety of unexplained newborn rashes, including infant atopic eczema, may be influenced by in utero–conditioned mast cells. Conversely, it is interesting to speculate that IgE-loaded mast cells may equip newborns with early-life protection against threatening infections.

A substantial body of evidence supports the idea that the development of allergic disease involves an "allergic march," which starts in the infant skin and subsequently develops into food allergy and then respiratory allergy (*10*). Msallam *et al.* demonstrated that loading of fetal mast cells with maternal IgE is transient, gone by 6 weeks of age in mice; this time period is a critical window for long-term immune polarization, as exemplified by the recent recognition that early-life exposure to allergens is protective for the development of food hypersensitivity (*11*).

An immediate implication of the results is the occurrence of vertical transmission of anaphylaxis. However, this is not a phenomenon readily observed in humans because infants rarely have anaphylaxis and mothers seldom pass specific allergies (e.g., to penicillin or peanut) to their offspring (*11*, *12*). Perhaps this is due to the short lifespan of the surface-bound IgE, estimated to be 70 days (*13*), meaning that maternal IgE would be gone by the time most infants begin to develop acute allergic reactions when solid foods are introduced. Instead, mothers pass on the tendency to develop allergies but not specific antigen sensitization. Although this has been attributed to the transfer of genetic variants in allergy susceptibility genes and commensal microbiota, the findings of Msallam *et al.* raise the possibility that in utero events, most notably the priming of mast cells with surface IgE, may contribute to a variety of subsequent immune responses, perhaps by promoting the continuation of the type 2 immune polarization that is characteristic of neonates (*14*). ■

REFERENCES AND NOTES

1. N. P. Azouz, M. E. Rothenberg, *J. Clin. Invest.* **129**, 1419 (2019).
2. C. A. Liu *et al.*, *J. Allergy Clin. Immunol.* **112**, 899 (2003).
3. R. Msallam *et al.*, *Science* **370**, 941 (2020).
4. R. Gentek *et al.*, *Immunity* **48**, 1160 (2018).
5. K. Bønnelykke, C. B. Pipper, H. Bisgaard, *J. Allergy Clin. Immunol.* **121**, 646 (2008).
6. D. D. Patel, J. B. Bussel, *J. Allergy Clin. Immunol.* **146**, 467 (2020).
7. F. D. Finkelman, M. Wills-Karp, *J. Allergy Clin. Immunol.* **121**, 603 (2008).
8. S. Zhang, H. Cherwinski, J. D. Sedgwick, J. H. Phillips, *J. Immunol.* **173**, 6786 (2004).
9. O. Malbec, M. Daëron, *Immunol. Rev.* **217**, 206 (2007).
10. H. Han, F. Roan, S. F. Ziegler, *Immunol. Rev.* **278**, 116 (2017).
11. G. Du Toit *et al.*, *N. Engl. J. Med.* **372**, 803 (2015).
12. G. Pouessel *et al.*, *Clin. Exp. Allergy* **50**, 74 (2020).
13. M. G. Lawrence *et al.*, *J. Allergy Clin. Immunol.* **139**, 422 (2017).
14. S. L. Prescott, *Curr. Opin. Allergy Clin. Immunol.* **3**, 125 (2003).

ACKNOWLEDGMENTS

I thank numerous colleagues for helpful discussions, including S. Sicherer, M. Young, A. Devonshire, A. Assa'ad, and S. Durrani, as well as S. Hottinger for editorial assistance.

10.1126/science.abe8283

GRAPHIC: KELLIE HOLOSKI/*SCIENCE*

Published by AAAS

INFECTIOUS DISEASE

The origin of diarrhea in rotavirus infection

Messengers from rotavirus-infected cells induce pathogenic signaling in neighboring cells

By **Megan Stanifer** *and* **Steeve Boulant**

Infectious diarrhea is a global health problem that affects more than a billion people and leads to half a million deaths in children annually (*1*). Among diarrhea-inducing viruses, rotavirus is one of the most important pathogens. Although a rotavirus vaccine has been licensed since 2006 and is part of the standard vaccination plan in more than 100 countries, there are differences in efficacy, particularly in developing countries (*2*). Therefore, it is critical to understand how rotavirus induces such extreme diarrhea episodes in infants and young children so as to provide new therapeutic approaches. On page 930 of this issue, Chang-Graham *et al.* (*3*) provide evidence in human and simian cells that intercellular signaling from rotavirus-infected cells to neighboring noninfected cells ultimately leads to diarrhea. This study shows that diarrhea can be controlled not by targeting the pathogen but by interfering with the intercellular messengers that drive pathology.

In infectious-disease research, two populations of cells should be distinguished: the infected cells and the noninfected neighboring cells (also called bystander cells). In rotavirus-induced pathogenesis, it has been suspected that bystander cells participate in life-threatening diarrhea by responding to viral and/or cellular factors that are secreted by infected cells (*4*, *5*). Chang-Graham *et al.* showed that upon rotavirus infection of human intestinal epithelial cells, both infected cells and bystander cells display increases in intracellular Ca^{2+}, released from the endoplasmic reticulum, that propagates to adjacent cells through paracrine signaling to form intercellular calcium waves (ICWs). These ICWs have been described to be responsible for the spatial coordination of cellular functions (*6*). However, the importance of ICWs in the development of diarrhea during rotavirus infection is currently unknown.

The virally encoded nonstructural protein 4 (NSP4) is responsible for the induction of intracellular Ca^{2+} waves in rotavirus-infected cells (*7*), likely acting as a "pore" protein mediating Ca^{2+} release from the endoplasmic reticulum (*8*). This protein exists in two forms: an intracellular form in the rotavirus-infected cells and a secreted virotoxin form. Thus, NSP4 has been the usual suspect for the onset and development of disease (*9*). However, Chang-Graham *et al.* showed that although NSP4 was critical for the initial increase in intracellular Ca^{2+} in infected cells, it was not required for ICW propagation to bystander cells. Instead, they identified adenosine diphosphate (ADP) as the extracellular messenger responsible for the development of ICWs. Release of nucleotides in the extracellular milieu induces ICWs (*10*). The authors showed that ADP released by infected cells acts on bystander cells through specific purinergic receptors to induce Ca^{2+} release in those cells. These findings are consistent with the central role of purinergic receptors and extracellular nucleotides in regulating gut homeostasis and communication between the intestinal epithelium and the microbial content of the gastrointestinal tract (*11*).

In addition to inducing ICWs, ADP-mediated signaling also induced the production of cellular factors (such as serotonin) that are responsible for the development of the rotavirus-associated pathology (see the figure). Serotonin is a neurotransmitter that bridges communication between the gut and the enteric nervous system. The intestinal epithelium is the largest producer of serotonin in the body, and as such, rotavirus infection of the intestinal epithelium and activation of the bystander cells induces a signaling storm that drives severe water loss.

It has been unclear how a rotavirus infection that leads to very few infected cells (at least at the onset of infection) can lead to the severe pathology of loss of barrier function and excessive water loss. Similarly, it remained unexplained how severe diarrhea could be observed in patients before the noticeable loss of structural integrity of the intestinal epithelium. With the findings that bystander cells are the main players in rotavirus-induced diarrhea, the study of Chang-Graham *et al.* provides a unifying view of how rotavirus induces pathologies. In this model, a few infected cells can release extracellular messengers that activate bystander cells that will in turn induce complex signaling that leads to pathology and disease development. This intercellular activation allows signal amplification because one infected cell can activate many bystander cells. Chang-Graham *et al.* found that not all bystander cells were activated by ADP, which suggests that within an epithelium, a subpopulation of bystander cells are responsible for disease development. The origin for this heterogeneous response of bystander cells to the paracrine signal secreted by rotavirus-infected cells remains unknown. However, the identification of the molecular basis for this spatially restricted response could provide ideas for therapeutic approaches aimed to control water loss and inflammation.

The understanding of other enteric viruses is more limited. There is little knowledge of the molecular mechanisms by which enteric

Rotavirus-induced diarrhea

After rotavirus infection, nonstructural protein 4 (NSP4) induces intracellular Ca^{2+} waves that mediate the release of adenosine diphosphate (ADP). ADP activates purinergic receptors on bystander cells, which leads to diarrhea. ADP also activates phospholipase C and release of inositol trisphosphate (IP_3), which amplifies intracellular and intercellular Ca^{2+} waves.

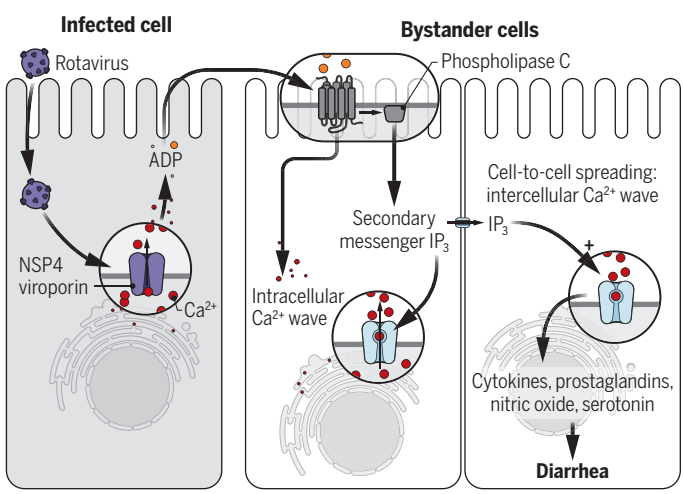

GRAPHIC: V. ALTOUNIAN/*SCIENCE*

University Hospital Heidelberg, Department of Infectious Diseases, Heidelberg, Germany. Email: m.stanifer@dkfz.de; s.boulant@dkfz.de

Published by AAAS

pathogens induce pathologies (inflammation, diarrhea, and vomiting). In the case of norovirus, only a few virus particles are sufficient to quickly induce severe diarrhea and vomiting. With the idea that severe pathology can develop in a bystander cell–dependent manner, despite only a few infected cells, perhaps research should also focus on bystander cells in the case of norovirus infection. Similarly, between 10 and 30% of coronavirus disease 2019 (COVID-19) patients have gastrointestinal symptoms (*12*), and there is evidence of severe acute respiratory syndrome coronavirus 2 (SARS-CoV-2) replication in the human intestinal epithelium (*13*, *14*). Although few infected cells have been detected in patient biopsies, bystander cells might be responsible for the gastrointestinal symptoms observed in COVID-19 patients.

Historically, infectious disease research has focused on the infected cell population because most analyses of host-pathogen interactions have been performed on bulk populations by using conditions in which most of the cells are infected by the pathogen of interest. With the development of single-cell methodologies, it is now possible to disentangle the participation of both the infected and noninfected bystander cells for the virus life cycle and induced pathologies. This will provide a better understanding of pathogenic mechanisms but also could provide new therapeutic targets to control the disease. This is exemplified by the study of Chang-Graham *et al*., which showed that blocking the formation of ICWs in bystander cells, through the inhibition of P2Y purinoceptor 1 (P2Y1), resulted in a decrease of rotavirus-induced diarrhea severity in mice. As such, targeting the pathogen or the infected cells might not be the sole option to control infectious diseases and their induced pathologies. ■

REFERENCES AND NOTES

1. World Health Organization, "Diarrhoeal disease" (2017); https://www.who.int/news-room/fact-sheets/detail/diarrhoeal-disease.
2. E. Burnett *et al*., *Lancet Glob. Health*. **8**, e1195 (2020).
3. A. L. Chang-Graham *et al*., *Science* **370**, eabc3621 (2020).
4. K. Hodges *et al*., *Gut Microbes*. **1**, 4 (2010).
5. K. Bányai *et al*., *Lancet*. **392**, 175 (2018).
6. L. Leybaert *et al*., *Physiol. Rev*. **92**, 1359 (2012).
7. P. Tian *et al*., *J. Virol*. **69**, 5763 (1995).
8. T. Pham *et al*., Sci. Rep. 7, 43487 (2017).
9. N. P. Sastri *et al*., in *Viral Gastroenteritis*, L. Svensson, U. Desselberger, M. Estes, H. Greenberg, Eds. (Academic Press, 2016), pp. 145–174.
10. Y. Osipchuk *et al*., *Nature*. **359**, 241 (1992).
11. A. Inami *et al*., *Int. J. Mol. Sci*. 10.3390/ijms19082371 (2018).
12. L. Lin *et al*., *Gut*. **69**, 997 (2020).
13. M. M. Lamers *et al*., *Science* **369**, 50 (2020).
14. M. L. Stanifer *et al*., *Cell Rep*. **32**, 107863 (2020).

ACKNOWLEDGMENTS

M.S. and S.B. are supported by research grants from the Deutsche Forschungsgemeinschaft: project nos. 415089553, 240245660, 278001972, and 272983813 to S.B. and 416072091 to M.S.

10.1126/science.abf1914

FLEXIBLE SENSORS

The more and less of electronic-skin sensors

Sensors can measure both strain and temperature or measure force without affecting touch

By **Xinyu Liu**[1,2]

Electronic skins (e-skins) are flexible electronic devices that emulate properties of human skin, such as high stretchability and toughness, perception of stimuli, and self-healing. These devices can serve as an alternative to natural human skin or as a human-machine interface (*1*–*3*). For on-skin applications, an e-skin should be multimodal (sense more than one external stimulus), have a high density of sensors, and have low interference with natural skin sensation. On pages 961 and 966 of this issue, You *et al*. (*4*) and Lee *et al*. (*5*), respectively, report advances of skin-like electronic devices. You *et al*. present a stretchable multimodal ionic-electronic (IE) conductor–based "IE^{M}-skin" that can measure both strain and temperature inputs without signal interference. Lee *et al*. describe an ultrathin capacitive pressure sensor based on conductive and dielectric nanomesh structures that can be attached to a human fingertip for grip pressure and force measurement without affecting natural skin sensation.

The human skin contains a large number of mechanoreceptors and thermoreceptors (nerve endings that sense deformation and temperature, respectively) that provide distinct perception of the spatial distributions of strain and temperature on our skin induced by touch stimulations (*6*). To replicate these sensory functions of the natural skin, different types of sensors that act as artificial receptors are integrated onto an e-skin for multimodal sensation (*7*). However, an e-skin containing a high-density array of sensory "pixels" of different types for sensing different physical quantities tends to have a complex structure and is challenging to manufacture.

A preferred strategy for realizing multimodal sensation on an e-skin is to use the same sensory unit for detecting different physical quantities without signal interference, an approach called decoupled multimodal sensing. Traditional stretchable sensors are sensitive to both strain and temperature and cannot be used as artificial multimodal receptors without signal interference. Targeting interference-free strain and temperature sensing by a single sensory unit, You *et al*. creatively used the ion relaxation dynamics of an ion conductor (an elastomer mixed with an ionic liquid) to decouple the strain and temperature measurement and developed the IE^{M}-skin composed of an array of artificial multimodal ionic receptors. They fabricated the IE^{M}-skin by sandwiching a thin layer of ion conductor with two layers of orthogonally patterned stretchable electrode strips (see the figure, top). A pixelated matrix of millimeter-sized artificial receptors formed between the top and bottom electrodes.

The electrical properties of each receptor are affected by the externally applied strain and temperature stimuli and can be measured through impedance measurement. You *et al*. used a strain-independent intrinsic electrical parameter of the ion conductor, the charge relaxation time, which reflects the ionic charge dynamics of the ion conductor and is equal to the ratio of material's dielectric constant and ion conductivity (*8*, *9*). The charge relaxation time is the signal readout for temperature and is not affected by the deformation of the IE^{M}-skin. For strain measurement, the bulk capacitance of the ion conductor is measured. The effect of temperature on the capacitance is eliminated through normalization against a reference capacitance at the temperature measured by the receptor. Thus, an external strain input only changes geometric parameters of the ion conductor, whereas a temperature input primarily modulates the intrinsic electrical properties (dielectric constant and ion conductivity) of the ion conductor.

Another enabling factor of the IE^{M}-skin design is its emulation of the epidermis and dermis bilayer of the human skin by suspending the receptor matrix layer over a low-friction interface layer filled with talcum powder. This design allows three-dimensional wrinkle-like deformations of the IE^{M}-skin under different contact modes (such as shear, pinch, tweak, and torsion) and permits the IE^{M}-skin to distinguish these contact modes through

[1]Department of Mechanical and Industrial Engineering, University of Toronto, Toronto, ON M5S 3G8, Canada. [2]Institute of Biomedical Engineering, University of Toronto, Toronto, ON M5S 3G9, Canada. Email: xyliu@mie.utoronto.ca

Published by AAAS

the measured temperature and strain profiles. Data confirm that the IE^M-skin can perform decoupled, real-time measurement of strain and temperature with high accuracy.

The IE^M-skin can serve as a human-machine interface that accepts tactile inputs of different contact modes and can be integrated into prosthetic and robotic devices to provide tactile and thermal feedback with high spatial resolution. The concept of using intrinsic electrical parameters, such as conductivity and dielectric constant of sensing materials, for strain-independent temperature sensing can be generalized to developing other types of stretchable multimodal sensors for humidity, chemicals, and biomolecules. One limitation is that the method for recognizing different tactile input modes through the measured temperature and strain profiles only works for interactions with hot or cold objects at temperatures different from that of the IE^M-skin. Alternative solutions may include the use of learning-based recognition models purely based on strain-distribution data or modulation of the temperature of the IE^M-skin (by adding a heating layer) based on the environment.

Skin-like electronic sensors also hold great potential for construction of hand-wearing devices such as instrumented gloves for quantifying tactile signals like force and pressure during finger or in-hand manipulation (*10*). Such data could facilitate the decoding of human hand sensation and its roles in object manipulation and enable better designs of robotic and prosthetic hands with biomimetic sensory feedback (*11*). Targeting imperceptible wearing and tactile sensing on fingertips, Lee *et al.* developed an ultrathin capacitive pressure sensor consisting of multilayers of conductive and dielectric nanomesh structures. This sensor design is derived from the design of conductive nanomesh electrodes proposed by Miyamoto *et al.* (*12*), which can be directly laminated on human skin during fabrication.

The electrode is fabricated by first electrospinning a water-soluble polymer, polyvinyl alcohol (PVA) into a multilayered mesh-like network of 300- to 500-nm-wide nanofibers. A 100-nm-thick gold layer is then deposited onto the PVA nanomesh sheet, and the gold-coated nanomesh sheet is transferred onto the skin surface. The sacrificial PVA nanofibers are washed off by water, but a residual layer of the dissolved PVA greatly facilitates the attachment of the resultant gold nanomesh layer onto the textured skin surface with excellent adhesion and conformal contact. The skin-integrated nanomesh electrode is stretchable and highly breathable and has exceptionally low bending stiffness, and so it creates no mechanical constraint or dermatological irritation to the skin.

To fabricate a nanomesh pressure sensor (see the figure, bottom), Lee *et al.* first laminated a nanomesh electrode on the skin surface and then sequentially attached a dielectric nanomesh layer made of electrospun polyurethane and parylene nanofibers and another nanomesh electrode layer to form a parallel-plate capacitor structure. Then, a nanomesh passivation layer of polyurethane nanofibers was attached to the top electrode layer with dissolved PVA nanofibers as the filler and adhesive. The total thickness of the nanomesh pressure sensor is ~13 μm. When fingers wearing such a pressure sensor grip an object, the grip force applied to the pressure sensor deforms the middle dielectric nanomesh layer and leads to a change in the capacitance measured between the top and bottom electrodes as the sensor readout.

Through object-gripping experiments performed by human participants, Lee *et al.* investigated the effect of the finger-integrated pressure sensor on the natural fingertip sensation and found no decrease of the sensory feedback caused by the attachment of the pressure sensor. They hypothesized that the ultrathin and compliant structure of the nanomesh pressure sensor renders the device imperceptible on the fingertip. In addition, the intimate and conformal adhesion of the sensor's bottom nanomesh electrode layer to the skin surface may also contribute to the negligible interference of the finger skin sensation by the sensor attachment. This sensor also shows excellent mechanical durability under cyclic compression, shearing, and surface friction, which is attributed to the high mechanical robustness of the multilayered nanomesh structure of the pressure sensor.

This work highlights another new application of the previously reported skin-integrated nanomesh electronics (*12*) to wearable physical sensing with unprecedented performance. Future work may involve the further examination of fundamental mechanisms for the on-skin imperceptibility of the nanomesh pressure sensor, the systematic study of the skin-integrated pressure sensor performance for grasping objects of different materials and properties (such as insulating versus conductive, hard versus soft, and smooth versus textured), and the scalable fabrication of pixelated nanomesh pressure sensors in a large area with high density. The nanomesh pressure sensor could record tactile signals of human-hand manipulation that could provide superior sensing performance and zero data artifacts over existing instrumented gloves and e-skins.

Multimodal sensation and nonobstructive skin integration are two important features that are desirable in e-skin designs. The studies reported by You *et al.* and Lee *et al.*, respectively, provide new solutions to better realize these attractive features with simplified device structures and enhanced sensing performance without impeding natural sensation. These results will inspire new sensor designs and lead to applications of e-skins as wearable health care monitoring, sensory prosthetic and robotic devices, and high-performance human-machine interfaces. ■

Improved electronic skins

Two goals in artificial touch sensors are to sense more than one stimulus with one receptor and to create wearable sensors that maintain natural skin sensation.

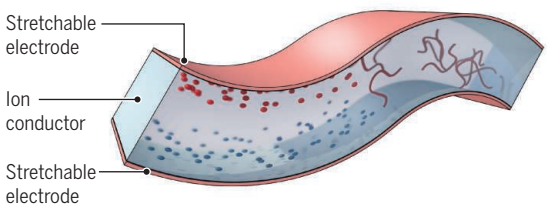

Receptor for decoupled sensing
For multimodal sensation, You *et al.* developed a stretchable ionic-electronic conductor receptor that detects both strain and temperature inputs without the signals interfering with each other.

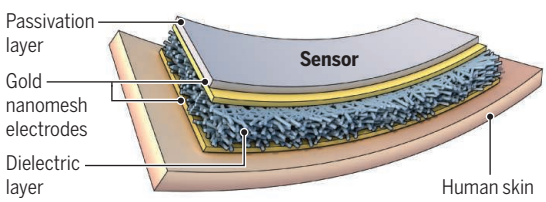

Nanomesh-based pressure sensor
For on-skin sensing, Lee *et al.* attached an ultrathin capacitive pressure sensor based on conductive and dielectric nanomesh structures to a human, which did not affect natural skin sensation.

GRAPHIC: C. BICKEL/*SCIENCE*

REFERENCES AND NOTES

1. J. C. Yang *et al.*, *Adv. Mater.* **31**, 1904765 (2019).
2. T. R. Ray *et al.*, *Chem. Rev.* **119**, 5461 (2019).
3. T. Someya, M. Amagai, *Nat. Biotechnol.* **37**, 382 (2019).
4. I. You *et al.*, *Science* **370**, 961 (2020).
5. S. Lee *et al.*, *Science* **370**, 966 (2020).
6. A. Zimmerman, L. Bai, D. D. Ginty, *Science* **346**, 950 (2014).
7. S. Jeon, S.-C. Lim, T. Q. Trung, M. Jung, N.-E. Lee, *Proc. IEEE* **107**, 2065 (2019).
8. C. Gainaru *et al.*, *J. Phys. Chem. B* **120**, 11074 (2016).
9. B. A. Mei, O. Munteshari, J. Lau, B. Dunn, L. Pilon, *J. Phys. Chem. C* **122**, 194 (2018).
10. S. Sundaram *et al.*, *Nature* **569**, 698 (2019).
11. E. D'Anna *et al.*, *Sci. Robot.* **4**, eaau8892 (2019).
12. A. Miyamoto *et al.*, *Nat. Nanotechnol.* **12**, 907 (2017).

ACKNOWLEDGMENTS

X.L. acknowledges support from the Natural Sciences and Engineering Research Council of Canada (RGPIN-2017-06374).

10.1126/science.abe7366

Published by AAAS

MOLECULAR MACHINES

The molecular wagon that stays on track

Single molecules are sent and received accurately over long distances across a surface

By **Friedrich Esch** and **Barbara A. J. Lechner**

Ever since the 2016 Nobel Prize in Chemistry was awarded "for the design and synthesis of molecular machines," growing attention has been aimed at connecting and embedding molecular machines into hierarchically more complex systems for sophisticated applications. Such connections would, for example, enable the targeted delivery of molecules over larger distances. An important question that arises in this context is what kind of transporter would do such a job, over what distances, and with what degree of precision. On page 957 of this issue, Civita *et al.* (*1*) found a distinct example of a bromine-terminated terfluorene molecule on a metal surface that can be sent and received deliberately across more than a hundred nanometers with atomic precision.

The bromine-terminated terfluorene molecules can be moved easily on a Ag(111) support by applying electric fields between the surface and a scanning tunneling microscopy (STM) tip. The close-packed rows of the metal support essentially act as railway tracks for the molecular wagons. To characterize this movement on the single-molecule level, the authors had to sense the molecule at specific start and end points. This required bringing the molecule on the desired track and locally inducing motion along that track. The beauty of the experiment by Civita *et al.* lies in the successful application of a two-probe STM setup: Each tip provides a separate probe and manipulation device at the start and end points of the movement. In addition, each tip can individually generate local fields. The experiment thus constitutes a near-ideal sender–receiver setup where atomic-scale cargo is transmitted.

Previous experiments have already demonstrated that molecules can be accelerated along a surface using an STM tip (*2*) and that preferential diffusion directions can be accessed by rotating the molecules (*3*, *4*), but they have never reached this long-distance precision and high level of motion control. The interaction of the bromine-terminated terfluorene molecule with the silver surface is unusually well suited for this application. The linear molecule consists of three stiff fluorene units linked by rotationally flexible junctions and is not bonded strongly to a particular adsorption site on the surface. The reason lies in lateral methyl distancers that lift the molecule, while guiding it with its long axis along the track of the close-packed rows. However, keeping the molecule safely on the track is only achieved by the additional terminal bromine substituents, which add a further interaction to the support atoms. Furthermore, the molecule–surface system has a permanent dipole moment pointing out of the surface that is the handle to induce lateral movement. The authors convincingly show that the electric fields

"The experiment thus constitutes a near-ideal sender–receiver setup where atomic-scale cargo is transmitted."

can be used to induce the movement from afar (150 nm) by both repulsion and attraction. The fortunate combination of all these properties leads to the particular mobility observed here, constituting a seminal quality and thus opening up important questions with regard to the design of hierarchical nanomachineries.

An interesting part of the experiment is that all molecules initially adsorb in locked-in, static orientations, upon deposition at low temperatures. Only after rotation by STM manipulation do the molecules snap to the track and become mobile. They reach a state with low lateral diffusion barriers along their long axis, which might point to incommensurability. One could speculate that the difficulty of dissipating the excess adsorption energy in this orientation is what keeps the molecules from adsorbing in the highly mobile orientation in the first place. Additionally, this might be the reason for the concomitant facile diffusion. The role of rotational flexibility along the long axis and of internal vibrational modes for the molecules' mobility will be interesting to assess.

From previous studies, we know that these aspects influence the long jumps in the diffusion path (*5*) and modulate the degree of incommensurability that can lead to particular diffusion behaviors, such as, for example, Lévy flights (*6*). In Civita *et al.*'s experimental setup, such an influence can be studied by systematic structural variation of the molecules. The two-tip setup, however, reaches its time resolution limit when it comes to understanding in more detail the acceleration and maximal velocities that the wagons can reach. For quantitative access to the thermally activated diffusion properties, helium spin-echo measurements would be the way forward (*7*). However, observations of this type require a considerable population of molecules moving along tracks in an equilibrium state, at temperatures where immobilization at steps and island edges can be overcome.

Civita *et al.* show that the possibility exists to reliably move molecules along tracks. Moving closer toward nanomachineries will require implementation into more-complex systems, opening up several challenges. Similar track–molecule systems have to be realized on functionalized supports. Also, reversible cargo attachment to the nanowagons and an adequate handover process need to be established. And easily addressable or alternative acceleration mechanisms that can be actioned by nanomachines have to be explored. Nanomachines might generate the required local fields or induce chemical reactions that steer the cargo transport by energy release into distinct degrees of freedom. One might even envisage the use of light to photostimulate reactions or to create optically rectified fields in plasmonic nanoreactors that control the reactant supply. The possibilities are boundless—exciting times lie ahead. ■

Department of Chemistry and Catalysis Research Center, Technical University of Munich, 85748 Garching, Germany. Email: bajlechner@tum.de

REFERENCES AND NOTES

1. D. Civita *et al.*, *Science* **370**, 957 (2020).
2. S. W. Hla, K. F. Braun, B. Wassermann, K. H. Rieder, *Phys. Rev. Lett.* **93**, 208302 (2004).
3. R. Otero *et al.*, *Nat. Mater.* **3**, 779 (2004).
4. B. Vasić *et al.*, *Nanoscale* **10**, 18835 (2018).
5. K. D. Dobbs, D. J. Doren, *J. Chem. Phys.* **97**, 3722 (1992).
6. W. D. Luedtke, U. Landman, *Phys. Rev. Lett.* **82**, 3835 (1999).
7. A. P. Jardine, H. Hedgeland, G. Alexandrowicz, W. Allison, J. Ellis, *Prog. Surf. Sci.* **84**, 323 (2009). f

10.1126/science.abe5959

Published by AAAS

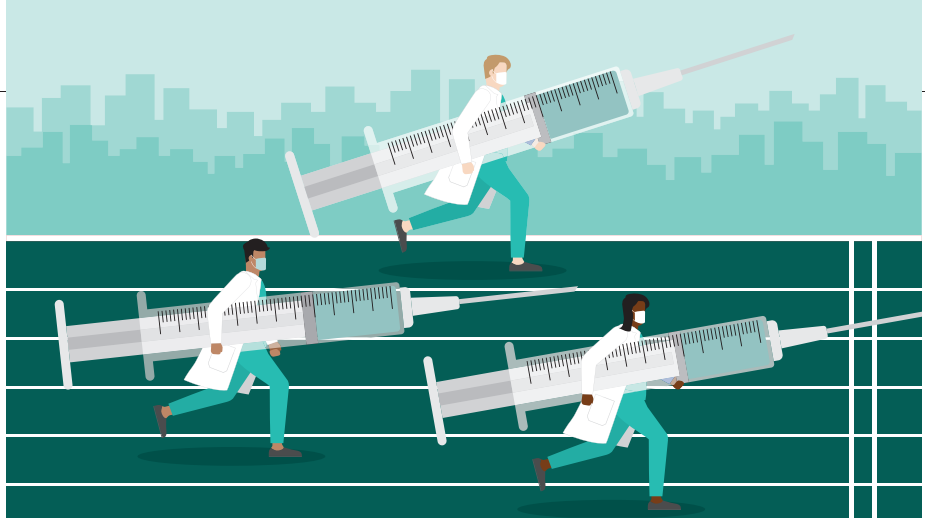

ILLUSTRATION: ADAPTED BY C. SMITH/*SCIENCE* FROM KORA_SUN/SHUTTERSTOCK

VIEWPOINT: COVID-19

Advancing new tools for infectious diseases

Therapeutics and vaccine development for infectious diseases could be transformed

By **Rajesh Gupta**

Several infectious diseases cause considerable mortality worldwide each year: Tuberculosis causes ~1.2 million deaths, diarrheal disease causes ~1.5 million deaths, and lower respiratory infections cause ~700,000 deaths in children under 5 years old (*1*). Yet the scale and speed of innovation in developing tools for coronavirus disease 2019 (COVID-19) dwarf the development of those for global infectious diseases, which disproportionally affect resource-limited countries. By August 2020, ~175 therapeutics and vaccines were in clinical trials for COVID-19 (*2*). By contrast, for 41 global infectious diseases or disease groups, only ~250 therapeutics and vaccines were in clinical trials in August 2019 (*3*). A robust product pipeline and abridged development time frame for COVID-19 has primarily been enabled by three factors: scientific advances, operational efficiencies, and large-scale at-risk financing. A clear, well-financed path from research through product procurement now exists for COVID-19, shortening timelines while increasing output. This could underpin an approach for global infectious diseases.

Recent scientific advances have revolutionized platform technologies and expanded the ability to rapidly identify therapeutic and vaccine candidates. High-throughput computational screening of molecular libraries against key pathogens and/or host targets has accelerated the ability to repurpose agents and identify entities against severe acute respiratory syndrome coronavirus 2 (SARS-CoV-2, which causes COVID-19) (*4*). Candidate compounds with existing clinical safety data quickly entered clinical trials, leading to the repurposing of dexamethasone and remdesivir to treat hospitalized COVID-19 patients. Monoclonal antibodies (mAbs) can potentially provide near-immediate therapy and/or prophylaxis by bypassing the need for a host-generated immune response (*5*), and at lower costs and higher volumes than previously assumed. Vaccines have benefited from innovations in vector modalities, manufacturing, antigen design, computational biology, protein engineering, and gene synthesis (*6*). Such innovations may provide the technological basis for targeting other global infectious diseases.

In response to COVID-19, the public health and regulatory communities are streamlining clinical development. Independently funded, designed, and conducted platform clinical trials, such as Accelerating COVID-19 Therapeutic Interventions and Vaccines (ACTIV), are structured under a single, adaptive "master" protocol to allow for continuous and consistent evaluation of multiple drug candidates, adding products as they become available and removing candidates as they are deemed futile. They also provide access to large, geographically diverse populations, and some have created or expanded operational structures in resource-limited countries (*7*). Timelines have been shortened because of accelerated regulatory reviews, flexible requirements to enter first-in-human trials, newer approaches to modeling population-specific issues, early approval mechanisms, and enhanced regulatory harmonization among countries (*8*). This increased efficiency in clinical trial execution and regulatory processes could be applied to other global infectious diseases.

Historically, investment in product development for global infectious diseases has been restricted owing to the lack of financial returns compared to more profitable areas of drug development, such as oncology. However, the threat that pandemic human coronaviruses (HCoVs) pose to the global economy, political stability, and people's lives has stimulated the private sector, public sector, and philanthropic groups to devote considerable financial and human resources to product development. Previous HCoV outbreaks led to initial development activities that were accelerated with COVID-19. Supplementing these efforts, the U.S. government has provided over $10 billion for COVID-19 therapeutics and vaccines. Other governments, including the European Union, United Kingdom, Germany, and Canada, are making substantial financial commitments, as are large funding institutions (*2*).

A fundamental principle behind this unprecedented funding is that financing for the entire product development process is made by the time a candidate enters early-stage clinical trials (*9*). This approach has mitigated the range of risks faced by different categories of developers (e.g., academia, nonprofit organizations, public-private partnerships, small biotechnology companies, and large multinational pharmaceutical companies) who may individually have widely varying risk-reward calculations. As a result, developers can simultaneously prepare for late-stage clinical trials, implement scaling up of manufacturing processes, and obtain advanced purchase commitments of large-scale supply—all during first-in-human clinical trials (*9*). Together, providing the full range of financing as early as possible in the product development process, articulating the need for multiple products, and acknowledging implicit failure of some candidates and platforms have overcome product development barriers. The result has been an extraordinary scale of therapeutic and vaccine development in the shortest time possible.

A similar product development framework could be created for global infectious diseases. Such a framework could attempt to resolve three long-standing challenges for these diseases: the lack of interest in

Vir Biotechnology, Inc., San Francisco, CA, USA.
Email: rgupta@vir.bio

Published by AAAS

developing products, resulting in a diminished initial pipeline of candidates; the large pipeline attrition points between preclinical activities and early-stage clinical trials and between early- and late-stage clinical trials (*10*) that occur because of the considerable increases in development costs of these two transition points; and the extended timelines for product development. If these challenges are addressed, a more robust initial pipeline could be created, more candidates could advance to early- and late-stage clinical trials, and more products could be approved in a shorter period.

A robust pipeline for global infectious diseases should include repurposed agents, mAbs, new chemical entities, and vaccines. Each of these categories possess strengths and limitations; thus, each may not prove beneficial for every disease. Repurposed agents may have existing preclinical data and clinical safety experience, putting them on the fastest development timelines. mAbs targeting proteins encoded by highly conserved regions of a pathogen's genome—thereby minimizing escape mutations and maximizing strain coverage—can be isolated from patients and modified to enhance their activities, for example, to extend half-life and induce host immune responses. New chemical entities could target families of pathogens to create "one-drug-multiple-bug" approaches to replace "one-drug-one-bug" approaches. Traditional vaccine platforms have a history of clinical validation and scaled production capacity. Emerging nucleic acid–based vaccine systems have promise for generating a candidate upon availability of a genomic sequence.

Several factors must be considered to rapidly build and advance such a pipeline. Arguably the most critical factor is to incentivize all development groups and encourage aggressive competition. Public sector and philanthropic financing should address the cost of research, clinical trials, manufacturing, and supply agreements, and such financing should be available at the earliest possible part of the product development process. This is essential to overcome developers' decision to avoid product development because of lack of a clear revenue model. This financing, in turn, could stimulate the levels of investment and activity from the private sector observed in COVID-19, including public-private partnerships to advance candidates. A fundamental biological understanding of coronaviruses existed prior to COVID-19 and is necessary to drive product development, but a similar biological understanding needs to be improved for many global infectious diseases (*11*). While under development for COVID-19, predictive, validated preclinical assays, animal models, and human challenge models for infectious diseases would provide faster, cost-efficient methods to eliminate candidates earlier in the development cycle (*12*, *13*).

Moreover, implementing high-quality, decentralized clinical trials and using existing clinical trial networks could reduce the need for each developer to create complex multicountry clinical trial processes and infrastructure while still maintaining consistent evaluation methods (*14*). Machine learning could help optimize clinical trial design and identify populations most likely to benefit from a candidate, thereby reducing the large sample sizes currently required for late-stage clinical trials (*15*). Consideration should be given to what accelerated and flexible regulatory processes may be adopted from COVID-19, and which regulatory agencies should serve as benchmark approvals for those diseases that predominantly affect resource-limited settings. The manufacturing supply chain may need to be improved for some technologies facing global constraints. Additionally, access, affordability, and availability will need to be addressed to ensure that innovations reach the populations in greatest need.

Implementing this strategy is not without risk, and there are challenges to overcome. Development of predictive models and biomarkers has proved difficult with COVID-19. The risk-benefit assessment for accelerated first-in-human testing during an unfolding pandemic may differ compared to that for endemic pathogens. Global capacity for late-stage clinical trials may initially be reached quickly in resource-limited settings. As seen with hydroxychloroquine, early approvals based on limited evidence can occur with compounds that ultimately demonstrate no benefit. The advanced financing available for COVID-19 candidates partially emerged from country-specific interests and, if repeated, may continue to foster inequitable access to new tools globally. Ultimately, the SARS-CoV-2 product development model may need optimization to realistically achieve success across multiple global infectious diseases.

Of the ~250 therapeutics and vaccines in clinical development for global infectious diseases, ~30% are for HIV and AIDS (*3*). The innovation in antiretroviral medicines was initially sparked by strong political will coupled with streamlined regulatory processes. Growing demand produced attractive returns from resource-wealthy countries. By contrast, the distinct regulatory pathways and government funding to address the growing problem of resistance to antimicrobial agents (such as antibiotics) could not overcome the lack of a revenue model, thereby bankrupting companies that successfully developed safe and efficacious therapies and curtailing development activities. For the recent outbreak of Zika virus beginning in 2015 in the Americas, the time frame from identification of genomic sequences to advancing a nucleic acid vaccine into phase 1 clinical trials occurred within 4 months; but the threat to high-income countries quickly subsided, resulting in stalled product development programs. After nearly 40 years of continuous outbreaks in Africa, the potential global spread of Ebola became evident during the 2014–2016 outbreak and spurred public-private partnerships that recently achieved approval of two vaccines and one therapeutic mAb combination (with a second, single therapeutic mAb under regulatory review).

Resource-limited countries are experiencing combined morbidity and mortality impacts from COVID-19: from the disease itself and from other global infectious diseases, owing, in large part, to diversion of resources. Which candidates in clinical trials for COVID-19 will reach regulatory approval, what limitations may come with licensed candidates, and the success of emerging technology platforms are all unknown. However, COVID-19 forced the world to construct a new product development approach, taking what was previously perceived as impossible and turning it into reality. How to implement this approach to address other global infectious diseases that continue to curtail global economic growth and devastate humanity must now be decided. ■

REFERENCES AND NOTES

1. Institute for Health Metrics and Evaluation, *Global Burden of Disease Study 2019*; https://bit.ly/3jjb5J9.
2. Policy Cures Research, COVID-19 R&D Tracker Update: 6 August 2020; https://bit.ly/3oqL9PI.
3. Policy Cures Research, *Neglected Diseases R&D Pipeline Tracker—August 2019*; https://bit.ly/2FU2r6m.
4. D. E. Gordon *et al*., *Nature* **583**, 459 (2020).
5. M. Marovich, J. R. Mascola, M. S. Cohen, *JAMA* **324**, 131 (2020).
6. B. S. Graham, *Science* **368**, 945 (2020).
7. L. Corey, J. R. Mascola, A. S. Fauci, F. S. Collins, *Science* **368**, 948 (2020).
8. J. L. Wilson *et al*., *Sci. Transl. Med.* **12**, eaax2550 (2020).
9. M. Slaoui, M. Hepburn, *N. Engl. J. Med.* **383**, 1701 (2020).
10. R. Rappuoli, S. Black, D. E. Bloom, *Sci. Transl. Med.* **11**, eaaw2888 (2019).
11. M. De Rycker, B. Baragaña, S. L. Duce, I. H. Gilbert, *Nature* **559**, 498 (2018).
12. J. Cohen, *Science* **368**, 221 (2020).
13. N. Eyal, M. Lipsitch, P. G. Smith, *J. Infect. Dis.* **221**, 1752 (2020).
14. COVID-19 Clinical Research Coalition, *Lancet* **395**, 1322 (2020).
15. W. R. Zame *et al*., *Stat. Biopharm. Res.* 10.1080/19466315.2020.1797867 (2020).

ACKNOWLEDGMENTS

Thanks to D. Gollaher, B. Hubby, M. Kamarck, I. Pleasure, S. Shome, H. W. Virgin, C. Wells, and G. Yamey for their insightful comments. R.G. is an employee and owns shares of Vir Biotechnology, Inc. The author's opinions expressed in this article do not necessarily reflect Vir's official policy.

10.1126/science.abe0773

Published by AAAS

RETROSPECTIVE

Georgina Mace (1953–2020)

Pioneering conservation biologist and sustainability scientist

By **Andy Purvis**[1,2] *and* **Kate E. Jones**[3,4]

Georgina Mace, who died on 19 September at the age of 67, did groundbreaking research assessing the state of biodiversity, how human actions have driven biodiversity loss, and how society might change to deliver a sustainable future. Intellectually fearless and possessing absolute integrity, Georgina selflessly supported and empowered countless researchers. One of the first conservation biologists and a pioneer for uniting disciplines to deliver evidence-based change, she provided the insights that underpin conservation laws and policies worldwide.

Georgina was born in Lewisham, London, in 1953. Her early fascination with biology led to a B.Sc. in zoology from the University of Liverpool in 1976 and then a Ph.D. from the University of Sussex on mammalian evolutionary ecology in 1979. Georgina joined the Zoological Society of London (ZSL) in the mid-1980s, where she used her quantitative skills to explore the genetic and ecological processes that can drive small populations extinct. This led to a remarkable career trajectory, in which she always tackled the next obstacle on the critical path toward better nature conservation, immersing herself in whatever field was necessary to do so.

The first step was her work on the International Union for Conservation of Nature (IUCN) Red List of Threatened Species. Recognizing the list's importance, Georgina—against advice—accepted the challenge of making it more useful for conservation. At the time, some listings reflected force of personality more than weight of evidence. By analyzing population ecological models, she and modeler Russell Lande derived five quantitative criteria that could be applied transparently and repeatably to any species to assess its risk of extinction. In piloting these revolutionary criteria through the approval process, Georgina's characteristically respectful, patient, logical, and focused arguments convinced the skeptics, bringing a rigor to Red List assessments that provided a robust basis to the legal protection of species. This enabled comprehensive assessments of all species across major taxonomic groups and led to analyses of which features of species' ecology and life history made them more susceptible to human impacts and which threats posed the greatest risk.

The first comprehensive Red List assessments found that 12% of birds and 24% of mammals were threatened with extinction, prompting the global signatories to the United Nations (UN) Convention on Biological Diversity (CBD) in 2002 to commit to substantially reducing the rate of biodiversity loss by 2010. To determine what the rate of biodiversity loss was, Georgina led the biodiversity component of the UN's Millennium Ecosystem Assessment in 2005, which marshaled all available evidence to show the rate and severity of ecosystem degradation. Georgina went on to influence the design of many of the science-based indicators of the global status and trends of biodiversity used to track progress toward internationally agreed-upon targets; she also helped to set up ZSL's Indicators and Assessments Unit in 2006 as a hub for such work.

The world failed to meet the CBD 2010 target. Realizing that nature being undervalued was a major problem, Georgina increasingly transcended disciplinary and science-policy boundaries. Her work on the unprecedented U.K. National Ecosystem Assessment (2009–2011) established a "natural capital" framework for decision-making, which viewed the state of nature as an asset. This and the 2010 Lawton Report ("Making Space for Nature"), on which she also worked, started a snowball effect on U.K. policy as the government explicitly acknowledged that addressing the decline in nature was first and foremost an economic problem with consequences for health and well-being. A 2011 Natural Environment White Paper made an astonishing key commitment not just to halt the decline in nature but to reverse the trends of the past century. The Natural Capital Committee (NCC)—the first organization of its kind, directly advising the U.K. government—was established in 2012 with Georgina as a founding member. On the NCC's recommendation, an innovative national 25 Year Environment Plan was published in 2018. The same principles underpin the Agriculture and Environment Bills currently under consideration by Parliament.

Our first collaborations with Georgina were so fascinating, so inspiring, and so enjoyable (she had a mischievous sense of humor) that we soon became hooked on the same challenges that absorbed her. We started working with her around the time when, in 2000, she became ZSL's director of science and head of its Institute of Zoology. She was an inspirational and transformative leader and role model. She demonstrated and encouraged crystal-clear strategic thinking, she listened to and supported everyone equally, and she never dominated the discussion or raised her voice (although keen observers could spot a raised eyebrow).

Despite Georgina's aversion to the limelight, she received countless awards, honors, and appointments. She was elected as a fellow of the Royal Society in 2002, won Japan's International Cosmos Prize in 2007, became the first female president of the British Ecological Society in 2011, and was made a Dame Commander of the Order of the British Empire in 2015 (but those who called her Dame Commander did so at their peril). After 23 years at ZSL, she moved to Imperial College London in 2006 to lead the Centre for Population Biology and then set up her own institute, the Centre for Biodiversity and Environment Research, at University College London in 2012. She stepped down as director in 2018 to concentrate on research and policy but still made time for everyone who needed her support and advice.

Georgina continued working until a few days before her death. Among her 2020 research papers are an analysis showing that it may not be too late to bend the curve of biodiversity and restore some of what has been lost and a framework to ensure that decisions about using nature do not shortchange future generations. As the links between how we use nature and the current pandemic become clearer, the momentum from world leaders to address biodiversity loss is growing. Georgina has left as her legacy the tools we need to coexist with nature. ■

[1]Department of Life Sciences, Natural History Museum, London, UK. [2]Department of Life Sciences, Imperial College London, Silwood Park, Ascot, UK. [3]Centre for Biodiversity and Environment Research, Department of Genetics, Evolution, and Environment, University College London, London, UK. [4]Institute of Zoology, ZSL, Regent's Park, London, UK. Email: kate.e.jones@ucl.ac.uk

10.1126/science.abf1559

PHOTO: JUSSI PUIKKONEN/KNAW

Published by AAAS

POLICY FORUM

BIOTECH REGULATION

Community-led governance for gene-edited crops

A post–market certification process could promote transparency and trust

By **Jennifer Kuzma**[1] *and* **Khara Grieger**[2]

In August 2020, the U.S. Department of Agriculture (USDA) began implementing new regulations for genetically engineered (GE) organisms, the SECURE (sustainable, ecological, consistent, uniform, responsible, efficient) rule (*1*). SECURE marks the first comprehensive reform of U.S. genetically modified (GM) crop oversight since the agency's initial approach in 1987 (and after several unsuccessful attempts to update its regulations over the past two decades) [see (*1*) for definitions of GE and GM crops]. The USDA estimates that under this substantial departure from its prior approach, 99% of GM plants will be exempt from premarket field testing and data-based risk assessment requirements (*2*). This rule has potential implications for international trade as the European Union (EU) is taking a more stringent approach to regulating gene-edited crops and will track them in the marketplace (*3*). We are also concerned that developers of gene-edited and GM (i.e., biotech) crops, who largely support the SECURE approach (*4*), are reconstituting the same conditions that led to public rejection and mistrust of the first generation of GM foods (*3*). To earn greater public trust and transparency, as well as enhance the ability to track gene-edited plants entering the marketplace, we therefore propose a "community-led and responsible governance" (CLEAR-GOV) coalition and certification process for biotech crop developers based on transparent information sharing about current and anticipated market uses of biotech crop varieties.

REGULATION OF BIOTECH CROPS

After a series of stakeholder meetings, the USDA Animal Plant Health Inspection Service (APHIS) proposed the new SECURE rule in mid-2019 and finalized the rule in May 2020. SECURE substantially changes the approach adopted by USDA-APHIS to regulating biotech crops. Because earlier generations of GM plants were engineered using plant-pest DNA sequences from *Agrobacterium*, the use of these sequences provided a regulatory basis for the USDA under its plant-pest regulatory authorities. But because this is no longer the only method used to genetically engineer plants, several plants have in the past decade gone unregulated by the USDA. SECURE recenters the regulations on "plant-pest risk" (defined as "the potential for direct or indirect injury to, damage to, or disease in any plant or plant product resulting from introducing or disseminating a plant pest, or the potential for exacerbating the impact of a plant pest"), as opposed to the mere presence of plant-pest sequences. We view this as positive, as many DNA fragments from plant pests have little to do with environmental or agricultural risk. Another positive attribute of SECURE is that if a plant contains a combination of a plant-trait–mechanism of action (MOA) that has already been reviewed by the USDA, the new product would be exempt from review. This allows the agency to expend limited resources on new biotech crops rather than variations of previous ones.

However, the SECURE rule has several shortcomings. First, in comparison to a proposed 2017 rule, it abandons a focus on noxious weed risks under the Plant Protection Act. A demonstrated category of risks from the first generation of GE crops centered around the evolution of resistant weeds (*5*). Although the USDA will review the "weedy impacts of the plant and its sexually compatible relatives" during its regulatory status review (RSR), if the crop does not pose an increased plant-pest risk, it is not subject to regulation [(*1*), p. 29835].

Second, it puts forth several regulatory exemptions based on whether the genetic change could conceivably have been achieved through conventional breeding, and these exemptions are not necessarily risk-based (*6*). Some gene-edited crops with single point mutations—or other changes from gene editing that could conceivably be found in the biotech crop's gene pool—may pose substantial risk. For example, small DNA mutations can lead to changes in the amounts of plant chemicals that are harmful to nontarget insects or human health (*7*). A 2016 report by the U.S. National Academies of Science, Engineering, and Medicine (NASEM) suggested screening both conventionally bred and GM crops for potential risks (6). Another NASEM report justified a closer look at GM crops in regulation given public concern and our shorter history with consuming them (*8*). Regulating new gene-edited crops makes sense from risk-based and public-legitimacy standpoints.

Third, and most important for our vision of CLEAR-GOV, most biotech crops will not go through regulatory pathways that require formal risk assessment, and opportunities for peer-review and public input are lacking. For example, developers will be able to self-determine whether their GE crop falls into an exempt area with no USDA-APHIS review or by requesting a letter of confirmation from USDA-APHIS. The USDA describes the confirmation process as "functionally equivalent to" the existing "Am I Regulated?" (AIR) process that has exempted over 100 GM crops, including many gene-edited crops, from USDA-APHIS regulation [(*1*), p. 29801]. Neither the AIR nor the new SECURE process provides opportunities for public, stakeholder, or expert input.

If a biotech crop is not exempt through the self-exemption or USDA confirmation process, it will undergo an RSR, a key decision point for whether a new biotech crop is regulated. This involves a scientific review of what is known about the host, its modification, and the environment to determine whether there is a potential plant pest risk. This is a crucial screening stage, yet it will not require publication of any risk or environmental assessment for notice and comment in the *Federal Register*. The USDA will, however, maintain a list of biotech crops that undergo the first step of the RSR process by plant, trait, and general MOA on its website [unless claimed as confidential business information (CBI) and thus kept out of public view].

If there is a potential plant-pest risk that is indicated from the RSR, USDA-APHIS will conduct a pest risk assessment in the second phase of the RSR (which overlaps with the agency's past permitting process) and publish it for comment in the *Federal Register*. After the plant-pest risk assessment, a determination will be made

[1]School of Public and International Affairs, Genetic Engineering and Society Center, NC State University, Raleigh, NC, USA. [2]Applied Ecology, Genetic Engineering and Society Center, NC State University, Raleigh, NC, USA. Email: jkuzma@ncsu.edu

Published by AAAS

USDA SECURE regulatory pathways for GE plants

This schematic depicts regulatory pathways and places for public information or input. It shows the general process and does not contain details for every step. The U.S. Department of Agriculture (USDA) may put forth new categories of exemptions owing to achievability by conventional breeding. These will also undergo public posting and a comment period before a potential plant–pest risk determination is made, however.

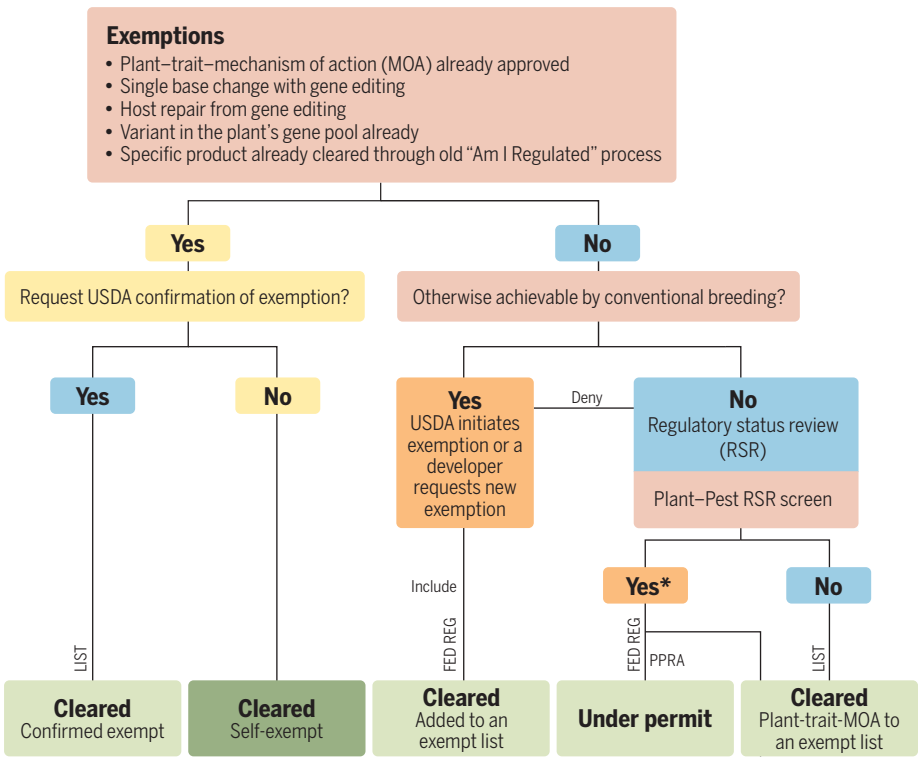

Issues considered by USDA to make a decision about which regulatory pathway applies

USDA makes a determination

Product developer makes a self-determination

USDA shares written assessments with the public in the Federal Register ("FED REG") for public comment prior to decision-making

USDA will keep a public record ("LIST") of some form on its website of the genetically engineered (GE) plant products cleared for the market (although the information on the LIST may be limited by confidential business information, or for confirmed exemptions may omit the phenotype and gene function)

No information will be required to be made publicly available

*If a potential plant–pest risk is identified, the developer has a choice to immediately apply for a permit or ask USDA for plant–pest risk assessment (PPRA). After assessment, USDA may determine a low likelihood of plant–pest risk and put the GE plant-trait-MOA on an exempt list, or require permitting conditions. SECURE, sustainable, ecological, consistent, uniform, responsible, efficient; GE:genetically engineered.

GRAPHIC: MELISSA THOMAS BAUM/*SCIENCE*

whether a permit is needed to limit environmental release in some way (e.g., to certain geographic regions). If no restrictions are put in place under a permit, the crop would be cleared for commercial use and interstate commerce.

COMMUNITY-LED RESPONSIBLE GOVERNANCE

The lack of information about biotech crops that will be exempt, as well as the deficit of opportunities for peer and public review of the basis for initial RSR decisions, is likely to exacerbate low levels of public trust (*9*). For example, according to the USDA's informational webinar on 5 August 2020, developers do not need to submit information about the function of the gene or the plant phenotype through the confirmation process, and the USDA will allow CBI to be removed under the same policy as with the AIR process. Furthermore, allowing developers with a clear conflict of interest to self-determine exemptions is likely to promote public skepticism, not confidence, as well as have potential implications for international trade. Therefore, we propose to augment formal government oversight of biotech crops with a voluntary certification process that will bolster transparency and increase the availability of public information and the ability to track gene-edited plants. The process that we suggest will also make possible external scientific peer review because of greater public information about the presence and use of GM crops.

In contrast to previous cooperative governance models for gene-edited crops that center on decision-making for environmental release (*10*), we focus on the sharing of basic information in pursuit of transparency, which is a cornerstone of responsible governance. As a starting point for community discussion about the content and structure of a CLEAR-GOV approach, we propose the following.

CERTIFICATION

To incentivize biotech developers' participation in greater information sharing, there should be rewards. Biotech crop developers would be able to obtain a CLEAR-GOV certification by contributing information about biotech crops and their market uses through open-access data repositories. Although this cannot guarantee public trust, a certification process could at least signify that the biotech crop producer is striving to become more transparent and trustworthy according to community-derived standards. As consumers increasingly include stewardship practices of products in purchasing behavior (*11*), a certification for biotech developers could help provide a win for consumers, industry, and regulatory officials in terms of having a better understanding of biotech crops on the market. Other certification programs have been successful, including those in forestry and farming of select commodities (*10, 12*). A verification scheme for gene-edited crops is currently being considered by a nonprofit coalition under the Center for Food Integrity (CFI) (*13*). Our approach differs from CFI's in that successful certification under CLEAR-GOV would be granted to developers who submit certain data and information to a publicly accessible repository. Minimum requirements of information in compliant formats would be required for CLEAR-GOV certification.

REPOSITORY OF HOST-TRAIT-PURPOSE-ENVIRONMENT-USE

Certification would depend on the sharing of data and information in the open-access repository whether or not the biotech crop is exempt from regulatory review or has cleared USDA regulations. Minimum categories of public information, in both common and scientific terms, would include the species and variety of plant, type of trait modified, the purpose of the trait modification (or improved quality), and the general areas where the crop is grown (without compromising farmer or field security).

Once a crop is sold on the market, CLEAR-GOV staff should work with the

Published by AAAS

biotech crop developer to compile a list of general food or other market uses for the biotech crop wherever possible. The list of uses would be linked to the plant host-trait-purpose-environment list and be available online. However, the identification of uses will be difficult for biotech crops that end up in larger commodity markets or food-ingredient streams. Certification in these cases will need to be made on a case-by-case basis to ensure that the desire for transparency is balanced with the limits of biotech crop developers' own knowledge of the use of their GM crop in the marketplace. The repository should also provide mechanisms for protecting privacy, confidentiality, and proprietary information and include options to balance the tensions between data provision and data protection.

Many biotech food ingredients and some gene-edited, whole-plant foods will not require labeling at the point of sale to consumers under the National Bioengineered Food Disclosure Standard (*14*). Thus, CLEAR-GOV would fill a critical gap for consumer access to information about the presence of a biotech crop on the market for multiple reasons. Regulatory databases will not be enough to ensure transparency for four reasons. First, if the biotech crop is not regulated by USDA SECURE (e.g., falls into the self-exempt category or the USDA's categorical exemptions), there will not be a publicly available record of that biotech crop being used in the United States. Second, CLEAR-GOV ensures that a minimal amount of information (e.g., plant host, trait, purpose, and potential uses) is available. This information could otherwise be claimed as CBI in regulatory documents. Third, CLEAR-GOV is designed to make it easier for consumers and stakeholders to find all biotech crop information in one place. Given the multiple and complex regulatory pathways under SECURE and through other agencies in the Coordinated Framework, many people may not know where to look for regulatory clearance information. Finally, CLEAR-GOV will translate plant-host, trait, purpose, and possible uses into nontechnical terms that are understandable to the public, whereas regulatory submissions often do not. As new types of biotech crops evolve for new purposes, the repository will need to be adaptive, flexible, and continuously improved and updated.

COMMUNITY-LED COALITION

We propose that CLEAR-GOV be operationalized through a coalition formed under the aegis of a new nonprofit organization (NPO) without a prior history in biotech crops, so it is not viewed as biased from the start. NPO staff must have expertise to support open-access data repository infrastructure and oversee data quality. The coalition should be cofunded by government (nonregulatory) agencies, public-sector donors, and private-sector funds if they are distanced from biotech crop producers. For example, studies on monarch butterfly impacts from GM crops were commissioned by a multisector coalition (*15*).

Coalition leadership should consist of nonconflicted, expert staff in the social and natural sciences, law, agriculture and business, data sciences, and ethics. A stakeholder advisory board with people from industry, government, environmental and consumer NGOs, trade organizations, and academe would provide input to devise the certification process. A public advisory group composed of consumers, indigenous and marginalized groups, and community groups would also help develop the certification. Members of the public will be one category of end users for the CLEAR-GOV data repository and therefore, they have important perspectives on the provision of meaningful and understandable information.

"...we focus on the sharing of basic information in pursuit of transparency, which is a cornerstone of responsible governance."

Both advisory groups would be tasked with helping staff to detail the certification scheme, the type of information deposited, and the presentation of data on the public interface; reviewing and providing input for decisions to certify individual biotech crops and their developers; and periodically revisiting the repository design and making iterative improvements. Both coalition advisory groups and CLEAR-GOV staff would meet periodically together to gather input from biotech crop developers on the design and operations of the repository. Multisector coalitions have been employed in other cases to promote the sustainable production of commodities, and historical lessons should be derived from these experiences as the design and redesign of CLEAR-GOV take place (*10*, *12*).

Lessons can be drawn from other fields in which multistakeholder coalitions operate parallel or complementary to a regulatory agency. For instance, the Center for Science in the Public Interest has worked alongside federal regulatory agencies (including the U.S. Food and Drug Administration) and has housed independent databases on food safety. The U.S. National Nanotechnology Initiative has developed international Communities of Research between U.S. and EU researchers in the field of nanomaterial environmental, health, and safety topics and frequently exchanges information and dialogue regarding nanosafety, including collaborations on the development of databases and exchanges with industry partners.

EXPANSION TO OTHER AREAS

If CLEAR-GOV is successful in the above "phase 1" of the repository and certification, the coalition could consider expanding to promote the sharing of studies aimed at assessing the safety of biotech crops. CLEAR-GOV may even expand to fill a gap for convening and funding more holistic assessments of the risks and benefits of biotech crops from sustainability and socioeconomic perspectives.

We realize that it may be challenging for biotech developers to embrace the concept of providing transparent, open data regarding new GM crops through such a data repository. However, the benefits of doing so may help overcome concerns about transparency and trust that have lingered since the intense debates of the first generation of GM foods. Coalitions for responsible governance such as CLEAR-GOV could fill a critical governance gap as roles for federal agencies diminish and a plethora of new biotech products enter the market. ■

REFERENCES AND NOTES

1. *Fed. Regist.* **85**, 29790 (2020).
2. E. Stokstad, *Science* (2020). 10.1126/science.abc8305
3. See summary of comments on proposed rule in (1). See remarks in (2).
4. J. Kuzma, *Issues Sci. Technol.* **35**, 80 (2018).
5. M. L. Zapiola, C. A. Mallory-Smith, *PLOS ONE* **12**, e0173308 (2017).
6. National Academies of Sciences, Engineering, and Medicine, *Genetically Engineered Crops: Experiences and Prospects* (National Academies Press, 2016).
7. P. Morandini, *N. Biotechnol.* **27**, 482 (2010).
8. National Academies of Sciences, Engineering, and Medicine, *Genetically Modified Pest-Protected Plants: Science and Regulation* (National Academies Press, 2000).
9. J. de Jonge, J. C. M. van Trijp, I. A. van der Lans, R. J. Renes, L. J. Frewer, *Appetite* **51**, 311 (2008).
10. N. R. Jordan *et al.*, *EMBO Rep.* **18**, 1683 (2017).
11. A. Risius, M. Janssen, U. Hamm, *Appetite* **113**, 246 (2017).
12. Steering Committee of the State-of-Knowledge Assessment of Standards and Certification, "Toward sustainability: The roles and limitations of certification" (RESOLVE Inc., 2012).
13. Center for Food Integrity, "Coalition for Responsible Gene Editing in Agriculture"; https://foodintegrity.org/programs/gene-editing-agriculture/.
14. G. Jaffe, Biotech Blog: *The Final National Bioengineered Food Disclosure Standard* (2019); https://cspnet.org.
15. Pew Initiative on Food and Biotechnology, "Three years later: Lessons from the Monarch Butterfly controversy" (2002); www.pewtrusts.org/en/about/news-room/press-releases-and-statements/2002/05/30/three-years-later-lessons-learned-from-the-monarch-butterfly-controversy.

ACKNOWLEDGMENTS

We thank F. Gould and reviewers for feedback.

10.1126/science.abd1512

Published by AAAS

LINGUISTICS

Alphabets and their origins

A new documentary series surveys the inception and evolution of the written word

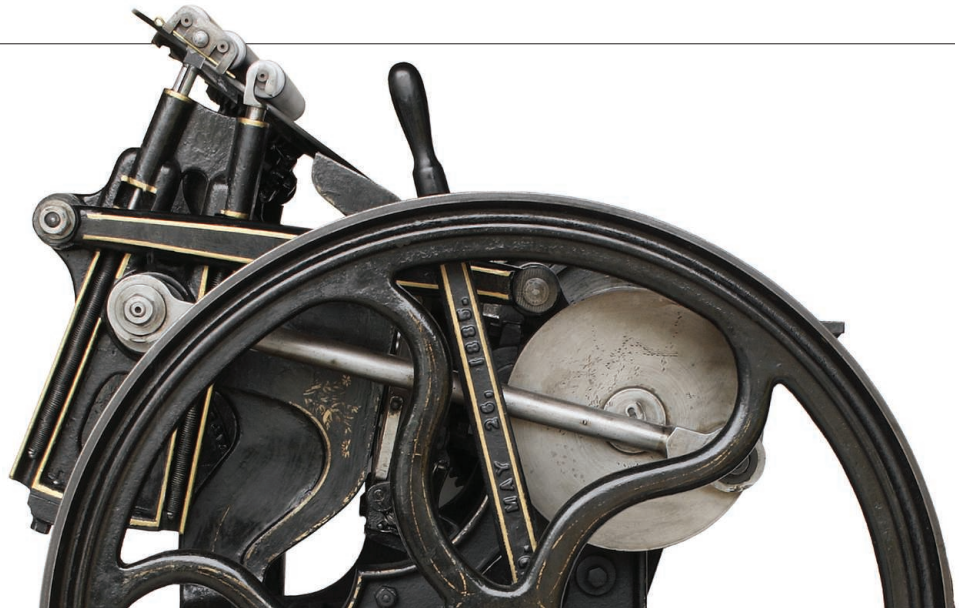

Latin alphabetic letter forms matched perfectly the movable metal type used in the first printing presses.

PHOTO: ISTOCK.COM/NEBARI

By **Andrew Robinson**

Written communication is among the greatest inventions in human history, yet reading and writing are skills most of us take for granted. After we learn them at school, we seldom stop to think about the mental-cum-physical process that turns our language and thoughts into symbols on a piece of paper or computer screen, or the reverse process whereby our brains extract meaning from written symbols.

The neural correlates of reading remain a mystery to neuroscientists. They once assumed that an auditory pathway in the brain was used for alphabetic symbols and a visual pathway for Chinese characters but have since discovered experimentally that both neural pathways are used together—if in differing proportions—in each instance. Meanwhile, key aspects of writing's development have yet to be demystified by archaeologists and philologists. Was there a single origin, circa 3100 BCE—either cuneiform in Mesopotamia or hieroglyphs in Egypt—or did writing arise in multiple places independently? When and how did Chinese characters, first identified on Shang oracle bones dated to circa 1200 BCE, originate? And what prompted the invention of the radically simple alphabetic principle, circa 1800 BCE, in a script that contains certain signs resembling Egyptian hieroglyphs?

The Secret History of Writing—a BBC television series broadcast in three parts, two of which have been adapted as NOVA's *A to Z: The First Alphabet* and *A to Z: How Writing Changed the World*—explores these questions and more. Both versions of the series are intelligent, articulate, and visually imaginative, discussing five millennia of writing—by hand, by printing, and by computer keyboard. The programs feature notable scholars of many scripts and cultures, such as Assyriologist Irving Finkel, Egyptologist Pierre Tallet, and Sinologist Yongsheng Chen, interviewed by Lydia Wilson, an academic with expertise in medieval Arabic philosophy and the winning ability to interrogate authorities at their own level while rendering their views broadly understandable and engaging.

A to Z: The First Alphabet
David Sington, director
NOVA, 2020.
54 minutes.

A to Z: How Writing Changed the World
David Sington, director
NOVA, 2020.
54 minutes.

The idea for the series grew from a long-standing friendship between writer-director David Sington and calligrapher Brody Neuenschwander, who charismatically demonstrates his skill at penning ancient and modern scripts, using materials such as Egyptian papyrus, European parchment, and Islamic paper.

At one point, Neuenschwander observes that Latin alphabetic letter forms, unlike calligraphic scripts such as Chinese and Arabic, were ideally shaped for the movable metal type created by Johannes Gutenberg in the 1450s—a technology that enabled the growth of European literacy and the European scientific revolution beginning in the 16th century. The pairing was so ideal, in fact, that the Gutenberg Bible fooled some scholars for centuries, who believed it was handwritten and cataloged it as such. "I think Gutenberg would have been delighted by our confusion, because what he was trying to achieve with the printing of this book was to produce a book, by a new technique, that people would think was just as good as the manuscripts that they were used to buying and reading," observes archivist Giles Mandelbrote. He was trying to do "something new that would seem old."

In another scene, Finkel, a lifelong scholar of cuneiform at the British Museum, avidly dissects a few signs on early clay tablets to explain the rebus principle, which permits the sounds of pictograms, written together, to express the sound of an unrelated, nonpictographic word. Thus, for example, the plainly pictographic Sumerian sign for barley, pronounced "she," can be written beside the pictographic sign for milk, pronounced "ga," to create two signs read as "shega," meaning something like "beautiful." As Finkel reasonably speculates, rebuses are so "obvious" that they could have been developed in languages anywhere in the world, supporting the hypothesis that writing may have arisen on multiple, separate occasions.

Today, pictography has returned to writing in the form of international transport symbols and computerized emojis. Meanwhile, many young people in China, having become habituated to smartphone writing, are increasingly using the Romanized spelling known as Pinyin ("spell sound") and, as a result, some no longer know how to write Chinese characters.

Could smartphones, or the internet more generally, eventually lead to a universal writing system, independent of particular languages, like the one envisioned by polymath Gottfried Leibniz in 1698? It is unlikely, in my view, and, according to Wilson, undesirable. "A world of perfect communication is also a world of cultural uniformity," she cautions. ■

The reviewer is the author of *The Story of Writing: Alphabets, Hieroglyphs and Pictograms* (Thames and Hudson, 2007) and *Writing and Script: A Very Short Introduction* (Oxford Univ. Press, 2009). Email: andrew@andrew-robinson.org

10.1126/science.abf4509

Published by AAAS

CORONAVIRUS

Probing COVID's complexity in real time

The pandemic is as much about society, leaders, and values as it is about a pathogen

By **Samuel V. Scarpino**

In 2019, the Global Health Security (GHS) Index ranked the United States as the most prepared country in the world for a pandemic. Just over a year later, the United States has not only failed to control coronavirus disease 2019 (COVID-19), many consider the nation's response to the pandemic to be one of the worst in the world. Was the GHS Index biased? Or did the country's preparedness change drastically during this period?

Answering these questions requires understanding the pandemic as a complex system—one that reveals our greatest strengths and most debilitating weaknesses. In his provocative new book, *Apollo's Arrow,* Nicholas Christakis uses such an approach, drawing on his experience as both a hospice physician and a leading network scientist to integrate societal, technological, and biological data into a single cohesive narrative of the unfolding pandemic. Not surprisingly, the book is far-ranging, covering relevant aspects of epidemiology, human behavior, social networks, technology, immunology, and applied mathematics.

The book's title refers to a plague that befell the Achaean troops in *The Iliad*, which was brought about by the Greek god Apollo in response to the bad behavior of the Achaean leader Agamemnon—a fitting analogy for our current predicament. Christakis turns to another literary analogy to further illuminate the complexity of human behavior during pandemics, which can range from fear-induced debilitation to profound acts of courage, with a short story by Ernest Hemingway about a soldier, a nurse, and a patient dying of the 1918 flu. (The nurse demonstrates incredible heroism by caring for the patient until he dies, whereas the soldier cannot even bring himself to embrace the nurse, his lover, for fear of infection.) Within the past 6 months, we have seen similarly divergent responses to the current pandemic, from recovered individuals selflessly donating plasma to defiant customers who refuse (sometimes violently) to wear a mask while out in public.

As Christakis repeatedly shows, the United States could have taken a different path. "The *upward* trajectory as the pandemic initially took root in each nation was grimly similar," he observes. While countries such as Vietnam, Mongolia, New Zealand, and Japan quickly implemented test-trace-isolate strategies, which accounted for the role of so-called "superspreading" events in COVID-19 transmission, and were able to control the epidemic, other countries, including the United States, the United Kingdom, and India, failed to do so, revealing the joint effects of underfunded public health systems and a lack of experience dealing with diseases that, like COVID-19, require a complex-systems approach to control.

Medical staff collect a driver's blood for a COVID-19 virus antibody test in Inglewood, California, on 19 June 2020.

PHOTO: MARK RALSTON/AFP/GETTY IMAGES

"In many real-world social networks, most people have very few contacts and a small minority have many connections," notes Christakis, highlighting one of the many factors that can influence disease transmission. This variability in social contact network structure, coupled with human behavior and pathogen biology, can result in epidemics where a minority of infected individuals give rise to a majority of cases. COVID-19 exploits this variation, perpetuating itself largely by way of superspreading events.

Conventional public health wisdom in the United States suggests that forward-looking contact tracing is essential for preventing epidemics. However, for diseases that rely heavily on superspreading events for sustained transmission, backward-facing case investigation is often even more important. As Christakis repeatedly shows, seemingly trivial differences in the public health response to COVID-19—for example, Japan's focus on "cluster-busting" versus the investment in contact tracing in the United States—can lead to large differences in outcome. Such dependence is the hallmark of complex systems.

In the United States, the COVID-19 pandemic has been aggravated by long-standing racism and xenophobia. Communities of color, Native Americans, and recent immigrants too often have reduced access to health care, a higher disease burden, and greater economic insecurity, argues Christakis, and the outcomes for those in these communities who contract the virus have been staggering. Native Americans, Blacks, and Hispanics, for example, have thus far experienced at least twice the population-adjusted rate of mortality. Here, Christakis echoes growing cries that we must confront and repair the long-standing health inequalities borne by nonwhite communities.

There is no shortage of books that argue that pandemics are complex or ones that discuss the public health issues raised in *Apollo's Arrow*, and it is unlikely that there will be a shortage of future works that dissect domestic and international responses to the COVID-19 pandemic. What sets Christakis's work apart is that it was written in real time by an expert who astutely shows how pandemics are as much about our societies, values, and leaders as they are about pathogens. ■

Apollo's Arrow: The Profound and Enduring Impact of Coronavirus on the Way We Live
Nicholas A. Christakis
Little, Brown, 2020. 384 pp.

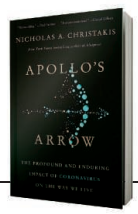

The reviewer is at the Network Science Institute, Northeastern University, Boston, MA 02115, USA, and the Santa Fe Institute, Santa Fe, NM 87501, USA. Email: s.scarpino@northeastern.edu

10.1126/science.abe9731

Published by AAAS

The repeal of a rule prohibiting roads within Alaska's Tongass National Forest has put the temperate rainforest at risk.

PHOTO: YEGOROV/SHUTTERSTOCK

Edited by **Jennifer Sills**

Retraction

The authors of the Report "Secondary siRNAs result from unprimed RNA synthesis and form a distinct class" (*1*) have been made aware of duplications in Fig. 2D and supplementary figures S1C and S3C. We attempted to find the original data from 2007, but all authors have left the Hubrecht Institute, where the work was performed, and the data could not be located. Although other data in the paper were consistent with the conclusions supported by Fig. 2D and figs. S1C and S3C, all data were taken into account in the review of the paper, and the loss of these figures weakens the conclusions. Therefore, in the spirit of full transparency, we have decided to retract the paper.

Titia Sijen[1], Florian A. Steiner[2], Karen L. Thijssen[3], Ronald H. A. Plasterk[4]*
[1]Netherlands Forensic Institute, 2497GB The Hague, Netherlands. [2]University of Geneva, 1211 Geneva, Switzerland. [3]Rotterdam, Netherlands. [4]Frame Cancer Therapeutics, 1098XG Amsterdam, Netherlands.
*Corresponding author.
Email: ronald.plasterk@frametherapeutics.com

REFERENCES AND NOTES

1. T. Sijen, F. A. Steiner, K. L. Thijssen, R. H. A. Plasterk, *Science* **315**, 244 (2007).

10.1126/science.abf4837

Eroded protections threaten U.S. forests

Despite record-breaking mega-fires in 2020 (*1*), the U.S. Department of Agriculture (USDA) recently removed the 2001 Roadless Rule protection for 9.37 million acres of Tongass National Forest in Alaska (*2*). The intact and fire-resistant Tongass temperate rainforest is home to valuable biodiversity and functions as an important carbon sink, making it vital in combatting both global extinction risk and climate change (*3*, *4*). In light of catastrophic fires and rapid climate change, the government needs to rigorously and transparently evaluate costs and benefits before repealing any environmental protections.

Ending the rule prohibiting roads in the Tongass exposes 165,000 acres of old-growth rainforest to logging (*2*) and leaves the remaining rainforest vulnerable to degradation from road-building and potential mining and fossil fuel extraction (*5*, *6*). Industrial expansion has ecological repercussions through increased emissions, diminished carbon sequestration, and reduced fire resistance (*6*) as well as potential downstream socio-economic effects for local fishery and tourism industries (*7*). The Roadless Rule repeal was opposed by several local tribes and 96% of the quarter million letters submitted by the public (*2*, *7*). The repeal will also enable an economically unviable timber program that has cost U.S. taxpayers more than half a billion dollars in losses since 1980 (*8*).

The government's decision to erode protection of Tongass National Park sets a precedent to roll back protections for other remaining intact forests (*9*) that provide critical carbon storage, protection against species extinction, and refuge against the effects of climate and fire-season intensification (*2*, *3*, *10*). Instead of forcing taxpayers to subsidize an ecologically and financially shortsighted initiative, activities such as native reforestation should be implemented. Strategic reforesting, particularly after fires, can provide short- and long-term benefits for the environment, society, and economy by increasing carbon storage (*11*), reducing erosion, providing habitat for displaced wildlife, and supporting the long-term sustainability of industries like tourism and carbon farming (*12*). In the face of global climate change and intensifying fire seasons, the U.S. government should be seeking to fortify rather than repeal evidence-based protections in a way that supports ecological, social, and economic objectives.

Katharina-Victoria Pérez-Hämmerle[1,2]*, Katie Moon[3,4], Hugh P. Possingham[2,5], Maria Jose Martinez-Harms[6], James E. M. Watson[1,2,7]
[1]School of Earth and Environmental Sciences, The University of Queensland, St. Lucia, Brisbane, QLD 4067, Australia. [2]Centre for Biodiversity and Conservation Science, The

Published by AAAS

University of Queensland, Brisbane, QLD 4072, Australia. [3]Public Service Research Group, School of Business, University of New South Wales, Canberra, ACT 2601, Australia. [4]Centre for Ecosystem Science, School of Biological, Earth and Environmental Sciences, University of New South Wales, Sydney, NSW 2052, Australia. [5]School of Biological Sciences, University of Queensland, Brisbane, QLD 4072, Australia. [6]Center for Applied Ecology and Sustainability (CAPES), Pontificia Universidad Católica de Chile, Santiago, Chile. [7]Wildlife Conservation Society, Global Conservation Program, Bronx, NY 10460, USA.
*Corresponding author.
Email: k.perezhammerle@uq.edu.au

REFERENCES AND NOTES

1. P. E. Higuera, J. T. Abatzoglou, *Glob. Change Biol*. 10.1111/gcb.15388 (2020).
2. USDA, Forest Service, "Special Areas; Roadless Area Conservation; National Forest System Lands in Alaska," *Federal Register* (2020).
3. S. L. Maxwell *et al*., *Sci. Adv*. **5**, eaax2546 (2019).
4. J. W. Coulston *et al*., in "Moving from status to trends: Forest Inventory and Analysis (FIA) symposium 2012," R. S. Morin, G. C. Liknes, Eds. (Gen. Tech. Rep. NRS-P-105. Newtown Square, PA: USDA, Forest Service, Northern Research Station [CD-ROM]), pp. 170–176.
5. W. F. Laurance, M. Goosem, S. G. Laurance, *Trends Ecol. Evol*. **24**, 659 (2009).
6. P. Potapov *et al*., *Sci. Adv*. **3**, e1600821 (2017).
7. USDA, Forest States, "Alaska Roadless Rule: Draft Environmental Impact Statement, Public Comment Report" (2020).
8. Taxpayers for Common Sense, "Cutting our losses after 40 years of money-losing timber sales in the Tongass" (2020).
9. M. B. Mascia, S. Pailler, *Conserv. Lett*. **4**, 9 (2011).
10. J. E. M. Watson *et al*., *Nat. Ecol. Evol*. **2**, 599 (2018).
11. G. M. Domke *et al*., *Proc. Natl. Acad. Sci. U.S.A*. **117**, 24649 (2020).
12. R. Chazdon, P. Brancalion, *Science* **365**, 24 (2019).

10.1126/science.abf5654

Space debris puts exploration at risk

Humans have now lived aboard the International Space Station (ISS) for 20 years (*1*). As we look toward the next 20 years, we must address the dangers that space debris poses to both manned missions and crucial satellites. National policy-makers and international organizations must develop actionable rules and regulations that preserve our ability to explore space.

With tens of millions of pieces of space junk rocketing around our planet at thousands of kilometers an hour, debris is a substantial threat to our expanding networks of satellites and even the ISS itself (*2*–*4*). The European Space Agency (ESA) puts much of the blame on the failure to properly dispose of expiring satellites (*2*). The recently signed Artemis Accords similarly point to the value of "end-of-mission planning and implementation [and…] post-mission disposal" in reducing debris (*5*). With the rapid expansion of the satellite orbital population—many of which are relatively cheaply produced with comparatively high failure rates (*6*)—this problem will likely get much worse before it gets better.

Unfortunately, Cold War cooperation led to rules designed primarily for nation states, not for the corporations that are now launching literally thousands of new satellites. Meanwhile, the nation states have mostly neglected to implement the necessary local space regulations that would promote the long-term sustainability of equitable space exploration. This tragedy of the commons will damage the space environment and eventually impair commercial space endeavors. Space debris threatens efforts ranging from the emerging mini-satellite mega-constellations that aim to democratize internet access to space tourism. In a worst case scenario, orbital debris could start a self-sustaining cascade of destruction that would litter the Low Earth Orbit with enough debris to make it effectively unusable (*7*).

To maintain a sustainable space environment, all states and their nationals must take responsibility for reducing the creation of new space debris. Both nations and private corporations should design more reliable satellites that are less likely to malfunction, deorbit satellites before they become inoperable and hazardous, and promote the emerging private-sector industries that are collecting defunct satellites and repairing and refueling older satellites. Developing public-private collaborations can enhance the tracking of even small man-made particles zooming around in orbit.

The United Nations' Committee on the Peaceful Uses of Outer Space (COPUOS) may be the most appropriate forum to accomplish these goals. COPUOS can provide both the desperately needed development of norms, the required regulatory support, and the necessary scientific and technical expertise to direct these efforts. During the past 20 years, astronauts on the ISS have conducted space-based research representing the work of scientists from more than 100 countries (*1*), and science diplomacy has often prefaced cross-boundary collaboration on Earth. We must preserve the amazing opportunities space exploration provides by developing better sustainable practices before it is too late.

Dov Greenbaum
Zvi Meitar Institute for Legal Implications of Emerging Technologies, IDC Herzliya, Herzliya, Israel; Harry Radzyner Law School, IDC Herzliya, Herzliya, Israel, and Department of Molecular Biophysics and Biochemistry, Yale University, New Haven, CT 06510, USA.
Email: dov.greenbaum@aya.yale.edu

REFERENCES AND NOTES

1. National Aeronautics and Space Administration, "International Space Station facts and figures" (2020); www.nasa.gov/feature/facts-and-figures.
2. ESA, "The current state of space debris" (2020); www.esa.int/Safety_Security/Space_Debris/The_current_state_of_space_debris.
3. ESA, "Space Debris by the numbers" (2020); www.esa.int/Safety_Security/Space_Debris/Space_debris_by_the_numbers.
4. R. Khatchadourian, "The elusive peril of space junk," *The New Yorker* (2020).
5. "The Artemis Accords: Principles for cooperation in the civil exploration and use of the Moon, Mars, Comets, and Asteroids for peaceful purposes" (2020), pp. 6–7; www.nasa.gov/specials/artemis-accords/img/Artemis-Accords-signed-13Oct2020.pdf.
6. S. A Jacklin, "Small-satellite mission failure rates," NASA Technical Memorandum (2019); https://ntrs.nasa.gov/citations/20190002705.
7. D. J. Kessler, *J. Spacecraft Rockets* **18**, 357 (1981).

10.1126/science.abf2682

TECHNICAL COMMENT ABSTRACTS

Comment on "Ancient origins of allosteric activation in a Ser-Thr kinase"

Yeonwoo Park, Jaeda E. J. Patton, Georg K. A. Hochberg, Joseph W. Thornton

Hadzipasic *et al*. (Reports, 21 February 2020, p. 912) used ancestral sequence reconstruction to identify historical sequence substitutions that putatively caused Aurora kinases to evolve allosteric regulation. We show that their results arise from using an implausible phylogeny and sparse sequence sampling. Addressing either problem reverses their inferences: Allostery and the amino acids that confer it were not gained during the diversification of eukaryotes but were lost in a subgroup of Fungi.
Full text: dx.doi.org/10.1126/science.abc8301

Response to Comment on "Ancient origins of allosteric activation in a Ser-Thr kinase"

Christopher Wilson and Dorothee Kern

Park *et al*. question one out of seven findings from Hadzipasic *et al*.: whether TPX2 allosterically regulates the oldest Aurora. We had already addressed the two concerns raised—sparse sequence sampling and not forcing the gene to the species tree—before publication. Moreover, we believe their ancestral sequence reconstruction would be consistent with a nonallosteric common ancestor, and we show large sequence differences caused by species tree–enforced gene trees.
Full text: dx.doi.org/10.1126/science.abd0364

ERRATA

Erratum for the Report "Activation of methane: A selective industrial route to methanesulfonic acid" (previously titled "Activation of methane to CH_3^+: A selective industrial route to methanesulfonic acid") by C. Díaz-Urrutia and T. Ott, *Science* **369**, eabe0416 (2020). Published online 7 August 2020; 10.1126/science.abe0416

Erratum for the Report "Global distribution of earthworm diversity" by H. R. P. Phillips *et al*., *Science* **369**, eabd9834 (2020). Published online 31 July 2020; 10.1126/science.abd9834

Published by AAAS

Cite as: Y. Park *et al.*, *Science* 10.1126/science.abc8301 (2020).

Comment on "Ancient origins of allosteric activation in a Ser-Thr kinase"

Yeonwoo Park[1]*, Jaeda E. J. Patton[1]*, Georg K. A. Hochberg[2], Joseph W. Thornton[3,4]†

[1]Committee on Genetics, Genomics and Systems Biology, University of Chicago, Chicago, IL, USA. [2]Max Planck Institute for Terrestrial Microbiology, Marburg, Germany. [3]Department of Human Genetics, University of Chicago, Chicago, IL, USA. [4]Department of Ecology and Evolution, University of Chicago, Chicago, IL, USA.

*These authors contributed equally to this work.

†Corresponding author. Email: joet1@uchicago.edu

Hadzipasic *et al.* (Reports, 21 February 2020, p. 912) used ancestral sequence reconstruction to identify historical sequence substitutions that putatively caused Aurora kinases to evolve allosteric regulation. We show that their results arise from using an implausible phylogeny and sparse sequence sampling. Addressing either problem reverses their inferences: Allostery and the amino acids that confer it were not gained during the diversification of eukaryotes but were lost in a subgroup of Fungi.

How allosteric regulation of proteins arose during evolution is a critical question in evolutionary biochemistry. Using ancestral sequence reconstruction (ASR) and biochemical experiments, Hadzipasic *et al.* (*1*) claim to have identified historical sequence substitutions that caused the acquisition of allostery from a nonallosteric ancestor during the evolution of Aurora kinase (AURK), a eukaryotic cell cycle regulator that is allosterically activated in animals by the TPX2 protein. Inferred ancestral sequences are conditional upon the set of extant sequences used and the phylogeny that describes their relationships, but Hadzipasic *et al.*'s sequence sampling was extremely sparse, and the phylogeny they used is implausible. We therefore investigated these shortcomings and their effects on the reconstruction of AURK evolution.

The phylogeny inferred by Hadzipasic *et al.* (Fig. 1A) is highly incongruent with the established phylogeny of eukaryotes (Fig. 1B). The Hadzipasic *et al.* phylogeny groups animals and plants together to the exclusion of fungi, but the monophyly of Opisthokonta (fungi, animals, and their unicellular relatives) has been extensively corroborated (*2*, *3*). Hadzipasic *et al.* also place microsporidians as the most basally branching eukaryotic lineage, despite strong evidence for their inclusion within Fungi (*4*). These incongruences are crucial to the claims of Hadzipasic *et al.*, because the nodes on their phylogeny between which allostery is claimed to have evolved represent ancestral species that in fact never existed: Aur_{ANC2}, the nonallosteric precursor, would be AURK in the last common ancestor of all eukaryotes except microsporidians, and Aur_{ANC3}, the first allosteric protein, would be AURK in the last common ancestor of animals and plants to the exclusion of fungi.

Hadzipasic *et al.* suggest that their AURK gene tree might be incongruent with the accepted species phylogeny because of gene duplication and loss, but this scenario is implausible: It requires an elaborate history of three gene duplications before the most recent common ancestor of eukaryotes, followed by 14 gene losses distributed so precisely that only a single resulting paralog has been retained in every eukaryote that has been sequenced (Fig. 1C). Hadzipasic *et al.* also suggest horizontal gene transfer (HGT) as a possible cause, but this would require a complex scenario in which every single AURK sequence on the phylogeny except for one descends from an HGT event, with every transfer replacing the recipient's original copy and leaving no trace of the event in any extant genome (Fig. 1D); this scenario is especially implausible because HGT between multicellular eukaryotes is rare (*5*).

A more likely cause of the incongruence of Hadzipasic *et al.*'s tree with the species phylogeny is long branch attraction (LBA) (*6*). The branches leading to microsporidians and ascomycetes may have been moved from their established position near animals toward the root, where they attach to an extremely long branch leading to the nearest outgroup [Polo-like kinases (PLKs)]. Microsporidians have previously been found to be subject to systematic LBA that moves them to an artifactual position as basal eukaryotes, especially when sampling in the Fungi is sparse (*7*). Strong support for misplaced branches is consistent with systematic bias caused by LBA (*7*).

We therefore repeated ASR using Hadzipasic *et al.*'s sequence set of AURKs and PLKs, but we constrained the phylogeny to follow established species relationships (Fig. 1, B and E). We focused on the 15 sequence states from Aur_{ANC3} that experimentally confer allostery when introduced into the nonallosteric Aur_{ANC2} (Fig. 1F). We found that the direction of these substitutions is almost completely reversed relative to the trajectory proposed by Hadzipasic *et al.* (Fig. 1, E to G). The deepest AURK ancestor (AncEukarya) now contains 14 of the 15 states associated with allostery and only one of the nonallosteric states; the other 14 nonallosteric states were all gained within the Fungi. Repairing the major topological errors in Hadzipasic *et al.*'s phylogeny is therefore sufficient to remove the evidence for their paper's central claims.

We next studied the effect of improved sequence sampling. AURKs are present across eukaryotes, but the sequence set analyzed by Hadzipasic *et al.* included only 19 AURKs; all but three of these were from animals and fungi, which account for only a small fraction of eukaryotic diversity. Within fungi, only ascomycetes and a single microsporidian were represented, and only a single species each of plant and amoeba were included. We therefore acquired and aligned 324 AURK and 315 PLK protein sequences, broadly sampled from five major eukaryotic taxa (Fig. 2A): Fungi, Holozoa (animals and unicellular relatives), Archaeplastida (plants and green and red algae), Amoebozoa (amoebae), and SAR (stramenopiles, alveolates, and rhizarians). Within Fungi, we included 137 AURKs from numerous taxonomic groups to better resolve the phylogenetic position of Fungi and the amino acid states within it.

We used this alignment to reconstruct ancestral sequences on three phylogenies: (i) the unconstrained maximum likelihood (ML) phylogeny, which recovers almost all the established species relationships—including the sister relationship of Fungi and Holozoa—except that Amoebozoa and some SAR sequences are pulled toward the root (Fig. 2B); (ii) the "maximum congruence" (MC) phylogeny, which is constrained to reflect established species relationships among the major groups (Fig. 2, A and C); and (iii) a "Fungi-out" phylogeny, which has the same constraints, but with Fungi as the first-branching eukaryotic lineage (Fig. 2D). The likelihood difference between the ML and MC trees is not significant [$P = 0.36$, Shimodaira-Hasegawa test (*8*)], and the latter requires no auxiliary events such as gene duplications/losses or horizontal transfers, so we consider the MC phylogeny to be the best supported. The Fungi-out phylogeny is implausible, but it allows us to isolate the effect of improving sampling on ASR by imposing the critical features of the Hadzipasic *et al.* phylogeny.

On all three trees, AncEukarya again has predominantly allosteric states and only one or two of the 15 nonallosteric states that Hadzipasic *et al.* inferred as ancestral (Fig. 2, F to H). All other nonallosteric residues are again derived within Fungi. This result arises because the allosteric states are found not only in animals and plants but also in non-ascomycete fungi and other eukaryotic groups, which Hadzipasic *et al.* did not include. Improved sequence sampling alone, even on the Fungi-out phylogeny, is therefore sufficient to reverse the direction of evolution of the experimentally important substitutions compared with that inferred by Hadzipasic *et al.*

On the most plausible MC phylogeny, AncEukarya contains the allosteric state at 11 of 15 sites. The four missing states are not universally required for allostery, because they are absent in one or more extant allosteric AURKs (Fig. 2E) (*9*–*11*). The best-supported hypothesis is therefore that AURK of AncEukarya was allosteric, and this feature was lost along the lineage leading to ascomycetes; experiments will be necessary for a direct test. This scenario is consistent with the taxonomic distribution of AURK's allosteric effector TPX2. Hadzipasic *et al.* claim that TPX2 evolved after the origin of the AURK protein and before the emergence of allostery, but a reciprocal BLAST search identifies TPX2 orthologs in all major eukaryotic taxa, including all fungal groups except ascomycetes (*12*). The history of TPX2 therefore tracks exactly with the best-supported history of AURK allostery: presence in the eukaryotic ancestor, loss in ascomycetes.

Finally, our analysis indicates that the basal placement of fungi in the phylogeny of Hadzipasic *et al.* is likely attributable to LBA. The first line of defense against LBA is improved sampling to break up long branches (*13*). When we analyzed more sequences with greater taxonomic diversity—including numerous fungal groups that branch off the established phylogeny between Microsporidiae and ascomycetes, as well as basally branching groups within the other high-level eukaryotic taxa—support for Hadzipasic *et al.*'s topology was eliminated, and the canonical position of Fungi was restored with strong support (Fig. 2B). One reason for the sparse sampling in Hadzipasic *et al.* may have been the use of software to coestimate phylogeny and alignment, which is computationally demanding and therefore limited to very small datasets; although coestimation is appealing in theory, the AURK sequences align with little ambiguity, and the compromised sampling necessitated by this approach led to severe phylogenetic error.

This case illustrates the importance of sound phylogenetic practice when using ASR. Comprehensive sequence sampling is essential, especially from taxa that attach to the phylogeny near the nodes of interest and that can break up long branches. Single-protein datasets may not have sufficient signal to resolve difficult phylogenetic problems or overcome LBA, so congruence with well-established rela-

tionships should be assessed, and the effect of imposing those relationships on the reconstruction should be explored. Confidence in the functional properties of reconstructed ancestral proteins should always be assessed by examining the distribution of functions among extant sequences across the phylogeny; if a very nonparsimonious history is implied, extra scrutiny is warranted. In the current case, characterization of other extant AURKs—particularly in non-ascomycete fungi, Amoebozoa, and SAR—is essential. These kinds of practices can provide multiple safety checks against erroneous inference by ASR.

REFERENCES AND NOTES

1. A. Hadzipasic, C. Wilson, V. Nguyen, N. Kern, C. Kim, W. Pitsawong, J. Villali, Y. Zheng, D. Kern, Ancient origins of allosteric activation in a Ser-Thr kinase. *Science* **367**, 912–917 (2020). doi:10.1126/science.aay9959 Medline
2. S. L. Baldauf, J. D. Palmer, Animals and fungi are each other's closest relatives: Congruent evidence from multiple proteins. *Proc. Natl. Acad. Sci. U.S.A.* **90**, 11558–11562 (1993). doi:10.1073/pnas.90.24.11558 Medline
3. J. del Campo, I. Ruiz-Trillo, Environmental survey meta-analysis reveals hidden diversity among unicellular opisthokonts. *Mol. Biol. Evol.* **30**, 802–805 (2013). doi:10.1093/molbev/mst006 Medline
4. P. J. Keeling, N. M. Fast, Microsporidia: Biology and evolution of highly reduced intracellular parasites. *Annu. Rev. Microbiol.* **56**, 93–116 (2002). doi:10.1146/annurev.micro.56.012302.160854 Medline
5. S. M. Soucy, J. Huang, J. P. Gogarten, Horizontal gene transfer: Building the web of life. *Nat. Rev. Genet.* **16**, 472–482 (2015). doi:10.1038/nrg3962 Medline
6. H. Philippe, H. Brinkmann, D. V. Lavrov, D. T. J. Littlewood, M. Manuel, G. Wörheide, D. Baurain, Resolving difficult phylogenetic questions: Why more sequences are not enough. *PLOS Biol.* **9**, e1000602 (2011). doi:10.1371/journal.pbio.1000602 Medline
7. H. Brinkmann, M. van der Giezen, Y. Zhou, G. Poncelin de Raucourt, H. Philippe, An empirical assessment of long-branch attraction artefacts in deep eukaryotic phylogenomics. *Syst. Biol.* **54**, 743–757 (2005). doi:10.1080/10635150500234609 Medline
8. H. Shimodaira, M. Hasegawa, Multiple Comparisons of Log-Likelihoods with Applications to Phylogenetic Inference. *Mol. Biol. Evol.* **16**, 1114–1116 (1999). doi:10.1093/oxfordjournals.molbev.a026201
9. P. A. Eyers, E. Erikson, L. G. Chen, J. L. Maller, A novel mechanism for activation of the protein kinase Aurora A. *Curr. Biol.* **13**, 691–697 (2003). doi:10.1016/S0960-9822(03)00166-0 Medline
10. E. Tomaštíková, D. Demidov, H. Jeřábková, P. Binarová, A. Houben, J. Doležel, B. Petrovská, *Plant Mol. Biol. Rep.* **33**, 1988–1995 (2015). doi:10.1007/s11105-015-0890-x
11. N. Ozlü, M. Srayko, K. Kinoshita, B. Habermann, E. T. O'toole, T. Müller-Reichert, N. Schmalz, A. Desai, A. A. Hyman, An essential function of the C. elegans ortholog of TPX2 is to localize activated aurora A kinase to mitotic spindles. *Dev. Cell* **9**, 237–248 (2005). doi:10.1016/j.devcel.2005.07.002 Medline
12. See supplementary information at Dryad (https://doi.org/10.5061/dryad.cvdncjt2b).
13. S. M. Hedtke, T. M. Townsend, D. M. Hillis, Resolution of phylogenetic conflict in large data sets by increased taxon sampling. *Syst. Biol.* **55**, 522–529 (2006). doi:10.1080/10635150600697358 Medline
14. M. Anisimova, O. Gascuel, Approximate likelihood-ratio test for branches: A fast, accurate, and powerful alternative. *Syst. Biol.* **55**, 539–552 (2006). doi:10.1080/10635150600755453 Medline

ACKNOWLEDGMENTS

We thank members of the Thornton laboratory for comments. Supported by NIH grants R01GM131128 (J.W.T.), R01GM121931 (J.W.T.), and T32-007197 (J.E.J.P.). See (*12*) for description of methods and supplementary table, phylogenies, alignments, and ancestral sequence reconstructions.

18 May 2020; accepted 23 October 2020
Published online 20 November 2020
10.1126/science.abc8301

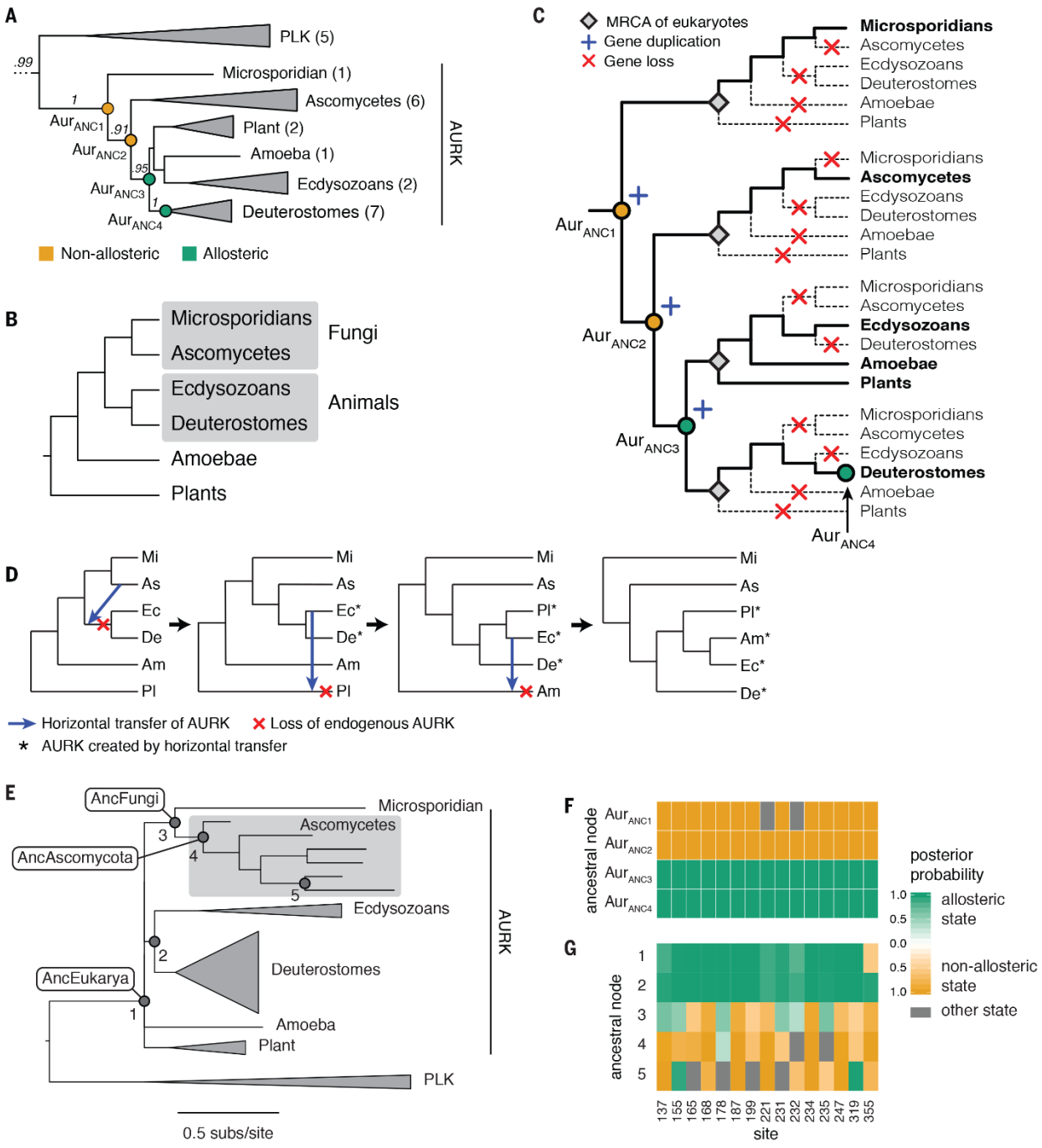

Fig. 1. A plausible phylogeny reverses Hadzipasic *et al.*'s ancestral reconstructions. (**A**) The phylogeny of AURKs and their nearest outgroup (PLKs) used by Hadzipasic *et al*. Parentheses indicate the number of sequences in each clade. Circles mark the experimentally characterized ancestors, colored by presence or absence of the allosteric response to TPX2. Numbers in italics show the inferred posterior probability of each clade. (**B**) The established phylogeny of the taxa in (A). (**C**) Minimum number of gene duplications and losses required to reconcile (A) phylogeny with (B). (**D**) Minimum number of gene transfer and replacement events required to reconcile (A) phylogeny with (B). Other scenarios with an equal or greater number of events are also possible. (**E**) AURK phylogeny when sequences in Hadzipasic *et al*. were reanalyzed given the constraint in (B). Ancestral sequences reconstructed in (G) are labeled. (**F**) Ancestral reconstruction on the phylogeny of Hadzipasic *et al*. (A). Inferred ancestral states are displayed for a group of 15 sites that experimentally confer allostery when the states from Aur_{ANC3} (green) replace those in Aur_{ANC2} (orange); gray, other amino acid states. Row labels correspond to nodes in (A). Site numbers are based on human AURKA. (**G**) Maximum a posteriori ancestral states reconstructed on the constrained AURK phylogeny in (E). Sites, states, and colors are as in (F). Shading (color scale at right) shows the posterior probability of each state.

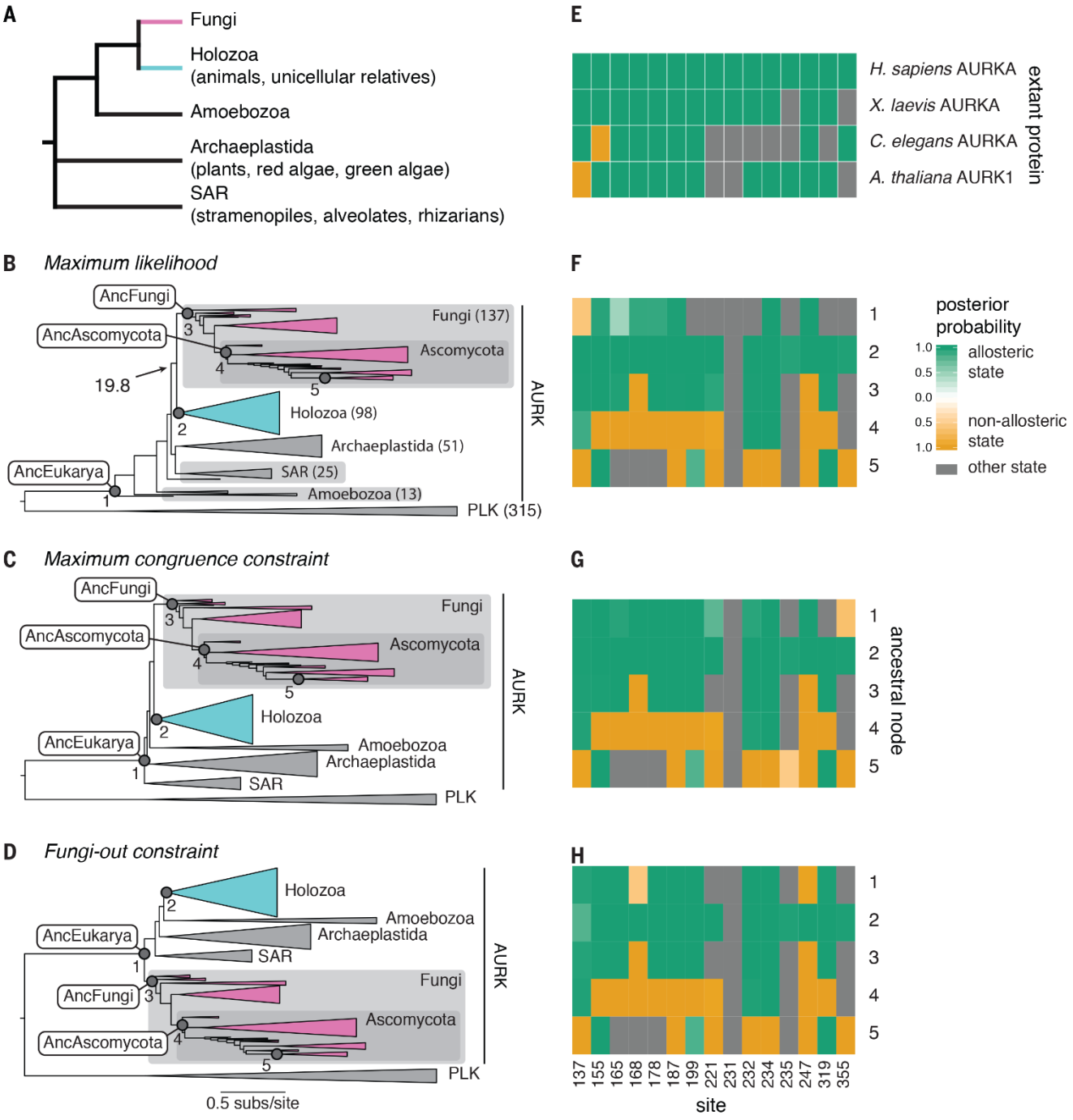

Fig. 2. Improved sequence sampling reverses Hadzipasic *et al.*'s ancestral reconstructions. (**A**) The established phylogeny of the major eukaryotic groups. Polytomy and branching order are not established. (**B**) Maximum likelihood (ML) phylogeny when AURK and PLK are densely sampled. Numbers in parentheses indicate the number of sequences in each group. Node labels denote reconstructed ancestral sequences. Fungi and Holozoa are pink and cyan, respectively. Branch label with arrow is the approximate likelihood ratio statistic for Fungi + Holozoa [$P < 0.01$ by χ^2 approximation (*14*)]. (**C**) ML phylogeny given the constraint in (A). (**D**) ML phylogeny given the constraint in (A), except that Fungi are constrained to split first. (**E**) Most states that confer allostery in Hadzipasic *et al*. are not conserved in extant AURKs that are allosterically regulated by TPX2. Green and orange respectively denote allosteric and nonallosteric states from Hadzipasic *et al*.; gray, other states. Site numbers are in (H). (**F** to **H**) Reconstructed sequences on the phylogenies in (B), (C), and (D), respectively. The maximum a posteriori states at the 15 sites that experimentally confer allostery or nonallostery are shown, colored as in (E) and shaded by their posterior probability. Row numbers correspond to ancestral nodes in (B) to (D).

Cite as: C. Wilson, D. Kern, *Science* 10.1126/science.abd0364 (2020).

Response to Comment on "Ancient origins of allosteric activation in a Ser-Thr kinase"

Christopher Wilson and Dorothee Kern*

Department of Biochemistry and Howard Hughes Medical Institute, Brandeis University, Waltham, MA 02453, USA.

*Corresponding author. Email: dkern@brandeis.edu

Park *et al.* question one out of seven findings from Hadzipasic *et al.*: whether TPX2 allosterically regulates the oldest Aurora. We had already addressed the two concerns raised—sparse sequence sampling and not forcing the gene to the species tree—before publication. Moreover, we believe their ancestral sequence reconstruction would be consistent with a nonallosteric common ancestor, and we show large sequence differences caused by species tree–enforced gene trees.

The key findings in Hadzipasic *et al.* (*1*) are that (i) autophosphorylation is the ancient allosteric regulation for Aurora kinases; (ii) a gradual increase in allosteric activation took place during the holozoan evolution; (iii) an allosteric network in Aurora exists that, when mutated, alters allosteric activity; (iv) allosteric activation by TPX2 is entirely encoded in the kinase; (v) the interface between Aurora and TPX2 is co-conserved; (vi) evolution of specificity in signaling happens on binding affinity; and (vii) the oldest ancestral Aurora is not allosterically activated by TPX2.

The comment by Park *et al.* (*2*) questions only the seventh finding, on the basis of differences in the computation of ancestral sequence reconstruction (ASR). Notably, even though the ASR calculations differ, we believe the outcome is consistent with, rather than contradicting, the finding. The two concerns raised are (i) the small number of modern sequences used in the ASR calculations and (ii) the mismatch between the gene tree and the species tree. We had these same concerns and extensively investigated both points before publication:

1. The reason for the original sparse sampling was the use of BALi-Phy (*3*) to coestimate phylogeny and alignment using Bayesian statistics, a commonly used method in the field. After the completion of several years of experiments, we tested our concerns about the smaller number of modern sequences used by repeating the computational part of ASR with more than 500 sequences using a maximum likelihood (ML) approach, very similar to (*2*). By then, newer software was available, and the field, including the Thornton lab, had demonstrated that ML trees are in several cases comparable in quality to Bayesian trees. Therefore, we created a ML tree with more than 500 collected sequences from Uniport with an identity cutoff of 99%. We aligned the obtained sequences with PRANK (*4*). We used IQ-TREE (*5*) to simultaneously search for a best-fit model and constructed a ML tree with rapid bootstrapping and SH-aLRT to estimate node supports. Notably, the resulting tree contained the same general topology as in our Bayes-based tree (Fig. 1) with robust support at the relevant nodes. We did not include this additional analysis in the supplementary materials because of the agreement with the original tree and ancestors and because all experiments were performed on the original ancestors. We shared this information, including Fig. 1, with Park *et al.* before they submitted their Comment to *Science*.

2. Park *et al.*'s concern that the gene tree does not match the species tree is well known and controversially discussed in the field. We cite and state (*1*): "Discrepancies between gene trees and species trees are common…" (*6*–*9*). We also had tried to force the gene tree to the species tree. Unlike other cases where S-aware trees have been used to produce ancestors, the difference between the gene and species tree is large for Aurora; consequently, we found that forcing the gene tree onto the species tree resulted in large penalties. The best-fitting tree still differed significantly from the species tree and resembled the maximum a posteriori tree. Fungi were placed distant from the animals because the gene sequences differ more from animals than the plant sequences do. We disagree with a general approach of forcing gene trees to species trees, as done in figure 2 of (*2*).

Park *et al.*'s calculations alone highlight an issue with forcing the gene tree to the species tree: The sequences for their ancestor 1, which is the one questioned by the authors (AncEukarya), are very different between their ML tree and an ML tree that is forced onto the species tree (Fig. 2). They differ by 25% (yellow), significantly more than our nonallosteric Anc2 and allosteric Anc3 (10%). This comparison be-

tween the ASR from their ML and maximum congruence constraint (MCC) tree challenges their logic of restraining the gene tree topology to match a species tree for the Aurora system and their conclusion that both approaches give very similar results.

The question is whether the differences in ASR calculations matter for the outcome. We believe Park *et al.*'s ASR calculations would be consistent with our conclusion that TPX2 does not allosterically activate the oldest ancestor. These are the essential points for interpreting computational results without experimentally measuring the properties of those ancestors:

1. Their oldest ancestor 1, which the authors speculate will be allosterically regulated by TPX2 binding, is very likely not regulated by TPX2: In Fig. 2, AncAur_Eukarya_ML (F) has only 6 of the 15 required residues in the allosteric network (dark green); all others either have the incorrect residue (8 residues, yellow and gray) or too low posterior probabilities (1 residue, light green). We had experimentally determined that the majority of these 15 residues are necessary for allosteric TPX2 activation [figures 4 and S11 of (*1*)]. The "nonallosteric state" and "other state" [figure 2 of (*2*)] are all "nonallosteric" because they have different amino acids than the correct one. From our experimental data (*1*), an Aurora ancestor with a subset of only six correct residues in this allosteric network would not show allosteric activation.

2. Their ancestor 2 agrees with our findings that this node has all the allosteric network residues because this is the last common ancestor for Holozoa [ancestor 2 in figure 2F of (*2*)]. Their ancestor 3 node has no experimental counterpart in our study.

3. Park's ancestors 4 and 5 are in the Fungi kingdom, for which no allosteric activation is expected because fungal AurA are not activated by TPX2 binding (they lost the AurA binding motif of TPX2). Therefore, the loss of TPX2 activation in the Fungi kingdom is another point on which we agree with Park *et al.*, and we interpret this as the reason why fungi diverge further in the Aur gene tree.

In summary, we believe the outcome of Park *et al.*'s calculations is consistent with our key findings that the oldest regulation is autophosphorylation, and allosteric regulation by TPX2 was dialed in (*1*). The significant differences in overall sequence and critical positions in their ancestor sequences derived from a gene ML tree and a gene ML tree with congruence constraint to the species tree (Fig. 2) would, in our view, argue against constraining the gene tree to the species tree in this system. However, this question is under active investigation in the field and can only be answered by comparing both computational approaches in combination with experimental interrogation of the derived ancestral sequences. The Comment authors have convincingly performed such experimental tests for their systems (*10*–*13*). Such tests would be informative for the Aur ancestors suggested in Park *et al.* Allosteric enzyme activation is a difficult task to resurrect compared to only ligand binding. Apart from this methodological disagreement, the experimental results in (*1*) stand independent on the detailed phylogenetic tree: allosteric activation by either autophosphorylation or TPX2 binding, gradual dialing in of that second activation along the evolutionary trajectory in holozoans, identification of the allosteric network spanning a large portion of the kinase, co-conservation of the interface between Aurora and TPX2, and evolution of selectivity in activation by the correct activator via binding affinity.

REFERENCES

1. A. Hadzipasic, C. Wilson, V. Nguyen, N. Kern, C. Kim, W. Pitsawong, J. Villali, Y. Zheng, D. Kern, Ancient origins of allosteric activation in a Ser-Thr kinase. *Science* **367**, 912–917 (2020). doi:10.1126/science.aay9959 Medline
2. Y. Park, J. E. J. Patton, G. K. A. Hochberg, J. W. Thornton, Comment on "Ancient origins of allosteric activation in a Ser-Thr kinase". *Science* **370**, eabc8301 (2020).
3. M. A. Suchard, B. D. Redelings, BAli-Phy: Simultaneous Bayesian inference of alignment and phylogeny. *Bioinformatics* **22**, 2047–2048 (2006). doi:10.1093/bioinformatics/btl175 Medline
4. A. Löytynoja, Phylogeny-aware alignment with PRANK. *Methods Mol. Biol.* **1079**, 155–170 (2014). Medline
5. L.-T. Nguyen, H. A. Schmidt, A. von Haeseler, B. Q. Minh, IQ-TREE: A fast and effective stochastic algorithm for estimating maximum-likelihood phylogenies. *Mol. Biol. Evol.* **32**, 268–274 (2015). doi:10.1093/molbev/msu300 Medline
6. R. Nichols, Gene trees and species trees are not the same. *Trends Ecol. Evol.* **16**, 358–364 (2001). doi:10.1016/S0169-5347(01)02203-0 Medline
7. W. P. Maddison, Gene Trees in Species Trees. *Syst. Biol.* **46**, 523–536 (1997). doi:10.1093/sysbio/46.3.523
8. N. Takahata, Gene genealogy in three related populations: Consistency probability between gene and population trees. *Genetics* **122**, 957–966 (1989). Medline
9. P. Pamilo, M. Nei, Relationships between gene trees and species trees. *Mol. Biol. Evol.* **5**, 568–583 (1988). Medline
10. J. W. Thornton, E. Need, D. Crews, Resurrecting the ancestral steroid receptor: Ancient origin of estrogen signaling. *Science* **301**, 1714–1717 (2003). doi:10.1126/science.1086185 Medline
11. G. C. Finnigan, V. Hanson-Smith, T. H. Stevens, J. W. Thornton, Evolution of increased complexity in a molecular machine. *Nature* **481**, 360–364 (2012). doi:10.1038/nature10724 Medline
12. M. J. Harms, G. N. Eick, D. Goswami, J. K. Colucci, P. R. Griffin, E. A. Ortlund, J. W. Thornton, Biophysical mechanisms for large-effect mutations in the evolution of steroid hormone receptors. *Proc. Natl. Acad. Sci. U.S.A.* **110**, 11475–11480 (2013). doi:10.1073/pnas.1303930110 Medline
13. A. N. McKeown, J. T. Bridgham, D. W. Anderson, M. N. Murphy, E. A. Ortlund, J. W. Thornton, Evolution of DNA specificity in a transcription factor family produced a new gene regulatory module. *Cell* **159**, 58–68 (2014). doi:10.1016/j.cell.2014.09.003 Medline

ACKNOWLEDGMENTS

D.K. is a Howard Hughes Medical Institute Investigator.

1 September 2020; accepted 5 November 2020
Published online 20 November 2020
10.1126/science.abd0364

Fig. 1. Improved sequence sampling results in reconstruction similar to that in (*1*). Aurora homologs' ML tree using more than 500 sequences, with ultrafast bootstraps (left number) and SH-aLRT statistic (right number) shown at the relevant nodes.

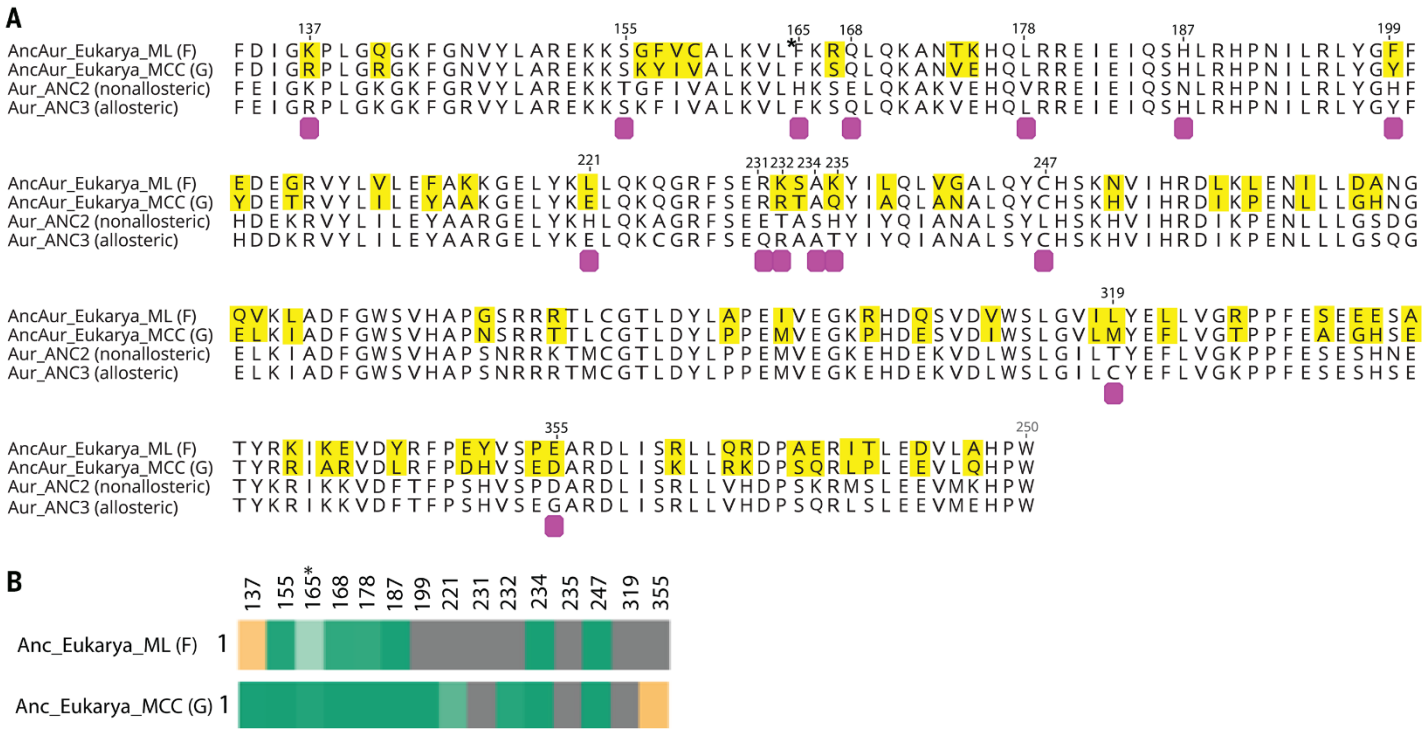

Fig. 2. Ancestral sequences from Park *et al.* argue against a species enforced gene tree and suggest agreement with our finding in (*1*) of incomplete allosteric network in oldest ancestor. (A) Comparison of the sequences of the oldest ancestor 1 in the ML tree [AncEukarya_ML (F)] and MCC tree [AncEukarya_MCC (G)] showing that the sequences differ by 25% when constraining the gene tree to the species tree (highlighted in yellow) (*2*), a finding that argues against a species enforced gene tree. Also shown are the two critical ancestors in (*1*), Aur_ANC2 and Aur_ANC3, which were shown experimentally to be nonallosteric and allosteric, respectively, in (*1*), differing by only 10%. Of the 15 positions of the allosteric network (indicated by pink symbols below), only six have the correct amino acid in the network in Anc_-Eukarya_ML (F). (B) The same 15 positions as in (A), represented as in figure 2, F and G, of (*2*) (posterior below 0.5 indicated by an asterisk). Accordingly, the oldest ancestor produced by the ML tree with expanded sampling is expected to be nonallosteric, consistent with our findings.

PRIZE ESSAY

GENOMICS, PROTEOMICS, AND SYSTEMS BIOLOGY

Tracking development at the cellular level

Single-cell genomic methods enable developmental mapping of entire organisms

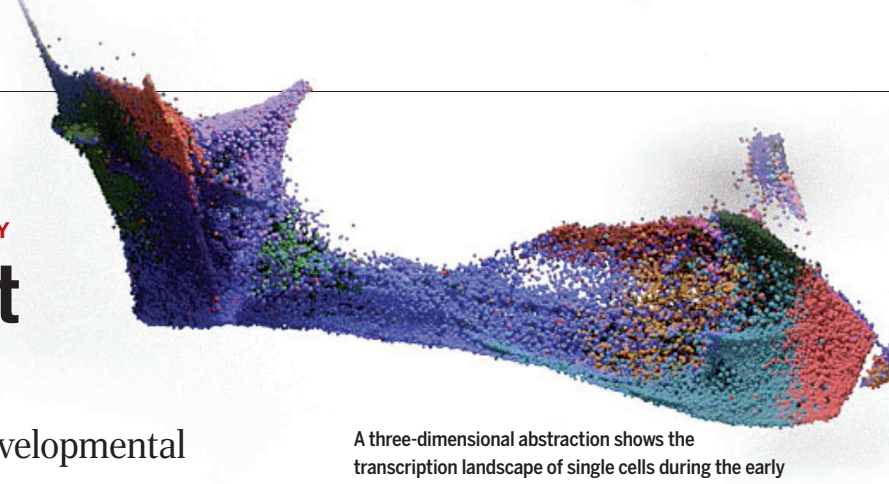

A three-dimensional abstraction shows the transcription landscape of single cells during the early development of the mouse central nervous system.

By **Junyue Cao**

We each developed from a single cell—a fertilized egg—that divided and divided and eventually gave rise to the trillions of cells, of hundreds of types, that constitute the tissues and organs of our adult bodies. Advancing our understanding of the molecular programs underlying the emergence and differentiation of these diverse cell types is of fundamental interest and will affect almost every aspect of biology and medicine.

Recently, technological advances have made it possible to directly measure the gene expression patterns of individual cells (*1*). Such methods can be used to clarify cell types and to determine the developmental stage of individual cells (*2*). Single-cell transcriptional profiling of successive developmental stages has the potential to be particularly informative, as the data can be used to reconstruct developmental processes, as well as characterize the underlying genetic programs (*3*, *4*).

When I began my doctoral studies in Jay Shendure's lab at the University of Washington, available single-cell sequencing techniques relied on the isolation of individual cells within physical compartments and thus were limited in terms of both throughput and cost. As a graduate student, I developed four high-throughput single-cell genomic techniques to overcome these limitations (*5*–*8*). Leveraging these methods, I profiled millions of single-cell transcriptomes from organisms, in species that included worms, mice, and humans. By quantifying the dynamics of embryonic development at single-cell resolution, I was able to map out the global genetic programs that control cell proliferation and differentiation at the whole-organism scale.

Laboratory of single-cell genomics and population dynamics, Rockefeller University, New York, NY, USA.
Email: jcao@rockefeller.edu

COMPREHENSIVE SINGLE-CELL TRANSCRIPTIONAL PROFILING OF A MULTICELLULAR ORGANISM

By the 1980s, biologists had documented every developmental step in the nematode *Caenorhabditis elegans*, from a single-cell embryo to the adult worm, and mapped the connections of all of the worm's neurons (*9*). However, although the nematode worm has a relatively small cell number (558 cells at hatching), a comprehensive understanding of the molecular basis for the specification of these cell types remains difficult.

To resolve cellular heterogeneity, I first developed a method to specifically label the transcriptomes of large numbers of single cells, which we called sci-RNA-seq (single-cell combinatorial indexing RNA sequencing) (*5*). This method is based on combinatorial indexing, a strategy using split-pool barcoding of nucleic acids to label vast numbers of single cells within a single experiment (*9*).

A genomic technique for tracking cellular development

High-throughput single-cell genomic methods enable a global view of cell type diversification by transcriptome and epigenome

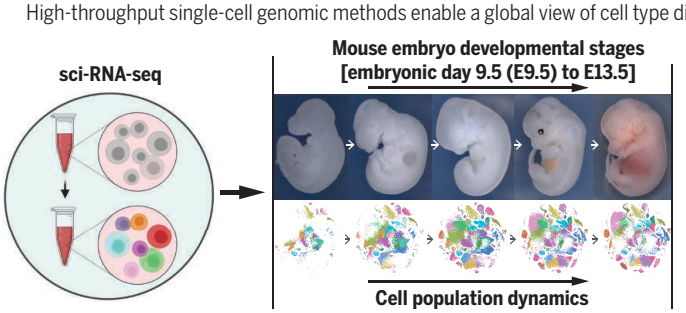

Single-cell transcriptome profiling of cell dynamics at organism scale
Single-cell RNA sequencing by combinatorial indexing (sci-RNA-seq), with its improved version (sci-RNA-seq3), enables high-throughput single-cell transcriptome profiling of over 2 million cells in a single experiment, by assigning each cell a specific molecular barcode without physically isolating a single cell (left). The technique is applied to tracking cell dynamics from undistinguished cellular precursors to becoming the animal's brain, heart, and all major organs in a mouse model (right). t-Distributed stochastic neighbor embedding (t-SNE) plots (bottom) show cell population dynamics across developmental stages (embryo photos shown on the top), colored by cell types.

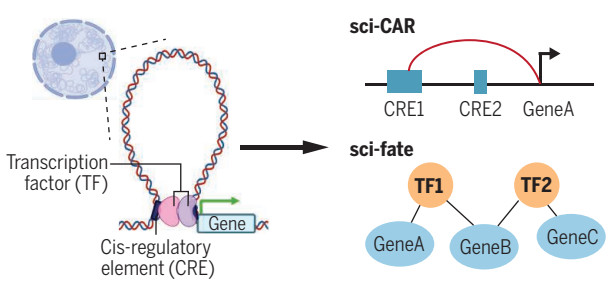

Single-cell genomics for deciphering gene regulatory mechanisms
Gene expression is tightly controlled by its linked cis-regulatory elements and transcription factors (TFs) (left). Two new methods, single-cell combinatorial indexing chromatin accessibility and mRNA (sci-CAR) and single-cell combinatorial indexing and mRNA labeling (sci-fate), were developed to delineate the epigenetic codes underlying gene regulation (right). sci-CAR profiles both transcriptome and epigenome (chromatin accessibility) from the same cell and links CREs to their gene targets based on their covariance across thousands of cells. Sci-fate recovers the gene regulatory network, including TFs and target genes, by profiling both TF expression and newly synthesized RNA across many cells.

CREDITS: (TOP TO BOTTOM) COLE TRAPNELL; N. DESAI/*SCIENCE* FROM CAO *ET AL.* (*7*) AND BIORENDER

Published by AAAS

In this study, I profiled nearly 50,000 cells from *C. elegans* at the L2 stage, which is more than 50-fold "shotgun cellular coverage" of its somatic cell composition. We further defined consensus expression profiles for 27 cell types and identified rare neuronal cell types corresponding to as few as one or two cells in the L2 worm. This was the first study to show that single-cell transcriptional profiling is sufficient to separate all major cell types from an entire animal.

THE SINGLE-CELL TRANSCRIPTIONAL LANDSCAPE OF MAMMALIAN ORGANOGENESIS

C. elegans development follows a tightly controlled genetic program. Other multicellular organisms, such as mice and humans, have much more developmental flexibility. However, conventional approaches for mammalian single-cell profiling lack the throughput and resolution to obtain a global view of the molecular states and trajectories of the rapidly diversifying and expanding cell types.

To investigate cell state dynamics in mammalian development, I developed an even more scalable single-cell profiling technique, sci-RNA-seq3 (*7*), and used it to trace the development path of 2 million mouse cells as they traversed diverse paths in a 4-day window of development corresponding to organogenesis (embryonic day 9.5 to embryonic day 13.5). From these data, we characterized the dynamics of cell proliferation and key regulators for each cell lineage, a potentially foundational resource for understanding how the hundreds of cell types forming a mammalian body are generated in development. This was, and remains, the largest publicly available single-cell transcriptional dataset. The sci-RNA-seq3 method enabled this dataset to be generated rapidly, within a few weeks, by a single individual.

SINGLE-CELL PROFILING OF EPIGENETIC REGULATORY CODES IN CELL FATE DETERMINATION

A major challenge regarding current single-cell assays is that nearly all such methods capture just one aspect of cellular biology (typically mRNA expression), limiting the ability to relate different components to one another and to infer causal relationships. Another technique that I developed, sci-CAR (single-cell combinatorial indexing chromatin accessibility and mRNA) (*6*), was created with the goal of overcoming this limitation, allowing the user to jointly profile the epigenome (chromatin accessibility) and transcriptome (mRNA). I applied sci-CAR to the mouse whole kidneys, recovering all major cell types and linking cis-regulatory sites to their target genes on the basis of the covariance of chromatin accessibility and transcription across large numbers of single cells.

To further explore the gene regulatory mechanisms, I invented sci-fate (*8*), a new method that identifies the temporal dynamics of transcription by distinguishing newly synthesized mRNA transcripts from "older" mRNA transcripts in thousands of individual cells. Applying the strategy to cancer cell state dynamics in response to glucocorticoids, we were able to link transcription factors (TFs) with their target genes on the basis of the covariance between TF expression and the amount of newly synthesized RNA across thousands of cells.

SUMMARY OF FINDINGS

In summary, my dissertation involved developing the technical framework for quantifying gene expression and chromatin dynamics across thousands to millions of single cells and applying these technologies to profile complex, developing organisms. The methods that I developed enable such projects to be achievable by a single individual, rather than requiring large consortia. Looking ahead, I anticipate that the integration of single-cell views of the transcriptome, epigenome, proteome, and spatial-temporal information throughout development will enable an increasingly complete view of how life is formed. ■

GRAND PRIZE WINNER

Junyue Cao

Junyue Cao received his undergraduate degree from Peking University and a Ph.D. from the University of Washington. After completing his postdoctoral fellowship at the University of Washington, Junyue Cao started his lab as an assistant professor and lab head of single-cell genomics and population dynamics at the Rockefeller University in 2020. His current research focuses on studying how a cell population in our body maintains homeostasis by developing genomic techniques to profile and perturb cell dynamics at single-cell resolution.

CATEGORY WINNER: ECOLOGY AND EVOLUTION

Orsi Decker

Orsi Decker completed her undergraduate degree at Eötvös Loránd University in Budapest, Hungary. She went on to receive her master's degree in Ecology and Evolution at the University of Amsterdam. Decker completed her doctoral research at La Trobe University in Melbourne, Australia, where she investigated the extinctions of native digging mammals and their context-dependent impacts on soil processes. She is currently a postdoctoral researcher at La Trobe University, where she is examining how land restoration efforts could be improved to regain soil functions through the introduction of soil fauna to degraded areas. **www.sciencemag.org/content/370/6519/925.1**

CATEGORY WINNER: MOLECULAR MEDICINE

Dasha Nelidova

Dasha Nelidova completed her undergraduate degrees at the University of Auckland, New Zealand. She completed her Ph.D. in neurobiology at the Friedrich Miescher Institute for Biomedical Research in Basel, Switzerland. Nelidova is currently a postdoctoral researcher at the Institute of Molecular and Clinical Ophthalmology Basel, where she is working to develop new translational technologies for treating retinal diseases that lead to blindness. **www.sciencemag.org/content/370/6519/925.2**

CATEGORY WINNER: CELL AND MOLECULAR BIOLOGY

William E. Allen

William E. Allen received his undergraduate degree from Brown University in 2012, M.Phil. in Computational Biology from the University of Cambridge in 2013, and Ph.D. in Neurosciences from Stanford University in 2019. At Stanford, he worked to develop new tools for the large-scale characterization of neural circuit structure and function, which he applied to understand the neural basis of thirst. After completing his Ph.D., William started as an independent Junior Fellow in the Society of Fellows at Harvard University, where he is developing and applying new approaches to map mammalian brain function and dysfunction over an animal's life span. **www.sciencemag.org/content/370/6519/925.3**

PHOTOS: (TOP TO BOTTOM) COURTESY OF J. CAO; COURTESY OF O. DECKER; COURTESY OF D. NELIDOVA; COURTESY OF W. ALLEN

REFERENCES AND NOTES

1. D. Ramsköld *et al.*, *Nat. Biotechnol.* **30**, 777 (2012).
2. C. Trapnell, *Genome Res.* **25**, 1491 (2015).
3. D. E. Wagner *et al.*, *Science* **360**, 981 (2018).
4. K. Davie *et al.*, *Cell* **174**, 982 (2018).
5. J. Cao *et al.*, *Science* **357**, 661 (2017).
6. J. Cao *et al.*, *Science* **361**, 1380 (2018).
7. J. Cao *et al.*, *Nature* **566**, 496 (2019).
8. J. Cao, W. Zhou, F. Steemers, C. Trapnell, J. Shendure, *Nat. Biotechnol.* **38**, 980 (2020).
9. D. A. Cusanovich *et al.*, *Science* **348**, 910 (2015).

10.1126/science.abf1686

Published by AAAS

PRIZE ESSAY

CATEGORY WINNER: ECOLOGY AND EVOLUTION

Orsi Decker

Orsi Decker completed her undergraduate degree at Eötvös Loránd University in Budapest, Hungary. She went on to receive her master's degree in Ecology and Evolution at the University of Amsterdam. Decker completed her doctoral research at La Trobe University in Melbourne, Australia, where she investigated the extinctions of native digging mammals and their context-dependent impacts on soil processes. She is currently a postdoctoral researcher at La Trobe University, where she is examining how land restoration efforts could be improved to regain soil functions through the introduction of soil fauna to degraded areas. **www.sciencemag.org/content/370/6519/925.1**

ECOLOGY AND EVOLUTION

Losing Australia's native gardeners

The loss of the country's digging mammals compromises the continent's arid soil health

By **Orsi Decker**

When many of us think of outback Australia, we imagine desolate sands stretching out to the horizon, with either droughts or flooding rains. But what if this state of desolation is a result of the European colonization, poor land management, and native species extinctions driven by introduced plants and animals? What if the infertile soils that exist in the country today were once productive, with plant and animal communities maintaining a sensitive balance that reduced the impact of droughts and capitalized on flooding rains? What if our ideas of functioning ecosystems are the end-product of shifting baselines (*1*)?

DIGGING MAMMALS ARE CRUCIAL FOR HEALTHY SOILS

As a graduate student in the Insect Ecology lab at La Trobe University, I studied the ecologically extinct digging mammals of Australia to better understand their long-lost functions and to model historic functions of a world now largely lost: the world of pre-European Australia. The once widespread native digging mammals include a diverse group of charismatic animals that evolved to survive the desert heat but not to escape from introduced cats and foxes (*2*). These include bettong and potoroo species (*Potoroidae* spp.), bilbies (*Macrotis lagotis*), numbats (*Myrmecobius fasciatus*), and bandicoots (*Peramelidae* spp.), all of which are now mostly restricted to predator-free areas such as islands and fenced reserves (*3*).

Digging mammals create small pits while foraging for food, which turns over the soil (*4*). The pits capture organic material, seeds, and, most importantly, water (*5*). In this way, these creatures are the keen gardeners of their own habitat, constantly turning over and fertilizing the soil while creating up to 200 pits per night for a grand total of about 4 tonnes of soil turned over per individual per year (*6*, *7*). (This metric only includes foraging and does not account for burrowing activities.)

Through my research, I discovered that the loss of these animals has profoundly altered soil functioning. Other researchers have documented the effect of foraging pits on soil processes; however, my research represents an attempt to determine the "landscape-scale" effects of digging mammals on soil functions. To do this, I compared predator-free reserves that support reintroduced native digging mammals with adjacent control areas in southern Australia where these mammals are extinct.

After taking 1334 soil samples from five predator-free reserves and five control areas, we determined that the loss of digging mammals has had a pronounced impact on soils. Soil organic material and available carbon, nitrogen, and phosphorus were all higher in reserves (*8*). Increased soil carbon indicates an increased water-holding capacity, which is crucial in dry, sandy soils (*9*). The plant-available forms of nitrogen and phosphorus are scarce in many soil types (*10*); therefore, mechanisms increasing these elements will likely support greater rates of plant establishment and growth (*11*). These results suggest that native digging mammals increase carbon sequestration and the water-holding capacity of soils and may therefore be able to mitigate some of the effects of drought (*12*). This is extremely important in a warming climate (*13*).

To respond to extreme environmental conditions, soils must also be resilient. The presence of healthy microbial communities is vital to this resilience (*14*). Microscopic communities, it turns out, are also affected by digging mammals, and the diversity of microbes is higher in the mammal sanctuaries (*15*, *16*). Our preliminary research indicates that beneficial bacterial species, such as nitrogen-fixing and antipathogenic species, were associated with sanctuaries.

Department of Ecology, Environment, and Evolution, Latrobe University, Melbourne, VIC, Australia.
Email: o.decker@latrobe.edu.au

PHOTO: COURTESY OF O. DECKER

Published by AAAS

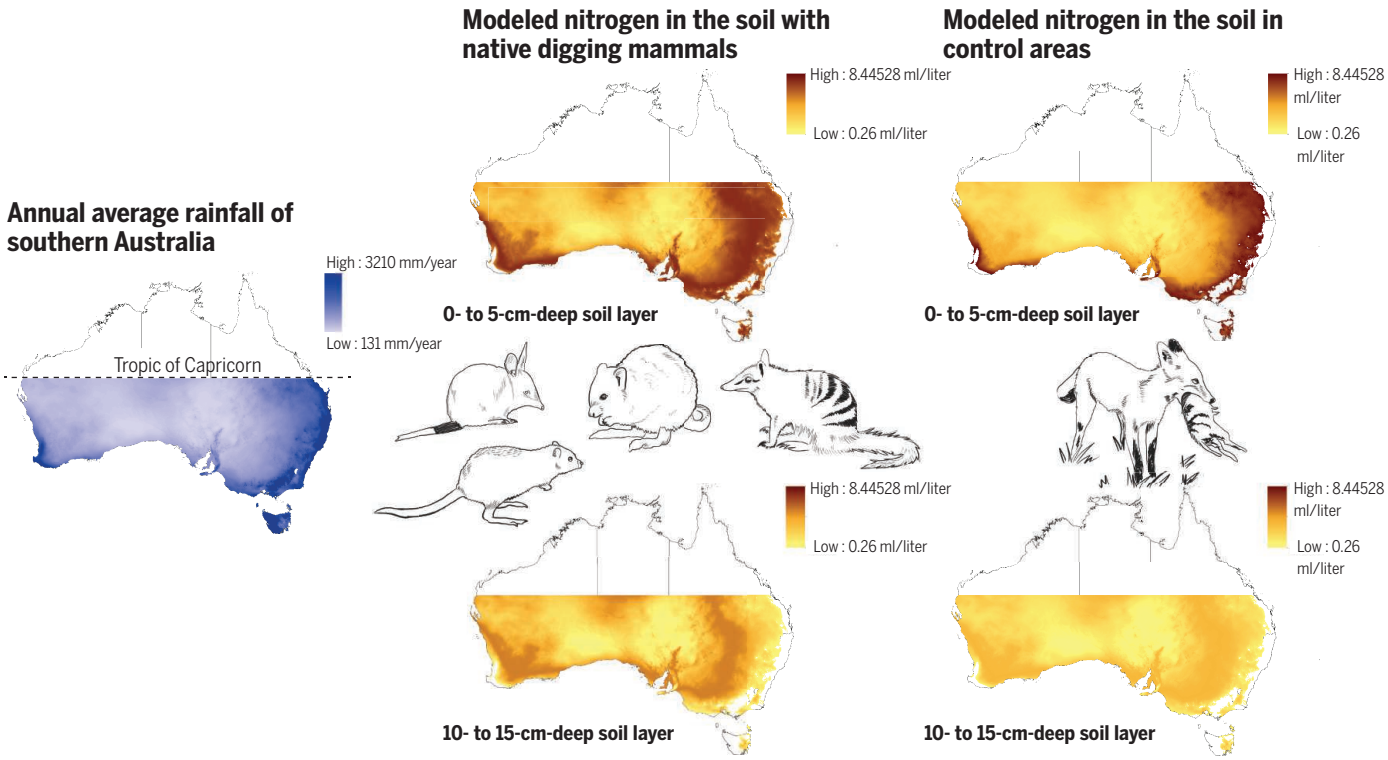
Annual average rainfall of southern Australia
High : 3210 mm/year
Low : 131 mm/year
Tropic of Capricorn
Modeled nitrogen in the soil with native digging mammals
High : 8.44528 ml/liter
Low : 0.26 ml/liter
0- to 5-cm-deep soil layer
High : 8.44528 ml/liter
Low : 0.26 ml/liter
10- to 15-cm-deep soil layer
Modeled nitrogen in the soil in control areas
High : 8.44528 ml/liter
Low : 0.26 ml/liter
0- to 5-cm-deep soil layer
High : 8.44528 ml/liter
Low : 0.26 ml/liter
10- to 15-cm-deep soil layer

Modeled difference in soil available nitrogen between an Australian continent with abundant native digging mammals and an Australian continent in which native digging mammals are extinct or very rare. Average annual rainfall is shown, excluding the tropical regions (left). Modeled soil nitrogen (in milliliters per liter of soil) can be seen in the topsoil (0- to 5-cm-deep soil layer) and subsoil (10- to 15-cm-deep soil layer) in reserves (middle). Modeled values are shown in areas without native digging mammals (right). The greatest differences are in the semiarid regions (medium blue on rainfall map) between reserves and control areas. Areas where annual rainfall is >900 mm/year were excluded because we did not have sites that received rainfall above that amount.

GRAPHIC: N. DESAI/*SCIENCE* FROM O. DECKER

DRY CLIMATES BENEFIT FROM DIGGING MORE THAN WET CLIMATES

The loss of Australia's digging mammals has occurred in a range of ecosystems (*17*, *18*) and has been followed by the loss of their ecological functions across much of the continent. This made me wonder if digging activities affected the environment differently across the continent, because species roles can be context-dependent (*19*, *20*).

Imagine, for example, one garden in a dry area and one in a relatively wet climate. In the dry garden, a small amount of fertilizer and moisture will boost the growth of many plants, but the same effort in the wet garden will not have as much of an effect. This, I hypothesized, could be similar with digging mammals: Their activity might change soil properties in dry areas, where natural disturbances compensate for the lack of rainfall (*21*), but not in more productive systems (*9*). To determine if this was the case, we set up a landscape-scale study of four ecosystem types along a precipitation gradient of 150 to 900 mm/year.

My Ph.D. project showed that native digging mammals have a context-dependent effect (see the figure). The benefits of digging mammals were the greatest in arid and semiarid ecosystems but much reduced in temperate systems. Arid and semiarid environments are commonly thought to be infertile. However, my research suggests that the presence of native fauna could cause such areas to thrive, creating refuges from climate change and providing new incentives for species conservation.

Predicting the aftermath of species loss is not always easy. However, in this case, it is clear that we are losing important ecological functions that might otherwise mitigate the effects of climate change. As the world becomes hotter, many temperate regions will become semiarid (*22*, *23*) and begin to look more like Australia. Across all such regions, it is important to recognize beneficial natural processes that offer climate solutions and make it a priority to conserve these processes and the organisms in their natural habitat. ■

REFERENCES AND NOTES

1. M. Soga, K. J. Gaston, *Front. Ecol. Environ.* **16**, 222 (2018).
2. C. N. Johnson, J. L. Isaac, *Austral Ecol.* **34**, 35 (2009).
3. C. R. Dickman, in *Fencing for Conservation*, M. Somers, M. Hayward, Eds. (Springer, 2012), pp. 43–63.
4. P. A. Fleming *et al.*, *Mammal Rev.* **44**, 94 (2014).
5. A. I. James, D. J. Eldridge, *Biol. Conserv.* **138**, 351 (2007).
6. M. J. Garkaklis, J. S. Bradley, R. D. Wooller, *J. Arid Environ.* **56**, 569 (2004).
7. N. T. Munro *et al.*, *PeerJ* **7**, e6622 (2019).
8. O. Decker, D. J. Eldridge, H. Gibb, *Ecography* **42**, 1370 (2019).
9. A. T. Austin *et al.*, *Oecologia* **141**, 221 (2004).
10. J. J. Elser *et al.*, *Ecol. Lett.* **10**, 1135 (2007).
11. L. T. Bennett, M. A. Adams, *J. Arid Environ.* **48**, 289 (2001).
12. O.-Y. Yu, B. Raichle, S. Sink, *Int. J. Energy Environ. Eng.* **4**, 44 (2013).
13. Intergovernmental Panel on Climate Change (IPCC), "Climate change 2014: Synthesis report. Contribution of Working Groups I, II, and III to the Fifth Assessment Report of the Intergovernmental Panel on Climate Change," Core Writing Team, R. K. Pachauri, L. A. Meyer, Eds. (IPCC, Geneva, 2014).
14. M. Delgado-Baquerizo *et al.*, *Nat. Commun.* **7**, 10541 (2016).
15. L. J. Clarke, L. S. Weyrich, A. Cooper, *Mol. Ecol.* **24**, 3194 (2015).
16. S. J. Dundas *et al.*, *Biodivers. Conserv.* **27**, 3071 (2018).
17. J. C. Z. Woinarski, A. A. Burbidge, P. L. Harrison, *Proc. Natl. Acad. Sci. U.S.A.* **112**, 4531 (2015).
18. A. D. Chapman, "Numbers of living species in Australia and the world" (Report, Australian Government, 2009).
19. K. H. Johnson, K. A. Vogt, H. J. Clark, O. J. Schmitz, D. J. Vogt, *Trends Ecol. Evol.* **11**, 372 (1996).
20. C. Mullan Crain, M. D. Bertness, *Bioscience* **56**, 211 (2006).
21. W. G. Whitford, F. R. Kay, *J. Arid Environ.* **41**, 203 (1999).
22. J. Huang, H. Yu, X. Guan, G. Wang, R. Guo, *Nat. Clim. Chang.* **6**, 166 (2016).
23. A. Rajaud, N. Noblet-Ducoudré, *Clim. Change* **144**, 703 (2017).

10.1126/science.abf1706

Published by AAAS

PRIZE ESSAY

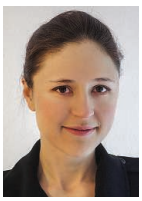

CATEGORY WINNER: MOLECULAR MEDICINE

Dasha Nelidova
Dasha Nelidova completed her undergraduate degrees at the University of Auckland, New Zealand. She completed her Ph.D. in neurobiology at the Friedrich Miescher Institute for Biomedical Research in Basel, Switzerland. Nelidova is currently a postdoctoral researcher at the Institute of Molecular and Clinical Ophthalmology Basel, where she is working to develop new translational technologies for treating retinal diseases that lead to blindness. **www.sciencemag.org/content/370/6519/925.2**

MOLECULAR MEDICINE

Engineering near-infrared vision

An optogenetic technology inspired by snakes could aid those with incomplete blindness

By **Dasha Nelidova**[1,2]

Photoreceptor degeneration, including age-related macular degeneration and retinitis pigmentosa, is a leading cause of blindness worldwide. Repair of retinal neurons by optogenetics—a technology that sensitizes neurons to light through the transfer of genes for light-sensitive proteins of microbial origin (*1*, *2*)—has entered clinical trials (*3*, *4*). Trials began in 2018 in patients with advanced retinitis pigmentosa and minimal remaining vision (*4*).

Optogenetic proteins are sensitive only to the brightest visible light, at intensities that overwhelm surviving functional photoreceptors. Yet, in a number of blinding diseases, light-sensitive and light-insensitive photoreceptor zones coexist within the same retina. In macular degeneration, for example, cone photoreceptors of the central retina lose their light sensitivity. Surrounding photoreceptors remain viable, and peripheral vision is largely unaffected. A key challenge for new translational technologies that aim to restore image-acquiring properties of the retina is the compatibility of such technologies with remaining vision.

We reasoned that sensitizing the retina to wavelengths that functional photoreceptors are unable to detect (>900 nm) could supplement deteriorating natural vision, without interfering with the ability to see the visible spectrum. Inspired by infrared vision in snakes, we developed nanogenetic molecular tools that allowed blind mice and ex vivo human retinas to detect near-infrared (NIR) light (*5*).

SNAKE VISION: TWO IMAGES SUPERIMPOSED

Snakes can see the world in two different ways. Like humans, they make use of their eyes to detect wavelengths of the visible spectrum (400 to 700 nm). In addition, several species can also generate thermal images (*6*). Snakes detect infrared light (1 to 30 μm) using temperature-sensitive transient receptor potential (TRP) cation channels expressed in a specialized "pit" organ (*6*). Infrared and visible spectrum images superimpose within the brain (*7*), presumably enabling the animals to react to the environment with greater precision than what is possible by using only a single image. Snakes can switch back and forth between the two imaging systems or use both simultaneously (*7*, *8*).

TRP channels could potentially be targeted to mammalian retinal cell types to make them sensitive to infrared radiation. However, infrared light would raise vibrational energies of water molecules throughout the eye. Shorter wavelength NIR light would be preferable because NIR has lower water absorption, although this same feature also makes direct NIR illumination an inefficient activator of TRP channels.

ENGINEERING RETINAL CELLS TO DETECT NIR

To develop a more efficient NIR light detector for retinal cell types, we engineered a dual system that consists of a genetic and a nanomaterial component (see the figure). The genetic half of the sensor consists of TRP channels, engineered to incorporate an extracellular protein epitope tag recognizable by a specific antibody (*9*). The nanomaterial half of the sensor consists of gold nanorods conjugated to an antibody against the epitope (*10*). Gold nanorods serve as antennas for NIR light and convert light into local heat through surface plasmon resonance (*11*), driving photocurrents through antibody-bound TRP channels. Subretinal microinjection of virally packaged TRP and nanorods delivered the sensor components to cones.

Our initial system was based on TRP vanilloid 1 (TRPV1) channels and gold nanorods with absorption maxima at 915 nm. We began by inserting a 6x-His epitope tag into the middle of the first TRPV1 extracellular loop, measuring sizes of evoked currents before and after the modification, and confirmed that channels remained functional. Next, we used adeno-associated virus (AAV)–mediated gene transfer to transduce cone photoreceptors of blind mice with the nanogenetic sensor. To measure neural ac-

[1]Institute of Molecular and Clinical Ophthalmology Basel, Basel, Switzerland. [2]University of Oxford, Oxford, UK. Email: dasha.nelidova@iob.ch

PHOTO: COURTESY OF D. NELIDOVA

Published by AAAS

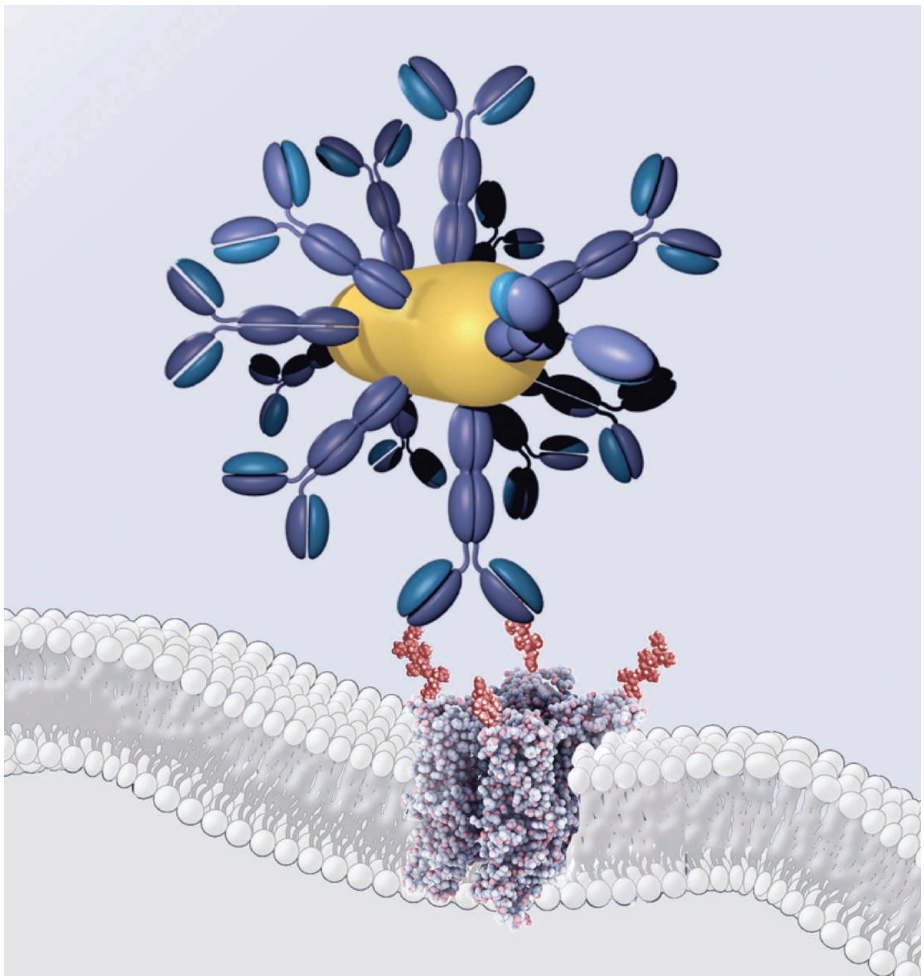

Components of the near-infrared light sensor. Engineered transient-receptor-potential channels (lilac) express protein epitope tags (red) in extracellular domains and bind extracellular antibody-conjugated gold nanorods.

IMAGE: VERONIQUE JUVIN/SCIARTWORK

tivity, we performed two-photon calcium imaging of individual neurons within the retina and primary visual cortex.

Expression of the nanogenetic sensor in cones rendered blind retinas to be sensitive to NIR light. Cone photoreceptors (retinal input) and retinal ganglion cells (retinal output) responded vigorously to 915-nm light, and NIR-evoked retinal activity propagated to the brain. This allowed treated mice to use their newly acquired NIR vision to perform behavioral tasks.

In complementary experiments, we confirmed that NIR light was unable to activate wild-type cones and did not affect their visible light responses. Similarly, awake, wild-type mice failed to exploit NIR light cues during behavioral training.

TUNABLE LIGHT SENSORS

Nanorod properties depend on size and shape (*11*). By changing the length of the gold nanorods from ~80 nm to ~120 nm, we tuned NIR vision to a different NIR wavelength (980 nm). Wavelength tuning is important for several reasons. Certain NIR wavelengths might be better tolerated by patients than others. Also, maximum permissible light doses for the human eye depend on the wavelength. Additionally, NIR vision requires eye goggles that project images composed of specific NIR wavelengths onto the retina. Compatibility with current and future NIR projectors requires tunable NIR detectors.

GAINING FUNCTION BY TWEAKING THERMOSENSITIVE PROTEINS

Across the animal kingdom, multiple variants of thermosensitive proteins can be found, and more can be created through mutagenesis. Channels, tags, and antibodies can be modified to gain additional desirable properties. We selected TRP ankyrin 1 (TRPA1) channels from the Texas rat snake because of their lower thermal thresholds and inserted the newer epitope tag OLLAS (*Escherichia coli* OmpF Linker and mouse Langerin fusion sequence) (*12*) into the first extracellular loop. Mice transfected with engineered TRPA1 channels were better able to anticipate water rewards when lights were dimmed as compared with mice transfected with TRPV1, indicating an improvement in the sensitivity of the sensor. (Both TRPA1- and TRPV1-transduced animals performed behavioral tasks as well as wild-type animals that were trained by using visible light.)

TOWARD HUMAN NIR VISION

The next step was to validate findings in blind human retinas. To do this, we targeted TRPV1 and gold nanorods to light-insensitive photoreceptors of adult human ex vivo retinal explants. (We had previously developed a cocktail of molecules to keep human retinas alive for 8 weeks post mortem, giving gene expression time to take hold.) We then recorded NIR light–evoked calcium activity and saw fast, strong activation of human photoreceptors and downstream retinal neurons, including ganglion cells.

Taken together, these experiments provide proof of principle for the potential therapeutic translation of this technology. Light intensities required to drive genetically encoded NIR sensors met existing safety standards that specify exposure limits for the human eye, and we further demonstrated that components of the sensor may be exchanged, with predictable final outcomes. In the future, targeted central repair would allow an island of NIR sensitivity to be built in a sea of natural vision. Parallel developments in surgery (*13*) and NIR projectors with eye-tracking capabilities (*4*) make targeted central repair feasible. Ultimately, the user may be able to self-select the region of the electromagnetic spectrum most useful to view the external world, a decision guided by the state of their retina and ambient light conditions. ■

REFERENCES AND NOTES

1. J. A. Sahel, B. Roska, *Annu. Rev. Neurosci.* **36**, 467 (2013).
2. V. Busskamp *et al.*, *Science* **329**, 413 (2010).
3. S. Makin, *Nat. Outlook* 10.1038/d41586-019-01107-8 (2019).
4. Dose-escalation Study to Evaluate the Safety and Tolerability of GS030 in Subjects With Retinitis Pigmentosa (PIONEER). Clinical Trials ID: NCT03326336 (2018).
5. D. Nelidova *et al.*, *Science* **368**, 1108 (2020).
6. E. O. Gracheva *et al.*, *Nature* **464**, 1006 (2010).
7. E. A. Newman, P. H. Hartline, *Science* **213**, 789 (1981).
8. E. A. Newman, P. H. Hartline, *Sci. Am.* **246**, 116 (1982).
9. S. A. Stanley *et al.*, *Science* **336**, 604 (2012).
10. P. P. Joshi, S. J. Yoon, W. G. Hardin, S. Emelianov, K. V. Sokolov, *Bioconjug. Chem.* **24**, 878 (2013).
11. Z. Qin, J. C. Bischof, *Chem. Soc. Rev.* **41**, 1191 (2012).
12. S. H. Park *et al.*, *J. Immunol. Methods* **331**, 27 (2008).
13. A. M. Maguire *et al.*, *N. Engl. J. Med.* **358**, 2240 (2008).

ACKNOWLEDGMENTS

I thank my thesis adviser, B. Roska, and all molecular and clinical research colleagues at the Institute of Molecular and Clinical Ophthalmology Basel for their enthusiasm, advice, and help. I also thank our collaborators, especially A. Szabo, without whom human retinal experiments would not have been possible.

10.1126/science.abf1710

Published by AAAS

PRIZE ESSAY

CATEGORY WINNER: CELL AND MOLECULAR BIOLOGY

William E. Allen

William E. Allen received his undergraduate degree from Brown University in 2012, M.Phil. in Computational Biology from the University of Cambridge in 2013, and Ph.D. in Neurosciences from Stanford University in 2019. At Stanford, he worked to develop new tools for the large-scale characterization of neural circuit structure and function, which he applied to understand the neural basis of thirst. After completing his Ph.D., William started as an independent Junior Fellow in the Society of Fellows at Harvard University, where he is developing and applying new approaches to map mammalian brain function and dysfunction over an animal's life span.

www.sciencemag.org/content/370/6519/925.3

CELL AND MOLECULAR BIOLOGY

Brain mapping, from molecules to networks

Bridging multiple levels of brain function reveals the neural basis of thirst motivation

By **William E. Allen**

Charting what the pioneering neuroanatomist Santiago Ramón y Cajal called the "impenetrable jungle" of the brain (*1*) presents one of biology's greatest challenges. How do billions of neurons, wired through trillions of connections, work together to produce cognition and behavior?

Like an orchestra, wherein many instruments played simultaneously produce a sound greater than the sum of its parts, thought and behavior emerge from communication between ensembles of molecularly distinct neurons distributed throughout vast neural circuits. Although we know much about the properties of individual genes, cells, and circuits (see the figure, panel A), a vast gap lies between the function of each brain component and an animal's behavior. Bridging this gap has proven technically and conceptually difficult.

Inspired by the fact that the development of high-throughput DNA sequencing led geneticists to shift focus from individual genes to the entire genome, I wanted to develop approaches that could simultaneously link multiple levels of the brain, from molecules to neurons to brain-wide neural networks. My goal was to capture a global perspective while maintaining the high resolution and specificity necessary to understand the function of individual components at each level. This new viewpoint, I hoped, would reveal how the collective properties of the brain's building blocks give rise to behavior.

MAPPING MOTIVATED BEHAVIOR FROM GENES TO CIRCUITS

During my doctoral studies at Stanford University with Karl Deisseroth and Liqun Luo, I developed new methods to map the architecture and activity of mammalian neural circuits. I applied these approaches to understand the neural basis of thirst, a fundamental regulator of behavior (*2*).

Society of Fellows, Harvard University, Cambridge, MA, USA. Email: weallen@fas.harvard.edu

Need-based motivational drives, such as hunger and thirst, direct animals to satisfy specific physiological imperatives important for survival (*3*). Despite decades of research, at the beginning of my studies it was unclear how the activity of neurons that sense these needs causes an animal to engage in specific motivated behaviors (e.g., eating or drinking) to maintain homeostasis (*3*). Thirst, a relatively simple yet important drive, thus seemed the perfect model system for investigating multiple levels in the brain.

I first traced thirst motivational drive from cellular gene expression to a circuit mechanism. Using a new version of targeted recombination in active populations (TRAP2), a tool to genetically label neurons according to their activity, I found that neurons in the median preoptic nucleus (MnPO) of the hypothalamus became activated in thirsty mice (*4*) (see the figure, panel C). Single-cell RNA sequencing revealed that these neurons formed a single molecularly defined cell type.

Artificial activation of these neurons caused mice to drink water within seconds, whereas their inhibition prevented mice from drinking, which suggested that these MnPO neurons were master regulators of thirst. Drinking water also gradually reduced the activity of these neurons. Finally, activation of these neurons was aversive. Together, these results suggested a surprising "drive reduction" model of thirst motivation: Genetically hard-wired thirst neurons become active when mice need hydration, which causes mice to drink water.

This ability to ascribe specific functional relevance to genetically defined neurons inspired me to develop new techniques to map cells within their native tissue architecture in even greater molecular detail. To this end, I co-developed STARmap, an approach for highly multiplexed in situ RNA sequencing to measure the expression of hundreds of genes simultaneously within a brain section at the level of single mRNA molecules (*5*) (see the figure, panel B). In combination with genetic markers of activity, this technique powerfully describes the molecular identity of behaviorally activated neurons and their neighbors at single-cell resolution.

PHOTO: COURTESY OF W. ALLEN

Published by AAAS

New large-scale, high-resolution approaches to bridging multiple levels of brain function

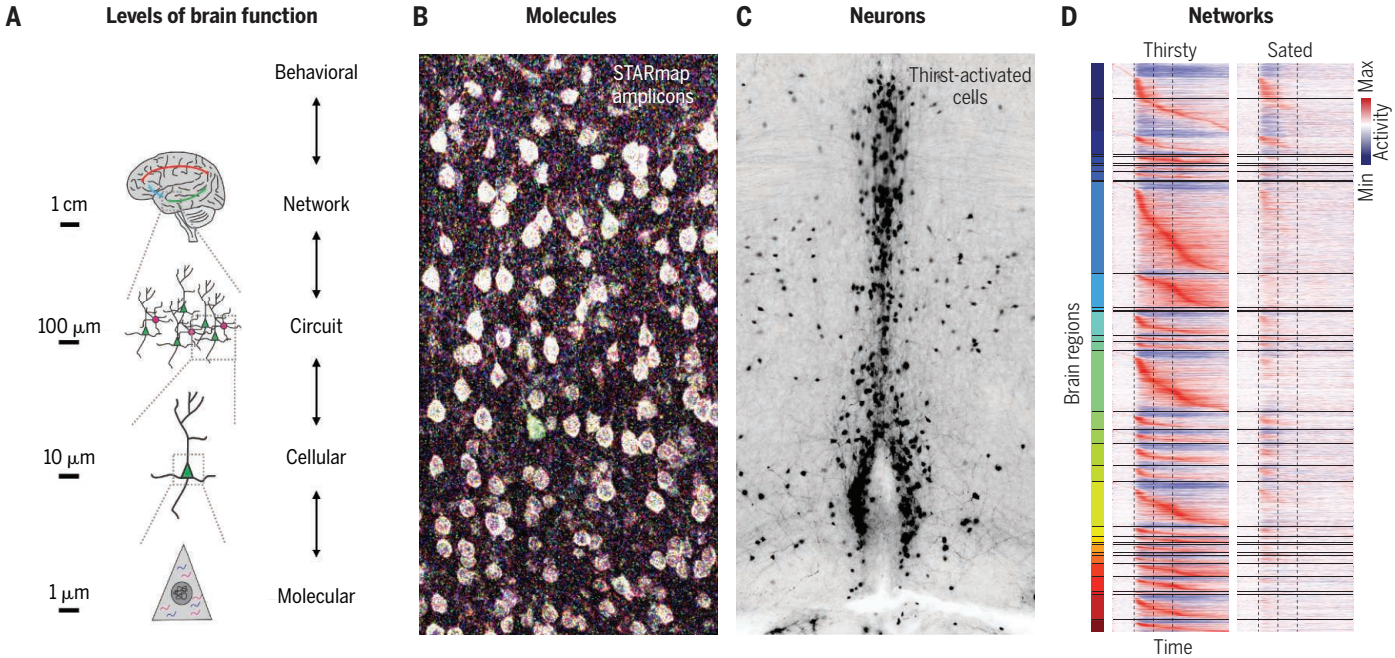

A new approach to brain function mapping. (A) An illustration of the levels of brain function and how they are interlinked. (B to D) New approaches to bridging levels: (B) STARmap amplicons barcoding 1020 RNA species simultaneously with single-molecule resolution in the mouse visual cortex. (C) Genetic labeling of neurons according to activity reveals thirst neurons in the median preoptic nucleus of the hypothalamus, used to identify the motivational mechanism of thirst drive. (D) Brain-wide activity map of the response of thousands of neurons across dozens of brain regions to a water-predicting sensory cue, in thirsty or sated mice, reveals widespread broadcasting of thirst state.

LINKING INDIVIDUAL NEURONS TO BRAIN-WIDE NETWORKS

Despite these insights, a question remained: How do thirst-sensitive neurons deep in the brain coordinate activity in distributed circuits spanning sensory perception, cognition, and motor output to produce motivated behavior? I found that MnPO thirst neurons projected to many brain regions potentially serving different behavioral roles (*4*), but the gap between individual neurons and brain-wide networks was daunting.

Earlier in graduate school, I had developed several new microscopy techniques to characterize brain-wide (*6*) or neocortex-wide (*7*) activity, which revealed that global neural activity was present during even simple motivated behaviors. However, because of the mammalian brain's opacity, these approaches were limited in their ability to record fast neural activity throughout the brain at the scale required to understand thirst motivation.

Fortunately, however, developments in microelectronics enabled me to construct global maps of neuronal activity with microsecond-level temporal resolution. Using advanced "Neuropixels" probes (*8*), thin silicon needles that can be acutely inserted into the brain to record the electrical signals of hundreds of neurons simultaneously, I developed an experimental approach to record the activity of huge neuronal ensembles across the brain and reconstruct the anatomical location of each recorded cell (*9*).

Applying this technique, I mapped the brain-wide flow of activity through ~24,000 single neurons during thirst-motivated behavior (*9*) (see the figure, panel D). My experiments revealed that this simple behavior produced an unexpectedly global coordination of activity throughout the brain. By observing how activity changed as mice drank water, as well as directly stimulating hypothalamic thirst neurons, I showed that this activity wave was dependent on the animal's motivational state.

Surprisingly, the activity of a few hundred thirst neurons instantly modulated the state of the entire brain. Even more surprisingly, I found many neurons, distributed throughout the brain, that directly encoded thirst. These results suggest that even simple behaviors, such as thirst, are emergent properties of the entire brain.

I hope these new approaches will at last enable us to comprehend the rules that transform distributed patterns of electrical activity in neural circuits into thoughts, emotions, and perceptions. Understanding how molecules, neurons, and networks interact to shape these rules will have a sweeping impact on our understanding of brain function in health and disease. ■

GRAPHIC: N. DESAI/*SCIENCE* FROM W. ALLEN, WANG *ET AL.* (5), ALLEN *ET AL.* (4), ALLEN *ET AL.* (9)

REFERENCES AND NOTES

1. "Mas, por desgracia, faltábanos el arma poderosa con que descuajar la selva impenetrable de la substancia gris..." (*10*).
2. C. A. Zimmerman, D. E. Leib, Z. A. Knight, *Nat. Rev. Neurosci.* **18**, 459 (2017).
3. S. M. Sternson, *Neuron* **77**, 810 (2013).
4. W. E. Allen *et al.*, *Science* **357**, 1149 (2017).
5. X. Wang *et al.*, *Science* **361**, eaat5691 (2018).
6. L. Ye *et al.*, *Cell* **165**, 1776 (2016).
7. W. E. Allen *et al.*, *Neuron* **94**, 891 (2017).
8. J. J. Jun *et al.*, *Nature* **551**, 232 (2017).
9. W. E. Allen *et al.*, *Science* **364**, eeav3932 (2019).
10. S. Ramón y Cajal, *Recuerdos de mi vida: Historia de mi labor científica* (Moya, Madrid, 1917).

10.1126/science.abf1711

Published by AAAS

RESEARCH

IN *SCIENCE* JOURNALS

Edited by **Michael Funk**

NEUROSCIENCE

Threat detection starts in the eyes

When a mouse sees something that quickly becomes larger in its visual field, perhaps indicating an attacking predator, it runs. Kim *et al*. identified a small group of neurons in the mouse retina that selectively respond to such looming visual stimuli and are required for innate defensive behaviors in response. These neurons perform this specific computation by integrating inputs from nearby neurons in a selective manner. Thus, neural circuits within the eyes, even before the information reaches the brain, perform specific computations to mediate innate, evolutionarily conserved behaviors. —TK

Sci. Adv. 10.1126/sciadv.abc9920 (2020).

Neural circuits in the retina help mice and other animals detect looming threats, such as a lunging predator.

ANTIBIOTIC RESISTANCE

PBT2 pumps up polymyxins

Bacterial resistance to antibiotics is a growing worldwide problem, and *Enterobacterales* with resistance to the polymyxin class of antibiotics are a critical threat. De Oliveira *et al*. repurposed a hydroxyquinoline compound called PBT2, currently in phase 2 clinical trials for neurodegenerative diseases, to break polymyxin antibiotic resistance in four different Gram-negative pathogens, including *Klebsiella pneumoniae* and *Pseudomonas aeruginosa*. In vitro, treatment with PBT2 disrupted the abundance of zinc and iron in the resistant bacteria, whereas in immunocompetent septic mice, PBT2 combined with polymyxins resulted in improved survival with reduced bacterial dissemination. These findings, although exciting, need to be confirmed in humans. —MN

Sci. Transl. Med. **12**, eabb3791 (2020).

DEVELOPMENTAL BIOLOGY

Functional screen for microcephaly genes

Genetic screens are widely used to identify regulators in biological processes. Human screens are currently limited to two-dimensional cell cultures, which lack the ability to score tissue-dependent gene function. Esk *et al*. combined CRISPR-Cas9 screening with barcoded cellular lineage tracing to enable loss-of-function screening in three-dimensional human cerebral organoid tissue. By testing microcephaly candidate genes, the endoplasmic reticulum was found to control extracellular matrix protein secretion regulating tissue integrity and brain size. This genetic screen in human brain tissue implicates multiple pathways in microcephaly and provides a tool for systematic testing of genes in organoids. —BAP

Science, this issue p. 935

WATER PHASES

Liquid-liquid transitions under pressure

Theoretical simulations suggest that deeply supercooled water undergoes a transition between high- and low-density forms, but this transition is difficult to study experimentally because it occurs under conditions in which ice crystallization is extremely rapid. Kim *et al*. combined x-ray lasers for rapid structure determination with infrared femtosecond pulses for rapid heating of amorphous ice layers formed at about 200 kelvin. The heating process created high-density liquid water at increased pressures. As the layer expanded and decompressed, low-density liquid domains appeared and grew on time scales between 20 nanoseconds and 3 microseconds, which was much faster than competing ice crystallization. —PDS

Science, this issue p. 978

PHOTO: IMAGE SOURCE/GETTY IMAGES

Published by AAAS

IN OTHER JOURNALS

Edited by **Caroline Ash** *and* **Jesse Smith**

STELLAR ASTROPHYSICS

A relic star cluster under the floor

Globular clusters (GCs) are gravitationally bound assemblies of thousands to millions of stars that orbit in the outskirts of large galaxies. GCs consist of old stars with low metallicity containing low proportions of chemical elements heavier than hydrogen and helium. However, GCs appear to have a minimum metallicity, known as the floor, implying that at least some of those elements were required for their formation. Larsen *et al*. have found a GC in the nearby Andromeda Galaxy with a metallicity beneath the floor. This unexpected discovery will inform models of GC formation and incorporation into galaxies. —KTS

Science, this issue p. 970

ZIKA VIRUS

Domesticating Zika virus

Why hasn't Zika virus (ZIKV) disease caused as much devastation in Africa, its continent of origin, as it has in the Americas? Outside of Africa, this flavivirus is transmitted by a ubiquitous mosquito subspecies, *Aedes aegypti aegypti*, which emerged from the African forerunner subspecies *A. aegypti formosus* and acquired a preference for human blood and a peridomestic lifestyle. Now, this subspecies colonizes many intertropical cities, aided by climate change and human trash. Aubry *et al*. tested 14 laboratory mosquito colonies for their relative susceptibility to ZIKV. Quantitative trait locus mapping showed differences on chromosome 2 between mosquitoes from Gabon and Guadeloupe. Mouse infection experiments revealed that African mosquitoes transmitted a smaller virus inoculum than the South American insects. Increased susceptibility coupled with the ability of *A. aegypti aegypti* to breed in any discarded object containing water has amplified the problematic nature of this virus as it has circumnavigated the world. —CA

Science, this issue p. 991

A feeding female *Aedes aegypti* mosquito, the primary species that transmits Zika virus

PHOTOS: B. G. THOMSON/SCIENCE SOURCE; NOKURO/ALAMY STOCK PHOTO

CORONAVIRUS

A strong cocktail against SARS-CoV-2

Severe acute respiratory syndrome coronavirus 2 (SARS-CoV-2) infection is initiated by the trimeric spike protein that decorates the virus and binds the ACE2 receptor. Antibodies against the spike that neutralize viral infection have potential as therapeutics. Tortorici *et al*. describe two very potent antibodies, S2E12 and S2M11. Electron microscopy structures characterized the binding and showed that S2E12 traps the spike in a conformation that cannot bind ACE2. Both antibodies protected hamsters against SARS-CoV-2 challenge and may be useful in antibody cocktails to combat the virus and prevent the development of resistance. —VV

Science, this issue p. 950

GEOPHYSICS

Finding the Emperor's head

Volcanic island and seamount chains form from deep-seated plumes of hot material upwelling through the mantle. The most famous of these is the Hawaiian-Emperor seamount chain. However, a large volcanic structure associated with a plume head that should precede the chain has long been missing. Wei *et al*. finally identified the likely location of this structure in the mantle under eastern Russia. The structure was likely subducted 20 million to 30 million years ago, and the location helps constrain several geodynamic processes. —BG

Science, this issue p. 983

LIGHT POLLUTION

Too bright to breed

Most coral species reproduce through broadcast spawning. For such a strategy to be successful, coordination has had to evolve such that gametes across clones are released simultaneously. Over millennia, lunar cycles have facilitated this coordination, but the recent development of bright artificial light has led to an overpowering of these natural signals. Ayalon *et al*. tested for the direct impact of different kinds of artificial light on different species of corals. The authors found that multiple lighting types, including cold and warm light-emitting diode (LED) lamps, led to loss of synchrony and spawning failure. Further, coastal maps of artificial lighting globally suggest that it threatens to interfere with coral reproduction worldwide and that the deployment of LED lights, the blue light of which penetrates deeper into the water column, is likely to make the situation even worse. —SNV

Curr. Biol. 10.1016/j.cub.2020.10.039 (2020).

Night light from coastal cities overpowers natural signals for coral spawning from neighboring reefs.

SIGNAL TRANSDUCTION

How RAS mutations really work

Mutations in the small guanosine triphosphatase RAS occur in many human tumors and are thought to act by activating the mitogen-activated protein kinase (MAPK, also called ERK) signaling pathway. Gillies *et al*. used imaging of live single cells to measure MAPK activity in cells expressing a single wild-type or mutant isoform of human RAS. The dynamic range of the signaling pathway and its growth factor responsiveness were surprisingly

Published by AAAS

INFECTIOUS DISEASE

Undercover parasites

The protozoan *Plasmodium falciparum* is transmitted from mosquitoes to humans, where it replicates in red blood cells to cause malaria. In many countries where malaria is endemic, most transmission occurs during the rainy season, so how does the parasite persist during the dry season? Andrade *et al.* analyzed *P. falciparum* from the blood of Malian individuals during the dry season and found that they had low numbers of parasites and no symptoms. Compared with the febrile cases that occur during the rainy season, parasites in asymptomatic infections exhibit distinct gene expression patterns and reduced binding to the endothelium lining blood vessels. Asymptomatic cases also show longer circulation and continual clearance of infected red blood cells by the spleen. Such low-level infections do not stimulate an acute immune response and can persist until the next transmission season, when mosquitoes can breed and resume transmission. —GKA

Nat. Med. 10.1038/s41591-020-1084-0 (2020).

The rainy season in Mali is the trigger for mosquito breeding and transmission of persistent infections of human malaria parasites.

unperturbed. Although RAS mutants are biochemically more active, negative feedback and other regulatory mechanisms still exert control. The oncogenic effects of RAS mutations could reflect a small increase in baseline activity of the pathway. RAS mutations may be common in cancer in part because they can be constrained and thus do not lead to cell death. —LBR

Mol. Syst. Biol. **16**, e9518 (2020).

TRANSPOSONS

Transposable drivers or passengers?

Transposable element activity has been associated with cancer genomes, but whether this activity drives cancers or is incidental to tumorigenesis has been difficult to resolve. Tiwari *et al*. tested the function of the oncogene p53 on LINE1s, transposable elements found in human cells. Oncogene p53 stimulates repressive histone marks on LINE1s, which keeps them from replicating. If p53 becomes mutated in human cells, the epigenetic repressors on the LINE1s are not maintained. This allows LINE1s to become hyperactivate and replicate within the genome. In some cases, this causes chromosomal breakage, a hallmark of p53 loss-of-function cancers, and stimulates inflammation. Thus, when function is lost in p53 mutants and LINE1 activity increases, an acute oncogenic crisis looms. —LMZ

Genes Dev. **34**, 1439 (2020).

PHYSICS

Testing an exotic magnet

In quantum spin liquid (QSL), an exotic state of matter predicted to occur in certain materials, spins remain in a liquid-like state down to the lowest temperatures. A theoretical realization of a QSL is the Kitaev model, where spins reside on a two-dimensional hexagonal lattice. The layered material $RuCl_3$ is thought to display the Kitaev model physics. Modic *et al*. studied magnetic anisotropy in $RuCl_3$. They focused on the magnetotropic coefficient, which reflects the rigidity of a material to rotation in a magnetic field. In a certain temperature range, the coefficient scaled linearly with the magnetic field, indicating that the relevant energy scales were those set by temperature and magnetic field rather than by magnetic interactions intrinsic to the material. —JS

Nat. Phys. 10.1038/s41567-020-1028-0 (2020).

ORGANOMETALLICS

A crystallographic conundrum

X-ray crystallography is often construed as the most direct means of characterizing molecular structure. Nonetheless, it still relies on an accurate assessment of elemental composition to begin with. Amemiya *et al*. report a strange case in which a structure previously assigned to a cadmium carbonyl compound appears much more consistent with a rhenium carbonyl. Although the initial refinement statistics seemed reasonable, the ratio of displacement parameters for the metal versus the ligand atoms was unusually small. The authors further concluded that coordinative carbon and chlorine sites in the ligands were more likely to be nitrogen and sulfur, respectively. —JSY

Chem. Sci. 10.1039/d0sc04596a (2020).

PEPTIDE TOXINS

Redirecting a wasp's sting

Venomous animals typically produce peptides and proteins that have potent biological activities through their interaction with membranes or cellular targets. Silva *et al*. analyzed the sequence and structure of a short peptide toxin from the wasp *Vespula lewisii* and reengineered it into an antimicrobial peptide. Modifications to the end of the peptide reduced toxicity to mammalian cells while preserving the ability to disrupt the outer membrane of Gram-negative bacteria. Antimicrobial activity in mouse infection models demonstrated promising potential for the original design and various analogs. —MAF

Proc. Natl. Acad. Sci. U.S.A. **117**, 26936 (2020).

PHOTO: ANDREW AITCHISON/ALAMY STOCK PHOTO

Published by AAAS

ALSO IN *SCIENCE* JOURNALS

Edited by **Michael Funk**

CORONAVIRUS

Tackling other infectious diseases

The severe acute respiratory syndrome coronavirus 2 (SARS-CoV-2) pandemic has pushed drug discovery and clinical testing to a pace previously considered impossible. In a Perspective, Gupta discusses how the structure of drug development for coronavirus disease 2019 (COVID-19) can be implemented to treat other infectious diseases that kill millions globally each year. By focusing research, implementing operational efficiencies, and ensuring large-scale financing, the author suggests that extensive drug development pipelines can be built to tackle other severe infections. —GKA

Science, this issue p. 913

FIRE ECOLOGY

Fire's growing impacts on ecosystems

Fire has played a prominent role in the evolution of biodiversity and is a natural factor shaping many ecological communities. However, the incidence of fire has been exacerbated by human activity, and this is now affecting ecosystems and habitats that have never been fire prone or fire adapted. Kelly *et al*. review how such changes are already threatening species with extinction and transforming terrestrial ecosystems and discuss the trends causing changes in fire regimes. They also consider actions that could be taken by conservationists and policy-makers to help sustain biodiversity in a time of changing fire activity. —AMS

Science, this issue p. 929

VIROLOGY

Riding the calcium waves

Rotavirus causes severe diarrhea and vomiting in children worldwide, yet how infection causes these diseases remains poorly understood. A leading theory is that virus-infected cells secrete paracrine signaling molecules that dysregulate epithelial cells. Chang-Graham *et al*. found that rotavirus-infected cells trigger cell-to-cell signaling that manifests as intercellular calcium waves (see the Perspective by Stanifer and Boulant). This signal results from the repeated release of adenosine 5′-diphosphate by rotavirus-infected cells. This release activates receptors on nearby uninfected cells, resulting in a calcium signal. The intercellular calcium waves activate chloride and serotonin secretion, which contributes to diarrhea and vomiting. Blocking this paracrine signal could represent a target for antidiarrheal pharmacotherapy. —SMH

Science, this issue p. 930; see also p. 909

PHOTOSYNTHESIS

Green to the core

Light from the Sun powers most life on today's Earth in some way. The core of the photosynthetic apparatus where charge separation occurs, the reaction center (RC), is thought to have originated a single time and diverged, yielding new kinds of complexes adapted to different tasks and environments. Chen *et al*. now present an important missing puzzle piece in our understanding of the evolution of RCs: a cryo–electron microscopy structure of the homodimeric type I RC from a green sulfur bacterium bound to a light-harvesting protein. The observed cofactor and pigment arrangement explain biochemical features of this RC and will aid in our understanding of how a single ancestral RC gave rise to the range of structures and functions seen in RCs today. —MAF

Science, this issue p. 931

NEURODEGENERATION

Two ways to get tangled?

Neurodegeneration in Alzheimer's disease dementia is associated with neurofibrillary tangles composed of aggregated tau protein. Darwich *et al*. describe an additional form of autosomal-dominant dementia with neurofibrillary tangles linked to a hypomorph mutation in valosin-containing protein (VCP). VCP was found to disaggregate pathologic tau, and the hypomorph mutation increased tau accumulation in cells and mice. These findings highlight the role of protein turnover in maintaining neuronal health and suggest that VCP may provide a therapeutic target for Alzheimer's disease. —SMH

Science, this issue p. 932

WILDLIFE DISEASE

Climate change alters disease risks

Climate change appears to be provoking changes in the patterns and intensity of infectious diseases. For example, when conditions are cool, amphibians from warm climates experience greater burdens of infection by chytrid fungus than hosts from cool regions. Cohen *et al*. undertook a global metanalysis of 383 studies to test whether this "thermal mismatch" hypothesis holds true over the gamut of host-pathogen relationships. The authors combined date and location data with a selection of host and parasite traits and weather data. In the resulting model, fungal disease risk increased sharply under cold abnormalities in warm climates, whereas bacterial disease prevalence increased sharply under warm abnormalities in cool climates. Warming is projected to benefit helminths more than other parasites, and viral infections showed less obvious relationships with climate change. —CA

Science, this issue p. 933

NEURODEVELOPMENT

Unlocking retinal regeneration in mice

Zebrafish can regenerate damaged retinal tissue, but mice cannot. Hoang *et al*. found that tracking changes in gene expression and chromatin accessibility upon injury revealed clues as to why retinal glial cells in zebrafish could generate new neurons but the same cell type in mice could not. In zebrafish, activated Müller glial cells shift into a proliferative phase, whereas in mice, a genetic network returns the glial cells to quiescence. A few transcription factors enforce quiescence in the mouse, and disruption of these allowed Müller glia to proliferate and generate new neurons after retinal injury. —PJH

Science, this issue p. 934

DEVELOPMENTAL BIOLOGY

Cells and the path of least resistance

For processes encompassing proper embryonic development, adult homeostasis, tumor cell dissemination, and immunity, certain cells must translocate from their site of origin. Migrating cells navigate physical features of their microenvironment; however, the in vivo importance of tissue topography for pathfinding is mostly unknown. Studying fruit flies, Dai *et al*. used border cells within the ovarian egg chamber to study path selection. Live imaging, genetics, mathematical modeling, and simulations showed that tissue microtopography provides an energetically favorable path of least resistance, whereas chemoattractants supply orthogonal guidance information and cell-cell adhesion contributes traction. The results provide insight into how cells integrate and prioritize topographical, adhesive, and chemoattractant cues to choose one path among many. —BAP

Science, this issue p. 987

Published by AAAS

IMMUNOLOGY

Maternal IgE activates fetal mast cells

Mast cells (MCs) are immune cells that participate in allergic reactions through their activation by immunoglobulin E (IgE) antibodies. MCs arise early during mammalian development, but it is unclear whether IgE-mediated activation occurs in fetal tissues and what the source of IgE stimulation is. Msallam *et al*. show that human and mouse fetal MCs can be sensitized by IgE of maternal origin, which crosses the placental barrier through the fetal neonatal Fc receptor (see the Perspective by Rothenberg). Prenatal maternal sensitization conferred transient allergen sensitivity after birth and resulted in the development of postnatal skin and airway inflammation in the offspring after their first exposure to allergen. Thus, both maternal IgE and fetal MCs may influence mother-to-child transmission of allergic disease during gestation. —PNK

Science, this issue p. 941; see also p. 907

MATERIALS SCIENCE

Feeling temperature and touch

The range of receptors in our skin make it possible to sense when we are touching an object and also gives us a general sense of the temperature of that object. Achieving this in an artificial skin-like material has been a challenge because most of the approaches for sensing touch are themselves temperature sensitive. You *et al*. studied the ion relaxation dynamics in a conductive elastomeric film (see the Perspective by Liu). They show that the ion relaxation time can be used as a strain-insensitive intrinsic variable for detecting temperature and the capacitance can be used as a temperature-insensitive extrinsic variable for sensing the strain, thus decoupling the two so that their signals do not interfere with each other. —MSL

Science, this issue p. 961; see also p. 910

MATERIALS SCIENCE

A soft touch

Measuring the force it takes for a hand to grasp an object requires sensors to be placed on the fingertips, but these sensors will interfere with or affect how much force ends up being applied. Lee *et al*. developed a nanomesh sensor built from a series of electrospun materials (see the Perspective by Liu). Using a robotic tester, they show that this device can repeatably detect the pressure involved in gripping an object. They also show that the sensors can be attached to human fingers and that this does not affect the force used to grasp an object. —MSL

Science, this issue p. 966; see also p. 910

SURFACE SCIENCE

Telegraphing molecules

Scanning tunneling microscope (STM) tips have long been used to manipulate atoms and molecules through direct interactions. Civita *et al*. now show that at cryogenic temperatures, the bias voltage from an STM tip can propel a large organic molecule, dibromoterfluorene, long distances—tens of nanometers along straight tracks on the flat silver (111) surface (see the Perspective by Esch and Lechner). This electrostatic effect requires the molecule to be oriented along the track, and derivatives lacking bromide groups would change direction. In a dual-tip setup, changing the bias voltage sent and received molecules between two specific points about 60 nanometers apart. —PDS

Science, this issue p. 957; see also p. 912

ANTIFUNGAL DISCOVERY

Prospecting for antifungal molecules

Marine bacteria produce a plethora of natural products that often have unusual chemical structures and corresponding reactivity, which sometimes translate into a valuable biological function. Zhang *et al*. used a metabolomic screen to zero in on microbial strains from the microbiome of a sea squirt that produces a high diversity of chemical structures. They then screened these molecules for inhibition of fungi (see the Perspective by Cowen). A polycyclic molecule dubbed turbinmicin possessed potent antifungal activity against the multidrug-resistant fungal pathogens *Candida auris* and *Aspergillus fumigatus*. Preliminary mechanism-of-action and mouse toxicity studies suggest that this molecule works though a fungus-specific pathway and is well tolerated at therapeutic doses. —MAF

Science, this issue p. 974; see also p. 906

CANCER THERAPY

Unmasking sensitivity to chemotherapy

Although the activity of the epidermal growth factor receptor (EGFR) pathway is increased in triple-negative breast cancers (TNBCs), these tumors are generally insensitive to EGFR inhibitors. Cruz-Gordillo *et al*. found that insensitivity to the EGFR inhibitor erlotinib was due to the prosurvival protein Mcl-1. *MCL1* expression in TNBC cells was promoted by the ELP family of transcription-elongation regulators, particularly ELP4. These findings suggest that combining erlotinib with an Mcl-1 inhibitor might be effective in TNBC patients. —LKF

Sci. Signal. **13**, eabb9820 (2020).

DENDRITIC CELLS

Distinct dendritic cell responses

Dendritic cells (DCs) are critical for activating naïve T cells by presenting antigens and providing costimulation, processes that are enhanced by cytokine signals from the surrounding environment. Girard *et al*. used single-cell proteogenomics and flow cytometry to examine cell type–specific responses of human peripheral blood monocyte and DC subsets to type I interferon. Interferon-β induced maturation of the recently identified $CD1c^+$ $CD5^-$ DC3 subset, which was characterized by distinct expression of the costimulatory molecule GITRL, a tumor necrosis factor family ligand, and driven by nuclear factor κB signaling. These results identify conserved and cell type–specific features of the type I interferon response of human mononuclear phagocyte subsets, including the molecular signals that monocytes and DCs may leverage to instruct T cells. —CO

Sci. Immunol. **5**, eabe0347 (2020).

Published by AAAS

REVIEW SUMMARY

FIRE ECOLOGY

Fire and biodiversity in the Anthropocene

Luke T. Kelly*, Katherine M. Giljohann, Andrea Duane, Núria Aquilué, Sally Archibald, Enric Batllori, Andrew F. Bennett, Stephen T. Buckland, Quim Canelles, Michael F. Clarke, Marie-Josée Fortin, Virgilio Hermoso, Sergi Herrando, Robert E. Keane, Frank K. Lake, Michael A. McCarthy, Alejandra Morán-Ordóñez, Catherine L. Parr, Juli G. Pausas, Trent D. Penman, Adrián Regos, Libby Rumpff, Julianna L. Santos, Annabel L. Smith, Alexandra D. Syphard, Morgan W. Tingley, Lluís Brotons

BACKGROUND: Fire has shaped the diversity of life on Earth for millions of years. Variation in fire regimes continues to be a source of biodiversity across the globe, and many plants, animals, and ecosystems depend on particular temporal and spatial patterns of fire. Although people have been using fire to modify environments for millennia, the combined effects of human activities are now changing patterns of fire at a global scale—to the detriment of human society, biodiversity, and ecosystems. These changes pose a global challenge for understanding how to sustain biodiversity in a new era of fire. We synthesize how changes in fire activity are threatening species with extinction across the globe, highlight forward-looking methods for predicting the combined effects of human drivers and fire on biodiversity, and foreshadow emerging actions and strategies that could revolutionize how society manages fire for biodiversity in the Anthropocene.

ADVANCES: Our synthesis shows that interactions with anthropogenic drivers such as global climate change, land use, and biotic invasions are transforming fire activity and its impacts on biodiversity. More than 4400 terrestrial and freshwater species from a wide range of taxa and habitats face threats associated with modified fire regimes. Many species are threatened by an increase in fire frequency or intensity, but exclusion of fire in ecosystems that need it can also be harmful. The prominent role of human activity in shaping global ecosystems is the hallmark of the Anthropocene and sets the context in which models and actions must be developed. Advances in predictive modeling deliver new opportunities to couple fire and biodiversity data and to link them with forecasts of multiple drivers including drought, invasive plants, and urban growth. Making these connections also provides an opportunity for new actions that could revolutionize how society manages fire. Emerging actions include reintroduction of mammals that reduce fuels, green fire breaks comprising low-flammability plants, strategically letting wildfires burn under the right conditions, managed evolution of populations aided by new genomics tools, and deployment of rapid response teams to protect biodiversity assets. Indigenous fire stewardship and reinstatement of cultural burning in a modern context will enhance biodiversity and human well-being in many regions of the world. At the same time, international efforts to reduce greenhouse gas emissions are crucial to reduce the risk of extreme fire events that contribute to declines in biodiversity.

OUTLOOK: Conservation of Earth's biological diversity will be achieved only by recognition of and response to the critical role of fire in shaping ecosystems. Global changes in fire regimes will continue to amplify interactions between anthropogenic drivers and create difficult trade-offs between environmental and social objectives. Scientific input will be crucial for navigating major decisions about novel and changing ecosystems. Strategic collection of data on fire, biodiversity, and socioeconomic variables will be essential for developing models to capture the feedbacks, tipping points, and regime shifts characteristic of the Anthropocene. New partnerships are also needed to meet the challenges ahead. At the local and regional scale, getting more of the "right" type of fire in landscapes that need it requires new alliances and networks to build and apply knowledge. At the national and global scale, biodiversity conservation will benefit from greater integration of fire into national biodiversity strategies and action plans and in the implementation of international agreements and initiatives such as the UN Convention on Biological Diversity. Placing the increasingly important role of people at the forefront of efforts to understand and adapt to changes in fire regimes is central to these endeavors. ■

PHOTO CREDITS: J. CARMODY / AUSTRALIAN BROADCASTING CORPORATION (TOP LEFT). AAP PHOTOS (TOP RIGHT). A. DE LANGE (BOTTOM LEFT). J. R. WELCH (BOTTOM RIGHT)

Interactions between fire and anthropogenic drivers such as global climate change, land use, and invasive species are reshaping ecosystems worldwide. A hotter and drier climate causes more extreme fire weather in southeastern Australia and significant loss of biota. Human-caused ignitions at the interface of urban areas and forests increase the risk of large, severe fires in the western United States, with growing human and ecological costs. In South Africa, fynbos shrublands depend on recurrent fire, yet invasive woody species can promote high-intensity fires that harm native plants and seedbanks. Changes in climate, land use, and species redistributions are underpinned by socioeconomic drivers. In many parts of the world, cessation of traditional fire practices has been linked with detrimental outcomes for biodiversity. In the fire-dependent savannas (cerrado) of Brazil, deliberate use of fire by Indigenous and local peoples, such as the Xavante, can have positive effects on biodiversity.

The list of author affiliations is available in the full article online.
*Corresponding author. Email: ltkelly@unimelb.edu.au
Cite this article as L. T. Kelly *et al.*, *Science* **370**, eabb0355 (2020). DOI: 10.1126/science.abb0355

READ THE FULL ARTICLE AT
https://doi.org/10.1126/science.abb0355

REVIEW

FIRE ECOLOGY

Fire and biodiversity in the Anthropocene

Luke T. Kelly[1]*, Katherine M. Giljohann[2], Andrea Duane[3], Núria Aquilué[3,4], Sally Archibald[5,6], Enric Batllori[7,8], Andrew F. Bennett[9], Stephen T. Buckland[10], Quim Canelles[3], Michael F. Clarke[9], Marie-Josée Fortin[11], Virgilio Hermoso[3], Sergi Herrando[12], Robert E. Keane[13], Frank K. Lake[14], Michael A. McCarthy[2], Alejandra Morán-Ordóñez[3], Catherine L. Parr[5,15,16], Juli G. Pausas[17], Trent D. Penman[1], Adrián Regos[18,19], Libby Rumpff[2], Julianna L. Santos[1], Annabel L. Smith[20,21], Alexandra D. Syphard[22,23,24], Morgan W. Tingley[25], Lluís Brotons[3,7,26]

Fire has been a source of global biodiversity for millions of years. However, interactions with anthropogenic drivers such as climate change, land use, and invasive species are changing the nature of fire activity and its impacts. We review how such changes are threatening species with extinction and transforming terrestrial ecosystems. Conservation of Earth's biological diversity will be achieved only by recognizing and responding to the critical role of fire. In the Anthropocene, this requires that conservation planning explicitly includes the combined effects of human activities and fire regimes. Improved forecasts for biodiversity must also integrate the connections among people, fire, and ecosystems. Such integration provides an opportunity for new actions that could revolutionize how society sustains biodiversity in a time of changing fire activity.

Fire has shaped the diversity of life on Earth for millions of years (*1*). Variation in fire regimes enables many plants to complete their life cycles (*2*), creates habitats for a range of animals (*3*), and maintains a diversity of ecosystems (*4*). Although people have used fire to modify environments for millennia (*5*–*7*), the cumulative effects of human activities are now changing patterns of fire at a global scale—to the detriment of human society, biodiversity, and ecosystems.

Many recent fires have burned ecosystems where fire has historically been rare or absent, from the tropical forests of Southeast Asia (*8*) and South America (*9*) to the tundra of the Arctic Circle (*10*). Large, severe fires have also been observed in areas with a long history of recurrent fire, and this is consistent with predictions of increased wildfire activity in the boreal forests of Canada and Russia (*11*, *12*) and the mixed forests and shrublands of Australia, southern Europe, and the western United States (*13*–*15*). Conversely, fire-dependent grassland and savanna ecosystems in countries such as Brazil, Tanzania, and the United States have had fire activity reduced and even excluded (*16*–*18*). These emerging changes pose a global challenge for understanding how to sustain biodiversity in a new era of fire. This requires improved knowledge of the interactions among fire, biodiversity, and human drivers and new insights into conservation actions that will be effective in this changing environment.

In this review, we explore the causes and consequences of fire-induced changes to biodiversity in the Anthropocene, the current era characterized by the prominent role of human activity in shaping global ecosystems. We start by synthesizing how changes in fire activity threaten species with extinction across the globe. Next, we examine how multiple human drivers are causing these changes in fire activity and biodiversity. We then highlight forward-looking methods for predicting changes in ecosystems and forecasting the positive and negative effects of fire on biodiversity. Finally, we foreshadow emerging actions and strategies that could revolutionize how society manages biodiversity in ecosystems that experience fire. Our review concludes that conservation of Earth's biodiversity is unlikely to be achieved without incorporating the critical role of fire in national biodiversity strategies and action plans and in the implementation of international agreements and initiatives such as the UN Convention on Biological Diversity.

Extinction risk in a fiery world

A central concept in fire science is the fire regime, which describes the type, frequency, intensity, seasonality, and spatial dimensions of recurrent fire (*19*). Many species are adapted to a particular fire regime, so substantial changes to these fire characteristics can harm populations (*20*) and shift ecosystems (*21*). For example, plants that require fire to release seeds can be threatened by fire intervals shorter than the time needed for them to mature and reestablish a seed bank or by fire intervals longer than seed and plant life spans (*22*). For animals, changes in the frequency and intensity of fire can reduce the availability of key resources for foraging and shelter, limit the capacity to recolonize regenerating habitats, and, in the case of severe fires, directly increase mortality (*23*).

We reviewed the 29,304 terrestrial and freshwater species categorized as threatened with extinction by the International Union for the Conservation of Nature (IUCN) (*24*) and found that for at least 4403 (15%), modification of fire regimes is a recorded threat. Changes in fire activity threaten a range of taxonomic groups that have been assessed comprehensively or through sampling representative species or multiple regions, from birds, dragonflies, and mammals to gymnosperms, legumes, and monocots (Fig. 1A). Some groups, such as gymnosperms, are at greater risk of fire-driven extinction: Changed fire activity is a threat to 28% of these taxa classified as critically endangered, endangered, or vulnerable (Fig. 1A).

Changes in fire activity threaten biodiversity in habitat types worldwide (Fig. 1B). Proportionally, the threat from changed fire activity to species at risk of extinction is greater for savannas (28%), closely followed by grasslands (26%), rocky areas (26%), shrublands (26%), and forests (19%) (Fig. 1B).

Across nine taxonomic groups that have been assessed systematically (Fig. 1A), we found that at least 1071 species are categorized as threatened by an increase in fire frequency or intensity and 55 species by exclusion of fire. This delineation, however, oversimplifies the nature of threats; for example, it masks the relationship in some ecosystems

[1]School of Ecosystem and Forest Sciences, University of Melbourne, Parkville, Victoria 3010, Australia. [2]School of BioSciences, University of Melbourne, Parkville, Victoria 3010, Australia. [3]InForest JRU (CTFC-CREAF), 25280 Solsona, Lleida, Spain. [4]Centre d'Étude de la Forêt, Université du Québec à Montréal, Montreal, Quebec H3C 3P8, Canada. [5]Centre for African Ecology, School of Animal, Plant and Environmental Sciences, University of the Witwatersrand, Johannesburg, South Africa. [6]Natural Resources and the Environment, CSIR, Pretoria, South Africa. [7]CREAF, Edifici C. Autonomous, University of Barcelona, 08193 Bellaterra, Barcelona, Spain. [8]Department of Evolutionary Biology, Ecology, and Environmental Sciences, University of Barcelona, 08028 Barcelona, Spain. [9]Department of Ecology, Environment and Evolution, Centre for Future Landscapes, La Trobe University, Bundoora, Australia. [10]Centre for Research into Ecological and Environmental Modelling, University of St Andrews, St Andrews, Fife KY16 9LZ, UK. [11]Department of Ecology & Evolutionary Biology, University of Toronto, Toronto, Ontario M5S 3B2, Canada. [12]Catalan Ornithological Institute, Natural History Museum of Barcelona, 08019 Barcelona, Catalonia, Spain. [13]U.S. Department of Agriculture Forest Service Rocky Mountain Research Station, Missoula Fire Sciences Laboratory, Missoula, MT 59808, USA. [14]U.S. Department of Agriculture Forest Service Pacific Southwest Research Station, Albany, CA 94710, USA. [15]Department of Earth, Ocean & Ecological Sciences, University of Liverpool, Liverpool, UK. [16]Department of Zoology & Entomology, University of Pretoria, Pretoria, South Africa. [17]Centro de Investigaciones sobre Desertificación (CIDE-CSIC), 46113 Montcada, Valencia, Spain. [18]Departamento de Zooloxía, Xenética e Antropoloxía Fisica, Universidade de Santiago de Compostela, Santiago de Compostela, Spain. [19]CIBIO/InBIO, Research Center in Biodiversity and Genetic Resources, ECOCHANGE Group, Vairão, Portugal. [20]School of Agriculture and Food Science, University of Queensland, Gatton 4343, Australia. [21]Zoology, School of Natural Sciences, Trinity College Dublin, Dublin 2, Ireland. [22]Vertus Wildfire, San Francisco, CA 94108, USA. [23]San Diego State University, San Diego, CA 92182, USA. [24]Conservation Biology Institute, Corvallis, OR 97333, USA. [25]Ecology and Evolutionary Biology, University of California, Los Angeles, CA 90095, USA. [26]Spanish Research Council (CSIC), 08193 Bellaterra, Barcelona, Spain.
*Corresponding author. Email: ltkelly@unimelb.edu.au

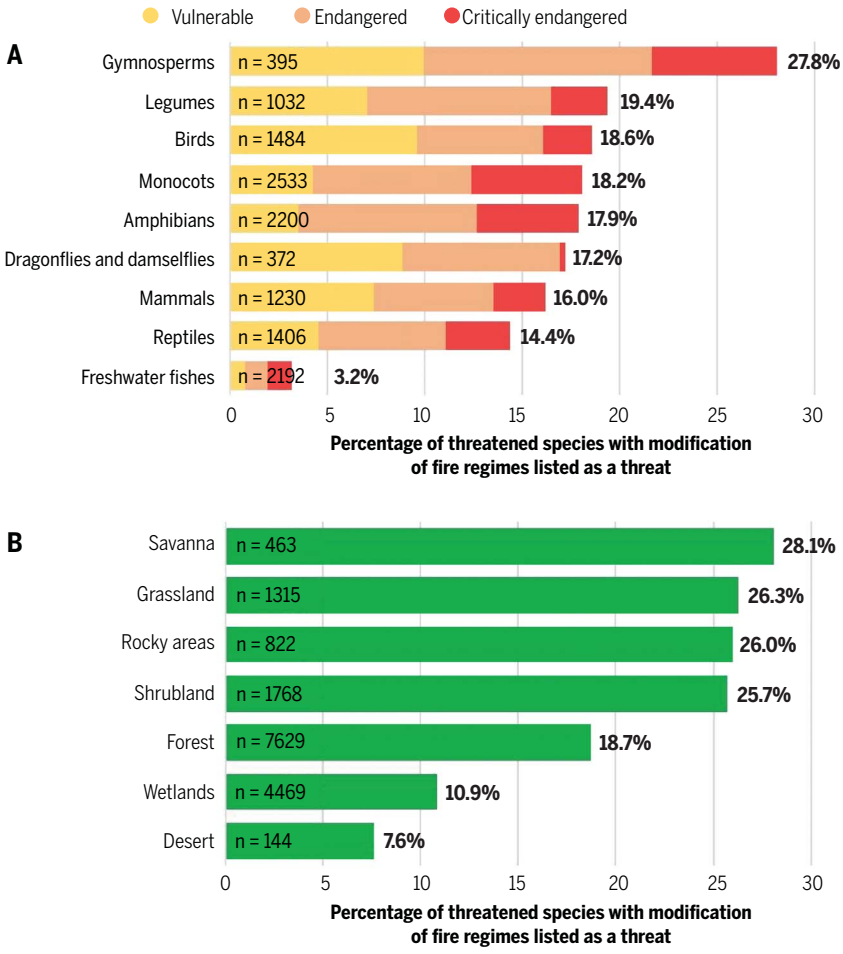

Fig. 1. Fire-driven extinction risk by taxonomic group and habitat type. (**A**) The percentage of threatened species (those classified as critically endangered, endangered, or vulnerable) for which modification of fire regimes is a threat (defined as threat type "Natural system modifications - Fire and fire suppression" in the IUCN Red List) for nine taxonomic groups. *n* is the total number of threatened species within each taxonomic group. Selected species include those globally assessed for the IUCN Red List, from groups assessed either comprehensively (amphibians, birds, gymnosperms, mammals), through a sampled approach of global data (dragonflies and damselflies, legumes, monocots, reptiles), or across several regions (freshwater fishes). The estimated percentages of species in each group that has been assessed include: gymnosperms, 91%; legumes, 17%; birds, 100%; monocots, 10%; amphibians, 84%; dragonflies and damselflies, 72%; mammals, 90%; reptiles, 71%; and freshwater fishes, 61%. (**B**) The percentage of threatened species for which modification of fire regimes is a threat for seven selected habitat types. *n* is the total number of threatened species, of the nine taxonomic groups within each habitat type [as defined in the IUCN Red List (*24*)].

between fire exclusion and subsequent intense wildfire from fuel accumulation. Nevertheless, important differences within and between habitat types emerge when the direction of fire regime change is considered. For example, of the species categorized as threatened by an increase or decrease in fire activity in forests (Fig. 1B), exclusion of fire is a threat to 17% of those in temperate forests and only 1% of those in tropical moist montane forests.

Changes in fire activity also threaten other levels of biodiversity. Assessments undertaken through the IUCN Red List of Ecosystems show that altered fire regimes, in combination with other drivers, threaten whole ecosystems with collapse, including the Cape Flats Sand Fynbos of South Africa and the mountain ash (*Eucalyptus regnans*) forests of Australia (*25*). Many biodiversity hotspots remain inadequately studied, and unprecedented recent fires such as the 12.6 million ha of vegetation burned in eastern Australia from late 2019 to early 2020 (*26*) mean that numerous species may have declined since their status was assessed. Thus, we are likely underestimating the total number of species threatened by ongoing changes in fire regimes.

Drivers of change in the Anthropocene

Among the profound consequences of the Anthropocene is the acceleration of Earth toward a hotter climate and a markedly different biosphere (*27*). Fire is both a consequence of and a contributor to this acceleration (*28*) but it is not acting alone: Interactions between fire and anthropogenic drivers such as global climate change, land use, and invasive species are reshaping ecosystems worldwide. Recent work describing global fire regimes has shown that patterns of fire are closely linked to climate, vegetation, and human activity (*7*, *17*, *29*, *30*). Here, we synthesize linked changes in biodiversity and fire regimes and how they are shaped by three groups of direct drivers arising from human actions (Fig. 2 and table S1), as well as indirect socioeconomic drivers that underpin them (*31*). Our focus is on taxa and ecosystems likely to be threatened by the pace and magnitude of such change while recognizing that some taxa stand to benefit from these changes.

Global climate change

Anthropogenic climate change, including rising atmospheric CO_2 and a hotter global climate, modifies fire regimes by changing fuels, ignitions, and fire weather (*32*). These changes in turn alter the composition of ecosystems and the nature of species interactions. A prime example is fire interacting with more-severe droughts. In the Mediterranean Basin, abrupt shifts in ecosystems from forest to shrubland are triggered by large fire events followed by at least one extreme drought year (*33*). Elsewhere, intensifying droughts are contributing to more widespread fires in tropical forests in Amazonia, the Congo Basin, and Southeast Asia, with high mortality of thin-barked trees (*34*). More frequent or more intense climate-induced fires even threaten forests with a long history of high-intensity fire. For example, successive fires that occur before trees can set seed and reproduce are reshaping the species composition of temperate forests in Australia (*35*), subalpine forests in the United States (*36*), and boreal forests in Canada (*11*) and Russia (*12*). Such changes have cascading effects on the biota. For example, high-intensity fires in boreal forests in Alaska negatively affect microbes and fungi through soil heating (*37*) and by reducing the cover of lichens, a critical food source for caribou (*Rangifer tarandus*) (*38*).

Land-use change

Humans alter fire regimes through land-use changes associated with agriculture, forestry, and urbanization and by intentionally starting or suppressing fires (*6*, *7*, *13*). How changes in land use affect fuels, fire, and biodiversity varies depending on the type of activity and ecosystem.

Until recent decades, tropical broadleaf forests of the Afrotropical, Indomalayan, and Neotropical realms rarely experienced large fires (*8*, *39*). Contemporary land use,

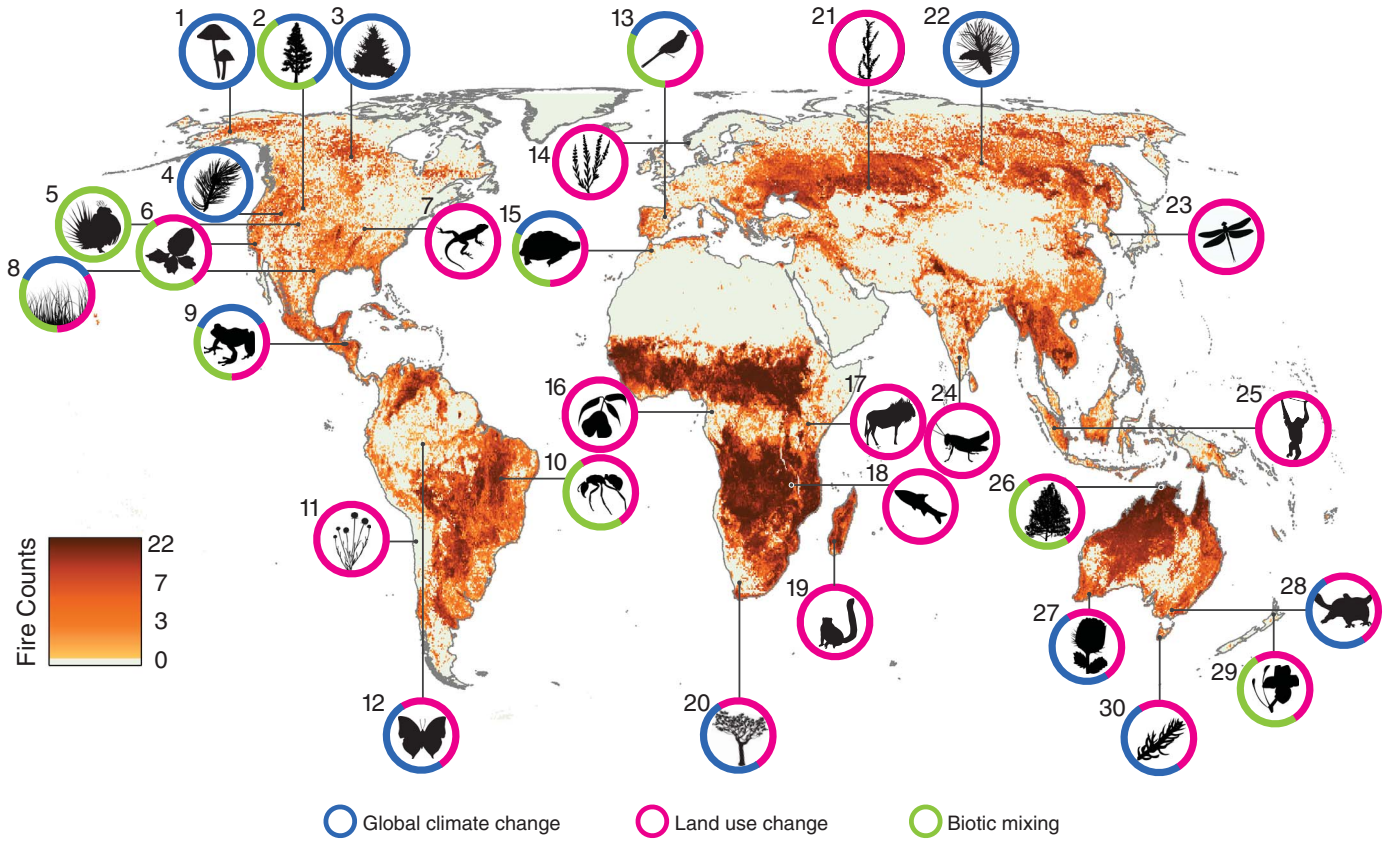

Fig. 2. Global portrait of linked changes in fire and biodiversity. Examples of documented and predicted fire-driven changes in biodiversity are shown. Details of the anthropogenic drivers associated with each of these changes are provided in the main text or table S1, following the numbered key. Examples are overlaid on a map of the number of times a fire was recorded from 2000 to 2019 in a given 500 m by 500 m MODIS pixel averaged across the 10 km by 10 km pixels displayed on the map.

including deforestation fires to clear primary forest for agriculture, often promotes more frequent and severe fires. In the Amazon basin, logging, habitat fragmentation, and climate change act synergistically to increase the risk of larger and more severe fires (*39*). This can drive abrupt change from forest to derived savannas (*40*). Cascading effects on a host of forest fauna have been observed, including declines in ant and butterfly communities (*40*, *41*) (Fig. 3). In tropical forests in Indonesia, massive wildfires caused by land clearing threaten some of the world's most biodiverse ecosystems and emblematic species such as the orangutan (*Pongo borneo*) (*8*).

By contrast, fire has been markedly reduced and almost eliminated from some grassy ecosystems, such as the Serengeti-Mara savanna of Tanzania, through increased livestock grazing and habitat fragmentation (*18*). This has led to woody encroachment, which threatens wild populations of large herbivores (Fig. 3) (*42*). Fire exclusion in the hyperdiverse Brazilian Cerrado is threatening biodiversity in areas where recurrent fire, which limits woody encroachment, has been impeded by habitat fragmentation and fire suppression policies. Where forests have encroached into unburned Cerrado, plant species richness has declined by 27% and ant richness by 35% (*43*). In other areas, such as parts of the Great Plains of North America, a century or more of active fire suppression has led to the replacement of grassland with juniper (*Juniperus* spp.) woodland (*16*).

Urbanization and habitat modification are important drivers of fire regimes (*13*) and of biodiversity (*44*) in Mediterranean-type and temperate ecosystems. In Southern California, native chaparral shrublands support exceptionally high plant diversity. Short intervals between fires, associated with increased ignitions near urban areas, trails, and roads, are converting chaparral into vegetation dominated by exotic herbs (*45*). In the Mediterranean Basin, expansion of urban areas is linked with agricultural land abandonment: After rural depopulation, mosaics of farmland and open forest have shifted to more fire-prone shrublands and forests (*46*). Larger and more severe wildfires are expected to negatively affect forest-dwelling birds, but some open-country species will benefit from more frequent fires (*47*). In temperate mountain ash forests of Australia, the cumulative impacts of logging and extensive wildfires have removed large trees, placing populations of arboreal mammals that nest in old trees, such as Leadbeater's possum (*Gymnobelideus leadbeateri*), at increased risk of extinction (*48*).

Biotic mixing

Humans have redistributed species across the globe (*49*) and, in doing so, have created novel assemblages that modify fuels, fire regimes, and postfire dynamics (*50*). In many parts of the world, invasive plants have increased flammability and fire frequency (*22*, *51*). For example, in deserts and shrublands of the western United States, invasive cheatgrass (*Bromus tectorum*) increases fuel loads and continuity, which alters regional fire regimes (*52*). In turn, increased fire frequency reduces habitat for the greater sage-grouse (*Centrocercus urophasianus*), a bird that prefers to forage in dense sagebrush (*53*). Invasive animals can also modify fire regimes by altering fuels (*54*). The introduction of exotic vertebrate herbivores to New Zealand generated open conditions favorable for frequent low-intensity fires and contributed to the conversion of

A Exclusion of fire threatens wild herbivores in savanna ecosytems in the Serengeti-Mara, Tanzania.

B Deforestation fires cause shifts in vegetation with cascading effects on fauna in Amazonia, Brazil.

Fig. 3. Some tropical ecosystems are experiencing too much fire and others not enough. (**A**) Frequent fires are a key aspect of African savanna ecosystems that support a large portion of the world's remaining wild large mammals. However, fire activity in the Serengeti-Mara of Tanzania has been reduced, and some areas no longer experience fire. This could increase shrub encroachment (top left; photo by S. Archibald) and the displacement of wild herbivores that prefer open areas (top right; photo by D. D'Auria) (*18*, *42*). (**B**) The Amazon basin is home to ~10 to 15% of the world's terrestrial biodiversity. In southeast Amazonia (bottom left; photo by P. M. Brando), human drivers increase deforestation fires and uncontrolled fires. This is driving shifts from humid forest to drier forests or derived savannas. Cascading effects on fauna include the decline of forest butterfly species such as the leaf wing butterfly (*Zaretis itys*) [bottom right; photo by Morales/agefotostock (*40*)].

temperate forests to shrublands (*55*). Invasive animals can also affect biodiversity through their influence on the postfire recovery of species: In Australia, an increase in the activity of the red fox (*Vulpes vulpes*) and feral cat (*Felis catus*), as well as their greater hunting success in postfire environments, increases mortality of native animals (*56*).

Disruption of biotic interactions and the removal of species can also shape fire and biodiversity associations. Experimental evidence indicates that removal of large grazing mammals in Africa and North America alters ecosystem structure and increases fire activity (*57*). Indeed, our review of IUCN Red List data indicates that modification of fire activity has contributed to the recent extinction of 37 species, including a suite of marsupials in Australia whose digging and foraging activity may have influenced fire regimes (*58*).

Socioeconomic drivers

Demographic, economic, political, and institutional factors underpin changes in land use and other direct drivers of fire regimes and their impact on biodiversity (*6*, *15*, *59*). Contemporary changes in human population size and distribution shape fire regimes worldwide, with corresponding pressures on biodiversity and ecosystems (*17*, *60*). In the Amazon basin, increases in deforestation and uncontrolled fires have underlying societal causes, including market demand for beef, soybean, and timber, as well as transportation and energy projects and weak institutional governance (*9*, *61*). Political and social institutions also are important. After the collapse of the Soviet Union, the abandonment of large areas of cropland in Kazakhstan provided opportunities for the restoration of steppe grasslands. However, in some recovering grasslands, the removal of grazing animals and the subsequent increase in fire activity has reduced plant species richness. (*62*). Conflicts are a largely unrecognized driver of changes in fire regimes: An endangered dragonfly, *Asiagomphus coreanus*, inside the demilitarized zone between South Korea and North Korea is threatened by anthropogenic fire used to reduce vegetation for increased visibility (*24*).

Even before the acceleration of social and ecological changes in the mid-1900s (*31*), cessation of traditional fire practices in many parts of the world transformed landscapes. For example, colonialism in the southwestern United States disrupted fire-dependent human cultures with cascading effects for ecosystems, including dense stands of conifer forests replacing previously open vegetation (*63*). In Australia, changes arising from the displacement of Indigenous peoples and their purposeful

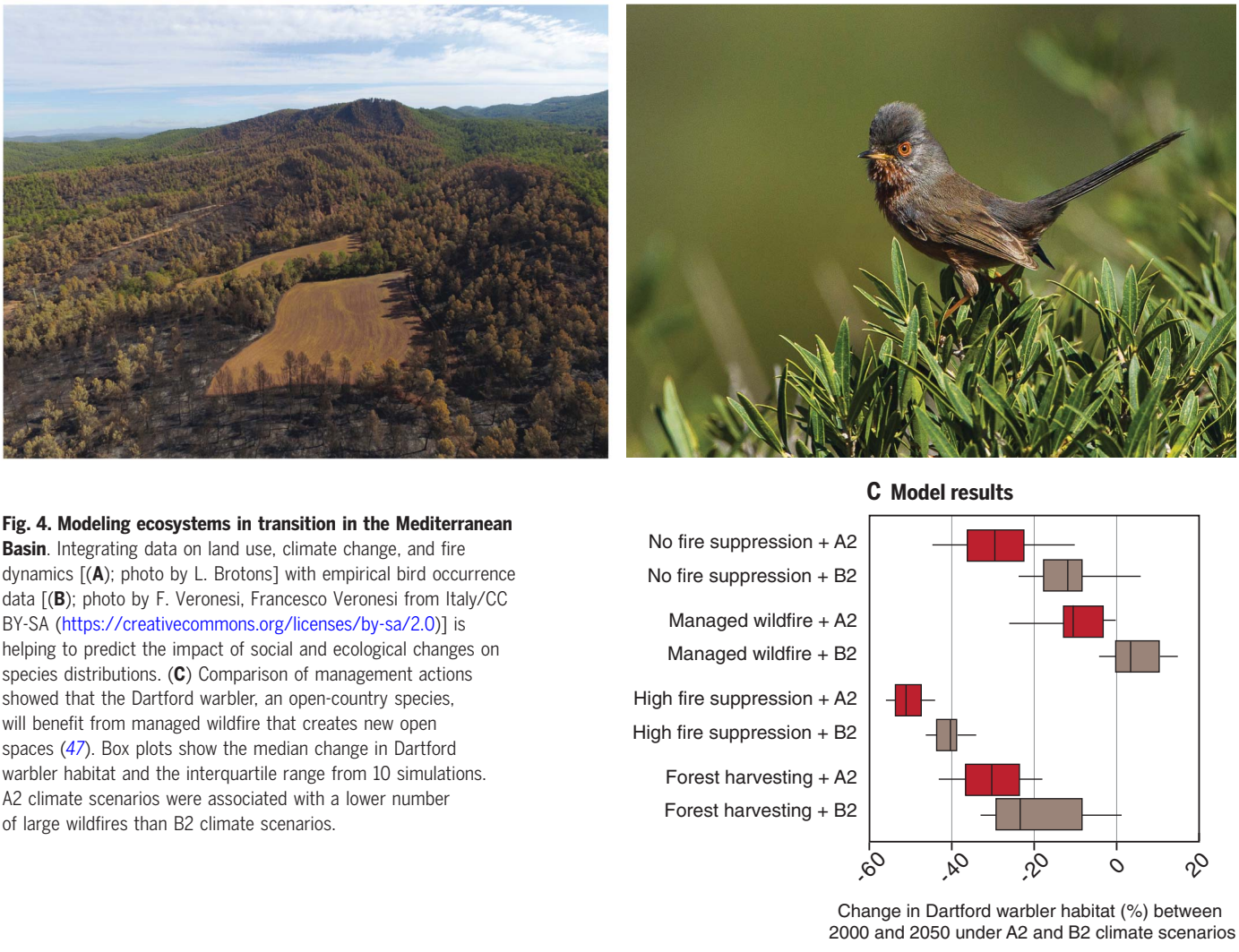
A Recently burnt pine-oak forest and farmland
B Dartford warbler (Sylvia undata)
C Model results
No fire suppression + A2
No fire suppression + B2
Managed wildfire + A2
Managed wildfire + B2
High fire suppression + A2
High fire suppression + B2
Forest harvesting + A2
Forest harvesting + B2
-60
-40
-20
0
20
Change in Dartford warbler habitat (%) between 2000 and 2050 under A2 and B2 climate scenarios

Fig. 4. Modeling ecosystems in transition in the Mediterranean Basin. Integrating data on land use, climate change, and fire dynamics [(**A**); photo by L. Brotons] with empirical bird occurrence data [(**B**); photo by F. Veronesi, Francesco Veronesi from Italy/CC BY-SA (https://creativecommons.org/licenses/by-sa/2.0)] is helping to predict the impact of social and ecological changes on species distributions. (**C**) Comparison of management actions showed that the Dartford warbler, an open-country species, will benefit from managed wildfire that creates new open spaces (*47*). Box plots show the median change in Dartford warbler habitat and the interquartile range from 10 simulations. A2 climate scenarios were associated with a lower number of large wildfires than B2 climate scenarios.

use of fire have been linked with extinctions of mammals (*24*), transformation of vegetation types (*5*), and decline of species such as the endemic Tasmanian pine (*Athrotaxis selaginoides*) (*64*). Cessation of traditional fire practices continues to affect species and ecosystems today (*5*).

Improving the forecast for biodiversity

To underpin new and emerging approaches to conservation in the Anthropocene, an urgent task is to better quantify how biodiversity responds to changing fire regimes. This requires a mix of empirical studies, manipulative experiments, and modeling. Various methods are available to predict changes in fire behavior and fire effects (*65*), changes to biodiversity (*66*), and anthropogenic drivers (*67*). Here, we focus on methods that couple information on fire and biodiversity, particularly those that incorporate human drivers.

A surge of empirical studies has explored the relationship between biodiversity and the spatial and temporal variation in fire regimes (sometimes called "pyrodiversity") (*3*). For example, a continent-wide assessment of savanna ecosystems in Africa showed that pyrodiversity was important in wet savannas, where areas with large variation in fire size, intensity, and timing had 27% more mammal species and 40% more bird species than areas with low variation in fire regimes (*68*). Studies in California found that the diversity of pollinators, plants, and birds in mixed-conifer forests was higher in areas with greater spatial variation in fire interval and severity (*69*, *70*). Linking such information on fire patterns and biodiversity with projections of future wildfires or management actions provides a powerful way to forecast future changes to ecosystems. For example, modeling has been used to identify alternative strategies for prescribed burning to reduce wildfire risk for populations of the iconic koala (*Phascolarctos cinereus*) in southeastern Australia (*71*).

Advances in predictive modeling also deliver new opportunities to couple fire and biodiversity data with likely trajectories of multiple drivers. For instance, coupling a dynamic fire-succession model with species distribution models enabled projection of the impact of alternative management and climate change scenarios on bird communities in northeastern Spain (*47*). Letting some wildfires burn in mild weather conditions was predicted to create new open spaces that would benefit open-habitat species (*47*) (Fig. 4). Forest harvesting for bioenergy production, an important socioeconomic consideration, also benefited some species by offsetting the loss of open habitats through a reduction in severe fires. Integrating projections of climate, wildfires, and species distributions offers an opportunity

to design nature reserves that are effective now and in the future (47).

Process-based models that incorporate biological mechanisms such as demography and dispersal offer a robust way to model potential relationships between fire and biodiversity that may be outside the range of past conditions (66). For example, an individual-based model was used to examine the response of Hooker's banksia (*Banksia hookeriana*), a shrub species in southwestern Australia, to climate-mediated shifts in seed production, postfire recruitment, and shortened fire intervals (72). Modeling revealed that the effects of multiple stressors will threaten population persistence; a drier climate reduces the range of fire intervals that enable seed production and seedling recruitment, and the intervals between fires are projected to become shorter (72). Process-based models can also guide strategic management of populations of tree and shrub species when changes in fire regimes interact with habitat fragmentation (73), pathogens (74), and urban growth (75).

Currently, predictive models of biodiversity do not incorporate empirical data on evolutionary responses to fire, yet some aspects of biodiversity are rapidly evolving in the face of changing fire regimes. In Chile, where shrublands have experienced human-driven increases in fire frequency, anthropogenic fires are shaping the evolution of seed traits in a native herb, including seed pubescence and shape, with fire selecting plants with thicker pericarps (76). Variation in fire-related traits caused by heritable genetic variation between individuals has been assessed only for a small number of plant species but indicates moderate evolutionary potential (77). There are exciting opportunities to apply models and tools developed by evolutionary biologists, such as the breeder's and Price's equations (66), to forecast fire-driven evolutionary changes in the Anthropocene.

Feedbacks among fire, biodiversity, and other natural and anthropogenic drivers of biodiversity are important and have been assessed using a variety of methods (39, 59, 78, 79). However, new approaches to quantifying feedbacks between social and ecological systems are needed. A promising technique is the use of agent-based models that quantify how changes in the environment create feedbacks that influence the likelihood of human actions (80). Such models can incorporate feedbacks between fire-driven changes in vegetation and the likelihood of human actors (e.g., family forest owners and homeowners) taking actions such as prescribed burning. In mountain forests in the United States, incorporating social and environmental interactions that influence the probability of planned fire and wildfire helped to quantify the effect of alternative fire management strategies on wildlife such as birds and mammals (80).

Emerging strategies and actions

The prominent role of human activity in shaping ecosystems at planetary scales is the hallmark of the Anthropocene and sets the context for emerging strategies and actions. First, it demands that scientists, stakeholders, and decision-makers confront the diverse and often synergistic changes to the environment that are occurring worldwide and emphasizes the need for new, bolder conservation initiatives. Second, it places the increasingly important role of people at the forefront of efforts to understand and adapt to ecosystem changes. Third, by linking people and local land uses with ecosystems, there is a greater likelihood of finding effective, place-based solutions to suit species and ecosystems.

A suite of emerging actions, some established but receiving increasing attention, others new and innovative, could be effective in promoting biodiversity in a new era of fire (Table 1). We summarize these (nonmutually exclusive) actions under three themes: (i) fire regimes that are managed by being tailored to species or ecosystems, (ii) approaches that focus on "whole ecosystems" (and not just on fire), and (iii) approaches that recognize the critical role of people.

A first set of approaches involves actively managing fire to suit particular species or ecosystems. This means ensuring the right amount, pattern, and timing of fire in landscapes that need it and less fire in those that do not. Temperate forests in the western United States, for example, have had a century-long history of fire suppression. A new prospect in temperate ecosystems is forest managers letting wildfires burn when conditions are not extreme (81) to promote mixed-severity fires that advantage a range of species (70). For example, in Yellowstone National Park, a policy of permitting lightning-ignited fires to burn has created more diverse landscapes (81) that support a high species richness of plants and their pollinators (69). Some fire-excluded forests in southern Australia, southern Europe, and the western United States have such high levels of fuels that mechanical treatments combined with prescribed fire may be needed to reduce the potential for biodiversity losses associated with high-intensity wildfire (15, 82).

For innovative fire management in the Anthropocene, careful planning and deep knowledge of an ecosystem and its biota will be important to ensure the appropriate fire regime to achieve conservation objectives (3, 68), whether the aim is to promote critical habitat features such as hollow-bearing trees (48), functional resources such as seed banks (20), or landscapes with diverse fire histories (70).

Although fire suppression threatens some ecosystems, targeted suppression can be a positive strategy to protect vulnerable species and ecosystems in fire-dependent and fire-sensitive ecosystems alike. For example, the fire-sensitive Wollemi pine (*Wollemia nobilis*) is an endangered Gondwanan relic with less than 200 individuals in a single rainforest valley in eastern Australia. During extensive wildfires in 2020, firefighters used targeted suppression to save this species (83). In subalpine vegetation of the western United States, surviving trees in whitebark pine (*Pinus albicaulis*) forests devastated by an exotic pathogen are actively protected by targeted fire suppression because they represent the seed source for future populations (84). Active fire suppression also has benefits in areas where it can reduce an uncharacteristically high fire frequency arising from increased human-caused ignitions associated with urban expansion (45).

A second set of approaches focuses on whole ecosystems, not just fire. Ecosystems can be particularly vulnerable to changes in fire regimes when already stressed by other threats and the synergies emerging from these threats (39). For example, populations of plants and animals affected by extreme drought, or those that occur in disconnected patches or are under pressure from exotic predators, are more likely to be threatened by fire when it interacts with these other disturbances (56, 72, 73). A whole-ecosystem approach that manages fire in the context of wider restoration and conservation actions is more likely to be effective (79). For example, strategic rewetting of drained peatlands and replanting with fire-resistant mosses is a promising technique for reducing fire frequency and promoting biodiversity in boreal forests in Canada (85). In the Amazon rainforest, a large-scale restoration project involving local citizens and national actors has been proposed to increase the total area and connectivity of rainforest habitat (86).

Reintroduction of species that have key functional roles offers an innovative opportunity to promote ecological processes that moderate fire regimes (57). For example, the reintroduction of a digging marsupial (*Isoodon fusciventer*) in an urban reserve in western Australia led to reduction of surface fuel loads and the predicted rate of fire spread (58). Digging animals modify fuels by creating foraging pits and burrows; the reintroduction of previously common digging species is an exciting prospect for restoring fire-prone ecosystems (58). In Africa, reintroducing native grazing animals such as the white rhinoceros (*Ceratotherium simum*) creates patchy fire regimes (57). Habitats created by these native megaherbivores differ from areas heavily grazed by livestock and provide habitat for birds, insects, and plants (57). Reintroduction of species to assist in the management of fire will likely

A Yurok and Karuk ignitors burning under oaks to accomplish multiple objectives

B Fire improves Huckleberry (*Vaccinium* spp.) growth, an important food plant for animals and people

Fig. 5. Pyrodiversity with purpose in temperate forests of the western United States. (**A**) The Klamath-Siskiyou region is home to Indigenous peoples with different languages and histories. After more than a century of policies that promoted fire suppression, newly developed collaborations led by Indigenous communities and including scientists and local stakeholders are being formed to reinstate Indigenous fire practices. This cultural burning diversifies the frequency, seasonality, and intensity of fires and results in a fine-scale mosaic of disturbance history (photo by F. Lake). (**B**) Reinstating Indigenous burning, coupled with other cultural practices such as hunting, gathering, and tending of habitats for resources, supports a wide range of biodiversity, including species used for food, materials, medicines, and ceremonial purposes (*91*) (photo by F. Lake).

be most valuable in ecosystems that have experienced an increase in fire activity.

Many circumstances require the simultaneous management of multiple threats or drivers to achieve benefits for biodiversity. Invasion of highly flammable herbaceous species can exacerbate increased fire frequency, causing a positive grass-fire feedback cycle now evident across a range of deserts, shrublands, and savannas (*51*, *52*). Preventing or breaking this cycle in which invasive grasses replace woody plants relies on coordination among fire managers, conservation practitioners, and local communities to not only reduce ignitions but also to detect and remove invasive species as early as possible. In other cases, hotter burns may be applied to tackle encroachment by unwanted woody plants through the judicious use of "fire storms," such as in temperate grasslands of the central United States and savanna ecosystems in southern Africa (*16*, *87*). Simultaneous management of fire regimes and invasive animals can also be beneficial; for example, fire management to create unburned refuges while also controlling introduced mammalian predators is expected to benefit diverse populations of native wildlife across Australia (*56*).

Evolutionarily informed approaches for managing whole ecosystems are a newer prospect. Options for building ecological resilience to fire include managing for larger, better-connected populations to ensure the maintenance of genetic variation (*88*). A more radical approach is to use translocations to enhance gene flow and increase species' adaptability in fire-prone environments (*88*). For example, knowledge of within-species variation in plant traits, such as time to reproductive maturity, could be used by land managers to select populations for translocation that are better equipped to deal with changes in fire frequency. Modeling studies indicate that managed relocations outside of a species' known geographic range could also be effective in addressing population decline caused by high fire-frequency and land-use change (*75*). An increasingly important measure to increase ecosystem resilience to changes in fire regimes is to identify fire and climate refuges and ensure that they remain connected to secure habitats now and in the future (*89*).

Immediate measures to promote postfire recovery are crucial for whole-ecosystem management. However, there is much to learn about the most effective actions for rapid recovery. After the megafires in eastern Australia in 2019–2020, large-scale efforts are under way to assess the value of feeding stations, reducing browsing pressure by introduced herbivores, controlling invasive predators, and creating artificial shelters (*26*). For plants, rapid recovery actions include aerial seeding (*90*), seed collection (*75*), and restoration plantings (*84*). The benefits of restoration plantings are likely to apply to a range of taxa, including populations of freshwater fish and frogs threatened by postfire runoff of soil and sediments into streams (*24*).

A third set of approaches focuses on the critical role of people. Restoring and promoting landscapes that benefit people creates opportunities to balance biodiversity with other values in many regions of the world. Learning from previous and contemporary management by local and Indigenous people and promoting collaborative fire management are valuable steps in promoting fire regimes that benefit people and biodiversity (*91*–*94*). For example, reinstating Indigenous burning practices in the Klamath-Siskiyou bioregion in the western United States supports a wide range of species used as resources for food, materials, medicines, and ceremonial purposes (*91*) (Fig. 5). In the western deserts of Australia, hunting fires used by the indigenous Martu people increase vegetation diversity and support high populations of endemic mammals and reptiles. In the absence of the Martu, the more extensive lightning-ignited fires reduce biodiversity (*92*).

Diversified agriculture can also provide a range of habitats for plants and animals and shape fire regimes that benefit biodiversity. For instance, agricultural and forestry practices in the Mediterranean Basin that promote mosaics of low-flammability crops, orchards and oak trees reduce the risk of large, intense fires (*46*) and provide habitats for species-rich communities of birds (*47*). In China, more than 364,000 km of green firebreaks – strips of low flammability vegetation – have been planted in a range of terrestrial ecosystems and have the potential to promote biodiversity while reducing fire activity where it is unwanted (*95*).

Challenges and opportunities

Global changes in fire regimes will continue to amplify interactions between anthropogenic drivers and create challenges for biodiversity conservation and ecosystem adaptation. But

Table 1. New and emerging actions for sustaining biodiversity in ecosystems that experience fire.

Emerging approach	Reference
Managed wildfire whereby wildfires are allowed to burn naturally in fire-prone ecosystems and are suppressed only under specific conditions	(*81*)
Targeted fire suppression to protect vulnerable populations or ecosystems, aided by real-time data	(*84*)
Reintroduction of grazing and fossorial animals that regulate fire regimes for the benefit of threatened species or whole ecosystems	(*57*)
Simultaneous management of fire and other drivers such as invasive plants and animals	(*56*)
Use of extreme weather conditions to create "firestorms" that can be used to reduce woody plant encroachments in savannas and grasslands	(*87*)
Building evolutionary resilience by maintaining large and connected populations with genetic variation, identifying and protecting refuges, and increasing adaptability to future fire regimes by translocation	(*88*)
Rapid response and recovery teams that enact emergency conservation management including providing refuges for animals, planting and reseeding to promote rapid revegetation, and, in extreme situations, ex situ conservation	(*26*)
Indigenous fire stewardship and reinstatement of cultural burning in a modern context to enhance biodiversity, ecosystems, and human well-being	(*91*)
Diversified agricultural systems that moderate fire regimes and provide habitats for a range of species	(*46*)
Green firebreaks comprising low-flammability species planted at strategic locations to help reduce fire spread while providing refuges for biota	(*95*)

there are exciting opportunities for finding solutions that benefit both people and nature.

Historical or novel ecosystems

Restoring historical fire regimes is often regarded as the best approach for biodiversity and ecological resilience (*22*). However, recreating historical fire regimes in landscapes that are highly modified by climate change, new land-uses, and invasive species, will not necessarily lead to effective biodiversity conservation (*96*). Conserving organisms requires evidence of how ecosystems may respond to fires that are modified by, and subject to, new stressors. Direct measures of species, populations and ecosystems and their change through time, will help in identifying the fire characteristics that best promote biodiversity. The path forward requires deep knowledge of both historical and contemporary landscapes.

Linking biodiversity, ecosystem services, and human well-being

Promoting fire regimes that benefit biodiversity is difficult partly because of the need to simultaneously consider multiple values. In Mediterranean-type ecosystems, expansion of urban areas is bringing more people into proximity with wildfire activity, making human safety a priority in fire planning (*13*, *15*, *59*). Fires also sustain livelihoods (*92*, *94*) and influence ecosystem services such as water, climate, pest control and soil regulation (*97*), and these too are important considerations for local communities and policy makers. Developing strategies and actions that enhance diverse social and ecological values is not necessarily straightforward, but explicitly recognizing trade-offs and uncertainty between competing values can help navigate this complexity (*44*, *71*).

Creating innovative partnerships and policies

At local and regional scales, getting more of the 'right' type of fire in landscapes entails forging new alliances to build and apply knowledge. Indigenous-led fire stewardship is an example of a bottom-up approach to fostering partnerships between Indigenous and non-Indigenous institutions that aim to share and implement understanding of cultural burning practices which, in turn, can improve cultural connections and enhance ecosystems (*91*, *93*). Another example of forging new alliances comes from the city of Paradise, California, burned in 2018 in the catastrophic 'Camp Fire'. Partnerships among scientists, conservation organizations and urban planners are redesigning the city by strategically locating less-flammable land-uses, such as orchards or parklands, and creating opportunities to achieve social and ecological goals (*98*). Sharing knowledge through training and education is crucial for integrating biodiversity into fire policy.

At national and global scales, biodiversity conservation will benefit from greater integration of fire into conservation policy. The United Nations Convention on Biological Diversity guides national and international efforts to protect species and ecosystems. A range of stakeholders, including signatory countries, nongovernment organizations and scientists, are currently negotiating a new Global Biodiversity Framework of goals and targets for the decade to 2030. Together with other drivers, changed fire regimes will affect proposed goals for increasing 'the area, connectivity and integrity of natural ecosystems' and reducing 'the number of species that are threatened' (*99*). Explicitly incorporating fire regimes in the formulation of the new Global Biodiversity Framework provides an opportunity to develop innovative policies to set and achieve biodiversity targets. Emerging global initiatives that bring together scientists with a wide range of stakeholders, such as the Intergovernmental Science-Policy Platform on Biodiversity and Ecosystem Services (IPBES), provide a foundation through which new biodiversity policies and scenarios could be developed and assessed. At the same time, international efforts to reduce greenhouse gas emissions, such as the Paris Agreement, remain crucial.

Monitoring and manipulating ecosystems

Assessing the effectiveness of conservation actions requires strategic collection of data on fire, biodiversity, and anthropogenic drivers. Data that inform a mechanistic understanding are essential for early warnings of regime shifts and their consequences (*48*, *66*). Experiments have provided a large body of knowledge, but more examples of large-scale manipulations of ecosystems are needed to assess new initiatives such as green fire breaks, and translocations

aimed at increasing adaptive capacity. However, experiments that address ecological questions are not necessarily designed in ways that most effectively influence management (*100*). Adaptive management aims to resolve this dilemma by identifying a plan for addressing critical knowledge gaps, testing alternative actions and monitoring outcomes to improve future management (*100*).

Conclusions

Conservation of Earth's biological diversity will be achieved only by recognition of, and response to, the critical role of fire in shaping ecosystems. More than 4400 terrestrial and freshwater species, from a wide range of taxa and regions, face threats associated with inappropriate fire regimes. Innovative science and new partnerships across a range of sectors are crucial for navigating big decisions about new and changing ecosystems – whether it be consideration of fire in the context of meeting global biodiversity targets, safeguarding regional ecosystem services, or protecting homes and habitats. Placing the increasingly important role of people and their relationships with biodiversity at the forefront of efforts to understand and adapt to changes in fire regimes is central to these endeavors.

REFERENCES AND NOTES

1. T. He, B. B. Lamont, J. G. Pausas, Fire as a key driver of Earth's biodiversity. *Biol. Rev. Camb. Philos. Soc.* **94**, 1983–2010 (2019). doi: 10.1111/brv.12544; pmid: 31298472
2. P. W. Rundel *et al.*, Fire and plant diversification in Mediterranean-climate regions. *Front. Plant Sci.* **9**, 851 (2018). doi: 10.3389/fpls.2018.00851; pmid: 30018621
3. L. T. Kelly, L. Brotons, Using fire to promote biodiversity. *Science* **355**, 1264–1265 (2017). doi: 10.1126/science.aam7672; pmid: 28336625
4. J. G. Pausas, W. J. Bond, Alternative biome states in terrestrial ecosystems. *Trends Plant Sci.* **25**, 250–263 (2020). doi: 10.1016/j.tplants.2019.11.003; pmid: 31917105
5. M. S. Fletcher, T. Hall, A. N. Alexandra, The loss of an indigenous constructed landscape following British invasion of Australia: An insight into the deep human imprint on the Australian landscape. *Ambio* (2020). doi: 10.1007/s13280-020-01339-3; pmid: 32378038
6. S. Archibald, Managing the human component of fire regimes: Lessons from Africa. *Philos. Trans. R. Soc. London Ser. B* **371**, 20150346 (2016). doi: 10.1098/rstb.2015.0346; pmid: 27216516
7. D. M. J. S. Bowman *et al.*, The human dimension of fire regimes on Earth. *J. Biogeogr.* **38**, 2223–2236 (2011). doi: 10.1111/j.1365-2699.2011.02595.x; pmid: 22279247
8. R. A. Chisholm, L. S. Wijedasa, T. Swinfield, The need for long-term remedies for Indonesia's forest fires. *Conserv. Biol.* **30**, 5–6 (2016). doi: 10.1111/cobi.12662; pmid: 26612785
9. J. Barlow, E. Berenguer, R. Carmenta, F. França, Clarifying Amazonia's burning crisis. *Glob. Change Biol.* **26**, 319–321 (2020). doi: 10.1111/gcb.14872; pmid: 31729092
10. F. S. Hu *et al.*, Arctic tundra fires: Natural variability and responses to climate change. *Front. Ecol. Environ.* **13**, 369–377 (2015). doi: 10.1890/150063
11. E. Whitman, M. A. Parisien, D. K. Thompson, M. D. Flannigan, Short-interval wildfire and drought overwhelm boreal forest resilience. *Sci. Rep.* **9**, 18796 (2019). doi: 10.1038/s41598-019-55036-7; pmid: 31827128
12. K. Barrett *et al.*, Postfire recruitment failure in Scots pine forests of southern Siberia. *Remote Sens. Environ.* **237**, 111539 (2020). doi: 10.1016/j.rse.2019.111539
13. T. Schoennagel *et al.*, Adapt to more wildfire in western North American forests as climate changes. *Proc. Natl. Acad. Sci. U.S.A.* **114**, 4582–4590 (2017). doi: 10.1073/pnas.1617464114; pmid: 28416662
14. M. M. Boer, V. Resco de Dios, R. A. Bradstock, Unprecedented burn area of Australian mega forest fires. *Nat. Clim. Chang.* **10**, 171–172 (2020). doi: 10.1038/s41558-020-0716-1
15. F. Moreira *et al.*, Wildfire management in Mediterranean-type regions: Paradigm change needed. *Environ. Res. Lett.* **15**, 011001 (2020). doi: 10.1088/1748-9326/ab541e
16. D. Twidwell, C. H. Bielski, R. Scholtz, S. D. Fuhlendorf, Advancing fire ecology in 21st century rangelands. *Rangeland Ecol. Manag.* (2020). doi: 10.1016/j.rama.2020.01.008
17. N. Andela *et al.*, A human-driven decline in global burned area. *Science* **356**, 1356–1362 (2017). doi: 10.1126/science.aal4108; pmid: 28663495
18. J. R. Probert *et al.*, Anthropogenic modifications to fire regimes in the wider Serengeti-Mara ecosystem. *Glob. Change Biol.* **25**, 3406–3423 (2019). doi: 10.1111/gcb.14711; pmid: 31282085
19. A. M. Gill, Fire and the Australian flora: A review. *Aust. For.* **38**, 4–25 (1975). doi: 10.1080/00049158.1975.10675618
20. R. G. Miller *et al.*, Mechanisms of fire seasonality effects on plant populations. *Trends Ecol. Evol.* **34**, 1104–1117 (2019). doi: 10.1016/j.tree.2019.07.009; pmid: 31399287
21. J. E. Keeley, J. G. Pausas, Distinguishing disturbance from perturbations in fire-prone ecosystems. *Int. J. Wildland Fire* **28**, 282–287 (2019). doi: 10.1071/WF18203
22. J. E. Keeley, W. J. Bond, R. A. Bradstock, J. G. Pausas, P. W. Rundel, *Fire in Mediterranean Ecosystems: Ecology, Evolution and Management* (Cambridge: Cambridge Univ. Press, 2012).
23. D. G. Nimmo *et al.*, Animal movements in fire-prone landscapes. *Biol. Rev. Camb. Philos. Soc.* **94**, 981–998 (2019). doi: 10.1111/brv.12486; pmid: 30565370
24. International Union for the Conservation of Nature (IUCN), "The IUCN red list of threatened species," Version 2019-3 (IUCN, 2019); www.iucnredlist.org.
25. International Union for the Conservation of Nature (IUCN), "The IUCN red list of ecosystems," 14 April 2020 (IUCN, 2020); https://iucnrle.org/.
26. B. A. Wintle, S. Legge, J. C. Z. Woinarski, After the megafires: What next for Australian wildlife? *Trends Ecol. Evol.* **35**, 753–757 (2020). doi: 10.1016/j.tree.2020.06.009; pmid: 32680597
27. W. Steffen *et al.*, Trajectories of the Earth System in the Anthropocene. *Proc. Natl. Acad. Sci. U.S.A.* **115**, 8252–8259 (2018). doi: 10.1073/pnas.1810141115; pmid: 30082409
28. D. M. J. S. Bowman *et al.*, Fire in the Earth system. *Science* **324**, 481–484 (2009). doi: 10.1126/science.1163886; pmid: 19390038
29. S. Archibald, C. E. R. Lehmann, J. L. Gómez-Dans, R. A. Bradstock, Defining pyromes and global syndromes of fire regimes. *Proc. Natl. Acad. Sci. U.S.A.* **110**, 6442–6447 (2013). doi: 10.1073/pnas.1211466110; pmid: 23559374
30. B. Rogers, J. K. Balch, S. J. Goetz, C. E. R. Lehmann, M. Turetsky, Focus on changing fire regimes: Interactions with climate, ecosystems, and society. *Environ. Res. Lett.* **15**, 030201 (2018). doi: 10.1088/1748-9326/ab6d3a
31. S. Díaz *et al.*, Pervasive human-driven decline of life on Earth points to the need for transformative change. *Science* **366**, eaax3100 (2019). doi: 10.1126/science.aax3100; pmid: 31831642
32. R. A. Bradstock, A biogeographic model of fire regimes in Australia: Current and future implications. *Glob. Ecol. Biogeogr.* **19**, 145–158 (2010). doi: 10.1111/j.1466-8238.2009.00512.x
33. E. Batllori *et al.*, Compound fire-drought regimes promote ecosystem transitions in Mediterranean ecosystems. *J. Ecol.* **107**, 1187–1198 (2019). doi: 10.1111/1365-2745.13115
34. P. M. Brando *et al.*, Droughts, wildfires, and forest carbon cycling: A pantropical synthesis. *Annu. Rev. Earth Planet. Sci.* **47**, 555–581 (2019). doi: 10.1146/annurev-earth-082517-010235
35. T. A. Fairman, C. R. Nitschke, L. T. Bennett, Too much, too soon? A review of the effects of increasing wildfire frequency on tree mortality and regeneration in temperate eucalypt forests. *Int. J. Wildland Fire* **25**, 831–848 (2016). doi: 10.1071/WF15010
36. M. G. Turner, K. H. Braziunas, W. D. Hansen, B. J. Harvey, Short-interval severe fire erodes the resilience of subalpine lodgepole pine forests. *Proc. Natl. Acad. Sci. U.S.A.* **116**, 11319–11328 (2019). doi: 10.1073/pnas.1902841116; pmid: 31110003
37. S. R. Holden, B. M. Rogers, K. K. Treseder, J. T. Randerson, Fire severity influences the response of soil microbes to a boreal forest fire. *Environ. Res. Lett.* **11**, 035004 (2016). doi: 10.1088/1748-9326/11/3/035004
38. K. Joly, P. A. Duffy, T. S. Rupp, Simulating the effects of climate change on fire regimes in Arctic biomes: Implications for caribou and moose habitat. *Ecosphere* **3**, 1–18 (2012). doi: 10.1890/ES12-00012.1
39. M. A. Cochrane, C. P. Barber, Climate change, human land use and future fires in the Amazon. *Glob. Change Biol.* **15**, 601–612 (2009). doi: 10.1111/j.1365-2486.2008.01786.x
40. L. N. Paolucci, J. H. Schoereder, P. M. Brando, A. N. Andersen, Fire-induced forest transition to derived savannas: Cascading effects on ant communities. *Biol. Conserv.* **214**, 295–302 (2017). doi: 10.1016/j.biocon.2017.08.020
41. R. B. de Andrade, J. K. Balch, J. Y. O. Carreira, P. M. Brando, A. V. L. Freitas, The impacts of recurrent fires on diversity of fruit-feeding butterflies in a south-eastern Amazon forest. *J. Trop. Ecol.* **33**, 22–32 (2017). doi: 10.1017/S0266467416000559
42. M. P. Veldhuis *et al.*, Cross-boundary human impacts compromise the Serengeti-Mara ecosystem. *Science* **363**, 1424–1428 (2019). doi: 10.1126/science.aav0564; pmid: 30923217
43. R. C. R. Abreu *et al.*, The biodiversity cost of carbon sequestration in tropical savanna. *Sci. Adv.* **3**, e1701284 (2017). doi: 10.1126/sciadv.1701284; pmid: 28875172
44. D. A. Driscoll *et al.*, Resolving future fire management conflicts using multicriteria decision making. *Conserv. Biol.* **30**, 196–205 (2016). doi: 10.1111/cobi.12580; pmid: 26148692
45. A. D. Syphard, T. J. Brennan, J. E. Keeley, Drivers of chaparral type conversion to herbaceous vegetation in coastal Southern California. *Divers. Distrib.* **25**, 90–101 (2019). doi: 10.1111/ddi.12827
46. F. Moreira, G. Pe'er, Agricultural policy can reduce wildfires. *Science* **359**, 1001 (2018). pmid: 29496872
47. A. Regos, V. Hermoso, M. D'Amen, A. Guisan, L. Brotons, Trade-offs and synergies between bird conservation and wildfire suppression in the face of global change. *J. Appl. Ecol.* **55**, 2181–2192 (2018). doi: 10.1111/1365-2664.13182
48. D. B. Lindenmayer, C. Sato, Hidden collapse is driven by fire and logging in a socioecological forest ecosystem. *Proc. Natl. Acad. Sci. U.S.A.* **115**, 5181–5186 (2018). doi: 10.1073/pnas.1721738115; pmid: 29712832
49. G. T. Pecl *et al.*, Biodiversity redistribution under climate change: Impacts on ecosystems and human well-being. *Science* **355**, eaai9214 (2017). doi: 10.1126/science.aai9214; pmid: 28360268
50. J. G. Pausas, J. E. Keeley, Abrupt climate-independent fire regime changes. *Ecosystems (N. Y.)* **17**, 1109–1120 (2014). doi: 10.1007/s10021-014-9773-5
51. M. L. Brooks *et al.*, Effects of invasive alien plants on fire regimes. *Bioscience* **54**, 677–688 (2004). doi: 10.1641/0006-3568(2004)054[0677:EOIAPO]2.0.CO;2
52. E. J. Fusco, J. T. Finn, J. K. Balch, R. C. Nagy, B. A. Bradley, Invasive grasses increase fire occurrence and frequency across US ecoregions. *Proc. Natl. Acad. Sci. U.S.A.* **116**, 23594–23599 (2019). doi: 10.1073/pnas.1908253116; pmid: 31685633
53. C. Riginos *et al.*, Potential for post-fire recovery of greater sage-grouse habitat. *Ecosphere* **10**, e02870 (2019). doi: 10.1002/ecs2.2870
54. C. N. Foster *et al.*, Animals as agents in fire regimes. *Trends Ecol. Evol.* **35**, 346–356 (2020). doi: 10.1016/j.tree.2020.01.002; pmid: 32187509
55. G. L. W. Perry, J. M. Wilmshurst, J. Ogden, N. J. Enright, Exotic mammals and invasive plants alter fire-related thresholds in southern temperate forested landscapes. *Ecosystems* **18**, 1290–1305 (2015). doi: 10.1007/s10021-015-9898-1
56. B. A. Hradsky, Conserving Australia's threatened native mammals in predator-invaded, fire-prone landscapes. *Wildl. Res.* **47**, 1–15 (2020). doi: 10.1071/WR19027
57. C. N. Johnson *et al.*, Can trophic rewilding reduce the impact of fire in a more flammable world? *Philos. Trans. R. Soc. London B.* **373**, 20170443 (2018). doi: 10.1098/rstb.2017.0443; pmid: 30348870
58. C. M. Ryan, R. J. Hobbs, L. E. Valentine, Bioturbation by a reintroduced digging mammal reduces fuel loads in an urban reserve. *Ecol. Appl.* **30**, e02018 (2020). doi: 10.1002/eap.2018; pmid: 31596973
59. M. A. Moritz *et al.*, Learning to coexist with wildfire. *Nature* **515**, 58–66 (2014). doi: 10.1038/nature13946; pmid: 25373675
60. A. D. Syphard, J. E. Keeley, A. H. Pfaff, K. Ferschweiler, Human presence diminishes the importance of climate in

driving fire activity across the United States. *Proc. Natl. Acad. Sci. U.S.A.* **114**, 13750–13755 (2017). doi: 10.1073/pnas.1713885114; pmid: 29229850
61. C. A. Nobre *et al*., Land-use and climate change risks in the Amazon and the need of a novel sustainable development paradigm. *Proc. Natl. Acad. Sci. U.S.A.* **113**, 10759–10768 (2016). doi: 10.1073/pnas.1605516113; pmid: 27638214
62. A. Brinkert, N. Hölzel, T. V. Sidorova, J. Kamp, Spontaneous steppe restoration on abandoned cropland in Kazakhstan: Grazing affects successional pathways. *Biodivers. Conserv.* **25**, 2543–2561 (2016). doi: 10.1007/s10531-015-1020-7
63. M. J. Liebmann *et al*., Native American depopulation, reforestation, and fire regimes in the Southwest United States, 1492-1900 CE. *Proc. Natl. Acad. Sci. U.S.A.* **113**, E696–E704 (2016). doi: 10.1073/pnas.1521744113; pmid: 26811459
64. A. Holz, S. W. Wood, C. Ward, T. T. Veblen, D. M. J. S. Bowman, Population collapse and retreat to fire refugia of the Tasmanian endemic conifer *Athrotaxis selaginoides* following the transition from Aboriginal to European fire management. *Glob. Change Biol.* **26**, 3108–3121 (2020). doi: 10.1111/gcb.15031; pmid: 32125058
65. R. E. Keane *et al*., Representing climate, disturbance, and vegetation interactions in landscape models. *Ecol. Modell.* **309–310**, 33–47 (2015). doi: 10.1016/j.ecolmodel.2015.04.009
66. M. C. Urban *et al*., Improving the forecast for biodiversity under climate change. *Science* **353**, aad8466 (2016). doi: 10.1126/science.aad8466; pmid: 27609898
67. P. H. Verburg *et al*., Methods and approaches to modelling the Anthropocene. *Glob. Environ. Change* **39**, 328–340 (2016). doi: 10.1016/j.gloenvcha.2015.08.007
68. C. M. Beale *et al*., Pyrodiversity interacts with rainfall to increase bird and mammal richness in African savannas. *Ecol. Lett.* **21**, 557–567 (2018). doi: 10.1111/ele.12921; pmid: 29441661
69. L. C. Ponisio *et al*., Pyrodiversity begets plant-pollinator community diversity. *Glob. Change Biol.* **22**, 1794–1808 (2016). doi: 10.1111/gcb.13236; pmid: 26929389
70. M. W. Tingley, V. Ruiz-Gutiérrez, R. L. Wilkerson, C. A. Howell, R. B. Siegel, Pyrodiversity promotes avian diversity over the decade following forest fire. *Proc. Biol. Sci.* **283**, 20161703 (2016). doi: 10.1098/rspb.2016.1703; pmid: 27708152
71. P. D. Bentley, T. D. Penman, Is there an inherent conflict in managing fire for people and conservation? *Int. J. Wildland Fire* **26**, 455–468 (2017). doi: 10.1071/WF16150
72. J. Henzler, H. Weise, N. J. Enright, S. Zander, B. Tietjen, A squeeze in the suitable fire interval: Simulating the persistence of fire-killed plants in a Mediterranean-type ecosystem under drier conditions. *Ecol. Modell.* **389**, 41–49 (2018). doi: 10.1016/j.ecolmodel.2018.10.010
73. A. I. T. Tulloch, J.-B. Pichancourt, C. R. Gosper, A. Sanders, I. Chadès, Fire management strategies to maintain species population processes in a fragmented landscape of fire-interval extremes. *Ecol. Appl.* **26**, 2175–2189 (2016). doi: 10.1002/eap.1362; pmid: 27755728
74. H. M. Regan, C. I. Bohórquez, D. A. Keith, T. J. Regan, K. E. Anderson, Implications of different population model structures for management of threatened plants. *Conserv. Biol.* **31**, 459–468 (2017). doi: 10.1111/cobi.12831; pmid: 27596063
75. T. C. Bonebrake *et al*., Fire management, managed relocation, and land conservation options for long-lived obligate seeding plants under global changes in climate, urbanization, and fire regime. *Conserv. Biol.* **28**, 1057–1067 (2014). doi: 10.1111/cobi.12253; pmid: 24606578
76. S. Gómez-González, C. Torres-Díaz, C. Bustos-Schindler, E. Gianoli, Anthropogenic fire drives the evolution of seed traits. *Proc. Natl. Acad. Sci. U.S.A.* **108**, 18743–18747 (2011). doi: 10.1073/pnas.1108863108; pmid: 22065739
77. M. C. Castellanos, S. C. González-Martínez, J. G. Pausas, Field heritability of a plant adaptation to fire in heterogeneous landscapes. *Mol. Ecol.* **24**, 5633–5642 (2015). doi: 10.1111/mec.13421; pmid: 26460597
78. S. Archibald *et al*., Biological and geophysical feedbacks with fire in the Earth System. *Environ. Res. Lett.* **13**, 033003 (2017). doi: 10.1088/1748-9326/aa9ead
79. D. M. J. S. Bowman *et al*., Pyrodiversity is the coupling of biodiversity and fire regimes in food webs. *Philos. Trans. R. Soc. Lond. B Biol. Sci.* **371**, 20150169 (2016). doi: 10.1098/rstb.2015.0169; pmid: 27216526
80. T. A. Spies *et al*., Using an agent-based model to examine forest management outcomes in a fire-prone landscape in Oregon, USA. *Ecol. Soc.* **22**, art25 (2017). doi: 10.5751/ES-08841-220125
81. G. Boisramé, S. Thompson, B. Collins, S. Stephens, Managed wildfire effects on forest resilience and water in the Sierra Nevada. *Ecosystems (N. Y.)* **20**, 717–732 (2017). doi: 10.1007/s10021-016-0048-1
82. S. L. Stephens *et al*., Is fire "for the birds"? How two rare species influence fire management across the US. *Front. Ecol. Environ.* **17**, 391–399 (2019). doi: 10.1002/fee.2076
83. A. Morton, "Dinosaur trees: Firefighters save endangered Wollemi pines from NSW bushfires," *The Guardian*, 15 January 2020; https://www.theguardian.com/australia-news/2020/jan/15/dinosaur-trees-firefighters-save-endangered-wollemi-pines-from-nsw-bushfires.
84. R. E. Keane, Managing wildfire for whitebark pine ecosystem restoration in western North America. *Forests* **9**, 648 (2018). doi: 10.3390/f9100648
85. G. Granath, P. A. Moore, M. C. Lukenbach, J. M. Waddington, Mitigating wildfire carbon loss in managed northern peatlands through restoration. *Sci. Rep.* **6**, 28498 (2016). doi: 10.1038/srep28498; pmid: 27346604
86. T. E. Lovejoy, C. Nobre, Amazon tipping point: Last chance for action. *Sci. Adv.* **5**, eaba2949 (2019). doi: 10.1126/sciadv.aba2949; pmid: 32064324
87. I. P. J. Smit, G. P. Asner, N. Govender, N. R. Vaughn, B. W. van Wilgen, An examination of the potential efficacy of high-intensity fires for reversing woody encroachment in savannas. *J. Appl. Ecol.* **53**, 1623–1633 (2016). doi: 10.1111/1365-2664.12738
88. C. M. Sgrò, A. J. Lowe, A. A. Hoffmann, Building evolutionary resilience for conserving biodiversity under climate change. *Evol. Appl.* **4**, 326–337 (2011). doi: 10.1111/j.1752-4571.2010.00157.x; pmid: 25567976
89. A. J. H. Meddens *et al*., Fire refugia: What are they, and why do they matter for global change? *Bioscience* **68**, 944–954 (2018). doi: 10.1093/biosci/biy103
90. O. D. Bassett, L. D. Prior, C. M. Slijkerman, D. Jamieson, D. M. J. S. Bowman, Aerial sowing stopped the loss of alpine ash (Eucalyptus delegatensis) forests burnt by three short-interval fires in the Alpine National Park, Victoria, Australia. *For. Ecol. Manage.* **342**, 39–48 (2015). doi: 10.1016/j.foreco.2015.01.008
91. F. K. Lake, A. C. Christianson, "Indigenous fire stewardship," in *Encyclopedia of Wildfires and Wildland-Urban Interface (WUI) Fires*, Manzello S, Ed. (Springer, 2019); .doi: 10.1007/978-3-319-51727-8_225-1
92. R. Bliege Bird, D. Nimmo, Restore the lost ecological functions of people. *Nat. Ecol. Evol.* **2**, 1050–1052 (2018). doi: 10.1038/s41559-018-0576-5; pmid: 29867099
93. J. Mistry, B. A. Bilbao, A. Berardi, Community owned solutions for fire management in tropical ecosystems: Case studies from Indigenous communities of South America. *Philos. Trans. R. Soc. London B.* **371**, 20150174 (2016). doi: 10.1098/rstb.2015.0174; pmid: 27216507
94. J. R. Welch, E. S. Brondízio, S. S. Hetrick, C. E. Coimbra Jr., Indigenous burning as conservation practice: Neotropical savanna recovery amid agribusiness deforestation in Central Brazil. *PLOS ONE* **8**, e81226 (2013). doi: 10.1371/journal.pone.0081226; pmid: 24349045
95. X. Cui *et al*., Green firebreaks as a management tool for wildfires: Lessons from China. *J. Environ. Manage.* **233**, 329–336 (2019). doi: 10.1016/j.jenvman.2018.12.043; pmid: 30584964
96. A. D. Barnosky *et al*., Merging paleobiology with conservation biology to guide the future of terrestrial ecosystems. *Science* **355**, eaah4787 (2017). doi: 10.1126/science.aah4787; pmid: 28183912
97. J. G. Pausas, J. E. Keeley, Wildfires as an ecosystem service. *Front. Ecol. Environ.* **17**, 289–295 (2019). doi: 10.1002/fee.2044
98. Conservation Biology Institute, The Nature Conservancy, Paradise Parks and Recreation, "Paradise nature-based fire risk resilience project" (Corvallis, OR, 2020).
99. Convention on Biological Diversity, "Preparations for the post-2020 biodiversity framework" (CBD, 2020); https://www.cbd.int/conferences/post2020.
100. B. W. van Wilgen, N. Govender, I. P. J. Smit, S. MacFadyen, The ongoing development of a pragmatic and adaptive fire management policy in a large African savanna protected area. *J. Environ. Manage.* **132**, 358–368 (2014). doi: 10.1016/j.jenvman.2013.11.003; pmid: 24365711

ACKNOWLEDGMENTS

We thank the Centre Tecnològic Forestal de Catalunya for hosting the workshop that led to this paper, and the people of Solsona for welcoming our international team. We thank C. Kelly for codesigning the figures and two reviewers for valuable comments.: **Funding:** The workshop leading to this paper was funded by the Centre Tecnològic Forestal de Catalunya and the ARC Centre of Excellence for Environmental Decisions. L.T.K. was supported by a Victorian Postdoctoral Research Fellowship (Victorian Government), a Centenary Fellowship (University of Melbourne), and an Australian Research Council Linkage Project Grant (LP150100765). A.R. was supported by the Xunta de Galicia (Postdoctoral Fellowship ED481B2016/084-0) and the Foundation for Science and Technology under the FirESmart project (PCIF/MOG/0083/2017). A.L.S. was supported by a Marie Skłodowska-Curie Individual Fellowship (746191) under the European Union Horizon 2020 Programme for Research and Innovation. L.R. was supported by the Australian Government's National Environmental Science Program through the Threatened Species Recovery Hub. L.B. was partially supported by the Spanish Government through the INMODES (CGL2014-59742-C2-2-R) and the ERANET-SUMFORESTS project FutureBioEcon (PCIN-2017-052). This research was supported in part by the U.S. Department of Agriculture, Forest Service, Pacific Southwest Research Station. All opinions, findings, and conclusions or recommendations expressed here are those of the authors and do not necessarily reflect the views of the USDA Forest Service or Tribes. **Author contributions:** All authors contributed to the conceptualization of ideas and research goals during a 1-week workshop in Solsona, Spain, and/or follow up meetings in Tucson, Arizona. L.T.K., L.B., A.D., and K.M.G. led the workshop. L.T.K. wrote the original draft. All authors contributed to reviewing and editing the paper. L.T.K. prepared visual materials with assistance from A.L.S., E.B., and S.A. J.L.S., K.M.G., and L.T.K. synthesized IUCN Red List data. **Competing interests:** The authors declare no competing interests. **Data and materials availability:** The IUCN Red List of Threatened Species is available at https://www.iucnredlist.org/.

SUPPLEMENTARY MATERIALS

science.sciencemag.org/content/370/6519/eabb0355/suppl/DC1
Table S1
References (*101*–*107*)

10.1126/science.abb0355

RESEARCH ARTICLE SUMMARY

VIROLOGY

Rotavirus induces intercellular calcium waves through ADP signaling

Alexandra L. Chang-Graham, Jacob L. Perry, Melinda A. Engevik, Kristen A. Engevik, Francesca J. Scribano, J. Thomas Gebert, Heather A. Danhof, Joel C. Nelson, Joseph S. Kellen, Alicia C. Strtak, Narayan P. Sastri, Mary K. Estes, Robert A. Britton, James Versalovic, Joseph M. Hyser*

INTRODUCTION: Rotavirus (RV) causes severe diarrheal disease in children worldwide by broadly dysregulating intestinal homeostasis. The mechanisms of RV diarrhea are multifactorial and still not completely understood. RV infects epithelial enterocytes and enteroendocrine cells at the tip and middle of villi in the small intestine, but not all of the cells susceptible to RV are infected during disease. A hallmark of RV infection is that RV dysregulates host cell calcium signaling pathways to increase cytosolic calcium, which is required for RV replication.

RATIONALE: A long-held concept in how RV infection causes life-threatening diarrhea—despite a small percentage of infected cells—is that RV-infected cells release potent signaling molecules that can dysregulate neighboring, uninfected cells. Previous studies have found increased levels of signaling molecules during RV infection, such as RV enterotoxin nonstructural protein 4 (NSP4), nitric oxide (NO), and prostaglandins (PGE2). However, whether signaling molecule(s) spread from infected to uninfected cells is not clear. Examination of the intercellular signaling between infected and uninfected cells during RV infection may provide insights into the pathophysiology of RV and other viral diarrheas.

RESULTS: In this study, we used long-term live fluorescence calcium imaging throughout RV infection to show that RV-infected cells produce paracrine signals that manifest as intercellular calcium waves (ICWs), an intercellular communication pathway in which increases in cytosolic calcium occur in an expanding circular pattern from a central initiating cell. We observed RV-induced ICWs in both cell lines and human intestinal enteroids (HIEs). Blocking previously known RV-induced paracrine signaling pathways (enterotoxin NSP4, NO, and PGE2) did not inhibit the ICWs, but the addition of apyrase, an enzyme that degrades extracellular adenosine 5′-triphosphate (ATP) and adenosine 5′-diphosphate (ADP), greatly reduced the ICWs. The RV-induced ICWs were mediated by extracellular ADP, which activates P2Y1 purinergic receptors on neighboring cells. ICWs were blocked by P2Y1 antagonists or CRISPR-Cas9 knockout of the P2Y1 receptor. Inhibiting the paracrine ADP signal reduced RV replication and inhibited the RV-induced increases in *COX2* and *iNOS* expression that mediate PGE2 and NO production, respectively. Blocking ADP signaling also decreased RV-induced serotonin release from HIEs and fluid secretion in an HIE swelling assay. Furthermore, BPTU and MRS2500, small molecule inhibitors of the P2Y1 receptor, reduced RV diarrhea severity in neonatal mice.

CONCLUSION: The current concept of RV pathogenesis proposes that paracrine signaling from RV-infected cells dysregulates surrounding uninfected cells and contributes to life-threatening diarrhea. Here, characterization of ICWs originating from RV-infected cells has provided direct experimental proof for the role of virus-induced paracrine signaling in gastrointestinal pathophysiology. Furthermore, ADP signaling provides both a potent paracrine signal and the most dominant calcium signal observed in RV infection. These results point to purinergic signaling as a therapeutic target for developing antidiarrheal drugs for RV and potentially other viral diarrheas. Our studies provide direct evidence that viruses can exploit purinergic signaling and intercellular calcium waves to potentially amplify pathophysiological signaling that is important for disease. ■

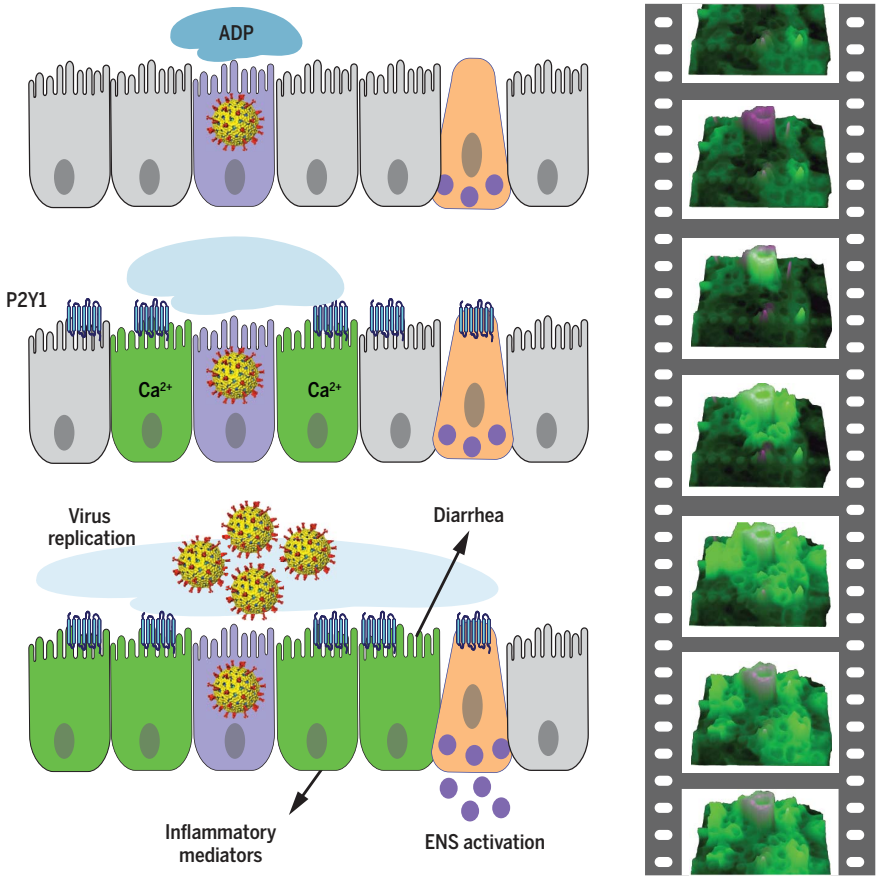

ADP released from rotavirus-infected cells drives pathogenesis. (Top) Rotavirus-infected intestinal epithelial cells release ADP, which diffuses to neighboring, uninfected cells. (Middle) ADP activates the purinergic P2Y1 receptor, which increases intracellular calcium, observed as an intercellular calcium wave (see filmstrip, right). (Bottom) ADP and P2Y1 activation triggers the release of inflammatory mediators, fluid secretion contributing to diarrhea, and the release of serotonin from enteroendocrine cells to activate the enteric nervous system (ENS).

The list of author affiliations is available in the full article online.
*Corresponding author. Email: joseph.hyser@bcm.edu
Cite this article as A. L. Chang-Graham *et al.*, *Science* **370**, eabc3621 (2020). DOI: 10.1126/science.abc3621

READ THE FULL ARTICLE AT
https://doi.org/10.1126/science.abc3621

RESEARCH ARTICLE

VIROLOGY

Rotavirus induces intercellular calcium waves through ADP signaling

Alexandra L. Chang-Graham[1,2], Jacob L. Perry[1,2], Melinda A. Engevik[3,4], Kristen A. Engevik[1,2], Francesca J. Scribano[1,2], J. Thomas Gebert[1,2], Heather A. Danhof[1,2], Joel C. Nelson[1], Joseph S. Kellen[1,2], Alicia C. Strtak[1,2], Narayan P. Sastri[1], Mary K. Estes[1,2,5], Robert A. Britton[1,2], James Versalovic[3,4], Joseph M. Hyser[1,2]*

Rotavirus causes severe diarrheal disease in children by broadly dysregulating intestinal homeostasis. However, the underlying mechanism(s) of rotavirus-induced dysregulation remains unclear. We found that rotavirus-infected cells produce paracrine signals that manifested as intercellular calcium waves (ICWs), observed in cell lines and human intestinal enteroids. Rotavirus ICWs were caused by the release of extracellular adenosine 5′-diphosphate (ADP) that activated P2Y1 purinergic receptors on neighboring cells. ICWs were blocked by P2Y1 antagonists or CRISPR-Cas9 knockout of the P2Y1 receptor. Blocking the ADP signal reduced rotavirus replication, inhibited rotavirus-induced serotonin release and fluid secretion, and reduced diarrhea severity in neonatal mice. Thus, rotavirus exploited paracrine purinergic signaling to generate ICWs that amplified the dysregulation of host cells and altered gastrointestinal physiology to cause diarrhea.

Rotavirus (RV) causes severe diarrhea and vomiting in children worldwide, resulting in ~258 million diarrheal episodes and ~128,000 deaths annually (*1*). The mechanisms of RV diarrhea are multifactorial and not completely understood. RV infects the enterocytes and enteroendocrine cells at the tip and middle of villi in the small intestine (*2*–*4*). Not all cells susceptible to RV are infected, however, and diarrhea occurs before the onset of histopathologic changes (*2*, *5*–*7*). During infection, RV dysregulates host cell calcium (Ca^{2+}) signaling pathways to increase cytosolic Ca^{2+}, which is required for RV replication. The RV nonstructural protein 4 (NSP4) drives these changes in Ca^{2+} homeostasis as both an endoplasmic reticulum–localized viroporin and a secreted enterotoxin (*8*–*10*). These perturbations to host Ca^{2+} signaling activate autophagy, disrupt the cytoskeleton and tight junctions, and trigger fluid secretion pathways (*9*, *11*–*14*).

A long-held concept in how RV infection causes life-threatening diarrhea is that RV-infected cells release potent signaling molecules that dysregulate neighboring, uninfected cells (*6*, *15*, *16*). This notion is based on previous observations of increased signaling molecules during RV infection, including enterotoxin NSP4, prostaglandins (PGE2), and nitric oxide (NO) (*9*, *17*–*19*). In this theory, enterotoxin NSP4 binds to neighboring, uninfected enterocytes to activate Ca^{2+}-activated chloride channels and cause secretory diarrhea (*20*–*22*), and PGE2 and NO further activate fluid secretion processes (*23*, *24*). Simultaneously, dysregulation of neighboring enteroendocrine cells triggers Ca^{2+}-dependent release of serotonin, which stimulates the enteric nervous system both to activate vomiting centers in the central nervous system and to activate secretory reflex pathways in the gastrointestinal tract (*4*, *7*). Thus, this concept of RV-induced diarrhea addresses how a limited infection at the middle-to-upper villi may cause widespread dysregulation of host physiology and life-threatening disease. However, this cell-to-cell functional signaling has not been directly observed during a RV infection, and the signaling pathways remain incompletely understood.

In this study, we found that RV-infected cells signal to uninfected cells through an extracellular purinergic signaling pathway. This pathway was a dominant driver of observed RV disease processes, including replication, up-regulation of PGE2- and NO-producing enzymes, serotonin secretion, fluid secretion, and diarrhea in a neonatal mouse model. Thus, viruses may exploit host paracrine signaling pathways to amplify pathophysiology.

Low multiplicity of infection reveals intercellular calcium waves

RV greatly increases cytosolic Ca^{2+} during infection and disrupts host Ca^{2+}-dependent processes to cause disease (*25*–*27*). We used African green monkey kidney MA104 cells stably expressing the genetically encoded calcium indicator (GECI) GCaMP5G or GCaMP6s to observe changes in cytosolic Ca^{2+} during RV infection using live-cell time-lapse epifluorescence imaging. We mock- or RV (strain SA114F)–infected MA104-GCaMP cells at a low multiplicity of infection (MOI) (0.01) to distinguish Ca^{2+} changes in infected cells compared with those in neighboring, uninfected cells. RV-infected cells were identified using immunofluorescence (IF) staining for RV antigen after imaging, and these IF images were superimposed on the time-lapse movies (Fig. 1A). Although mock-infected cells had minimal changes in GCaMP fluorescence, RV-infected cells exhibited large fluctuations in fluorescence—and thus cytosolic Ca^{2+}—as discrete signaling events (*28*). These signaling events increased cytosolic Ca^{2+} in the RV antigen–positive cell, and we observed successive increases in cytosolic Ca^{2+} in neighboring, uninfected cells over a time interval of 30 s (Fig. 1A and movie S1). We quantified the Ca^{2+}-eliciting signal from infected to uninfected cells using a previously described criterion in which changes in normalized relative fluorescence >5% constituted a Ca^{2+} spike (*28*). To systematically and reproducibly characterize the signals in RV-infected and neighboring, uninfected cells, we visualized the cell monolayer as a grid, similar to previously described analysis techniques (*29*–*31*) (Fig. 1B and fig. S1A). The number and average magnitude of the RV-induced Ca^{2+} transients decreased in the neighboring 5 (NB+5) and 10 (NB+10) cells (Fig. 1B, blue and purple traces). Quantification of the number and magnitude of Ca^{2+} spikes of the infected, the NB+5, and the NB+10 cells showed a significant decrease with distance from the infected cell (Fig. 1, C and D). Thus, RV-infected cells signaled to surrounding uninfected cells and elicited a Ca^{2+} signaling response.

Next, we sought to confirm that the Ca^{2+} signaling in the neighboring cells was not caused by RV infection undetected by antibody staining. MA104-GCaMP cells were mock-inoculated or infected with a recombinant SA11 clone 3 strain expressing an mRuby3 fluorescent reporter (SA11cl3-mRuby3) (*28*) at MOI 0.01 and imaged for ~3 to 22 hours post-infection (hpi)—conditions we used throughout this study unless noted otherwise. We found no increase in mRuby3 fluorescence in the mock-infected cells, and there was a steep increase in fluorescence in RV-infected cells by hours 6 to 12 of imaging that correlated with increased Ca^{2+} signaling (Fig. 1E and movie S2). Notably, the NB+3 cell also had robust Ca^{2+} signaling that paralleled the infected cell, but the lack of increase in mRuby3 fluorescence demonstrated that it was not infected (Fig. 1E). There was a similar decrease in the number of Ca^{2+} spikes and the average Ca^{2+} spike magnitudes in the NB+3 and NB+5 cells that

[1]Department of Molecular Virology and Microbiology, Baylor College of Medicine, Houston, TX, USA. [2]Alkek Center for Metagenomic and Microbiome Research, Baylor College of Medicine, Houston, TX, USA. [3]Department of Pathology and Immunology, Baylor College of Medicine, Houston, TX, USA. [4]Department of Pathology, Texas Children's Hospital, Houston, TX, USA. [5]Department of Medicine, Gastroenterology and Hepatology, Baylor College of Medicine, Houston, TX, USA.
*Corresponding author. Email: joseph.hyser@bcm.edu

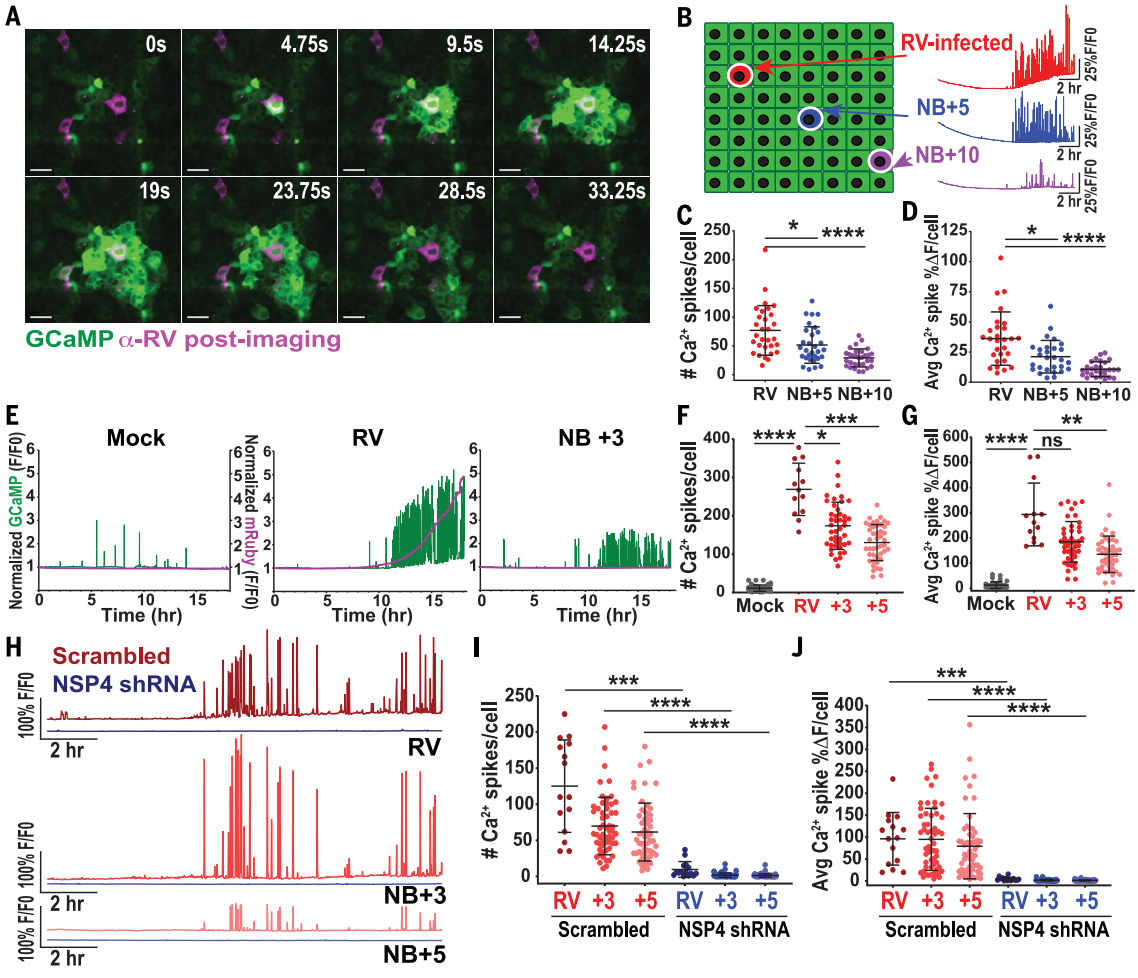

Fig. 1. Rotavirus-infected cells trigger calcium signaling in neighboring uninfected cells. (**A**) MA104-GCaMP cells infected with rotavirus (RV SA114F) at MOI 0.01 and imaged at ~12 hpi. Cells were fixed and immunostained at 24 hpi for RV (pink), images superimposed. Scale bars, 100 μm. (**B**) Cell monolayer schematic: RV-infected cell (red), NB+5 cells (blue), and NB+10 cells (purple). Representative single-cell Ca^{2+} traces with normalized GCaMP fluorescence (F/F_0) are shown. (**C** and **D**) Ca^{2+} spikes per cell in RV-infected and neighboring (NB) cells, (n = 30 cells) (C) and average magnitude of Ca^{2+} spikes per cell in RV-infected and NB cells (D) (n = 28 cells, data representative of N = 3 independent experiments). (**E**) Representative Ca^{2+} traces from MA104-GCaMP cells mock- or RV (SA11cl3-mRuby3)–infected and the NB+3 cell imaged 3 to 21 hpi. Left axes indicate GCaMP normalized fluorescence (green), and right axes indicate mRuby3 normalized fluorescence (pink). (**F** and **G**) Ca^{2+} spikes (F) and average magnitude of Ca^{2+} spikes per cell in RV-infected, NB +3, and +5 cells (G) (data combined from N = 3 independent experiments). (**H**) Representative Ca^{2+} traces from MA104-GCaMP-shRNA scrambled or NSP4 cells infected with RV (SA11cl3-mRuby3) and NB+3 and NB+5 cells imaged from ~4 to 20 hpi. (**I** and **J**) Ca^{2+} spikes in RV-infected and NB+3 and NB+5 uninfected cells in scrambled or NSP4 shRNA cells (I) and average magnitude of Ca^{2+} spikes per cell in RV-infected and NB cells (J) (data combined from N = 3 independent experiments). [(C), (D), (F), (G), (I), and (J)] Kruskal-Wallis with Dunn's multiple comparisons test used. Data represented as means ± SD; ns, not significant; *P < 0.05; **P < 0.01; ***P < 0.001; ****P < 0.0001.

correlated with increasing distance from the infected cell (Fig. 1, F and G). Thus, the Ca^{2+} signaling in the neighboring cell was not caused by infection of that cell but was a result of signals activated by a nearby RV-infected cell.

We next determined whether knockdown of NSP4 would reduce the Ca^{2+} signals in infected and uninfected cells because RV-induced changes in Ca^{2+} homeostasis are driven by NSP4. We used MA104-GCaMP cells expressing NSP4-targeted short hairpin RNA (shRNA) or a nontargeted scrambled shRNA (*28*). RV infection of the MA104-GCaMP-shRNA cells with SA114F decreased NSP4 expression by ~95% and significantly decreased Ca^{2+} signaling (*28*) (fig. S1, B and C). We infected the MA104-GCaMP cells expressing shRNA2, because they had the greatest percent knockdown, using RV SA11cl3-mRuby3, which has the same NSP4 sequence as RV SA114F. The Ca^{2+} signaling frequency and Ca^{2+} spike magnitudes were significantly decreased in the NSP4-targeted shRNA MA104-GCaMP cells, both in RV-infected cells and in NB+3 and NB+5 uninfected cells (Fig. 1, H to J, and movie S3). Thus, the RV-induced Ca^{2+} signal required expression of RV NSP4 and dysregulation of host Ca^{2+} homeostasis in the infected cell.

Adenosine 5′-diphosphate and the P2Y1 receptor mediate RV-induced intercellular calcium waves

The pattern of signaling observed between RV-infected cells and uninfected cells was a phenomenon called intercellular calcium waves (ICWs), in which increases in cytosolic Ca^{2+} occur in an expanding circular pattern from a central initiating cell (*31*–*33*). Several molecules have been implicated in ICW propagation and may communicate via gap junctions or through paracrine signaling (*33*). To test whether RV-induced ICWs propagated via gap junctions, we infected MA104-GCaMP cells and treated them with dimethyl sulfoxide (DMSO) vehicle or the gap junction blockers 18β-glycyrrhetinic acid and TAT-Gap19. There was no significant difference in the Ca^{2+} spikes in neighboring cells between the mock-, 18β-glycyrrhetinic acid–, or TAT-Gap19–treated cells, which supports the idea that the RV-induced ICWs did not propagate via gap junctions (Fig. 2A). This finding was consistent with a negative scrape loading–dye transfer assay, in which the lack of dye beyond the cells immediately adjacent to the scrape demonstrate a lack of gap junction intercellular communication (*34*, *35*) (fig. S2A). Next, we tested whether the extracellular enterotoxin form of NSP4 might be the signaling molecule responsible for propagating the ICWs. We treated

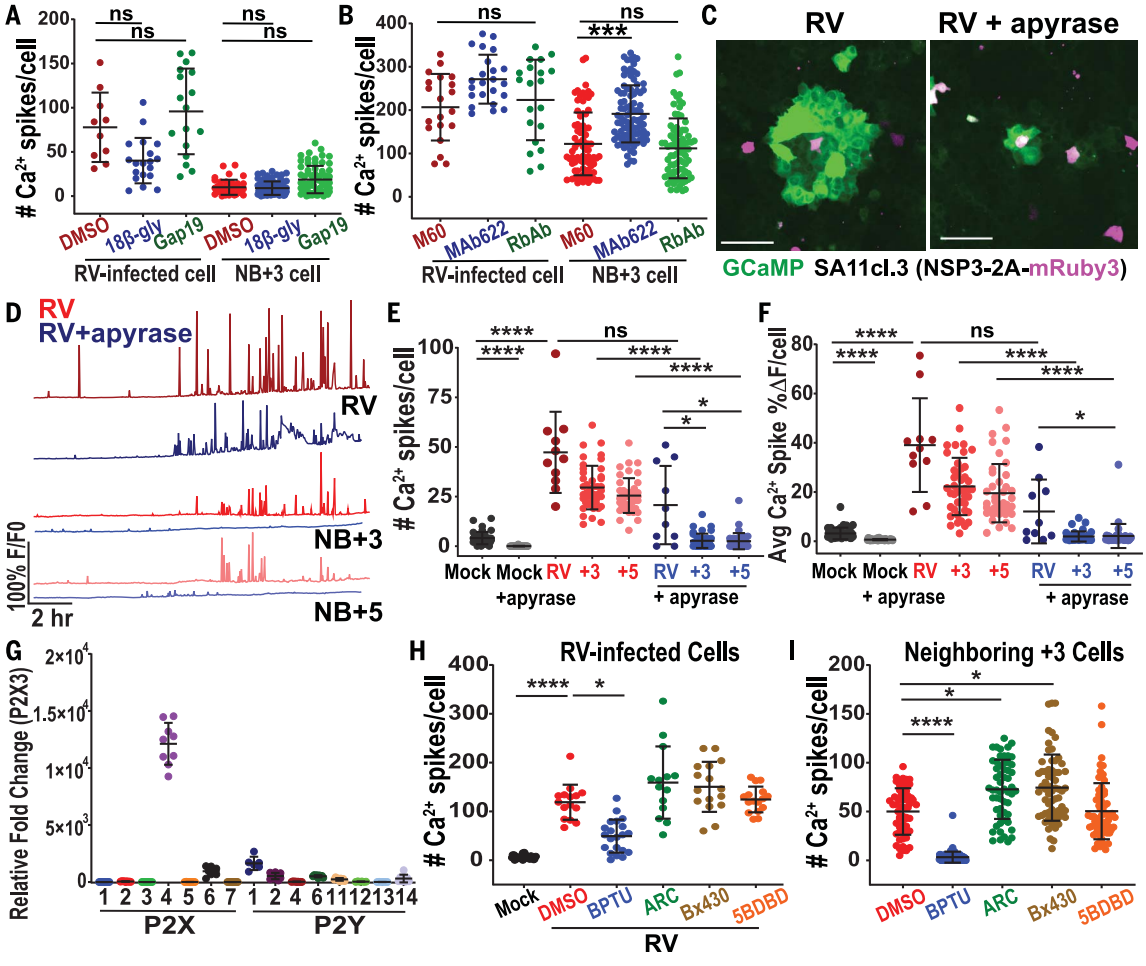

Fig. 2. Rotavirus induces ICWs by activating purinergic signaling. (**A** and **B**) Number of Ca^{2+} spikes in MA104-GCaMP cells in RV-infected (SA11cl3-mRuby3) at MOI 0.01 and NB+3 cell, treated with: (A) DMSO, 30 μM 18β-glycyrrhetinic acid (18β-gly) or 50 μM TAT-Gap19 (Gap19) and imaged ~8 to 24 hpi; or (B) anti-VP7 M60 MAb, anti-NSP4 MAb 622, or rabbit anti-NSP4 antisera 120 to 147 (Rb Ab) and imaged ~8 to 24 hpi (data combined from *N* = 3 independent experiments). (**C**) Representative images of ICWs in MA104-GCaMP cells infected with RV (SA11cl3-mRuby3) at MOI 0.1 and mock- or 10 U/ml apyrase–treated (5 U/ml apyrase VI and 5 U/ml apyrase VII) and imaged ~10 hpi. (**D**) Representative Ca^{2+} traces from ~8 to 25 hpi. (**E**) Ca^{2+} spikes in RV-infected and NB cells. (**F**) Average magnitude of Ca^{2+} spikes per cell in RV-infected and NB cells (data combined from *N* = 3 independent experiments). (**G**) qPCR of purinergic receptor mRNA normalized to 18S mRNA and fold change relative to P2X3 mRNA transcript levels in MA104 cells (data combined from *N* = 3 independent experiments). (**H** and **I**) Ca^{2+} spikes in MA104-GCaMP cells RV (SA114F)–infected (H) or neighboring (NB) cells (I) and treated with DMSO, 10 μM BPTU, 10 μM AR-C 118925XX (ARC), 10 μM Bx430, or 10 μM 5-BDBD (data combined from *N* = 3 independent experiments). [(A), (B), (E), (F), (H), (I)] Kruskal-Wallis with Dunn's multiple comparisons test used. Scale bars, 100 μm. Data represented as means ± SD; **P* < 0.05; ****P* < 0.001; *****P* < 0.0001.

RV-infected MA104-GCaMP cells with purified anti-NSP4 rabbit peptide antisera (amino acids 120 to 147) or anti-NSP4 monoclonal antibody 622, which bind to the enterotoxin domain and neutralize eNSP4-mediated Ca^{2+} flux (Fig. 2B) (*22*). Purified M60, a nonneutralizing anti-VP7 monoclonal antibody, was used as a control (*36*). We did not observe a significant reduction in Ca^{2+} spikes in the neighboring cells treated with anti-NSP4 antibodies, which suggests that enterotoxin NSP4 was not responsible for the RV-induced ICWs (Fig. 2B and movie S4). Previous studies have found increased PGE2 and NO during RV infection; thus, they potentially mediate RV-induced ICWs (*17*–*19*). However, adding PGE2 or the NO donor NOC-7 to MA104-GCaMP cells did not elicit a Ca^{2+} response, which demonstrates that these molecules could not directly transmit the RV-induced ICWs (fig. S2, B to E). Therefore, ICW propagation was mediated by an unidentified signaling molecule.

We then sought to determine whether adenosine 5′-triphosphate (ATP) was the signaling molecule responsible for the RV-induced ICWs. ATP is an important extracellular messenger and a common mediator of ICW signaling (*33*). We mock- or RV (SA11cl3-mRuby3)–infected MA104-GCaMP cells, and after infection, we mock-treated or treated with apyrase, an enzyme that degraded the purines ATP and adenosine 5′-diphosphate (ADP). Apyrase-treated wells showed a marked decrease in the area of Ca^{2+} signaling compared with that observed in untreated wells (Fig. 2C and movie S5). With apyrase treatment, the Ca^{2+} signaling frequency and amplitude were noticeably decreased in the uninfected NB+3 and NB+5 cells (Fig. 2D), which resulted in a significant decrease in the number of Ca^{2+} spikes and average Ca^{2+} spike magnitude in the NB+3 and NB+5 cells, but not in the RV-infected cells (Fig. 2, E and F). Thus, extracellular ATP and/or ADP propagated ICWs in RV infection.

Purinergic signaling—i.e., nucleotides as extracellular signaling molecules—is a key signaling pathway in intestinal physiology and involves multiple receptor subtypes. MA104 cells showed the greatest expression of the purinergic receptors *P2X4*, *P2X6*, *P2Y1*, *P2Y2*, and *P2Y14* (Fig. 2G). Relative mRNA expression levels of purinergic receptors did not substantially change with RV infection (fig. S3A and table S1). We first tested the ligand-gated ion channel P2X4 and the Gq/11 protein-coupled receptors P2Y1 and P2Y2 because they are strongly activated by ATP or ADP (*33*). We treated RV (SA11cl3-mRuby3)–infected MA104-GCaMP cells with small molecule inhibitors (Bx430 and 5BDBD for P2X4, BPTU for P2Y1, and AR-C 118925XX for P2Y2). The P2X4 inhibitors Bx430 and 5BDBD or the P2Y2 inhibitor AR-C 118925XX had no effect on RV-induced Ca^{2+} signaling. The P2Y1 blocker BPTU significantly decreased Ca^{2+} spikes in both the RV-infected cell and the NB+3 cells, and this

decrease was dose dependent (Fig. 2, H and I; fig. S3C; and movie S6). We tested the specificity of BPTU for the P2Y1 receptor and AR-C 118925XX for the P2Y2 receptor, which are strongly activated by ADP and ATP, respectively. The P2Y1 inhibitor BPTU significantly reduced the Ca^{2+} response in MA104-GCaMP cells from ADP but not in those from ATP (fig. S3D). Similarly, the P2Y2 inhibitor AR-C 118925XX significantly reduced the Ca^{2+} response from ATP but not that from ADP, which supports their specificity (fig. S3D).

Finally, we tested whether a different RV strain, Rhesus rotavirus (RRV), also elicited ICWs from RV-infected cells by the same mechanism. We mock- or RRV-infected MA104-GCaMP cells (MOI 0.05) and found that RRV-infected cells elicited ICWs that increased cytosolic Ca^{2+} in uninfected NB+3 and NB+5 cells (fig. S3E). Treatment with apyrase or BPTU significantly decreased the ICW signals only in the uninfected NB+3 and NB+5 cells (fig. S3E). Thus, cells infected with RRV also triggered ICWs through extracellular release of ADP and P2Y1 receptor activation, which demonstrates that this phenomenon was common to multiple RV strains.

RV induces ICWs in human intestinal enteroids

MA104 cells are a robust model system to study RV replication and form a simple, flat epithelium that facilitates microscopy studies. However, they are neither human nor intestinal in origin. To determine whether RV also causes ICWs in intestinal epithelial cells, we used jejunum-derived human intestinal enteroids (HIEs) stably expressing the GECI GCaMP6s (jHIE-GCaMP6s) (*28*). HIEs are a noncancerous in vitro model system established from human intestinal epithelial stem cells (*37*). They recapitulate the different epithelial cell types and support RV infection and replication, which makes them a biologically relevant system to study gastrointestinal pathophysiology (*38*–*40*). We infected jHIE-GCaMP6s monolayers with mock inoculum or the human RV strain Ito and imaged at 4 hpi (Fig. 3A and movie S7). We observed ICWs in both mock- and RV-infected jHIE-GCaMP6s monolayers; however, the areas of Ca^{2+} signaling were larger and occurred with greater frequency in the RV-infected monolayer than in the mock-infected or basal monolayer. To verify infection, we fixed the monolayers at 24 hpi, immunostained for RV antigen, and observed positive staining in the RV-infected monolayers (Fig. 3B). Thus, ICWs occurred under basal conditions in human intestinal epithelial cell models, but infection with RV increased the size of the ICWs.

Next, we investigated the mechanism of the RV-induced ICWs in the HIEs. To test gap

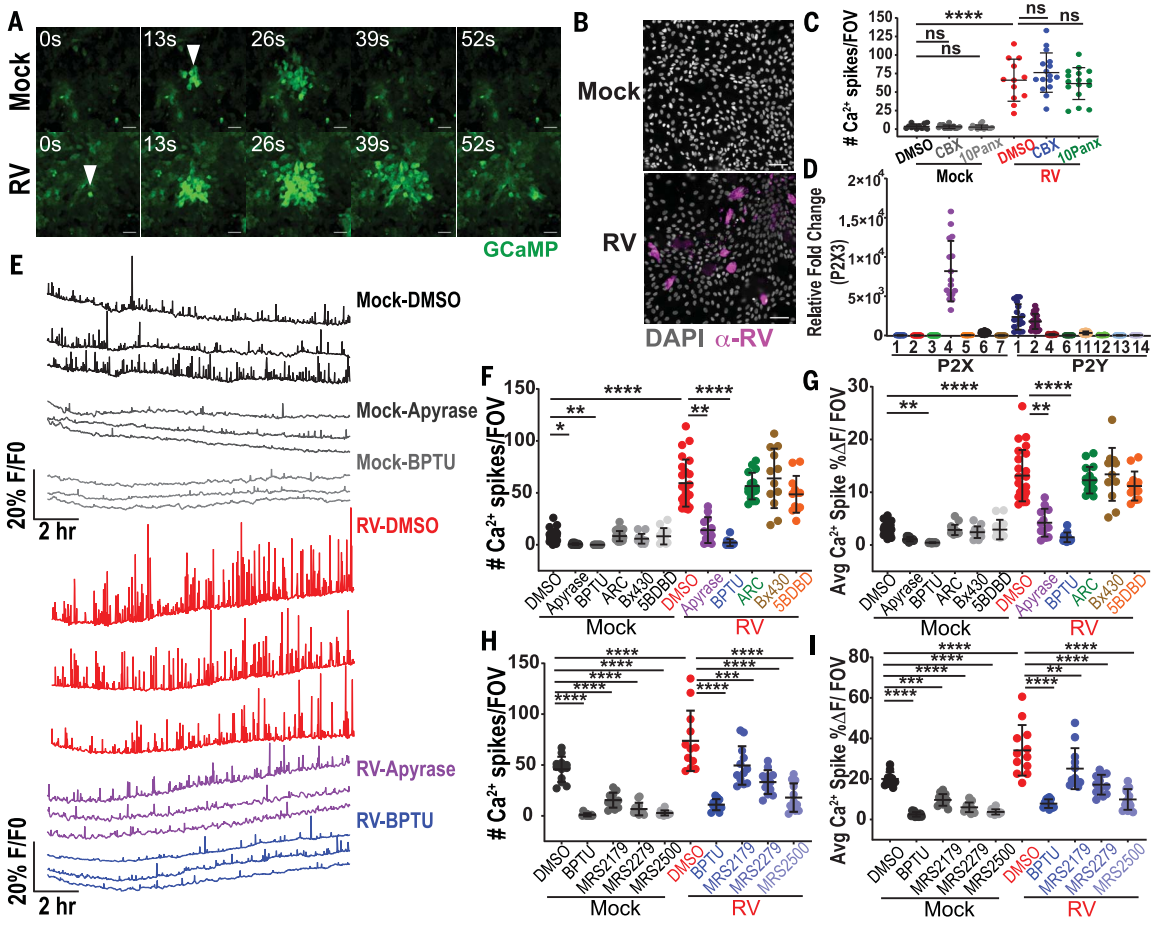

Fig. 3. Rotavirus infection induces ICWs in HIEs. (**A**) J3 jHIE-GCaMP6s monolayers mock- or RV (Ito)–infected produce ICWs originating at a cell (arrowheads), imaged at ~4 hpi. (**B**) IF images of (J3)HIE-GCaMP6s monolayers mock- or RV-infected, fixed at 24 hpi, and immunostained for RV antigen (pink) and counterstained with 4′,6-diamidino-2-phenylindole (DAPI) (gray). (**C**) Ca^{2+} spikes per FOV in (J3) HIEs mock- or RV-infected and treated with vehicle, 100 μM carbenoxolone (CBX), or 10 μM 10Panx at 8 to 22 hpi (data combined from *N* = 3 independent experiments). (**D**) qPCR of purinergic receptor mRNA normalized to 18*S* mRNA and fold change relative to P2X3 mRNA transcript levels in (J3)HIE monolayers (data combined from *N* = 3 independent experiments). (**E**) Representative Ca^{2+} traces per FOV of (J3)HIE-GCaMP6s monolayers either mock- or RV-infected and treated with DMSO, 100 U/ml apyrase, or 10 μM BPTU between 8.5 and 22 hpi. Mock- or RV-infected (J3)HIEs treated with DMSO, apyrase, or purinergic receptor blockers. (**F** and **G**) Ca^{2+} spikes per FOV in (J3)HIE-GCaMP6s monolayers treated with DMSO, 100 U/ml apyrase (50 U/ml apyrase VI and 50 U/ml apyrase VII), 10 μM BPTU, 10 μM AR-C 118925XX, 10 μM Bx430, or 10 μM 5-BDBD (F) and average magnitude of Ca^{2+} spikes per FOV for 8.5 to 22 hpi (G) (data combined from *N* = 3 independent experiments). (**H** and **I**) Ca^{2+} spikes per FOV of J2 jHIE-GCaMP6s monolayers mock- or RV-infected and treated with DMSO, 10 μM BPTU, 10 μM MRS2179, 10 μM MRS2279, or 10 μM MRS2500 (H) and average magnitude of Ca^{2+} spikes per FOV for 8 to 22 hpi (I) (data combined from *N* = 3 independent experiments). [(C), (H), and (I)] One-way ANOVA with Bonferroni's, and [(F) and (G)] Kruskal-Wallis with Dunn's multiple corrections test used. Scale bars, 50 μm. Data represented as means ± SD; **P* < 0.05; ***P* < 0.01; ****P* < 0.001; *****P* < 0.0001.

junction transmission, we treated mock- or RV (Ito)–infected jHIE-GCaMP6s monolayers with DMSO vehicle, the glycyrrhetinic acid-derivative carbenoxolone (CBX), or the pannexin blocker ^{10}Panx. We were unable to perform single-cell analysis for these experiments because individual jHIE cells were much smaller and more mobile than MA104 cells. Instead, we measured the GCaMP6s fluorescence over the whole field of view (FOV) (~455 μm^2). Although we observed statistically greater Ca^{2+} spikes in RV-infected than in mock-infected monolayers, CBX or ^{10}Panx did not significantly decrease the number of Ca^{2+} spikes per FOV in mock- or RV-infected monolayers (Fig. 3C). The scrape loading–dye transfer was also negative in jHIE monolayers, which further demonstrated a lack of gap junction intercellular communication (fig. S2A). Adding PGE2 or NOC-7 to jHIE-GCaMP6s cells also did not elicit a Ca^{2+} response (fig. S2, F to I). Thus, RV-induced ICWs in HIEs do not occur by gap junctions, PGE2, or NO, and basal ICWs do not appear to have significant gap junction transmission.

In jHIE monolayers, *P2X4*, *P2Y1*, and *P2Y2* had the highest expression levels, similar to that of MA104 cells (Fig. 2G and Fig. 3D). The relative mRNA expression levels of purinergic receptors did not substantially change with RV (Ito) infection (fig. S3B and table S1). To test the involvement of the different purinergic receptors in ICWs, we mock- or RV (Ito)–infected jHIE-GCaMP6s monolayers and treated with DMSO vehicle, apyrase, BPTU, AR-C 118925XX, Bx430, or 5BDBD. We found that apyrase and BPTU treatment decreased the Ca^{2+} signaling and amplitude in RV-infected monolayers (Fig. 3E and movie S8). Quantification verified a significant decrease in the number of Ca^{2+} spikes per FOV and in the average Ca^{2+} spike magnitude with apyrase or BPTU treatment compared with the DMSO vehicle control in the RV-infected monolayers (Fig. 3, F and G). Notably, BPTU and apyrase treatment also reduced the number of Ca^{2+} spikes in mock-inoculated monolayers (Fig. 3F). This suggests that there was purinergic receptor-induced Ca^{2+} signaling in jHIEs under basal conditions that was exploited during RV infection.

Genetic variation may influence whether RV infection can cause ICWs because jHIEs are human-derived cultures. We created an additional jHIE-GCaMP6s line derived from a different individual (J2). We mock- and RV-infected these jHIE-GCaMP6s monolayers and treated with a panel of P2Y1 receptor blockers (BPTU, MRS2179, MRS2279, and MRS2500). All of the P2Y1 blockers significantly decreased the number of Ca^{2+} spikes per FOV and the average Ca^{2+} spike magnitude when compared with DMSO vehicle control for both the mock- and RV-infected monolayers (Fig. 3, H and I). Thus, RV-induced ICWs in intestinal epithelial cells occurred by extracellular ADP signaling and the P2Y1 receptor, the same as in MA104 cells.

CRISPR-Cas9 P2Y1 receptor knockout reduces ICWs

The P2Y1 purinergic receptor exhibits greater activation with ADP than with ATP, which suggests that ADP mediates the ICWs in RV infection (*41*). This is consistent with the reduced cytoplasmic ATP concentrations found in RV-infected cells (*42*). To test whether ADP was the signaling molecule associated with the ICWs, we infected MA104-GCaMP cells with RV (SA114F) and then treated with apyrase grade VI—which had a high adenosine triphosphatase (ATPase)/adenosine diphosphatase (ADPase) activity ratio—or apyrase grade VII—which had a low ATPase/ADPase activity ratio. Treatment with apyrase grade VII, but not grade VI, significantly decreased the number of Ca^{2+} spikes and the spike magnitude in RV-infected wells, supporting the idea that ADP was the signaling molecule in RV-induced ICWs (Fig. 4, A and B). To further test that the P2Y1 receptor was required for RV-induced ICWs, we genetically knocked out the P2Y1 receptor in MA104-GCaMP cells using lentivirus encoding CRISPR-Cas9 with small-guide RNAs targeted for the P2Y1 receptor gene (MA104-GCaMP-P2Y1ko). Genotyping analysis revealed several mutations in the sequence downstream of the guide RNA in three clonal populations of cells (fig. S4, A and B). To test the P2Y1 knockout (KO) phenotype, we added ADP to parental and MA104-GCaMP-P2Y1ko cells and found a significantly decreased Ca^{2+} response in the KO cells compared with the parental cells, consistent with a lack of P2Y1 receptor function (Fig. 4C).

Next, we sought to determine whether KO of the P2Y1 receptor would also prevent ICWs during RV infection. Fixing and immunostaining for RV antigen at 24 hpi showed positive staining for RV in parental and P2Y1ko cells, confirming that the P2Y1 KO did not prevent infection (Fig. 4D). We next tested whether RV-infected MA104-GCaMP-P2Y1ko cells still released ADP to confirm that the P2Y1 KO was specific to receptor function and did not affect ADP release, which could be responsible for decreased ICWs. We mock- or RV (SA114F)–infected parental or P2Y1ko cells, washed off inoculum, and added ARL 67156, an ecto-ATPase inhibitor, to block the degradation of released nucleotides from cellular ectoATPases. Approximately 5 to 6 hpi, we transferred the mock- or infected-cell supernatant to uninfected MA104-GCaMP cells to measure the Ca^{2+} response as a sensor of released ADP. We found a significantly greater increase in GCaMP fluorescence in RV-infected than in mock-infected supernatants (Fig. 4E). However, there was no significant difference in the extent of that increase between parental- or P2Y1ko-derived supernatants (Fig. 4E). To show specificity of this Ca^{2+} signal to ADP and P2Y1, we treated the uninfected sensor MA104-GCaMP cells with BPTU, which significantly lessened the increase in GCaMP fluorescence from both parental and P2Y1ko supernatants (Fig. 4E). Thus, the Ca^{2+} response from both parental- and P2Y1ko-derived supernatants was predominantly caused by ADP. Also, there was no significant difference between adding parental- or P2Y1ko-derived supernatants to the BPTU-treated sensor cells, which supports the idea that RV-infected P2Y1ko cells still release ADP (Fig. 4E). Last, we tested whether RV-infected P2Y1ko cells had decreased ICWs. We mock- or RV (SA114F)–infected MA104-GCaMP (parental) or MA104-GCaMP-P2Y1ko cells. In the P2Y1ko cells, there was decreased Ca^{2+} signaling, Ca^{2+} spikes, and average Ca^{2+} spike magnitude in the NB+3 and NB+5 cells compared with the parental, though not in the RV-infected cell (Fig. 4, F to H, and movie S9). Additional treatment of apyrase VII to the P2Y1ko cells only modestly decreased the Ca^{2+} spikes in neighboring cells (Fig. 4, G and H).

Similarly, we tested the effect of genetic KO of the P2Y1 receptor on ICWs in RV-infected jHIEs (jHIE-GCaMP6s-P2Y1ko). Genotyping analysis revealed two P2Y1 KO enteroid populations composed of an insertional mutation and a deletion in the sequence downstream of the guide RNA (fig. S4, C and D). Phenotypic KO was confirmed by a reduced Ca^{2+} response to ADP in jHIE-GCaMP6s-P2Y1ko enteroids compared with parental enteroids (Fig. 5A). We created an additional jHIE-GCaMP6s enteroid line with CRISPR-Cas9 KO of the P2Y2 receptor (jHIE-GCaMP6s-P2Y2ko). Genotyping analysis of the P2Y2ko enteroids detected two alleles with deletion mutations downstream of the guide RNA sequence (fig. S5, A and B). To test the P2Y2 KO phenotype, we added nonhydrolyzable ATP-γS to parental and P2Y2ko enteroids and found a significantly decreased Ca^{2+} response in the P2Y2ko jHIEs (Fig. 5B). As with the P2Y1ko MA104 cells, immunostaining the jHIE monolayers for RV antigen at 24 hpi showed similar levels of positive staining for RV in parental, P2Y1ko, and P2Y2ko enteroids, demonstrating equivalent susceptibility to RV infection (Fig. 5, C and D). Mock or RV (Ito) infection of the parental, jHIE-GCaMP6s-P2Y1ko, or jHIE-GCaMP6s-P2Y2ko resulted in significantly fewer Ca^{2+} signaling events, Ca^{2+} spikes per FOV, and smaller average Ca^{2+} spike magnitude in the P2Y1 KO jHIEs, but not in P2Y2 KO jHIEs (Fig. 5, E to G, and movie S10). Notably, there were also significantly fewer Ca^{2+} spikes per FOV and average Ca^{2+} spike magnitude in the P2Y1 KO enteroids compared with parental or P2Y2 KO enteroids in mock inoculation (Fig. 5, F and G). Thus, ADP and the P2Y1 receptor mediated the ICWs in RV infection and reduced basal ICW signaling.

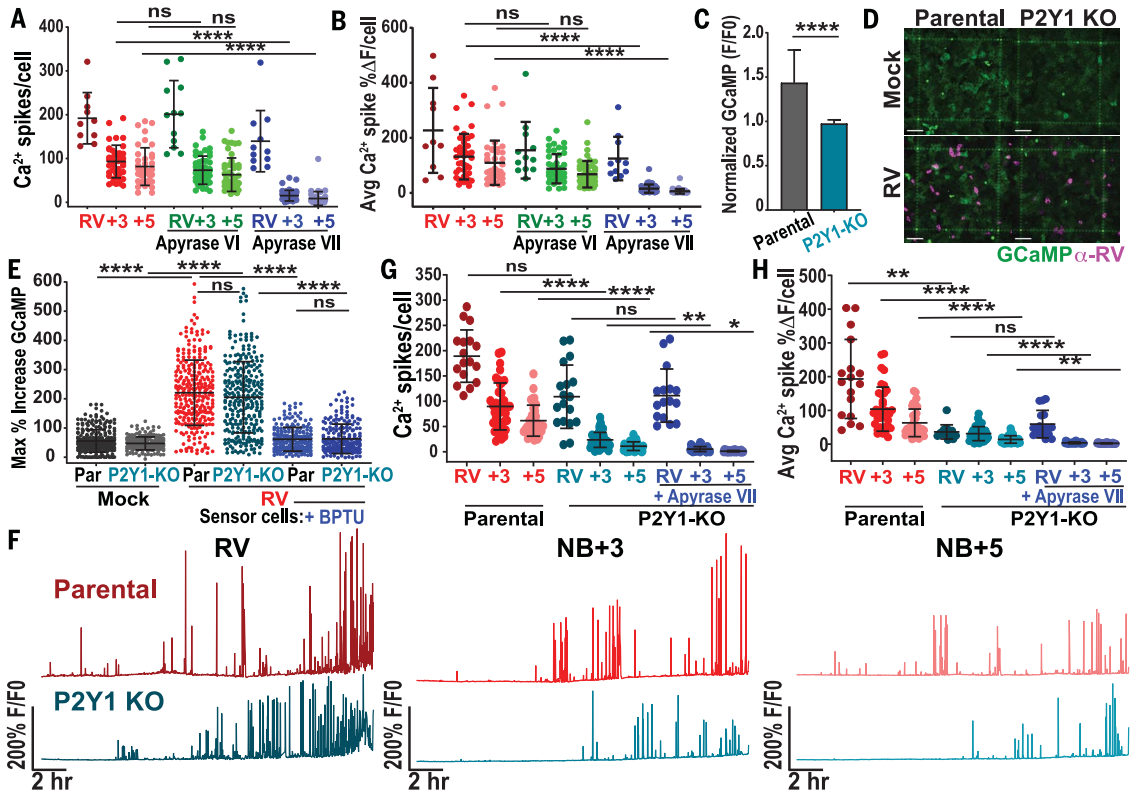

Fig. 4. CRISPR-Cas9 KO of P2Y1 receptor reduces ICWs. (**A** and **B**) MA104-GCaMP cells infected with rotavirus (RV SA114F) at MOI 0.01 and mock- or treated with apyrase grade VI or grade VII, imaged ~3 to 25 hpi. (A) Ca^{2+} spikes per RV-infected cell and NB+3 and NB+5 cells and (B) the average magnitude of Ca^{2+} spikes per cell in RV-infected and NB cells (data combined from *N* = 3 independent experiments). (**C**) Normalized GCaMP fluorescence increase in parental or P2Y1 KO MA104-GCaMP cells treated with 1 nM ADP (*n* = 27 cells, data combined from *N* = 3 independent experiments, Mann-Whitney statistical test). (**D**) Parental or P2Y1 KO MA104-GCaMP monolayers mock- or RV-infected, fixed at 24 hpi, and immunostained for RV antigen (pink). Scale bars, 100 μm. (**E**) Maximum percent increase in GCaMP fluorescence of MA104-GCaMP cells (± 10 μM BPTU) after addition of supernatant from mock- or RV (SA114F)–infected parental (Par) or P2Y1 KO MA104-GCaMP cells (MOI 5, harvested ~5 to 6 hpi) (*n* ≥ 210 cells per condition, data combined from *N* = 3 independent experiments). (**F**) Representative Ca^{2+} traces of parental or P2Y1 KO cells infected with RV (SA11cl3-mRuby3). (**G** and **H**) Ca^{2+} spikes per cell in RV-infected or NB+3 or NB+5 cell (G) and average magnitude of Ca^{2+} spikes/cell (H) (data combined from *N* = 3 independent experiments). [(A), (B), (E), (G), and (H)] Kruskal-Wallis with Dunn's multiple comparisons test used. Data represented as means ± SD; **P* < 0.05; ***P* < 0.01; *****P* < 0.0001.

Purinergic signaling increases RV replication and expression of interleukin-1α, iNOS, and COX2

Extracellular ATP reduces the replication of several viruses through activation of P2X7 receptors, which specifically bind ATP (*43*, *44*). Less is known about the role of ADP in cellular signaling or its effects on viral infection and replication. We first tested the effect of purinergic blockers on RV replication. New infectious yield from RV (SA114F)–infected MA104 cells was significantly decreased when treating cells with apyrase or BPTU after inoculation by ~92 and ~90%, respectively (Fig. 6A). No significant decrease was observed when adding AR-C 118925XX, Bx430, 5BDBD, or the nonselective P2 receptor antagonists suramin and PPADS (Fig. 6A). Furthermore, RV infectious yield was also reduced from RV (SA11cl3-mRuby)–infected MA104-GCaMP-P2Y1ko cells compared with parental MA104-GCaMP cells by ~95% (Fig. 6B). Thus, blocking ADP signaling and the P2Y1 receptor decreased RV replication.

Extracellular ATP is also known to have proinflammatory functions and activate components of the innate immune system such as macrophages (*45*, *46*). RV increases expression and release of the inflammatory cytokine interleukin-1α (IL-1α), which is highly expressed in epithelial cells (*47*, *48*). Furthermore, strong cytosolic Ca^{2+} agonists can induce the secretion of IL-1α independent of inflammasome activation (*49*). To determine whether RV-induced ICWs increase IL-1α, we mock- or RV (Ito)–infected jHIE monolayers and treated with apyrase or BPTU. RV infection significantly increased *IL-1α* expression levels over mock infection, and treatment with apyrase or BPTU inhibited this increase (Fig. 6C). Thus, RV-induced ICWs and ADP signaling increased *IL-1α* expression and mediated the inflammatory response from HIEs.

Because increased PGE2 and NO have been found during RV infection, we also investigated whether RV-induced ICWs could stimulate their production (*17*–*19*). Purinergic signaling stimulates cyclooxygenase-2 (*COX2*) expression and PGE2 release from Caco-2 and rat-derived IEC-6 cell lines and activates inducible nitric oxide synthase (*iNOS*) expression and NO production (*50*, *51*). We mock- or RV (Ito)–infected jHIE monolayers and treated with apyrase or BPTU. RV significantly increased both *COX2* and *iNOS* expression levels over mock infection, and treatment with apyrase or BPTU inhibited this increase (Fig. 6, D and E). Both RV-induced ICWs and ADP signaling increased the expression of *COX2* and *iNOS* and thus potentially caused the increased PGE2 and NO observed in RV infections.

Blocking purinergic signaling reduces serotonin and fluid secretion

RV infection causes a multifactorial secretory diarrhea, and two-thirds of the fluid secretion is attributed to enteric nervous system (ENS) activation (*7*). RV infection stimulates the release of serotonin from enterochromaffin cells

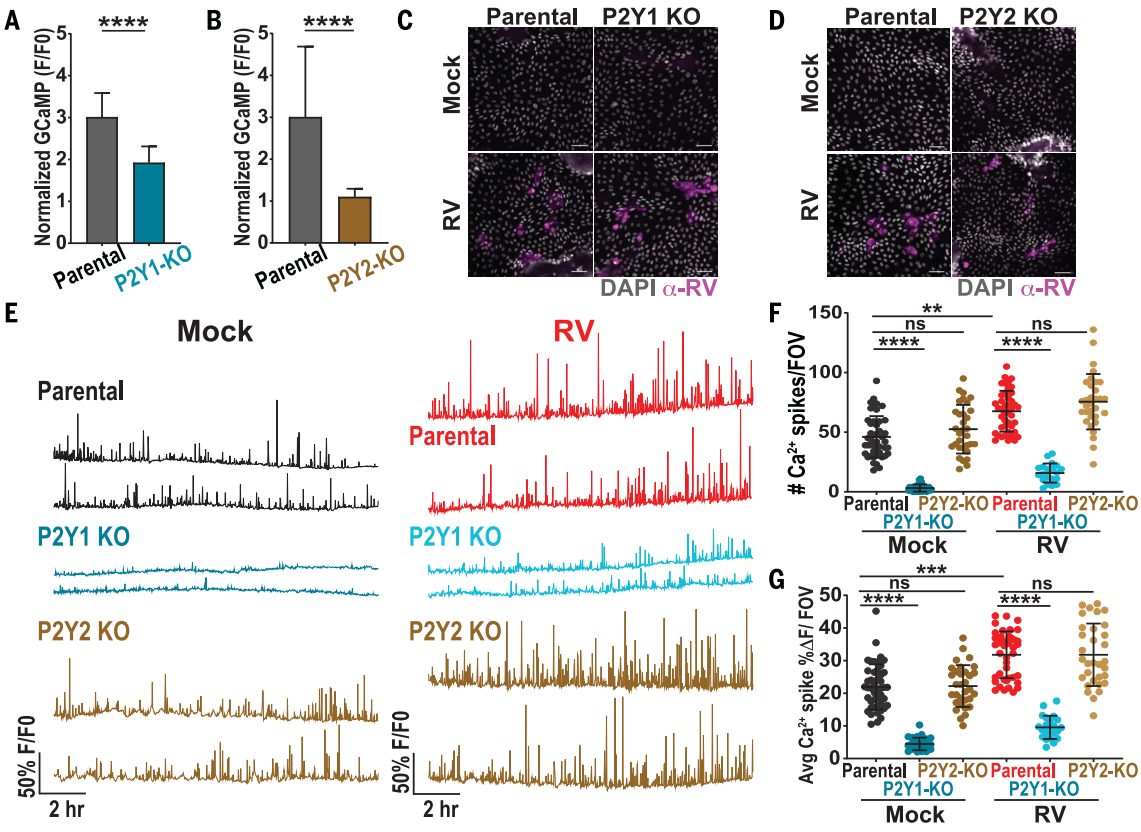

Fig. 5. CRISPR-Cas9 KO of P2Y1 receptor in jHIEs reduces ICWs. (**A** and **B**) Normalized GCaMP fluorescence increase in parental or P2Y1 KO (J2)HIE-GCaMP6s monolayers treated with 10 nM ADP (n = 75 cells, data combined from N = 3 independent experiments) (A) and parental or P2Y2 KO (J2)HIE-GCaMP6s monolayers treated with 10 μM ATP-γS (n = 30 cells, data representative of N = 3 independent experiments) (B). (**C** and **D**) Parental or P2Y1 KO jHIE-GCaMP6s or parental or P2Y2 KO jHIE-GCaMP6s monolayers mock- or RV-infected, fixed at 24 hpi, and immunostained for RV antigen (pink) and counterstained with DAPI (gray). (**E**) Representative Ca^{2+} traces per FOV of mock- or RV-infected parental, P2Y1 KO jHIE-GCaMP6s, or P2Y2 KO jHIE-GCaMP6s monolayers. (**F** and **G**) Ca^{2+} spikes per FOV (F) and average magnitude of Ca^{2+} spikes per FOV (G). [(A) and (B)] Mann-Whitney test or [(F) and (G)] Kruskal-Wallis with Dunn's multiple corrections test used. Scale bars, 50 μm. Data represented as means ± SD; $^{**}P < 0.01$; $^{***}P < 0.001$; $^{****}P < 0.0001$.

to activate the ENS, and blocking serotonin decreases diarrhea, making serotonin release a key mechanism for RV-induced diarrhea (*4*, *52*). To determine whether RV-induced ADP signaling stimulated serotonin secretion, we mock- or RV (Ito)–infected jHIE monolayers and treated with DMSO vehicle, apyrase, or BPTU. After 24 hours, we found significantly increased serotonin in the supernatant of RV-infected jHIE monolayers compared with mock infection, which was significantly inhibited by treatment with apyrase or BPTU (Fig. 6F). Furthermore, treatment of RV-infected monolayers with ω-agatoxin, a P-type voltage-gated Ca^{2+} channel blocker, significantly inhibited the RV-induced secretion of serotonin, which supports the idea that the measured serotonin was from cellular release rather than RV-induced cell death (Fig. 6F). We found similar results when infecting jHIE transwells, a more polarized model of epithelium, with RV. Treatment with BPTU significantly decreased serotonin measured in both the apical and basolateral compartments compared with DMSO vehicle (Fig. 6G). Thus, ADP signaling stimulated serotonin secretion during RV infection.

RV infection also activates secretory pathways in epithelial cells through the stimulation of chloride secretion, which drives paracellular movement of water. We tested whether ADP signaling was important for RV-induced epithelial fluid secretion using the enteroid swelling assay, in which an increase in fluid secretion causes an increase in the lumen of three-dimensional (3D) enteroid cultures (*38*, *53*). We mock- or RV-infected 3D jHIE-GCaMP6s enteroids, treated with DMSO vehicle or BPTU, and found that BPTU treatment significantly decreased the percentage of swelling in mock- and RV-infected enteroids (Fig. 6H and movie S11). Thus, ADP signaling stimulated epithelial fluid secretion in RV infection.

Finally, we determined whether inhibition of the P2Y1 receptor would attenuate RV-induced diarrhea in a neonatal mouse model. BPTU consistently had the most potent inhibition of Ca^{2+} spikes and average Ca^{2+} spike magnitude in HIEs (Fig. 3, H and I), and it binds to an allosteric pocket on the external surface of the P2Y1 receptor (*54*). We tested a drug treatment model in which 6- to 8-day-old C57Bl/6J pups were orally gavaged with RRV and then gavaged with BPTU or vehicle control on days 1 to 4 postinfection. RRV is more pathogenic than SA11 in C57Bl/6J pups and causes a moderate diarrhea (*55*, *56*). RRV also causes ICWs similar to SA11 and thus is appropriate for assessing whether BPTU treatment can reduce the diarrhea phenotype in vivo (fig. S3E). Stools were assessed each day, and watery, mucus, and yellow stools were indicators of diarrhea. Peak diarrhea occurred at 2 days postinfection (dpi) in both DMSO- and BPTU-treated pups, but the percentage of pups with diarrhea decreased significantly by 4 dpi (Fig. 6I). BPTU-treated pups had significantly less-severe diarrhea as measured by their mean diarrheal score (Fig. 6J). Intestinal cross sections from the duodenum, jejunum, and ileum of RV-infected pups treated with DMSO or BPTU were relatively similar with no histopathological features at 5 dpi (fig. S6A). We

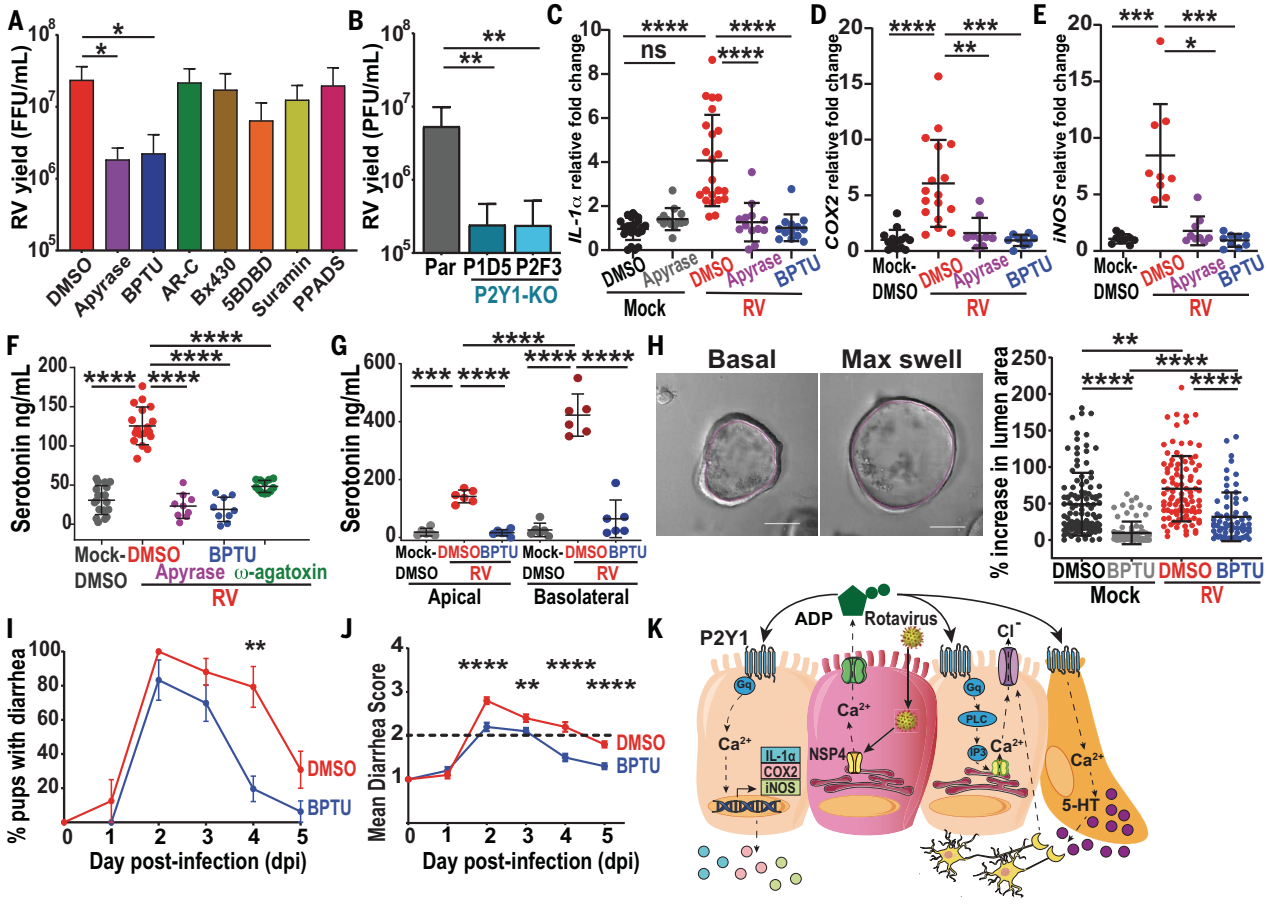

Fig. 6. Purinergic signaling contributes to rotavirus disease processes. (**A**) Rotavirus yield from SA114F-infected MA104 cells treated with DMSO vehicle, 10 U/ml apyrase, 10 μM BPTU, 10 μM AR-C 118925XX, 20 μM Bx430, 20 μM 5-BDBD, 300 μM suramin, or 10 μM PPADS by fluorescent focus assay (data combined from *N* = 3 independent experiments). FFU, focus-forming units. (**B**) Plaque assay yield of RV (SA114F)–infected MA104-GCaMP (Par) or MA104-GCaMP P2Y1 KO cells (data combined from *N* = 3 independent experiments). (**C** to **E**) qPCR of mRNA transcripts normalized to 18*S* mRNA transcripts and fold change relative to the mock-DMSO transcript levels in (J3)HIE monolayers mock- or RV (Ito)–infected and treated with DMSO vehicle, 100 U/ml apyrase, or 10 μM BPTU (data combined from *N* = 3 independent experiments). (**F** and **G**) Serotonin secretion from RV (Ito)–infected jHIE (F) monolayers and (G) transwells treated with DMSO, 100 U/ml apyrase, 10 μM BPTU, or 300nM ω-agatoxin (data combined from *N* = 3 independent experiments). (**H**) Enteroid swelling assay: 3D jHIE-GCaMP6s enteroids mock- or RV (Ito)–infected and treated with DMSO or 10 μM BPTU. Cross-sectional area of the internal lumen (pink outline) used for percent increase between basal and maximum swelling (left panels). Scale bar, 100 μm (*n* ≥ 68 HIEs per condition, data combined from *N* = 3 independent experiments). (**I** and **J**) C57Bl/6J mouse pups with diarrhea infected with RRV and vehicle- or BPTU-treated (I) and the mean diarrhea score (J) (data combined from four cages of each condition, 26 to 30 pups total per condition; means ± SEM). (**K**) Summary model of RV-induced ICWs mediated by extracellular ADP. [(A), (F), and (G)] One-way ANOVA with Bonferroni multiple comparisons test, [(C), (D), (E), and (H)] Kruskal-Wallis with Dunn's multiple comparisons test, and [(B), (I), and (J)] Mann-Whitney test were used. [(A) to (H)] Data represented as means ± SD. **P* < 0.05; ***P* < 0.01; ****P* < 0.001; *****P* < 0.0001.

then tested whether treatment with MRS2500, a water-soluble small molecule P2Y1 receptor blocker with a different mechanism of inhibition from BPTU, would similarly attenuate RV diarrhea (*54*). In these studies, there were similar percentages of pups with diarrhea on days 1 to 5 postinfection (fig. S6B). However, pups treated with MRS2500 had significantly less-severe diarrhea at the peak of diarrhea on days 3 to 4 postinfection compared with pups treated with control saline (fig. S6C). Thus, blocking the P2Y1 receptor decreased diarrhea severity and caused diarrhea to resolve more quickly than in the DMSO-treated animals.

The current concept of RV pathogenesis proposes that paracrine signaling from RV-infected cells dysregulates surrounding uninfected cells and contributes to life-threatening diarrhea and/or vomiting. RV elevates cytosolic Ca^{2+} during infection and increases paracrine signaling molecules such as eNSP4, PGE2, and NO, but functional signaling from RV-infected cells to uninfected cells had not yet been determined (*9*, *18*, *19*). Thus, the primary goal of this study was to investigate the role and identify the mechanisms of intercellular signaling during RV infection. Using long-term live-cell fluorescence imaging to detect signaling between infected and uninfected cells, our work describes the direct observation of ICWs originating from RV-infected cells and provides experimental proof for the widely held paracrine signaling idea as summarized in Fig. 6K.

Extracellular purinergic signaling is a well-conserved communication system found in single-celled bacteria and protozoa as well as in plants and higher-order eukaryotes (*57*). Though this signaling is most commonly ATP, RV activated ADP- and P2Y1 receptor–mediated ICWs, and this was the most dominant Ca^{2+} signal observed during RV infection. Mechanical stress and cell swelling are two major triggers of ATP secretion from intact, nonneuronal cells (*33*). Because RV disrupts the actin cytoskeleton and greatly increases intracellular Ca^{2+} during infection, we speculate that cell-shape changes or cellular swelling may be

sufficient to cause mechanical stress and ADP release (*58*, *59*). RV exploited ADP signaling in host cells to benefit its replication, but it also increased hallmarks of RV disease such as fluid and serotonin secretion. Furthermore, treatment of neonatal mice with two mechanistically different small molecule P2Y1 receptor inhibitors attenuated RV diarrhea. Thus, activation of purinergic signaling was biologically relevant to RV disease. Although eNSP4 can induce diarrhea in animal models, here eNSP4 was not involved in ICWs or purinergic signaling and may induce fluid secretion through an alternative pathway (*9*, *20*). Blocking ADP signaling and the P2Y1 receptor reduced the RV-induced expression of *COX2* and *iNOS* that drives production of PGE2 and NO, respectively. This suggests that ICWs and ADP signaling induced production of these additional paracrine signaling molecules. RV-induced *IL-1α* expression was decreased upon blocking ADP signaling; thus, ADP signaling may also be upstream of other inflammatory responses such as interferon pathways increased in RV infection (*47*, *60*). Activating ICWs and ADP signaling may be a common strategy for enteric viruses to amplify dysregulation of host cells. Thus, targeting the P2Y1 receptor may be an effective host-directed approach to treating viral diarrhea and other inflammatory pathways.

ICWs and extracellular ADP signaling may be a broadly important form of communication in the gastrointestinal epithelium. Basal ICWs in jHIEs were reduced when treated with apyrase and P2Y1 blockers, and P2Y1 receptor KO enteroids had significantly reduced Ca^{2+} signaling. Because ATP-mediated ICWs are activated in wound-healing responses (*61*, *62*), tonic purinergic signaling may also be important for maintaining epithelial barrier integrity and epithelial-to-epithelial cell communication of damage, stretch, and compression forces. Purinergic signaling regulates responses to injury and restitution by mediating the innate immune system (*46*). Basal, ADP-based ICWs may also have a role in the balance of pro- and anti-inflammatory signaling from the epithelium. Furthermore, extracellular ATP signaling in the gastrointestinal tract stimulates epithelial ion transport (*63*), which suggests that basal ICWs could stimulate fluid secretion and hydrate the mucus layer. Finally, ADP-driven ICWs may mediate communication from the epithelium to the ENS directly or signal to the lamina propria and endothelium as part of tissue-level homeostasis. ICWs in intestinal epithelium and HIE models have not been widely studied, and the possible physiological roles of their ICWs remain to be characterized. Because the epithelium is the primary interface between the environment and the host, understanding how it coordinates and communicates is critical for developing therapeutics when it becomes dysregulated in disease states.

Together, these studies identify ADP as the signaling compound that elicited a paracrine signal involved in RV diarrhea and vomiting responses. Reduction of ADP signaling and ICWs decreased many known aspects of RV disease, including serotonin release, epithelial fluid secretion, and diarrhea in a neonatal mouse model. Paracrine purinergic signaling and ICWs may be a common strategy among enteric viruses to amplify their dysregulation of host systems. Thus, targeting the P2Y1 receptor may be an effective approach for treating viral diarrhea.

Materials and methods

Cells and rotaviruses

MA104 cells (African green monkey kidney cells) (ATCC CRL-2378.1) and HEK293T cells (ATCC CRL-3216) were cultured in high glucose Dulbeccos modified Eagle's medium (DMEM) supplemented with 10% fetal bovine serum (FBS) and Antibiotic/Antimycotic (Invitrogen) at 37°C in 5% CO_2. The rotavirus human strain Ito, used for all HIE infections, was prepared as previously described (*38*). Rotavirus strains SA114F and Rhesus RV (RRV) were produced from in-house stocks. Recombinant and SA11 clone 3-mRuby3 was produced previously (*28*). All viruses were propagated in MA104 cells in serum-free DMEM supplemented with 1 μg/ml Worthington's Trypsin, and after harvest stocks were subjected to three freeze-thaw cycles and activated with 10 μg/ml Worthington's Trypsin for 30 min at 37°C before use.

Rotavirus diarrhea mouse model

C57Bl/6J dams with natural litters (purchased from Center for Comparative Medicine, Baylor College of Medicine) were used and housed in standard cages with food and water provided ad libitum. Mouse pups, both male and female at natural ratios, were housed with their dam throughout the experiment. Animal experiments were approved by the Baylor College of Medicine Institutional Animal Care and Use Committee (IACUC), approved protocol AN-6903. All experiments were performed in accordance with the recommendations in the Guide for the Care and Use of Laboratory Animals of the National Institutes of Health.

Six- or 7-day-old mouse pups were orally gavaged with 1.5×10^7 PFU/ml of RRV, a dosage sufficient to cause diarrhea in 100% of pups. The inoculum was mixed with sterile-filtered green food dye (3% by volume) for visualization of the gavage. For BPTU experiments, pups were orally gavaged with BPTU (4 mg/kg) (4 cages, n = 30 pups) or an equivalent volume of DMSO vehicle control (4 cages, n = 26 pups) suspended in pharmaceutical grade corn oil on days 1 to 4 postinfection. For MRS2500 experiments, pups were orally gavaged with MRS2500 (4 mg/kg) (9 cages, n = 60 pups) suspended in pharmaceutical grade normal saline or an equivalent volume of saline control (8 cages, n = 46 pups) on days 1 to 4 postinfection. Cages receiving control or drug treatment were assigned at random.

Each day, mouse pups were gently palpated on the abdomen to express and visualize feces. Stools were assessed on a scale between 1 and 4 for volume, color, and consistency as described previously (*9*); an average score of ≥2 was considered diarrhea. For scoring consistency, select experiments were scored by an observer blinded to experimental condition. Percentage of pups with diarrhea was calculated as the number of stools with a diarrhea score ≥2 divided by the number of stools collected per cage per day. Pups from which a stool sample could not be collected on that day were not counted for percent diarrhea or mean diarrhea severity calculations.

Chemicals

BPTU, AR-C 118925XX, Bx430, 5-BDBD, MRS2179, MRS2279, MRS2500, 10-Panx, suramin, TAT-Gap19, PPADS (Pyridoxalphosphate-6-azophenyl-2',4'-disulfonic acid), NOC-7, prostaglandin E2, ARL 67156, and ω-agatoxin were purchased from Tocris Bioscience. Apyrase grade VI (catalog no. A6410) and apyrase grade VII (catalog no. A6535) were purchased from Sigma-Aldrich. 18β-glycyrrhetinic acid and carbenoxolone were purchased from Santa Cruz Biotechnology.

Antibodies

To detect RV by IF, we used rabbit anti-RV strain Alabama (*12*) (1:80,000) and the secondary antibody donkey anti–rabbit IgG H&L AlexaFluor 568 (Invitrogen, A10042) (1:2000). For Western blots, we used rabbit anti-NSP4 aa120-147 (*64*) (1:3000) to detect RV NSP4, mouse anti-GAPDH monoclonal antibody (Novusbio, NB600-502) (1:5000) to detect GAPDH, and secondary antibodies alkaline phosphatase-conjugated goat anti–rabbit IgG or goat anti–mouse IgG (Southern Biotech, 4030-04, 1036-04) (1:2000). For eNSP4-blocking assays, we used purified anti-NSP4 rabbit antisera (120-147) (*22*), purified anti-NSP4 monoclonal antibody 622 generated against bacterially expressed SA11 NSP4 coiled-coil domain (amino acids 95 to 146) (*65*), and purified M60, a nonneutralizing anti-VP7 monoclonal antibody, was used as a control (*36*). Equal concentrations of antibody, estimated using protein OD_{280}, were added to RV-infected wells after inoculation.

Calcium indicator lentiviruses, cell lines, and enteroids

GCaMP5G (Addgene plasmid #31788), GCaMP6s (Addgene plasmid #40753), and G-CEPIA1er (Addgene plasmid #105012) were cloned into

pLVX-Puro. RGECO1.2 (Addgene plasmid #45494), R-CEPIA1er (Addgene plasmid #58216), and GCaMP6s were cloned into pLVX-IRES-Hygro. Lentivirus vectors for the GECI constructs were packaged in HEK293T cells as previously described (*66*) or produced commercially (Cyagen Biosciences, Inc.). MA104-GCaMP5G, MA104-GCaMP5G/RCEPIAer, MA104-RGECO1/GCEPIAer, and MA104-GCaMP6s-shRNA cell lines and the jHIE-GCaMP6s enteroids (enteroid line J3) were generated as previously described (*28*, *66*). Both MA104-GCaMP5G and MA104-GCaMP6s cells were used in these studies; we observed no difference in calcium responses with these two indicators and thus refer to both as MA104-GCaMP. Jejunum (J2) HIE cultures expressing GCaMP6s (in pLVX-IRES-Hygro) were created using lentivirus transduction as described previously and grown in high Wnt3a CMGF+ with 50 μg/ml hygromycin B for selection (*67*).

CRISPR-Cas9 KO cell lines and enteroids

Lentivirus constructs in pLentiCRISPRv2 vectors were purchased from GenScript Biotech Corp (USA) and were packaged in HEK293T cells as previously described (*66*). The CRISPR-Cas9–expression vectors encode a puromycin-resistance gene for drug selection. The following small guide RNAs were used: P2Y1-sg1 CTACAGCATGTGCACGACCG and P2Y2-sg1 TTTGTCACCACCAGCGCGCG. MA104-GCaMP6s cells (pLVX-IRES-Hygro) were transduced with the P2Y1 CRISPR-Cas9–expressing construct and at 72 hours posttransduction the cells were passaged in the presence of 50 μg/ml hygromycin B and 10 μg/ml puromycin to select for coexpression of GCaMP6s and CRISPR-Cas9. The J2-derived jHIE-GCaMP6s(hygro) enteroid cultures described above were transduced with the CRISPR-Cas9–expressing constructs to make two separate enteroid lines and grown with 50 μg/ml hygromycin B and 1 μg/ml puromycin to select for coexpression of GCaMP6s and CRISPR-Cas9.

Genotyping was performed on whole genomic DNA prepared using DirectPCR (Viagen) with Proteinase K (Qiagen) according to manufacturer's instructions. Genomic DNA was a template to polymerase chain reaction (PCR) amplify a region surrounding the P2Y1 or P2Y2 sgRNA-target sites using primers listed in table S2. PCR products were cloned into the pMiniT2.0 vector using the NEB PCR Cloning Kit (New England Biolabs). Five clones for P2Y1ko HIEs and five clones for P2Y2ko HIEs were picked and sequenced to determine the repertoire of alleles present in the HIE cultures. Sanger sequencing was performed by GENEWIZ (USA).

Phenotypic KO was tested through measurement of relative GFP fluorescence increase after addition of 1 nM ADP for MA104-GCaMP6s-P2Y1ko cells, 10 nM ADP for (J2)HIE-GCaMP6s-P2Y1ko enteroids and 10 μM ATP-γS for (J2) HIE-GCaMP6s-P2Y2ko enteroids compared with parental (J2)HIE-GCaMP6s-P2Y2ko enteroids. Experiments were performed at least three times with $n \geq 25$ cells per experiment analyzed.

Establishment of HIE cultures

The HIE cultures used in this study were generated previously and deposited into the Texas Medical Center Digestive Diseases Center (TMC-DDC) Gastrointestinal Experimental Model Systems (GEMS) Core (*37*, *38*). We used jejunal HIEs cultures J2 and J3, both from adult females, obtained from the GEMS core. Complete media with and without growth factors (CMGF+ and CMGF-, respectively) (*37*, *38*), differentiation media (*67*), high Wnt3a CMGF+ (hW-CMGF+) (*67*), and a Fluorobrite-DMEM based differentiation media (FB-Diff) were prepared as previously described (*28*). HIEs were grown in phenol red-free, growth factor–reduced Matrigel (Corning). HIE monolayers were prepared from three-dimensional cultures and seeded into optical-bottom 10-well Cellview chamber slides coated with dilute collagen IV (Sigma) as described previously (*68*, *69*). After 24 hours in CMGF+ and 10 μM Y-27632 Rock inhibitor, differentiation medium was used and changed every day for 4 to 5 days.

Microscopy and image analysis

For calcium imaging, MA104 cells and HIEs were imaged with a widefield epifluorescence Nikon TiE inverted microscope using a SPECTRAX LED light source (Lumencor) and either a 20x Plan Fluor (NA 0.45) phase contrast or a 20X Plan Apo (NA 0.75) differential interference contrast (DIC) objective. Fluorescence and transmitted light images were recorded using an ORCA-Flash 4.0 sCMOS camera (Hamamatsu), and Nikon Elements Advanced Research version 4.5 software was used for multipoint position selection, data acquisition, and image analysis. Images were read-noise subtracted using an average of 10 no-light acquisitions of the camera. Single cells were selected as regions of interest (ROIs) and fluorescence intensity measured for the experiment. The fluorescence intensity of the whole FOV was measured for HIE monolayers. Fluorescence intensity values were exported to Microsoft Excel and normalized to the baseline fluorescence. The number and magnitude of Ca^{2+} spikes were calculated as described previously (*28*). Ca^{2+} signals with a ΔF magnitude of >5% were counted as Ca^{2+} spikes for MA104-GCaMP cells and J3 HIE-GCaMP6s monolayers, which is based on our previously established threshold for Ca^{2+} spikes being >3 standard deviations above the mean ΔF. For J2 HIE-GCaMP6s monolayers, the mean Ca^{2+} transient increase per FOV for mock-infected jHIE monolayers was 5.4% (±1.0% standard deviation), which was greater than that for MA104 cells or J3 HIEs (*28*). Thus, using the threshold for Ca^{2+} spikes being >3 standard deviations above the mean, Ca^{2+} signals with a ΔF magnitude of >10% were counted as Ca^{2+} spikes for J2 HIE-GCaMP6s monolayers. Average relative fluorescence increase, or average magnitude of Ca^{2+} spikes, was calculated as the average percent increase in fluorescence from largest 50 Ca^{2+} spikes per cell or per FOV.

Long-term calcium imaging

MA104-GECI cells

Fluorobrite DMEM supplemented with 15mM HEPES, 1X sodium pyruvate, 1X Glutamax, and 1X nonessential amino acids (Invitrogen) was used for fluorescence Ca^{2+} imaging (FB-Plus). Confluent monolayers of MA104-GCaMP cells in gridded 8-well chamber slides (ibidi) were mock- or RV-infected in FBS-free media for 1 hour at the indicated MOI. The inoculum was removed and replaced with FB-Plus, and for experiments where noted, with DMSO vehicle or drugs at indicated concentrations. For experiments with gap junction blockers, either 30 μM 18β-glycyrrhetinic acid (18β-gly) or 50 μM TAT-Gap19 (Gap19) was added. For experiments with apyrase, either 10 U/ml of apyrase VI, 10 U/ml of apyrase VII, or a mixture of 5 U/ml of apyrase VI and 5 U/ml of apyrase VII was added. For experiments with purinergic receptor blockers, 10 μM BPTU, 10 μM AR-C 118925XX, 10 μM Bx430, or 10 μM 5-BDBD was used or otherwise noted. The slide was mounted into an Okolab microscope stage-top incubation chamber equilibrated to 37°C with a humidified 5% CO_2 atmosphere. In each experiment, 3 to 5 positions per well were selected and imaged every 1 min for ~3 to 22 hpi. Each imaging experiment was performed at least three times independently, and data shown are representative of one to three experiments combined.

GECI HIEs

For RV infection in monolayers, jHIE-GCaMP6s monolayers were washed once with CMGF- and treated with an inoculum of 50 μl CMGF- plus 30 μl MA104 cell lysate or RV (Ito) and incubated at 37°C and 5% CO_2 for 2 hours. Then inoculum was removed, and monolayers were washed once with FB-Diff before adding FB-Diff with DMSO or drugs at indicated concentrations. For experiments with apyrase, a mixture of 50 U/ml of apyrase VI and 50 U/ml of apyrase VII was added. For experiments with purinergic receptor blockers, 10 μM BPTU, 10 μM AR-C 118925XX, 10 μM Bx430, 10 μM 5-BDBD, 10 μM MRS2179, 10 μM MRS2279, or 10 μM MRS2500 was used. Monolayers were transferred to the stage-top incubator for imaging with four FOVs chosen per well and imaged every minute for ~7 to 22 hpi. Each imaging experiment was performed at least

three times independently, and data shown are representative of all replicates combined.

Supernatant transfer assay

Confluent monolayers of parental MA104-GCaMP or MA104-GCaMP-P2Y1ko cells in a flat-bottom 24-well cell culture plate (Corning) were mock- or RV-infected in FB-Plus for 1 hour at MOI 5. Inoculum was removed and replaced with 300 μl FB-Plus with 20 μM ARL 67156, an ecto-ATPase inhibitor. Reporter cells consisted of confluent monolayers of parental MA104-GCaMP cells in a flat-bottom 96-well cell culture plate (Greiner Bio One). Reporter cells were incubated for 1 hour before imaging with or without 10 μM BPTU in 50 μl FB-Plus.

After the onset of ICWs (~5 to 6 hpi, confirmed by epifluorescence microscopy), 50 μl of supernatant was collected from mock- or RV-infected wells and transferred to the reporter cells. Reporter cells were imaged every 2 s for 15 to 30 s for baseline and then for 1 to 2 min after addition. Change in GCaMP fluorescence for the 10 to 15 most-responsive cells per FOV were analyzed. Each imaging run was repeated three times per experimental condition, and the entire experiment performed at least three times independently. Data shown are representative of one to three experiments combined.

Enteroid swelling assay

Jejunum HIEs were split and grown in hW-CMGF+ for 2 days followed by differentiation medium for 1 day. jHIEs were gently washed using ice cold 1XPBS and suspended in inoculum of 50 μl MA104 cell lysate or RV (Ito) diluted with 150 μl CMGF- and incubated for 1 hour. Then HIEs were washed, resuspended in 25% Matrigel diluted in FB-Diff (with DMSO vehicle or BPTU) and pipetted onto 8-well chamber slides (Matek) precoated with Matrigel. Imaging positions were chosen so that between 30 and 50 enteroids were selected per experimental condition. Enteroids were imaged using the stage-top incubator with transmitted light and GFP fluorescence every 2 to 3 min for ~18 hours. Swelling was determined by measuring the cross-sectional area of the internal lumen at the beginning of the run compared with the time point of maximum swelling and calculating the percent increase. Area measurements were determined using the Nikon Elements AR version 4.5 software. Experiments were performed three times independently, and data shown are representative of all replicates combined, $n \geq 68$ HIEs per condition.

Scrape loading–dye transfer assay

Lucifer Yellow in Hank's Buffered Salt Solution (HBSS) (1 mg/ml) or Rhodamine 123 in H_2O (1 mg/ml) was diluted 1:100 in FB-Plus and added to MA104 or jHIE cell monolayers. Monolayers were scraped with a 26 *g* needle and incubated for 5 min at room temperature. Monolayers were then washed three times with FB-Plus and imaged. The mechanical disruption causes cells adjacent to the scrape to take up dye, which then is permeable to adjacent cells if there are functional gap junction channels. Images are representative of each experiment performed in triplicate.

Immunofluorescence

MA104 cells and HIEs were fixed using the Cytofix/Cytoperm kit (BD Biosciences) according to manufacturer instructions. Primary antibodies were diluted in 1X Perm/Wash and incubated with cells overnight at 4°C. The next day, the cells were washed three times with 1X Perm/Wash solution and then incubated with corresponding secondary antibodies for 1 hour at room temperature. Nuclei were stained with NucBlue Fixed Cell Stain (Life Technologies) for 5 min at room temperature and washed with 1X PBS for imaging. Experiments were performed three times independently.

Fluorescence focus assay

Fluorescence focus assays (FFAs) were performed as described previously with the following modifications (*13*). After inoculation with RV, MA104 cells were treated with DMSO, 10 U/ml apyrase, 10 μM BPTU, 10 μM AR-C 118925XX, 20 μM Bx430, 20 μM 5-BDBD, 300 μM suramin, or 10 μM PPADS. Then, cells and media at 24 hpi were freeze-thawed three times and activated with 10 μg/ml Worthington's Trypsin for 30 min at 37°C before use. Ten-fold dilutions were used to inoculate MA104 monolayers in 96-well plates for 1 hour and cells were fixed at 20 hpi with ice-cold methanol for ~20 min at 4°C, then washed three times with 1X phosphate buffered solution (PBS). Primary rabbit anti-rotavirus antisera (*12*) was used at 1:100,000 and incubated overnight at 4°C. Monolayers were washed three times with 1XPBS and then incubated with secondary antibody donkey anti-rabbit AlexaFluor 488 (1:2000) for 1 hour at 37°C and then washed three times with 1XPBS before imaging. FFA experiments were performed three times independently.

Plaque assay

Plaque assays were performed as described previously with the following modifications (*70*). Briefly, MA104 cells were seeded and grown to confluency in 6-well plates. Wells were infected at 10-fold dilutions in duplicate for 1 hour and media replaced with an overlay of 1.2% Avicel in serum-free DMEM supplemented with DEAE dextran, and 1 μg/ml Worthington's Trypsin, and, for indicated experiments, DMSO vehicle, apyrase, or purinergic receptor blocker drugs (*71*). The cells were incubated at 37°C/5% CO_2 for 48 to 72 hours before overlay was removed and cells stained with crystal violet to count plaques. Plaque assays of using MA104-GCaMP and MA104-GCaMP-P2Y1ko cells were performed three times independently, and data shown are representative of all replicates combined.

RNA extraction, reverse transcription, and quantitative PCR

Total RNA was extracted from HIE 96-well monolayers or MA104 cells grown to confluency in a 6-well plate using TRIzol reagent (Ambion). In RV-infection experiments, cells were harvested at 24 hpi. Total RNA was treated with Turbo DNase I (Ambion) and cDNA was generated from 250 ng RNA using the SensiFAST cDNA synthesis kit (Bioline). Quantitative PCR (qPCR) was performed using Fast SYBR Green (Life Technologies) with primers either designed in-house or published previously (*72*) (table S3) and using the QuantStudio real time thermocycler (Applied Biosciences). Target genes were normalized to the housekeeping gene ribosomal subunit 18*S* and relative expression was calculated using the ddCT method. Experiments were performed three times independently, and data shown are representative of all replicates combined. For *IL-1α*, *COX2*, and *iNOS* experiments, HIE monolayers were mock- or RV (Ito)–infected and then treated with DMSO, 100 U/ml apyrase, or 10 μM BPTU and normalized to 18*S* mRNA transcripts and relative to the Mock-DMSO condition.

Immunoblot analysis

RV NSP4 protein were detected by immunoblot analysis as previously described, with minor changes as follows (*64*). Confluent MA104 cell monolayers in 6-well tissue culture plates were mock- or RV (SA114F)–infected at MOI 0.01 and then harvested at 18 hpi. Cells were lysed using a 1X RIPA buffer solution [10 mM Tris-HCL pH 8.0, 1 mM EDTA, 1% Triton X-100, 0.1% sodium deoxycholate, 0.1% SDS, 140 mM NaCl, and 1 tablet complete mini protease inhibitor (Roche)] and passed through a Qiashredder (Qiagen). Lysed cells were boiled for 10 min at 100°C in SDS-PAGE sample buffer and separated on Tris-glycine 4 to 20% SDS-PAGE gels (BioRad). The detected NSP4 protein band was quantified for gel densitometry measurements using ImageJ software.

Measurement of serotonin release

Serotonin secretion by HIEs after stimulation with RV infection and treatment with DMSO, 100 U/ml apyrase, 10 μM BPTU, or 300 nM ω-agatoxin was quantified by enzyme-linked immunosorbent assay (ELISA) (Eagle Biosciences) according to the manufacturer's instructions. A standard curve of known serotonin concentrations was plotted against optical density at 450 nm with a limit of detection of 2.6 ng/ml (Infinite F200Pro, Tecan). Experiments in flat monolayers were performed three times independently and experiments in

transwells were performed three times independently. Data shown are representative of all replicates combined.

Statistical analysis

Biostatistical analyses were performed using GraphPad Prism (version 8.1) software (GraphPad Inc., La Jolla, CA). Outlier data points were removed using the ROUT method (Q = 1%). Statistical comparisons were made using the Mann-Whitney test, the one-way analysis of variance (ANOVA) with Tukey or Bonferroni multiple comparison's test, or the Kruskal-Wallis test with Dunn's multiple comparisons test. Parametric or nonparametric tests were used depending on Normality testing of the datasets. Differences between the groups were considered significant at $^*P < 0.05$, and the data are presented as means ± standard deviation unless otherwise noted.

REFERENCES AND NOTES

1. C. Troeger *et al*.., Rotavirus Vaccination and the Global Burden of Rotavirus Diarrhea Among Children Younger Than 5 Years. *JAMA Pediatr.* **172**, 958–965 (2018). doi: 10.1001/jamapediatrics.2018.1960; pmid: 30105384
2. G. P. Davidson *et al*., Immunofluorescence in duodenal mucosa of children with acute enteritis due to a new virus. *J. Clin. Pathol.* **28**, 263–266 (1975). doi: 10.1136/jcp.28.4.263; pmid: 1092720
3. W. G. Starkey *et al*., Kinetics, tissue specificity and pathological changes in murine rotavirus infection of mice. *J. Gen. Virol.* **67**, 2625–2634 (1986). doi: 10.1099/0022-1317-67-12-2625; pmid: 3025343
4. M. Hagbom *et al*., Rotavirus stimulates release of serotonin (5-HT) from human enterochromaffin cells and activates brain structures involved in nausea and vomiting. *PLOS Pathog.* **7**, e1002115 (2011). doi: 10.1371/journal.ppat.1002115; pmid: 21779163
5. L. M. Little, J. A. Shadduck, Pathogenesis of rotavirus infection in mice. *Infect. Immun.* **38**, 755–763 (1982). doi: 10.1128/IAI.38.2.755-763.1982; pmid: 6292110
6. A. P. Morris, M. K. Estes, VIII. Pathological consequences of rotavirus infection and its enterotoxin. *Am. J. Physiol. Gastrointest. Liver Physiol.* **281**, G303–G310 (2001). doi: 10.1152/ajpgi.2001.281.2.G303; pmid: 11447008
7. O. Lundgren *et al*., Role of the enteric nervous system in the fluid and electrolyte secretion of rotavirus diarrhea. *Science* **287**, 491–495 (2000). doi: 10.1126/science.287.5452.491; pmid: 10642552
8. J. M. Hyser, M. R. Collinson-Pautz, B. Utama, M. K. Estes, Rotavirus disrupts calcium homeostasis by NSP4 viroporin activity. *mBio* **1**, e00265-10 (2010). doi: 10.1128/mBio.00265-10; pmid: 21151776
9. J. M. Ball, P. Tian, C. Q. Zeng, A. P. Morris, M. K. Estes, Age-dependent diarrhea induced by a rotaviral nonstructural glycoprotein. *Science* **272**, 101–104 (1996). doi: 10.1126/science.272.5258.101; pmid: 8600515
10. P. Tian *et al*., The rotavirus nonstructural glycoprotein NSP4 mobilizes Ca2+ from the endoplasmic reticulum. *J. Virol.* **69**, 5763–5772 (1995). doi: 10.1128/JVI.69.9.5763-5772.1995; pmid: 7637021
11. K. Kunzelmann *et al*., Expression and function of epithelial anoctamins. *Exp. Physiol.* **97**, 184–192 (2012). doi: 10.1113/expphysiol.2011.058206; pmid: 21908539
12. S. E. Crawford, J. M. Hyser, B. Utama, M. K. Estes, Autophagy hijacked through viroporin-activated calcium/calmodulin-dependent kinase kinase-β signaling is required for rotavirus replication. *Proc. Natl. Acad. Sci. U.S.A.* **109**, E3405–E3413 (2012). doi: 10.1073/pnas.1216539109; pmid: 23184977
13. J. L. Zambrano *et al*., Rotavirus infection of cells in culture induces activation of RhoA and changes in the actin and tubulin cytoskeleton. *PLOS ONE* **7**, e47612 (2012). doi: 10.1371/journal.pone.0047612; pmid: 23082182
14. I. Beau, J. Cotte-Laffitte, R. Amsellem, A. L. Servin, A protein kinase A-dependent mechanism by which rotavirus affects the distribution and mRNA level of the functional tight junction-associated protein, occludin, in human differentiated intestinal Caco-2 cells. *J. Virol.* **81**, 8579–8586 (2007). doi: 10.1128/JVI.00263-07; pmid: 17553883
15. M. Hagbom, S. Sharma, O. Lundgren, L. Svensson, Towards a human rotavirus disease model. *Curr. Opin. Virol.* **2**, 408–418 (2012). doi: 10.1016/j.coviro.2012.05.006; pmid: 22722079
16. K. Hodges, R. Gill, Infectious diarrhea: Cellular and molecular mechanisms. *Gut Microbes* **1**, 4–21 (2010). doi: 10.4161/gmic.1.1.11036; pmid: 21327112
17. T. V. Sowmyanarayanan *et al*., Nitric oxide production in acute gastroenteritis in Indian children. *Trans. R. Soc. Trop. Med. Hyg.* **103**, 849–851 (2009). doi: 10.1016/j.trstmh.2009.05.003; pmid: 19552932
18. Y. Yamashiro, T. Shimizu, S. Oguchi, M. Sato, Prostaglandins in the plasma and stool of children with rotavirus gastroenteritis. *J. Pediatr. Gastroenterol. Nutr.* **9**, 322–327 (1989). doi: 10.1097/00005176-198910000-00010; pmid: 2614618
19. J. Rodríguez-Díaz *et al*., Role of nitric oxide during rotavirus infection. *J. Med. Virol.* **78**, 979–985 (2006). doi: 10.1002/jmv.20650; pmid: 16721855
20. A. P. Morris *et al*., NSP4 elicits age-dependent diarrhea and Ca2+-mediated I- influx into intestinal crypts of CF mice. *Am. J. Physiol. Gastrointest. Liver Physiol.* **277**, G431–G444 (1999). doi: 10.1152/ajpgi.1999.277.2.G431
21. J. Ousingsawat *et al*., Rotavirus toxin NSP4 induces diarrhea by activation of TMEM16A and inhibition of Na+ absorption. *Pflugers Arch.* **461**, 579–589 (2011). doi: 10.1007/s00424-011-0947-0; pmid: 21399895
22. N. Seo *et al*., Integrins α1β1 and α2β1 are receptors for the rotavirus enterotoxin. *Proc. Natl. Acad. Sci. U.S.A.* **105**, 8811–8818 (2008). doi: 10.1073/pnas.0803934105; pmid: 18587047
23. S. Fujii *et al*., PGE 2 is a direct and robust mediator of anion/fluid secretion by human intestinal epithelial cells. *Sci. Rep.* **6**, 36795 (2016). doi: 10.1038/srep36795
24. F. H. Mourad, J. L. Turvill, M. J. G. Farthing, Role of nitric oxide in intestinal water and electrolyte transport. *Gut* **44**, 143–147 (1999). doi: 10.1136/gut.44.2.143; pmid: 9895365
25. F. Michelangeli, M. C. Ruiz, J. R. del Castillo, J. E. Ludert, F. Liprandi, Effect of rotavirus infection on intracellular calcium homeostasis in cultured cells. *Virology* **181**, 520–527 (1991). doi: 10.1016/0042-6822(91)90884-E; pmid: 1849676
26. J. M. Hyser, M. K. Estes, Pathophysiological Consequences of Calcium-Conducting Viroporins. *Annu. Rev. Virol.* **2**, 473–496 (2015). doi: 10.1146/annurev-virology-100114-054846; pmid: 26958925
27. S. E. Crawford *et al*., Rotavirus infection. *Nat. Rev. Dis. Primers* **3**, 17083 (2017). doi: 10.1038/nrdp.2017.83; pmid: 29119972
28. A. L. Chang-Graham *et al*., Rotavirus Calcium Dysregulation Manifests as Dynamic Calcium Signaling in the Cytoplasm and Endoplasmic Reticulum. *Sci. Rep.* **9**, 10822 (2019). doi: 10.1038/s41598-019-46856-8; pmid: 31346185
29. W. Zhang, B. J. Segura, T. R. Lin, Y. Hu, M. W. Mulholland, Intercellular calcium waves in cultured enteric glia from neonatal guinea pig. *Glia* **42**, 252–262 (2003). doi: 10.1002/glia.10215; pmid: 12673831
30. C. D'hondt, B. Himpens, G. Bultynck, Mechanical stimulation-induced calcium wave propagation in cell monolayers: The example of bovine corneal endothelial cells. *J. Vis. Exp.* **77**, e50443 (2013). doi: 10.3791/50443; pmid: 23892350
31. M. J. Sanderson, A. C. Charles, E. R. Dirksen, Mechanical stimulation and intercellular communication increases intracellular Ca2+ in epithelial cells. *Cell Regul.* **1**, 585–596 (1990). doi: 10.1091/mbc.1.8.585; pmid: 2078569
32. A. H. Cornell-Bell, S. M. Finkbeiner, M. S. Cooper, S. J. Smith, Glutamate induces calcium waves in cultured astrocytes: Long-range glial signaling. *Science* **247**, 470–473 (1990). doi: 10.1126/science.1967852; pmid: 1967852
33. L. Leybaert, M. J. Sanderson, Intercellular Ca(2+) waves: Mechanisms and function. *Physiol. Rev.* **92**, 1359–1392 (2012). doi: 10.1152/physrev.00029.2011; pmid: 22811430
34. P. Babica, I. Sovadinová, B. L. Upham, in *Gap Junction Protocols*, M. Vinken, S. R. Johnstone, Eds. (Humana Press, 2016), pp. 133–144.
35. B. L. Upham, I. Sovadinová, P. Babica, Gap junctional intercellular communication: A functional biomarker to assess adverse effects of toxicants and toxins, and health benefits of natural products. *J. Vis. Exp.* **2016**, 1–9 (2016). doi: 10.3791/54281; pmid: 28060274
36. K. R. Emslie *et al*., Expression of the rotavirus SA11 protein VP7 in the simple eukaryote Dictyostelium discoideum. *J. Virol.* **69**, 1747–1754 (1995). doi: 10.1128/JVI.69.3.1747-1754.1995; pmid: 7853513
37. T. Sato *et al*., Long-term expansion of epithelial organoids from human colon, adenoma, adenocarcinoma, and Barrett's epithelium. *Gastroenterology* **141**, 1762–1772 (2011). doi: 10.1053/j.gastro.2011.07.050; pmid: 21889923
38. K. Saxena *et al*., Human Intestinal Enteroids: A New Model To Study Human Rotavirus Infection, Host Restriction, and Pathophysiology. *J. Virol.* **90**, 43–56 (2015). doi: 10.1128/JVI.01930-15; pmid: 26446608
39. J. Foulke-Abel *et al*., Human enteroids as an ex-vivo model of host-pathogen interactions in the gastrointestinal tract. *Exp. Biol. Med.* **239**, 1124–1134 (2014). doi: 10.1177/1535370214529398; pmid: 24719375
40. N. C. Zachos *et al*., Human enteroids/colonoids and intestinal organoids functionally recapitulate normal intestinal physiology and pathophysiology. *J. Biol. Chem.* **291**, 3759–3766 (2016). doi: 10.1074/jbc.R114.635995; pmid: 26677228
41. C. Léon *et al*., The P2Y1 receptor is an ADP receptor antagonized by ATP and expressed in platelets and megakaryoblastic cells. *FEBS Lett.* **403**, 26–30 (1997). doi: 10.1016/S0014-5793(97)00022-7; pmid: 9038354
42. K. G. Dickman *et al*., Rotavirus alters paracellular permeability and energy metabolism in Caco-2 cells. *Am. J. Physiol. Gastrointest. Liver Physiol.* **279**, G757–G766 (2000). doi: 10.1152/ajpgi.2000.279.4.G757; pmid: 11005763
43. C. Zhang *et al*., Virus-Triggered ATP Release Limits Viral Replication through Facilitating IFN-β Production in a P2X7-Dependent Manner. *J. Immunol.* **199**, 1372–1381 (2017). doi: 10.4049/jimmunol.1700187; pmid: 28687662
44. D. Ferrari, M. Idzko, T. Müller, R. Manservigi, P. Marconi, Purinergic Signaling: A New Pharmacological Target Against Viruses? *Trends Pharmacol. Sci.* **39**, 926–936 (2018). doi: 10.1016/j.tips.2018.09.004; pmid: 30292585
45. S. Zumerle *et al*., Intercellular Calcium Signaling Induced by ATP Potentiates Macrophage Phagocytosis. *Cell Rep.* **27**, 1–10. e4 (2019). doi: 10.1016/j.celrep.2019.03.011; pmid: 30943393
46. C. Cekic, J. Linden, Purinergic regulation of the immune system. *Nat. Rev. Immunol.* **16**, 177–192 (2016). doi: 10.1038/nri.2016.4; pmid: 26922909
47. P. P. Hernández *et al*., Interferon-λ and interleukin 22 act synergistically for the induction of interferon-stimulated genes and control of rotavirus infection. *Nat. Immunol.* **16**, 698–707 (2015). doi: 10.1038/ni.3180; pmid: 26006013
48. N. C. Di Paolo, D. M. Shayakhmetov, Interleukin 1α and the inflammatory process. *Nat. Immunol.* **17**, 906–913 (2016). doi: 10.1038/ni.3503; pmid: 27434011
49. O. Gross *et al*., Inflammasome activators induce interleukin-1α secretion via distinct pathways with differential requirement for the protease function of caspase-1. *Immunity* **36**, 388–400 (2012). doi: 10.1016/j.immuni.2012.01.018; pmid: 22444631
50. Y. Ohtani, M. Minami, M. Satoh, Expression of inducible nitric oxide synthase mRNA and production of nitric oxide are induced by adenosine triphosphate in cultured rat microglia. *Neurosci. Lett.* **293**, 72–74 (2000). doi: 10.1016/S0304-3940(00)01478-6; pmid: 11065141
51. E. Degagné *et al*., P2Y2 receptor transcription is increased by NF-κ B and stimulates cyclooxygenase-2 expression and PGE2 released by intestinal epithelial cells. *J. Immunol.* **183**, 4521–4529 (2009). doi: 10.4049/jimmunol.0803977; pmid: 19734210
52. S. Bialowas *et al*., Rotavirus and Serotonin Cross-Talk in Diarrhoea. *PLOS ONE* **11**, e0159660 (2016). doi: 10.1371/journal.pone.0159660; pmid: 27459372
53. J. F. Dekkers *et al*., A functional CFTR assay using primary cystic fibrosis intestinal organoids. *Nat. Med.* **19**, 939–945 (2013). doi: 10.1038/nm.3201; pmid: 23727931
54. D. Zhang *et al*., Two disparate ligand-binding sites in the human P2Y1 receptor. *Nature* **520**, 317–321 (2015). doi: 10.1038/nature14287; pmid: 25822790
55. E. C. Mossel, R. F. Ramig, Rotavirus genome segment 7 (NSP3) is a determinant of extraintestinal spread in the neonatal mouse. *J. Virol.* **76**, 6502–6509 (2002). doi: 10.1128/JVI.76.13.6502-6509.2002; pmid: 12050363
56. R. F. Ramig, The effects of host age, virus dose, and virus strain on heterologous rotavirus infection of suckling mice. *Microb. Pathog.* **4**, 189–202 (1988). doi: 10.1016/0882-4010(88)90069-1; pmid: 2848173
57. A. Verkhratsky, G. Burnstock, Biology of purinergic signalling: Its ancient evolutionary roots, its omnipresence and its multiple functional significance. *BioEssays* **36**, 697–705 (2014). doi: 10.1002/bies.201400024; pmid: 24782352
58. J. P. Brunet *et al*., Rotavirus infection induces an increase in intracellular calcium concentration in human intestinal epithelial cells: Role in microvillar actin alteration. *J. Virol.* **74**,

2323–2332 (2000). doi: 10.1128/JVI.74.5.2323-2332.2000; pmid: 10666263
59. Z. Berkova, S. E. Crawford, S. E. Blutt, A. P. Morris, M. K. Estes, Expression of rotavirus NSP4 alters the actin network organization through the actin remodeling protein cofilin. *J. Virol.* **81**, 3545–3553 (2007). doi: 10.1128/JVI.01080-06; pmid: 17229686
60. K. Saxena *et al*., A paradox of transcriptional and functional innate interferon responses of human intestinal enteroids to enteric virus infection. *Proc. Natl. Acad. Sci. U.S.A.* **114**, E570–E579 (2017). doi: 10.1073/pnas.1615422114; pmid: 28069942
61. H. Takada, K. Furuya, M. Sokabe, Mechanosensitive ATP release from hemichannels and Ca^{2+} influx through TRPC6 accelerate wound closure in keratinocytes. *J. Cell Sci.* **127**, 4159–4171 (2014). doi: 10.1242/jcs.147314; pmid: 25097230
62. Y. J. Sung *et al*., Intercellular calcium waves mediate preferential cell growth toward the wound edge in polarized hepatic cells. *Exp. Cell Res.* **287**, 209–218 (2003). doi: 10.1016/S0014-4827(03)00160-5; pmid: 12837277
63. I. Novak, Purinergic signalling in epithelial ion transport: Regulation of secretion and absorption. *Acta Physiol.* **202**, 501–522 (2011). doi: 10.1111/j.1748-1716.2010.02225.x; pmid: 21073662
64. J. M. Hyser, C. Q. Y. Zeng, Z. Beharry, T. Palzkill, M. K. Estes, Epitope mapping and use of epitope-specific antisera to characterize the VP5* binding site in rotavirus SA11 NSP4. *Virology* **373**, 211–228 (2008). doi: 10.1016/j.virol.2007.11.021; pmid: 18164740
65. N. P. Sastri *et al*., Structural plasticity of the coiled-coil domain of rotavirus NSP4. *J. Virol.* **88**, 13602–13612 (2014). doi: 10.1128/JVI.02227-14; pmid: 25231315
66. J. L. Perry, N. K. Ramachandran, B. Utama, J. M. Hyser, Use of genetically-encoded calcium indicators for live cell calcium imaging and localization in virus-infected cells. *Methods* **90**, 28–38 (2015). doi: 10.1016/j.ymeth.2015.09.004; pmid: 26344758
67. A. L. Chang-Graham *et al*., Human intestinal enteroids with inducible neurogenin-3 expression as a novel model of gut hormone secretion. *Cell. Mol. Gastroenterol. Hepatol.* **8**, 209–229 (2019). doi: 10.1016/j.jcmgh.2019.04.010; pmid: 31029854
68. K. L. VanDussen *et al*., Development of an enhanced human gastrointestinal epithelial culture system to facilitate patient-based assays. *Gut* **64**, 911–920 (2015). doi: 10.1136/gutjnl-2013-306651; pmid: 25007816
69. K. Ettayebi *et al*., Replication of human noroviruses in stem cell–derived human enteroids. *Science* **353**, 1387–1393 (2016). doi: 10.1126/science.aaf5211; pmid: 27562956
70. M. K. Estes, D. Y. Graham, C. P. Gerba, E. M. Smith, Simian rotavirus SA11 replication in cell cultures. *J. Virol.* **31**, 810–815 (1979). doi: 10.1128/JVI.31.3.810-815.1979; pmid: 229253
71. M. Matrosovich, T. Matrosovich, W. Garten, H.-D. Klenk, New low-viscosity overlay medium for viral plaque assays. *Virol. J.* **3**, 63 (2006). doi: 10.1186/1743-422X-3-63; pmid: 16945126
72. J. P. Maynard *et al*., P2X3 purinergic receptor overexpression is associated with poor recurrence-free survival in hepatocellular carcinoma patients. *Oncotarget* **6**, 41162–41179 (2015). doi: 10.18632/oncotarget.6240; pmid: 26517690

ACKNOWLEDGMENTS

We would like to thank X.-L. Zeng and X. Yu for their help with enteroid cultures and media. Additional thanks to the Baylor College of Medicine (BCM) Center for Comparative Medicine and technicians for their care of the animals. **Funding:** This work was supported in part by NIH grants K01DK093657, R03DK110270, R01DK115507 [primary investigator (PI) J.M.H.]; R01AI080656 and U19AI116497 (PI: M.K.E.); and R01AI123278 and U01 AI124290 (PI: R.A.B.). Trainee support for A.L.C.-G. was provided by NIH grants F30DK112563 (PI: A.L.C.-G.) and the BCM Medical Scientist Training Program, and support for both A.L.C.-G. and A.C.S. was provided by the Integrative Molecular and Biomedical Sciences Graduate Program (no. T32GM008231; PI: D. Nelson). Training support for M.A.E. was provided by NIH grant K01DK123195 (PI: M.A.E.). Training support for K.A.E. was provided by NIH grant T32DK07644 (PI: R. Shulman). Training support for H.A.D. was provided by NIH grant F32AI136404 (PI: H.A.D.). Training support for J.T.G. was provided by the McNair M.D./Ph.D. Scholars Program at Baylor College of Medicine. This project was also supported in part by PHS grant P30DK056338, which supports the Texas Medical Center Digestive Diseases Center (TMC-DDC) Gastrointestinal Experimental Model Systems (GEMS) Core and the Cellular and Molecular Morphology Core. Fluorescence-activated cell sorting of cell lines utilized the BCM Cytometry and Cell Sorting Core with funding from the CPRIT Core Facility Support Award (CPRIT-RP180672), the NIH (CA125123 and RR024574), and the expert assistance of J. M. Sederstrom. **Author contributions:** J.M.H., A.L.C.-G., J.L.P., M.A.E., K.A.E., H.A.D., R.A.B., J.V., and M.K.E. designed the experiments and discussed the data. J.M.H., A.L.C.-G., J.L.P., F.J.S., J.T.G., A.C.S., J.C.N., and J.S.K. conducted the calcium imaging experiments and analyzed the data with J.M.H. and A.L.C.-G. J.L.P. conducted the fluorescent focus assays, plaque assays, and genotyping and analyzed data with J.M.H. J.L.P. and A.L.C.-G. created the CRISPR-Cas9 KO lines. M.A.E. and K.A.E. conducted and analyzed qPCR experiments with A.L.C.-G. H.A.D. performed and analyzed the serotonin ELISAs. A.L.C.-G. conducted and analyzed the enteroid imaging assays. J.M.H., A.L.C.-G., and K.A.E. performed the mouse experiments, and M.A.E. performed immunohistochemistry. N.P.S and M.K.E. provided key reagents including the anti-NSP4 antibodies. J.M.H. and A.L.C.-G. wrote the manuscript, and all of the authors contributed to revisions of the paper. All authors had access to the study data, reviewed, and approved the final manuscript. **Competing interests:** The authors declare no competing interests with this work. **Data and materials availability:** All data are available in the manuscript or the supplementary materials. Correspondence and requests for materials should be addressed to J.M.H.

SUPPLEMENTARY MATERIALS

science.sciencemag.org/content/370/6519/eabc3621/suppl/DC1
Figs. S1 to S6
Tables S1 to S3
MDAR Reproducibility Checklist
Movies S1 to S11

View/request a protocol for this paper from *Bio-protocol*.

22 April 2020; accepted 16 October 2020
10.1126/science.abc3621

RESEARCH ARTICLE SUMMARY

PHOTOSYNTHESIS

Architecture of the photosynthetic complex from a green sulfur bacterium

Jing-Hua Chen, Hangjun Wu, Caihuang Xu, Xiao-Chi Liu, Zihui Huang, Shenghai Chang, Wenda Wang, Guangye Han, Tingyun Kuang*, Jian-Ren Shen*, Xing Zhang*

INTRODUCTION: Photosynthetic reaction centers (RCs) harvest light energy and convert it into chemical energy, a process that ultimately sustains most life on Earth. RCs are classified as type I (Fe-S type) or type II (quinone type) on the basis of their terminal electron acceptors. Most extant RCs are heterodimers represented by photosystems I and II (PSI and PSII), and they are evolved from homodimeric RCs similar to those seen in green sulfur bacteria (GSB) and heliobacteria. GSB grow in the absence of oxygen, capturing sunlight energy with a light-harvesting structure known as the chlorosome. Fenna-Matthews-Olson proteins (FMO) transfer this energy to a type I RC (GsbRC) to initiate charge-separation and electron-transfer reactions.

RATIONALE: Energy-transfer efficiencies within the chlorosome, from chlorosome to FMO, or within FMO are nearly 100%. However, the efficiency drops to between 35 and 75% for energy transfer from FMO to GsbRC and is substantially lower than the nearly 100% efficiency for transfer from the light-harvesting antenna to the PSI RC in oxygenic photosynthetic organisms. To date, the structures of all typical RCs have been determined except that of the RC from GSB. To reveal the structural characteristics of GsbRC and the basis for the lower energy-transfer efficiency from FMO to GsbRC, we solved the structure of the FMO-GsbRC supercomplex from the GSB *Chlorobaculum tepidum* at 2.7-Å resolution by cryo–electron microscopy.

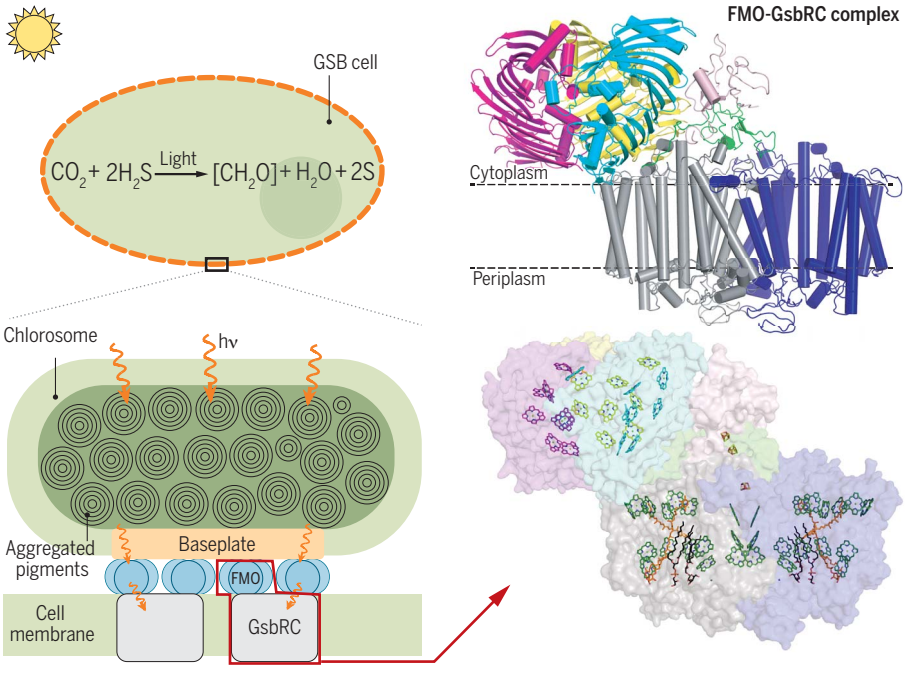

Photosynthetic apparatus of GSB and atomic structure of the FMO-RC complex. GSB perform photosynthesis by using light energy to transform substrates of carbon dioxide and hydrogen sulfide to organic compounds, water, and sulfur. One unit of the photosynthetic apparatus in GSB contains a peripheral antenna chlorosome, light-harvesting FMO, and a membrane-embedded RC. The energy absorbed by the chlorosome is transferred through FMO to the RC to initiate charge-separation and electron-transfer reactions. The overall structure and cofactor arrangements in this supercomplex help explain rates of energy transfer and the evolution of features observed in oxygenic photosystems. h, Planck's constant; ν, photon frequency.

RESULTS: The structure contains one FMO trimer attached at a distal end of the homodimeric GsbRC, and the edge-to-edge distance between the bacteriochlorophylls of FMO and GsbRC is >21 Å. This distance is considerably longer than that seen in other photosynthetic systems and thus explains the reduced efficiency of energy transfer between these two complexes. The GsbRC binds 26 bacteriochlorophylls *a* and 4 chlorophylls *a*, among which the chlorophylls *a* are assigned to the first and second electron acceptors in the electron-transfer chain. No quinones were found between the secondary electron acceptor A_0 and the Fe-S cluster, and the arrangement of the chlorophylls in the two branches of the electron-transfer chain is approximately symmetric at the current resolution. The total number of (bacterio)chlorophylls, 30, is substantially less than the 60 (bacterio)chlorophylls in the heliobacterial RC and the 87 chlorophylls in the PSI core but is close to the 35 chlorophylls in the PSII core. The 30 (bacterio)chlorophylls in our structure are located at conserved positions relative to those of other RCs and are arranged into two layers, representing common features of both type I and II RCs. We observed a carotenoid derivative between the two layers (instead of linker chlorophylls seen in other RCs); this may represent an ancestral feature of RCs. In each layer, chlorophylls are clustered into two separated groups, similar to the arrangement of the PSII core but in contrast to that of other type I RCs.

CONCLUSION: The structure of the GsbRC explains the imperfect efficiency of energy transfer from FMO to GsbRC and reveals a number of features that may represent an ancestral form of both type I and II RCs. These features include a homodimeric core with fewer pigments associated, a conserved core protein structure, distinctive pigment arrangement similar to that seen in PSII instead of PSI, and a chlorobactene derivative located between the two chlorophyll layers within the membrane. With this structure, we now have a complete set of structures from different groups of photosynthetic organisms, allowing us to examine the evolution of photosystems in greater detail. By revealing the arrangement of proteins and pigments, including features of both type I and II RCs, the structure provides valuable insight into how extant members of this family of proteins diverged from a common RC ancestor. ■

The list of author affiliations is available in the full article online.
*Corresponding author. Email: xzhang1999@zju.edu.cn (X.Z.); shen@cc.okayama-u.ac.jp (J.-R.S.); kuangty@ibcas.ac.cn (T.K.)
Cite this article as J.-H. Chen *et al.*, *Science* **370**, eabb6350 (2020). DOI: 10.1126/science.abb6350

READ THE FULL ARTICLE AT
https://doi.org/10.1126/science.abb6350

RESEARCH ARTICLE

PHOTOSYNTHESIS

Architecture of the photosynthetic complex from a green sulfur bacterium

Jing-Hua Chen[1,2], Hangjun Wu[1,2], Caihuang Xu[1], Xiao-Chi Liu[3], Zihui Huang[1], Shenghai Chang[1,2], Wenda Wang[3], Guangye Han[3], Tingyun Kuang[3]*, Jian-Ren Shen[3,4]*, Xing Zhang[1,2,5]*

The photosynthetic apparatus of green sulfur bacteria (GSB) contains a peripheral antenna chlorosome, light-harvesting Fenna-Matthews-Olson proteins (FMO), and a reaction center (GsbRC). We used cryo–electron microscopy to determine a 2.7-angstrom structure of the FMO-GsbRC supercomplex from *Chlorobaculum tepidum*. The GsbRC binds considerably fewer (bacterio) chlorophylls [(B)Chls] than other known type I RCs do, and the organization of (B)Chls is similar to that in photosystem II. Two BChl layers in GsbRC are not connected by Chls, as seen in other RCs, but associate with two carotenoid derivatives. Relatively long distances of 22 to 33 angstroms were observed between BChls of FMO and GsbRC, consistent with the inefficient energy transfer between these entities. The structure contains common features of both type I and type II RCs and provides insight into the evolution of photosynthetic RCs.

Photosynthesis converts light energy from the Sun into chemical energy, thereby sustaining most life forms on Earth. Light energy is first captured by various antenna systems and is subsequently transferred to a membrane-embedded pigment-protein complex termed the reaction center (RC) to initiate a series of charge-separation and electron-transfer reactions. RCs are classified as type I (Fe-S type) or type II (quinone type) according to their terminal electron acceptors (*1*), and all oxygenic photosynthetic organisms contain both type I and II RCs. Most extant type I and all known type II RCs are heterodimers that were most likely evolved from a common homodimeric RC, similar to those seen in green sulfur bacteria (GSB) and heliobacteria (*2*–*4*). In particular, the heterodimeric photosystem I (PSI) is believed to be evolved from a homodimeric RC, similar to the extant RCs of either GSB or heliobacteria (*4*). To date, structures of RCs representing all typical photosynthetic organisms have been determined except the RC structures of GSB and *Acidobacteria*, which provide important information regarding the distinct mechanisms of light–energy conversion and the evolution of photosynthetic RCs.

GSB in the *Chlorobi* phylum are strictly anaerobic and can grow under extremely low light intensities (*5*) by using a photosynthetic apparatus that consists of three coupled modules: a large light-harvesting chlorosome (*6*), a soluble energy transmitter FMO (Fenna-Matthews-Olson protein) (*7*), and a membrane-embedded type I RC (*8*). The chlorosome is an elliptical vesicle enclosing a large number of self-assembled antenna molecules [e.g., bacteriochlorophylls (BChls), carotenoids, and quinones] attached to a paracrystalline baseplate made up of CsmA proteins and BChls (*9*). FMO connects chlorosomes to RCs at the cytoplasmic side of cell membrane and is a homotrimer in which each FMO monomer binds eight BChls *a* (*10*). The RC of *Chlorobaculum tepidum* (GsbRC), a model GSB in the *Chlorobiaceae* family, comprises six subunits: a homodimer of two 82-kDa core subunits (PscA), a 24-kDa Fe-S protein (PscB), two 20-kDa cytochrome (PscC) proteins, and a 17-kDa protein (PscD) (*8*, *11*, *12*). Previous analysis suggested that each GsbRC binds 16 BChls *a*, including a pair of BChls *a*′ (the stereoisomer at the 13^2 position of ring E of BChl *a*) with a characterized absorption maximum near 840 nm (corresponding to the "special pair" BChls of RC); four Chls *a*; and four derivatives of chlorobactenes or γ-carotenes (*8*, *13*, *14*). The pair of BChls *a*′ absorbing energy at 840 nm is termed P_{840} and is the special pair of GsbRC that not only accepts energy transferred from FMO but also serves as the primary electron donor in the electron-transfer chain (ETC) (*8*).

The energy-transfer efficiencies among pigments within the chlorosome, within FMO, or from chlorosome to FMO are reported to be near 100% (*15*, *16*). However, this value drops to 35 to 75% for energy transfer between FMO and GsbRC examined either in vitro or in vivo (*17*–*20*), which is substantially lower than the nearly 100% efficiency of energy transfer from light-harvesting antenna to RC of PSI in oxygenic photosynthetic organisms (*21*). To date, the structural basis for this drop in energy-transfer efficiency from FMO to GsbRC remains unknown. We determined the structure of FMO-GsbRC at 2.7-Å resolution by cryo–electron microscopy (cryo-EM) (Fig. 1, Materials and methods, figs. S1 and S2, table S1, and movie S1), which revealed distinctive features of this antenna-RC complex and provided the basis for explaining its energy-transfer dynamics as well as structural insights into the evolution of photosystems.

Structure of the FMO-GsbRC supercomplex

The cryo-EM structure of FMO-GsbRC consists of an RC dimer associated with an FMO trimer with dimensions of ~160 Å by 120 Å by 100 Å (Fig. 1 and movie S1), as reported previously at nanometer resolution (*22*, *23*). We identified seven subunits in the whole supercomplex: four from the RC (PscA-1, PscA-2, PscB, and PscD) and three from the FMO trimer (FMO-1, -2, and -3) (Fig. 1, B to D, and movie S2). The PscC subunit (see supplementary materials for more details) and the second FMO trimer were not observed in the cryo-EM structure, probably because of their weak association with the GsbRC, which resulted in their loss during sample preparation. We identified 67 cofactors in the FMO-GsbRC: 26 BChls *a*, 4 Chls *a*, 4 lipids (two phosphatidyl glycerols and two monogalactosyl diglycerides), 2 chlorobactenes [labeled as F26 in the Protein Data Bank (PDB) file], 2 chlorobactene esters (labeled as F39), 3 Fe_4S_4 clusters, and 2 calcium ions in GsbRC, as well as 24 BChls *a* in FMO (Fig. 1, B to D, fig. S3, and movie S3).

The GsbRC core is a homodimer of PscA that includes both transmembrane and extrinsic regions (Fig. 1B). The Fe_4S_4 cluster F_X is coordinated by two pairs of cysteine residues (Cys^{527} and Cys^{536}) at the interface between PscA-1 and PscA-2, similar to that in heliobacterial RC (HbRC) and PSI (*24*, *25*). The transmembrane region of each PscA consists of 11 transmembrane helices (TMHs), which can be divided into an antenna domain (TMHs 1 to 6) and an electron-transfer (ET) domain (TMHs 7 to 11) (fig. S4A). The sequence identities between PscA of GsbRC, PshA of HbRC, and PsaA and PsaB of cyanobacterial PSI range from 18 to 21%, and the spatial organizations of GsbRC TMHs are similar to those of L and M of purple bacterial RC (PbRC), PshA of HbRC, PsaA and PsaB of cyanobacterial PSI, and CP43, D1, D2, and CP47 of PSII, with root mean square deviations (RMSDs) between their Cα atoms ranging from 2.5 to 4.0 Å (fig. S4, B to E) (*24*–*27*).

[1]Department of Pathology of Sir Run Run Shaw Hospital and Department of Biophysics, Zhejiang University School of Medicine, Hangzhou, 310058 Zhejiang, China. [2]Center of Cryo-Electron Microscopy, Zhejiang University, Hangzhou, 310058 Zhejiang, China. [3]Photosynthesis Research Center, Key Laboratory of Photobiology, Institute of Botany, Chinese Academy of Sciences, 100093 Beijing, China. [4]Research Institute for Interdisciplinary Science and Graduate School of Natural Science and Technology, Okayama University, 700-8530 Okayama, Japan. [5]Zhejiang Laboratory for System and Precision Medicine, Zhejiang University Medical Center, 1369 West Wenyi Road, Hangzhou, 311121 Zhejiang, China.
*Corresponding author. Email: xzhang1999@zju.edu.cn (X.Z); shen@cc.okayama-u.ac.jp (J.-R.S.); kuangty@ibcas.ac.cn (T.K.)

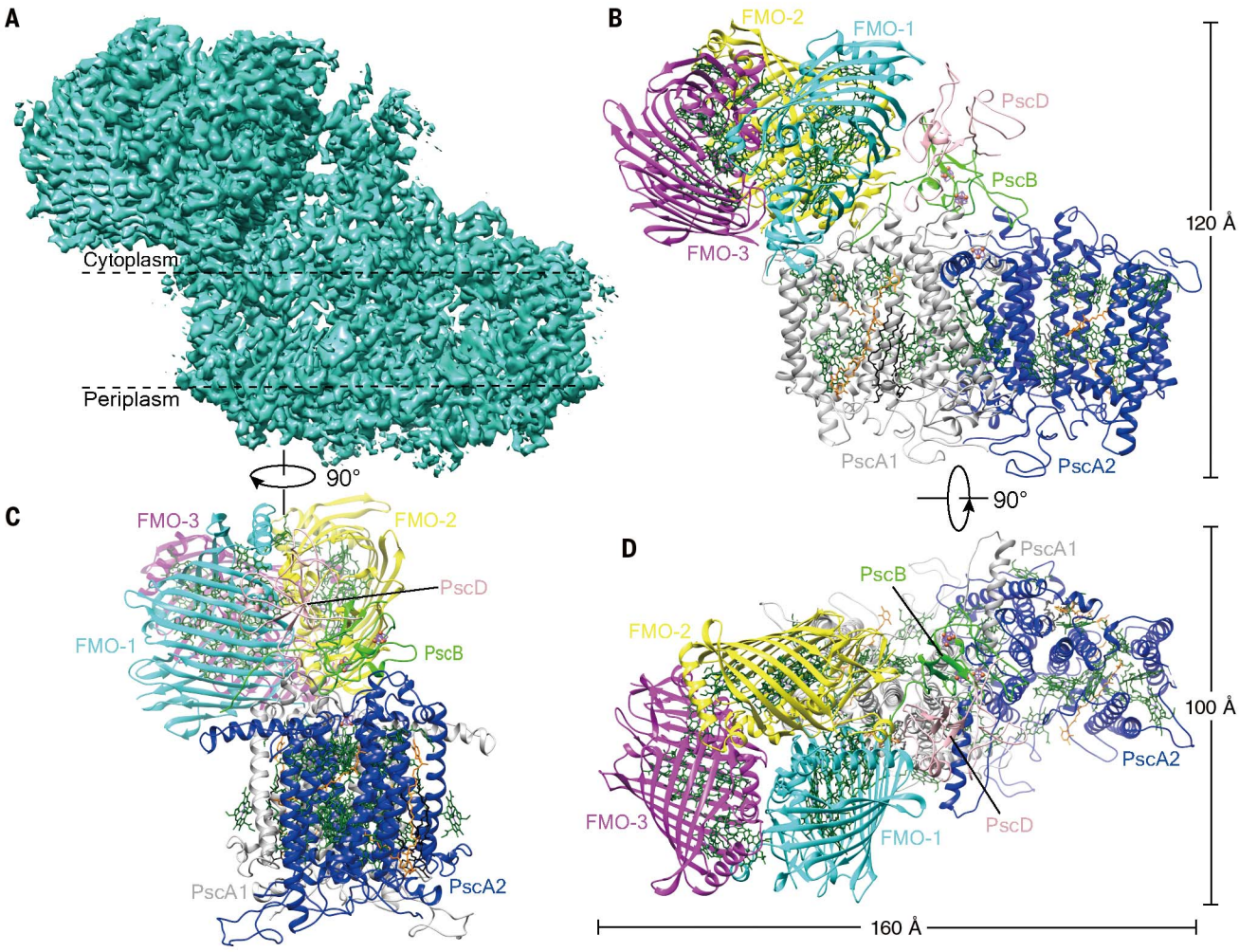

Fig. 1. Cryo-EM structure of FMO-GsbRC. (**A**) Map and (**B** to **D**) structure of FMO-GsbRC with views from the (B) front, (C) side, and (D) top (from the cytoplasmic side). The cofactors are shown in dark green for (B)Chls, black for lipids, and orange for carotenoids.

However, the structures of extrinsic regions, especially at the periplasmic side, are largely different (fig. S4, B to E), likely reflecting their distinctive interactions with different electron donors.

Two extrinsic subunits, PscB and PscD, are located at the cytoplasmic surface of the complex. Although the functions of these subunits are similar to those of PSI PsaC and PsaD, respectively, PscB and PscD are not homologous to PsaC and PsaD but are products of convergent evolution (*2*, *28*). We modeled residues 130 to 223 out of 231 in PscB and residues 20 to 117 out of 144 in PscD (see supplementary materials for details). PscB binds two Fe_4S_4 clusters and binds to the GsbRC homodimer at a position near the C_2 axis (Fig. 1, B and D), thus interacting with both PscA-1 and PscA-2. The structure and location of PscB resemble those of PsaC in PSI (fig. S5, A and C) (*24*). However, the structure of PscD differs substantially from that of PsaD in PSI, with an RMSD value of 6.8 Å between their C_α atoms (fig. S5B, D and E), despite their similar biochemical characteristics (*8*). Both PscB and PscD interact not only with each other but also with FMO and the GsbRC core, which may be essential for stabilizing the FMO-GsbRC complex (*29*) (Fig. 1, B and C).

The FMO is composed of three identical subunits, each binding eight BChls (BChls 1 to 8) as in the previous crystal structure (*10*) (fig. S6, A to C). The FMO trimer attaches to the cytoplasmic side of one of the PscA subunits at a distal end of GsbRC. The C_3 symmetry axis of the FMO trimer inclines ~75° against the surface plane of the PscA homodimer (fig. S6, D and E), instead of ~90° as reported previously (*30*–*32*). This orientation may facilitate energy transfer from the FMO to GsbRC as discussed below. A second FMO trimer was not observed in the current structure but was suggested to be present in the isolated FMO_2-GsbRC complex (*32*). This second FMO may bind to the other distal end, as shown in fig. S7.

The ETC in GsbRC

The ETC in GsbRC includes three pairs of (B)Chls and three Fe_4S_4 clusters (F_X, F_A, and F_B) arranged into two branches along the core dimer axis from the peripheral side to the cytoplasmic side (Fig. 2) (*8*). The primary donor is a special pair of BChls *a*′ (P_{840}) coordinated by His^{621} from two PscAs, with a planar-to-planar distance shorter than 3.5 Å. The cofactors in the third pair (termed A_0) along the ETC are Chls *a*, consistent with previous spectroscopic and biochemical studies (*33*–*36*). The cofactors in the second pair (termed A_{CC}) are tentatively identified from their densities as two Chls *a*, as the densities were not clear enough to allow distinguish between Chl *a* and BChl *a*. However, our assignment is consistent with the previous report that four Chls *a* at 670 nm are arranged symmetrically and have pronounced excitonic coupling on the basis of the linear dichroism and circular dichroism spectra of GsbRC (*13*). The central magnesium

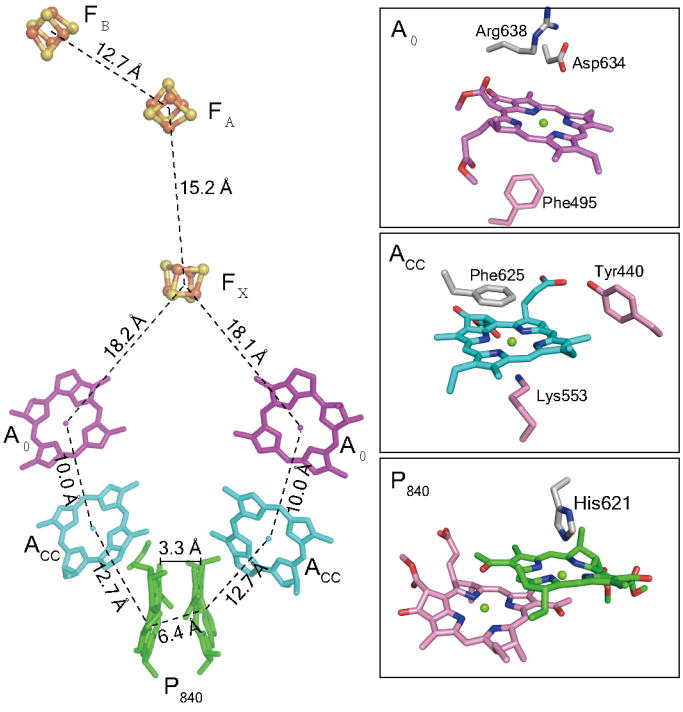

Fig. 2. Cofactor arrangement along the ETC in GsbRC. The panels at right show the coordinating environment for the three (B)Chl cofactors. Residues from PscA that coordinate the (B)Chls are shown in gray, and those from the second PscA are in pink.

atoms of A_{CC} are coordinated by PscA-Lys^{553} instead of water found in the homodimeric HbRC and the heterodimeric PSI (*24*, *25*), and no ligand for A_0 is identified in the structure (Fig. 2).

The electron-transfer rate decreases exponentially with increasing distance between neighboring cofactors of the ETC (*37*). The distances between the GsbRC ET cofactors are more similar to those in HbRC than to those in PSI, and the arrangement of the cofactors in the two branches is approximately symmetric at the current resolution, which suggests that electron transfer in GsbRC could proceed through both branches (Fig. 2 and fig. S8, A to C) (*25*). The distance between A_0 and F_X in GsbRC (18.0 Å) is close to that in HbRC (17.9 Å) but shorter than that in PSI (~20 Å) (*24*, *25*). In PSI, a quinone is located between A_0 and F_X and functions as the secondary electron acceptor (A_1) to mediate electron transfer from A_0 to F_X (*24*). No such quinone molecules were identified in the structure of HbRC, and the relatively shorter distance between A_0 and F_X in HbRC may allow a direct electron transfer between them without an intermediate cofactor (*25*). In GsbRC, the role of quinone in electron transfer between A_0 and F_X is controversial. Although one or two menaquinone-7 molecules have been reported to bind to GsbRC and function as the electron acceptor A_1 (*38*, *39*), other studies have suggested that menaquinone-7 is not required for the forward electron transfer (*40*). Our high-performance liquid chromatography (HPLC) analysis identified virtually no menaquinone-7, but a trace amount was detected in the isolated FMO-GsbRC sample by ultra-performance liquid chromatography–quadrupole time-of-flight mass spectrometry (UPLC-QTOF/MS). This amount is far below a stoichiometry of one menaquinone-7 per GsbRC (see fig. S9 and supplementary text for more details). We observed a weak, hooklike feature in the EM map at a position ~3 Å from the chlorin plane of A_0 (fig. S8, D and E), which could be modeled as menaquinone-7; however, the identity of this molecule is not certain from the structure, and the position is inconsistent with a role in ET between A_0 and F_x.

Arrangements of pigments in GsbRC

The 30 (B)Chls in GsbRC are substantially fewer than the 60 BChls in HbRC and the 87 Chls in the PSI core but are close to the 35 Chls in the PSII core (*24*–*26*) (Fig. 3 and movie S5). Notably, the binding sites of these 30 (B)Chls are largely conserved in HbRC and PSI with only slight shifts in the positions and orientations of a few (B)Chls. Compared with those in GsbRC, the additional (B)Chls in HbRC and PSI mainly distribute at the peripheral regions and gap regions between the two separate (B)Chl clusters (Fig. 3) (*24*, *25*). Furthermore, 26 of the 30 (B)Chls from GsbRC have similar positions to those of the Chls in PSII (Fig. 3B). This arrangement of pigments represents the common features of both type I and II RCs. The different amount of pigments in GsbRC, HbRC, and PSI may reflect their different evolutionary statuses. It can be postulated that in the initial stages of evolution, the RCs binds fewer pigments, therefore a large amount of peripheral antenna (such as the chlorosome in GSB) is attached to harvest the light energy. During evolution, RCs can bind more pigments in their proteins and lose the large antenna proteins such as those seen in HbRC and PSI. An alternative explanation is that the additional (B)Chls observed in HbRC and PSI were lost in GsbRC during evolution. However, in view of the structural features of GsbRC, such as the homodimer and the lack of a quinone in ETC, the latter possibility is unlikely.

The 30 (B)Chls in GsbRC include 6 central ET (B)Chls and 24 peripheral antenna BChls (Fig. 3A). When viewed perpendicular to the membrane plane, the antenna BChls in GsbRC are organized into two distinct clusters, with each cluster located in a PscA subunit and separated by more than 28 Å (edge to edge) (fig. S10A). This distribution pattern is similar to that seen in PSII (Fig. 3B and fig. S10B). By contrast, the antenna (B)Chls in HbRC and PSI are arranged around the three pairs of central (B)Chls, forming a closed ring across two RC subunits with distances of neighboring (B)Chls shorter than 14.5 Å (edge to edge) (Fig. 3, C and D and fig. S10, C and D). Two BChls (A814 and a814) in GsbRC are located at positions similar to those of two Chl_Z molecules bound to D1 and D2 of PSII RC, and they are all separated from other (B)Chls, in contrast to the two corresponding BChls in HbRC and PSI that have rather closely positioned (B)Chls. These features indicate that the organization of (B)Chls in the GsbRC more closely resembles that in PSII rather than that in HbRC and PSI.

When viewed parallel to the membrane plane, the 30 (B)Chls in GsbRC are arranged into two separated layers (the cytoplasmic and periplasmic layers), similar to the (B)Chl arrangements in PSII, HbRC, and PSI (Fig. 4, A to D, fig. S11A, and movie S5). Most (B)Chls in each layer are close to neighboring (B)Chls, with Mg-to-Mg distance shorter than 14 Å (fig. S11, B and C). The shortest Mg-to-Mg distance between the two (B)Chl layers in GsbRC is 15.3 Å, similar to that in PSII (16.3 Å), HbRC (15.2 Å), and PSI (17.2 Å). The longer distances between the two (B)Chl layers would diminish the energy-transfer efficiency exponentially by a factor of 6 (*37*), and the present structure thus suggests that the energy transfer between the two layers would be slightly less efficient than that within each layer. In PSII, HbRC, and PSI, there are additional linker (B)Chls located between the two layers that have Mg-to-Mg distances of 9.4 to 11.7 Å, thereby facilitating energy transfer between the two layers (Fig. 4, B to D). However, no such linker (B)Chls were found in GsbRC, suggesting a less efficient energy transfer between the two (B)Chls layers. We observed a long (~52 Å), continuous EM density connecting

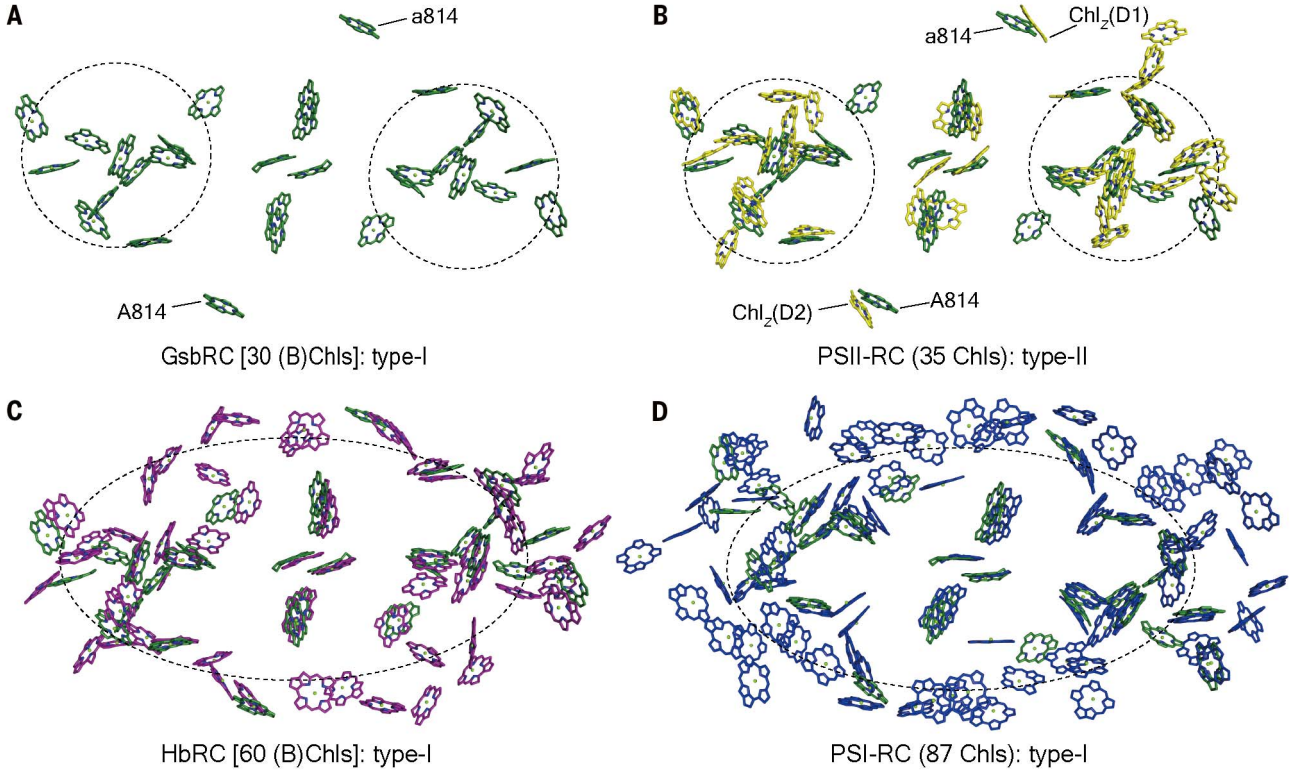

Fig. 3. Distribution of (B)Chls in GsbRC, PSII, HbRC, and PSI RCs. (**A** and **B**) Arrangement of (B)Chls in GsbRC (A) (dark green) and their superposition with those of PSII (B) (yellow). Two separated (B)Chl clusters around the ETCs in GsbRC and PSII are indicated by dashed circles. (**C** and **D**) Superposition of (B)Chls of GsbRC (dark green) with those of HbRC (C) (purple) and PSI RC (D) (blue). Dashed ellipses indicate closed (B)Chl rings surrounding the ETCs in both HbRC and PSI RC. The number of (B)Chls in each RC is noted. All models are viewed perpendicular to the membrane plane. The PDB IDs of PSII RC, HbRC, and PSI RC are 3WU2 (*26*), 5V8K (*25*), and 1JB0 (*24*), respectively.

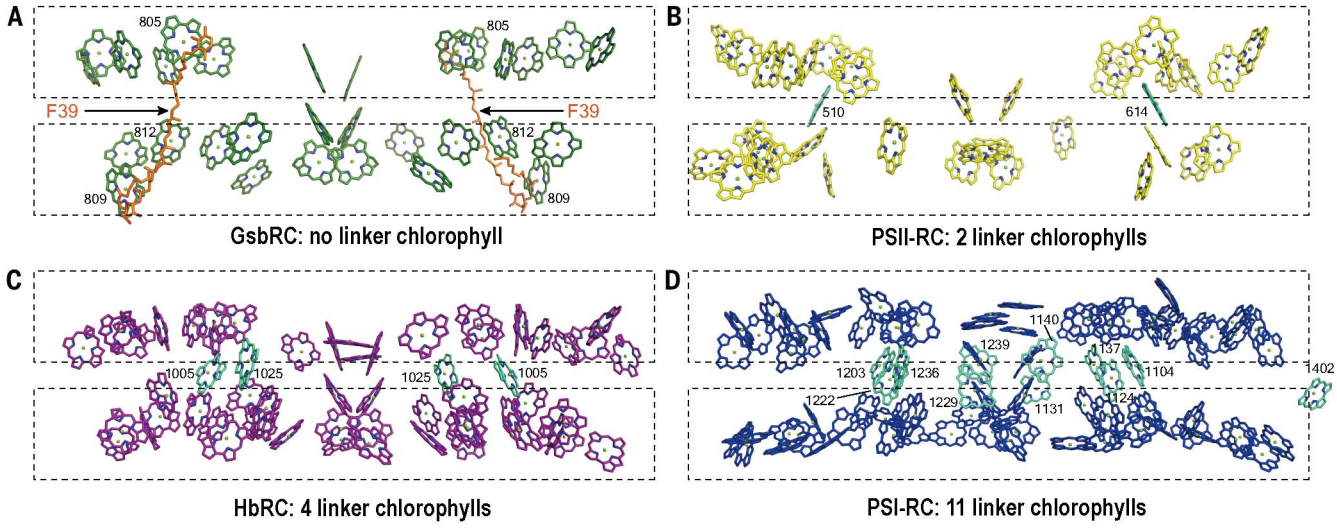

Fig. 4. Comparisons of the two (B)Chl layers in GsbRC, PSII, HbRC, and PSI RCs. (**A** to **D**) Distribution of (B)Chls in two layers viewed from the side of the membrane in GsbRC (A), PSII (B), HbRC (C), and PSI (D). Two F39 molecules are found between the two layers in GsbRC (A), in contrast to linker Chls (colored in green-blue) in the other RCs [2 in PSII RC (B), 4 in HbRC (C), and 11 in PSI RC (D)]. The PDB IDs of PSII, HbRC, and PSI are 3WU2 (*26*), 5V8K (*25*), and 1JB0 (*24*), respectively.

the two (B)Chl layers in each PscA subunit (Fig. 4A). Both length and characteristic features of the density match those of a hydroxychlorobactene glucoside laurate (designated F39), a chlorobactene derivative with a glycosyl tail (Fig. 4A, fig. S3, and movie S6) (*41*). The aromatic head of F39 is 5.3 Å from the porphyrin ring of BChl A805 in the cytoplasmic (B)Chl layer, and its glycosyl tail is parallel to the BChl chlorin planes of BChls A809 and A812 in the periplasmic (B)Chl layer (Fig. 4A and fig. S11D). This F39 molecule may absorb and transfer energy to either of the two layers or may dissipate excess energy from pigments in either of the two layers under strong light conditions. However, it would not mediate energy transfer between the two BChl layers, as this would necessitate a highly "uphill" energy-transfer step.

Possible energy-transfer pathways from FMO to GsbRC

In GSB, light energy absorbed by the chlorosome is transferred to the RC through FMO (*20*). The energy-transfer efficiencies of intra-chlorosome, chlorosome-to-FMO, and intra-FMO transfer are considered to be near to 100%, and an obvious drop in energy-transfer efficiency occurs from FMO to GsbRC (<50% in vitro and ~75% in vivo) (*17*–*20*). This low energy-transfer efficiency between FMO and GsbRC is in sharp contrast to the near-100% efficiency of transfer from light-harvesting complex I (LHCI) to the PSI RC (*21*), suggesting differences in how these elements are connected.

In our structure, the two BChl-8s of FMO-2 and FMO-3 are located at the uppermost surface that should be the interface between FMO and the chlorosome (Fig. 5). These BChls will thus receive energy from the chlorosome. This arrangement is different from that described in previous reports, which have argued that the FMO binds to GsbRC with its C_3 symmetry axis perpendicular to the cell membrane, in which all three BChl-8s from three FMO subunits acquire energy equally from the chlorosome (*30*, *31*). BChls within each FMO monomer generally have edge-to-edge distances of 6 to 7 Å. However, BChl-8 is isolated from the other seven BChls in the same FMO monomer with edge-to-edge distances of 17 to 18 Å, but it is close to BChl-1 of the adjacent monomer at edge-to-edge distances of 7 to 8 Å (fig. S6, A to C). Thus, the energy received by BChl-8 will be distributed rapidly to BChl-1 in the adjacent monomer and subsequently throughout the entire monomer. This observation is consistent with previously reported inter-monomer energy transfer (*42*, *43*). Eventually, the energy would be transferred to the BChl-3s of the FMO-1 and FMO-2 that are closest to the BChls in GsbRC and have the lowest energy level, as suggested previously (*42*, *43*) (Fig. 5A).

Between FMO and GsbRC, the BChl-3s of FMO-1 and FMO-2 have edge-to-edge distances of ~22 and ~23 Å to BChl-808 and BChl-810 of GsbRC, respectively. However, the BChl-3 in FMO-3 has a much longer distance (~33 Å) to the GsbRC BChls. Thus, the energy received by the FMO would be transferred through the BChl-3s of FMO-1 and FMO-2 to BChl-808 and BChl-810 of GsbRC (Fig. 5, A and B).

The BChl-to-BChl distances between FMO and GsbRC described above are considerably longer than those between the LHCI and PSI. As many as 10 Chls have been found in the gap space between the higher-plant LHCI and PSI core, and thus the edge-to-edge distances between Chls of LHCI and PSI RC are shortened to between 8 and 13 Å (*44*–*46*). These gap Chls likely function to mediate effective energy transfer from LHCI to PSI RC. In FMO-GsbRC, no such gap (B)Chls exist between FMO and GsbRC, resulting in longer distances from the three FMO monomers to the closest BChls (A808 and A810) of GsbRC in the cytoplasmic (B)Chl layer (Fig. 5B). We observed a group of aromatic and histidine residues between BChl-3 and BChl-4 of FMO-2 and BChls A805 and A810 of GsbRC (Fig. 5C), but whether these residues contribute to energy-transfer mediation remains unclear.

In GsbRC, the energy transferred from one FMO would be restricted primarily in the PscA-1 subunit owing to the separated BChl clusters in the GsbRC core (Fig. 3A and Fig. 4A), in contrast to the unconfined distribution of (B)Chls over a ring across the core subunits in HbRC and PSI (Fig. 3, C and D). The energy transferred from FMO may finally be transferred to the special pair BChls (P_{840}) through BChls A811 and A815 in GsbRC, because these two BChls are located closest to P_{840} with edge-to-edge distances of 12.0 and 13.4 Å, respectively (Fig. 5E).

Notably, these discussions are based on the distances of (B)Chls only, but the energy-transfer efficiencies also depend on the relative orientations of the chlorin rings and relative energy levels of the associated pigments, the latter of which are regulated by the protein environment. Thus, an explicit description of the energy-transfer pathways and efficiencies will require detailed theoretical calculations using the experimental coordinates reported here.

The cryo-EM structure of FMO-GsbRC reveals many characteristic features of a homodimeric type I RC, with fewer pigments associated, a chlorobactene derivative, and a distinctive pigment arrangement that establishes the energy-transfer pathways within FMO-GsbRC. These results provide a basis for a more comprehensive examination of the energy- and electron-transfer functions of this supercomplex through both experimental and theoretical approaches. A notable feature of the FMO-GsbRC supercomplex (a type I RC) is that the arrangement of its pigments is instead similar to that of the PSII RC (a type II RC), represented by two distinct (B)Chl clusters surrounding the ETC (B)Chls and fewer pigments than in the HbRC and PSI RC. GsbRC thus exhibits features of both type I and II RCs and may provide insight into how these structures are diverged from a common ancestor. Such an ancestor may have served as the origin of the extant RCs and may have evolved to type I RCs by incorporating more pigments, as well as to type II RCs by losing the Fe-S cluster and using quinone as the terminal electron acceptor.

Materials and methods

Purification of the FMO-GsbRC complex

The FMO-GsbRC complex was isolated and purified from *C. tepidum* as previously described with some modifications (*12*). Cells of *C. tepidum* TLS (ATCC 49652) were grown in 2-liter glass bottles for 7 to 10 days under white light illumination of 2400 lux at 47°C. To avoid oxidization of the RC, ascorbic acid was added to all buffers used in the following steps immediately before use, and all operations were performed under weak light. Cells were harvested by centrifugation at 2000 × g for 10 min at 4°C, and the pellet was resuspended to 0.2 g/ml with a Tris buffer (20 mM Tris-HCl, pH 8.0) supplemented with DNase I and 10 mM ascorbic acid and then disrupted six times at 2300 bar with a cell disruptor (JNBIO) equipped with a cooling system. The cell lysate was centrifuged at 30,000 × g for 20 min, and the supernatant was collected and centrifuged again at 120,000 × g for 40 min. Membranes containing the RC and FMO proteins were collected and solubilized with Triton X-100 at a final concentration of 3% (w/v) for 70 min on ice. Unsolubilized membrane fragments were removed by centrifugation at 120,000 × g for 40 min, and the supernatant containing the FMO-GsbRC complex was collected and further purified through an anion exchange column using the media of Q-Sepharose High Performance (GE). The column was pre-equilibrated with a salt-free buffer (20 mM Tris-HCl, pH 8.0, 10 mM ascorbic acid, 0.03% Triton X-100), and the FMO-GsbRC supercomplex was then eluted with the same buffer containing 250 mM NaCl. The sample eluted was concentrated to a small volume and subjected to separation by sucrose density gradient centrifugation (SDGC) at 200,000 × g for 14 hours. Three bands were obtained from the sucrose density gradient centrifugation (fig. S1), among which B1 and B2 are free pigments, detached FMO in mixture with RC, respectively, and B3 is the FMO-GsbRC supercomplex. The B3 band was collected and concentrated to a proper concentration to be used for the cryo-EM experiment.

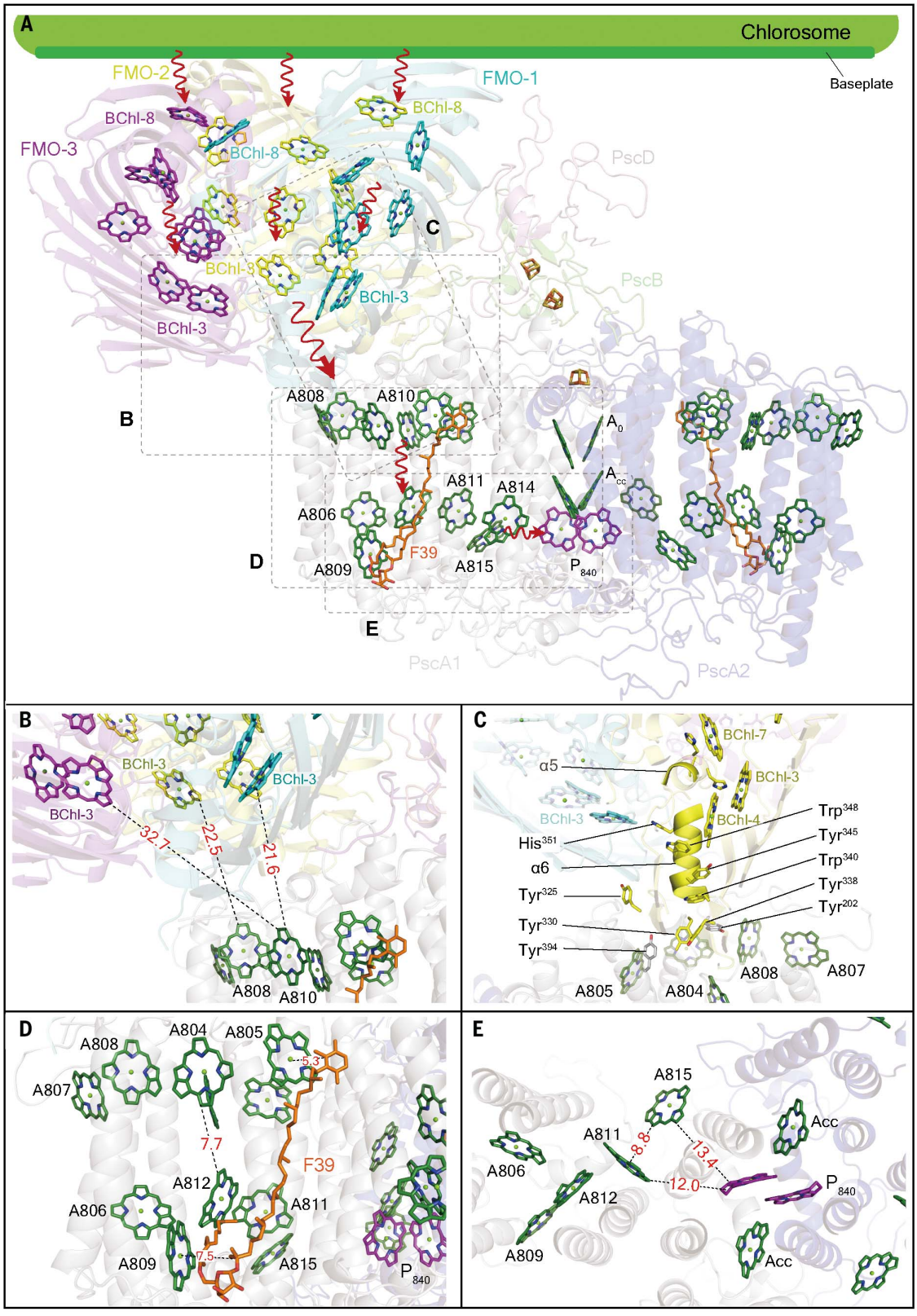

Fig. 5. Possible energy-transfer pathways in FMO-GsbRC. (**A**) Putative energy-transfer pathways from chlorosome to FMO and eventually to GsbRC (see text for details). Dashed boxes are enlarged in (B) to (E). (**B**) Connections of BChls at the interface between FMO and GsbRC. (**C**) Two short α helices (α5 and α6) of an FMO subunit locate at the interface between FMO and GsbRC. These helices may play important roles in mutual energy transfer. (**D**) The chlorobactene ester (labeled as F39) locates between the two BChl layers. (**E**) Two antenna BChls (A811 and A815) locate between the bulk BChls of GsbRC and ETC in the periplasmic BChl layer. This arrangement likely mediates energy transfer from the antenna BChls to P_{840}. The red numbers in (B) to (E) indicate distances in angstroms.

Cryo-EM sample preparation and data collection

An aliquot of a 2.5-μl purified FMO-GsbRC sample was applied to a holey carbon grid covered with graphene-oxide (Quantifoil R1.2/1.3, Au, 300 mesh). After 90 s, the grids were blotted for 6.5 s at a humidity of 100% and 8°C and plunge-frozen in liquid ethane using a Vitrobot (FEI). Using SerialEM (*47*), cryo-EM images of FMO-GsbRC were recorded with an FEI Titan Krios electron microscope operated at 300 kV under a nominal magnification of 22,500. The microscope was carefully aligned before data collection, including the coma-free alignment to minimize the effects of beam tilt. The dose rate of the electron beam was set to ~8 e^-/s per physical pixel, and a total of 7773 cryo-image stacks were recorded on a Gatan K2 summit camera at 4 frames/s for 10 s using the super-resolution mode with a total dose of ~47 $e^-/Å^2$ on the specimen, and additional 1383 cryo-image stacks were collected with the sample stage tilted to 30° to overcome the problem of a preferred orientation of the particles in ice. Defocus values were set from −1.5 to −2.5 μm.

Cryo-EM image processing

The drift correction and dose-weighting of all image stacks were performed with MotionCor2 to generate 2× binned images with a pixel size of 1.307 Å per pixel (*48*). All following image processing steps were accomplished with cryoSPARC (*49*). A total of 3,947,008 raw particles were automatically picked, and the local defocus and astigmatism values of individual particles were determined. Initial particle screening with two-dimensional (2D) classification resulted in 1,308,701 particles; further screenings by two cycles of 3D classifications produced 268,430 particles for further 3D refinements, including a 3D refinement, a nonuniform 3D refinement, and four cycles of local 3D refinements, to achieve a final density map at 2.71-Å resolution (FSC ≥ 0.143) with cryoSPARC (*49*) (fig. S2). The resolution was further estimated to be 2.73 Å (FSC ≥ 0.143) by refinement with RELION (*50*) and 2.96 Å (FSCref ≥ 0.5) with Phenix (*51*) (fig. S2). C_1 symmetry was used in the 3D classifications and refinements. CryoSPARC data were converted to the RELION format with the UCSF PYEM (*52*). The final map was sharpened with a B-factor of −93 $Å^2$. Notably, the sample is not homogeneous; by 2D classification, we obtained three types of particles in the cryo-EM images, which are FMO, GsbRC, and FMO-GsbRC with a ratio of ~3:1.5:1.

Modeling and refinement

The model of FMO trimer was built by directly fitting the high-resolution crystal structure of FMO from *Chlorobaculum tepidum* (PDB ID: 3ENI) into the corresponding density map using UCSF Chimera (*10*, *53*). The model of the core structure of GsbRC (PscA dimer) was built using the crystal structure of RC from *Heliobacterium modesticaldum* (PDB ID: 5V8K) as a reference model from which all cofactors and regions outside the membrane were removed (*25*). The backbones of the transmembrane domains of HbRC were fitted into the map and the amino acid sequences were then manually mutated to the corresponding sequences of PscA which were obtained by translating the coding gene. The remaining fragment was further built manually with COOT (*54*). The model of PscB was built initially using the Fe_4-S_4 cluster binding domain of PsaC in the structure of PSI (PDB ID: 1JB0). As no homologous proteins with an identity higher than 30% to PscD were found in the PDB, the model of PscD was built manually by placing poly-alanine residues into the map as the backbone and adjusting the side chains with COOT. The cofactors (BCL, CLA, LHG, LMG, SF4, and CA) in the FMO-GsbRC complex were fitted with corresponding high-resolution structures from PDB. The models of chlorobactene and the modified carotenoid (hydrochlorobactene glucoside laurate) were built using the eLBOW tool in Phenix (*51*, *55*).

The initial model of the FMO-GsbRC complex was refined in real space against the EM map with Phenix (*51*). The refined model was edited again with COOT to reduce the related parameters to a reasonable range (*54*). The final model was obtained by several iterative operations of the above steps. Without NCS restraint, the C_α RMSDs of the three FMO and two PscA subunits are ~0.35 and ~0.32 Å, respectively, and no unambiguous asymmetry was observed at the current resolution. The NCS restraint was applied for the final model refinement with Phenix. Figures were prepared with UCSF Chimera and PyMOL (Molecular Graphics System, LLC) (*53*, *56*). The sequence identity and similarity are estimated by the tool EMBOSS Needle (*57*).

Analysis of menaquinones in the FMO-GsbRC supercomplex

Quinones of the FMO-GsbRC sample were analyzed by HPLC with a Prominence LC-20A HPLC system (Shimadzu) equipped with an analytical Discovery C18 column (4.6 mm by 25 cm) (Supelco, Sigma-Aldrich), as described previously (*58*). The solvents used for elution consisted of solvent A (methanol:acetonitrile: water, 42:33:25 by volume) and solvent B (methanol:acetonitrile:ethyl acetate, 50:20:30 by volume), and the elution was performed as follows: at the time of injection, 30% B; a linear increase from 30% B to 100% B in 52 min; constant 100% B for 6 min; and a return to 30% B in 2 min. The flow rate was 1.0 ml/min, and the column temperature was 35°C. The eluent was monitored at 270 nm. To identify menaquinone-7 (MK-7) in FMO-GsbRC, a standard MK-7 sample (Cerilliant, lot number FN10101902) was analyzed under the same conditions.

Quinones in the FMO-GsbRC sample was further analyzed by UPLC-QTOF/MS. The sample was first separated by LC with a Waters UPLC system (Waters Corp., Milford, MA, USA) equipped with a ZORBAX-SB C18 column (100 mm by 4.6 mm i.d., 1.8 μm). The mobile phases used were solvent A (methanol:water, 90:10 by volume) and solvent B (isopropanol: acetonitrile, 50:50 by volume), and the column was eluted with three steps of linear gradients of 0/0, 15/100, 23/100, (min/B%). An aliquot of 5-μl sample was injected to the column set at 40°C. The flow rate was 0.6 ml/min, and the eluent was detected at 270 nm. The LC was coupled with an MS system of AB Triple TOF 5600^{plus} (AB SCIEX, Framingham, MA, USA), and the MS conditions were as follows: APCI mode, Positive ion mode; source voltage, +5.5 kV; source temperature, 550°C; declustering potential (DP), 100 V; collision energy (CE), 10 eV. The pressure of Gas 1 (Air) and Gas 2 (Air) were set to 50 psi, and the pressure of Curtain Gas (N2) was set to 35 psi. The maximum allowed error was set to ±5 ppm. The IDA-based auto-MS^2 was performed on the eight most intense metabolite ions in a cycle of full scan (1 s). The scan range of m/z of precursor ion and product ion was set as 100 to 1500 Da and 50 to 1500 Da, respectively. For MS/MS acquisition mode, the parameters were almost the same except that the collision energy (CE) was set at 40 ± 20 eV, ion release delay (IRD) at 67, ion release width (IRW) at 25.

The exact mass calibration was performed automatically before each analysis by employing the Automated Calibration Delivery System.

REFERENCES AND NOTES

1. J. P. Allen, J. C. Williams, Photosynthetic reaction centers. *FEBS Lett.* **438**, 5–9 (1998). doi: 10.1016/S0014-5793(98)01245-9; pmid: 9821949
2. G. S. Orf, C. Gisriel, K. E. Redding, Evolution of photosynthetic reaction centers: Insights from the structure of the heliobacterial reaction center. *Photosynth. Res.* **138**, 11–37 (2018). doi: 10.1007/s11120-018-0503-2; pmid: 29603081
3. T. Cardona, A. W. Rutherford, Evolution of photochemical reaction centres: More twists? *Trends Plant Sci.* **24**, 1008–1021 (2019). doi: 10.1016/j.tplants.2019.06.016; pmid: 31351761
4. A. Ben-Shem, F. Frolow, N. Nelson, Evolution of photosystem I - from symmetry through pseudo-symmetry to asymmetry. *FEBS Lett.* **564**, 274–280 (2004). doi: 10.1016/S0014-5793(04)00360-6; pmid: 15111109
5. J. F. Imhoff, "The family *Chlorobiaceae*" in *The Prokaryotes*, E. Rosenberg, E. F. DeLong, S. Lory, E. Stackebrandt, F. Thompson, Eds. (Springer, 2014), pp. 501–514.
6. J. T. Nielsen *et al.*, *In situ* high-resolution structure of the baseplate antenna complex in *Chlorobaculum tepidum*. *Nat. Commun.* **7**, 12454 (2016). doi: 10.1038/ncomms12454; pmid: 27534696
7. R. E. Fenna, B. W. Matthews, Chlorophyll arrangement in a bacteriochlorophyll protein from *Chlorobium limicola*. *Nature* **258**, 573–577 (1975). doi: 10.1038/258573a0
8. G. Hauska, T. Schoedl, H. Remigy, G. Tsiotis, The reaction center of green sulfur bacteria. *Biochim. Biophys. Acta* **1507**, 260–277 (2001). doi: 10.1016/S0005-2728(01)00200-6; pmid: 11687219
9. M. O. Pedersen, J. Underhaug, J. Dittmer, M. Miller, N. C. Nielsen, The three-dimensional structure of CsmA:

A small antenna protein from the green sulfur bacterium *Chlorobium tepidum*. *FEBS Lett.* **582**, 2869–2874 (2008). doi: 10.1016/j.febslet.2008.07.020; pmid: 18652828
10. A. Camara-Artigas, R. E. Blankenship, J. P. Allen, The structure of the FMO protein from *Chlorobium tepidum* at 2.2 A resolution. *Photosynth. Res.* **75**, 49–55 (2003). doi: 10.1023/A:1022406703110; pmid: 16245093
11. T. M. Wahlund, C. R. Woese, R. W. Castenholz, M. T. Madigan, A thermophilic green sulfur bacterium from New Zealand hot springs, *Chlorobium tepidum* sp. nov. *Arch. Microbiol.* **156**, 81–90 (1991). doi: 10.1007/BF00290978
12. C. Hager-Braun *et al*., Stable photobleaching of P_{840} in *Chlorobium* reaction center preparations: Presence of the 42-kDa bacteriochlorophyll a protein and a 17-kDa polypeptide. *Biochemistry* **34**, 9617–9624 (1995). doi: 10.1021/bi00029a039; pmid: 7626630
13. H. P. Permentier *et al*., Composition and optical properties of reaction centre core complexes from the green sulfur bacteria *Prosthecochloris aestuarii* and *Chlorobium tepidum*. *Photosynth. Res.* **64**, 27–39 (2000). doi: 10.1023/A:1026515027824; pmid: 16228441
14. C. Griesbeck, C. Hager-Braun, H. Rogl, G. Hauska, Quantitation of P_{840} reaction center preparations from *Chlorobium tepidum*: Chlorophylls and FMO-protein. *Biochim. Biophys. Acta Bioenerg.* **1365**, 285–293 (1998). doi: 10.1016/S0005-2728(98)00081-4
15. T. P. Causgrove, D. C. Brune, J. Wang, B. P. Wittmershaus, R. E. Blankenship, Energy transfer kinetics in whole cells and isolated chlorosomes of green photosynthetic bacteria. *Photosynth. Res.* **26**, 39–48 (1990). pmid: 24420408
16. Z. G. Fetisova, A. M. Freiberg, K. E. Timpmann, Long-range molecular order as an efficient strategy for light harvesting in photosynthesis. *Nature* **334**, 633–634 (1988). doi: 10.1038/334633a0
17. C. Francke, S. C. M. Otte, M. Miller, J. Amesz, J. M. Olson, Energy transfer from carotenoid and FMO-protein in subcellular preparations from green sulfur bacteria. Spectroscopic characterization of an FMO-reaction center core complex at low temperature. *Photosynth. Res.* **50**, 71–77 (1996). doi: 10.1007/BF00018222; pmid: 24271823
18. G. He, D. M. Niedzwiedzki, G. S. Orf, H. Zhang, R. E. Blankenship, Dynamics of energy and electron transfer in the FMO-reaction center core complex from the phototrophic green sulfur bacterium *Chlorobaculum tepidum*. *J. Phys. Chem. B* **119**, 8321–8329 (2015). doi: 10.1021/acs.jpcb.5b04170; pmid: 26061391
19. N. C. M. Magdaong, D. M. Niedzwiedzki, R. G. Saer, C. Goodson, R. E. Blankenship, Excitation energy transfer kinetics and efficiency in phototrophic green sulfur bacteria. *Biochim. Biophys. Acta Bioenerg.* **1859**, 1180–1190 (2018). doi: 10.1016/j.bbabio.2018.07.012; pmid: 30075116
20. J. Dostál, J. Pšenčík, D. Zigmantas, *In situ* mapping of the energy flow through the entire photosynthetic apparatus. *Nat. Chem.* **8**, 705–710 (2016). doi: 10.1038/nchem.2525; pmid: 27325098
21. N. Nelson, Plant photosystem I—The most efficient nano-photochemical machine. *J. Nanosci. Nanotechnol.* **9**, 1709–1713 (2009). doi: 10.1166/jnn.2009.SI01; pmid: 19435029
22. G. Tsiotis, C. Hager-Braun, B. Wolpensinger, A. Engel, G. Hauska, Structural analysis of the photosynthetic reaction center from the green sulfur bacterium *Chlorobium tepidum*. *Biochim. Biophys. Acta Bioenerg.* **1322**, 163–172 (1997). doi: 10.1016/S0005-2728(97)00073-X
23. H. W. Rémigy *et al*., The reaction center complex from the green sulfur bacterium *Chlorobium tepidum*: A structural analysis by scanning transmission electron microscopy. *J. Mol. Biol.* **290**, 851–858 (1999). doi: 10.1006/jmbi.1999.2925; pmid: 10398586
24. P. Jordan *et al*., Three-dimensional structure of cyanobacterial photosystem I at 2.5 A resolution. *Nature* **411**, 909–917 (2001). doi: 10.1038/35082000; pmid: 11418848
25. C. Gisriel *et al*., Structure of a symmetric photosynthetic reaction center-photosystem. *Science* **357**, 1021–1025 (2017). doi: 10.1126/science.aan5611; pmid: 28751471
26. Y. Umena, K. Kawakami, J.-R. Shen, N. Kamiya, Crystal structure of oxygen-evolving photosystem II at a resolution of 1.9 Å. *Nature* **473**, 55–60 (2011). doi: 10.1038/nature09913; pmid: 21499260
27. L. J. Yu, M. Suga, Z. Y. Wang-Otomo, J.-R. Shen, Structure of photosynthetic LH1-RC supercomplex at 1.9 Å resolution. *Nature* **556**, 209–213 (2018). doi: 10.1038/s41586-018-0002-9; pmid: 29618814
28. M. Büttner *et al*., Photosynthetic reaction center genes in green sulfur bacteria and in photosystem 1 are related. *Proc. Natl. Acad. Sci. U.S.A.* **89**, 8135–8139 (1992). doi: 10.1073/pnas.89.17.8135; pmid: 1518838
29. Y. Tsukatani, R. Miyamoto, S. Itoh, H. Oh-Oka, Function of a PscD subunit in a homodimeric reaction center complex of the photosynthetic green sulfur bacterium *Chlorobium tepidum* studied by insertional gene inactivation. Regulation of energy transfer and ferredoxin-mediated $NADP^+$ reduction on the cytoplasmic side. *J. Biol. Chem.* **279**, 51122–51130 (2004). doi: 10.1074/jbc.M410432200; pmid: 15371432
30. A. N. Melkozernov, J. M. Olson, Y.-F. Li, J. P. Allen, R. E. Blankenship, Orientation and excitonic interactions of the Fenna–Matthews–Olson bacteriochlorophyll *a* protein in membranes of the green sulfur bacterium *Chlorobium tepidum*. *Photosynth. Res.* **56**, 315–328 (1998). doi: 10.1023/A:1006082513522
31. J. Wen, H. Zhang, M. L. Gross, R. E. Blankenship, Membrane orientation of the FMO antenna protein from *Chlorobaculum tepidum* as determined by mass spectrometry-based footprinting. *Proc. Natl. Acad. Sci. U.S.A.* **106**, 6134–6139 (2009). doi: 10.1073/pnas.0901691106; pmid: 19339500
32. D. Bína, Z. Gardian, F. Vácha, R. Litvín, Native FMO-reaction center supercomplex in green sulfur bacteria: An electron microscopy study. *Photosynth. Res.* **128**, 93–102 (2016). doi: 10.1007/s11120-015-0205-y; pmid: 26589322
33. M. Kobayashi *et al*., The primary electron acceptor of green sulfur bacteria, bacteriochlorophyll 663, is chlorophyll *a* esterified with Δ2,6-phytadienol. *Photosynth. Res.* **63**, 269–280 (2000). doi: 10.1023/A:1006480629059; pmid: 16228437
34. M. Kobayashi, Study of precise pigment composition of photosystem I-type reaction centers by means of normal-phase HPLC. *J. Plant Res.* **109**, 223–230 (1996). doi: 10.1007/BF02344549
35. E. J. van de Meent *et al*., The nature of the primary electron acceptor in green sulfur bacteria. *Biochim. Biophys. Acta Bioenerg.* **1102**, 371–378 (1992). doi: 10.1016/0005-2728(92)90137-Q
36. M. Iwaki, S. Itoh, S. Kamei, H. Matsubara, H. Oh-oka, Time-resolved spectroscopy of chlorophyll-*a* like electron acceptor in the reaction center complex of the green sulfur bacterium *Chlorobium tepidum*. *Plant Cell Physiol.* **40**, 1021–1028 (1999). doi: 10.1093/oxfordjournals.pcp.a029483
37. M. Şener *et al*., Förster energy transfer theory as reflected in the structures of photosynthetic light-harvesting systems. *ChemPhysChem* **12**, 518–531 (2011). doi: 10.1002/cphc.201000944; pmid: 21344591
38. S. Takaichi, H. Oh-oka, Pigment composition in the reaction center complex from the thermophilic green sulfur bacterium, *Chlorobium tepidum*: Carotenoid glucoside esters, menaquinone and chlorophylls. *Plant Cell Physiol.* **40**, 691–694 (1999). doi: 10.1093/oxfordjournals.pcp.a029594
39. B. Kjaer *et al*., Menaquinone-7 in the reaction center complex of the green sulfur bacterium *Chlorobium vibrioforme* functions as the electron acceptor A_1. *Biochemistry* **37**, 3237–3242 (1998). doi: 10.1021/bi973121t; pmid: 9536963
40. A. Van der Est, H. Scheller, C. Hager-Braun, G. Hauska, D. Stehlik, "Forward electron transfer in chlorobium reaction centres studied by transient EPR" in *Photosynthesis: Mechanisms and Effects*, G. Garab, Ed. (Springer, 1998), pp. 547–550.
41. S. Takaichi *et al*., New carotenoids from the thermophilic green sulfur bacterium *Chlorobium tepidum*: 1′,2′-dihydro-γ-carotene, 1′,2′-dihydrochlorobactene, and OH-chlorobactene glucoside ester, and the carotenoid composition of different strains. *Arch. Microbiol.* **168**, 270–276 (1997). doi: 10.1007/s002030050498; pmid: 9297463
42. A. Kell, K. Acharya, V. Zazubovich, R. Jankowiak, On the controversial nature of the 825 nm exciton band in the FMO protein complex. *J. Phys. Chem. Lett.* **5**, 1450–1456 (2014). doi: 10.1021/jz5001165; pmid: 26269993
43. A. Kell, A. Y. Khmelnitskiy, T. Reinot, R. Jankowiak, On uncorrelated inter-monomer Förster energy transfer in Fenna-Matthews-Olson complexes. *J. R. Soc. Interface* **16**, 20180882 (2019). doi: 10.1098/rsif.2018.0882; pmid: 30958204
44. X. Qin, M. Suga, T. Kuang, J.-R. Shen, Photosynthesis. Structural basis for energy transfer pathways in the plant PSI-LHCI supercomplex. *Science* **348**, 989–995 (2015). doi: 10.1126/science.aab0214; pmid: 26023133
45. Y. Mazor, A. Borovikova, I. Caspy, N. Nelson, Structure of the plant photosystem I supercomplex at 2.6 Å resolution. *Nat. Plants* **3**, 17014 (2017). doi: 10.1038/nplants.2017.14; pmid: 28248295
46. A. Ben-Shem, F. Frolow, N. Nelson, Crystal structure of plant photosystem I. *Nature* **426**, 630–635 (2003). doi: 10.1038/nature02200; pmid: 14668855
47. D. N. Mastronarde, E. M. Serial, A program for automated tilt series acquisition on Tecnai microscopes using prediction of specimen position. *Microsc. Microanal.* **9**, 1182–1183 (2003). doi: 10.1017/S1431927603445911
48. S. Q. Zheng *et al*., MotionCor2: Anisotropic correction of beam-induced motion for improved cryo-electron microscopy. *Nat. Methods* **14**, 331–332 (2017). doi: 10.1038/nmeth.4193; pmid: 28250466
49. A. Punjani, J. L. Rubinstein, D. J. Fleet, M. A. Brubaker, cryoSPARC: Algorithms for rapid unsupervised cryo-EM structure determination. *Nat. Methods* **14**, 290–296 (2017). doi: 10.1038/nmeth.4169; pmid: 28165473
50. S. H. Scheres, RELION: Implementation of a Bayesian approach to cryo-EM structure determination. *J. Struct. Biol.* **180**, 519–530 (2012). doi: 10.1016/j.jsb.2012.09.006; pmid: 23000701
51. P. D. Adams *et al*., R. J. Read, D. C. Richardson, J. S. Richardson, T. C. Terwilliger, P. H. Zwart, PHENIX: A comprehensive Python-based system for macromolecular structure solution. *Acta Crystallogr. D* **66**, 213–221 (2010). doi: 10.1107/S0907444909052925; pmid: 20124702
52. D. Asarnow, E. Palovcak, Y. Cheng, asarnow/pyem: UCSF pyem v0.5, Version v0.5, Zenodo (2019); .doi: 10.5281/zenodo.3576630
53. E. F. Pettersen *et al*., UCSF Chimera—A visualization system for exploratory research and analysis. *J. Comput. Chem.* **25**, 1605–1612 (2004). doi: 10.1002/jcc.20084; pmid: 15264254
54. P. Emsley, K. Cowtan, Coot: Model-building tools for molecular graphics. *Acta Crystallogr. D* **60**, 2126–2132 (2004). doi: 10.1107/S0907444904019158; pmid: 15572765
55. N. W. Moriarty, R. W. Grosse-Kunstleve, P. D. Adams, electronic Ligand Builder and Optimization Workbench (eLBOW): A tool for ligand coordinate and restraint generation. *Acta Crystallogr. D* **65**, 1074–1080 (2009). doi: 10.1107/S0907444909029436; pmid: 19770504
56. W. L. DeLano, The PyMOL Molecular Graphics System (DeLano Scientific, 2002); www.pymol.org.
57. F. Madeira *et al*., The EMBL-EBI search and sequence analysis tools APIs in 2019. *Nucleic Acids Res.* **47**, W636–W641 (2019). doi: 10.1093/nar/gkz268; pmid: 30976793
58. C. Francke, H. P. Permentier, E. M. Franken, S. Neerken, J. Amesz, Isolation and properties of photochemically active reaction center complexes from the green sulfur bacterium *Prosthecochloris aestuarii*. *Biochemistry* **36**, 14167–14172 (1997). doi: 10.1021/bi9716837; pmid: 9369489

ACKNOWLEDGMENTS

All cryo-EM data were collected in the Center of Cryo-Electron Microscopy (CCEM), Zhejiang University. We thank C. Ma from the Protein facility, Zhejiang University School of Medicine, for sample purification; S. Schein for editing our manuscript; and the staff at the Analysis Center of Agrobiology and Environmental Sciences, Zhejiang University, for their help with the HPLC and UPLC-QTOF/MS experiments. **Funding:** This work was supported by the National Key Research and Development Program of China (2017YFA0504803 and 2018YFA0507700 to X.Z., 2017YFA0503700 to J.-R.S.), the Fundamental Research Funds for the Central Universities (2018XZZX001-13 to X.Z.), the Chinese Academy of Sciences Key Research Program of Frontier Sciences (QYZDY-SSW-SMC003 to J.-R.S.), a Strategic Priority Research Program of CAS (XDB17000000 to J.-R.S.), a National Basic Research Program of China (2015CB150100 to J.-R.S. and T.K.), and Natural Science Foundation of Zhejiang Province, China (LQ17C050001 to H.W.). **Author contributions:** T.K., J.-R.S., and X.Z. initialized and supervised the project, analyzed the data, interpreted the structures, and wrote the paper. J.-H.C. prepared the sample, analyzed data, built atomic models, interpreted the structures, prepared figures, and wrote the paper. C.X. and Z.H. collected and processed the data. H.W. analyzed data and prepared figures. S.C., W.W., and G.H. assisted in the sample preparation and quinone analysis. X.-C.L. participated in sample preparation and data collection. All authors discussed and commented on the results and the manuscript. **Competing interests:** The authors declare no competing interests. **Data and materials availability:** Atomic coordinates and the cryo-EM map have been deposited in the Protein Data Bank (PDB ID: 6M32) and the Electron Microscopy Data Bank (accession numbers and EMD-30069), respectively. All other data are presented in the main text or supplementary materials.

SUPPLEMENTARY MATERIALS

science.sciencemag.org/content/370/6519/eabb6350/suppl/DC1
Supplementary Text
Figs. S1 to S12
Table S1
References (*59*–*64*)
Movies S1 to S6
MDAR Reproducibility Checklist

View/request a protocol for this paper from *Bio-protocol*.

17 March 2020; accepted 9 September 2020
10.1126/science.abb6350

RESEARCH ARTICLE SUMMARY

NEURODEGENERATION

Autosomal dominant VCP hypomorph mutation impairs disaggregation of PHF-tau

Nabil F. Darwich*, Jessica M. Phan*, Boram Kim, EunRan Suh, John D. Papatriantafyllou, Lakshmi Changolkar, Aivi T. Nguyen, Caroline M. O'Rourke, Zhuohao He, Sílvia Porta, Garrett S. Gibbons, Kelvin C. Luk, Sokratis G. Papageorgiou, Murray Grossman, Lauren Massimo, David J. Irwin, Corey T. McMillan, Ilya M. Nasrallah, Camilo Toro, Geoffrey K. Aguirre, Vivianna M. Van Deerlin, Edward B. Lee†

INTRODUCTION: Alzheimer's disease (AD) is a fatal neurodegenerative disease in which progressive brain degeneration compromises cognitive function. AD neurodegeneration is tightly associated with abnormal neuronal inclusions called neurofibrillary tangles, which are composed of aggregated tau protein. The importance of tau protein in dementia is highlighted by various known autosomal-dominant mutations in *MAPT* (microtubule-associated protein tau), the gene that encodes for tau, that are associated with frontotemporal lobar degeneration with tau inclusions (FTLD-tau). Identifying additional disease-causing genes that affect tau accumulation, including genes involved in protein quality control and tau clearance, has the potential to reveal previously unknown mechanisms that maintain neuronal health.

RATIONALE: Two families were identified with autosomal-dominant dementia linked to a p.Asp395Gly mutation in *VCP*. Valosin-containing protein (VCP) is a AAA+ [adenosine triphosphatases (ATPases) associated with diverse cellular activities] protein and uses energy from adenosine 5′-triphosphate (ATP) hydrolysis to unfold substrates to assist the dismantling of macromolecular complexes. Other *VCP* mutations have been identified in a disease called multisystem proteinopathy (MSP), which is associated with neuronal TDP-43 [TAR DNA-binding protein 43] protein inclusions. The mechanisms by which p.Asp395Gly *VCP* leads to neurodegeneration are unknown.

RESULTS: Two kindred were identified with an autosomal-dominant inheritance pattern of frontotemporal degeneration linked to a p.Asp395Gly *VCP* mutation. We have named this disease vacuolar tauopathy because of the presence of neuronal vacuoles and tau aggregates. Tau aggregates were morphologically and biochemically similar to AD neurofibrillary tangles. Moreover, the presence of vacuoles and neurofibrillary tangles in the brain were inversely correlated. Degenerating brain regions such as the frontal neocortex exhibited tau aggregation, whereas nondegenerating brain regions such as the visual cortex exhibited vacuolization. To further characterize the p.Asp395Gly VCP mutation, we assessed recombinant VCP proteins for ATPase activity in an in vitro assay. This approach demonstrated that p.Asp395Gly VCP exhibited a partial loss of ATPase activity, in contrast with MSP mutations, which increase ATPase activity. Given that VCP unfolds protein substrates, we hypothesized that VCP may disaggregate pathologic tau aggregates. Indeed, VCP appeared to partially disaggregate pathologic tau aggregates derived from AD human brain tissues, and the p.Asp395Gly mutation impaired this activity. VCP activity against pathologic tau was energy (ATP) dependent and required polyubiquitination of the tau substrate. In addition, expression of p.Asp395Gly VCP in a cell culture model of tau aggregation was associated with enhanced accumulation of cellular tau aggregates. Last, we generated mice in which the p.Asp395Gly mutation was knocked in, which exhibited a minimal phenotype when unchallenged. However, upon initiating tau aggregation through microinjection of pathologic AD tau extracts into the mouse brain, mutant VCP mice showed an increase in tau accumulation compared with that of wild-type animals.

CONCLUSION: We describe a partial loss-of-function mutation in *VCP* that was associated with a neurodegenerative disease, which we named vacuolar tauopathy. VCP appeared to exhibit activity that promoted the disruption of tau aggregates in an energy- and polyubiquitin-dependent manner. Furthermore, the p.Asp395Gly VCP mutation enhanced tau aggregation in a cell culture model system and in a knock-in mouse model. These results highlight a potential role for protein disaggregation in the maintenance of neuronal health. Furthermore, our findings suggest that VCP may provide a potential therapeutic target in the development of future AD therapies. ■

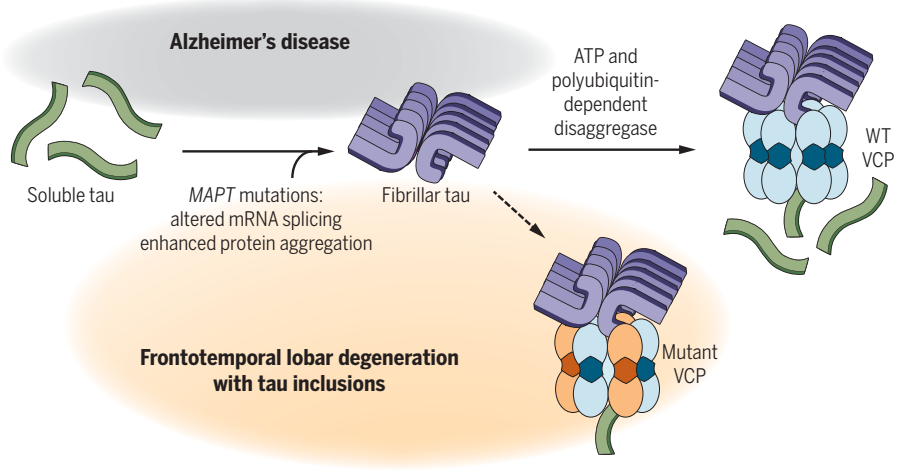

Vacuolar tauopathy and VCP function. Model of tau aggregation, highlighting different mechanisms that lead to neurodegeneration in AD and FTLD-tau. Tau is a soluble protein (green) that forms highly structured fibrils (purple) in AD. Tau aggregates are also a hallmark of FTLD-tau. Autosomal dominant FTLD-tau mutations in *MAPT*, the gene that encodes tau protein, can alter splicing or enhance tau protein aggregation, which results in the accumulation of insoluble tau inclusions in neurons and glia. VCP (blue) appears to exhibit disaggregase activity against pathologic tau. This activity is dependent on the availability of energy (ATP) and the presence of polyubiquitin on tau protein aggregates. Vacuolar tauopathy is an autosomal-dominant form of dementia linked to a p.Asp395Gly *VCP* mutation (orange-red). Neurodegeneration in vacuolar tauopathy was associated with tau aggregates of similar biochemical composition and morphology as those seen in Alzheimer's disease. The accumulation of insoluble tau aggregates in vacuolar tauopathy appeared to be in part due to a partial loss of tau disaggregase function associated with the p.Asp395Gly *VCP* mutation. WT, wild-type.

The list of author affiliations is available in the full article online.
*These authors contributed equally to this work.
†Corresponding author. Email: edward.lee@pennmedicine.upenn.edu
Cite ths article as N. F. Darwich *et al.*, *Science* **370**, eaay8826 (2020). DOI: 10.1126/science.aay8826

READ THE FULL ARTICLE AT
https://doi.org/10.1126/science.aay8826

RESEARCH ARTICLE

NEURODEGENERATION

Autosomal dominant VCP hypomorph mutation impairs disaggregation of PHF-tau

Nabil F. Darwich[1]*, Jessica M. Phan[1]*, Boram Kim[1], EunRan Suh[2], John D. Papatriantafyllou[3], Lakshmi Changolkar[2], Aivi T. Nguyen[1], Caroline M. O'Rourke[1], Zhuohao He[2]†, Sílvia Porta[2], Garrett S. Gibbons[2], Kelvin C. Luk[2], Sokratis G. Papageorgiou[4], Murray Grossman[5], Lauren Massimo[5], David J. Irwin[5], Corey T. McMillan[5], Ilya M. Nasrallah[6], Camilo Toro[7], Geoffrey K. Aguirre[5], Vivianna M. Van Deerlin[2], Edward B. Lee[1]‡

Neurodegeneration in Alzheimer's disease (AD) is closely associated with the accumulation of pathologic tau aggregates in the form of neurofibrillary tangles. We found that a p.Asp395Gly mutation in *VCP* (valosin-containing protein) was associated with dementia characterized neuropathologically by neuronal vacuoles and neurofibrillary tangles. Moreover, VCP appeared to exhibit tau disaggregase activity in vitro, which was impaired by the p.Asp395Gly mutation. Additionally, intracerebral microinjection of pathologic tau led to increased tau aggregates in mice in which p.Asp395Gly *VCP* mice was knocked in, as compared with injected wild-type mice. These findings suggest that p.Asp395Gly *VCP* is an autosomal-dominant genetic mutation associated with neurofibrillary degeneration in part owing to reduced tau disaggregation, raising the possibility that VCP may represent a therapeutic target for the treatment of AD.

Alzheimer's disease (AD) and other tauopathies are progressive and fatal neurologic diseases characterized by tau protein aggregation and neurodegeneration (*1*–*3*). Autosomal-dominant mutations that result in AD pathologies have been linked mechanistically to the production or aggregation of pathologic proteins (*4*). Less is known about which endogenous disaggregating factors play an etiologic role in neurodegenerative disease. Valosin-containing protein (VCP; also known as p97) is a member of the AAA+ protein family [adenosine triphosphatases (ATPases) associated with diverse cellular activities] (*5*, *6*) and uses the energy from adenosine 5′-triphosphate (ATP) hydrolysis to extract proteins from various macromolecular complexes (*7*). *VCP* is an essential gene and is expressed across central nervous system (CNS) cell types (*8*, *9*). We report here that the loss of VCP tau disaggregase function is associated with autosomal-dominant dementia, suggesting that impaired tau turnover can promote neurofibrillary degeneration.

[1]Translational Neuropathology Research Laboratory, Department of Pathology and Laboratory Medicine, Perelman School of Medicine at the University of Pennsylvania, PA, USA. [2]Center for Neurodegenerative Disease Research, Department of Pathology and Laboratory Medicine, Perelman School of Medicine at the University of Pennsylvania, PA, USA. [3]Medical Center of Athens, Memory Disorders Clinic and Day Care Center for Third Age "IASIS," Athens, Greece. [4]First University Department of Neurology, Eginiteio University Hospital, National and Kapodistrian University of Athens, Athens, Greece. [5]Department of Neurology, Perelman School of Medicine at the University of Pennsylvania, PA, USA. [6]Department of Radiology, Perelman School of Medicine at the University of Pennsylvania, PA, USA. [7]NIH Undiagnosed Diseases Program, National Human Genome Research Institute, MD, USA.
*These authors contributed equally to this work.
†Present address: Interdisciplinary Research Center on Biology and Chemistry, Shanghai Institute of Organic Chemistry, Chinese Academy of Sciences, Shanghai 201210, China.
‡Corresponding author. Email: edward.lee@pennmedicine.upenn.edu

Results

p.Asp395Gly VCP is associated with autosomal-dominant frontotemporal degeneration

We identified two families from the United States and Greece (*10*) with an autosomal-dominant inheritance pattern of frontotemporal degeneration (FTD) (Fig. 1, A and B). Targeted, exome, and whole-genome sequencing of the U.S. family identified a *VCP* mutation (c.1184A>G, p.Asp395Gly, NM_007126.5) in three affected family members that was absent in the unaffected parent (Fig. 1A and table S1). The Greek family also demonstrated an autosomal-dominant inheritance pattern of FTD, with p.Asp395Gly (c.1184A>G) *VCP* identified in the affected proband but absent in both unaffected siblings (Fig. 1B and table S1). Neither family exhibited muscle or bone disease. Whole-genome sequencing revealed that *VCP* c.1184A>G was the only rare (allele frequency <0.1%) protein coding variant shared by the three affected U.S. siblings and the Greek proband (table S2). Haplotype data extracted from whole-genome sequencing indicated that *VCP* c.1194A>G did not seem to originate from a common founder (Fig. 1C). *MAPT* (microtubule-associated protein tau) mutations were absent in both families.

Neuropathologic characterization of vacuolar tauopathy

An autopsy was performed on the U.S. proband. The brain weighed 1090 g and exhibited severe circumscribed frontal atrophy that was consistent with frontotemporal lobar degeneration (Fig. 1D). Microscopic analysis revealed marked gray matter neuronal vacuolization (Fig. 1E). Vacuoles appeared to be immunoreactive for the endocytic marker EEA1 (early endosome antigen 1) (Fig. 1E), with less than 1% of vacuoles positive for lysosomal markers (Fig. 1E, CD68 and Lamp1). VCP staining showed granular staining in the neuropil but was negative in vacuoles (Fig. 1E). Vacuoles were negative for markers of endoplasmic reticulum, multivesicular bodies, and autophagosomes (calnexin, CD63, and LC3B) (fig. S1A). Ultrastructural analysis revealed electron-lucent, membrane-bound vacuoles (Fig. 1E). These findings suggested that these vacuoles may be endocytic in origin, with rare vacuoles exhibiting lysosomal features.

Neuron loss affected the frontal, temporal, and parietal neocortices, together with abundant tau protein aggregates (Fig. 1F and fig. S1B). TDP-43 [TAR DNA-binding protein 43], Aβ, α-synuclein, and prion protein aggregates were absent (fig. S1, C and D). Tau protein aggregates were morphologically identical to the neurofibrillary tangles (NFTs) found in AD. Tau inclusions were strongly reactive with Thioflavin S (ThS) and Gallyas silver stain and were immunoreactive with antibodies specific to phosphorylated tau (PHF1), three-repeat tau, four-repeat tau, and ubiquitin (Fig. 1F and fig. S1E). Tau aggregates were also immunoreactive to GT-38, an antibody that recognizes a conformation specific to AD tau (Fig. 1F) (*11*). Accumulation of three-repeat and four-repeat sarkosyl-insoluble tau was confirmed biochemically, and VCP protein expression appeared normal (Fig. 1G and fig. S1F). Electron microscopy of biochemically extracted insoluble tau protein demonstrated paired helical filaments (PHFs) (Fig. 1F). Thus, the tau pathology of p.Asp395Gly *VCP* was characterized by accumulation of NFTs of similar composition to those found in AD.

Distribution of neuronal vacuolization and neurofibrillary degeneration

Neuronal vacuolization and neurofibrillary degeneration were inversely related (Fig. 2A). Regional analysis indicated that vacuoles were most prominent in the occipital neocortex with fewer vacuoles rostrally, in contrast with NFTs, which were most abundant in the frontal neocortex with fewer along a caudal gradient (Fig. 2B and fig. S1G). Reactive astrocytosis and microgliosis were seen in regions with neurofibrillary degeneration (Fig. 2, A and B, and fig. S1G). White matter was unaffected by vacuoles or tauopathy. Thus, in contrast with NFTs, vacuoles appeared not to be directly associated with degeneration, differentiating them from the vacuoles of prion disease, the rimmed vacuoles of inclusion body myopathy,

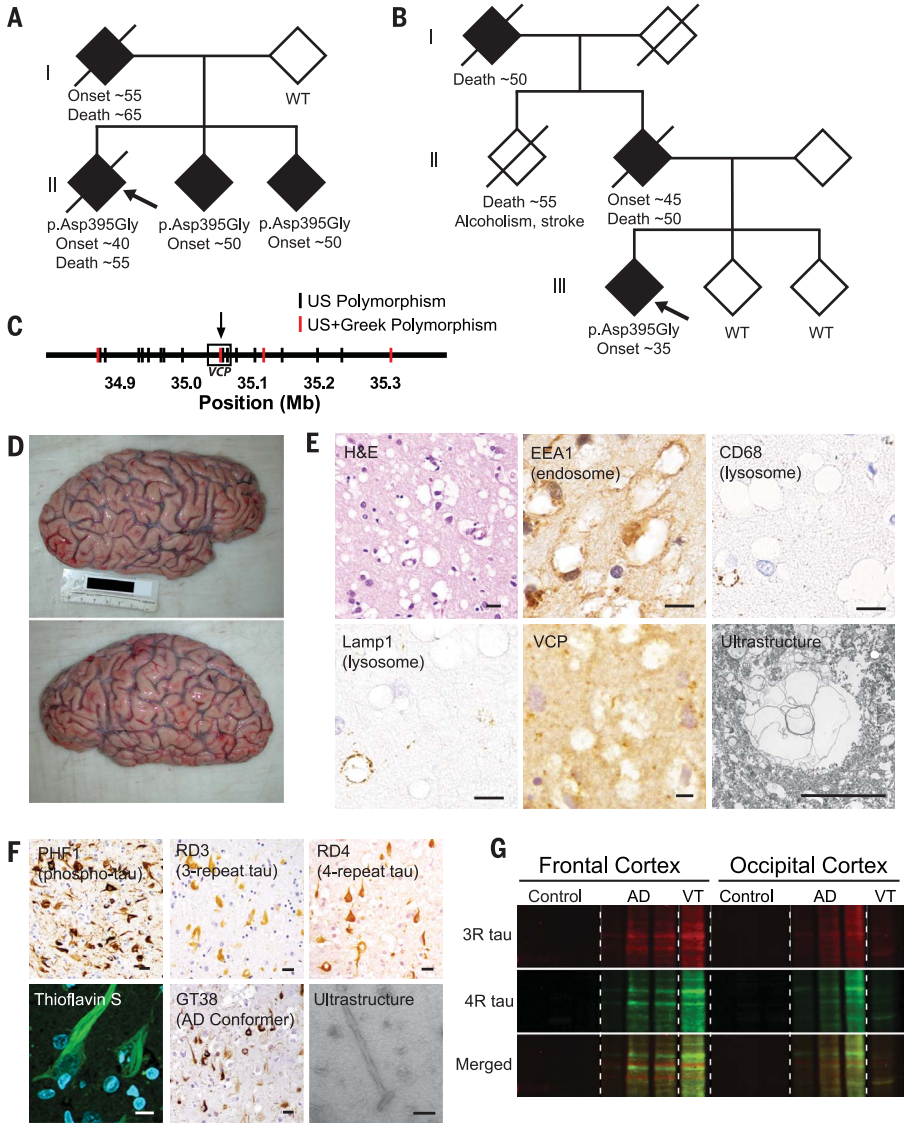

Fig. 1. p.Asp395Gly *VCP* is associated with VT. (**A** and **B**) Family pedigrees for the kindred from (A) the United States or (B) Greece showing an autosomal-dominant pattern of inheritance, with shaded shapes denoting individuals with FTD. *VCP* genotype and approximate age of disease onset and death are listed, if available. Proband is indicated with an arrow. (**C**) Distinct *VCP* haplotypes suggest absence of a common founder mutation. Genotype data was extracted from whole-genome sequencing in which polymorphisms shared between the three affected U.S. siblings but absent in their unaffected parent are in black, and polymorphisms that are additionally found in the affected Greek individual are indicated in red. *VCP* is designated by the box, with the arrow indicating the location of the p.Asp395Gly *VCP* mutation. (**D**) Gross photographs of VT brain showing circumscribed frontal atrophy. (**E**) Vacuolar neuropathology. Representative hematoxylin and eosin (H&E), antibody immunostain, or electron microscopic ultrastructure images are shown. Scales bars, 10 μm. (**F**) Neuropathology of tau aggregates. Representative antibody immunostain, ThS stain, or electron microscopic ultrastructure images are shown. Scale bars, 10 μm, except for electron microscopy, which is 200 nm. (**G**) Biochemical analysis of pathologic tau. Sarkosyl-insoluble frontal and occipital neocortex lysates from control, AD, or VT were immunoblotted for three-repeat (RD3, red) and four-repeat tau (anti-4R tau, green).

or the nonspecific microvacuolar superficial spongiosus common to many neurodegenerative diseases.

To confirm that p.Asp395Gly VCP was associated with tauopathy, magnetic resonance imaging (MRI) and ^{18}F-flortaucipir (formerly ^{18}F-AV-1451) positron emission tomography (PET) imaging was performed on a living affected sibling who demonstrated frontotemporal atrophy coinciding with tau tracer retention in a frontotemporal distribution (Fig. 2C and fig. S2). In addition, frontal cerebral biopsy of the affected Greek proband also confirmed the presence of tauopathy consisting of NFTs (Fig. 2D). Moreover, mean diffusivity (MD) from diffusion tensor imaging of the Greek proband demonstrated "cortical ribboning," most prominently affecting the occipital lobe, which is a known feature of vacuolated cortex (Fig. 2E) (*12*). Thus, vacuolar pathology was most prominent in caudal neocortical regions (Fig. 2F), which showed minimal radiologic and pathologic evidence of neurodegeneration. By contrast, tau accumulation correlated with cerebral atrophy, neuron loss, and reactive gliosis (Fig. 2G).

These atypical neuropathologic features, together with the absence of the p.Asp395Gly variant of *VCP* from multiple genetic databases [1000 Genomes Project, the Alzheimer's Disease Genetic Consortium, and the Genome Aggregation Database (gnomAD)], suggested that this mutation results in a distinct neurodegenerative disease that we have named vacuolar tauopathy (VT). Despite its distinctiveness, the similarities in morphology and composition of tau aggregates in VT and AD suggested that VCP may be involved in regulating the formation or dissolution of NFTs.

p.Asp395Gly VCP is a hypomorph mutation

Previously identified *VCP* mutations cause multisystem proteinopathy (MSP), a pleiotropic degenerative disease that affects the muscle, bone, and nervous system and sometimes manifests as frontotemporal lobar degeneration with TDP-43 inclusions (FTLD-TDP) (*13*–*15*). MSP mutations with autopsy confirmed that FTLD-TDP uniformly lie in the cleft between the N-terminal and D1 ATPase domains (Fig. 3A, cyan). Furthermore, these MSP mutations increase ATPase activity (*16*, *17*) and unfolding activity (*18*, *19*), suggesting that MSP is associated with gain-of-function *VCP* mutations.

By contrast, p.Asp395Gly *VCP* appeared to be associated with tauopathy in the absence of muscle or bone disease, and the mutation is found within the lid subdomain of the D1 ATPase domain (Fig. 3A, red). Amino acid position 395 is the N-cap of a short α-helix. Because the N-cap of an α-helix does not have amino acids above for hydrogen bonding, the helix is stabilized by the N-cap's side chain hydrogen bonding within the interior of the α-helix. Aspartic acid (D) is among the most stabilizing of N-cap amino acids, whereas glycine (G) is destabilizing (*20*, *21*). Asp395 is conserved from humans to plants to bacteria (Fig. 3B). Furthermore, position-specific scoring matrix (PSSM) scores for position 395 were calculated for VCP and its homologs (Fig. 3C). The positive PSSM score suggested that D has been evolutionarily selected and is functional at this position. The gnomAD database contains a single instance of the relatively conservative p.Asp395Glu variant, which is of uncertain

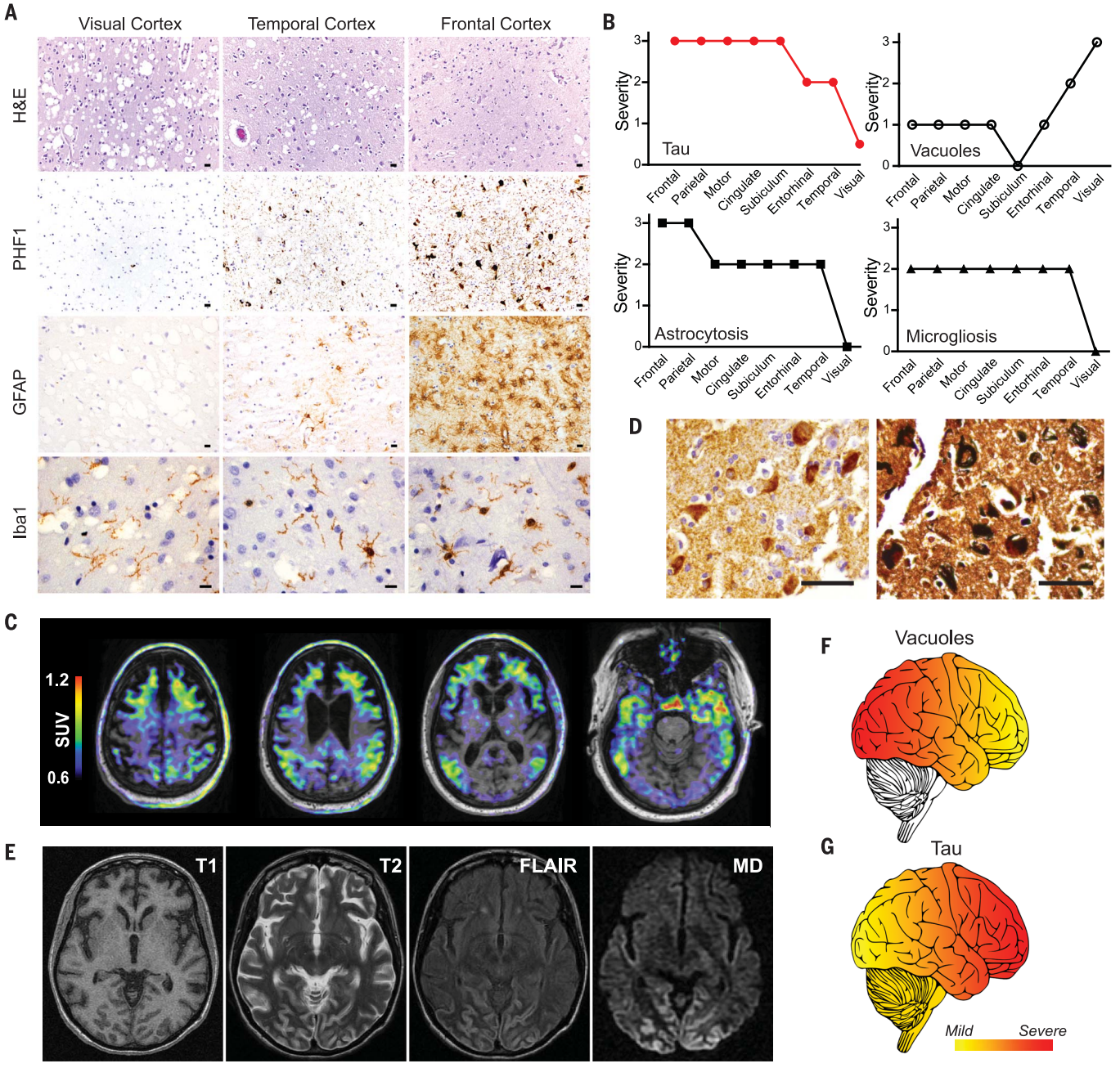

Fig. 2. Inverse regional relationship between vacuoles and neurofibrillary degeneration in VT. (**A**) Rostral to caudal gradient of vacuoles versus neurofibrillary degeneration. Representative H&E, PHF1 (phospho-tau), GFAP (astrocyte), and Iba1 (microglia) stained images from occipital-visual, temporal, and frontal neocortical regions are shown. Scale bars, 10 μm. (**B**) Regional scoring of tau accumulation, vacuoles, astrogliosis, and microgliosis. Cortical brain regions were scored for severity of tau (red), vacuoles (circles), astrogliosis (squares), and microgliosis (triangles). Severity scores ranged from 0 (none) to 3 (severe). (**C**) Neuroimaging of affected kindred. Overlaid T1-weighted MRI and tau PET images from affected p.Asp395Gly VCP carrier pseudocolored to standard uptake values (SUVs). (**D**) Cerebral biopsy of Greek proband demonstrates NFTs. Shown are representative images of AT8 (phospho-tau, left) and Gallyas silver (right) stained sections from a frontal neocortex biopsy. Scale bars, 50 μm (left) and 20 μm (right). (**E**) Neuroimaging of Greek proband. MRI neuroimaging images are shown, including T1, T2, fluid-attenuated inversion recovery (FLAIR), and MD from diffuse tensor imaging. (**F** and **G**) Schematic showing the distribution of (F) vacuole or (G) tau pathology is illustrated (yellow, mild; red, severe), where vacuoles were most severe in caudal neocortical regions in contrast with tau aggregates, which were most severe in rostral neocortical regions.

significance given its rarity and the lack of accompanying phenotype data. By contrast, the negative PSSM score associated with glycine (G) at this position has been evolutionarily selected against and may be detrimental to VCP function. Multiple in silico analyses predicted that p.Asp395Gly has a deleterious effect on VCP function (fig. S3A). In addition to being conserved among VCP homologs, this residue is found in the same corresponding lid subdomain location of several AAA+ ATPase domains (Fig. 3D), including the D2 ATPase domain of VCP, NSF, and Rix7. Overall, these analyses suggested that Asp395 may be important for VCP function.

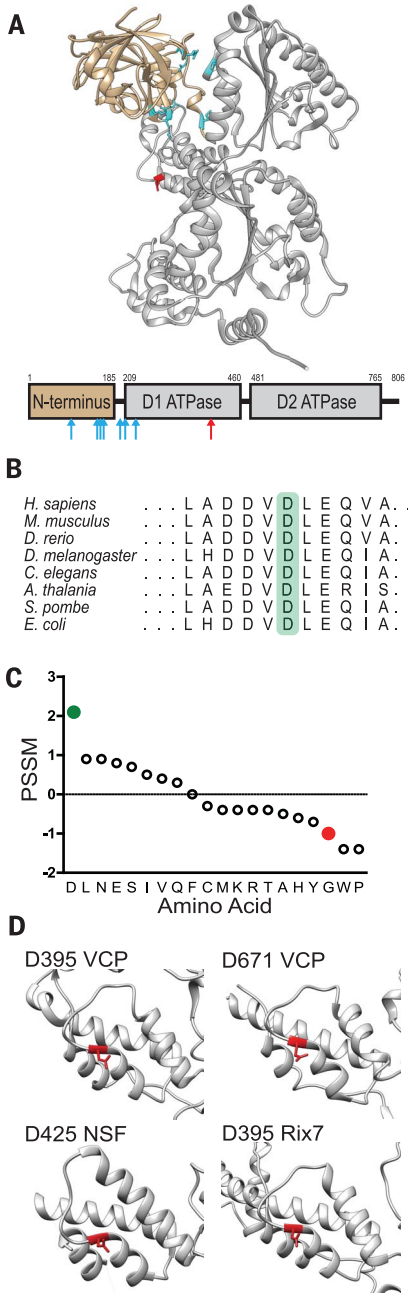
A
1
185
209
460
481
765
806
N-terminus
D1 ATPase
D2 ATPase
B
H. sapiens . . . L A D D V D L E Q V A. .
M. musculus . . . L A D D V D L E Q V A. .
D. rerio . . . L A D D V D L E Q V A. .
D. melanogaster . . . L H D D V D L E Q I A. .
C. elegans . . . L A D D V D L E Q I A. .
A. thalania . . . L A E D V D L E R I S. .
S. pombe . . . L A D D V D L E Q I A. .
E. coli . . . L H D D V D L E Q I A. .
C
PSSM
3
2
1
0
-1
-2
D L N E S I V Q F C M K R T A H Y G W P
Amino Acid
D
D395 VCP
D671 VCP
D425 NSF
D395 Rix7

Fig. 3. In silico analysis of D395 *VCP*.
(**A**) Structure of VCP monomer. N-terminal domain is tan, D1 and D2 ATPase domains are gray, MSP mutations are cyan, and VT mutation is red (PDB 5C19). The primary structure of VCP is underneath with the same color scheme; mutations are indicated with arrows. (**B**) Conservation of D395 VCP across species (highlighted in green). (**C**) PSSM scores for conservation in *VCP* homologs for amino acids, including aspartic acid (D, green) and glycine (G, red). (**D**) Common aspartic acid N-cap in AAA+ proteins. The structures of several AAA+ proteins are shown with D395, or its equivalent, indicated in red (VCP PDB 5C19, NSF PDB 1NSF, Rix7 PDB 6MAT).

To determine the effect of p.Asp395Gly on VCP activity, we performed Michaelis-Menten enzyme kinetics on purified recombinant VCP proteins (Fig. 4A and fig. S3B, UniProtKB: Q01853). As expected, the MSP mutation p.Asp232Glu increased VCP ATPase activity (Fig. 4A, MSP, blue) compared with wild type (Fig. 4A, black), whereas the D2 mutation p.Glu578Gln (Walker B mutation in the D2 ATPase domain) that inactivates ATPase hydrolysis decreased VCP ATPase activity (Fig. 4A, dark red). The p.Asp395Gly mutation decreased VCP ATPase activity (Fig. 4A, red), resulting in a 30.3% reduction in maximum velocity (V_{max}) (Fig. 4B) and no significant change in Michaelis constant (K_m) (Fig. 4C).

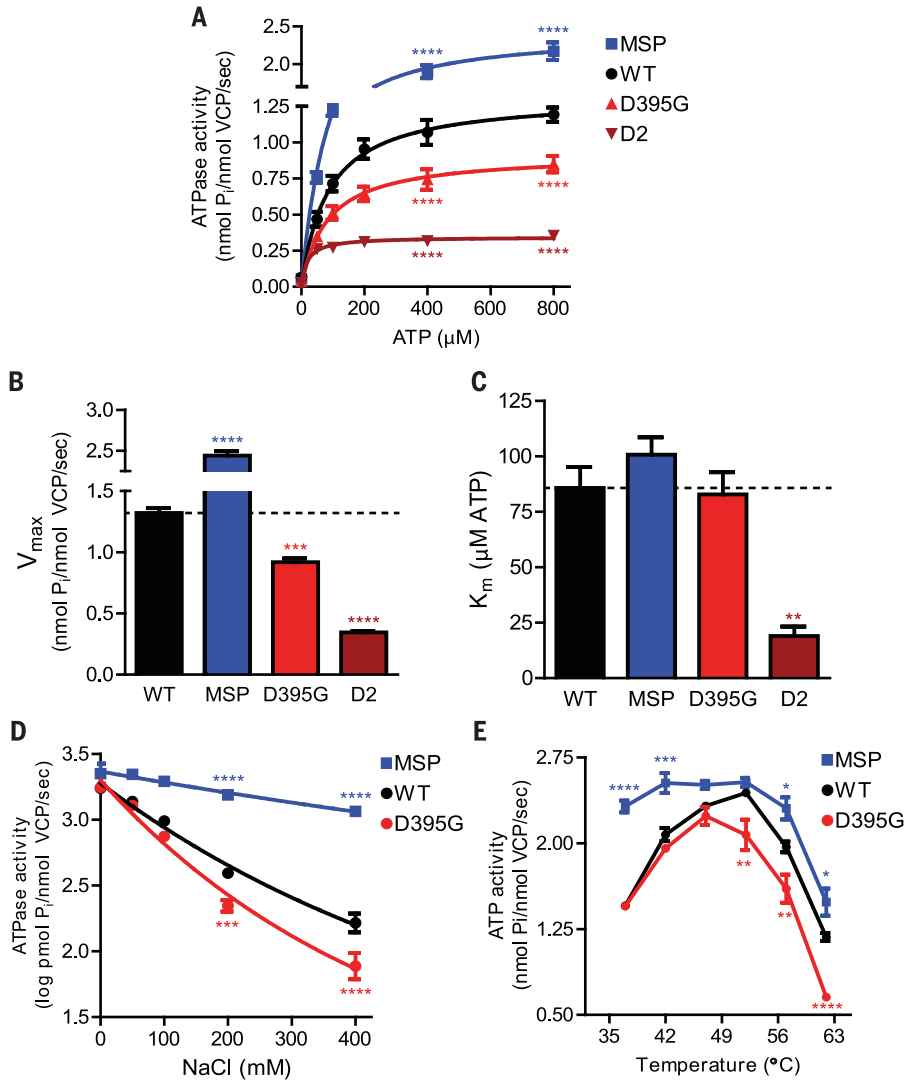

Fig. 4. ATPase activity of mutant VCP proteins. (**A**) Michaelis-Menten kinetic ATPase analysis. Recombinant WT, MSP, p.Asp395Gly, and D2 VCP proteins were assessed for ATPase activity over a range of ATP concentrations (n = 3 replicates). ATPase activity shown as mean ± SEM (two-way ANOVA: mutation $P < 0.0001$; ATP $P < 0.0001$; interaction $P < 0.0001$; Bonferroni posthoc shown for only 400 and 800 μM ATP ****$P < 0.0001$). (**B**) V_{max} values and (**C**) K_m from Michaelis-Menten kinetics (n = 3 replicates). Data are shown as mean ± SEM (one-way ANOVA: V_{max} $P < 0.0001$; K_m $P = 0.0005$; Bonferroni posthoc **$P < 0.01$, ***$P < 0.001$, ****$P < 0.0001$). (**D**) Salt denaturation of recombinant VCP proteins. VCP ATPase activity was assessed across NaCl concentrations (n = 5 replicates). ATPase activity is shown as mean ± SEM (two-way ANOVA: mutation $P < 0.0001$; NaCl $P < 0.0001$; interaction $P < 0.0001$; Bonferroni posthoc shown for only 200 and 400 mM NaCl ***$P < 0.001$, ****$P < 0.0001$). (**E**) Heat activation and denaturation of recombinant VCP proteins. VCP ATPase activity was assessed across temperature (n = 3 replicates). ATPase activity is shown as mean ± SEM (two-way ANOVA: mutation $P < 0.0001$; temperature $P < 0.0001$; interaction $P < 0.0001$; Bonferroni posthoc *$P < 0.05$, **$P < 0.01$, ***$P < 0.001$, ****$P < 0.0001$).

We hypothesized that p.Asp395Gly may result in local protein destabilization that may manifest as enhanced sensitivity to denaturation. Thus, we tested recombinant VCP proteins for ATPase activity in the presence of increasing salt concentration (Fig. 4D and fig. S3C). MSP mutant protein was relatively resistant to salt denaturation, whereas p.Asp395Gly mutant protein displayed increased sensitivity to salt denaturation. We also tested the ATPase activity of VCP with increasing temperature. VCP is known to heat-activate before heat-inactivating at higher temperatures because of denaturation (Fig. 4E, black, and fig. S3C) (*22*). Although MSP mutant protein heat inactivated at a similar temperature compared with WT VCP protein, p.Asp395Gly mutant protein heat inactivated at lower temperatures. Overall, these data supported the hypothesis that p.Asp395Gly is a hypomorph mutation.

ATP- and polyubiquitin-dependent PHF-tau disaggregase

Recent studies have demonstrated that VCP can unfold protein substrates in an ATP-dependent manner (*18*, *19*, *23*–*26*). Immunohistochemistry of VT brain demonstrated granular VCP staining adjacent to but excluded from NFTs (Fig. 5, A and C). By contrast, AD tissues showed wild-type (WT) VCP localized to NFTs, dystrophic neurites within neuritic plaques, and tau-positive neuropil threads (Fig. 5, B and C), raising the possibility that VCP interacts with pathologic tau in AD.

Because VCP colocalizes with tau aggregates in AD and the partial loss-of-function p.Asp395Gly mutation is associated with tau accumulation, we hypothesized that VCP may be a tau disaggregase. To assess this, we treated pathologic tau aggregates purified from human AD brain tissue (*27*) with recombinant VCP protein together with VCP cofactors (UFD1L and NPLOC4) (fig. S3, B and D) and either ATP or ATPγS, a nonhydrolyzable ATP analog. Tau aggregate levels were measured by using ThS, which undergoes a fluorescence shift when bound to pathologic tau fibrils (*28*). VCP exhibited a 30.1% ATP-dependent reduction in ThS signal (Fig. 5D). Furthermore, the gain-of-function MSP mutant protein (blue) led to a further decrease of ThS signal, whereas the loss-of-function p.Asp395Gly (red) and D2 mutant (maroon) proteins led to increased ThS signal (16.3% decrease versus 23.0 and 30.0% increases, respectively) (Fig. 5E).

Recent structural evidence suggests that VCP is a ubiquitin-dependent segregase that requires at least five conjugated polyubiquitins (*25*, *26*). We predicted that VCP would not have activity against recombinant protein aggregates because of the absence of polyubiquitination. In vitro aggregated recombinant tau, α-synuclein, or TDP-43 were incubated with VCP, VCP cofactors, and either ATP or ATPγS, which demonstrated that VCP had no activity against recombinant protein aggregates on the basis of ThS signal or sedimentation analysis (Fig. 5F and fig. S3E). Rather, VCP appeared to require polyubiquitin for substrate recognition because addition of monoclonal antibodies specific to ubiquitin (αUb) was able to block VCP activity against AD tissue–derived pathologic tau, whereas nonspecific isotype control antibodies had no effect (Fig. 5G). Similarly, addition of recombinant polyubiquitin (pUb) blocked VCP activity, whereas recombinant mono-ubiquitin (mUb) did not block VCP activity (Fig. 5G). These data suggested that polyubiquitin mediates substrate recognition by VCP.

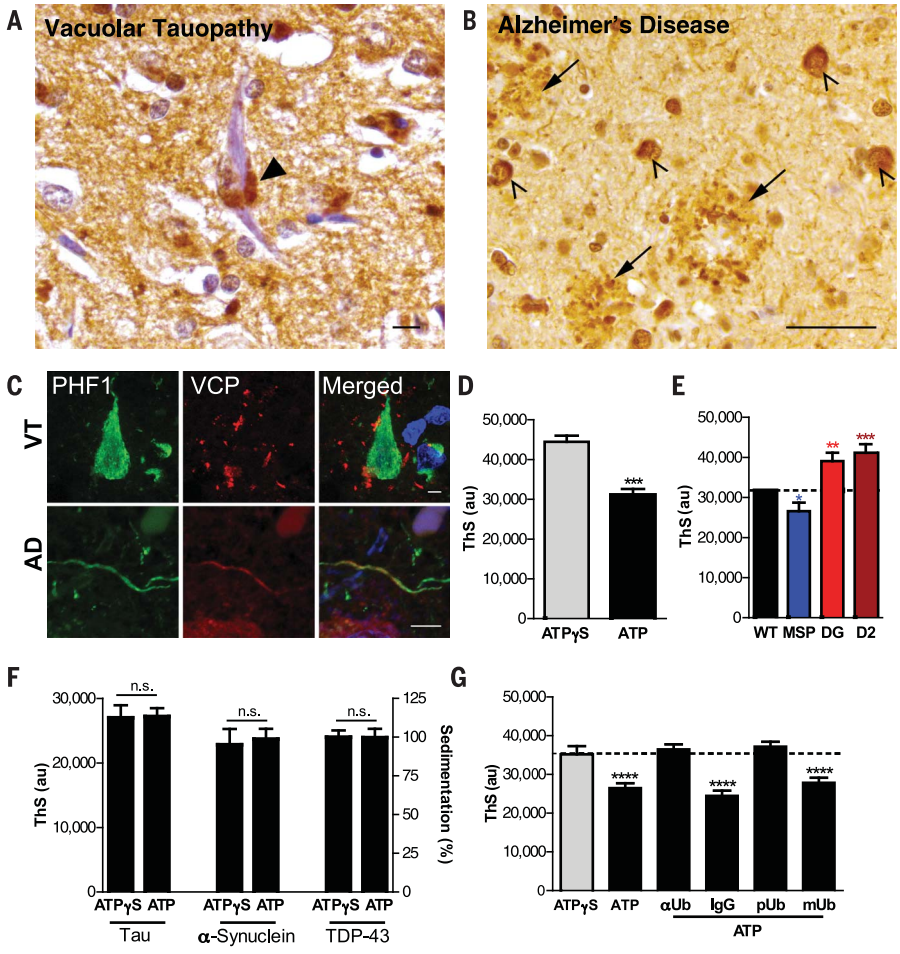

Fig. 5. ATP- and polyubiquitin-dependent tau disaggregase activity of VCP. (**A**) VT neocortex showing granular VCP immunostaining (arrowhead) adjacent to a NFT. Scale bar, 10 μm. (**B**) AD neocortex showing VCP immunostaining within NFTs (arrows) and dystrophic neurites in neuritic plaques (arrowheads). Scale bar, 50 μm. (**C**) Localization of VCP and tau in human VT and AD tissues. Double immunofluorescence of VCP (green) and PHF1 (phospho-tau, red) in VT (top) and AD (bottom). Scale bars, 5 μm. (**D**) Recombinant VCP activity against pathologic PHF-tau. Shown is ThS fluorescence after incubation of human AD tissue–derived pathologic tau with recombinant VCP, UFD1, NPLOC4, and either ATPγS or ATP (n = 5 replicates). ThS signal is shown as mean ± SEM (two-tailed t test, ***P = 0.0003). (**E**) Mutant VCP activities against pathologic PHF-tau. Shown is ThS fluorescence after incubation of pathologic tau with recombinant WT, MSP, p.Asp395Gly (DG), or D2 VCP (n = 5 replicates). ThS signal is shown as β ± SEM (mixed effects model, MSP *P = 0.0272; **DG P = 0.0036; ***D2 P = 0.0005). (**F**) VCP activity against recombinant protein aggregates. Recombinant tau, α-synuclein, or TDP-43 aggregates were incubated with VCP, VCP cofactors, and ATPγS or ATP. ThS fluorescence signal is shown as a mean ± SEM for tau (n = 3 replicates) and α-synuclein (n = 3 replicates). Sedimentation data are shown as mean percent of average of ATPγS samples ± SEM for TDP-43 (n = 5 replicates). Pairwise testing with two-tail t test resulted in nonsignificance (n.s.). (**G**) Polyubiquitin-dependence of VCP activity against pathologic PHF-tau. Shown is ThS fluorescence after addition of anti-ubiquitin monoclonal antibody (αUb), nonspecific isotype control (IgG), recombinant polyubiquitin (pUb), or recombinant monoubiquitin (mUb) to VCP, VCP cofactors, pathologic tau, and ATP (black with underline, n = 5 replicates). Reactions with only VCP, VCP cofactors, pathologic tau, and either ATP or ATPγS (black and gray bar, respectively) were run in parallel as controls. ThS fluorescence signal is shown as β ± SEM (mixed effects model: ATP, αUb, pUb ****P < 0.0001).

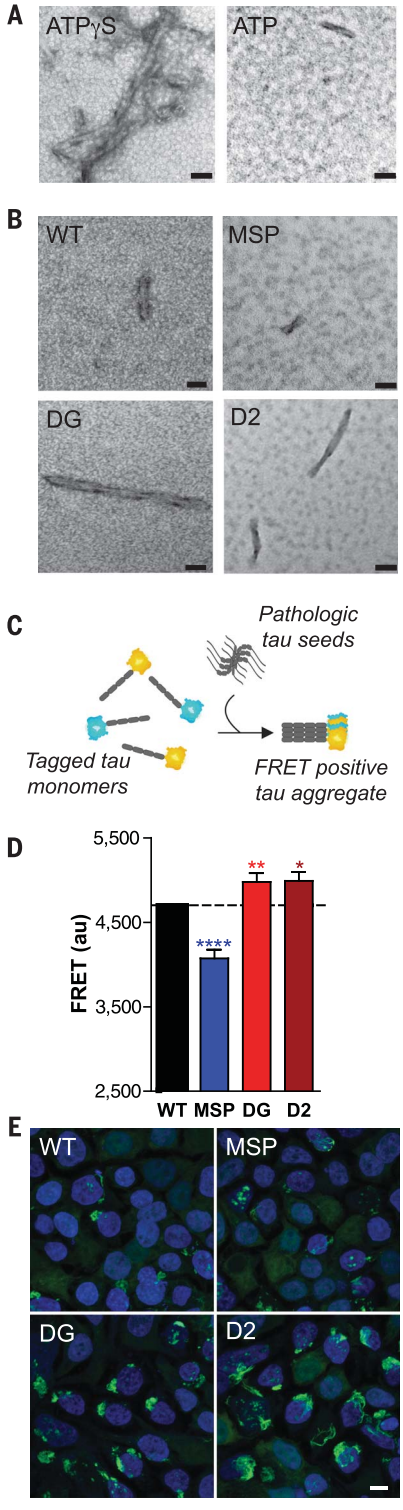

Fig. 6. VCP activity against pathologic tau fibrils and cellular tau aggregates. (**A**) Electron microscopy of human AD tissue–derived PHF tau fibrils after treatment with recombinant VCP, UFD1, NPLOC4, and either ATPγS or ATP (n = 3 replicates). Scales bars, 50 nm. (**B**) Electron microscopy of VCP tau disaggregase reactions with recombinant WT VCP protein versus MSP, p.Asp395Gly (DG), and D2 mutant VCP proteins (n = 3 replicates). Scales bars, 50 nm. (**C**) Schematic of tau seeding in tau biosensor cells. (**D** and **E**) Biosensor cells expressing WT or mutant VCP were transduced with human AD tissue–derived pathologic tau (n = 5 replicates). (D) FRET signal was assessed by means of flow cytometry and shown as β ± SEM (mixed effects model: MSP ****P < 0.0001; **DG P = 0.0095, *D2 P = 0.0126). (E) Representative confocal fluorescence microscopy images of biosensor cells with intracellular tau aggregates (green) and 4′,6-diamidino-2-phenylindole (DAPI) nuclear counterstain (blue). Scale bar, 10 μm.

To provide orthogonal evidence for VCP activity against PHF tau, disaggregase reactions were examined by means of negative-staining electron microscopy, which revealed that VCP reduced the abundance of pathologic tau fibrils in an ATP-dependent manner (Fig. 6A) that was partially mitigated by the p.Asp395Gly mutation (Fig. 6B). These data suggested that VCP exhibits an ATP-dependent disaggregase activity against pathologic tau aggregates derived from human AD brain. Furthermore, tau disaggregase activity of VCP mutant proteins appeared to correlate with ATPase activity in that the gain-of-function MSP mutation increased VCP tau disaggregase activity, whereas loss-of-function VT and D2 mutations decreased VCP tau disaggregase activity.

To confirm that VCP affects tau aggregates, we used a biosensor cell line engineered to develop intracellular aggregates upon seeding with proteopathic tau (*29*). When introduced to these cells, pathologic tau aggregates nucleate the aggregation of tau reporter proteins, resulting in a fluorescence resonance energy transfer (FRET) signal as a measure of intracellular tau aggregation (Fig. 6C). Biosensor cells overexpressing WT or mutant forms of VCP were transduced with AD brain–derived tau. Relative to WT VCP, biosensor cells expressing p.Asp395Gly VCP exhibited higher FRET signal and increased intracellular tau aggregation, similar to what was observed with the ATPase-deficient D2 mutant VCP (Fig. 6D). By contrast, biosensor cells expressing MSP mutant VCP exhibited reduced FRET signal and reduced intracellular tau aggregation (Fig. 6D). Confocal microscopy of biosensor cells confirmed that cells expressing p.Asp395Gly VCP exhibited increased intracellular tau aggregates (Fig. 6E).

Tau accumulation in p.Asp395Gly knock-in mice

To confirm our in vitro findings and to test p.Asp395Gly *VCP*'s role in tau pathogenesis, we generated a mutant mouse line in which p.Asp395Gly was knocked-in (DG) by use of CRISPR-Cas9 (fig. S4A) (*30*). Although DG mice exhibited decreased litter size, non-Mendelian breeding, and mildly decreased 1-year survival (fig. S4, B to D), no overt neurodegeneration was observed. RNA-sequencing revealed essentially no significantly altered transcripts in DG mice (fig. S4, E to G), and biochemical and immunohistochemical analysis did not reveal changes in VCP, tau, and other proteostasis related factors (p62, EEA1, LC3, and ubiquitin) (fig. S4, H and I). Thus, mutant p.Asp395Gly *VCP* did not result in any overt CNS developmental phenotype and appeared to be insufficient to initiate tau aggregation, which was consistent with our hypothesis that VCP acts as a disaggregase downstream of tau aggregation, which does not occur spontaneously in mice.

To initiate tau aggregation, 3-month-old +/+, DG/+, and DG/DG mice (WT, heterozygous, and homozygous p.Asp395Gly, respectively) were stereotaxically microinjected intracerebrally with pathologic AD tau in the dorsal hippocampus and overlying cortex and assessed 3 months after injection for tau pathology. Semiquantitiative scores of AT8-positive tau aggregates were used to generate brain heat maps to visualize the distribution and severity of tau pathology. Although the distribution of tau pathology was similar across all genotypes (Fig. 7A), DG/+ and DG/DG mice appeared to exhibit more tau pathology in several brain

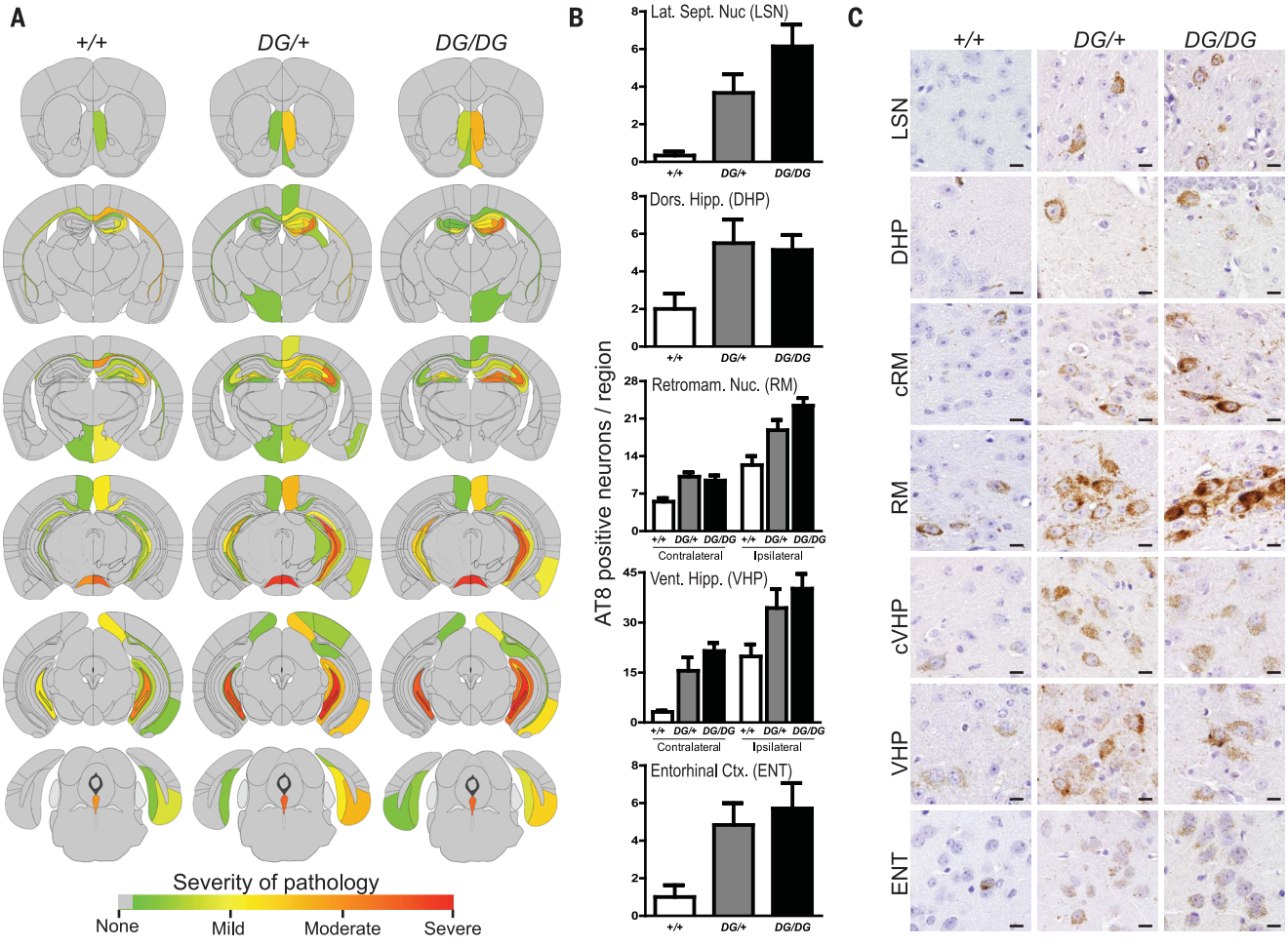

Fig. 7. p.Asp395Gly VCP exacerbates tau pathology in vivo. (**A**) Semiquantitative analysis of AT8-positive phospho-tau pathology. Shown are 6-month old WT (+/+), heterozygous p.Asp395Gly (DG/+), and homozygous p.Asp395Gly (DG/DG) knock-in mice analyzed 3 months after injection of pathologic tau in the right dorsal hippocampus and overlying cortex (n = 6 or 7 mice per genotype). Semiquantitative scores were averaged across mice of the same genotype and mapped onto coronal brain maps (gray = no pathology, red = severe pathology). (**B**) Regional quantitative analysis of AT8-positive phospho-tau pathology. The number of AT8-positive neurons was counted across different brain regions, shown as β ± SEM (mixed effects model: DG/+ P = 0.0005; DG/DG P < 0.0001). (**C**) Tau pathology in p.Asp395Gly knock-in mice. Representative AT8 immunostained images are shown. Scale bars, 10 μm. LSN, lateral septal nucleus; DHP, dorsal hippocampus; RM, retromammillary nucleus; VHP, ventral hippocampus; ENT, entorhinal cortex; c, contralateral.

regions. Selected brain regions that are neuroanatomically connected to the injection site were then quantitatively assessed for AT8-positive tau aggregates. DG/+ and DG/DG mice demonstrated an increase in the number of affected neurons across all examined regions (Fig. 7B). More severe pathology was present in both anterior and posterior regions as well as in connected regions contralateral to the injection site (Fig. 7, B and C). A mixed-effects linear regression model demonstrated that DG/+ and DG/DG mice exhibited significantly more AT8-positive neurons relative to those of WT mice (DG/+, P = 0.0005; DG/DG, P < 0.0001) (fig. S5, A and B). Iba1 and glial fibrillary acidic protein (GFAP) immunohistochemical staining showed minimal to no reactive gliosis in response to accumulation of tau aggregation because this paradigm specifically models tau aggregation without confounding downstream neurodegeneration (fig. S5C). Moreover, injecting VCP mutant mice with control human brain lysates or AD lysates that were immunodepleted of tau did not induce tau aggregation (fig. S5D). These data indicated that p.Asp395Gly *VCP* exacerbates tau pathology in vivo and were consistent with our in vitro data, suggesting that VCP may function as a pathologic tau disaggregase.

Discussion

We report a genetic mutation that impairs tau aggregate turnover, resulting in neurodegeneration, that is distinct from previously described genetic mutations linked to the production or aggregation propensity of tau. We posit that neurons in VT are at increased susceptibility to tau aggregation, resulting in downstream neurodegeneration. This also represents an instance of convergent allelic heterogeneity in which different mutations of a single gene (*VCP*) result in different underlying diseases (VT versus MSP) that can manifest with the same clinical phenotype (FTD). Moreover, our data suggest that VCP can function as a tau disaggregase and that a mutation in the lid subdomain can impair VCP ATPase and tau disaggregase activity. Because the lid subdomain is highly conserved across VCP homologs, understanding the structure and function of the lid subdomain may further our understanding of the dynamic processes that underlie VCP disaggregase activity. Last, although much attention has been afforded to the biosynthetic and aggregation pathways that lead to abnormal protein inclusions in AD and related disorders, these findings indicate that disaggregation

pathways may play a causal role in neurodegeneration and suggests that modulating VCP activity may represent a new therapeutic target for the treatment of AD and other tauopathies.

Materials and methods

Cloning and mutagenesis

N-terminal histidine tagged wild-type VCP was obtained from Addgene (plasmid #12373, gift from Axel Brunger). Untagged NPLOC4 (pCOLA-Duet, Novagen, NcoI/EcoR1) and N-terminal histidine tagged UFD1 (pET-Duet, Novagen, NcoI/HindIII) were obtained from Hermann Schindelin. Full-length human tau was inserted in pRK172 vector using NdeI/EcoR1, full-length human α-synuclein was inserted in pRK172 vector using NdeI/HindIII, and full-length human TDP-43 with a C-terminal histidine tag was inserted in pCOLD vector (CNDR, University of Pennsylvania). QuikChange II site-directed mutagenesis kit (Agilent Technology) was used to generate desired mutations. Plasmid sequences were confirmed with Sanger sequencing.

Recombinant protein purification

For VCP, plasmids were transformed into *Escherichia coli* Rosetta (DE3) cells (Novagen) following manufacturer's instructions. Cells were grown in Terrific Broth supplemented with kanamycin and induced at OD_{600} ~0.600 with 1 mM IPTG for 18 hours at 15°C. Cells were collected by centrifugation at 4,000×g for 15 min at 4°C and then resuspended in lysis buffer (100 mM Tris pH 7.4, 500 mM KCl, 5 mM $MgCl_2$, 1 mM ATP, 5% glycerol, 2 mM β-mercaptoethanol, 20 mM imidazole, 1 mg/mL lysoszyme, EDTA-free Complete Protease Inhibitor (Roche)) for 30 min at 4°C. Following sonication, lysates were cleared by centrifugation at 27,500×g for 30 min at 4°C. 2.5 mL of Ni-NTA Agarose (Qiagen) was added to the supernatant and nutated for 30 min at 4°C. The resin was washed three times with 20 mL of wash buffer 1 (50 mM HEPES pH 7.4, 150 mM KCl, 5 mM $MgCl_2$, 1 mM ATP, 5% glycerol, 2 mM β-mercaptoethanol, EDTA-free Complete Protease Inhibitor (Roche)) and then three additional times with 20 mL of wash buffer 2 (1 M KCl in wash buffer 1). VCP was eluted with 350 mM imidazole in wash buffer 1. Elute was concentrated using an Amicon Ultra-15 centrifugal unit (Millipore) and loaded onto a precalibrated Superose-6 gel filtration column (GE Healthcare) at 4°C. 0.5 mL fractions were collected in 50 mM HEPES pH 7.5, 150 mM NaCl, 2 mM $MgCl_2$, 5% glycerol, 1 mM β-mercaptoethanol. Protein concentrations was determined using the Bradford Assay (Bio-Rad). Fractions were then concentrated to 5 mg/mL using an Amicon Ultra–0.5 mL centrifugal unit (Millipore), snap frozen, and stored in liquid nitrogen. Additionally, expression plasmid was isolated from each protein preparation and confirmed by Sanger sequencing. Each preparation's purity was assessed by gel electrophoresis.

For UFD1L and NPLOC4, plasmids were expressed similarly to VCP. Cultures were combined and then lysed in lysis buffer (50 mM Tris pH 7.4, 500 mM KCl, 5 mM $MgCl_2$, 5% glycerol, 2 mM β-mercaptoethanol, and 20 mM imidazole). Purification was identical to VCP except resin was washed with lysis buffer then eluted with lysis buffer plus 300 mM imidazole. Elute was loaded onto a Superdex 200 Increase 10/300 GL (GE Healthcare) column precalibrated with 20 mM HEPES pH 7.4, 250 mM KCl, 1 mM $MgCl_2$, 5% glycerol, and 1 mM β-mercaptoethanol.

For tau, plasmids were expressed in *E. coli* BL21 (DE3) cells (Agilent Technology). After induction, bacterial pellets were resuspended in 100 mM MES pH 7.5, 750 mM NaCl, 2 mM NaF, 1 mM EGTA, 0.5 mM $MgSO_4$, 1 mM PMSF, and protease inhibitors and then heated to 100°C for 10 min and centrifuged at 70,000×g for 30 min. Supernatants were then dialyzed into 20 mM piperazine-N,N'-bis(2-ethanesulfonic acid) pH 6.5, 10 mM Nacl, 1 mM EGTA, 1 mM $MgSO_4$, 2 mM DTT, 0.1 mM PMSF and then separated on a HiTrap Sepharose HP IEX cation-exchange column (GE Healthcare) and eluted with a 0 to 400 mM NaCl gradient.

For α-synuclein, plasmids were expressed in *E. coli* BL21 (DE3) cells (Agilent Technologies). Bacterial pellets were then resuspended in 50 mM Tris pH 7.4, 750 mM NaCl, 1 mM EDTA, and protease inhibitors, and then heated to 100°C for 10 min, and centrifuged at 70,000×g for 30 min. Supernatants were separated using a Superdex 200 gel filtration column (GE Healthcare). Fractions containing α-synuclein were concentrated using a Centriprep-10 (Millipore), dialyzed in 10 mM Tris pH 7.5, and subsequently separated on a Mono Q column (Amersham Pharmacia Biotech) and eluted with a 0 to 500 mM NaCl gradient.

For TDP-43, plasmids were expressed in *E. coli* BL21 (DE3)-RIL cells (Agilent Technologies). Bacterial pellets were lysed in 20 mM sodium phosphate pH 7.8, 4 M urea, 500 mM NaCl. Solubilized protein was then bound onto a Ni-NTA column (Qiagen) and eluted with 20 mM sodium phosphate pH 7.8, 4 M urea, 500 mM NaCl and 200 mM imidazole prior to dialyzing into 20 mM Tris pH 8.0, 1M NaCl, 10 mM $MgCl_2$, 1 mM $CaCl_2$, and 50% glycerol.

Recombinant poly- and mono-ubiquitin were purchased (rPeptide).

Recombinant protein aggregation

Recombinant proteins were aggregated as previously described (*31*, *32*). Recombinant α-synuclein at 5 mg/ml in PBS pH 7.0 was incubated with agitation at 37°C for 5 days. Recombinant tau at 40 μM was mixed with 40 μM low molecular weight heparin and 2 mM DTT in PBS pH 7.0 and incubated with agitation at 37°C for 5 days. Recombinant TDP-43 protein at 1 mg/ml in 20mM Tris pH 8.0, 1 M NaCl, 10 mM $MgCl_2$, 1 mM $CaCl_2$ and 9% glycerol was incubated with agitation at 37°C overnight, centrifuged at 100,000×g for 60 min at 4°C, and resuspended in PBS.

ATPase activity assay

ATPase activity was determined using the EnzCheck phosphatase assay kit (Molecular Probes). ATPase activity was measured in a 96 well flat bottom plate (Fisher Scientific) by a microplate reader (Spark 20M, Tecan). 50 nM of VCP was incubated in 100 μL ATPase reaction buffer (25 mM HEPES, pH 7.5, 100 mM NaCl, 10 mM $MgCl_2$) containing 0, 50, 100, 200, 400, or 800 μM ATP. The absorbance at 360 ± 5 nm was measured at 45 s intervals for a total of 30 min at 37°C. The amount of inorganic phosphate released was quantified based on a phosphate standard curve (0 to 150 μM) performed on the same plate. Initial enzyme velocity was determined by fitting the data to a linear regression model. Enzyme velocities were then plotted against ATP concentration for Michaelis-Menten kinetic analysis. Samples were run in duplicate. NaCl inactivation assays were conducted in a similar fashion but in the presence of 0, 50, 100, 200, or 400 mM NaCl with 800 μM ATP. For heat activation/inactivation, 50 nM of VCP was incubated in 100 μL ATPase reaction buffer containing 50 mM NaCl and 800 μM ATP. Reactions were incubated for 20 min at 37, 42, 47, 52, 57, or 62°C in a Veriti Thermal Cycler (Applied Biosystems). After 20 min, the reaction was stopped by incubation at 4°C for 2 min and phosphate levels were determined using the EnzCheck phosphatase assay kit based on a phosphate standard curve performed on the same plate.

VCP tau disaggregase assays

50 nM pathologic tau, 100 nM VCP, and 300 nM UFD1L+NPLOC4 were incubated with 5 mM ATPγS or ATP in 25 mM HEPES pH 7.4, 100 mM KCl, 2 mM $MgCl_2$, 1 mM β-mercaptoethanol at 42°C for 30 min. For ThS measurements, 1% Sarkosyl was added to reaction and centrifuged at 186,000 × g for 30 min at 4°C. The pellet was resuspended in 10 mM MOPS pH 6.5, 5 μM ThS to measure emission at 480 nm. Disaggregase reactions were also absorbed onto carbon/formvar-coated copper grids (Electron Microscopy Sciences) for visualization with a Joel 1010 electron microscope in a blinded manner. Recombinant protein aggregates (100 nM recombinant tau, 100 nM α-synuclein, or 600 nM TDP-43) were incubated with 300 nM VCP and 900 nM UFD1L+NPLOC4, and 5 mM ATP. For tau and α-synuclein, ThS

measurements were then performed as described above. TDP-43 was analyzed by sedimentation because TDP-43 aggregates are not strongly positive for ThS. TDP-43 aggregates were centrifuged at 186,000×g for 30 min at 4°C. Pellets were immunoblotted for TDP-43 by SDS PAGE.

FRET biosensor experiments

Tau RD P301S FRET Biosensor (ATCC) were maintained in DMEM (Invitrogen) with 10% FBS (Atlanta Biologicals) and 1% Pen-Strep (Invitrogen) at 37°C. Plasmids containing wild-type or mutant VCP were transfected using Lipofectamine 2000 (Thermo Fisher). 24 hours later, pathologic tau lysates were added to biosensor cells using Lipofectamine 2000 (Thermo Fisher). 24 hours later, cells were analyzed by flow cytometry (LSR-II, BD Biosciences) to obtain median FRET fluorescence signal intensity.

Mice

Mice were bred and maintained in a pathogen-free facility at the University of Pennsylvania. Experiments were completed in accordance to the Institutional Animal Care and Use Committee (IACUC) of the University of Pennsylvania. Using an established protocol (30), the University of Pennsylvania Transgenic and Chimeric Mouse facility generated knock in animals. CRISPR-Cas9 components were injected into a fertilized oocyte then implanted into a pseudopregnant C57BL/6J mice (Jackson Laboratory). Single-guide RNA (sgRNA:AACAGGTAGAGTGGTGATAA) and single-stranded oligo donor nucleotide (ssODN:GGAATACCTGATGCTACAGGACGTTTGGAGATTCTTCAGATCCATACCAAGAACATGAAACTGGCAGATGATGTGGGCTTGGAACAGGTAGAGTGGTGATAAGGCCTGACCAGAATTTAGGATAGCTCTGTTTTAGGAGGTTGCAAATTACAAACATAGCCTAAGAAAGAGGCTTCATACCAGAAATACAAACTTGGGGA) were used to generate D395G mutant mice (fig. S4A). Because human and mouse VCP are identical at the protein level, the mouse genome was only altered by 3 base pairs. The first mutation led to the p.Asp395Gly mutation and the other silent, cis, non-coding mutation occurs in an intron to destroy the PAM site to prevent re-cutting by the Cas9 enzyme. Therefore, wild-type, heterozygous, and homozygous mice are wild-type, heterozygous, or homozygous on both the p.Asp395Gly and PAM site, respectively. Two founders were confirmed by Sanger sequencing to have D395G and no off-target mutations in the top 5 predicted off-target sites. Founders were bred with wild-type C57BL/6J mice for three generations prior to mouse experiments. For litter analyses, p.Asp395Gly mice were compared to PAM mice. PAM mice are wild-type in terms of VCP protein sequence but only harbor the non-coding PAM site mutation. Wild-type, heterozygous, and homozygous PAM mice exhibited no observable phenotype. Other lifespan, biochemical, molecular and histologic analyses compared p.Asp395Gly mice to WT C57BL/6J mice.

For intracerebral injections, mice were anesthetized with ketamine-xylazine-acepromazine and placed in a stereotaxic frame (David Kopf Instruments). Mice were aseptically injected with human AD pathologic tau in the right dorsal hippocampus and overlying cortex (bregma: −2.5mm, lateral: +2mm, depth: −2.4 mm and −1.4 mm from skull) with a Hamilton syringe. Each injection site received 2.5 μL of inoculum at 0.4 μg tau/μL as previously described (*27*, *33*).

RNA-sequencing

Mice were sacrificed by transcardiac perfusion with PBS. Brain regions were dissected, weighed, and frozen on dry ice. For RNA-sequencing, RNA from anterior cortex were extracted using RNeasy RNA extraction kit (Qiagen) following manufacturer's instruction. RNA integrity was determined using the RNA Nanochip 6000 kit and an Agilent 2100 bioanalyzer (Agilent). Biological replicates were barcoded, pooled, and sequenced in a single lane on a HiSeq 2000 for 150 × 2 base pair paired-end RNA sequencing at the University of Pennsylvania Next Generation Sequencing Core Facility. Reads were mapped to the mouse genome (mm10) using the RNA-Seq Unified Mapper (RUM) and gene expression differences were analyzed using EdgeR with statistical significance set at a false discovery rate (FDR) of <5%.

Immunoblotting

For human brain, samples were homogenized in a high salt buffer containing 10 mM Tris pH 7.5, 500 mM NaCl, 2 mM EDTA, 1 mM DTT, 10% sucrose containing protease and phosphatase inhibitors (PhosphoSTOP, Roche). Samples were then spun at 55,000×g for 30 min at 4°C and supernatant was collected for VCP immunoblotting. Pellets were homogenized in buffer containing 10 mM Tris, 500 mM NaCl, 2 mM EDTA, 1 mM DTT, and 30% sucrose and spun at 55,000×g for 30 min at 4°C to float and remove myelin. The resulting pellet was homogenized in buffer containing 2% sarkosyl and 50 mM Tris pH 7.6, followed by centrifugation at 55,000×g for 30 min at 4°C. Supernatant was collected and the sarkosyl-insoluble pellets were homogenized at room temperature in buffer containing 2% SDS and 50 mM Tris pH 7.6. Samples were spun at 55,000×g for 30 min at room temperature and supernatant was collected for tau immunoblotting.

For mouse brain, samples were sonicated using a probe sonicator (Sonics Vibra-cell) in ice-cold radio immunoprecipitation assay (RIPA) buffer containing 50 mM Tris pH 8.0, 150 mM NaCl, 1% Triton X-100, 0.5% sodium deoxycholate, and 0.1% SDS containing protease and phosphatase inhibitors. Sonicated samples were then spun at 55,000×g for 30 min at 4°C and supernatant was collected. Pellets were further extracted with 2% SDS buffer containing protease and phosphatase inhibitors at room temperature. Samples were spun at 55,000×g for 30 min at room temperature and supernatant was collected.

Brain lysate protein concentrations were quantified using BCA analysis (Pierce, Thermo Fisher). 50 μg of protein was run on either an 8% or 14% sodium dodecyl sulfate–polyacrylamide gel electrophoresis (SDS-PAGE) gel and transferred using the Trans-Blot Turbo system (Biorad, Hercules) to either nitrocellulose or polyvinylidene difluoride (PVDF) membranes. Membranes were then blocked in 5% non-fat milk for 1 hour at room temperature and immunoblotted with primary antibodies overnight at 4°C (table S3). IR dye secondary antibodies (Licor) were used to detect protein on a Licor Odyssey.

Purification of pathologic tau

AD brains with histologically confirmed tau pathology were used to extract insoluble pathologic tau as previously reported (*27*). ~12 g of frontal cortical gray matter from AD or control cases were homogenized in high-salt buffer (10 mM Tris pH 7.4, 800 mM NaCl, 0.1% Sarkosyl, 10% sucrose) and centrifuged at 10,000×g for 10 min at 4°C. Supernatant was filtered and additional Sarkosyl was added to 1%. Samples were nutated for 1 hour at room temperature and then centrifuged at 300,000×g for 1 hour at 4°C. The 1% Sarkosyl-insoluble pellet containing pathological tau was resuspended in PBS. Immunodepletion of tau from AD lysates was described previously (*33*). Anti-tau antibodies (R2295, Tau5, and K9JA) were conjugated to Dynabeads M-280 Toxylactivated (Fisher Scientific) according to manufacturer's instructions. Tau immunodepletion was performed by adding 200 μL of pathologic tau lysate with anti-tau antibody-bead complexes and rotating overnight at 4°C. A magnet was used to remove the Dynabeads, and this process was performed six times to obtain lysates with a final tau concentration of 0.61 ng/μL tau.

Immunohistochemistry

Six μm formalin-fixed, paraffin-embedded tissue sections were stained using immunohistochemistry or immunofluorescence as previously described (*34*) using antibodies listed in table S3. Semiquantitative analysis of mouse tau pathology was performed by grading coronal mouse sections as 0 to 3 (0 = no pathology, 3 = severe pathology) for each mouse. Averaged scores from each genotype were used to generate heat maps representing amount and distribution of tau pathology. Quantitative analysis was performed by manual counting of number of AT8-positive neurons in designated brain

regions. Analysis was conducted blinded to genotype.

Human subjects research

Approval was obtained from the Attikon University General Hospital's Bioethics Committee and the University of Pennsylvania IRB (702681, 298201, 824867). Informed consent was obtained from all participants or their next of kin surrogate. Consents did not include language permitting public sharing of genomic data.

Neuroimaging

Tau PET imaging was performed on an Ingenuity TF PET/CT scanner (Philips). Images were acquired over 30 min starting 75 min after intravenous injection of 370MBq (10 mCi) ^{18}F-flortaucipir (previously called ^{18}F-AV-1451). PET volumes were acquired at 2 mm^3 isotropic resolution over six five-minute frames and after correction for signal attenuation and patient head motion the acquisition frames were summed across volumes. T1 magnetization-prepared rapid acquisition with gradient echo MRI was performed with isotropic 1 mm voxel size. PET and MRI images were aligned using MIM (MIM Software).

Statistics

Statistical analyses were performed using the GraphPad Prism 5.0 or Rstudio 3.0.1+. Student's *t* test, one- or two-way analysis of variance (ANOVA) with Bonferroni multiple comparisons correction posthoc tests, or linear mixed effects regression models were used in this study.

REFERENCES AND NOTES

1. H. Braak, I. Alafuzoff, T. Arzberger, H. Kretzschmar, K. Del Tredici, Staging of Alzheimer disease-associated neurofibrillary pathology using paraffin sections and immunocytochemistry. *Acta Neuropathol.* **112**, 389–404 (2006). doi: 10.1007/s00401-006-0127-z; pmid: 16906426
2. G. G. Kovacs, Tauopathies. *Handb. Clin. Neurol.* **145**, 355–368 (2017). doi: 10.1016/B978-0-12-802395-2.00025-0; pmid: 28987182
3. M. G. Spillantini, M. Goedert, Tau pathology and neurodegeneration. *Lancet Neurol.* **12**, 609–622 (2013). doi: 10.1016/S1474-4422(13)70090-5; pmid: 23684085
4. V. M. Lee, M. Goedert, J. Q. Trojanowski, Neurodegenerative tauopathies. *Annu. Rev. Neurosci.* **24**, 1121–1159 (2001). doi: 10.1146/annurev.neuro.24.1.1121; pmid: 11520930
5. J. van den Boom, H. Meyer, VCP/p97-mediated unfolding as a principle in protein homeostasis and signaling. *Mol. Cell* **69**, 182–194 (2018). doi: 10.1016/j.molcel.2017.10.028; pmid: 29153394
6. P. I. Hanson, S. W. Whiteheart, AAA+ proteins: Have engine, will work. *Nat. Rev. Mol. Cell Biol.* **6**, 519–529 (2005). doi: 10.1038/nrm1684; pmid: 16072036
7. H. Meyer, M. Bug, S. Bremer, Emerging functions of the VCP/p97 AAA-ATPase in the ubiquitin system. *Nat. Cell Biol.* **14**, 117–123 (2012). doi: 10.1038/ncb2407; pmid: 22298039
8. M. Uhlén *et al*., Proteomics. Tissue-based map of the human proteome. *Science* **347**, 1260419 (2015). doi: 10.1126/science.1260419; pmid: 25613900
9. Y. Zhang *et al*., An RNA-sequencing transcriptome and splicing database of glia, neurons, and vascular cells of the cerebral cortex. *J. Neurosci.* **34**, 11929–11947 (2014). doi: 10.1523/JNEUROSCI.1860-14.2014; pmid: 25186741
10. E. M. Ramos *et al*., Frontotemporal dementia spectrum: First genetic screen in a Greek cohort. *Neurobiol. Aging* **75**, 224.e1–224.e8 (2019). doi: 10.1016/j.neurobiolaging.2018.10.029; pmid: 30528349
11. G. S. Gibbons *et al*., Detection of Alzheimer disease (AD)–specific tau pathology in AD and nonAD Tauopathies by immunohistochemistry with novel conformation-selective tau antibodies. *J. Neuropathol. Exp. Neurol.* **77**, 216–228 (2018). doi: 10.1093/jnen/nly010; pmid: 29415231
12. P. Demaerel, L. Heiner, W. Robberecht, R. Sciot, G. Wilms, Diffusion-weighted MRI in sporadic Creutzfeldt-Jakob disease. *Neurology* **52**, 205–208 (1999). doi: 10.1212/WNL.52.1.205; pmid: 9921880
13. M. Neumann *et al*., TDP-43 in the ubiquitin pathology of frontotemporal dementia with VCP gene mutations. *J. Neuropathol. Exp. Neurol.* **66**, 152–157 (2007). doi: 10.1097/nen.0b013e31803020b9; pmid: 17279000
14. G. D. Watts *et al*., Inclusion body myopathy associated with Paget disease of bone and frontotemporal dementia is caused by mutant valosin-containing protein. *Nat. Genet.* **36**, 377–381 (2004). doi: 10.1038/ng1332; pmid: 15034582
15. J. P. Taylor, Multisystem proteinopathy: Intersecting genetics in muscle, bone, and brain degeneration. *Neurology* **85**, 658–660 (2015). doi: 10.1212/WNL.0000000000001862; pmid: 26208960
16. A. Manno, M. Noguchi, J. Fukushi, Y. Motohashi, A. Kakizuka, Enhanced ATPase activities as a primary defect of mutant valosin-containing proteins that cause inclusion body myopathy associated with Paget disease of bone and frontotemporal dementia. *Genes Cells* **15**, 911–922 (2010). doi: 10.1111/j.1365-2443.2010.01428.x; pmid: 20604808
17. D. Halawani *et al*., Hereditary inclusion body myopathy-linked p97/VCP mutations in the NH2 domain and the D1 ring modulate p97/VCP ATPase activity and D2 ring conformation. *Mol. Cell. Biol.* **29**, 4484–4494 (2009). doi: 10.1128/MCB.00252-09; pmid: 19506019
18. E. E. Blythe, K. C. Olson, V. Chau, R. J. Deshaies, Ubiquitin- and ATP-dependent unfoldase activity of P97/VCP•NPLOC4•UFD1L is enhanced by a mutation that causes multisystem proteinopathy. *Proc. Natl. Acad. Sci. U.S.A.* **114**, E4380–E4388 (2017). doi: 10.1073/pnas.1706205114; pmid: 28512218
19. E. E. Blythe, S. N. Gates, R. J. Deshaies, A. Martin, Multisystem proteinopathy mutations in VCP/p97 increase NPLOC4·UFD1L binding and substrate processing. *Structure* **27**, 1820–1829.e4 (2019). doi: 10.1016/j.str.2019.09.011; pmid: 31623962
20. P. C. Lyu, M. I. Liff, L. A. Marky, N. R. Kallenbach, Side chain contributions to the stability of alpha-helical structure in peptides. *Science* **250**, 669–673 (1990). doi: 10.1126/science.2237416; pmid: 2237416
21. K. T. O'Neil, W. F. DeGrado, A thermodynamic scale for the helix-forming tendencies of the commonly occurring amino acids. *Science* **250**, 646–651 (1990). doi: 10.1126/science.2237415; pmid: 2237415
22. C. Song, Q. Wang, C. C. Li, ATPase activity of p97-valosin-containing protein (VCP). D2 mediates the major enzyme activity, and D1 contributes to the heat-induced activity. *J. Biol. Chem.* **278**, 3648–3655 (2003). doi: 10.1074/jbc.M208422200; pmid: 12446676
23. M. M. Olszewski, C. Williams, K. C. Dong, A. Martin, The Cdc48 unfoldase prepares well-folded protein substrates for degradation by the 26S proteasome. *Commun. Biol.* **2**, 29 (2019). doi: 10.1038/s42003-019-0283-z; pmid: 30675527
24. N. O. Bodnar *et al*., Structure of the Cdc48 ATPase with its ubiquitin-binding cofactor Ufd1-Npl4. *Nat. Struct. Mol. Biol.* **25**, 616–622 (2018). doi: 10.1038/s41594-018-0085-x; pmid: 29967539
25. E. C. Twomey *et al*., Substrate processing by the Cdc48 ATPase complex is initiated by ubiquitin unfolding. *Science* **365**, eaax1033 (2019). doi: 10.1126/science.aax1033; pmid: 31249135
26. I. Cooney *et al*., Structure of the Cdc48 segregase in the act of unfolding an authentic substrate. *Science* **365**, 502–505 (2019). doi: 10.1126/science.aax0486; pmid: 31249134
27. J. L. Guo *et al*., Unique pathological tau conformers from Alzheimer's brains transmit tau pathology in nontransgenic mice. *J. Exp. Med.* **213**, 2635–2654 (2016). doi: 10.1084/jem.20160833; pmid: 27810929
28. P. Friedhoff, A. Schneider, E. M. Mandelkow, E. Mandelkow, Rapid assembly of Alzheimer-like paired helical filaments from microtubule-associated protein tau monitored by fluorescence in solution. *Biochemistry* **37**, 10223–10230 (1998). doi: 10.1021/bi980537d; pmid: 9665729
29. B. B. Holmes *et al*., Proteopathic tau seeding predicts tauopathy in vivo. *Proc. Natl. Acad. Sci. U.S.A.* **111**, E4376–E4385 (2014). doi: 10.1073/pnas.1411649111; pmid: 25261551
30. J. Henao-Mejia *et al*., Generation of genetically modified mice using the CRISPR-Cas9 genome-editing system. *Cold Spring Harb. Protoc.* **2016**, prot090704 (2016). doi: 10.1101/pdb.prot090704; pmid: 26832688
31. K. C. Luk *et al*., Pathological α-synuclein transmission initiates Parkinson-like neurodegeneration in nontransgenic mice. *Science* **338**, 949–953 (2012). doi: 10.1126/science.1227157; pmid: 23161999
32. G. S. Gibbons *et al*., GFP-mutant human tau transgenic mice develop tauopathy following CNS injections of Alzheimer's brain-derived pathological tau or synthetic mutant human tau fibrils. *J. Neurosci.* **37**, 11485–11494 (2017). doi: 10.1523/JNEUROSCI.2393-17.2017; pmid: 28986461
33. Z. He *et al*., Amyloid-β plaques enhance Alzheimer's brain tau-seeded pathologies by facilitating neuritic plaque tau aggregation. *Nat. Med.* **24**, 29–38 (2018). doi: 10.1038/nm.4443; pmid: 29200205
34. E. B. Lee *et al*., Expansion of the classification of FTLD-TDP: Distinct pathology associated with rapidly progressive frontotemporal degeneration. *Acta Neuropathol.* **134**, 65–78 (2017). doi: 10.1007/s00401-017-1679-9; pmid: 28130640

ACKNOWLEDGMENTS

We thank T. M. Bardakjian, H. Brown, E. Chung, L. Dratch, S. Huang, A. Wang, E. McCarty Wood, B. Zhang, the National Prion Disease Pathology Surveillance Center (M. Cohen and K. Glisic), and the Center for Neurodegenerative Disease Research for their assistance, and the patients and families to whom this research is dedicated. **Funding:** This study was supported by grants from the NIH (F30AG058317, R56AG063344, P30AG010124, P01AG017586, and P01AG066597), the BrightFocus Foundation (A2018802S), and a Clinical Scientist Development Award from the Doris Duke Charitable Foundation. The NIH Undiagnosed Diseases Program is funded by the Common Fund, Office of the Director, NIH. **Author contributions:** N.F.D., J.M.P., and E.B.L. conceived of and designed the experiments, analyzed results, and wrote the manuscript. N.F.D., J.M.P., B.K., L.C., A.T.N., C.M.O., Z.H., S.P., G.S.G., K.C.L., and E.B.L. performed the experiments. E.S., J.D.P., S.G.P., M.G., L.M., D.J.I., C.T.M., I.M.N., C.T., G.K.A., and V.M.V.D. provided clinical, genetic, and neuroimaging data. All authors edited the manuscript. **Competing interests:** The authors declare no competing interests. A.T.N. is currently affiliated with the Mayo Clinic, Rochester, Minnesota. Z.H. is currently affiliated with the Chinese Academy of Sciences, Shanghai, China. **Data and materials availability:** All transcriptome data are deposited in NCBI's Gene Expression Omnibus (accession no. GSE156831). Human genomics data are available upon request subject to a data use agreement to ensure maintenance of personal privacy. Requests for data or materials should be addressed to edward.lee@pennmedicine.upenn.edu.

SUPPLEMENTARY MATERIALS

science.sciencemag.org/content/370/6519/eaay8826/suppl/DC1
Figs. S1 to S5
Tables S1 to S3
MDAR Reproducibility Checklist

View/request a protocol for this paper from *Bio-protocol*.

25 July 2019; resubmitted 16 July 2020
Accepted 17 September 2020
Published online 1 October 2020
10.1126/science.aay8826

RESEARCH ARTICLE SUMMARY

WILDLIFE DISEASE

Divergent impacts of warming weather on wildlife disease risk across climates

Jeremy M. Cohen*, Erin L. Sauer, Olivia Santiago†, Samuel Spencer†, Jason R. Rohr

INTRODUCTION: Infectious disease outbreaks among wildlife have surged in recent decades alongside global climate change. However, the circumstances under which climate change is most likely to promote or inhibit infectious disease remain unknown for several reasons. First, researchers know little about how climate change will alter disease risk across hosts and parasites with diverse life history traits (e.g., host thermal biology, habitat, and parasite transmission mode). Second, not all parasites will be affected by climate change, but it remains unclear how the relative risk of disease caused by bacteria, viruses, fungi, and helminths is changing. Third, impacts of temperature abnormalities and variability, rather than increasing mean temperatures alone, remain largely unexplored. Finally, it is not clear which regions of the globe may become more amenable to disease and which may become less suitable.

RATIONALE: Recently, the thermal mismatch hypothesis has emerged to predict how infection risk is affected by temperature across climate zones in an amphibian-disease system. This hypothesis suggests that hosts adapted to cooler and warmer climates should be at greatest risk of infection under abnormally warm and cool conditions, respectively, because smaller-bodied parasites are more likely to maintain performance over a wider range of temperatures than larger-bodied hosts but are limited by extreme conditions. However, thermal mismatches may not affect diverse hosts and parasites equally because wildlife host and parasite traits can greatly influence disease outcomes. For example, thermal mismatches might exert an especially strong influence over disease outcomes in ectothermic hosts because their immune responses are highly temperature-dependent.

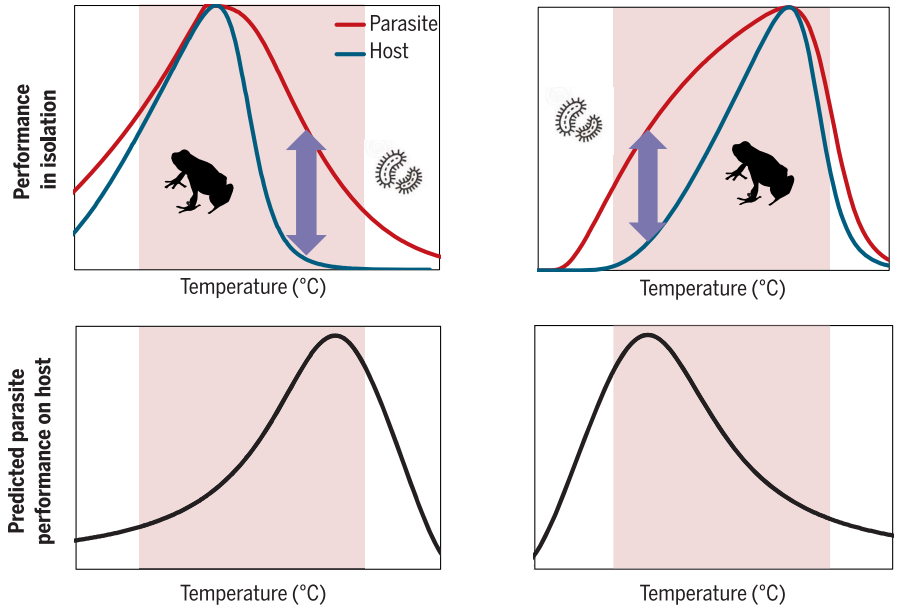

The thermal mismatch hypothesis. Predicted patterns of thermal host and parasite performance in isolation (top, left and right) versus patterns of host-parasite interactions (bottom, left and right). Because smaller organisms generally have broader thermal performance curves in isolation than larger organisms, peak parasite growth on hosts is likely at temperatures at which host performance is poor (arrows in top left and top right; curves in bottom left and bottom right). Cold-adapted hosts (left, top and bottom) and warm-adapted hosts (right, top and bottom) should thus experience maximal parasite growth at relatively warm and cool temperatures, respectively. Shaded areas span intermediate temperatures over which relationships between temperature and parasite performance on host are likely to be approximately linear.

To address this challenge, we examined how disease risk was affected by temperature for diverse wildlife hosts and parasites that vary in ecologically important traits across a worldwide climatic gradient. We amassed a global, spatiotemporal dataset describing parasite prevalence across 7346 wildlife populations and 2021 host-parasite combinations. Further, we compiled long-term climate records at each location and short-term weather records during each survey. Our modeling approach investigated how relationships between parasite prevalence and weather depend on local climate and host and parasite traits. Finally, we projected broad-scale changes in disease risk based on thermal mismatches and ensemble climate change model predictions.

RESULTS: We found that on average, hosts from cool and warm climates experienced increased disease risk at abnormally warm and cool temperatures, respectively, as predicted by the thermal mismatch hypothesis. This effect was greatest among hosts that are ectothermic and nonmigratory and among systems in which the parasite is directly transmitted (without vectors or intermediate hosts). However, the thermal mismatch effect was similar in terrestrial and freshwater systems. Projections based on climate change models indicate that ectothermic wildlife hosts from temperate and tropical zones may experience sharp increases and moderate reductions in disease risk, respectively, though the magnitude of these changes depends on parasite taxa. Prevalence of helminth parasites increased most in temperate zones, whereas fungal parasite prevalence decreased most in tropical zones.

CONCLUSION: Cold-adapted hosts may experience increasing disease risk during abnormally warm periods. Meanwhile, the risk to warm-adapted hosts may increase during cool periods and mildly decrease during warm periods. Further, these effects are dependent on the identity and traits of the parasite and the host. Our results highlight the complexity of the influences of climate change on diverse host-parasite dynamics, whereas our broad-scale predictions suggest contrasting impacts of climate change across climate zones and diverse parasites. As climate change accelerates, hosts adapted to cooler or milder climates may suffer increasing risk of infectious disease outbreaks, whereas those adapted to warmer climates could see mild reductions in infectious disease risk. ■

The list of author affiliations is available in the full article online.
*Corresponding author. Email: jeremy3cohen@gmail.com
†These authors contributed equally to this work.
Cite this article as J. M. Cohen *et al.*, *Science* **370**, eabb1702 (2020). DOI: 10.1126/science.abb1702

READ THE FULL ARTICLE AT
https://doi.org/10.1126/science.abb1702

RESEARCH ARTICLE

WILDLIFE DISEASE

Divergent impacts of warming weather on wildlife disease risk across climates

Jeremy M. Cohen[1,2]*, Erin L. Sauer[1,2], Olivia Santiago[1]†, Samuel Spencer[1]†, Jason R. Rohr[1,3]

Disease outbreaks among wildlife have surged in recent decades alongside climate change, although it remains unclear how climate change alters disease dynamics across different geographic regions. We amassed a global, spatiotemporal dataset describing parasite prevalence across 7346 wildlife populations and 2021 host-parasite combinations, compiling local weather and climate records at each location. We found that hosts from cool and warm climates experienced increased disease risk at abnormally warm and cool temperatures, respectively, as predicted by the thermal mismatch hypothesis. This effect was greatest in ectothermic hosts and similar in terrestrial and freshwater systems. Projections based on climate change models indicate that ectothermic wildlife hosts from temperate and tropical zones may experience sharp increases and moderate reductions in disease risk, respectively, though the magnitude of these changes depends on parasite identity.

In recent years, ecological communities have experienced increases in mean environmental temperatures and weather variability (*1*), as well as simultaneous increases in outbreaks of emerging infectious diseases (*2*, *3*). However, complex links between climate change and infectious disease risk in wildlife remain difficult to untangle for several reasons (*4*–*6*). First, despite positive relationships between warmer temperatures and disease in many host-parasite systems [e.g., (*7*, *8*)], warming could plausibly reduce risk in many cases [e.g., if the parasite performs poorly under warmer conditions (*6*)]. Second, few studies have explored how disease risk is affected by temperature abnormalities, even though increasing temperature variability is a hallmark of climate change [however, see (*9*, *10*)]. Third, although host or parasite traits often influence disease outcomes (*11*), it is difficult to predict how disease risk is shifting across hosts and parasites with diverse life history traits (*4*, *5*).

The thermal mismatch hypothesis has recently emerged to explain how abnormal temperatures alter infection risk in an amphibian-disease system (*12*–*14*). This hypothesis suggests that hosts adapted to cooler and warmer climates should be at greatest infection risk under abnormally warm and cool conditions (thermal mismatches), respectively (see summary figure). The hypothesis assumes that all organisms are physiologically adapted to their local climate but that smaller-bodied parasites generally have broader thermal tolerances than larger-bodied hosts, meaning that the parasites can maintain performance over a wider range of temperatures [perhaps because they acclimate or adapt to new conditions faster (*15*)]. Sometimes, parasites may even directly reduce the thermal breadths of their hosts (*10*). Thus, host infection risk is hypothesized to peak at temperatures at which host performance is low but parasite performance remains high. Further, all organisms are expected to be limited by extremes that exceed their critical thermal minima or maxima (*15*). Therefore, infection risk is expected to be maximized during unusually cool conditions in warm environments and warm conditions in cool environments. Although thermal performance curves are inherently nonlinear, the hypothesis predicts that, under intermediate conditions where hosts occur at threshold densities needed for transmission (*16*), infection risk can be effectively modeled as a linear relationship with temperature. Importantly, the hypothesis is robust to violations of the aforementioned assumptions (fig. S1). The thermal mismatch hypothesis could offer a tool for understanding the impacts of climate change and disease across regions because it suggests that under abnormally warm conditions, hosts from cooler climates should experience higher disease risk, whereas hosts from warmer climates may experience no change or a reduction in risk.

The thermal mismatch hypothesis has been broadly supported on the basis of continental and global-scale analyses of survey records of the fungal pathogen *Batrachochytrium dendrobatidis* across 394 amphibian host species and 1396 populations (*12*–*14*). Additionally, experimental infections revealed that hosts from warm climates experienced the greatest *B. dendrobatidis* infection loads and mortality under cool conditions, and vice versa (*13*), even when amphibians were able to thermoregulate (*17*), and a meta-analysis indicated that host mortality risk in the lab also increased under thermal mismatches (*18*). However, this hypothesis has only been shown to affect disease risk in amphibians infected with *B. dendrobatidis*, a system with an ectothermic host and ectoparasite that might be especially sensitive to environmental conditions. Several wildlife host and parasite traits influence disease outcomes, including host thermal biology, habitat, parasite taxa, and transmission mode (*12*). For example, thermal mismatches might exert a stronger influence over disease outcomes in ectothermic hosts than endothermic hosts because the body temperatures and immune responses of ectotherms are more dependent on environmental temperature (*19*). Thus, it remains unclear how temperature abnormalities influence the risk of disease outbreaks across diverse host-parasite systems from disparate climates.

Modeling changing infectious disease risk

Our primary goal was to assess how thermal mismatches, or short-term weather fluctuations, affect shifts in disease risk under long-term climate change across diverse host-parasite systems. To accomplish this, we compiled a population-level spatiotemporal parasite prevalence dataset from wildlife surveys reported in the literature. We limited our dataset to short-term surveys of wild animals, reported from precise geographic locations (see the Materials and methods). Our dataset contained 7346 population-level survey records from 355 studies on seven continents and represented 309 parasite lineages, 1381 host species from 52 taxonomic orders, and 2021 host-parasite combinations (figs. S2 and S3). The dataset contained a diverse assemblage of host taxa (31% birds, 30% amphibians, 22% fish, 9% mammals, 7% insects, and 1% reptiles) and parasite taxa (31% protozoa, 28% fungi, 23% viruses, 11% helminths, 6% bacteria, and 1% arthropods) from terrestrial (62%) and freshwater (38%) systems. We further collected the dates and locations of all surveys and compiled (i) local weather data provided by the Climate Research Unit (*20*) to estimate the temperature and precipitation during the month(s) of each survey (hereafter, "weather") and (ii) local long-term climate data (1970–2000 mean temperatures, hereafter, "climate") provided by Worldclim (*21*).

We fit five binomial mixed-effects models to examine how interactions between climate, weather, and various traits or features (host thermal biology, host habitat preference, host migratory distance, parasite taxa, and parasite transmission complexity) influenced parasite prevalence in hosts, which served as an indicator of disease risk. Thermal mismatches were

[1]Department of Integrative Biology, University of South Florida, Tampa, FL, USA. [2]Department of Forest and Wildlife Ecology, University of Wisconsin–Madison, Madison, WI, USA. [3]Department of Biological Sciences, University of Notre Dame, Notre Dame, IN, USA.
*Corresponding author. Email: jeremy3cohen@gmail.com
†These authors contributed equally to this work.

represented as statistical interactions between climate and weather variables (hereafter, "thermal mismatch interaction"), whereas three-way interactions evaluated how traits or taxa influenced the strength of thermal mismatch effects (hereafter, "trait-dependent thermal mismatch interactions"). We then generated model predictions at the 10th and 90th percentiles (~5° and ~22°C) of 30-year mean temperature, representative of cold and warm climates, respectively. Given our hypothesis, we expected to find negative thermal mismatch interactions, suggesting that infection risk among hosts from cooler climates increased at warm temperatures, and vice versa. Each model controlled for monthly precipitation and the four other traits or features as fixed effects and included study and host taxa as random effects. Our models assume linear relationships between temperature and parasite prevalence covering the intermediate portions of the temperature spectrum, as predicted by the thermal mismatch hypothesis (see Materials and methods). Survey data were not spatially autocorrelated, and thus we did not control for autocorrelation (fig. S4).

Relationships between climate, weather, and disease

All models (tables S2 to S6) produced a significant, negative two-way interaction between climate and weather; thus, thermal mismatches broadly influenced parasite prevalence in our dataset of diverse host-parasite interactions (thermal mismatch interaction: climate × weather; model coefficient (β) = −0.003, $p < 0.0001$). Impacts of thermal mismatches on parasite prevalence were highly dependent on host and parasite traits. Model comparisons demonstrated that, whereas thermal mismatch interactions always improved models, the greatest model improvements in Akaike information criterion (AIC), Nagelkerke's pseudo-R^2, and chi-square values were observed with trait-dependent thermal mismatch interactions (except habitat; table S1).

As predicted, partial residual (PR) plots revealed that ectothermic hosts from relatively cool or warm climates experienced the greatest parasite prevalence when temperatures were unusually warm or cool, respectively (trait-dependent thermal mismatch interaction–thermal biology; $p < 0.0001$; Fig. 1, A and B, and table S2). However, endotherms experienced the greatest parasite prevalence during cold weather. This could be an effect of cold-induced physiological changes in endotherms that can be immunosuppressive (*22*) or increasing transmission rates of airborne pathogens in cool, less humid air (*23*). Further, we expected that the effects of thermal mismatches on parasite prevalence may be less detectable in long-distance migrant hosts because these hosts experience greater variation in climate and have more flexibility to avoid adverse weather. Indeed,

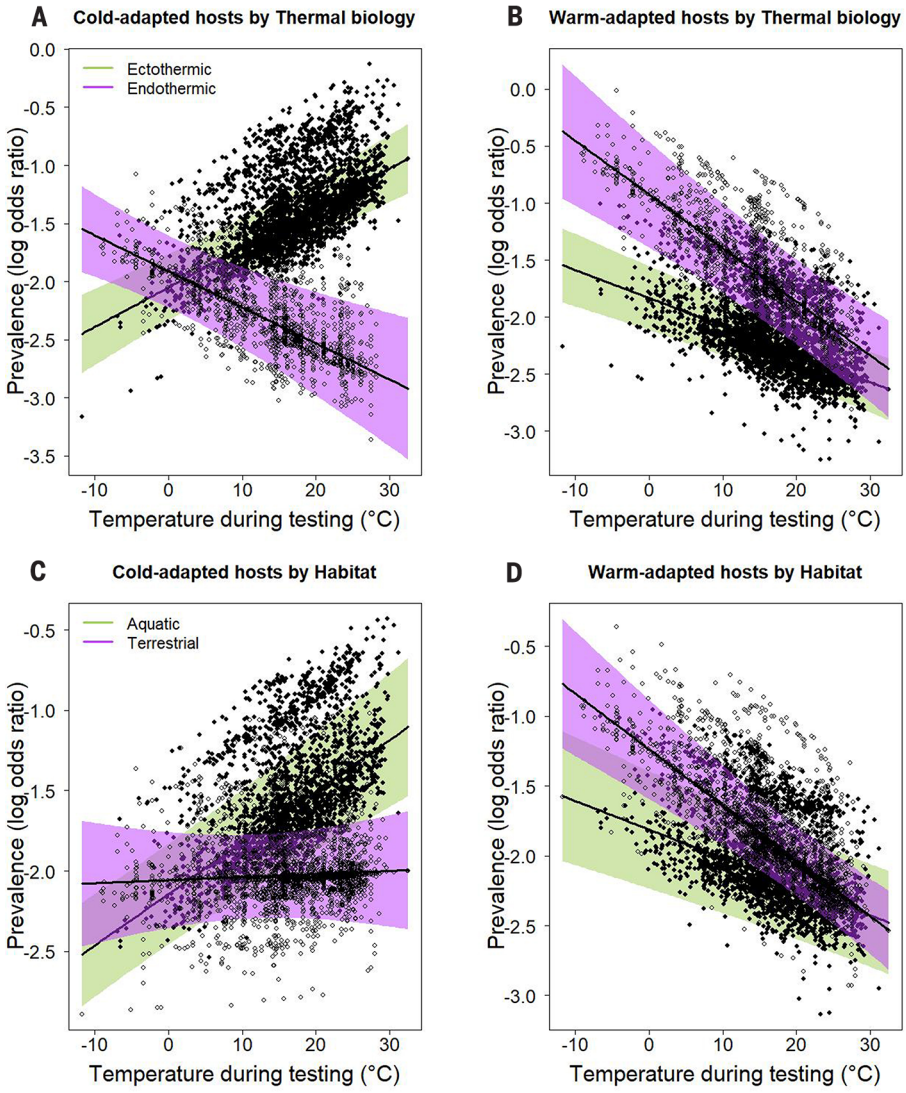

Fig. 1. Thermal mismatch effects on parasite prevalence depend on host thermal biology but not habitat. (**A** to **D**) Partial residual plots from binomial mixed-effects models display the significant three-way interactions among long-term climate, weather, and either host thermal biology [(A) and (B)] or habitat [(C) and (D)] that affect parasite prevalence (as log-odds ratios). Points represent host populations, and shading shows 95% confidence bands; green bands and solid points represent ectothermic and aquatic hosts, whereas purple bands and open points represent endothermic and terrestrial hosts. Cold-adapted (prediction at 10th percentile climate of ~5°C) hosts are represented in (A) and (C), and warm-adapted (prediction at 90th percentile climate of ~22°C) hosts are represented in (B) and (D). The models suggest that ectothermic and endothermic hosts from cooler climates typically experience higher and lower prevalence under warm conditions, respectively (A). Meanwhile, all warm-adapted hosts experience high prevalence when conditions are cool (B). Cold-adapted aquatic hosts experience greater parasite prevalence at warm temperatures than terrestrial hosts (C), though all warm-adapted hosts experience greater prevalence at cool temperatures (D), as predicted by the thermal mismatch hypothesis.

PR plots revealed that this was the case (trait-dependent thermal mismatch interaction–migratory distance; $p < 0.0001$; fig. S5, A and B, and table S3), although we caution that long-distance migrant hosts experience conditions over the annual cycle that often differ from the climate of the survey location.

We expected that terrestrial hosts experience greater parasite prevalence under thermal mismatches than aquatic hosts because environmental temperatures are typically less variable in water than in air, despite exceptions [e.g., perched wetlands (*24*)]. Surprisingly, all hosts experienced similarly high parasite prevalence after thermal mismatches (trait-dependent thermal mismatch interaction–habitat; $p = 0.24$; Fig. 1, C and D, and table S4), though terrestrial hosts were not as likely to experience high

parasite prevalence under warm temperatures in cold climates [possibly because aquatic hosts have evolved narrower thermal breadths (*15*)]. Finally, we observed increased parasite prevalence after thermal mismatches in host-parasite interactions with a directly transmitted parasite (trait-dependent thermal mismatch interaction–transmission mode; $p < 0.0001$; fig. S5, C and D, and table S6) rather than an indirectly transmitted parasite (relying on intermediate hosts or vectors; fig. S5, C and D), possibly because of the inherent complications present in these systems that might impede detection of temperature effects. For example, indirectly transmitted parasites may benefit from behavioral thermoregulation of intermediate hosts at high temperatures, which can provide shelter and thus mitigate the effects of unusually warm weather conditions in cold-adapted parasites.

Although we expected to see thermal mismatch effects across parasite taxa—including bacteria, viruses, fungi, and helminths—we predicted that the strength of effects in cool or warm climates depends on taxon. For example, fungal parasites might have a particularly strong advantage when infecting warm-adapted hosts at cold temperatures because many fungi perform best at cool or intermediate temperatures (*25*), whereas the opposite might be true for parasites that often grow well under warm temperatures, such as helminths (*26*). Indeed, the impacts of thermal mismatches on parasite prevalence were highly dependent on parasite taxa (Fig. 2 and table S5). Fungal prevalence exhibited the strongest thermal mismatch effect, increasing sharply under cold abnormalities in warm climates but more gradually under warm abnormalities in cool climates (Fig. 2). By contrast, helminth prevalence was positively related to temperature across climates, though this relationship was much stronger in cool climates (Fig. 2), suggesting that warming may benefit helminths more than other parasites. Several previous studies have found positive associations between helminth transmission and temperature [e.g., (*26*)], and helminth success in hosts is closely tied to host food consumption (*27*), which may be limited in abnormally cool conditions.

Bacterial prevalence decreased moderately under cool temperatures in warm climates but only slightly under warm temperatures in cool climates (Fig. 2). Finally, viral parasite prevalence increased under warm temperatures in cool climates but not cool temperatures in warm climates, though we advise caution in interpreting this result because viral infections progress quickly and thus hosts may be likely to clear infections or suffer mortality in time frames shorter than the monthly resolution of our weather data. These results were largely robust to reductions in model complexity (table S7) or shifts in the relative proportion of host taxa (figs. S6 to S8 and table S8).

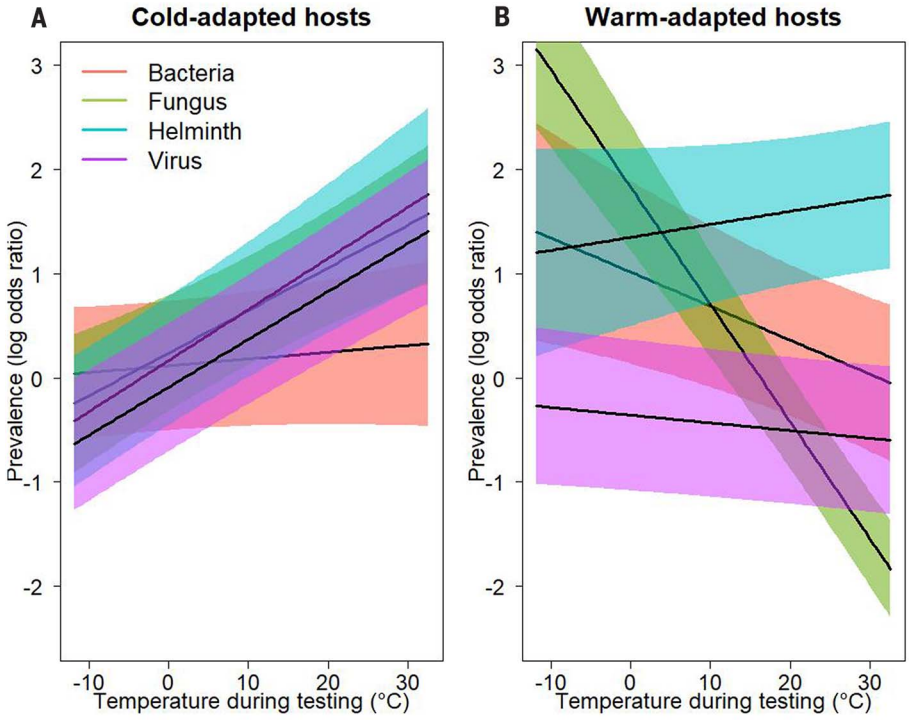

Fig. 2. Variation in thermal mismatch patterns among parasite taxa. (**A** and **B**) Partial residual plots from a binomial mixed-effects model display the significant three-way interactions among long-term climate, weather, and parasite taxa. Shading shows associated 95% confidence bands for four parasite taxa: bacteria (red), fungi (green), helminths (blue), or viruses (purple). Cold-adapted (prediction at 10th percentile climate of ~5°C) hosts are represented in (A), and warm-adapted (prediction at 90th percentile climate of ~22°C) hosts are represented in (B). The models suggest that hosts from cooler climates typically experience a higher prevalence of fungal, helminth, and viral parasites under warm conditions, whereas those from warmer climates experience a higher prevalence of fungal and bacterial parasites when conditions are cool.

Predicting changing disease risk across the globe

Our models indicate that climate change may increase disease risk for many wildlife hosts from cooler climates, whereas wildlife from warmer climates may experience reduced disease risk. Following these models, we aimed to explore global patterns of disease risk in wildlife under climate change. We generated nearly global predictions from our model results (excluding polar areas) for how prevalence of four parasite taxa (bacteria, fungi, helminths, and viruses) will change under projected annual mean temperatures in 2070 following various greenhouse gas emission scenarios [Representative Concentration Pathways (RCPs) 2.6, 4.5, 6.0, and 8.5 by the Community Climate System Model (*28*); see Materials and methods]. To generate these predictions, we represented climate with long-term mean temperature and weather with projected mean temperature under a given RCP. We then divided these predictions by predictions generated under the current climate (with long-term mean temperature representing climate and weather) to standardize the change in risk relative to the present.

The resulting maps show that climate change may increase parasite prevalence sharply at high latitudes and elevations but decrease it moderately at low latitudes (Fig. 3). Predictably, the magnitude of these effects increased at greater RCPs: Changes in parasite prevalence ranged from −22 to +66% at RCP-2.6 (95% of cells warming between 0.21° and 3.57°C) but ranged from −31 to +86% at RCP-8.5 (2.11° and 7.49°C). At RCP-8.5, predictions vary by parasite taxa, although warming is expected to increase parasite prevalence at high latitudes and decrease prevalence at low latitudes across all taxa (Fig. 4). Notably, fungal parasites exhibit the greatest increases in risk at high latitudes and greatest decreases in risk at low latitudes, whereas helminths benefit most from warming overall, decreasing only slightly at low latitudes (similar to predictions generated by Carlson *et al.* (*27*). Across all taxa, both our models and predictions found that cold-adapted hosts generally experienced steeper increases in parasite prevalence under warm conditions than warm-adapted hosts experienced under cool conditions, suggesting that climate change–driven increases in parasite prevalence for cold-adapted hosts may

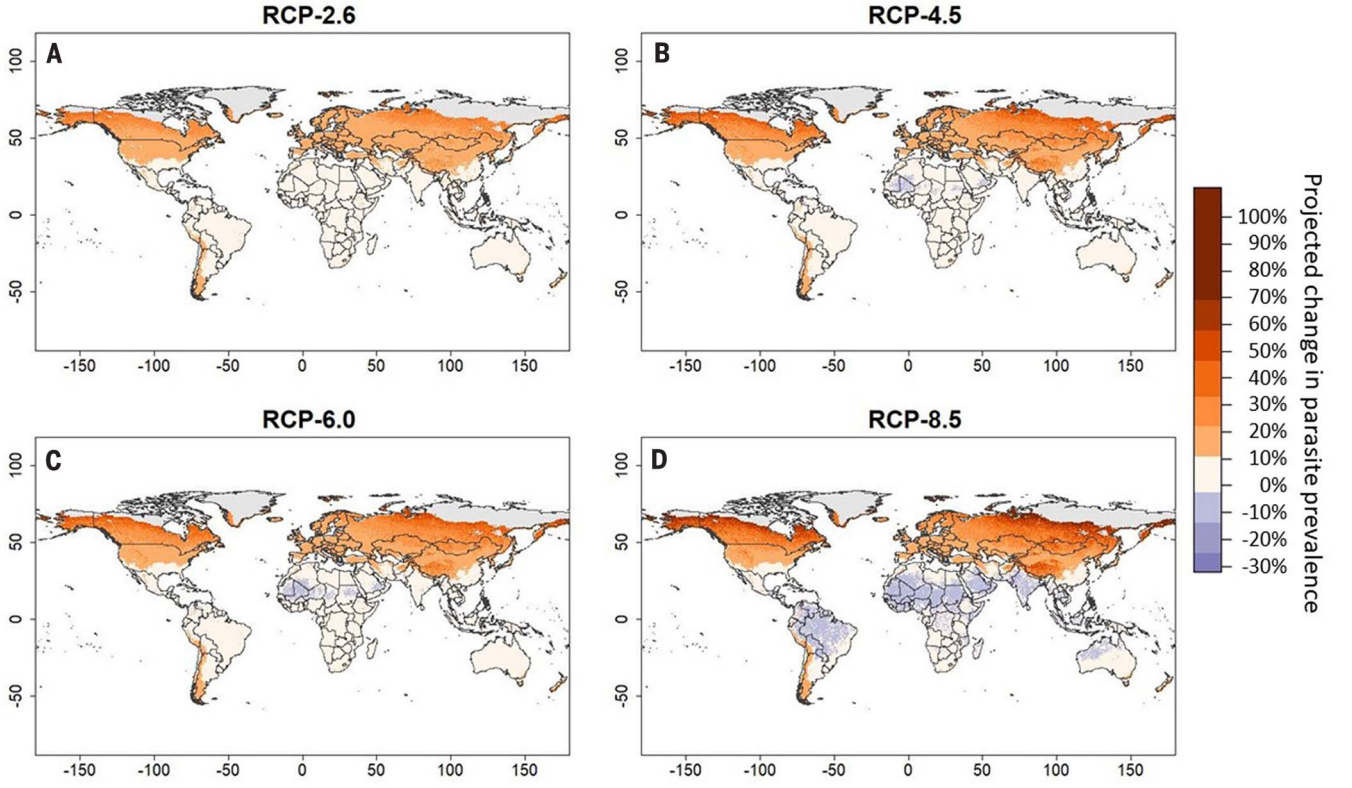

Fig. 3. Global projections of shifts in parasite prevalence under climate change. (**A** to **D**) Maps display projected change in overall parasite prevalence under four RCPs in 2070: 2.6 (A), 4.5 (B), 6.0 (C), and 8.5 (D). Parasite prevalence predictions were generated for each cell based on a binomial mixed-effects model containing a two-way thermal mismatch interaction between long-term climate and weather. Predictions were generated for the current climate as well as for each RCP scenario, in which projected mean temperatures substituted for survey temperatures. The proportional difference between the two projections is plotted.

exceed decreases in risk for warm-adapted hosts across systems. This pattern might be explained by the shape of most thermal performance curves, which are often left-skewed with a greater per-degree change in performance at temperatures above than below an organism's thermal optimum (*29*) [however, see (*30*) for exceptions]. Boreal zones appear likely to experience the greatest increases in parasite prevalence, adding an additional stressor to a region that is projected to experience some of the most pronounced changes to its climate (*28*). We caution that our predictions are highly generalized and are only a general expectation for global changes in disease risk under warming, because parasite species are given equal weight in this analysis regardless of their commonness in the environment or pathogenicity. Thus, we recommend against using these maps to make predictions about any single host-parasite system but present them as only a general expectation for global changes in disease occurrence under warming.

Conclusions

Here, we amassed a global spatiotemporal dataset of population-level parasite prevalence across thousands of wildlife populations worldwide and describe how temperature abnormalities influence parasite prevalence across diverse host-parasite systems from disparate climates. We show that cold-adapted hosts may experience increasing parasite prevalence, and thus disease risk, during abnormally warm periods. Meanwhile, risk to warm-adapted hosts may increase during cool periods and mildly decrease during warm periods. Further, these effects are dependent on the identity and traits of the parasite and the host. Our results highlight the complexity of the influences of climate change on diverse host-parasite dynamics, whereas our broad-scale predictions suggest contrasting impacts of climate change across climate zones and diverse parasites. As climate change accelerates, wildlife hosts adapted to cooler or milder climates may suffer increasing risk of infectious disease outbreaks, whereas those adapted to warmer climates could see mild reductions in infectious disease risk.

Materials and methods

Overview of data selection and extraction

We aimed to acquire spatiotemporal datasets describing population-level parasite prevalence across as many host-parasite systems as possible, defining a population as a group of hosts of the same species sampled at a single location and time. Because we aimed to test interacting effects of climate (30-year baseline mean temperature) and weather (temperature at the time of sampling) on host-parasite outcomes at the specific locations of each survey, our dataset was limited to records with information about location (to a 10th of a degree) and date (to month). We further limited our dataset to surveys among animal wildlife, excluding systems with human hosts and farmed or captive animal hosts because of the various complications arising from reporting, medical treatment, and climate-controlled buildings. We excluded any data acquired through antibody tests because these data do not reflect current parasite presence. Because our predictions only hold under intermediate local temperature conditions, we excluded two data points collected during very cold weather (<−10°C; our dataset had no surveys conducted above 30°C). In addition, we excluded marine systems because spatiotemporal data of equivalent resolution are not readily available. Finally, we limited our dataset to definitive hosts.

We used several strategies to gather appropriate datasets, including searching the

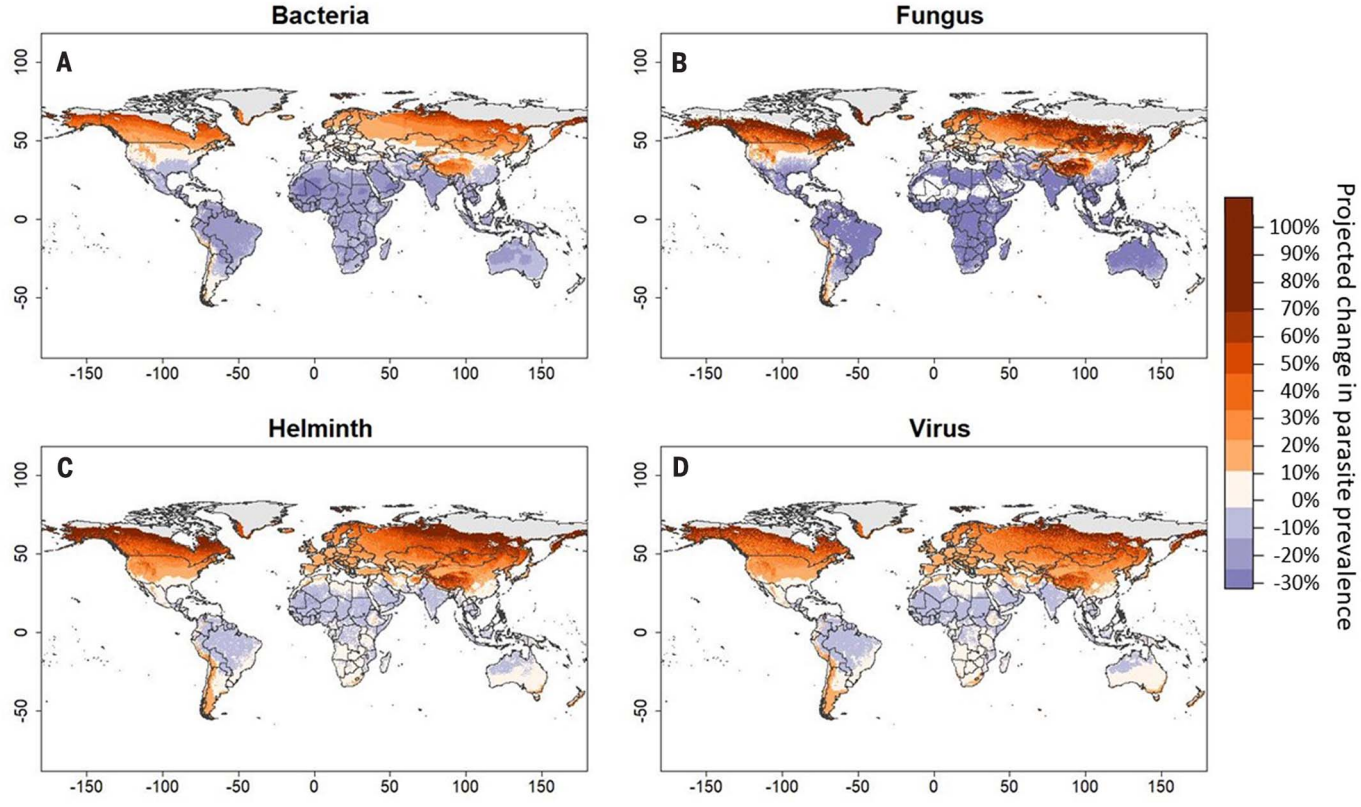

Fig. 4. Global projections of shifts in prevalence of four parasite taxa under climate change. (**A** to **D**) Maps display projected changes in parasite prevalence of four taxa—bacteria (A), fungi (B), helminths (C), and viruses (D)—in 2070 under RCP-8.5. Disease risk predictions were generated for each cell based on a binomial mixed-effects model containing a three-way thermal mismatch interaction between long-term climate, weather, and parasite taxa. Predictions were generated for current climate as well as RCP-8.5, and the proportional difference between the two projections is plotted.

literature (*31*–*223*), searching the internet for available datasets, assembling datasets from scratch for several host-parasite systems that are sampled frequently, and contacting various experts in disease ecology. Our internet search identified five available spatiotemporal datasets that we downloaded: (i) avian malaria data from Malavi (*224*), (ii) the Global Mammal Parasite Database [GMPD (*225*)], (iii) fish parasite data from the National Wild Fish Health Survey (NWFHS) database (https://www2.usgs.gov/ecosystems/disease/fishdisease.html), (iv) neotropical avian parasite data presented in Barrow *et al.* (*40*), and (v) honeybee data from McMahon *et al.* (*135*). We supplemented the Malavi and GMPD datasets with month and year of collection from the original published articles cited for each entry and excluded any entries describing captive hosts or missing geographic coordinates or for which we could not find dates. The NWFHS and Barrow *et al.* (*40*) databases were organized at the individual level and needed to be summarized to the population level. When summarizing individual-level data at the population level, we grouped individuals into populations based on species, identical location (geographic coordinates in decimal degrees, rounded to two decimal places), and month.

We also manually collected spatiotemporal survey data from the literature. First, we searched Web of Science for the term "disease survey*," yielding 1925 results from a wide variety of host-parasite systems, and extracted data from 28 papers that met our criteria. Second, we targeted several host-parasite systems for which we knew data would be available in the literature. We searched Web of Science for the term *Batrachochytrium dendrobatidis* (Bd), producing 1215 total results and extracting data from 159 papers. We also searched Web of Science for papers relating to iridoviruses, using the terms ("Frog virus 3" OR "Epizootic haematopoietic" OR "necrosis virus" OR "European sheatfish virus" OR "European catfish virus" OR "Regina ranavirus" OR "Santee-Cooper ranavirus" OR "Bohle iridovirus" OR "Red sea bream iridovirus" OR "White sturgeon iridovirus" OR "ranavirus"), obtaining 612 results and extracting data from 29 papers that reported iridovirus prevalence. Despite the focus on Bd and iridovirus, they accounted for only 21 and 5% of our dataset, respectively. We screened all papers using the *metagear* package (*226*) in R 3.4.2 (*227*) and manually extracted relevant data. All literature searches and data collection associated with these searches took place between May 2018 and February 2019, and all data were combined into a single dataset for analysis.

When extracting data from papers and databases, we recorded host and parasite species, number of hosts sampled, host life stage, number of infected and uninfected individuals or infection prevalence (if only one was given, the other was calculated), date of sampling, and geographic coordinates. When coordinates were not given in a paper or database, we searched named sites for coordinates on Google Maps. We only included field surveys conducted over a continuous period up to a maximum of 4 months and up to a maximum area of 50 km^2 to ensure that weather data were local and sufficiently short term. We collected taxonomic information and standardized all classifications according to the International Union for Conservation of Nature [IUCN (*228*)]. Prevalence data was bimodally distributed in our dataset, with many populations having no infection or 100% infection, and this pattern was consistent across time periods (fig. S9). Surveys were most common in summer regardless of latitude, though there was some variation (fig. S10).

We classified all parasites as either bacteria, viruses, protozoa, helminths, arthropods, or fungi (hereafter referred to as "parasite taxa") and classified them as having either direct or indirect life cycles. All hosts were classified as either ecto- or endothermic, terrestrial or aquatic, and migratory (long-distance migrants) or nonmigratory (short-distance migrants or residents). Amphibian habitat associations were classified based on Sodhi *et al.* (*229*). Birds were classified as terrestrial except for species in the orders Anseriformes, Charadriiformes (family Laridae only), Gaviiformes, Pelecaniformes, and Sphenisciformes (other aquatic taxa were not present in our dataset). Mammals, reptiles, and insects were assessed at the species level on the basis of the judgment of the data collectors. See below for definitions of the classifications.

Climate data

We extracted historic monthly mean temperature and total precipitation data from the University of East Anglia Climate Research Unit [CRU (*20*)] for the location and specific month(s) that each population was tested in the field [raster package (*230*)]. CRU data are the finest-scale global, historic climate data available, offered at a resolution of 0.5^{o2} cells (about 50 km^2) for each month dating to 1901. If sampling took place over the course of up to four consecutive months or less, and was not reported at the monthly level, then we averaged climate data across the sampling months. We did not use data collected over longer periods of time because doing so would have been inappropriate to seasonal analysis.

We collected annual mean temperature between 1970 and 2000 for each population (as a representative of mean temperature in their climate) on the basis of their locations using interpolated Worldclim rasters (*21*), which have been used in hundreds of previous ecological studies to represent long-term climate means. Long-term annual temperatures in the range of a species are a useful approximation of thermal tolerance (*19*, *231*). Though the time period is somewhat arbitrary, such high-resolution historic data are not available at a global scale for other time periods. In our view, this window adequately represents the historic mean conditions in a given area to which an organism has likely adapted.

Statistical analyses

All analyses were conducted in R 3.4.2 (*227*). We fit a series of four generalized linear mixed-effects models (GLMMs) with binomial distributions to test relationships between thermal mismatches, host or parasite traits, and parasite prevalence in wildlife using the package *glmmTMB* (*232*). Thermal mismatches were represented in models as statistical interactions between 30-year mean temperature (representing climate) and monthly mean temperature during sampling (representing weather) for a given host population at the location it was sampled. Because we expect that hosts adapted to warm conditions should have the greatest parasite prevalence under cool conditions and vice versa, the estimate of the coefficient of the two-way thermal mismatch interaction is hypothesized to be negative. In our five models, we tested for effects of three-way interactions (the thermal mismatch interactors and one of five host or parasite traits) on the number of infected and uninfected hosts (binomial response variable). Host or parasite traits were each categorical factors—either host thermal biology (ecto- or endotherm), host habitat type (summarized as terrestrial or aquatic based on where the host spends a majority of its time at its tested life stage), host migratory strategy (migratory or nonmigratory), parasite transmission complexity (direct or indirect; the latter representing parasites that are vector-transmitted or requiring an intermediate host), or parasite taxa (limited to virus, bacteria, fungus, protozoa, or helminth). Our goal in assessing the impacts of migration was to determine whether hosts migrating long distances were less affected by thermal mismatches, because they experience a greater range of climates than other species; thus, we considered all hosts migrating on average >200 km per year to be migratory (a category that included some birds, mammals, and fish) and others to be nonmigratory, even if they do migrate shorter distances. In the model testing for an interaction between thermal mismatch and parasite taxa, we subsetted the data to exclude insect parasitoids and protozoans because these categories were not fully crossed with our other fixed effects. We did not explicitly test for differences in relationships across host taxa because of redundancy between taxonomic group and our other traits, and we did not compare zoonotic systems with others because we lacked sufficient data in zoonotic systems.

In each model, we included the following as fixed effects: the absolute value of latitude, log-transformed total precipitation during the month(s) of sampling, and the other host or parasite traits that were not part of the three-way thermal mismatch interaction (excluding parasite transmission mode, which is highly redundant with parasite taxa). Because studies contained varying numbers of surveys, study was included as a random effect to account for nonindependence among sampling events within a study. Further, we included host taxonomic class as a random effect to ensure that outsized effects of a single taxonomic group did not sway the outcome of the models. Unfortunately, traditional phylogenetic correlation structures cannot be included in mixed models with a binomial error distribution because the distribution is only defined by a single parameter specifying both the mean and variance, whereas correlation structures affect only variance parameters.

To evaluate the importance of the thermal mismatch and its dependence on host, parasite, and environmental traits, we compared among nested models using AIC scores, Nagelkerke's pseudo-R^2 values [MuMIn package (*233*)], and chi-square values. Because highly complex models with partially correlated predictor variables can sometimes produce spurious results (though this is less of a concern when analyzing large datasets), we explored fitting simplified models corresponding to each of the five primary models that did not include any host or parasite taxa or traits other than main effects of terms included in interactions but were otherwise identical. Additionally, we explored fitting models in which major host taxa (birds, mammals, amphibians, invertebrates, and fish) were equally represented by randomly subsampling 2000 rows from the original dataset for each category. All results were visualized using the *visreg* package (*234*).

Spatial structure of the data

Unfortunately, the size of our dataset made controlling for spatial structure computationally unfeasible (requires accounting for >56 million distance estimates per model). Instead, we generated correlograms to evaluate spatial autocorrelation (Moran's I) at a sequence of distances up to 30° from each point. To reduce the computational burden, which increases exponentially with the number of records, we randomly subsampled 1000 rows from our dataset nine times and produced correlograms for each subsample [ncf package (*235*)].

Climate change projections

We generated two sets of global maps, projecting future change in parasite prevalence at four RCPs (different possible greenhouse gas trajectories predicted by climate models, with RCP-2.6 representing an optimistic climate change scenario and RCP-8.5 representing a business-as-usual model) or for four parasite taxa (bacteria, fungi, helminth, and virus). The RCP maps were based on a GLMM that tests how the two-way interaction between 30-year mean temperature and temperature during surveying predicts population-level parasite prevalence [glmmTMB package (*232*)]. The model contained log-transformed monthly precipitation and study as a random effect, though we did not include categorical fixed effects because this would necessitate assuming categorical values of host or parasite traits while generating model predictions and our goal was to keep the predictions general (study ID was randomized when making predictions). We first generated predictions for all cells on a global map (aggregated by mean to 0.21^{o2} resolution)

based on projections of 2070 annual mean temperature at four RCP scenarios (2.6, 4.5, 6.0, and 8.5) by the Community Climate System Model, version 4 [CCSM4 (*28*)]. For each cell, we used Bioclim 30-year mean temperature [bio1 (*21*)] as 30-year mean temperature and CCSM4 bio1 projections as the temperature during surveying. We then divided each of these by a "current climate" projection in which Bioclim 30-year mean temperature was used for both temperature variables. Resulting rasters show change in parasite prevalence globally and were plotted using the *raster* package (*230*) and color palettes from *RColorBrewer* (*236*).

Projections of parasite prevalence by taxa were based on a GLMM that tests the three-way interaction between both temperature terms and parasite taxa, a categorical variable with the four levels given above. Predictions were generated for current and future climate (RCP-8.5) based on 30-year temperature and temperature during sampling, respectively. All other methods were identical to those described above.

Data availability

All data and code compiled for this study are available on Github (*223*).

REFERENCES AND NOTES

1. Intergovernmental Panel on Climate Change (IPCC), "Climate change 2014: Synthesis report. Contribution of Working Groups I, II and III to the fifth assessment report of the Intergovernmental Panel on Climate Change," Core Writing Team, R. K. Pachauri, L. A. Meyer, Eds. (IPCC, Geneva, 2014).
2. K. E. Jones *et al*., Global trends in emerging infectious diseases. *Nature* **451**, 990–993 (2008). doi: 10.1038/nature06536; pmid: 18288193
3. L. Liang, P. Gong, Climate change and human infectious diseases: A synthesis of research findings from global and spatio-temporal perspectives. *Environ. Int.* **103**, 99–108 (2017). doi: 10.1016/j.envint.2017.03.011; pmid: 28342661
4. J. R. Rohr *et al*., Frontiers in climate change-disease research. *Trends Ecol. Evol.* **26**, 270–277 (2011). doi: 10.1016/j.tree.2011.03.002; pmid: 21481487
5. S. Altizer, R. S. Ostfeld, P. T. J. Johnson, S. Kutz, C. D. Harvell, Climate change and infectious diseases: From evidence to a predictive framework. *Science* **341**, 514–519 (2013). doi: 10.1126/science.1239401; pmid: 23908230
6. K. D. Lafferty, E. A. Mordecai, The rise and fall of infectious disease in a warmer world. *F1000 Res.* **5**, 2040 (2016). doi: 10.12688/f1000research.8766.1; pmid: 27610227
7. S. J. Ryan, C. J. Carlson, E. A. Mordecai, L. R. Johnson, Global expansion and redistribution of *Aedes*-borne virus transmission risk with climate change. *PLOS Negl. Trop. Dis.* **13**, e0007213 (2019). doi: 10.1371/journal.pntd.0007213; pmid: 30921321
8. S. H. Paull, P. T. Johnson, Experimental warming drives a seasonal shift in the timing of host-parasite dynamics with consequences for disease risk. *Ecol. Lett.* **17**, 445–453 (2014). doi: 10.1111/ele.12244; pmid: 24401007
9. T. R. Raffel *et al*., Disease and thermal acclimation in a more variable and unpredictable climate. *Nat. Clim. Chang.* **3**, 146–151 (2013). doi: 10.1038/nclimate1659
10. S. E. Greenspan *et al*., Infection increases vulnerability to climate change via effects on host thermal tolerance. *Sci. Rep.* **7**, 9349 (2017). doi: 10.1038/s41598-017-09950-3; pmid: 28839273
11. P. T. Johnson, J. C. de Roode, A. Fenton, Why infectious disease research needs community ecology. *Science* **349**, 1259504 (2015). doi: 10.1126/science.1259504; pmid: 26339035
12. J. M. Cohen *et al*., Impacts of thermal mismatches on chytrid fungus Batrachochytrium dendrobatidis prevalence are moderated by life stage, body size, elevation and latitude. *Ecol. Lett.* **22**, 817–825 (2019). doi: 10.1111/ele.13239; pmid: 30816626
13. J. M. Cohen *et al*., The thermal mismatch hypothesis explains host susceptibility to an emerging infectious disease. *Ecol. Lett.* **20**, 184–193 (2017). doi: 10.1111/ele.12720; pmid: 28111904
14. J. M. Cohen, D. J. Civitello, M. D. Venesky, T. A. McMahon, J. R. Rohr, An interaction between climate change and infectious disease drove widespread amphibian declines. *Glob. Change Biol.* **25**, 927–937 (2019). doi: 10.1111/gcb.14489; pmid: 30484936
15. J. R. Rohr *et al*., The complex drivers of thermal acclimation and breadth in ectotherms. *Ecol. Lett.* **21**, 1425–1439 (2018). doi: 10.1111/ele.13107; pmid: 30009486
16. J. O. Lloyd-Smith *et al*., Should we expect population thresholds for wildlife disease? *Trends Ecol. Evol.* **20**, 511–519 (2005). doi: 10.1016/j.tree.2005.07.004; pmid: 16701428
17. E. L. Sauer *et al*., Variation in individual temperature preferences, not behavioural fever, affects susceptibility to chytridiomycosis in amphibians. *Proc. Biol. Sci.* **285**, 20181111 (2018). doi: 10.1098/rspb.2018.1111; pmid: 30135162
18. E. L. Sauer *et al*., A meta-analysis reveals temperature, dose, life stage, and taxonomy influence host susceptibility to a fungal parasite. *Ecology* **101**, e02979 (2020). doi: 10.1002/ecy.2979; pmid: 31960949
19. C. A. Deutsch *et al*., Impacts of climate warming on terrestrial ectotherms across latitude. *Proc. Natl. Acad. Sci. U.S.A.* **105**, 6668–6672 (2008). doi: 10.1073/pnas.0709472105; pmid: 18458348
20. I. Harris, P. D. Jones, T. J. Osborn, D. H. Lister, Updated high-resolution grids of monthly climatic observations—the CRU TS3.10 dataset. *Int. J. Climatol.* **34**, 623–642 (2014). doi: 10.1002/joc.3711
21. S. E. Fick, R. J. Hijmans, WorldClim 2: New 1-km spatial resolution climate surfaces for global land areas. *Int. J. Climatol.* **37**, 4302–4315 (2017). doi: 10.1002/joc.5086
22. N. J. Morley, J. W. Lewis, Temperature stress and parasitism of endothermic hosts under climate change. *Trends Parasitol.* **30**, 221–227 (2014). doi: 10.1016/j.pt.2014.01.007; pmid: 24613288
23. B. D. Dalziel *et al*., Urbanization and humidity shape the intensity of influenza epidemics in U.S. cities. *Science* **362**, 75–79 (2018). doi: 10.1126/science.aat6030; pmid: 30287659
24. U. Nickus, K. Bishop, M. Erlandsson, C. D. Evans, M. Forsius, H. Laudon, D. M. Livingstone, D. Monteith, H. Thies, "Direct impacts of climate change on freshwater ecosystems" in *Climate Change Impacts on Freshwater Ecosystems*, M. Kernan, R. W. Battarbee, B. Moss, Eds. (2010), pp. 38–64.
25. J. W. Deacon, *Fungal Biology* (Wiley, 2013).
26. R. M. Anderson, J. G. Mercer, R. A. Wilson, N. P. Carter, Transmission of *Schistosoma mansoni* from man to snail: Experimental studies of miracidial survival and infectivity in relation to larval age, water temperature, host size and host age. *Parasitology* **85**, 339–360 (1982). doi: 10.1017/S0031182000055323; pmid: 7145476
27. C. J. Carlson *et al*., Parasite biodiversity faces extinction and redistribution in a changing climate. *Sci. Adv.* **3**, e1602422 (2017). doi: 10.1126/sciadv.1602422; pmid: 28913417
28. P. R. Gent *et al*., The community climate system model version 4. *J. Clim.* **24**, 4973–4991 (2011). doi: 10.1175/2011JCLI4083.1
29. M. J. Angilletta Jr., Estimating and comparing thermal performance curves. *J. Therm. Biol.* **31**, 541–545 (2006). doi: 10.1016/j.jtherbio.2006.06.002
30. P. K. Molnár, A. P. Dobson, S. J. Kutz, Gimme shelter—The relative sensitivity of parasitic nematodes with direct and indirect life cycles to climate change. *Glob. Change Biol.* **19**, 3291–3305 (2013). doi: 10.1111/gcb.12303; pmid: 23801641
31. A. A. Aguirre *et al*., Pathology of fibropapillomatosis in olive ridley turtles *Lepidochelys olivacea* nesting in Costa Rica. *J. Aquat. Anim. Health* **11**, 283–289 (1999). doi: 10.1577/1548-8667(1999)011<0283:POFIOR>2.0.CO;2
32. M. N. Al-Sabi *et al*., PCR detection of *Angiostrongylus vasorum* in faecal samples of dogs and foxes. *Parasitol. Res.* **107**, 135–140 (2010). doi: 10.1007/s00436-010-1847-5; pmid: 20372926
33. T. Anderson, A. DeJardin, D. K. Howe, J. P. Dubey, M. L. Michalski, *Neospora caninum* antibodies detected in Midwestern white-tailed deer (*Odocoileus virginianus*) by Western blot and ELISA. *Vet. Parasitol.* **145**, 152–155 (2007). doi: 10.1016/j.vetpar.2006.11.012; pmid: 17194547
34. W. M. Arjo, E. M. Gese, C. Bromley, A. Kozlowski, E. S. Williams, Serologic survey for diseases in free-ranging coyotes (*Canis latrans*) from two ecologically distinct areas of Utah. *J. Wildl. Dis.* **39**, 449–455 (2003). doi: 10.7589/0090-3558-39.2.449; pmid: 12910777
35. I. M. Asmundsson, J. A. Mortenson, E. P. Hoberg, Muscleworms, Parelaphostrongylus andersoni (Nematoda: Protostrongylidae), discovered in Columbia white-tailed deer from Oregon and Washington: implications for biogeography and host associations. *J. Wildl. Dis.* **44**, 16–17 (2008). doi: 10.7589/0090-3558-44.1.16; pmid: 18263818
36. O. Bain, G. Wahl, A. Renz, *Onchocerca ramachandrini* n. sp. from the warthog in Cameroon. *Ann. Parasitol. Hum. Comp.* **68**, 139–143 (1993). doi: 10.1051/parasite/1993683139
37. S. M. Banks, D. C. Ashley, Parelaphostrongyliasis in white-tailed deer in Missouri. *J. Wildl. Dis.* **36**, 562–564 (2000). doi: 10.7589/0090-3558-36.3.562; pmid: 10941746
38. J. E. Barlough *et al*., Antibodies to marine caliciviruses in the Steller sea lion (*Eumetopias jubatus* Schreber). *J. Wildl. Dis.* **23**, 34–44 (1987). doi: 10.7589/0090-3558-23.1.34; pmid: 3820427
39. J. E. Barlough *et al*., Isolation of reptilian calicivirus *Crotalus* type 1 from feral pinnipeds. *J. Wildl. Dis.* **34**, 451–456 (1998). doi: 10.7589/0090-3558-34.3.451; pmid: 9706554
40. L. N. Barrow *et al*., Deeply conserved susceptibility in a multi-host, multi-parasite system. *Ecol. Lett.* **22**, 987–998 (2019). doi: 10.1111/ele.13263; pmid: 30912262
41. R. Beck *et al*., Trichinellosis in wolves from Croatia. *Vet. Parasitol.* **159**, 308–311 (2009). doi: 10.1016/j.vetpar.2008.10.068; pmid: 19081193
42. P. M. Beldomenico *et al*., Internal parasites of free-ranging guanacos from Patagonia. *Vet. Parasitol.* **118**, 71–77 (2003). doi: 10.1016/j.vetpar.2003.09.008; pmid: 14651877
43. L. C. Bender, P. B. Hall, *Leptospira interrogans* exposure in free-ranging elk in Washington. *J. Wildl. Dis.* **32**, 121–124 (1996). doi: 10.7589/0090-3558-32.1.121; pmid: 8627923
44. L. C. Bender, H. Li, B. C. Thompson, P. C. Morrow, R. Valdez, Infectious disease survey of gemsbok in New Mexico. *J. Wildl. Dis.* **39**, 772–778 (2003). doi: 10.7589/0090-3558-39.4.772; pmid: 14733271
45. J. Beringer, L. P. Hansen, D. E. Stallknecht, An epizootic of hemorrhagic disease in white-tailed deer in Missouri. *J. Wildl. Dis.* **36**, 588–591 (2000). doi: 10.7589/0090-3558-36.3.588; pmid: 10941752
46. B. Berón-Vera, E. A. Crespo, J. A. Raga, S. N. Pedraza, *Uncinaria hamiltoni* (Nematoda: Ancylostomatidae) in South American sea lions, *Otaria flavescens*, from northern Patagonia, Argentina. *J. Parasitol.* **90**, 860–863 (2004). doi: 10.1645/GE-182R; pmid: 15357082
47. A. Blanc *et al*., Serologic evidence of influenza A and B viruses in South American fur seals (*Arctocephalus australis*). *J. Wildl. Dis.* **45**, 519–521 (2009). doi: 10.7589/0090-3558-45.2.519; pmid: 19395764
48. K. Borchers, K. Frölich, Antibodies against equine herpesviruses in free-ranging mountain zebras from Namibia. *J. Wildl. Dis.* **33**, 812–817 (1997). doi: 10.7589/0090-3558-33.4.812; pmid: 9391966
49. G. H. Borst, H. C. Walvoort, P. J. Reijnders, J. S. van der Kamp, A. D. Osterhaus, An outbreak of a herpesvirus infection in harbor seals (*Phoca vitulina*). *J. Wildl. Dis.* **22**, 1–6 (1986). doi: 10.7589/0090-3558-22.1.1; pmid: 3005664
50. E. C. Burton, D. L. Miller, E. L. Styer, M. J. Gray, Amphibian ocular malformation associated with frog virus 3. *Vet. J.* **177**, 442–444 (2008). doi: 10.1016/j.tvjl.2007.05.006; pmid: 17604194
51. I. C. Cadavid-Sanchez, E. Amat, L. M. Gomez-Piñerez, Enterobacteria isolated from synanthropic flies (Diptera, Calyptratae) in Medellín, Colombia. *Caldasia* **37**, 319–332 (2015). doi: 10.15446/caldasia.v37n2.53594
52. S. A. Cameron *et al*., Patterns of widespread decline in North American bumble bees. *Proc. Natl. Acad. Sci. U.S.A.* **108**, 662–667 (2011). doi: 10.1073/pnas.1014743108; pmid: 21199943
53. M. G. Candela *et al*., Pathogens of zoonotic and biological importance in roe deer (*Capreolus capreolus*): Seroprevalence in an agro-system population in France. *Res. Vet. Sci.* **96**, 254–259 (2014). doi: 10.1016/j.rvsc.2014.02.003; pmid: 24576494
54. G. Carpi, F. Cagnacci, M. Neteler, A. Rizzoli, Tick infestation on roe deer in relation to geographic and remotely sensed climatic variables in a tick-borne encephalitis endemic area. *Epidemiol. Infect.* **136**, 1416–1424 (2008). doi: 10.1017/S0950268807000039; pmid: 18081949
55. O. Courtenay *et al*., Is *Mycobacterium bovis* in the environment important for the persistence of bovine

tuberculosis? *Biol. Lett.* **2**, 460–462 (2006). doi: 10.1098/rsbl.2006.0468; pmid: 17148430
56. A. F. Currylow, A. J. Johnson, R. N. Williams, Evidence of ranavirus infections among sympatric larval amphibians and box turtles. *J. Herpetol.* **48**, 117–121 (2014). doi: 10.1670/12-235
57. A. M. D'Aoust-Messier, P. Echaubard, V. Billy, D. Lesbarrères, Amphibian pathogens at northern latitudes: Presence of chytrid fungus and ranavirus in northeastern Canada. *Dis. Aquat. Organ.* **113**, 149–155 (2015). doi: 10.3354/dao02837; pmid: 25751857
58. H. Dautel, C. Dippel, R. Oehme, K. Hartelt, E. Schettler, Evidence for an increased geographical distribution of *Dermacentor reticulatus* in Germany and detection of *Rickettsia* sp. RpA4. *Int. J. Med. Microbiol.* **296** (suppl. 40), 149–156 (2006). doi: 10.1016/j.ijmm.2006.01.013; pmid: 16524777
59. W. R. Davidson, J. M. Crum, J. L. Blue, D. W. Sharp, J. H. Phillips, Parasites, diseases, and health status of sympatric populations of fallow deer and white-tailed deer in Kentucky. *J. Wildl. Dis.* **21**, 153–159 (1985). doi: 10.7589/0090-3558-21.2.153; pmid: 3999248
60. J. de la Fuente *et al*., Evidence of Anaplasma infections in European roe deer (*Capreolus capreolus*) from southern Spain. *Res. Vet. Sci.* **84**, 382–386 (2008). doi: 10.1016/j.rvsc.2007.05.018; pmid: 17655893
61. S. L. Deem, A. J. Noss, R. Villarroel, M. M. Uhart, W. B. Karesh, Disease survey of free-ranging grey brocket deer (*Mazama gouazoubira*) in the Gran Chaco, Bolivia. *J. Wildl. Dis.* **40**, 92–98 (2004). doi: 10.7589/0090-3558-40.1.92; pmid: 15137493
62. T. M. Doherty-Bone *et al*., Morbidity and mortality of the Critically Endangered Lake Oku clawed frog *Xenopus longipes*. *Endanger. Species Res.* **21**, 115–128 (2013). doi: 10.3354/esr00514
63. J. P. Dubey *et al*., Biologic and molecular characteristics of *Toxoplasma gondii* isolates from striped skunk (*Mephitis mephitis*), Canada goose (*Branta canadensis*), black-winged lory (*Eos cyanogenia*), and cats (*Felis catus*). *J. Parasitol.* **90**, 1171–1174 (2004). doi: 10.1645/GE-340R; pmid: 15562622
64. J. P. Dubey *et al*., Isolation and genetic characterization of Toxoplasma gondii from raccoons (*Procyon lotor*), cats (*Felis domesticus*), striped skunk (*Mephitis mephitis*), black bear (*Ursus americanus*), and cougar (*Puma concolor*) from Canada. *J. Parasitol.* **94**, 42–45 (2008). doi: 10.1645/GE-1349.1; pmid: 18372620
65. A. L. J. Duffus, B. D. Pauli, K. Wozney, C. R. Brunetti, M. Berrill, Frog virus 3-like infections in aquatic amphibian communities. *J. Wildl. Dis.* **44**, 109–120 (2008). doi: 10.7589/0090-3558-44.1.109; pmid: 18263826
66. L. A. Durden, D. J. Richardson, Ectoparasites of the striped skunk, *Mephitis mephitis*, in Connecticut, USA. *Comp. Parasitol.* **70**, 42–45 (2003). doi: 10.1654/1525-2647(2003)070[0042:EOTSSM]2.0.CO;2
67. N. W. Dyer, L. E. Huffman, Plague in free-ranging mammals in western North Dakota. *J. Wildl. Dis.* **35**, 600–602 (1999). doi: 10.7589/0090-3558-35.3.600; pmid: 10479100
68. J. H. Epstein *et al*., Identification of GBV-D, a novel GB-like flavivirus from old world frugivorous bats (*Pteropus giganteus*) in Bangladesh. *PLOS Pathog.* **6**, e1000972 (2010). doi: 10.1371/journal.ppat.1000972; pmid: 20617167
69. A. Farajollahi *et al*., Serologic evidence of West Nile virus infection in black bears (*Ursus americanus*) from New Jersey. *J. Wildl. Dis.* **39**, 894–896 (2003). doi: 10.7589/0090-3558-39.4.894; pmid: 14733286
70. M. Fernández *et al*., High prevalence of haemosporidians in reed warbler *Acrocephalus scirpaceus* and sedge warbler *Acrocephalus schoenobaenus* in Spain. *J. Ornithol.* **151**, 27–32 (2010). doi: 10.1007/s10336-009-0417-z
71. E. S. Ferrer, V. García-Navas, J. J. Sanz, J. Ortego, Molecular characterization of avian malaria parasites in three Mediterranean blue tit (*Cyanistes caeruleus*) populations. *Parasitol. Res.* **111**, 2137–2142 (2012). doi: 10.1007/s00436-012-3062-z; pmid: 22855242
72. E. Ferroglio, F. Tolari, E. Bollo, B. Bassano, Isolation of *Brucella melitensis* from alpine ibex. *J. Wildl. Dis.* **34**, 400–402 (1998). doi: 10.7589/0090-3558-34.2.400; pmid: 9577795
73. M. J. Forzán, J. Wood, Low detection of ranavirus DNA in wild postmetamorphic green frogs, *Rana* (*Lithobates*) *clamitans*, despite previous or concurrent tadpole mortality. *J. Wildl. Dis.* **49**, 879–886 (2013). doi: 10.7589/2013-03-051; pmid: 24502715
74. S. F. Fox, A. L. Greer, R. Torres-Cervantes, J. P. Collins, First case of ranavirus-associated morbidity and mortality in natural populations of the South American frog Atelognathus patagonicus. *Dis. Aquat. Organ.* **72**, 87–92 (2006). doi: 10.3354/dao072087; pmid: 17067077
75. T. J. Gaetano *et al*., Mapping correlates of parasitism in wild South African vervet monkeys (*Chlorocebus aethiops*). *Afr. J. Wildl. Res.* **44**, 56–70 (2014). doi: 10.3957/056.044.0105
76. M. Gauthier-Clerc *et al*., Serological survey of the king penguin, *Aptenodytes patagonicus*, in Crozet Archipelago for antibodies to infectious bursal disease, influenza A and Newcastle disease viruses. *Polar Biol.* **25**, 316–319 (2002). doi: 10.1007/s00300-001-0346-7
77. A. Gimeno, M. Meikl, A. Pitt, M. Winkler, U.-G. Berninger, Testing of fire salamanders around Salzburg for *Batrachochytrium salamandrivorans* within a school project. *Eco. Mont.* **7**, 72–76 (2015). doi: 10.1553/eco.mont-7-1s72
78. K. M. Good, A. Houser, L. Arntzen, P. C. Turnbull, Naturally acquired anthrax antibodies in a cheetah (*Acinonyx jubatus*) in Botswana. *J. Wildl. Dis.* **44**, 721–723 (2008). doi: 10.7589/0090-3558-44.3.721; pmid: 18689661
79. R. M. Goodman, D. L. Miller, Y. T. Ararso, Prevalence of ranavirus in Virginia turtles as detected by tail-clip sampling versus oral-cloacal swabbing. *Northeast. Nat.* **20**, 325–332 (2013). doi: 10.1656/045.020.0208
80. C. Gortázar, R. Villafuerte, J. Blanco, D. Fernández-De-Luco, Enzootic sarcoptic mange in red foxes in Spain. *Z. Jagdwiss.* **44**, 251–256 (1998).
81. M. J. Gray, D. L. Miller, J. T. Hoverman, First report of ranavirus infecting lungless salamanders. *Herpetol. Rev.* **40**, 316 (2009).
82. A. L. Greer, J. L. Brunner, J. P. Collins, Spatial and temporal patterns of *Ambystoma tigrinum* virus (ATV) prevalence in tiger salamanders *Ambystoma tigrinum nebulosum*. *Dis. Aquat. Organ.* **85**, 1–6 (2009). doi: 10.3354/dao02061; pmid: 19593927
83. C. S. Gresham, C. A. Gresham, M. J. Duffy, C. T. Faulkner, S. Patton, Increased prevalence of *Brucella suis* and pseudorabies virus antibodies in adults of an isolated feral swine population in coastal South Carolina. *J. Wildl. Dis.* **38**, 653–656 (2002). doi: 10.7589/0090-3558-38.3.653; pmid: 12238392
84. P. R. Grimstad, S. M. Schmitt, D. G. Williams, Prevalence of neutralizing antibody to Jamestown Canyon virus (California group) in populations of elk and moose in northern Michigan and Ontario, Canada. *J. Wildl. Dis.* **22**, 453–458 (1986). doi: 10.7589/0090-3558-22.4.453; pmid: 3503129
85. M.-H. Guislain *et al*., Ecological and biological factors involved in the transmission of *Echinococcus multilocularis* in the French Ardennes. *J. Helminthol.* **82**, 143–151 (2008). doi: 10.1017/S0022149X08912384; pmid: 18394209
86. E. M. Hall, E. J. Crespi, C. S. Goldberg, J. L. Brunner, Evaluating environmental DNA-based quantification of ranavirus infection in wood frog populations. *Mol. Ecol. Resour.* **16**, 423–433 (2016). doi: 10.1111/1755-0998.12461; pmid: 26308150
87. A. N. Hamir, D. E. Snyder, J. R. Lichtenfels, Cerebral larva migrans in a raccoon (*Procyon lotor*). *Vet. Pathol.* **36**, 618–620 (1999). doi: 10.1354/vp.36-6-618; pmid: 10568447
88. A. S. Hammer, H. H. Dietz, T. H. Andersen, L. Nielsen, M. Blixenkrone-Moeller, Distemper virus as a cause of central nervous disease and death in badgers (*Meles meles*) in Denmark. *Vet. Rec.* **154**, 527–530 (2004). doi: 10.1136/vr.154.17.527; pmid: 15134165
89. M. M. Henton, O. Zapke, P. A. Basson, *Streptococcus phocae* infections associated with starvation in Cape fur seals. *J. S. Afr. Vet. Assoc.* **70**, 98–99 (1999). doi: 10.4102/jsava.v70i2.763; pmid: 10855831
90. A. Hlinak *et al*., Serological survey of viral pathogens in bean and white-fronted geese from Germany. *J. Wildl. Dis.* **34**, 479–486 (1998). doi: 10.7589/0090-3558-34.3.479; pmid: 9706557
91. E. P. Hoberg, K. B. Aubry, J. D. Brittell, Helminth parasitism in martens (*Martes americana*) and ermines (*Mustela erminea*) from Washington, with comments on the distribution of *Trichinella spiralis*. *J. Wildl. Dis.* **26**, 447–452 (1990). doi: 10.7589/0090-3558-26.4.447; pmid: 2250320
92. J. Hoeve, D. G. Joachim, E. M. Addison, Parasites of moose (*Alces alces*) from an agricultural area of eastern Ontario. *J. Wildl. Dis.* **24**, 371–374 (1988). doi: 10.7589/0090-3558-24.2.371; pmid: 3373648
93. M. Hofmeyr, D. Hofmeyr, L. Nel, J. Bingham, A second outbreak of rabies in African wild dogs (*Lycaon pictus*) in Madikwe Game Reserve, South Africa, demonstrating the efficacy of vaccination against natural rabies challenge. *Anim. Conserv.* **7**, 193–198 (2004). doi: 10.1017/S1367943004001234
94. P. H. Holz *et al*., Virus survey in populations of two subspecies of bent-winged bats (*Miniopterus orianae bassanii* and *oceanensis*) in south-eastern Australia reveals a high prevalence of diverse herpesviruses. *PLOS ONE* **13**, e0197625 (2018). doi: 10.1371/journal.pone.0197625; pmid: 29795610
95. J. T. Hoverman, M. J. Gray, D. L. Miller, N. A. Haislip, Widespread occurrence of ranavirus in pond-breeding amphibian populations. *EcoHealth* **9**, 36–48 (2012). doi: 10.1007/s10393-011-0731-9; pmid: 22173292
96. M. Ionita, M. G. Varela, E. T. Lyons, T. R. Spraker, S. C. Tolliver, Hookworms (*Uncinaria lucasi*) and acanthocephalans (*Corynosoma* spp. and *Bolbosoma* spp.) found in dead northern fur seals (*Callorhinus ursinus*) on St. Paul Island, Alaska in 2007. *Parasitol. Res.* **103**, 1025–1029 (2008). doi: 10.1007/s00436-008-1087-0; pmid: 18587686
97. K. Ishiwata *et al*., Gnathostomiasis in wild boars from Japan. *J. Wildl. Dis.* **34**, 155–157 (1998). doi: 10.7589/0090-3558-34.1.155; pmid: 9476238
98. E. Isogai *et al*., Serological survey for Lyme disease in sika deer (*Cervus nippon yesoensis*) by enzyme-linked immunosorbent assay (ELISA). *Microbiol. Immunol.* **35**, 695–703 (1991). doi: 10.1111/j.1348-0421.1991.tb01603.x; pmid: 1808467
99. E. Isogai *et al*., *Borrelia burgdorferi* sensu lato in an endemic environment: Wild sika deer (*Cervus nippon yesoensis*) with infected ticks and antibodies. *Microbiol. Immunol.* **40**, 13–19 (1996). doi: 10.1111/j.1348-0421.1996.tb03311.x; pmid: 8871523
100. K. Ivanova, P. Zehtindjiev, J. Mariaux, B. B. Georgiev, Genetic diversity of avian haemosporidians in Malaysia: Cytochrome b lineages of the genera *Plasmodium* and *Haemoproteus* (Haemosporida) from Selangor. *Infect. Genet. Evol.* **31**, 33–39 (2015). doi: 10.1016/j.meegid.2015.01.004; pmid: 25577987
101. B. Jackson *et al*., Emerging infectious disease or evidence of endemicity? A multi-season study of beak and feather disease virus in wild red-crowned parakeets (*Cyanoramphus novaezelandiae*). *Arch. Virol.* **160**, 2283–2292 (2015). doi: 10.1007/s00705-015-2510-3; pmid: 26138559
102. E.-B. Jakubek, R. Farkas, V. Pálfi, J. G. Mattsson, Prevalence of antibodies against *Toxoplasma gondii* and *Neospora caninum* in Hungarian red foxes (*Vulpes vulpes*). *Vet. Parasitol.* **144**, 39–44 (2007). doi: 10.1016/j.vetpar.2006.09.011; pmid: 17045742
103. B. D. Jansen, J. R. Heffelfinger, T. H. Noon, P. R. Krausman, J. C. Devos Jr., Infectious keratoconjunctivitis in bighorn sheep, Silver Bell Mountains, Arizona, USA. *J. Wildl. Dis.* **42**, 407–411 (2006). doi: 10.7589/0090-3558-42.2.407; pmid: 16870866
104. J. A. Jarvinen, W. A. Hedberg, *Parelaphostrongylus tenuis* (Nematoda) in white-tailed deer (*Odocoileus virginianus*) in central Iowa. *J. Parasitol.* **79**, 116–119 (1993). doi: 10.2307/3283289; pmid: 8437050
105. T. Jenkins, I. P. Owens, Biogeography of avian blood parasites (*Leucocytozoon* spp.) in two resident hosts across Europe: Phylogeographic structuring or the abundance-occupancy relationship? *Mol. Ecol.* **20**, 3910–3920 (2011). doi: 10.1111/j.1365-294X.2011.05221.x; pmid: 21880082
106. D. O. Joly, F. Messier, The distribution of *Echinococcus granulosus* in moose: Evidence for parasite-induced vulnerability to predation by wolves? *Oecologia* **140**, 586–590 (2004). doi: 10.1007/s00442-004-1633-0; pmid: 15232731
107. D. O. Joly, F. Messier, Factors affecting apparent prevalence of tuberculosis and brucellosis in wood bison. *J. Anim. Ecol.* **73**, 623–631 (2004). doi: 10.1111/j.0021-8790.2004.00836.x
108. H. E. Jordan, F. A. Hayes, Gastrointestinal helminths of raccoons (*Procyon lotor*) from Ossabaw Island, Georgia. *J. Parasitol.* **45**, 249–252 (1959). doi: 10.2307/3274491; pmid: 13665459
109. F. Jori *et al*., An assessment of zoonotic and production limiting pathogens in rusa deer (*Cervus timorensis rusa*) from Mauritius. *Transbound. Emerg. Dis.* **61** (suppl. 1), 31–42 (2014). doi: 10.1111/tbed.12206; pmid: 24382104
110. D. Kálmán, L. Egyed, PCR detection of bovine herpesviruses from nonbovine ruminants in Hungary. *J. Wildl. Dis.* **41**, 482–488 (2005). doi: 10.7589/0090-3558-41.3.482; pmid: 16244057
111. A. J. Kamps, S. A. Dubay, J. Langenberg, R. K. Maes, Evaluation of trapper-collected Nobuto filter-paper blood samples for distemper and parvovirus antibody detection in

coyotes (*Canis latrans*) and raccoons (*Procyon lotor*). *J. Wildl. Dis.* **51**, 724–728 (2015). doi: 10.7589/2014-06-147; pmid: 25973631
112. V. Kharchenko, V. Kornyushin, E. Varodi, O. Malega, Occurrence of *Echinococcus multilocularis* (Cestoda, Taeniidae) in red foxes (*Vulpes vulpes*) from Western Ukraine. *Acta Parasitol.* **53**, 36–40 (2008). doi: 10.2478/s11686-008-0008-9
113. B. F. Kingscote, J. G. Bohac, Antibodies to bovine bacterial and viral pathogens in pronghorns in Alberta, 1983. *J. Wildl. Dis.* **22**, 511–514 (1986). doi: 10.7589/0090-3558-22.4.511; pmid: 2845155
114. C. E. Kirkpatrick, D. A. Leiby, D. Abraham, C. H. Duffy III, Gongylonema pulchrum Molin (Nematoda: Gongylonematidae) in black bears (*Ursus americanus* Pallas) from Pennsylvania. *J. Wildl. Dis.* **22**, 119–121 (1986). doi: 10.7589/0090-3558-22.1.119; pmid: 3951047
115. E. Kitamura, Y. Yokohata, M. Suzuki, M. Kamiya, Metazoan parasites of sika deer from east Hokkaido, Japan and ecological analyses of their abomasal nematodes. *J. Wildl. Dis.* **33**, 278–284 (1997). doi: 10.7589/0090-3558-33.2.278; pmid: 9131559
116. A. A. Kocan *et al*., Naturally occurring hepatozoonosis in coyotes from Oklahoma. *J. Wildl. Dis.* **35**, 86–89 (1999). doi: 10.7589/0090-3558-35.1.86; pmid: 10073352
117. H. Korsholm, C. Olesen, Preliminary investigations on the parasite burden and distribution of endoparasite species of muskox (*Ovibos moschatus*) and caribou (*Rangifer tarandus groenlandicus*) in West Greenland. *Rangifer* **13**, 185–189 (1993). doi: 10.7557/2.13.4.1056
118. J. Laakkonen, J. Sundell, T. Soveri, Lung parasites of least weasels in Finland. *J. Wildl. Dis.* **34**, 816–819 (1998). doi: 10.7589/0090-3558-34.4.816; pmid: 9813855
119. R. Lainson *et al*., Amazonian visceral leishmaniasis—Distribution of the vector *Lutzomyia longipalpis* (Lutz & Neiva) in relation to the fox *Cerdocyon thous* (linn.) and the efficiency of this reservoir host as a source of infection. *Mem. Inst. Oswaldo Cruz* **85**, 135–137 (1990). doi: 10.1590/S0074-02761990000100027; pmid: 2215228
120. L. Lamontagne, L. Sadi, R. Joyal, Serological evidence of bovine herpesvirus 1-related virus infection in the white-tailed deer population on Anticosti Island, Quebec. *J. Wildl. Dis.* **25**, 202–205 (1989). doi: 10.7589/0090-3558-25.2.202; pmid: 2541261
121. J. H. Landsberg *et al*., Co-infection by alveolate parasites and frog virus 3-like ranavirus during an amphibian larval mortality event in Florida, USA. *Dis. Aquat. Organ.* **105**, 89–99 (2013). doi: 10.3354/dao02625; pmid: 23872853
122. S. E. Little, D. E. Stallknecht, J. M. Lockhart, J. E. Dawson, W. R. Davidson, Natural coinfection of a white-tailed deer (*Odocoileus virginianus*) population with three *Ehrlichia* spp. *J. Parasitol.* **84**, 897–901 (1998). doi: 10.2307/3284616; pmid: 9794627
123. J. S. Liz, J. W. Sumner, K. Pfister, M. Brossard, PCR detection and serological evidence of granulocytic ehrlichial infection in roe deer (*Capreolus capreolus*) and chamois (*Rupicapra rupicapra*). *J. Clin. Microbiol.* **40**, 892–897 (2002). doi: 10.1128/JCM.40.3.892-897.2002; pmid: 11880411
124. G. López, J. Muñoz, R. Soriguer, J. Figuerola, Increased endoparasite infection in late-arriving individuals of a trans-Saharan passerine migrant bird. *PLOS ONE* **8**, e61236 (2013). doi: 10.1371/journal.pone.0061236; pmid: 23620731
125. B. Losson *et al*., Prevalence of *Echinococcus multilocularis* in the red fox (*Vulpes vulpes*) in southern Belgium. *Vet. Parasitol.* **117**, 23–28 (2003). doi: 10.1016/j.vetpar.2003.08.003; pmid: 14597275
126. H. L. Lutz *et al*., Parasite prevalence corresponds to host life history in a diverse assemblage of afrotropical birds and haemosporidian parasites. *PLOS ONE* **10**, e0121254 (2015). doi: 10.1371/journal.pone.0121254; pmid: 25853491
127. L. A. Magnarelli, J. W. Ijdo, K. C. Stafford III, E. Fikrig, Infections of granulocytic ehrlichiae and *Borrelia burgdorferi* in white-tailed deer in Connecticut. *J. Wildl. Dis.* **35**, 266–274 (1999). doi: 10.7589/0090-3558-35.2.266; pmid: 10231753
128. D. J. Marcogliese, Fecundity of sealworm (*Pseudoterranova decipiens*) infecting grey seals (*Halichoerus grypus*) in the Gulf of St. Lawrence, Canada: Lack of density-dependent effects. *Int. J. Parasitol.* **27**, 1401–1409 (1997). doi: 10.1016/S0020-7519(97)00129-X; pmid: 9421731
129. A. Martinez, A. Salinas, F. Martinez, A. Cantu, D. K. Miller, Serosurvey for selected disease agents in white-tailed deer from Mexico. *J. Wildl. Dis.* **35**, 799–803 (1999). doi: 10.7589/0090-3558-35.4.799; pmid: 10574545
130. A. Marzal, T. Albayrak, Geographical variation of haemosporidian parasites in Turkish populations of Krüper's Nuthatch *Sitta krueperi*. *J. Ornithol.* **153**, 1225–1231 (2012). doi: 10.1007/s10336-012-0853-z
131. A. Marzal, L. García-Longoria, J. M. Cárdenas Callirgos, R. N. M. Sehgal, Invasive avian malaria as an emerging parasitic disease in native birds of Peru. *Biol. Invasions* **17**, 39–45 (2015). doi: 10.1007/s10530-014-0718-x
132. B. K. McGee *et al*., Possible vector dissemination by swift foxes following a plague epizootic in black-tailed prairie dogs in northwestern Texas. *J. Wildl. Dis.* **42**, 415–420 (2006). doi: 10.7589/0090-3558-42.2.415; pmid: 16870868
133. S. McKEEVER, Observations on *Paragonimus kellicotti* Ward from Georgia. *J. Parasitol.* **44**, 324–327 (1958). doi: 10.2307/3274599; pmid: 13550027
134. R. G. McLean *et al*., The role of deer as a possible reservoir host of potosi virus, a newly recognized arbovirus in the United States. *J. Wildl. Dis.* **32**, 444–452 (1996). doi: 10.7589/0090-3558-32.3.444; pmid: 8827670
135. D. P. McMahon *et al*., Elevated virulence of an emerging viral genotype as a driver of honeybee loss. *Proc. Biol. Sci.* **283**, 20160811 (2016). doi: 10.1098/rspb.2016.0811; pmid: 27358367
136. L. N. Measures, J. P. Dubey, P. Labelle, D. Martineau, Seroprevalence of *Toxoplasma gondii* in Canadian pinnipeds. *J. Wildl. Dis.* **40**, 294–300 (2004). doi: 10.7589/0090-3558-40.2.294; pmid: 15362830
137. L. D. Mech, S. P. Tracy, Prevalence of giant kidney worm (*Dioctophyma renale*) in wild mink (*Mustela vison*) in Minnesota. *Am. Midl. Nat.* **145**, 206–210 (2001). doi: 10.1674/0003-0031(2001)145[0206:POGKWD]2.0.CO;2
138. C. Miaud *et al*., Ranavirus causes mass die-offs of alpine amphibians in the Southwestern Alps, France. *J. Wildl. Dis.* **52**, 242–252 (2016). doi: 10.7589/2015-05-113; pmid: 26967128
139. D. L. Miller *et al*., Pathologic findings in larval and juvenile anurans inhabiting farm ponds in Tennessee, USA. *J. Wildl. Dis.* **45**, 314–324 (2009). doi: 10.7589/0090-3558-45.2.314; pmid: 19395741
140. M. A. Moens, J. Pérez-Tris, Discovering potential sources of emerging pathogens: South America is a reservoir of generalist avian blood parasites. *Int. J. Parasitol.* **46**, 41–49 (2016). doi: 10.1016/j.ijpara.2015.08.001; pmid: 26348660
141. B. Molnar, C. Duchamp, K. Möstl, P.-A. Diehl, B. Betschart, Comparative survey of canine parvovirus, canine distemper virus and canine enteric coronavirus infection in free-ranging wolves of central Italy and south-eastern France. *Eur. J. Wildl. Res.* **60**, 613–624 (2014). doi: 10.1007/s10344-014-0825-0; pmid: 32214941
142. P. L. Moro *et al*., Intestinal parasites of the grey fox (*Pseudalopex culpaeus*) in the central Peruvian Andes. *J. Helminthol.* **72**, 87–89 (1998). doi: 10.1017/S0022149X00001048; pmid: 9639908
143. M. Mulvey, J. M. Aho, C. Lydeard, P. L. Leberg, M. H. Smith, Comparative population genetic structure of a parasite (*Fascioloides magna*) and its definitive host. *Evolution* **45**, 1628–1640 (1991). pmid: 28564131
144. R. Munro, H. Ross, C. Cornwell, J. Gilmour, Disease conditions affecting common seals (*Phoca vitulina*) around the Scottish mainland, September-November 1988. *Sci. Total Environ.* **115**, 67–82 (1992). doi: 10.1016/0048-9697(92)90033-O; pmid: 1594936
145. A. Burrells *et al*., Evidence of the three main clonal *Toxoplasma gondii* lineages from wild mammalian carnivores in the UK. *Parasitology* **140**, 1768–1776 (2013). doi: 10.1017/S0031182013001169; pmid: 23953298
146. E. Nilsson *et al*., Multiple cryptic species of sympatric generalists within the avian blood parasite *Haemoproteus majoris*. *J. Evol. Biol.* **29**, 1812–1826 (2016). doi: 10.1111/jeb.12911; pmid: 27262030
147. D. Nyamsuren *et al*., Exposure of Mongolian gazelles (*Procapra gutturosa*) to foot and mouth disease virus. *J. Wildl. Dis.* **42**, 154–158 (2006). doi: 10.7589/0090-3558-42.1.154; pmid: 16699158
148. D. W. Oates, M. C. Sterner, D. J. Steffen, Meningeal worm in free-ranging deer in Nebraska. *J. Wildl. Dis.* **35**, 101–104 (1999). doi: 10.7589/0090-3558-35.1.101; pmid: 10073356
149. D. W. Oates, M. C. Sterner, E. Boyd, Meningeal worm in deer from western Nebraska. *J. Wildl. Dis.* **36**, 370–373 (2000). doi: 10.7589/0090-3558-36.2.370; pmid: 10813621
150. K. Ohishi *et al*., Antibodies to human-related H3 influenza A virus in Baikal seals (*Phoca sibirica*) and ringed seals (*Phoca hispida*) in Russia. *Microbiol. Immunol.* **48**, 905–909 (2004). doi: 10.1111/j.1348-0421.2004.tb03610.x; pmid: 15557750
151. G. O'Neill, J. Whelan, The occurrence of *Corynosoma strumosum* in the grey seal, *Halichoerus grypus*, caught off the Atlantic coast of Ireland. *J. Helminthol.* **76**, 231–234 (2002). doi: 10.1079/JOH10.1076/2002117; pmid: 12363376
152. D. O'Toole, E. S. Williams, V. Welch, C. E. Nunamaker, C. Lynn, Subepidermal vesiculobullous filarial dermatitis in free-ranging American badgers (*Taxidea taxus*). *Vet. Pathol.* **30**, 343–351 (1993). doi: 10.1177/030098589303000403; pmid: 8212456
153. D. O'Toole, V. Welch, B. Williams, Immunohistochemistry of parasitic subepidermal vesiculobullous disease in American badgers (*Taxidea taxus*). *J. Vet. Diagn. Invest.* **6**, 72–76 (1994). doi: 10.1177/104063879400600113; pmid: 8011785
154. G. S. Pandey, A. Mweene, A. K. Suzuki, A. Nambota, T. Kaji, Dermatophilosis (*Cutaneous streptothricosis*) in Kafue lechwe (*Kobus leche kafuensis*). *J. Wildl. Dis.* **30**, 586–588 (1994). doi: 10.7589/0090-3558-30.4.586; pmid: 7760496
155. S. Pardal *et al*., Shorebird low spillover risk of mosquito-borne pathogens on Iberian wetlands. *J. Ornithol.* **155**, 549–554 (2014). doi: 10.1007/s10336-013-1036-2
156. G. A. Archer *et al*., Detection of copathogens in free-ranging eastern box turtles (*Terrapene carolina carolina*) in Illinois and Tennessee. *J. Zoo Wildl. Med.* **48**, 1127–1134 (2017). doi: 10.1638/2017-0148R.1; pmid: 29297797
157. J. Henning, P. Davies, J. Meers, Seropositivity to rabbit haemorrhagic disease virus in non-target mammals during periods of viral activity in a population of wild rabbits in New Zealand. *Wildl. Res.* **33**, 305–311 (2006). doi: 10.1071/WR03061
158. E. Lux, H. M. Mix, B. Zedev, *Damalinia* (*Tricholipeurus*) *zaganseeri*, n. sp. (Phthiraptera: Trichodectidae), a parasite from *Procapra gutturosa* (Artiodactyla: Bovidae) in Mongolia. *J. Med. Entomol.* **34**, 599–604 (1997). doi: 10.1093/jmedent/34.6.599; pmid: 9439112
159. A. Mannelli, U. Kitron, C. J. Jones, T. L. Slajchert, *Ixodes dammini* (Acari: Ixodidae) infestation on medium-sized mammals and blue jays in northwestern Illinois. *J. Med. Entomol.* **30**, 950–952 (1993). doi: 10.1093/jmedent/30.5.950; pmid: 8254647
160. E. S. Martinsen, I. F. Sidor, S. Flint, J. Cooley, M. A. Pokras, Documentation of malaria parasite (*Plasmodium* spp.) infection and associated mortality in a common loon (*Gavia immer*). *J. Wildl. Dis.* **53**, 859–863 (2017). doi: 10.7589/2016-08-195; pmid: 28665230
161. J. C. Pederson, L. A. Jensen, F. L. Andersen, Prevalence and distribution of *Elaeophora schneideri* Wehr and Dikmans, 1935 in mule deer in Utah. *J. Wildl. Dis.* **21**, 66–67 (1985). doi: 10.7589/0090-3558-21.1.66; pmid: 3157010
162. B. D. Perry, D. K. Nichols, E. S. Cullom, *Babesia odocoilei* Emerson and Wright, 1970 in white-tailed deer, *Odocoileus virginianus* (Zimmermann), in Virginia. *J. Wildl. Dis.* **21**, 149–152 (1985). doi: 10.7589/0090-3558-21.2.149; pmid: 3999247
163. M. J. Peterson *et al*., Infectious disease survey of Rio Grande wild turkeys in the Edwards Plateau of Texas. *J. Wildl. Dis.* **38**, 826–833 (2002). doi: 10.7589/0090-3558-38.4.826; pmid: 12528453
164. S. M. Pietrzak, O. J. Pung, Trypanosomiasis in raccoons from Georgia. *J. Wildl. Dis.* **34**, 132–136 (1998). doi: 10.7589/0090-3558-34.1.132; pmid: 9476234
165. J. R. Purvis, M. J. Peterson, N. O. Dronen, J. R. Lichtenfels, N. J. Silvy, Northern bobwhites as disease indicators for the endangered Attwater's prairie chicken. *J. Wildl. Dis.* **34**, 348–354 (1998). doi: 10.7589/0090-3558-34.2.348; pmid: 9577783
166. M. J. Pybus, Survey of hepatic and pulmonary helminths of wild cervids in Alberta, Canada. *J. Wildl. Dis.* **26**, 453–459 (1990). doi: 10.7589/0090-3558-26.4.453; pmid: 2250321
167. A. M. Ramey, C. R. Ely, J. A. Schmutz, J. M. Pearce, D. J. Heard, Molecular detection of hematozoa infections in tundra swans relative to migration patterns and ecological conditions at breeding grounds. *PLOS ONE* **7**, e45789 (2012). doi: 10.1371/journal.pone.0045789; pmid: 23049862
168. D. G. Renter, J. M. Sargeant, S. E. Hygnstorm, J. D. Hoffman, J. R. Gillespie, *Escherichia coli* O157:H7 in free-ranging deer in Nebraska. *J. Wildl. Dis.* **37**, 755–760 (2001). doi: 10.7589/0090-3558-37.4.755; pmid: 11763739
169. A. N. Reshetnikov *et al*., Detection of the emerging amphibian pathogens *Batrachochytrium dendrobatidis* and ranavirus in Russia. *Dis. Aquat. Organ.* **110**, 235–240 (2014). doi: 10.3354/dao02757; pmid: 25114047
170. H. P. Riemann, J. A. Howarth, R. Ruppanner, C. E. Franti, D. E. Behymer, Toxoplasma antibodies among bobcats and

other carnivores of norther California. *J. Wildl. Dis.* **11**, 272–276 (1975). doi: 10.7589/0090-3558-11.2.272; pmid: 1142562
171. H. P. Riemann, R. A. Thompson, D. E. Behymer, R. Ruppanner, C. E. Franti, Toxoplasmosis and Q fever antibodies among wild carnivores in California. *J. Wildl. Manage.* **42**, 198–202 (1978). doi: 10.2307/3800717
172. J. M. Rijks *et al*., Quantitative analysis of the 2002 phocine distemper epidemic in the Netherlands. *Vet. Pathol.* **45**, 516–530 (2008). doi: 10.1354/vp.45-4-516; pmid: 18587100
173. B. B. Rothermel *et al*., High occupancy of stream salamanders despite high ranavirus prevalence in a southern Appalachians watershed. *EcoHealth* **10**, 184–189 (2013). doi: 10.1007/s10393-013-0843-5; pmid: 23645459
174. B. B. Rothermel *et al*., Disease dynamics of red-spotted newts and their anuran prey in a montane pond community. *Dis. Aquat. Organ.* **118**, 113–127 (2016). doi: 10.3354/dao02965; pmid: 26912042
175. H. L. Ruhnke, S. Madoff, *Mycoplasma phocidae* sp. nov., isolated from harbor seals (*Phoca vitulina* L.). *Int. J. Syst. Bateriol.* **42**, 211–214 (1992). pmid: 1581181
176. D. J. Salkeld *et al*., The potential role of swift foxes (*Vulpes velox*) and their fleas in plague outbreaks in prairie dogs. *J. Wildl. Dis.* **43**, 425–431 (2007). doi: 10.7589/0090-3558-43.3.425; pmid: 17699080
177. D. Santiago-Alarcon, I. MacGregor-Fors, K. Kühnert, G. Segelbacher, H. M. Schaefer, Avian haemosporidian parasites in an urban forest and their relationship to bird size and abundance. *Urban Ecosyst.* **19**, 331–346 (2016). doi: 10.1007/s11252-015-0494-0
178. H. Sato, T. Inaba, Y. Ihama, H. Kamiya, Parasitological survey on wild carnivora in north-western Tohoku, Japan. *J. Vet. Med. Sci.* **61**, 1023–1026 (1999). doi: 10.1292/jvms.61.1023; pmid: 10535507
179. H. Sato, Y. Ihama, T. Inaba, M. Yagisawa, H. Kamiya, Helminth fauna of carnivores distributed in north-western Tohoku, Japan, with special reference to *Mesocestoides paucitesticulus* and *Brachylaima tokudai*. *J. Vet. Med. Sci.* **61**, 1339–1342 (1999). doi: 10.1292/jvms.61.1339; pmid: 10651058
180. S. Schmid, K. Fachet, A. Dinkel, U. Mackenstedt, F. Woog, Carrion crows (*Corvus corone*) of southwest Germany: Important hosts for haemosporidian parasites. *Malar. J.* **16**, 369 (2017). doi: 10.1186/s12936-017-2023-5;pmid: 28899382
181. D. M. Schock *et al*., Amphibian chytrid fungus and ranaviruses in the Northwest Territories, Canada. *Dis. Aquat. Organ.* **92**, 231–240 (2010). doi: 10.3354/dao02134; pmid: 21268986
182. F. M. Seesee, M. C. Sterner, D. E. Worley, Helminths of the coyote (*Canis latrans* Say) in Montana. *J. Wildl. Dis.* **19**, 54–55 (1983). doi: 10.7589/0090-3558-19.1.54; pmid: 6842734
183. T. A. Seimon *et al*., Avian hemosporidian parasite lineages in four species of free-ranging migratory waterbirds from Mongolia, 2008. *J. Wildl. Dis.* **52**, 682–687 (2016). doi: 10.7589/2015-11-311; pmid: 27243330
184. R. S. Seville, E. M. Addison, Nongastrointestinal helminths in marten (*Martes americana*) from Ontario, Canada. *J. Wildl. Dis.* **31**, 529–533 (1995). doi: 10.7589/0090-3558-31.4.529; pmid: 8592385
185. A. Silva-Iturriza, V. Ketmaier, R. Tiedemann, Profound population structure in the Philippine Bulbul *Hypsipetes philippinus* (Pycnonotidae, Aves) is not reflected in its *Haemoproteus haemosporidian* parasite. *Infect. Genet. Evol.* **12**, 127–136 (2012). doi: 10.1016/j.meegid.2011.10.024; pmid: 22108671
186. J. M. Simmons, W. S. Nicholson, E. P. Hill, D. B. Briggs, Occurrence of (*Dirofilaria immitis*) in gray fox (*Urocyon cinereoargenteus*) in Alabama and Georgia. *J. Wildl. Dis.* **16**, 225–228 (1980). doi: 10.7589/0090-3558-16.2.225; pmid: 7431520
187. T. Slajchert, U. D. Kitron, C. J. Jones, A. Mannelli, Role of the eastern chipmunk (*Tamias striatus*) in the epizootiology of Lyme borreliosis in northwestern Illinois, USA. *J. Wildl. Dis.* **33**, 40–46 (1997). doi: 10.7589/0090-3558-33.1.40; pmid: 9027689
188. D. E. Snyder, Indirect immunofluorescent detection of oocysts of Cryptosporidium parvum in the feces of naturally infected raccoons (*Procyon lotor*). *J. Parasitol.* **74**, 1050–1052 (1988). doi: 10.2307/3282233; pmid: 3057164
189. D. E. Snyder, *Capillaria procyonis* (Nematoda: Trichuroidea) eggs from the tongue of the raccoon (*Procyon lotor*). *J. Wildl. Dis.* **24**, 722–723 (1988). doi: 10.7589/0090-3558-24.4.722; pmid: 3193575
190. D. E. Snyder, G. C. Sanderson, M. Toivio-Kinnucan, B. L. Blagburn, *Sarcocystis kirkpatricki* n. sp. (Apicomplexa: Sarcocystidae) in muscles of raccoons (*Procyon lotor*) from Illinois. *J. Parasitol.* **76**, 495–500 (1990). doi: 10.2307/3282827; pmid: 2116513
191. K. K. Sørensen *et al*., Acute toxoplasmosis in three wild arctic foxes (*Alopex lagopus*) from Svalbard; one with co-infections of *Salmonella* Enteritidis PT1 and *Yersinia pseudotuberculosis* serotype 2b. *Res. Vet. Sci.* **78**, 161–167 (2005). doi: 10.1016/j.rvsc.2004.07.010; pmid: 15563924
192. M. J. Souza, M. J. Gray, P. Colclough, D. L. Miller, Prevalence of infection by Batrachochytrium dendrobatidis and ranavirus in eastern hellbenders (*Cryptobranchus alleganiensis alleganiensis*) in eastern Tennessee. *J. Wildl. Dis.* **48**, 560–566 (2012). doi: 10.7589/0090-3558-48.3.560; pmid: 22740521
193. A. Spitzen-van der Sluijs *et al*., Course of an Isolated ranavirus outbreak in a *Pelobates fuscus* population in The Netherlands. *J. Herpetological Med. Surg.* **26**, 117–121 (2016). doi: 10.5818/1529-9651-26.3-4.117
194. T. R. Spraker, J. K. Collins, W. J. Adrian, J. H. Olterman, Isolation and serologic evidence of a respiratory syncytial virus in bighorn sheep from Colorado. *J. Wildl. Dis.* **22**, 416–418 (1986). doi: 10.7589/0090-3558-22.3.416; pmid: 3735590
195. D. E. Stallknecht, W. R. Davidson, Antibodies to bluetongue and epizootic hemorrhagic disease viruses from white-tailed deer blood samples dried on paper strips. *J. Wildl. Dis.* **28**, 306–310 (1992). doi: 10.7589/0090-3558-28.2.306; pmid: 1318425
196. T. Stark *et al*., Death in the clouds: Ranavirus associated mortality in assemblage of cloud forest amphibians in Nicaragua. *Acta Herpetol.* **9**, 125–127 (2014). doi: 10.13128/Acta_Herpetol-13516
197. S. S. Stubblefield, D. B. Pence, R. J. Warren, Visceral helminth communities of sympatric mule and white-tailed deer from the Davis Mountains of Texas. *J. Wildl. Dis.* **23**, 113–120 (1987). doi: 10.7589/0090-3558-23.1.113; pmid: 3820412
198. J. N. Stuht, W. G. Youatt, Heartworms and lung flukes from red foxes in Michigan. *J. Wildl. Manage.* **36**, 166–170 (1972). doi: 10.2307/3799205
199. A. Svoboda, G. Marthinsen, L. Turcoková, J. T. Lifjeld, A. Johnsen, Identification of blood parasites in old world warbler species from the Danube River Delta. *Avian Dis.* **53**, 634–636 (2009). doi: 10.1637/8842-040409-Case.1; pmid: 20095169
200. P. Synek *et al*., Haemosporidian parasites of a European passerine wintering in South Asia: Diversity, mixed infections and effect on host condition. *Parasitol. Res.* **112**, 1667–1677 (2013). doi: 10.1007/s00436-013-3323-5; pmid: 23385972
201. E. Szöllosi *et al*., Determinants of distribution and prevalence of avian malaria in blue tit populations across Europe: Separating host and parasite effects. *J. Evol. Biol.* **24**, 2014–2024 (2011). doi: 10.1111/j.1420-9101.2011.02339.x; pmid: 21726328
202. S. Uni, Y. Suzuki, A. Katsumi, *Cercopithifilaria shohoi* n. sp. (Nematoda: Filarioidea) from the relict Bovidae, *Capricornis crispus*, in Japan. *Parasite* **5**, 119–126 (1998). doi: 10.1051/parasite/1998052119; pmid: 9754307
203. K. Urquhart *et al*., A survey of pathogens and metazoan parasites on wild sea trout (*Salmo trutta*) in Scottish waters. *ICES J. Mar. Sci.* **67**, 444–453 (2009). doi: 10.1093/icesjms/fsp271
204. H. Van Campen *et al*., Isolation of bovine viral diarrhea virus from a free-ranging mule deer in Wyoming. *J. Wildl. Dis.* **37**, 306–311 (2001). doi: 10.7589/0090-3558-37.2.306; pmid: 11310881
205. F. F. Vaz *et al*., Survey of pathogens in threatened wild red-tailed Amazon parrot (*Amazona brasiliensis*) nestlings in Rasa Island, Brazil. *Braz. J. Microbiol.* **48**, 747–753 (2017). doi: 10.1016/j.bjm.2017.03.004; pmid: 28629971
206. R. Ventim *et al*., Avian malaria infections in western European mosquitoes. *Parasitol. Res.* **111**, 637–645 (2012). doi: 10.1007/s00436-012-2880-3; pmid: 22427023
207. R. Ventim, L. Mendes, J. A. Ramos, H. Cardoso, J. Pérez-Tris, Local haemoparasites in introduced wetland passerines. *J. Ornithol.* **153**, 1253–1259 (2012). doi: 10.1007/s10336-012-0860-0
208. J. Vicente, C. Gortázar, High prevalence of large spiny-tailed protostrongylid larvae in Iberian red deer. *Vet. Parasitol.* **96**, 165–170 (2001). doi: 10.1016/S0304-4017(00)00425-8; pmid: 11230923
209. T. Vikøren *et al*., A severe outbreak of contagious ecthyma (orf) in a free-ranging musk ox (*Ovibos moschatus*) population in Norway. *Vet. Microbiol.* **127**, 10–20 (2008). doi: 10.1016/j.vetmic.2007.07.029; pmid: 17768017
210. R. W. Warne, B. LaBumbard, S. LaGrange, V. T. Vredenburg, A. Catenazzi, Co-infection by chytrid fungus and ranaviruses in wild and harvested frogs in the tropical Andes. *PLOS ONE* **11**, e0145864 (2016). doi: 10.1371/journal.pone.0145864; pmid: 26726999
211. I. Y. Warsame, M. Steen, Malignant catarrhal fever in wild Swedish moose (*Alces alces* L). *Rangifer* **9**, 51–57 (1989). doi: 10.7557/2.9.2.774
212. P. A. Webb *et al*., Epizootic vesicular stomatitis in Colorado, 1982: Some observations on the possible role of wildlife populations in an enzootic maintenance cycle. *J. Wildl. Dis.* **23**, 192–198 (1987). doi: 10.7589/0090-3558-23.2.192; pmid: 3035241
213. S. M. Whitfield *et al*., Infection and co-infection by the amphibian chytrid fungus and ranavirus in wild Costa Rican frogs. *Dis. Aquat. Organ.* **104**, 173–178 (2013). doi: 10.3354/dao02598; pmid: 23709470
214. E. S. Williams, E. T. Thorne, S. L. Anderson, J. D. Herriges Jr., Brucellosis in free-ranging bison (*Bison bison*) from Teton County, Wyoming. *J. Wildl. Dis.* **29**, 118–122 (1993). doi: 10.7589/0090-3558-29.1.118; pmid: 8445770
215. M. J. Wood *et al*., The epidemiology underlying age-related avian malaria infection in a long-lived host: The mute swan *Cygnus olor*. *J. Avian Biol.* **44**, 347–358 (2013). doi: 10.1111/j.1600-048X.2013.00091.x
216. K. Yagi, O. Bain, C. Shoho, *Onchocerca suzukii* n. sp. and *O. skrjabini* (= *O. tarsicola*) from a relict bovid, *Capricornis crispus*, in Japan. *Parasite* **1**, 349–356 (1994). doi: 10.1051/parasite/1994014349; pmid: 9140501
217. A. E. Yimam *et al*., First report of *Trichinella nativa* in red foxes (*Vulpes vulpes schrencki*) from Otaru City, Hokkaido, Japan. *Parasitol. Int.* **50**, 121–127 (2001). doi: 10.1016/S1383-5769(01)00073-3; pmid: 11438434
218. E. Yohannes, A. Križanauskienė, M. Valcu, S. Bensch, B. Kempenaers, Prevalence of malaria and related haemosporidian parasites in two shorebird species with different winter habitat distribution. *J. Ornithol.* **150**, 287–291 (2009). doi: 10.1007/s10336-008-0349-z
219. J. M. Zamparo, T. G. Andreadis, R. E. Shope, S. J. Tirrell, Serologic evidence of Jamestown Canyon virus infection in white-tailed deer populations from Connecticut. *J. Wildl. Dis.* **33**, 623–627 (1997). doi: 10.7589/0090-3558-33.3.623; pmid: 9249710
220. G. Zanella *et al*., *Mycobacterium bovis* in wildlife in France. *J. Wildl. Dis.* **44**, 99–108 (2008). doi: 10.7589/0090-3558-44.1.99; pmid: 18263825
221. P. Zehtindjiev *et al*., Occurrence of haemosporidian parasites in the paddyfield warbler, *Acrocephalus agricola* (Passeriformes, Sylviidae). *Acta Parasitol.* **54**, 295–300 (2009). doi: 10.2478/s11686-009-0052-0
222. P. Zehtindjiev *et al*., Dynamics of parasitemia of malaria parasites in a naturally and experimentally infected migratory songbird, the great reed warbler *Acrocephalus arundinaceus*. *Exp. Parasitol.* **119**, 99–110 (2008). doi: 10.1016/j.exppara.2007.12.018; pmid: 18280472
223. J. Cohen, jeremy-cohen/tmh-across-systems. Github (2008); https://github.com/jeremy-cohen/tmh-across-systems.
224. S. Bensch, O. Hellgren, J. Pérez-Tris, MalAvi: A public database of malaria parasites and related haemosporidians in avian hosts based on mitochondrial cytochrome *b* lineages. *Mol. Ecol. Resour.* **9**, 1353–1358 (2009). doi: 10.1111/j.1755-0998.2009.02692.x; pmid: 21564906
225. P. R. Stephens *et al*., Global mammal parasite database version 2.0. *Ecology* **98**, 1476–1476 (2017). doi: 10.1002/ecy.1799; pmid: 28273333
226. M. J. Lajeunesse, Facilitating systematic reviews, data extraction and meta-analysis with the metagear package for R. *Methods Ecol. Evol.* **7**, 323–330 (2016). doi: 10.1111/2041-210X.12472
227. R Core Team, R: A language and environment for statistical computing (R Foundation for Statistical Computing, Vienna, Austria, 2016).
228. IUCN, The IUCN Red List of Threatened Species, version 2015.2 (2015); www.iucnredlist.org.
229. N. S. Sodhi *et al*., Measuring the meltdown: Drivers of global amphibian extinction and decline. *PLOS ONE* **3**, e1636 (2008). doi: 10.1371/journal.pone.0001636; pmid: 18286193
230. R. J. Hijmans, raster: Geographic data analysis and modeling, R package version 2.2.31. (2014).

231. J. M. Sunday, A. E. Bates, N. K. Dulvy, Global analysis of thermal tolerance and latitude in ectotherms. *Proc. R. Soc. London Ser. B* **278**, 1823–1830 (2011). pmid: 21106582
232. M. E. Brooks *et al*., glmmTMB balances speed and flexibility among packages for zero-inflated generalized linear mixed modeling. *R J.* **9**, 378–400 (2017). doi: 10.32614/RJ-2017-066
233. K. Barton, MuMIn: Multi-model inference, R Package version 1.10.0 (2014).
234. P. Breheny, W. Burchett, visreg: Visualization of regression models, R package version 2 (2012).
235. O. Bjornstad, ncf: Spatial nonparametric covariance functions (2015).
236. E. Neuwirth, M. E. Neuwirth, Package "RColorBrewer," CRAN 2011-06-17 08:34:00. Apache License 2.0 (2011).

ACKNOWLEDGMENTS

We thank all of those who assembled disease or climatic datasets that were used in the analysis. We also thank E. Mordecai, T. Raffel, and the Rohr lab for their insightful thoughts on the manuscript. **Funding:** Funds were provided by grants to J.R.R. from the National Science Foundation (EF-1241889 and DEB-1518681) and the National Institutes of Health (R01TW010286-01). **Author contributions:** J.M.C. and J.R.R. devised ideas for the study. J.M.C., O.S., S.S., and E.L.S. compiled data from literature. J.M.C. compiled climate and weather data. J.M.C. conducted the statistical analyses. J.M.C. and J.R.R. wrote the first draft of the manuscript. All authors helped revise and improve the manuscript. O.S. and S.S. contributed equally and are listed alphabetically. **Competing interests:** The authors declare no competing interests. **Data and materials availability:** All data and code compiled for this study are available on Github (*223*).

SUPPLEMENTARY MATERIALS

science.sciencemag.org/content/370/6519/eabb1702/suppl/DC1
Figs. S1 to S10
Tables S1 to S8
MDAR Reproducibility Checklist

View/request a protocol for this paper from *Bio-protocol*.

4 February 2020; accepted 10 September 2020
10.1126/science.abb1702

RESEARCH ARTICLE SUMMARY

NEURODEVELOPMENT

Gene regulatory networks controlling vertebrate retinal regeneration

Thanh Hoang*, Jie Wang*, Patrick Boyd, Fang Wang, Clayton Santiago, Lizhi Jiang, Sooyeon Yoo, Manuela Lahne, Levi J. Todd, Meng Jia, Cristian Saez, Casey Keuthan, Isabella Palazzo, Natalie Squires, Warren A. Campbell, Fatemeh Rajaii, Trisha Parayil, Vickie Trinh, Dong Won Kim, Guohua Wang, Leah J. Campbell, John Ash, Andy J. Fischer, David R. Hyde†, Jiang Qian†, Seth Blackshaw†

INTRODUCTION: The ability to regenerate retinal neurons after injury varies drastically among vertebrate species. Teleost fish such as zebrafish can regenerate all major retinal cell types after injury by reprogramming Müller glia to a progenitor-like state. In the post-hatch chick, Müller glia can generate small numbers of neurons after injury but lose regenerative ability later in life. In contrast, mammalian Müller glia do not spontaneously regenerate lost retinal neurons. Although some genes that promote retinal regeneration have been identified, the core gene regulatory networks controlling Müller glia reprogramming remain largely unknown but can be identified through cross-species transcriptomic and epigenomic analysis.

RATIONALE: To identify injury-induced changes in Müller glia, we performed bulk RNA sequencing (RNA-seq) and assay for transposase-accessible chromatin with high-throughput sequencing (ATAC-seq) to separately profile gene expression and chromatin accessibility in both mouse and zebrafish. These assays included multiple time points following *N*-methyl-D-aspartate (NMDA) and light treatments, which damage inner retinal neurons and photoreceptors, respectively. We also conducted single-cell RNA-seq (scRNA-seq) to identify changes in gene expression after NMDA treatment and light damage, as well as after treatment with exogenous factors that induced injury-independent reprogramming, in mouse, zebrafish, and chick retinas. We then developed a computational tool, which we call integrated regulatory network analysis (IReNA), to integrate gene expression and chromatin accessibility in order to reconstruct regulatory networks of Müller glia in response to diverse stimuli. Finally, using loss-of-function approaches, we validated functions of candidate factors controlling Müller glia reprogramming.

RESULTS: We generated 100 RNA-seq and 40 ATAC-seq samples from zebrafish and mice, and obtained 105,666, 85,051, and 77,924 single retinal cells from zebrafish, chick, and mice, respectively. In all three species, Müller glia acquired a reactive state after treatments. In chick and zebrafish, Müller glia passed through this reactive state before becoming proliferative and neurogenic. In mice, however, Müller glia reverted to a resting state after injury. By integrating these datasets, we identified changes in gene expression and chromatin accessibility after each treatment. Cross-species analysis identified evolutionarily conserved and species-specific gene regulatory networks that control the transition of the quiescent, reactive, and proliferative Müller glia after stimulation. In mice, a dedicated network restored Müller glia to a quiescent state. In contrast, in zebrafish and chick, genes selectively expressed in reactive Müller glia promoted the transition to a proliferative and neurogenic progenitor state. Loss of function of genes selectively expressed in reactive Müller glia, such as *hmga1* and *yap1*, inhibited Müller glia reprogramming in zebrafish. In chick, pharmacological disruption of fatty acid–binding protein 5, 7, and 8 (FABP5/7/8) activity inhibited injury-induced transition from quiescence to neurogenic competence. Finally, deletion of nuclear factor I factors a, b, and x (*Nfia/b/x*), which maintain and restore a glial quiescent state, resulted in Müller glia reprogramming into retinal bipolar and amacrine interneurons in adult mice after injury.

CONCLUSION: We found that transition from quiescence through the reactive state is essential for Müller glia reprogramming in regeneration-competent species such as zebrafish and chick. Furthermore, proliferative and neurogenic competence are both suppressed by a dedicated gene regulatory network in mouse Müller glia. Cross-species RNA-seq and ATAC-seq data provide a comprehensive resource to study cellular responses to injury and Müller glia reprogramming. Our findings indicate that treatments targeting gene regulatory networks that repress neurogenic competence may help to facilitate reprogramming of mammalian Müller glia to neurons. ■

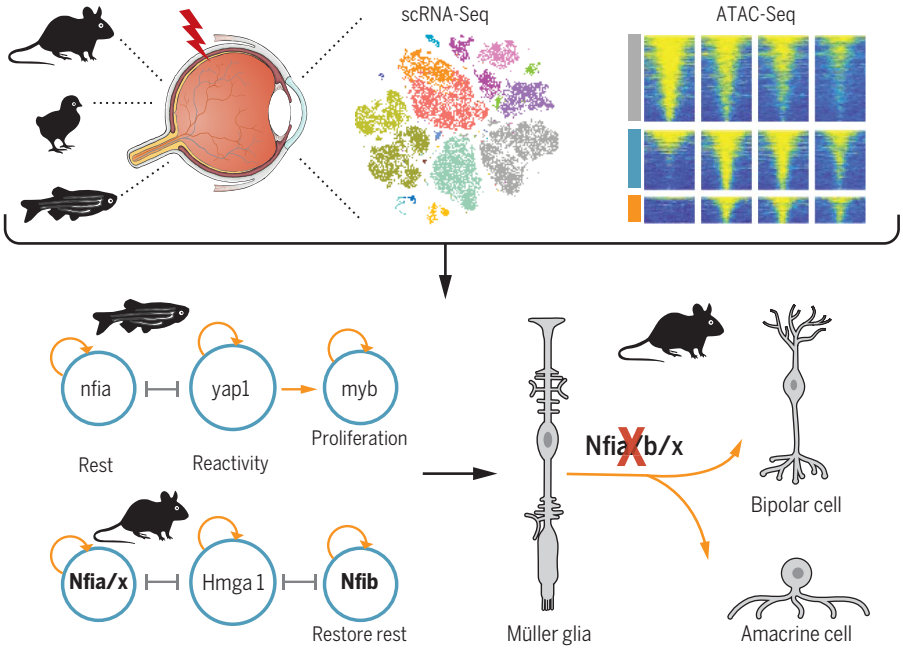

Control of retinal Müller glia reprogramming. RNA-seq and ATAC-seq were performed on Müller glia from zebrafish, chick, and mouse after different treatments. Integrative transcriptomic and epigenomic analysis revealed core regulatory networks controlling retinal regeneration. Loss of function of zebrafish genes expressed in reactive Müller glia blocked reprogramming, while in mouse Müller glia, disruption of *Nfia/b/x*, which maintain and restore quiescence, resulted in acquisition of neurogenic competence.

The list of author affiliations is available in the full article online.
*These authors contributed equally to this work.
†Corresponding author. Email: dhyde@nd.edu (D.R.H.); jiang.qian@jhmi.edu (J.Q.); sblack@jhmi.edu (S.B.)
Cite this article as T. Hoang *et al.*, *Science* **370**, eabb8598 (2020). DOI: 10.1126/science.abb8598

READ THE FULL ARTICLE AT
https://doi.org/10.1126/science.abb8598

RESEARCH ARTICLE

NEURODEVELOPMENT

Gene regulatory networks controlling vertebrate retinal regeneration

Thanh Hoang[1]*, Jie Wang[2]*, Patrick Boyd[3,4,5], Fang Wang[2], Clayton Santiago[1], Lizhi Jiang[1], Sooyeon Yoo[1]†, Manuela Lahne[3,4,5], Levi J. Todd[6], Meng Jia[3,4,5], Cristian Saez[1], Casey Keuthan[7], Isabella Palazzo[6], Natalie Squires[6], Warren A. Campbell[6], Fatemeh Rajaii[2], Trisha Parayil[1], Vickie Trinh[1], Dong Won Kim[1], Guohua Wang[2], Leah J. Campbell[3,4,5], John Ash[7], Andy J. Fischer[6], David R. Hyde[3,4,5]‡, Jiang Qian[2]‡, Seth Blackshaw[1,2,8,9,10,11]‡

Injury induces retinal Müller glia of certain cold-blooded vertebrates, but not those of mammals, to regenerate neurons. To identify gene regulatory networks that reprogram Müller glia into progenitor cells, we profiled changes in gene expression and chromatin accessibility in Müller glia from zebrafish, chick, and mice in response to different stimuli. We identified evolutionarily conserved and species-specific gene networks controlling glial quiescence, reactivity, and neurogenesis. In zebrafish and chick, the transition from quiescence to reactivity is essential for retinal regeneration, whereas in mice, a dedicated network suppresses neurogenic competence and restores quiescence. Disruption of nuclear factor I transcription factors, which maintain and restore quiescence, induces Müller glia to proliferate and generate neurons in adult mice after injury. These findings may aid in designing therapies to restore retinal neurons lost to degenerative diseases.

Loss of retinal neurons is a leading cause of blindness. Whereas mammals cannot regenerate lost retinal neurons, adult zebrafish regenerate all retinal neurons through reprograming Müller glia to a neurogenic progenitor-like state. In contrast, post-hatch chick Müller glia proliferate in response to injury, retain limited neurogenic competence, and produce small numbers of inner retinal neurons (*1*). In zebrafish, several injury-induced Müller glia genes that regulate neurogenic competence, such as *ascl1a* (*2*), promote Müller glia reprogramming. In mice, forced expression of *Ascl1* in Müller glia can reprogram these cells into functional inner retinal neurons (*3*). Conversely, inhibiting the Hippo pathway stimulates Müller glia proliferation in mice after injury but does not induce neurogenic competence (*4*, *5*).

To identify the genetic and epigenetic barriers to Müller glia proliferation and neurogenesis, we compared the molecular responses to retinal injury in multiple species with different regenerative abilities. We reconstructed evolutionarily conserved and species-specific gene regulatory networks controlling glial quiescence, reactivity, proliferation, and neurogenic competence. Our findings identify similarities and differences in the responses of Müller glia to injury in these species and reveal mechanisms that suppress neurogenic competence in mammalian Müller glia.

RNA-seq analysis of injury-regulated genes in Müller glia

To identify core gene regulatory networks that control Müller glia reprogramming in mouse and zebrafish, we examined two injury paradigms: light damage (outer retinal injury) and *N*-methyl-D-aspartate (NMDA) treatment (inner retinal injury) (*1*). We generated 100 bulk RNA sequencing (RNA-seq) libraries and 40 assay for transposase-accessible chromatin with high-throughput sequencing (ATAC-seq) libraries from fluorescence-activated cell sorting (FACS)–isolated Müller glia at multiple time points after injury (fig. S1, A to C, and table S1). Known Müller glia–specific genes were enriched in green fluorescent protein–positive (GFP^+) samples, while GFP^- samples were enriched for genes specific to other retinal cell types (fig. S1D and table S2). Principal component analysis of RNA-seq data revealed species-specific patterns of transcriptional changes after NMDA treatment and light damage. Transcriptional changes in mouse Müller glia occurred rapidly, within 3 hours after injury, but then reverted to a rest-like state (Fig. 1A). However, both NMDA treatment and light damage in zebrafish induced Müller glia to progressively diverge from the resting state (Fig. 1B).

We found 2198 differentially expressed genes (DEGs) in mice and 1600 DEGs in zebrafish that were common between NMDA treatment and light damage (expression correlation > 0.5, fig. S1E). These DEGs showed three groups of changes in both zebrafish and mouse. The first group was highly expressed in resting Müller glia and repressed after injury (Fig. 1, C and D). The remaining two groups exhibited rapid and slow injury-dependent induction, respectively. Gene Ontology analysis showed species-specific differences in DEGs. For instance, rapidly induced mouse Müller glia genes included components of the tumor necrosis factor (TNF), mitogen-activated protein kinase (MAPK), nuclear factor κB (NFκB), and Hippo pathways (Fig. 1E), whereas in zebrafish, they were enriched for ribosome biogenesis (Fig. 1F). Slowly induced mouse genes were enriched for ribosome biogenesis, whereas in zebrafish, they were enriched for cell cycle–related functions, reflecting the fact that zebrafish Müller glia reenter the cell cycle at 25 hours after light damage (*6*).

To identify species-specific genes that changed in Müller glia, including candidate regulators of neurogenic competence, we compared zebrafish and mouse DEGs and classified them into three categories (Fig. 1, G and H, and table S3). These include 547 DEGs lacking orthologs in the other species, 2483 DEGs with orthologs in both species but with species-specific changes, and 354 DEGs with different patterns of injury-induced changes in two species. In addition, we identified 368 genes that are not differentially expressed after injury but show significant differences in baseline expression between mouse and zebrafish Müller glia (Fig. 1G and table S3).

ScRNA-seq analysis of zebrafish, chick, and mouse retinas

To comprehensively identify genes regulating Müller glia reprogramming, we conducted single-cell RNA sequencing (scRNA-seq) of mouse, zebrafish, and chick retinas after NMDA treatment or light damage. We also treated retinas with exogenous factors that induce reprogramming independent of injury, such as TNFα and a gamma-secretase inhibitor (T+R) in zebrafish (*7*), and FGF2 and insulin (growth factors) in chick (*8*). In mice, we tested FGF2 and insulin combined with NMDA treatment, which induces limited proliferation but not neurogenic competence (*9*). We profiled 77,924 cells in mice,

[1]Solomon H. Snyder Department of Neuroscience, Johns Hopkins University School of Medicine, Baltimore, MD 21205, USA. [2]Department of Ophthalmology, Johns Hopkins University School of Medicine, Baltimore, MD 21205, USA. [3]Department of Biological Sciences, University of Notre Dame, Notre Dame, IN 46556, USA. [4]Center for Stem Cells and Regenerative Medicine, University of Notre Dame, Notre Dame, IN 46556, USA. [5]Center for Zebrafish Research, University of Notre Dame, Notre Dame, IN 46556, USA. [6]Department of Neuroscience, Ohio State University Wexner Medical Center, Columbus, OH 43210, USA. [7]Department of Ophthalmology, University of Florida School of Medicine, Gainesville, FL 32610, USA. [8]Department of Neurology, Johns Hopkins University School of Medicine, Baltimore, MD 21205, USA. [9]Center for Human Systems Biology, Johns Hopkins University School of Medicine, Baltimore, MD 21205, USA. [10]Institute for Cell Engineering, Johns Hopkins University School of Medicine, Baltimore, MD 21205, USA. [11]Kavli Neuroscience Discovery Institute, Johns Hopkins University School of Medicine, Baltimore, MD 21205, USA.
†Present address: Department of Pathology, Seoul National University Hospital, 71, Daehak-ro, Jongno-gu, Seoul 03082, South Korea.
*These authors contributed equally to this work.
‡Corresponding author. Email: dhyde@nd.edu (D.R.H.); jiang.qian@jhmi.edu (J.Q.); sblack@jhmi.edu (S.B.)

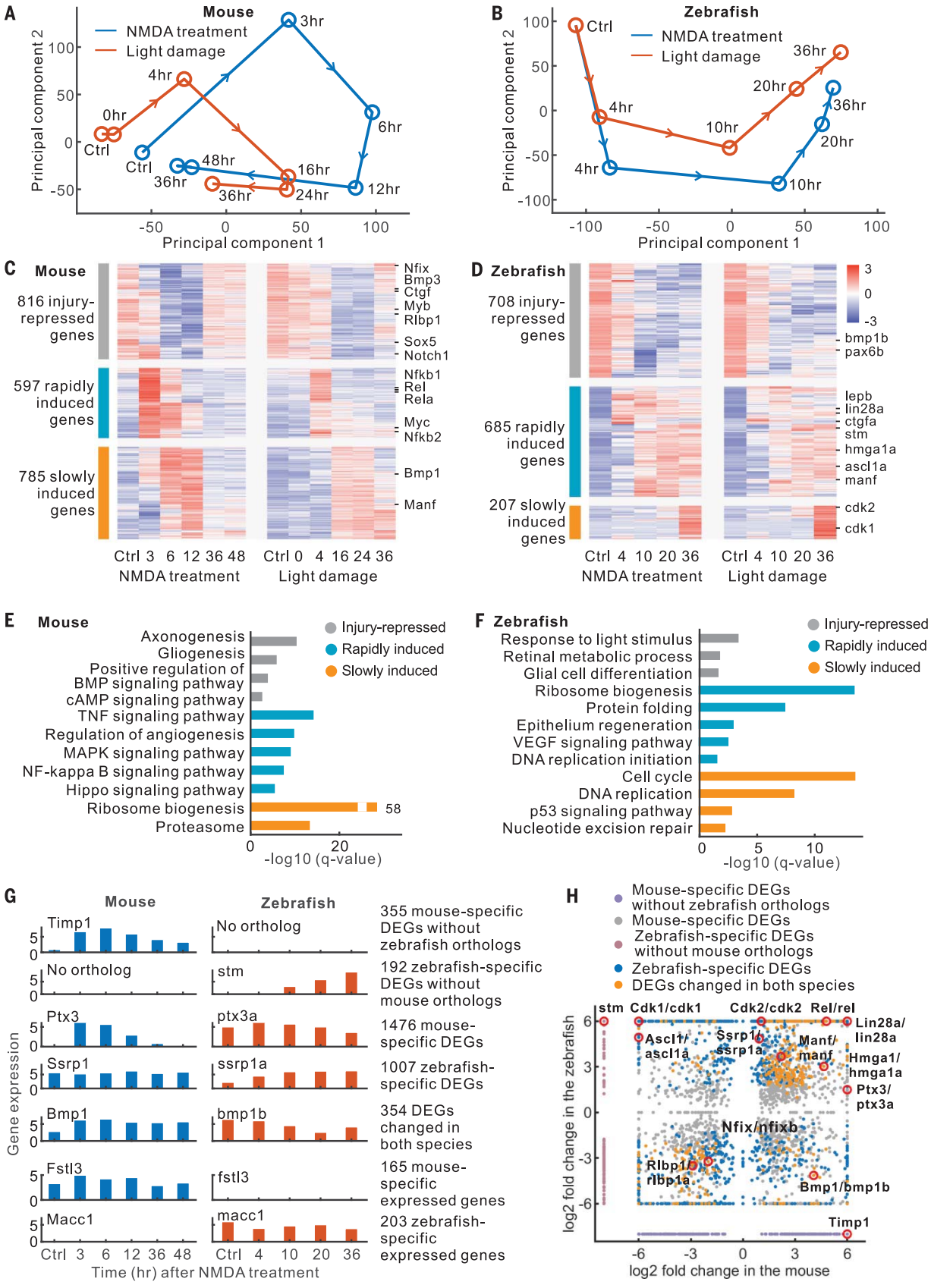

Fig. 1. RNA-seq analysis of mouse and zebrafish Müller glia. (**A** and **B**) Principal component analysis of RNA-seq data. (**C** and **D**) Expression profiles of DEGs. (**E** and **F**) Enriched functions of DEGs. BMP, bone morphogenetic protein; cAMP, cyclic adenosine monophosphate; VEGF, vascular endothelial growth factor. (**G**) Examples of DEGs and species-specific expressed genes. (**H**) Comparison of DEGs between mouse and zebrafish.

85,051 cells in chick, and 105,666 cells in zebrafish (fig. S2, A and B, and table S1).

Our scRNA-seq analysis separated cells into different clusters (Fig. 2, A to D, and figs. S2 and S3) that we annotated using known retinal cell type markers (table S4). We identified all major retinal cell types in each species, including a subset of zebrafish rod-restricted progenitor cells that expressed *nr2e3* and *neurod1* (Fig. 2D and fig. S2, F and G). Rod progenitors had 101 and 195 DEGs after NMDA treatment and light damage, respectively, 97 and 92% of which were also changed in Müller glia after injury (fig. S3D). We also identified resting and activated Müller glia in all three species after each treatment. Müller glia were overrepresented relative to their abundance in intact retina, accounting for 25.8, 38.2, and 16.7% of retinal cells in zebrafish, chick, and mouse, respectively, likely reflecting bias in cell survival and capture efficiency (*10*).

Finally, we compared transcriptomes and identified evolutionarily conserved and species-specific marker genes for each retinal cell type in all three species (Fig. 2E and table S5). We confirmed that *Mlc1*/*MLC1*/*mlc1* and *Inhba*/*INHBA*/*inhbab* are selectively expressed in Müller glia of all three species using single molecule fluorescence in situ hybridization (smFISH) and that *Cav2*/*cav2* are selectively expressed in mouse and zebrafish Müller glia (Fig. 2F and fig. S3E).

Trajectory analysis of Müller glia reprogramming

We conducted trajectory analysis of Müller glia after stimuli using scRNA-seq data. Consistent with bulk RNA-seq data (Fig. 1A), mouse Müller glia showed rapid changes in gene expression after NMDA treatment and light damage, then a gradual reversion toward a resting state (Fig. 3, A and B, and fig. S4). In contrast, zebrafish Müller glia showed progressive injury-induced transcriptional changes (Fig. 3C and fig. S5, A and B). T+R treatment produced changes in gene expression resembling both forms of injury (fig. S5, C and D). In zebrafish, we observed a side branch after both injury and T+R treatment (Fig. 3C and fig. S5, C and D), which was enriched for genes associated with the reactive state, such as *manf*, while the major branch showed increased expression of neurogenesis- and proliferation-related genes, such as *ascl1a* and *pcna* (fig. S5A). RNA velocity analysis (*11*) indicated that, after NMDA treatment, Müller glia transition from a resting state to a reactive state and then either proceed to a proliferative state or revert to a resting state (Fig. 3C). A similar response was observed in chick after NMDA or FGF2+insulin treatment (Fig. 3D and fig. S5, E to G). Furthermore, we calculated the dissimilarity of gene expression profiles in Müller glia after injury across species. We observed that both resting and activated Müller glia from mice and zebrafish were similar, as were proliferative Müller glia from zebrafish and chick (fig. S6, A and B). These results indicate that chick and zebrafish Müller glia undergo reprogramming by passing through a reactive state before reprogramming.

ScRNA-seq analysis indicated that 67.7% of the zebrafish DEGs and 48.4% of the mouse DEGs overlapped between light damage and NMDA treatment (fig. S6C). T+R treatment resembled both injury models in zebrafish, as did NMDA and FGF2+insulin treatment in chick. We identified evolutionarily conserved DEGs, including *Rlbp1*/*RLBP1*/*rlbp1a*, and species-specific DEGs, such as *Rela/b* in mouse and *lin28a* in zebrafish (Fig. 3, E and F; fig. S6, D to F; and table S6). Gene Ontology analysis identified functions enriched in both conserved and species-specific DEGs (fig. S6G).

Comparing zebrafish Müller glia reprogramming and development

To determine whether Müller glia–derived progenitors transcriptionally resemble progenitors observed during normal retinal development, we compared scRNA-seq data from developing zebrafish retinas with reprogrammed Müller glia. As in our previous work in mouse (*10*), we found two transcriptionally distinct retinal progenitor cells (RPCs) in the developing zebrafish retina: primary and neurogenic RPCs (Fig. 3G and fig. S7, A to C). We combined all RPCs and Müller glia and performed trajectory analysis. NMDA treatment, light damage, and T+R treatment all induced Müller glia to a state resembling multipotent RPCs but also induced a separate branch consisting of reactive Müller glia (Fig. 3H and figs. S7, D to G, and S8). Significant overlap was observed between genes differentially expressed during development and after reprogramming (figs. S7D and S8, A and F). For most overlapping genes (83.8%), there was a negative correlation between development and NMDA treatment, with decreasing developmental genes, such as *ascl1a*, increasing in expression in reprogrammed Müller glia and vice versa (Fig. 3I). These results imply that, after first passing through a reactive state, Müller glia reprogram by reversing the temporal pattern of gene expression associated with gliogenesis.

Gene regulatory networks controlling Müller glia reprogramming

To profile changes in chromatin accessibility in Müller glia, we performed ATAC-seq analysis after injury in zebrafish and mouse (fig. S9A). We identified differentially accessible chromatin regions (DARs) from NMDA-treated and light-damaged samples, of which 96% in mice and 90% in zebrafish are from promoter, intronic, and intergenic regions (fig. S9, B to D). Changes in chromatin accessibility correlated with changes in gene expression (Fig. 4, A and B, and fig. S9, E and F). We also observed species-specific changes in chromatin accessibility after injury (Fig. 4, A and B, and table S7). For instance, the *ascl1a* promoter became more accessible after injury in zebrafish but not in mice (fig. S10A). Likewise, we observed a mouse-specific increase in the promoter accessibility of genes that were induced after injury in mice but not zebrafish, such as *Rel* (fig. S10A).

To reconstruct gene regulatory networks controlling Müller glia reprogramming by integrating gene expression and chromatin accessibility data, we developed a method called integrated regulatory network analysis (IReNA; fig. S10B and see the Materials and methods section). We integrated bulk and single-cell RNA-seq data from zebrafish and mouse to obtain 10 modules of DEGs and Müller glia–expressed transcription factors (TFs) (Fig. 4, C and D; fig. S10, C and D; and table S8). In parallel, we analyzed ATAC-seq data to identify differentially accessible footprints that were used to infer regulatory relationships between TFs and DEGs. We constructed an integrated gene regulatory network for each module and generated an intramodular regulatory network for both zebrafish and mouse (Fig. 4, E and F; figs. S11 and S12; and table S9).

In zebrafish, we observed multiple active modules in resting Müller glia (rest-associated modules 1, 2, 3, 4, and 8), which are predicted to self-activate, promote expression of genes in other resting modules, and repress expression of genes in reactivity-associated modules (Fig. 4E, fig. S11, and table S10). TFs in these reactivity-associated modules (modules 5, 6, and 9) include *ascl1a*, *tgif1*, and *six3b*, which are necessary for zebrafish Müller glia reprogramming (*2*, *12*). TFs in the reactivity network likewise activate their own expression and repress genes in the rest-associated network. Downstream of the reactivity network lies a third set of modules (modules 7 and 10), which regulate genes associated with cell cycle progression. These include TFs known to regulate cell cycle entry, such as *myca* and *e2f3*, and neurogenesis, such as *olig2* and *foxn4* (Fig. 4E and fig. S11) (*13*–*15*). In zebrafish, the transition of Müller glia to a reactive state triggers either return to quiescence or acquisition of neurogenic and proliferative competence and full conversion to neurogenic progenitors (Fig. 4G).

In mice, we likewise observed three interconnected networks of modules (Fig. 4F, fig. S12, and table S10). As in zebrafish, the first network consists of TFs active in resting Müller glia (modules 1 and 2) (Fig. 4F). These include *Lhx2*, which represses reactive gliosis in mouse Müller glia (*16*), and Notch pathway genes such as *Hes1*. This rest-associated network is predicted to repress genes in a separate reactivity-associated network (modules 5, 6, 7, 9, and 10). TFs in the reactivity-associated network in turn are predicted to repress the rest-associated

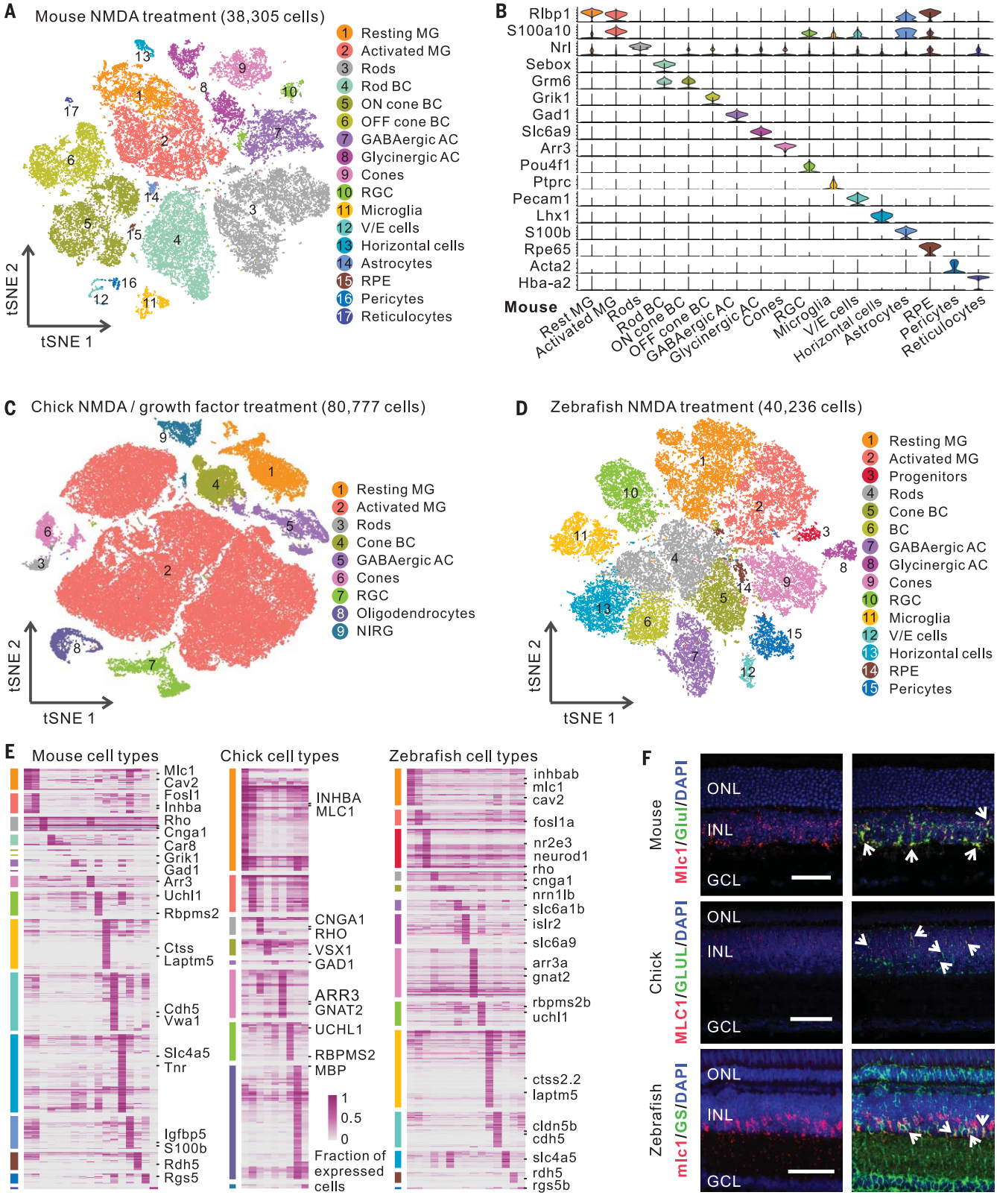

Fig. 2. ScRNA-seq analysis of mouse, chick, and zebrafish retinas. (**A**) Clustering of mouse retinal cells after NMDA treatment. (**B**) Expression of mouse retinal cell markers. (**C** and **D**) Clustering of chick and zebrafish retinal cells after NMDA or GF treatment. (**E**) Cell type–specific marker genes. Each column represents an individual cell type. (**F**) smFISH showing *Mlc1/MLC1/mlc1* expression in zebrafish, chick, and mouse Müller glia (MG). Immunostaining of glutamine synthetase (GS, the coding gene *glula/b*) was used in zebrafish. Arrows indicate colocalized signals. Scale bars, 50 μm. BC, bipolar cells; GABAergic, γ-aminobutyric acid–releasing; AC, amacrine cells; RGC, retinal ganglion cells; V/E cells, vascular/endothelial cells; RPE, retinal pigment epithelium; NIRG, nonastrocytic inner retinal glial cells; DAPI, 4′,6-diamidino-2-phenylindole; ONL, outer nuclear layer; INL, inner nuclear layer; GCL, ganglion cell layer.

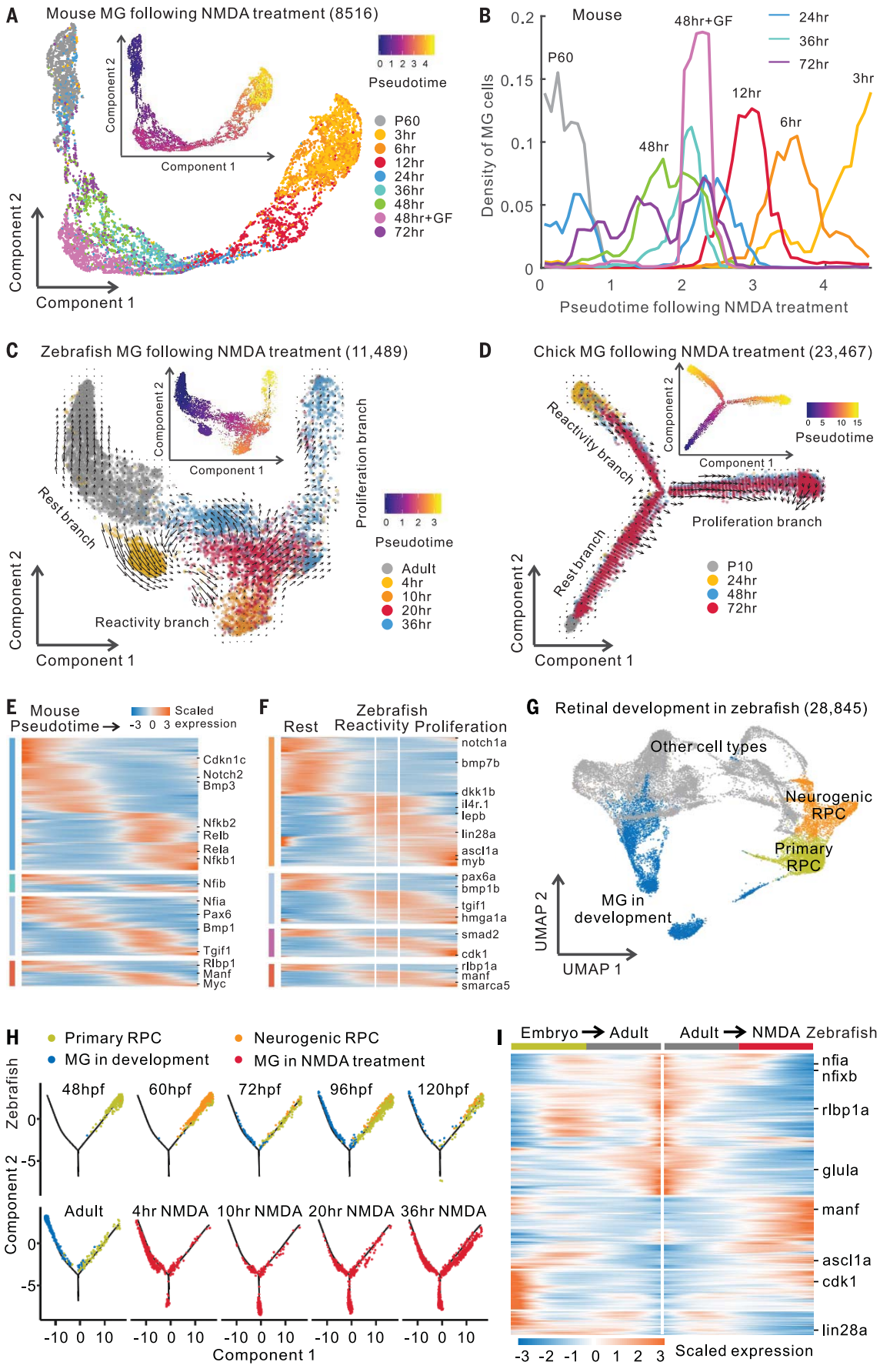

Fig. 3. Trajectory analysis of mouse, chick, and zebrafish Müller glia. (**A**) Trajectory of mouse MG after NMDA treatment. Inserted plot shows pseudotime of MG. P60, postnatal day 60; GF, growth factor (FGF2+insulin) treatment. (**B**) Quantification of mouse MG across the pseudotime. (**C** and **D**) Trajectory of zebrafish and chick MG after NMDA treatment. Arrows indicate the direction of MG transitions identified through RNA velocity analysis. (**E** and **F**) Expression of DEGs in mouse and zebrafish. Color bars on the left indicate categories of conserved and species-specific DEGs in fig. S6D. (**G**) Clustering of retinal cells during zebrafish development. (**H**) Trajectory of RPCs and MG from zebrafish development and NMDA treatment. Hours post-fertilization (hpf) are shown. (**I**) Pseudotemporal expression of DEGs shared by developing and NMDA-treated MG. Columns represent cells in pseudotime. Rows show genes changed in expression during MG development (embryo to adult) and NMDA treatment (adult to NMDA treatment).

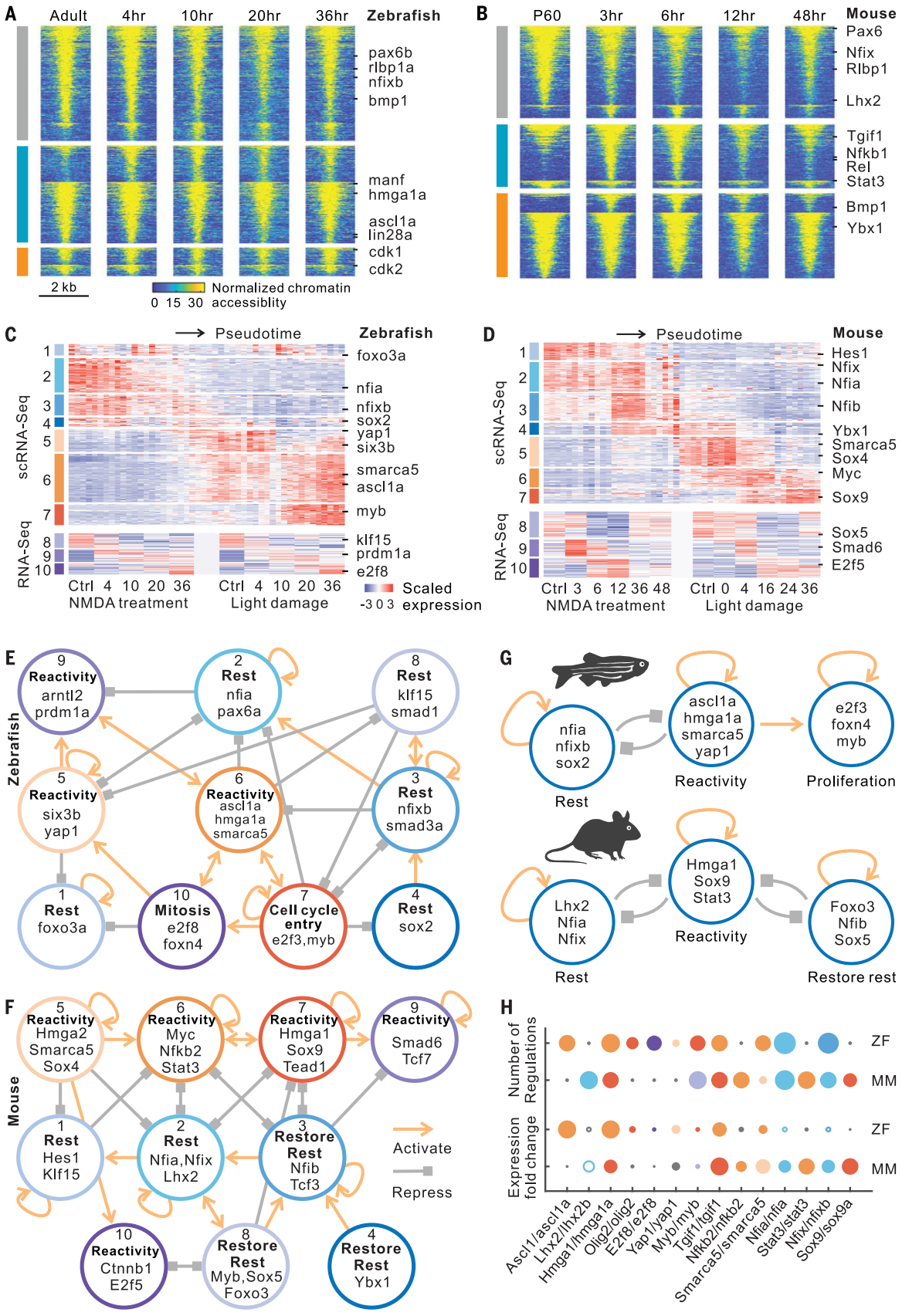

Fig. 4. ATAC-seq analysis and gene regulatory networks in Müller glia. (**A** and **B**) Changes in chromatin accessibility of injury-repressed (gray), rapidly induced (cyan), and slowly induced (orange) genes after NMDA treatment in zebrafish and mouse. Lines indicate differentially accessible regions, which are separated by their positive and negative correlations with gene expression in each group. (**C** and **D**) Candidate genes including transcription factors were divided into 10 modules in zebrafish and mouse. ScRNA-seq expression profiles contain 50-bin divisions of MG from all stimuli studied. (**E** and **F**) Intramodular regulatory networks in zebrafish and mouse. Colored circles represent modules. Connections indicate statistically significant regulations among modules. (**G**) Regulatory models in zebrafish and mouse. (**H**) Comparison of gene features between zebrafish (ZF) and mouse (MM). Colors represent modules. Small black circle indicates that the gene is absent from the network in the indicated species. Circle size represents either fold change of gene expression or the number of gene regulations. Hollow circle indicates decreased expression after treatment.

network, establishing a bistable regulatory relationship like that in zebrafish (Fig. 4, E and F). TFs in the reactivity-associated network include the NFκB pathway components (*Rela/b* and *Nfkb1/2*), which were also recently shown to repress Müller glia reprogramming in chick (*17*), as well as TFs that promote glial activation (*Stat3* and *Sox9*) (*18*, *19*) and the Hippo pathway target *Tead1*. Reversion to a resting state in mouse Müller glia is driven by a third network (modules 3, 4, and 8), which was not found in zebrafish (Fig. 4, E and F). This network is enriched for genes expressed in resting Müller glia, such as *Nfib and Sox5*, which are down-regulated immediately after injury but up-regulated at later stages (Fig. 4D). These modules are distinct from those predicted to maintain Müller glia in a resting state and may restore quiescence. The network analysis implies that the transition between rest, reactivity, and restoration of the resting state in mice is mediated by three separate bistable, autoactivating transcriptional regulatory networks (Fig. 4G).

Validation of genes regulating Müller glia reprogramming

To select candidates for functional analysis, we examined the degree of connectivity of each gene within regulatory networks and the fold change in gene expression during Müller glia reprogramming (Fig. 4H and table S11). We tested whether TFs predicted to regulate reactivity were required for Müller glia reprogramming in zebrafish. The high mobility group AT-hook 1 gene *hmga1a*/*Hmga1* was induced in reactive Müller glia in zebrafish and mouse (Fig. 4, G and H, and fig. S13A). Zebrafish *hmga1a* morphants showed fewer proliferating Müller glia than did controls (Fig. 5, A and C, and fig. S13, B and C). We next tested *yap1*, which was induced in the reactive state (Fig. 4, G and H, and fig. S13A) and is required for Müller glia to exit quiescence in both *Xenopus* and mice (*4*, *5*). *Yap1* morphants showed fewer proliferating Müller glia (Fig. 5, A and C). Injection of verteporfin, which inhibits the interaction of Yap1 and TEAD (*20*), also reduced proliferating Müller glia (Fig. 5, B and C). Morphants of both *smarca5*, a SWI/SNF-related chromatin regulator expressed in reactive Müller glia, and *myb*, which is expressed in proliferating progenitors, showed less Müller glia proliferation (fig. S13, D and E). All treatments that reduced Müller glia proliferation also inhibited photoreceptor regeneration, with significant reductions seen in rods and both red and blue cones (Fig. 5, D to F, and fig. S13, F to I). Additionally, scRNA-seq analysis of both *hmga1a* morphant and verteporfin-treated retinas showed fewer proliferating Müller glia and a corresponding increase in reactive Müller glia (Fig. 5, G and H, and figs. S13, J and K, and S14, A and B).

We identified both evolutionarily conserved genes and species-specific genes up-regulated in reactive Müller glia (table S6). For instance, fatty acid–binding proteins *FABP5*, *FABP7*, and *FABP8*/*PMP2* (FABPs) are selectively expressed in reactive chick Müller glia (fig. S14, C to E). Inhibiting FABPs using BMS309403 (*21*) resulted in fewer proliferating chick Müller glia after NMDA treatment (Fig. 5, I and J). ScRNA-seq analysis also showed that BMS309403 treatment decreased the fraction of proliferative Müller glia and led to a concomitant increase in the fraction of resting Müller glia compared with NMDA treatment alone (Fig. 5K and fig. S14, F and G), indicating that FABPs promote injury-induced transition from rest to a reprogrammed state.

We next investigated the role of mouse TFs predicted to promote glial quiescence by targeting the nuclear factor I (NFI) factors *Nfia*, *Nfib*, and *Nfix*, which were expressed at rest, down-regulated immediately after injury, and elevated at later stages (fig. S15A). We examined tamoxifen-fed *GlastCreER;CAG-lsl-Sun1-GFP;Nfia/b/x*$^{lox/lox}$ mice, in which NFIs were selectively deleted from Müller glia (fig. S15, B and C). Loss of *Nfia/b/x* reduced expression of genes enriched in resting glia, such as *Glul* and *Rlbp1*, but up-regulated genes associated with cell cycle regulation (*Ccnd1* and *Ccnd3*) and neurogenesis (*Ascl1*) (fig. S15, D to F). *Nfia/b/x*-deficient Müller glia proliferated more after injury than did controls, both with and without FGF2+insulin, with EdU$^+$/GFP$^+$ cells (EdU, 5-ethynyl-2′-deoxyuridine) observed in both inner and outer nuclear layers at 3 days after injury (Fig. 6A and fig. S15G). EdU$^+$ Müller glia in the outer nuclear layer disappear over time, indicating possible interkinetic nuclear migration of mitotic Müller glia. Müller glia–derived GFP$^+$ cells show the expression of the photoreceptor and bipolar cell marker CRX and amacrine, ganglion, and horizontal cell markers HuC/D and NeuN at 14 days after treatment (Fig. 6, B and C).

We analyzed cells generated from *Nfia/b/x*-deficient Müller glia using scRNA-seq 21 days after NMDA+FGF2+insulin treatment (fig. S15H). *Nfia/b/x*-deficient Müller glia produced several distinct cell populations, including proliferative Müller glia, neurogenic Müller glia, and bipolar- and amacrine-like cells (Fig. 6D). *Nfia/b/x*-deficient Müller glia significantly up-regulated genes associated with the reactive state, such as *Manf* (fig. S15I). Neurogenic Müller glia did not express cell cycle regulators. Conversely, proliferative *Nfia/b/x*-deficient Müller glia did not express neurogenic markers. RNA velocity analysis indicated that neurogenic Müller glia gave rise to bipolar and amacrine cells (Fig. 6E). These Müller glia–derived neurons expressed markers typical of mature bipolar and amacrine cells but did not express markers for other retinal cell types (fig. S15I). Expression of the on-center bipolar cell marker *PCP2* in the Müller glia–derived bipolar cells was confirmed by immunohistochemistry (fig. S15J). We observed 8.5% of CRX$^+$ neurons and 6.1% of HuC/D;NeuN$^+$ neurons derived from Müller glia colabeled with EdU (fig. S16, A and B). These data suggest that neurons arose from *Nfia/b/x*-deficient Müller glia through direct transdifferentiation. Native bipolar and amacrine cells showed similar expression profiles to neurons derived from *Nfia/b/x*-deficient Müller glia (fig. S16C). Verteporfin-mediated inhibition of YAP resulted in reduced proliferation and neurogenesis (fig. S16, D and E). Infection with AAV9-Flex-TdTomato showed that Müller glia–derived neurons had bipolar and amacrine-like morphologies (Fig. 6F and fig. S16F). Immunostaining for secretagogin (SCGN), a cone bipolar cell marker, indicates that Müller glia–derived bipolar cells extend processes to the inner plexiform layer at 2 months after injury (Fig. 6G and fig. S16G).

Discussion

This study reveals that Müller glia in all three species enter a reactive state after injury, in which mouse Müller glia arrest before returning to quiescence. However, most reactive Müller glia in zebrafish, and some in chick, pass through this state to become progenitors. Zebrafish genes essential for reprogramming, such as *six3b*, *tgif1*, and *lepb* (*12*, *22*, *23*), are up-regulated in reactive Müller glia. Inhibition of genes that are up-regulated in reactive Müller glia, such as *hmga1a*, *smarca5*, and *yap1* in zebrafish and *FABPs* in chick, blocks proliferation and neurogenesis. Whereas loss of function of *hmga1a* and *yap1* disrupts the transition from reactive to progenitor state, FABP inhibition blocks reprogramming by inhibiting transition from resting to reactive state. Some of these genes, including *yap1*, regulate neurogenic competence in the spinal cord (*24*, *25*), suggesting that these same mechanisms may broadly regulate central nervous system (CNS) regeneration.

Although activated mouse Müller glia transiently express cell cycle regulators and neurogenic factors, they rapidly return to quiescence. This is mediated by a dedicated gene regulatory network that includes NFI factors, which are up-regulated at later stages after injury, and restore reactive Müller glia to a resting state in mice. Deletion of *Nfia/b/x* in mouse Müller glia resulted in proliferation and formation of Müller glia–derived inner retinal neurons, which was suppressed by YAP inhibition. NFI factors thus maintain Müller glia quiescence, prevent expression of genes associated with transition to reactivity and/or progenitor-like stages, and suppress neurogenesis, much like in developing retina (*10*). While it has been previously shown that down-regulation of Notch signaling is sufficient for zebrafish Müller glia reprogramming

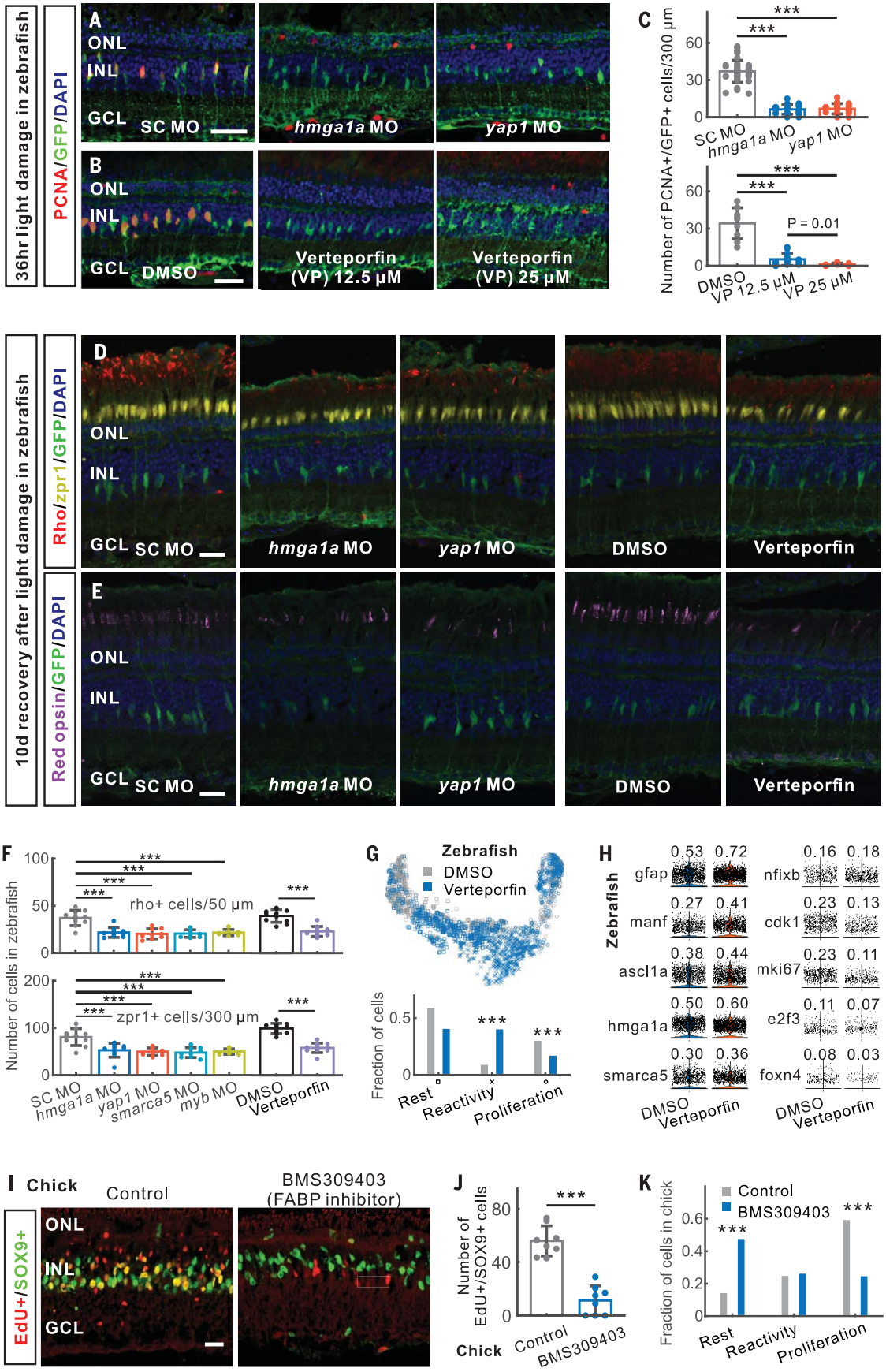

Fig. 5. Validation of genes regulating Müller glia reprogramming in zebrafish and chick. (**A** to **F**) In zebrafish, morpholino (MO)–mediated and verteporfin-treated knockdown of *hmga1a* and *yap1* inhibited MG proliferation [(A) to (C)] and neurogenesis [(D) to (F)] after light damage. (**G**) Distribution of DMSO- and verteporfin-treated MG in the trajectory. Bottom panel shows the fraction of DMSO- and verteporfin-treated MG in three branches. (**H**) Expression of verteporfin-induced genes in MG. The fraction of expressed cells is shown. (**I** and **J**) Inhibition of FABP5/7/8 using BMS309403 reduced progenitor formation at 48 hours after NMDA injury in chick. (**K**) Distribution of three states of MG in scRNA-seq of control and BMS309403-treated chick retinas at 48 hours after NMDA injury. SC, standard control. Scale bars, 20 μm. Error bars indicate standard deviation. ***$P < 0.001$.

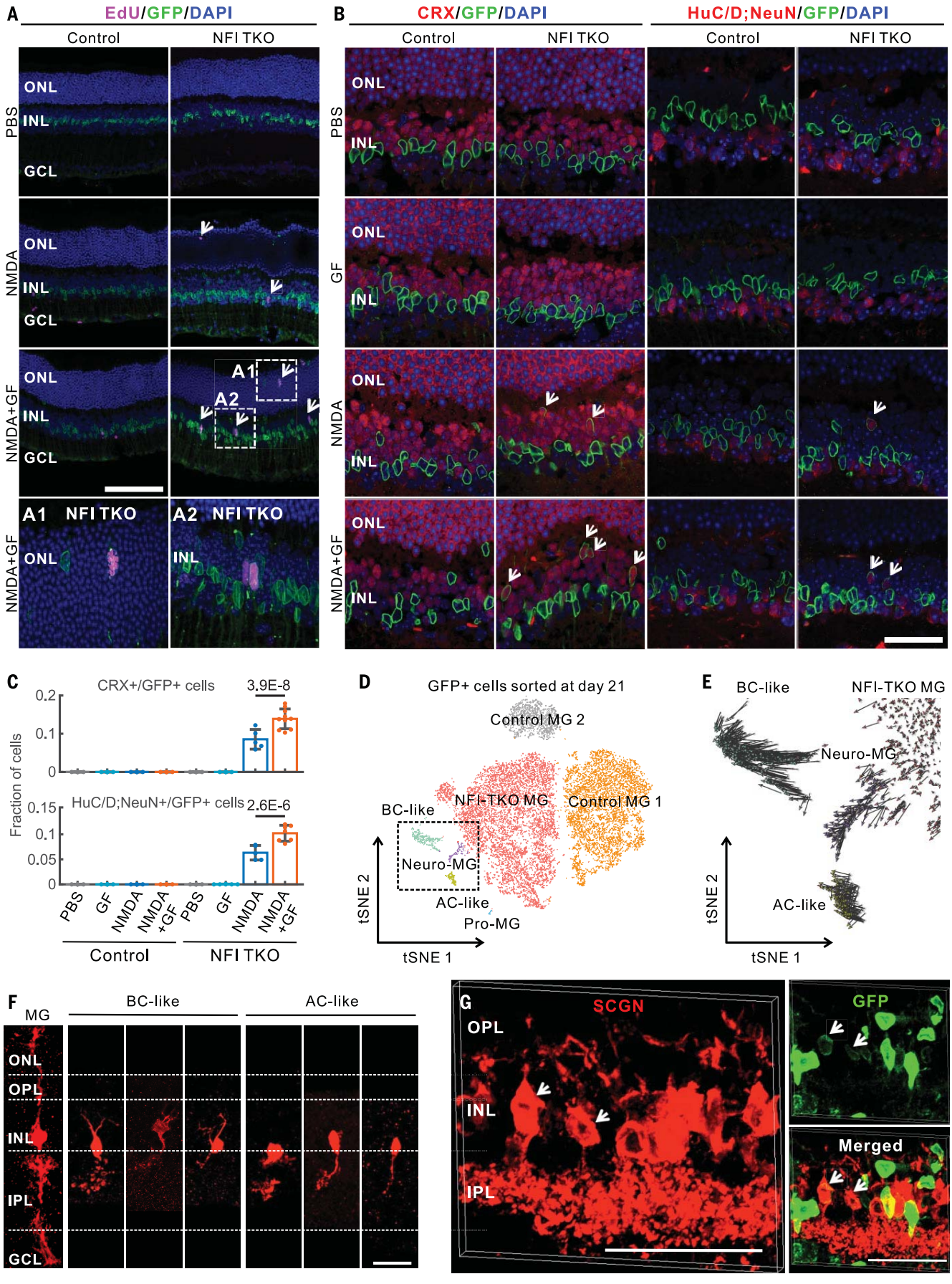
A
EdU/GFP/DAPI
Control
NFI TKO
PBS
NMDA
NMDA+GF
ONL
INL
GCL
A1
A2
A1 NFI TKO
A2 NFI TKO
B
CRX/GFP/DAPI
HuC/D;NeuN/GFP/DAPI
GF
C
CRX+/GFP+ cells
3.9E-8
HuC/D;NeuN+/GFP+ cells
2.6E-6
Fraction of cells
PBS
GF
NMDA
NMDA +GF
D
GFP+ cells sorted at day 21
Control MG 2
BC-like
NFI-TKO MG
Control MG 1
Neuro-MG
AC-like
Pro-MG
tSNE 1
tSNE 2
E
BC-like
NFI-TKO MG
Neuro-MG
AC-like
F
MG
BC-like
AC-like
IPL
G
SCGN
GFP
Merged

Fig. 6. Loss of *Nfia/b/x* enables mouse Müller glia proliferation and neurogenesis after injury. (**A**) EdU immunostainings of adult control and MG-specific *Nfia/b/x* knockout mice at 3 days after intravitreal injection with PBS, NMDA, or NMDA with growth factors (A1 and A2). (**B**) *Nfia/b/x*-deficient MG generated CRX^+ and HuC/D;$NeuN^+$ neurons (white arrows) at 14 days after injury. HuC/D and NeuN antibodies were mixed for these immunostainings. (**C**) Quantifications of CRX^+ and HuC/D;$NeuN^+$ neurons derived from *Nfia/b/x*-deficient MG glia at 14 days after injury. Error bars indicate standard deviation. (**D**) Clustering of GFP^+ cells flow-sorted from control and MG-specific *Nfia/b/x* knockout retina at 21 days after NMDA+GF treatment. Neuro-MG, neurogenic Müller glia; Pro-MG, proliferative Müller glia. (**E**) RNA velocity analysis of MG-derived cells in the dotted box from (D). (**F**) Morphological characterization of MG-derived neurons in *Nfia/b/x*-deficient retinas using AAV9-pCAG-Flex-TdTomato after 14 days of NMDA+GF treatment. (**G**) MG-derived bipolar cells in *Nfia/b/x*-deficient retinas at 2 months after NMDA +GF treatment were immunolabeled for secretagogin (SCGN). Bipolar cells extend processes to the OPL and IPL retinal layers (white arrows). Scale bars, 20 μm.

(*26*) and that *MYT1L*-dependent repression of non-neuronal genes is important for direct reprogramming to neuronal cell fate (*27*, *28*), our study highlights the importance of repressing cell type–specific genes in the context of cellular reprogramming.

Recently, it has been reported that downregulation of the RNA binding protein *Ptbp1* can convert Müller glia into retinal ganglion cells in adult mouse retina (*29*). However, we found that *Ptbp1* expression was maintained in reprogramed Müller glia after injury in both zebrafish and chick (fig. S17). Likewise, no significant change in *Ptbp1* expression was observed between control and neurogenic *Nfia/b/x*-deficient mouse Müller glia. These results do not support the hypothesis that dynamic expression of *Ptbp1* directly regulates Müller glia reprogramming.

Multiple independent mechanisms strongly repress neurogenic competence in mice, making it challenging to experimentally identify regulators of Müller glia reprogramming. In contrast, the limited neurogenic competence retained by the post-hatch chick facilitates functional analysis of both positive and negative candidate regulators of Müller glia reprogramming, making it an attractive system for analyzing regulators of retinal regeneration.

Injury-induced neurogenesis is limited or absent in the CNS of warm-blooded animals (*30*), in part as the result of active repression of regenerative competence. It has been hypothesized that this may reflect an evolutionary trade-off between regenerative competence and parasite resistance (*31*). Remaining in an activated state may allow CNS glia to efficiently restrict spread of infection, whereas regeneration would facilitate spread. This interpretation is supported by the fact that proinflammatory signals repress Müller glia reprogramming (*17*) and that evolutionary loss of injury-induced axonal regeneration typically tracks with loss of injury-induced neurogenic neurogenesis (*30*).

Materials and methods

Fish maintenance

Zebrafish (*Danio rerio*) lines AB, *albino;*Tg[*gfap:GFP*]*mi2001* (*32*) and *albino;*Tg[*gfap*:EGFP]*nt11* (*33*) were maintained in the Center for Zebrafish Research at the University of Notre Dame Freimann Life Science Center. Six- to twelve-month-old adult zebrafish were maintained under a 14 hours light/10 hours dark cycle at 28.5°C. All experimental protocols were approved by the University of Notre Dame Institutional Animal Care and Use Committee (IACUC) committee and are in compliance with the Association for Research in Vision and Ophthalmology (ARVO) statement for the use of animals in vision research.

Chick maintenance

The use of animals in these experiments was in accordance with the guidelines established by the National Institutes of Health and the Ohio State University. Newly hatched wild-type leghorn chickens (*Gallus gallus domesticus*) were obtained from Meyer Hatchery (Polk, OH). Postnatal chicks were kept on a cycle of 12 hours light/12 hours dark (lights on at 8:00 a.m.). Chicks were housed in a stainless steel brooder at about 25°C and received water and Purina chick starter ad libitum.

Mice maintenance

CD1 mice were purchased from Charles River Laboratories (Wilmington, MA). *GLASTCreERT2* and *Sun1-sGFP* transgenic mice were provided by J. Nathans (*16*, *34*). *GLASTCreERT2;Sun1-sGFP* were generated by breeding and subsequent backcrossing. To induce *Cre* recombination, *GLASTCreERT2;Sun1-sGFP* mice at ~2 weeks of age were intraperitoneally injected with tamoxifen in corn oil for two consecutive days at 1 mg per dose. To generate Müller glia–specific loss of function mutants of *Nfia/b/x* genes, 3-week-old *GLASTCreERT2;Nfia/bx$^{lox/lox}$;Sun1-sGFP* mice were fed tamoxifen diet for 3 weeks, followed by 2 weeks on normal diet. All mice were housed in a climate-controlled pathogen-free facility on a 14 hours light/10 hours dark cycle. All experimental procedures were preapproved by the IACUC of the Johns Hopkins University School of Medicine.

Retinal damage paradigms in fish

To damage rods and cones, adult *albino;*Tg[*gfap*:EGFP]*nt11* fish were dark-adapted for 14 days then placed in constant light (20,000 lux) at 32°C for up to 72 hours (*35*). Fish were euthanized by anesthetic overdose of 0.2% 2-phenoxyethanol in system water.

To damage amacrine and ganglion cells, adult Tg[*gfap:GFP*]*mi2001* zebrafish were anesthetized in 0.1% 2-phenoxyethanol and intravitreally injected with 0.5 μl of 100 mM *N*-methyl-D-aspartic acid (NMDA) (Sigma-Aldrich; St. Louis, MO) (*36*). The fish were revived and placed in a 32°C dark incubator for up to 36 hours before euthanization.

TNFα and RO4929097 treatment in fish

Recombinant TNFα was expressed in *Escherichia coli* and purified as previously described (*26*). Undamaged adult Tg[*gfap:GFP*]*mi2001* fish were anesthetized and intravitreally injected with 0.5 μl of TNFα (1.5 mg/ml) and intraperitoneally injected with 50 μl 0.75 mM RO4929097 (Selleckchem; Houston, TX) every 12 hours. The fish were revived and placed in a 32°C dark incubator for up to 72 hours before euthanization.

Intraocular injections in chicks

Chickens were anesthetized via inhalation of 2.5% isoflurane in oxygen. Intraocular injections performed as described previously (*37*). For all experiments, the right eyes of chicks were injected with the test compound and the contralateral left eyes were injected with a vehicle as a control. Compounds were injected in 20 μl sterile saline with 0.05 mg/ml bovine serum albumin added as a carrier. Compounds used in these studies included NMDA (38.5 or 154 g per dose; Sigma-Aldrich), FGF2 (200 ng per dose; R&D Systems), insulin (1 μg per dose; Sigma-Aldrich), and BMS309403 (500 ng per dose; Tocris). EdU (2 μg) was injected to label proliferating cells. Injection conditions are included in each figure.

NMDA treatment and light damage in mice

For NMDA treatment, adult mice, either CD1 or *GLASTCreERT2;Sun1-sGFP* mice at ~2 months of age, were anesthetized with isoflurane inhalation. Two microliters of 100 mM NMDA in phosphate-buffered saline (PBS) were intravitreally injected using a syringe with a 33G blunt-ended needle. Light damage was performed as previously described (*18*).

For NMDA and growth factor (GF) treatment of NFI triple-knockout (TKO) mice, adult *GLASTCreERT2;Nfia/bx$^{lox/lox}$;Sun1-sGFP* and *GLASTCreERT2;Sun1-sGFP* control mice, both in CD1 background, were intravitreally injected with 2 μl of 100 mM NMDA or 2 μl of 100 mM NMDA with 100 ng/μl FGF2 and 1 μg/μl insulin (N+GF treatment), followed by 2 μl of 500 ng/μl EdU at 24 and 48 hours after the first injection. For the N+GF treatment group, 2 μl of 100 ng/μl FGF2 and 1 μg/μl Insulin was co-injected with each EdU injection. Contralateral eyes were

injected with PBS and EdU as the controls. For long term EdU chasing, EdU was administered daily via intraperitoneal injection at 50 mg/kg in PBS for 10 days. Retina were collected at the indicated time points for immunohistochemistry and FACS.

For morphological examination of Müller glia and Müller glia–derived neurons, *GLASTCreERT2;Nfia/b/x*$^{lox/lox}$*;Sun1-sGFP* and *GLASTCreERT2;Sun1-sGFP* control mice were intravitreally injected with 1 μl of AAV9-pCAG-Flex-Tdtomato (Addgene #28306) at 1×10^{13} vg/ml and treated with a tamoxifen diet for 3 weeks. Morphology of GFP/TdTomato$^+$ Müller glia and Müller glia–derived neurons was examined on day 14 after N+GF treatment.

Zebrafish retinal dissociation, cell sorting, and methanol fixation

Zebrafish were euthanized in 0.2% 2-phenoxyethanol, and retinas were dissected and placed in Leibowitz medium (Thermo Fisher). Retinas were subsequently placed in 20 U/ml papain (10 retinas per 1 ml) (Worthington), and incubated at 28°C for 30 min with gentle agitation. Cells were pelleted and resuspended in PBS containing 0.1 mg/ml leupeptin (Sigma-Aldrich) and 10 U/ml DNaseI (Roche). Cells were filtered through a 70-μm filter (Miltenyi Biotec), kept on ice until sorting, and incubated with 5 μg/ml propidium iodide (PI; Life Technologies).

Cells were transferred into a 5-ml FACS tube and loaded into a FACS AriaII. Gating was set using dissociated retinas from *albino* zebrafish both unstained and PI stained and unstained Tg[*gfap*:EGFP]*nt11* zebrafish. GFP$^+$ and GFP$^-$ cells were sorted directly into Trizol LS (Life Technologies) and immediately flash frozen.

For scRNA-seq, cells were methanol-fixed after the 10x Genomics protocol. Dissociated cells were pelleted, resuspended in 100 μl Dulbecco's PBS in cryovials and added with 900 μl −20°C methanol dropwise while slowly vortexing. Cells were left on ice for 15 min and then placed directly in −80°C.

Mouse retinal cell dissociation and FACS

Mice were euthanized by CO_2, and eye globes were removed and kept in ice-cold 1x PBS. The neural retinas were dissected, and cells were dissociated using Papain Dissociation System (LK003150, Worthington). For FACS experiments, dissociated cell pellets were resuspended in ice-cold PBS containing 2% heat-inactivated fetal bovine serum (FBS) and 5 units/ml DNaseI). For scRNA-seq experiments, dissociated cells were then resuspended with ice-cold PBS containing 0.04% bovine serum albumin (BSA) and 0.5 U/μl RNase inhibitor. Cells were filtered through a 50-μm filter, and cell count and viability assessed by Trypan blue staining.

Cells were sorted using a Sony SH800S Cell Sorter. Retinal cells from nontransgenic mice were used to set the gating threshold for GFP$^+$ cells. Cells were flow-sorted into GFP$^+$ and GFP$^-$ fractions into ice-cold PBS containing a final concentration of 10% heat-activated FBS. For ATAC-seq, cells were kept on ice until use. For bulk RNA-seq, cells were centrifuged at 500*g* for 5 min, resuspended in 700 μl QIAzol lysis reagent (miRNAeasy Mini Kit), and stored at −80°C until RNA extraction.

Immunohistochemistry and imaging in mice

Mouse eye globes were collected and fixed in 4% paraformaldehyde in PBS for 2 hours at room temperature. Eyes were washed with PBS, and retina were placed in 30% sucrose overnight at 4°C. Retina were then embedded, cryosectioned at 20-μm thickness, and stored at −80°C. Sections were dried at 37°C for 20 min and washed 3 × 5 min with PBS before incubation with a blocking buffer (0.2% Triton, 5% horse serum in PBS) for 2 hours at room temperature. For CRX, HuC/D, and NeuN immunostaining, retinal sections were treated with 100 mM sodium citrate pH 6.0 at −80°C for 30 min for antigen retrieval before the blocking step. Sections were then incubated with primary antibodies at indicated concentrations in the blocking buffer (table S12) overnight at 4°C. EdU staining was performed by following the manufacturer instructions. Images were acquired using the confocal Zeiss LSM 700. EdU$^+$/GFP$^+$ cells were counted and averaged from >6 random whole sections for each retina. For examining neurogenesis in NFI TKO mice, immunohistochemistry for CRX, a photoreceptor and bipolar cell marker (*38*) was performed. To maximize the possibility of detecting Müller glia–derived neurons, two pan-neuronal antibodies, HuC/D and NeuN, which are amacrine/ganglion/horizontal cell markers, were mixed for the immunostainings. CRX$^+$/GFP$^+$ and HuC/D; NeuN$^+$/GFP$^+$ cells were counted from six images taken across >4 random sections per retina. The fraction of CRX$^+$/GFP$^+$ and HuC/D;NeuN$^+$/GFP$^+$ cells was calculated from total GFP$^+$ cells. Each data point in the quantification bar graphs was calculated from an individual retina. For morphological characterization of neurons, 10 to 20 *z*-stacked confocal images (0.15 to 0.35 μm per image) were taken for GFP/TdTomato$^+$ cells and GFP/SCNG$^+$ cells at day 14 and 2 months after N+GF treatment.

Injection and electroporation of morpholinos in zebrafish

Morpholino-mediated knockdown was performed in dark-adapted *albino;*Tg[*gfap*:EGFP]*nt11* fish as previously described (*39*). After morpholino electroporation, fish were intravitreally injected with NMDA and placed in a 32°C dark incubator for 36 hours, or they were placed in constant intense light for either 36 or 72 hours. The following previously validated morpholinos were used in this study: Standard Control: 5′-CCTCTTACCTCAGTTACAATTTATA-3′ (Gene Tools); *pcna*: 5′-TGAACCAGACGTGCCTCAAACATTG-3′ (*39*); *myb:* 5′-GCCGCCTCGCCATCCCGCTGTTCG-3′ (*40*); *smarca5*: 5′-CTTCTTCCCGCTGCTGCTCCATGCT-3′ (*41*); *hmga1a*: 5′-CTGTGTCCTTGCCAGAATCACTCAT-3′ (*42*); and *yap1*: 5′-CTCTTCTTTCTATCCAACAGAAACC-3′ (*43*).

Verteporfin injection

Verteporfin (#SML0534, Millipore Sigma) was resuspended to 3.48 mM in 100% dimethyl sulfoxide (DMSO). For zebrafish, verteporfin was diluted with water to the desired working concentration (either 12.5 or 25 μM). Dark-adapted *albino;*Tg[*gfap*:EGFP]*nt11* fish were anesthetized and 0.5 μl of either verteporfin or DMSO was intravitreally injected and the fish were exposed to constant light damage. Every 12 hours, the intravitreal injections were repeated until 36 hours, when fish were euthanized and retinal sections analyzed.

For mice, verteporfin was diluted to 30 μM in PBS and intravitreally co-injected with NMDA+FGF2+insulin into *GLASTCreERT2;Nfia/b/x*$^{lox/lox}$*;Sun1-sGFP* mice at 2 μl per eye. This was followed by two doses of verteporfin with FGF2+insulin and EdU at 24 and 48 hours later, as described above. Mice also received daily intraperitoneal injection of verteporfin (6 mg/kg) for seven consecutive days starting from the first verteporfin injection. DMSO was used as the control. Retinal samples were colected at the indicated time points for immunohistochemistry.

Immunohistochemistry and imaging in zebrafish

Immunohistochemistry was performed as described previously (*26*). Cryosections (14 μm) were prepared, processed, and incubated with primary antibodies (table S12) at room temperature overnight. Confocal imaging was performed using a Nikon A1R laser scanning confocal microscope. Images were obtained from sections from the center of the dorsal retina containing the optic nerve. Quantification was performed using 6.5-μm *z*-stacks and cell counts normalized to either 50 or 300 μm. Data were statistically analyzed using one-way ANOVA with Tukey's post-hoc test if more than two groups were compared, otherwise Student's *t* test with unequal variances was used.

Immunohistochemistry and imaging in chick

Chicks were euthanized by CO_2. Tissues were fixed, sectioned, and immunolabeled as described previously (*37*). Working dilutions and sources of antibodies are listed in table S12. Draq5 (10μM; Thermo Fisher) was added to the secondary antibody solution to label nuclei.

For EdU labeling, immunolabeled sections were fixed in 4% formaldehyde in PBS for 5 min at room temperature, washed for 5 min with PBS, permeabilized with 0.5% Triton X-100 in PBS for 1 min at room temperature, and washed twice for 5 min in PBS. Sections were incubated

for 30 min at room temperature in 2M Tris, 50 mM $CuSO_4$, Alexa Fluor 568 Azide (Thermo Fisher), and 0.5 M ascorbic acid in distilled H_2O.

Confocal images were obtained using Leica SP8 imaging. Cell counts were performed on representative images. To avoid the possibility of region-specific differences within the retina, cell counts were consistently made from the same region of the retina for each dataset.

RNAscope in situ hybridization

RNA in situ hybridization was performed using RNA probes (table S13) and RNAscope Multiplex Fluorescent Reagent Kit V2 Assay (#323100-USM, ACDBio) by following the protocol for fixed-frozen tissue. Briefly, zebrafish, chick, and mouse retina were fixed and cryosectioned as described above for immunohistochemistry. Retinal sections were processed using standard RNAscope protocol with some modifications: Hydrogen peroxide treatment was reduced to 5 min, target retrieval step was omitted, and Protease III treatment was reduced to 15 min. Images were acquired using the confocal Zeiss LSM 700.

RNA extraction and RT-qPCR

RNA was extracted from both GFP^+ and GFP^- cell fractions using miRNAeasy Mini Kit (#217004, Qiagen). For quantitative reverse transcription polymerase chain reaction (RT-qPCR), RNA samples were first reverse-transcribed into cDNA using random primers and Superscript IV reverse transcriptase (#18091050, Thermo Fisher). The qPCR assays were performed on the cDNA using GoTaq Green Master Mix (#M7122, Promega) using a StepOnePlus Real-Time instrument (Thermo Fisher). Intron-spanning primers were designed to specifically quantify targeted mRNA transcripts. Glyceraldehyde 3-phosphate dehydrogenase (*Gapdh*) expression was used as the endogenous control (table S13).

Bulk RNA-seq

Flow-sorted RNA samples were sent to the Deep Sequencing and Microarray Core (Johns Hopkins University) for library preparation and sequencing. Briefly, ribosomal RNA was depleted, and total RNA was captured from the RNA samples using Illumina TruSeq Stranded RNA LT kit Ribo-Zero Gold (#15032619, Illumina). Around 8 to 10 libraries were pooled and sequenced for paired-end 75 cycles using the NextSeq 500 system with ~400 million to 500 million reads per run, resulting in between ~45 million and 55 million reads per library.

Single-cell RNA-seq (scRNA-seq)

For fresh samples (table S1), cells were resuspended with ice-cold PBS containing 0.04% BSA and 0.5 U/μl RNase inhibitor. For methanol-fixed samples, fixed cells were processed according to 10x Genomics protocol for methanol-fixed cells. Briefly, methanol-fixed cells were centrifuged at 3000*g* for 10 min at 4°C and washed three times in an iced-cold resuspension buffer containing PBS, 1% BSA, and 0.5 U/μl RNAse inhibitors. Dissociated cells were resuspended in the resuspension buffer and filtered through a 50-μl cell filter. Cells (~10,000) were loaded into a 10x Genomics Chromium Single Cell system (10x Genomics, CA) using v2 chemistry following manufacturer's instructions. Libraries were pooled and sequenced on Illumina NextSeq with ~200 million reads per library.

ATAC-seq

Sorted cells (~50,000 to 75,000) from GFP^+ samples were used for ATAC library preparation. Nuclear isolation and all centrifugation steps were carried out on ice in a 4°C cold room. Briefly, cells were spun down at 500*g* for 5 min. Cells were rinsed with ice-cold PBS without disturbing cell pellets and centrifuged again at 500*g* for 5 min. Cells were lysed by adding 50 μl of ice-cold cell lysis buffer (10 mM Tris-Cl pH 7.4, 10 mM NaCl, 3 mM $MgCl_2$) containing 0.03% octylphenoxy poly(ethyleneoxy) ethanol (IGEPAL) and protease inhibitors (one tablet per 7 ml of lysis buffer) and mixing three times by pipetting. Cells were then immediately spun down at 500*g* for 10 min and washed with 150 μl of ice-cold lysis buffer without IGEPAL and protease inhibitors. For tagmentation, cell nuclei were incubated with 2.5 μl enzyme in 50 μl total volume at 37°C in a thermocycler (Illumina Nextera DNA library prep kit, #FC1211030). DNA was cleaned up using MinElute PCR purification kit (#28006, Qiagen) and eluted in 10 μl of EB buffer.

ATAC-seq DNA was amplified, and the number of PCR cycles were calculated as described (*44*). PCR products (10 μl) were run on a 1.5% agarose gel for expected DNA pattern. PCR products were then cleaned up by double-sized selection using AMPure beads (Agencourt APure XP, Beckman Coulter, #A63880) to remove large and small DNA fragments. This was performed by using 1:0.5 and 1:1.6 ratio of sample to AMPure beads (v/v). Completed ATAC-seq libraries (8 to 10) were then analyzed by Fragment Bioanalyzer and sequenced for paired-end 75 cycles using the NextSeq 500 system with ~400 million to 500 million reads per run.

Bulk RNA-seq data analysis

Using bulk RNA-seq, we measured gene expression profiles of 50 GFP^+ (GFP-positive, Müller glia, MG) and 50 GFP^- (GFP-negative, non-Müller glia, non-MG) samples, with at least two biological replicates for each time point or condition (table S1). All raw sequencing data from mouse and zebrafish were separately mapped to the GRCm38/mm10 and GRCz10/danRer10 genome assembly using STAR (*45*). The mappability (the percentage of sequencing reads that were uniquely mapped to the reference genome) on average is 87.5% in mice and 60.7% in zebrafish. Lower mappability in zebrafish could be attributed to the relatively less well annotated zebrafish reference genome.

We calculated FPKM (fragments per kilobase of exon per million) using raw counts of genes. We performed *t* test of paired GFP^+/GFP^- samples from NMDA treatment and light damage to identify GFP^+ or GFP^- specific genes [fold change > 2 and false discovery rate (FDR) < 0.01, table S2]. To identify genes that are not differentially expressed after injury but that show significant differences in baseline expression between species, we ranked the genes on the basis of their expression levels in each species. We then performed Wilcoxon rank test between two species to identify species-specific expressed genes in Müller glia (fold change > 1.5 and FDR < 0.05).

Using EdgeR (*46*), we identified DEGs relative to control samples (fold change > 1.5 and FDR < 0.05). To identify model-independent DEGs (common DEGs) that are consistently changed between NMDA treatment and light damage, we calculated Pearson's correlation coefficients between models for each species. Meanwhile, we shuffled the expression of each gene through randomly reordering the samples and obtained 0.5 correlation as the threshold of the correlation. We selected DEGs for further analysis if their expression correlation was >0.5.

To identify evolutionarily conserved and species-specific genes (table S3), we first identified orthologs between mouse and zebrafish (or chick) on the basis of vertebrate ortholog information from the Mouse Genome Informatics database (www.informatics.jax.org/). If multiple orthologs were mapped between species, we chose the DEG with the highest fold change. If no gene was differentially expressed, we selected genes that had the highest expression correlation between two models.

In addition, we performed K-means analysis of GFP^+ samples to separate DEGs into three groups, including injury-repressed genes, rapidly induced genes, and slowly induced genes. Function enrichment analysis on genes was conducted in R package "clusterProfiler" (*47*). The principal components were obtained through principal component analysis (*48*).

Quality control and clustering of scRNA-seq data

We analyzed 19, 12, and 27 scRNA-seq libraries from mouse, chick, and zebrafish, respectively (table S1). Chick raw reads from scRNA-seq were mapped to *Gallus_gallus*-5.0/galGal5 genome. Gene-cell matrices were generated using Cell Ranger 2.1.1 from 10x Genomics. We calculated the number of genes and the number of unique molecular identifiers (UMIs). We removed low-quality cells (chick: <200 genes or <500 UMIs; mouse and zebrafish: <200 genes or <1000 UMIs). On average, we obtained ~1000 to 1500 genes and ~2500 to 3250 UMIs per cell.

For single cells from each treatment, we first identified variable genes that had 0.1 to 8 mean expression level and >1 dispersion. Using variable genes, we combined all samples from the same treatment and performed clustering analysis of single cells using Seurat (*49*). Clusters were identified through K-nearest neighbors and a shared nearest neighbor modularity optimization and then visualized using *t*-distributed stochastic neighbor embedding (tSNE) (*50*). No obvious batch effects were observed among samples (figs. S2 and S3). No clear evidence for molecular heterogeneity of Müller glia were observed in the unstimulated control retina from any species examined.

Identification of cell doublets in scRNA-seq

To identify cell doublets in scRNA-seq data, we developed a new algorithm. First, we performed single-cell clustering and identified marker genes for each cluster or cell type. For each marker, we next calculated the gene power (GP) using GP = 2 × abs(AUC − 0.5), where AUC is the area under the receiver operating characteristic curve of gene expression (*49*).

For each cell in cluster i, we then calculated the summed power (SP_i)

$$SP_i = \sum_{j=1}^{j=N_i} GP_{i,j}$$

where N_i is the number of markers in cluster i, and $GP_{i,j}$ is the gene power that indicates the capability of marker j to distinguish cluster i and the remaining clusters.

For all cells in cluster i, we used the bottom 0.1% value of SP_i as the threshold to determine whether the cell expresses markers from cluster i. The cell is regarded as a doublet if SP_i of a cell is above the threshold for two or more clusters, suggesting that the cell expresses markers from multiple clusters. In each scRNA-seq sample, we identified and removed 5 to 10% of cells as cell doublets.

Identification of cell types and markers for each cluster

We used known marker genes to annotate cell type for each cluster of cells (table S4). Most known marker genes were reported in mice. For chick and zebrafish, we identified orthologs of mouse marker genes and used those orthologs to determine cell types of clusters. Meanwhile, we identified new markers of cell types in each injury model and species by setting >0.3 gene power. By comparing these marker genes across species, we identified species-specific and conserved markers for each cell type (table S5).

Trajectory and pseudotime analysis of single cells

We constructed the trajectory of Müller glia in response to retinal injury and performed pseudotime analysis using variable genes through Monocle (*51*). Pseudotime was calculated by setting unstimulated Müller glia as the root. Unstimulated Müller glia were from P60 mouse, P10 chick, and adult zebrafish. Furthermore, we identified significantly changed genes (or DEGs) along pseudotime. We used the following criteria to identify DEGs: fraction of expressed cells > 0.01, single-cell expression difference > 0.1, and q-value < 0.001. Single-cell expression difference was calculated as

$$\text{Single-cell expression difference} = \text{Q95-expression} - \text{Q5-expression}$$

where Q95-expression and Q5-expression separtely represent 0.95 and 0.05 quantile of log-transformed single-cell expression values across all bins of pseudotime. We divided cells into 50 bins across pseudotime with equal pseudotime intervals. Bin-derived expressions were obtained by averaging expressions of all cells within each bin.

To identify model-independent DEGs, we also used bin-derived expressions to calculate single-cell expression correlations between two models. Similar to bulk RNA-seq analysis, we identified evolutionarily conserved and species-specific DEGs through cross-species scRNA-seq analysis (table S6).

We aligned Müller glia trajectories from two species using cellAlign (*52*). In alignment, we separated and sorted different states of Müller glia on the basis of pseudotime. DEGs shared by two species were used for trajectory alignment.

RNA velocity analysis

To minimize batch effect, we chose branch-specific (zebrafish and chick) or cell type–specific (mouse) genes for performing RNA velocity analysis (*11*). First, in zebrafish, we identified branch-specific genes in the trajectory of Müller glia after NMDA treatment. We then selected the top 50 specifically expressed genes for each branch. Among 150 genes obtained from three branches, we selected 92 genes that satisfy the following criteria [the number of cells detected spliced UMIs >10, and the number of cells detected unspliced UMIs (U) is from 1 to 300]. Other parameters were set to the default. The same approach was applied to chick and mouse. The gene sets for RNA velocity analysis were listed in table S14.

Comparison of zebrafish Müller glia from development and injury models

We first used Seurat to identify cell subpopulations in zebrafish development. Single-cell clustering was visualized through uniform manifold approximation and projection (UMAP) (*53*). Using known marker genes of retinal cell types (table S4), we annotated cell types for clusters. We then selected 12,680 primary RPCs, neurogenic RPCs, and Müller glia to construct a trajectory and identify DEGs during Müller glia development. To compare each injury model with retinal development in zebrafish, we combined 12,680 developmental cells with Müller glia in NMDA treatment, light damage, and T+R treatment. Meanwhile, we identified overlapped DEGs between retinal development and injury model. Using overlapped DEGs, we reconstructed the Müller glia trajectory for each injury model combined with cells obtained from developing retina. We used the heatmap to visualize changes for all overlapped DEGs in retinal development and NMDA treatment. The heatmap includes left and right divisions, which represent the process from embryo to adult, and the transition from unstimulated adult Müller glia to NMDA treatment, respectively.

Mapping and normalization of ATAC-seq

We performed ATAC-seq for 20 zebrafish GFP^+ and 20 mouse GFP^+ samples (table S1). After removing adapters using cutadapt (*54*), raw reads from zebrafish and mouse were separately aligned to GRCz10/danRer10 and GRCm38/mm10 reference genome using Bowtie2 with default parameters (*55*). We performed a similar analysis as the previous report (*56*). Briefly, we filtered reads from chromosome M and Y and included reads with mapping quality (MAPQ) score > 10. After removing duplicate reads and blacklisted regions, we called ATAC-seq peaks using MACS2 with parameters –nomodel –shift –100 –extsize 200 (*57*). In total, we identified 248,761 peaks in zebrafish and 119,718 peaks in mice. We counted the raw fragment (C_R) for each peak using high-throughput sequencing (HTSeq) (*58*). The normalized fragment (C_N) was calculated as

$$C_N = \log_2\left(\frac{C_R}{S_L} \times 100{,}000{,}000 + 1\right)$$

where S_L is the sequencing library size of the sample.

Differentially accessible regions and footprints from ATAC-seq

We identified DARs relative to controls using EdgeR (*46*). In total, we identified 56,939 DARs in zebrafish (fold change > 1.5 and FDR < 0.05) and 77,447 DARs in mice (fold change > 2 and FDR < 0.01).

To identify model-independent or common DARs, we calculated the correlation of chromatin accessibility between two injury models. We identified the cutoff of 0.5 on the basis of the correlation distribution of shuffled chromatin accessibility, which was obtained from randomly reordering samples. Finally, we separately identified 24,515 and 52,297 model-independent DARs in zebrafish and mouse (table S7). In DARs, we further identified footprints using DNase2TF (*59*).

Reconstructing integrated regulatory networks

To reconstruct regulatory networks by integrating bulk RNA-seq, scRNA-seq, and ATAC-seq data, we developed a method called integrated regulatory network analysis (IReNA) (fig. S10B). Common DEGs and common DARs across all treatments were used to identify core regulatory networks.

First, we identified Müller glia–expressed TFs using the following criteria: (i) highly expressed in Müller glia: expression level > 5 FPKM for bulk RNA-seq, or > 0.1 fraction of expressed cells for scRNA-seq; (ii) correlated expression patterns between NMDA and light damage: correlation > 0.5 in bulk RNA-seq, or > 0.2 in scRNA-seq; and (iii) differentially expressed in treatment versus control or species-specific expressed in Müller glia (identified from above RNA-seq and scRNA-seq analysis). We identified 192 and 212 candidate TFs in zebrafish and mouse, respectively.

Next, we used Müller glia–expressed TFs and significantly changed and species-specific expressed genes as candidate genes. Through K-means clustering, we separated candidate genes into 10 modules in each species, three modules of which consisted of genes only identified by bulk RNA-seq analysis. For each gene in the module, we used FIMO (find individual motif occurrences) to identify DNA motifs within its footprints (P value < 1.0×10^{-4}) (*60*). Binding motifs of TFs were extracted from TRANSFAC 2018.3 version. Meanwhile, we calculated the footprint occupancy score (FOS) for each footprint in each ATAC-seq sample. FOS was calculated as previously described (*56*)

$$\mathrm{FOS} = \min\left(-\log_2\frac{N_C+1}{N_L+1}, -\log_2\frac{N_C+1}{N_R+1}\right)$$

where N_C indicates counts of ATAC-seq inserts in the central region of the motif. N_L and N_R are separately one-third counts of ATAC-seq inserts in left and right flanking regions of the motif, as a triple size of the central region was chosen as the size of the flanking region. To further refine regulatory relationships between TFs and target genes, we included binding motifs with FOS > 1 in any one of ATAC-seq samples.

Finally, we used expression correlations between TFs and target genes to determine active (positively correlated) or repressive (negatively correlated) regulations. Correlation coefficients >0.5 and <−0.5 were selected for active and repressive regulations, respectively. We constructed regulatory networks of candidate genes consisting of 26,083 and 30,177 regulatory relationships in zebrafish and mouse, respectively (table S9).

Identification of transcription factors regulating each gene module

For each gene module, we calculated the probability (Pr) of each TF regulating the module through hypergeometric test

$$\Pr(x=k) = \frac{\binom{K}{k}\binom{N-K}{n-k}}{\binom{N}{n}}$$

where N is the total number of regulations, K is the number of all regulations targeting module A, n is the number of regulations from the TF, k is the number of regulations from the TF to module A, and the general form $\binom{a}{b}$ is a binomial coefficient. We separately calculated P values for active and repressive regulations. FDR was further calculated on the basis of P values.

Using FDR < 10×10^{-6} in zebrafish and FDR < 10×10^{-5} in mice, we separately identified 97 zebrafish TFs and mouse 156 TFs which significantly regulate at least one gene module. We further extracted regulatory networks consisting of these TFs from regulatory networks of candidate genes (figs. S11 and S12 and table S10).

Constructing intramodular regulatory networks

To determine regulatory relationships between two modules, we calculated the significance of regulations from module A to module B using hypergeometric test

$$\Pr(x=q) = \frac{\binom{Q}{q}\binom{M-Q}{m-q}}{\binom{M}{m}}$$

where M is the total number of regulations, Q is the number of all regulations from TFs in module A, m is the number of all regulations targeting module B, q is the number of regulations from module A to module B, and the general form $\binom{a}{b}$ is a binomial coefficient. We assessed the significance of active and repressive regulations, respectively. We set FDR < 0.02 in zebrafish and FDR < 0.001 in mice as the cutoff to obtain significant regulations between modules (Fig. 4, E and F).

Features of transcription factors in regulatory networks

W calculated the degree of each enriched TF in the regulatory network. The degree includes out-degree (number of genes regulated by TFs of interest) and in-degree (number of TFs regulating TFs of interest). For the regulatory network of candidate genes, we calculated the normalized degree (D_N) on the basis of the degree (D_R)

$$D_N = \frac{D_R}{D_T} \times 1000$$

where D_T is the total number of regulations in the gene regulatory network. For the regulatory network of enriched TFs, the same analysis was performed to calculate the normalized degree.

Mapping of new single cells to the original trajectory

To map new single cells to the original trajectory, we first calculated Pearson's correlation coefficients between new cells and original cells. To calculate the expression correlations, we chose the same set of variable genes that were used for constructing the trajectory. For each new cell, the most correlated cell from the original trajectory was then identified. Correspondingly, the location and state of the original cell were assigned to the new cell. We then obtained the distribution of new cells in the original trajectory.

REFERENCES AND NOTES

1. M. Lahne, M. Nagashima, D. R. Hyde, P. F. Hitchcock, Reprogramming Müller glia to regenerate retinal neurons. *Annu. Rev. Vis. Sci.* **6**, 171–193 (2020). doi: 10.1146/annurev-vision-121219-081808; pmid: 32343929
2. B. V. Fausett, J. D. Gumerson, D. Goldman, The proneural basic helix-loop-helix gene *Ascl1a* is required for retina regeneration. *J. Neurosci.* **28**, 1109–1117 (2008). doi: 10.1523/JNEUROSCI.4853-07.2008; pmid: 18234889
3. N. L. Jorstad *et al.*, Stimulation of functional neuronal regeneration from Müller glia in adult mice. *Nature* **548**, 103–107 (2017). doi: 10.1038/nature23283; pmid: 28746305
4. A. Hamon *et al.*, Linking YAP to Müller glia quiescence exit in the degenerative retina. *Cell Rep.* **27**, 1712–1725.e6 (2019). doi: 10.1016/j.celrep.2019.04.045; pmid: 31067458
5. E. M. Rueda *et al.*, The Hippo pathway blocks mammalian retinal Müller glial cell reprogramming. *Cell Rep.* **27**, 1637–1649.e6 (2019). doi: 10.1016/j.celrep.2019.04.047; pmid: 31067451
6. J. Wan, D. Goldman, Retina regeneration in zebrafish. *Curr. Opin. Genet. Dev.* **40**, 41–47 (2016). doi: 10.1016/j.gde.2016.05.009; pmid: 27281280
7. C. M. Nelson *et al.*, Tumor necrosis factor-alpha is produced by dying retinal neurons and is required for Muller glia proliferation during zebrafish retinal regeneration. *J. Neurosci.* **33**, 6524–6539 (2013). doi: 10.1523/JNEUROSCI.3838-12.2013; pmid: 23575850
8. A. J. Fischer, C. R. McGuire, B. D. Dierks, T. A. Reh, Insulin and fibroblast growth factor 2 activate a neurogenic program in Müller glia of the chicken retina. *J. Neurosci.* **22**, 9387–9398 (2002). doi: 10.1523/JNEUROSCI.22-21-09387.2002; pmid: 12417664
9. P. Schäfer, M. O. Karl, Prospective purification and characterization of Müller glia in the mouse retina regeneration assay. *Glia* **65**, 828–847 (2017). doi: 10.1002/glia.23130; pmid: 28220544
10. B. S. Clark *et al.*, Single-cell RNA-seq analysis of retinal development identifies NFI factors as regulating mitotic exit and late-born cell specification. *Neuron* **102**, 1111–1126.e5 (2019). doi: 10.1016/j.neuron.2019.04.010; pmid: 31128945
11. G. La Manno *et al.*, RNA velocity of single cells. *Nature* **560**, 494–498 (2018). doi: 10.1038/s41586-018-0414-6; pmid: 30089906
12. J. R. Lenkowski *et al.*, Retinal regeneration in adult zebrafish requires regulation of TGFβ signaling. *Glia* **61**, 1687–1697 (2013). doi: 10.1002/glia.22549; pmid: 23918319
13. V. Esain, J. H. Postlethwait, P. Charnay, J. Ghislain, FGF-receptor signalling controls neural cell diversity in the zebrafish hindbrain by regulating *olig2* and *sox9*. *Development* **137**, 33–42 (2010). doi: 10.1242/dev.038026; pmid: 20023158
14. S. M. Taylor, E. Giuffre, P. Moseley, P. F. Hitchcock, The MicroRNA, *miR-18a*, regulates NeuroD and photoreceptor differentiation in the retina of zebrafish. *Dev. Neurobiol.* **79**, 202–219 (2019). doi: 10.1002/dneu.22666; pmid: 30615274
15. M. Vitorino *et al.*, Vsx2 in the zebrafish retina: Restricted lineages through derepression. *Neural Dev.* **4**, 14 (2009). doi: 10.1186/1749-8104-4-14; pmid: 19344499
16. J. de Melo *et al.*, Injury-independent induction of reactive gliosis in retina by loss of function of the LIM homeodomain transcription factor Lhx2. *Proc. Natl. Acad. Sci. U.S.A.* **109**, 4657–4662 (2012). doi: 10.1073/pnas.1107488109; pmid: 22393024
17. I. Palazzo, K. Deistler, T. V. Hoang, S. Blackshaw, A. J. Fischer, NF-κB signaling regulates the formation of proliferating Müller glia-derived progenitor cells in the avian retina. *Development* **147**, dev183418 (2020). doi: 10.1242/dev.183418; pmid: 32291273
18. Y. Ueki, J. Wang, S. Chollangi, J. D. Ash, STAT3 activation in photoreceptors by leukemia inhibitory factor is associated with protection from light damage. *J. Neurochem.* **105**, 784–796 (2008). doi: 10.1111/j.1471-4159.2007.05180.x; pmid: 18088375
19. X. Wang, Q. Shu, Y. Ni, G. Xu, CRISPR-mediated SOX9 knockout inhibits GFAP expression in retinal glial (Müller) cells. *Neuroreport* **29**, 1504–1508 (2018). doi: 10.1097/WNR.0000000000001143; pmid: 30334860

20. Y. Liu-Chittenden *et al*., Genetic and pharmacological disruption of the TEAD-YAP complex suppresses the oncogenic activity of YAP. *Genes Dev.* **26**, 1300–1305 (2012). doi: 10.1101/gad.192856.112; pmid: 22677547
21. G. S. Hotamisligil, D. A. Bernlohr, Metabolic functions of FABPs—Mechanisms and therapeutic implications. *Nat. Rev. Endocrinol.* **11**, 592–605 (2015). doi: 10.1038/nrendo.2015.122; pmid: 26260145
22. R. A. Gorsuch *et al*., Sox2 regulates Müller glia reprogramming and proliferation in the regenerating zebrafish retina via Lin28 and Ascl1a. *Exp. Eye Res.* **161**, 174–192 (2017). doi: 10.1016/j.exer.2017.05.012; pmid: 28577895
23. X.-F. Zhao *et al*., Leptin and IL-6 family cytokines synergize to stimulate Müller glia reprogramming and retina regeneration. *Cell Rep.* **9**, 272–284 (2014). doi: 10.1016/j.celrep.2014.08.047; pmid: 25263554
24. M. H. Mokalled *et al*., Injury-induced ctgfa directs glial bridging and spinal cord regeneration in zebrafish. *Science* **354**, 630–634 (2016). doi: 10.1126/science.aaf2679; pmid: 27811277
25. M. H. Mokalled, L. Zhou, R. Mcadow, B. Burris, Zebrafish-inspired strategies for spinal cord repair. *FASEB J.* **34**, 1–1 (2020). doi: 10.1096/fasebj.2020.34.s1.04539
26. C. Conner, K. M. Ackerman, M. Lahne, J. S. Hobgood, D. R. Hyde, Repressing notch signaling and expressing TNFα are sufficient to mimic retinal regeneration by inducing Müller glial proliferation to generate committed progenitor cells. *J. Neurosci.* **34**, 14403–14419 (2014). doi: 10.1523/JNEUROSCI.0498-14.2014; pmid: 25339752
27. M. Mall *et al*., Myt1l safeguards neuronal identity by actively repressing many non-neuronal fates. *Nature* **544**, 245–249 (2017). doi: 10.1038/nature21722; pmid: 28379941
28. S. Chanda *et al*., Generation of induced neuronal cells by the single reprogramming factor ASCL1. *Stem Cell Reports* **3**, 282–296 (2014). doi: 10.1016/j.stemcr.2014.05.020; pmid: 25254342
29. H. Zhou *et al*., Glia-to-neuron conversion by CRISPR-CasRx alleviates symptoms of neurological disease in mice. *Cell* **181**, 590–603.e16 (2020). doi: 10.1016/j.cell.2020.03.024; pmid: 32272060
30. E. M. Tanaka, P. Ferretti, Considering the evolution of regeneration in the central nervous system. *Nat. Rev. Neurosci.* **10**, 713–723 (2009). doi: 10.1038/nrn2707; pmid: 19763104
31. A. Rattner, J. Nathans, An evolutionary perspective on the photoreceptor damage response. *Am. J. Ophthalmol.* **141**, 558–562.e2 (2006). doi: 10.1016/j.ajo.2005.10.045; pmid: 16490507
32. R. L. Bernardos, P. A. Raymond, GFAP transgenic zebrafish. *Gene Expr. Patterns* **6**, 1007–1013 (2006). doi: 10.1016/j.modgep.2006.04.006; pmid: 16765104
33. S. C. Kassen *et al*., Time course analysis of gene expression during light-induced photoreceptor cell death and regeneration in *albino* zebrafish. *Dev. Neurobiol.* **67**, 1009–1031 (2007). doi: 10.1002/dneu.20362; pmid: 17565703
34. A. Mo *et al*., Epigenomic signatures of neuronal diversity in the mammalian brain. *Neuron* **86**, 1369–1384 (2015). doi: 10.1016/j.neuron.2015.05.018; pmid: 26087164
35. T. S. Vihtelic, J. E. Soverly, S. C. Kassen, D. R. Hyde, Retinal regional differences in photoreceptor cell death and regeneration in light-lesioned albino zebrafish. *Exp. Eye Res.* **82**, 558–575 (2006). doi: 10.1016/j.exer.2005.08.015; pmid: 16199033
36. C. Powell, E. Cornblath, F. Elsaeidi, J. Wan, D. Goldman, Zebrafish Müller glia-derived progenitors are multipotent, exhibit proliferative biases and regenerate excess neurons. *Sci. Rep.* **6**, 24851 (2016). doi: 10.1038/srep24851; pmid: 27094545
37. A. J. Fischer, M. A. Scott, W. Tuten, Mitogen-activated protein kinase-signaling stimulates Müller glia to proliferate in acutely damaged chicken retina. *Glia* **57**, 166–181 (2009). doi: 10.1002/glia.20743; pmid: 18709648
38. D. D. Glubrecht, J.-H. Kim, L. Russell, J. S. Bamforth, R. Godbout, Differential CRX and OTX2 expression in human retina and retinoblastoma. *J. Neurochem.* **111**, 250–263 (2009). doi: 10.1111/j.1471-4159.2009.06322.x; pmid: 19686387
39. R. Thummel *et al*., Characterization of Müller glia and neuronal progenitors during adult zebrafish retinal regeneration. *Exp. Eye Res.* **87**, 433–444 (2008). doi: 10.1016/j.exer.2008.07.009; pmid: 18718467
40. Y.-C. Lin *et al*., c-Myb is an evolutionary conserved miR-150 target and miR-150/c-Myb interaction is important for embryonic development. *Mol. Biol. Evol.* **25**, 2189–2198 (2008). doi: 10.1093/molbev/msn165; pmid: 18667440
41. A. Aguirre *et al*., In vivo activation of a conserved microRNA program induces mammalian heart regeneration. *Cell Stem Cell* **15**, 589–604 (2014). doi: 10.1016/j.stem.2014.10.003; pmid: 25517466
42. S. H. Moussavi Nik *et al*., Alzheimer's disease-related peptide PS2V plays ancient, conserved roles in suppression of the unfolded protein response under hypoxia and stimulation of γ-secretase activity. *Hum. Mol. Genet.* **24**, 3662–3678 (2015). doi: 10.1093/hmg/ddv110; pmid: 25814654
43. Q. Jiang *et al*., *yap* is required for the development of brain, eyes, and neural crest in zebrafish. *Biochem. Biophys. Res. Commun.* **384**, 114–119 (2009). doi: 10.1016/j.bbrc.2009.04.070; pmid: 19393221
44. C. Zibetti, S. Liu, J. Wan, J. Qian, S. Blackshaw, Epigenomic profiling of retinal progenitors reveals LHX2 is required for developmental regulation of open chromatin. *Commun. Biol.* **2**, 142 (2019). doi: 10.1038/s42003-019-0375-9; pmid: 31044167
45. A. Dobin, T. R. Gingeras, Mapping RNA-seq reads with STAR. *Curr. Protoc. Bioinformatics* **51**, 11.14.1–11.14.19 (2015). doi: 10.1002/0471250953.bi1114s51; pmid: 26334920
46. M. D. Robinson, D. J. McCarthy, G. K. Smyth, edgeR: A Bioconductor package for differential expression analysis of digital gene expression data. *Bioinformatics* **26**, 139–140 (2010). doi: 10.1093/bioinformatics/btp616; pmid: 19910308
47. G. Yu, L.-G. Wang, Y. Han, Q.-Y. He, clusterProfiler: An R package for comparing biological themes among gene clusters. *OMICS* **16**, 284–287 (2012). doi: 10.1089/omi.2011.0118; pmid: 22455463
48. H. Abdi, L. J. Williams, Principal component analysis. *Wiley Interdiscip. Rev. Comput. Stat.* **2**, 433–459 (2010). doi: 10.1002/wics.101
49. A. Butler, P. Hoffman, P. Smibert, E. Papalexi, R. Satija, Integrating single-cell transcriptomic data across different conditions, technologies, and species. *Nat. Biotechnol.* **36**, 411–420 (2018). doi: 10.1038/nbt.4096; pmid: 29608179
50. G. C. Linderman, M. Rachh, J. G. Hoskins, S. Steinerberger, Y. Kluger, Fast interpolation-based t-SNE for improved visualization of single-cell RNA-seq data. *Nat. Methods* **16**, 243–245 (2019). doi: 10.1038/s41592-018-0308-4; pmid: 30742040
51. X. Qiu *et al*., Reversed graph embedding resolves complex single-cell trajectories. *Nat. Methods* **14**, 979–982 (2017). doi: 10.1038/nmeth.4402; pmid: 28825705
52. A. Alpert, L. S. Moore, T. Dubovik, S. S. Shen-Orr, Alignment of single-cell trajectories to compare cellular expression dynamics. *Nat. Methods* **15**, 267–270 (2018). doi: 10.1038/nmeth.4628; pmid: 29529018
53. E. Becht *et al*., Dimensionality reduction for visualizing single-cell data using UMAP. *Nat. Biotechnol.* **37**, 38–44 (2018). doi: 10.1038/nbt.4314; pmid: 30531897
54. M. Martin, Cutadapt removes adapter sequences from high-throughput sequencing reads. *EMBnet J.* **17**, 10–12 (2011). doi: 10.14806/ej.17.1.200
55. B. Langmead, S. L. Salzberg, Fast gapped-read alignment with Bowtie 2. *Nat. Methods* **9**, 357–359 (2012). doi: 10.1038/nmeth.1923; pmid: 22388286
56. J. Wang *et al*., ATAC-Seq analysis reveals a widespread decrease of chromatin accessibility in age-related macular degeneration. *Nat. Commun.* **9**, 1364 (2018). doi: 10.1038/s41467-018-03856-y; pmid: 29636475
57. J. Feng, T. Liu, B. Qin, Y. Zhang, X. S. Liu, Identifying ChIP-seq enrichment using MACS. *Nat. Protoc.* **7**, 1728–1740 (2012). doi: 10.1038/nprot.2012.101; pmid: 22936215
58. S. Anders, P. T. Pyl, W. Huber, HTSeq—a Python framework to work with high-throughput sequencing data. *Bioinformatics* **31**, 166–169 (2015). doi: 10.1093/bioinformatics/btu638; pmid: 25260700
59. M.-H. Sung, M. J. Guertin, S. Baek, G. L. Hager, DNase footprint signatures are dictated by factor dynamics and DNA sequence. *Mol. Cell* **56**, 275–285 (2014). doi: 10.1016/j.molcel.2014.08.016; pmid: 25242143
60. C. E. Grant, T. L. Bailey, W. S. Noble, FIMO: Scanning for occurrences of a given motif. *Bioinformatics* **27**, 1017–1018 (2011). doi: 10.1093/bioinformatics/btr064; pmid: 21330290

ACKNOWLEDGMENTS

We thank J. Nathans, A. Kolodkin, and W. Yap for comments on the manuscript; B. Kulemeka and the Freimann Life Science Center staff for raising zebrafish; and X. Zhou and J. Wang for curation of sequencing data. **Funding:** This work was supported by NIH grants U01EY027267 (D.R.H., S.B., J.Q., A.J.F., and J.A.), R01EY024519 (D.R.H.), R01EY029548 (J.Q.), K08EY027093 (F.R.), and R01EY020560 (S.B.). P.B. was partially supported by the Hiller Family Endowment for Stem Cell Research at the University of Notre Dame. M.L. was partially supported by the Center for Zebrafish Research at the University of Notre Dame. **Author contributions:** D.R.H., S.B., J.Q., A.J.F., and J.A. conceived of the project and supervised the research and experimental design. T.H. generated RNA-seq and ATAC-seq data, conducted functional studies in mouse, and analyzed scRNA-seq on *Nfia/b/x*-deficient mouse retina and developing zebrafish retina. J.W. performed sequencing data analysis, developed IReNA, and identified gene regulatory networks. F.W. and G.W. analyzed data from developing zebrafish retina. P.B., M.L., and L.J.C. performed light damage and NMDA damage paradigms in zebrafish and the TNFα+RO4929097 co-injections and cell sorting to isolate Müller glia and neuronal fractions for bulk RNA-seq, scRNA-seq, and ATAC-seq. P.B. and M.J. performed morpholino and verteporfin studies in zebrafish. L.J., C.Z., C. Sae, S.Y., F.R., V.T., T.P., and D.W.M. contributed to analysis of mouse functional data. C. San, N.S., and C.K. contributed to analysis of mouse gene expression data. L.J.T., N.S., W.A.C., and I.P. performed injections and conducted functional analyses in chick. **Competing interests:** The authors declare no competing interests. **Data and materials availability:** RNA-seq and ATAC-seq data are deposited in the Gene Expression Omnibus (GSE135406). All scRNA-seq data and source codes are available at GitHub https://github.com/jiewwwang/Single-cell-retinal-regeneration. RNA-seq, ATAC-seq, and scRNA-seq data can be queried interactively at https://proteinpaint.stjude.org/F/2019.retina.scRNA.html. All other data are available in the main manuscript or the supplementary materials. Materials requests should be directed to S.B..

SUPPLEMENTARY MATERIALS

science.sciencemag.org/content/370/6519/eabb8598/suppl/DC1
Figs. S1 to S17
Tables S1 to S14
MDAR Reproducibility Checklist

View/request a protocol for this paper from *Bio-protocol*.

23 March 2020; accepted 16 September 2020
Published online 1 October 2020
10.1126/science.abb8598

RESEARCH ARTICLE

DEVELOPMENTAL BIOLOGY

A human tissue screen identifies a regulator of ER secretion as a brain-size determinant

Christopher Esk[1]*, Dominik Lindenhofer[1]*, Simon Haendeler[1,2], Roelof A. Wester[1], Florian Pflug[2], Benoit Schroeder[2], Joshua A. Bagley[1], Ulrich Elling[1], Johannes Zuber[3,4], Arndt von Haeseler[2,5], Jürgen A. Knoblich[1,4]†

Loss-of-function (LOF) screens provide a powerful approach to identify regulators in biological processes. Pioneered in laboratory animals, LOF screens of human genes are currently restricted to two-dimensional cell cultures, which hinders the testing of gene functions requiring tissue context. Here, we present CRISPR–lineage tracing at cellular resolution in heterogeneous tissue (CRISPR-LICHT), which enables parallel LOF studies in human cerebral organoid tissue. We used CRISPR-LICHT to test 173 microcephaly candidate genes, revealing 25 to be involved in known and uncharacterized microcephaly-associated pathways. We characterized *IER3IP1*, which regulates the endoplasmic reticulum (ER) function and extracellular matrix protein secretion crucial for tissue integrity, the dysregulation of which results in microcephaly. Our human tissue screening technology identifies microcephaly genes and mechanisms involved in brain-size control.

Primary microcephaly is a neurodevelopmental disease characterized by a substantially reduced head circumference (*1*, *2*). Genetic primary microcephaly syndromes often involve only single gene mutations (*3*). Studying these genes has revealed mechanisms critical for neurogenesis and human brain-size control (*4*). Twenty-seven genes have been associated with microcephaly, with centriole and spindle biogenesis and DNA damage response representing the two most common pathways that are negatively affected (*1*). Clinical genomic sequencing data have linked >100 additional genes to the disease, most of which have not been characterized in depth (*3*). Studying these genes' roles in brain development and microcephaly is complicated by the lack of suitable model systems. Human two-dimensional (2D) cell culture and mouse models often fail to fully recapitulate patient phenotypes (*1*). Human 3D cerebral organoids provide an opportunity to study microcephaly genes in detail in a human-tissue context (*4*). However, cerebral organoids suffer from several drawbacks: Genetically ablating individual gene functions is time consuming, comparing large numbers of candidate genes is currently not possible, and systematic loss-of-function (LOF) approaches are not available. Here, we have developed a human brain tissue LOF assay, which is amenable to high-throughput screening. Using our tissue-screening approach, we have almost doubled the number of model-verified genes that are causative for microcephaly. Specifically, we show that the regulation of extracellular matrix (ECM) protein secretion by *IER3IP1* is involved in brain-size control and is implicated in microcephaly.

The success of pooled CRISPR-Cas9–mediated LOF screens for cell proliferation based on guide RNA (gRNA) abundance measurements (*5*) is critically dependent on three factors: (i) homogeneous clonal growth; (ii) large coverage of individual gRNAs; and (iii) sufficient cell-loss or proliferation phenotypes to score (*5*). In the case of a potential microcephaly screen in human organoids, these prerequisites are currently not met because of several factors: (i) a variability in organoid tissue development; (ii) a limited number of starting cells per organoid and thereby gRNA coverage; and (iii) an expected moderate microcephalic cell-loss phenotype, rather than total cell loss.

Establishing a LOF screening methodology in cerebral organoids

To reliably generate dorsal forebrain tissue—the brain region most affected by microcephaly—we adapted a published protocol (*4*, *6*) to serum-free media (fig. S1A). Expression analysis (fig. S1B and table S1) and fluorescent immunohistochemistry (IHC) (fig. S1, C to E) confirmed consistent and predominantly dorsal forebrain identity. Staining for an early neuronal marker revealed that neurogenesis in this protocol is barely detectable at day 17, whereas neurons are extensively present at days 28 and 42 (fig. S1, F and G). Single-cell RNA sequencing (scRNA-seq) analysis confirmed the enrichment of dorsal forebrain neural stem cells as well as the enrichment of excitatory neurons (fig. S2 and table S2).

To develop a CRISPR-Cas9–based LOF screen (*7*, *8*) in organoids, we generated an H9 human embryonic stem cell (hESC) line expressing the off-target reduced Cas9 variant eCas9-1.1 (eCas9) and a dTomato reporter (Fig. 1A) (*9*). eCas9 and reporter expression are suppressed by a lox-STOP-lox element until chemically induced by 4-hydroxytamoxifen (4-OHT)–mediated Cre activity. Inducible Cre activity is provided by a lentivirus, which also contains the gene-targeting gRNA, alongside selection elements. To functionally test the system for both 4-OHT–controlled induction of Cas9 expression and LOF generation, we performed mixing experiments (fig. S3A). In two independent infections, transgenic eCas9 cells were transduced with green fluorescent protein (GFP)–expressing viruses carrying either a nontargeting control or dTomato-targeting gRNA. These two cell populations were mixed with inert nontargeting control gRNA blue fluorescent protein (BFP)–expressing organoid carrier cells. Mixed organoids were treated with 4-OHT to activate eCas9 at day 6 and analyzed by flow cytometry over time. Upon treatment, we observed rapid and extensive induction of dTomato reporting on eCas9 expression (fig. S3, B to D). No dTomato signal was observed without activation, which suggests precise control of eCas9 expression. dTomato gRNAs caused loss of reporter signal, indicating eCas9 activity on its genomic target. To test whether we could observe a cell-loss phenotype as expected in microcephaly, we modified the mixing experiment to contain a gRNA targeting a cell proliferation gene, *RPL3* (Fig. 1, B to D, and fig. S4). We detected selective loss of targeted cells that was strictly dependent on the correct targeting gRNA and chemical induction. These data illustrate the ability of our system to selectively and inducibly generate LOF mutations on endogenous target genes, resulting in measurable cell-loss phenotypes in a tissue context.

Conventional screens using 2D cell culture systems rely on uniform cell growth to assay changes in sequencing-based gRNA abundance (*10*, *11*). In pooled screens, variability in cell growth cannot be distinguished from gRNA-mediated gene knockout (KO) effects. To determine the cell growth dynamics (*12*) in cerebral organoids, we performed a lineage tracing experiment using DNA barcoding. hESCs were infected with viral DNA barcode libraries, used to generate 3D cerebral organoids, or maintained in 2D; and barcode abundance was assessed over time (fig. S5, A and B, and table S3). Cells in 2D displayed equal growth behavior, indicated by a homogeneous

[1]Institute of Molecular Biotechnology of the Austrian Academy of Science (IMBA), Vienna BioCenter (VBC), Vienna, Austria. [2]Center for Integrative Bioinformatics Vienna (CIBIV), Max F. Perutz Laboratories, University of Vienna and Medical University of Vienna, VBC, Vienna, Austria. [3]Research Institute of Molecular Pathology (IMP), VBC, Vienna, Austria. [4]Medical University of Vienna, VBC, Vienna, Austria. [5]Bioinformatics and Computational Biology, Faculty of Computer Science, University of Vienna, Vienna, Austria.
*These authors contributed equally to this work.
†Corresponding author. Email: juergen.knoblich@imba.oeaw.ac.at

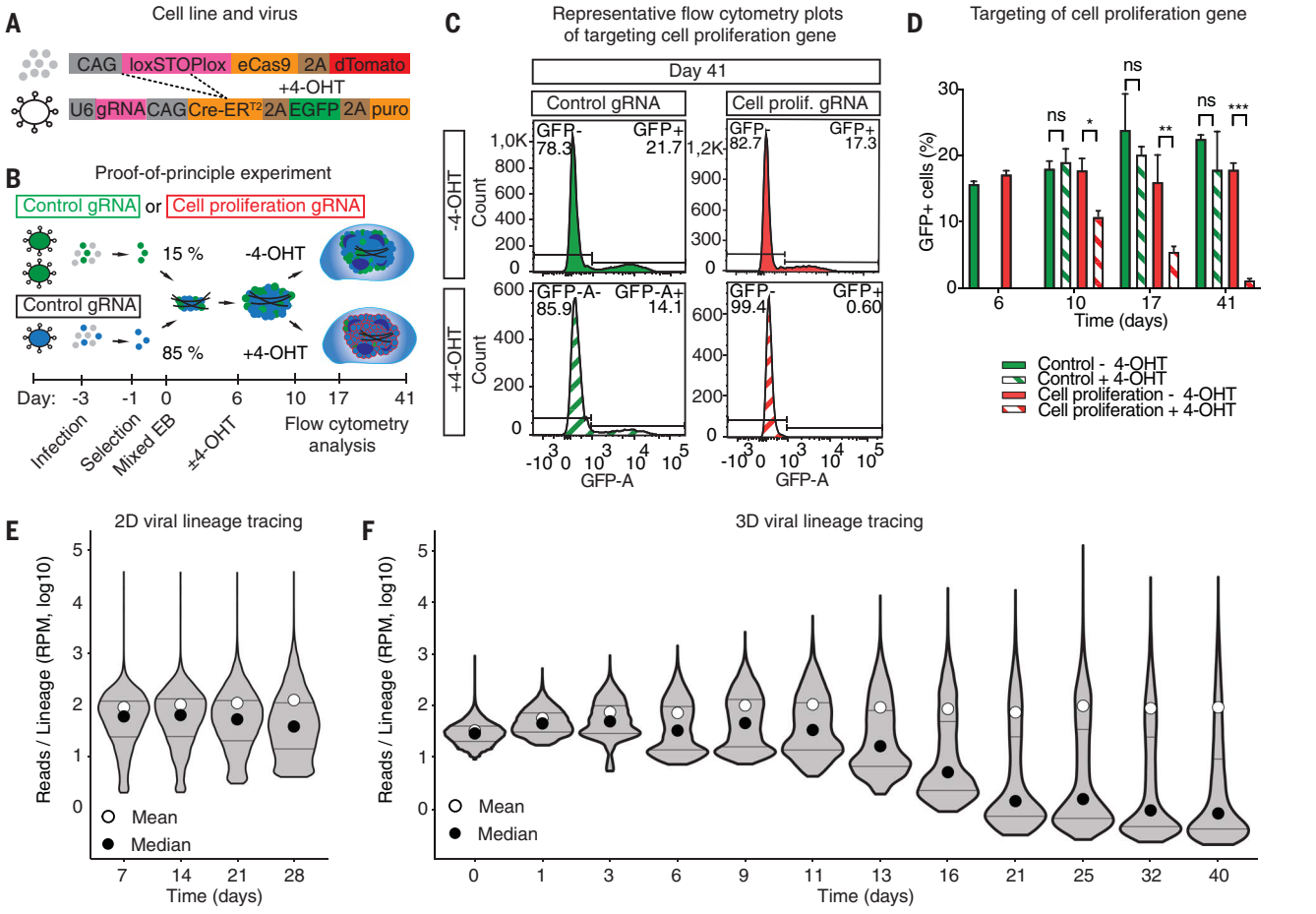

Fig. 1. Rapid LOF generation in lineage size–variable cerebral organoids. (**A**) Schematic of transgenic H9 hESCs and viral construct. EGFP, enhanced green fluorescent protein. (**B**) Outline of the proof-of-principle experiment. In two independent infections, a lentivirus introduced GFP together with a nontargeting control gRNA or a gRNA targeting a gene required for cell proliferation (RPL3), respectively. Separately, a lentivirus introduced BFP together with a nontargeting control gRNA. Both GFP and BFP hESCs were sorted by flow cytometry, mixed in the indicated ratios at embryoid body (EB) formation. Mixtures of control-gRNA-GFP: control-gRNA-BFP and cell-proliferation–gRNA–GFP:control-gRNA-BFP were analyzed over time. (**C**) Representative flow-cytometry histograms (GFP) for organoid mixtures at day 41. (**D**) GFP+ cells plotted for nontargeting control and cell proliferation gRNA, ±4-OHT treatment (n = 3 organoids). Data bars represent means ± SEM. *P = 0.03; **P = 0.004; and ***$P < 10^{-4}$ by two-way analysis of variance (ANOVA) with Sidak's multiple comparison test. ns, not significant. (**E** and **F**) 2D lineage (E) and 3D tracing data (F). Reads per lineage (RPM) were plotted for the indicated time points for each barcode.

lineage size distribution over time (Fig. 1E), consistent with immortalized 2D cell data (*13*). By contrast, lineages in cerebral organoid tissue grew unequally (Fig. 1F)—similarly to tissue stem cells (*14*)—and the increase in lineage size variability was highly reproducible over the course of organoid development (fig. S5, C and D). This unequal growth dynamic makes distinguishing cell number changes caused by inherent variability versus gRNA-mediated mutational effects difficult using conventional screening methods.

A screen for microcephaly candidate genes using dual barcoding

To overcome this problem, we devised a screening method to link gRNA information to lineage size and simultaneously reduce the noise in measurements of lineages containing low cell numbers. For this, we used DNA barcoding at two steps (Fig. 2A). First, each lentivirus introduces a unique lineage barcode (LB) alongside a gRNA, which enables us to distinguish individual lineages expressing a given gRNA (*15*). Second, during polymerase chain reaction (PCR) amplification, we uniquely barcoded individual genomically integrated templates corresponding to single cells [cell barcode (CB)] within a lineage to assay precise cell numbers. CB labeling involved a PCR strategy that excludes multilabeling of templates by nonsense-mediated primer exclusion (NOPE) (*16*) but does not require intermediate product purification, so as to minimize sample loss (fig. S6, A and B). To determine the detection of small lineages using CBs, sequenced PCR reactions from test cell samples containing different lineage sizes were analyzed with or without taking the CB into account (fig. S6C). For smaller lineages, CBs identified exact cell numbers whereas corresponding sequencing reads were variable, which indicates increased sensitivity for small lineages. This methodology overcomes the problems of variable tissue, unequal lineage growth, and low readout sensitivity of negative microcephalic selection—major obstacles for rapid parallel LOF screening in organoid cultures. We call this approach CRISPR–lineage tracing at cellular resolution in heterogeneous tissue (CRISPR-LICHT).

Using CRISPR-LICHT, we screened for microcephaly candidate genes in cerebral organoids (Fig. 2A). Candidates were taken from the Developmental Brain Disorder Database (DBDB) and a complimentary clinical test panel, which yielded 172 genes categorized by level of evidence (LOE) linking them to microcephaly (levels 1, 2, and 3 indicating strong, moderate, and weak, respectively) (*3*) (Fig. 2B). Four gRNAs per candidate gene together with nontargeting

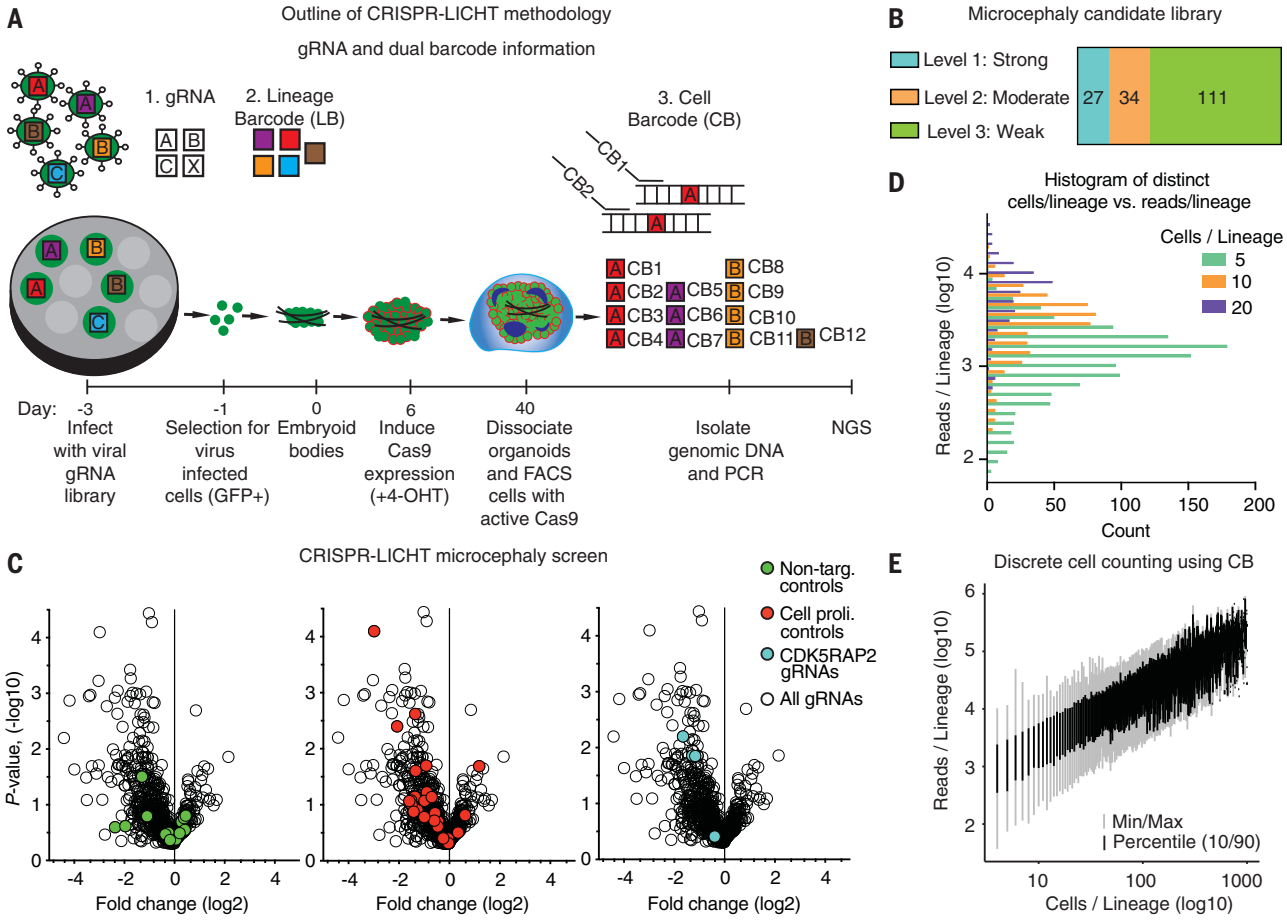

Fig. 2. Screening in human cerebral organoids using CRISPR-LICHT identifies microcephaly-associated genes. (**A**) Scheme describing the screening methodology. Stepwise introduction of gRNA and lineage barcode (LB) as well as cell barcode (CB) are indicated. FACS, fluorescence-activated cell sorting; NGS, next generation sequencing. (**B**) Overview of microcephaly candidate genes. In total, 172 genes were categorized by LOE (from DBDB) linking them to microcephaly (levels 1, 2, and 3 indicating strong. moderate, and weak, respectively). (**C**) Volcano plots depicting results of individual gRNAs in the CRISPR-LICHT microcephaly screen. Green indicates nontargeting controls, red indicates cell proliferation controls, and cyan indicates microcephaly control gene *CDK5RAP2*. (**D**) Histograms (reads per lineage) of lineages containing 5, 10, or 20 cells. (**E**) Point-range plot displaying screen data as cells per lineage versus reads per lineage. 10th and 90th percentiles are shown in black, and minimum and maximum values are shown in gray.

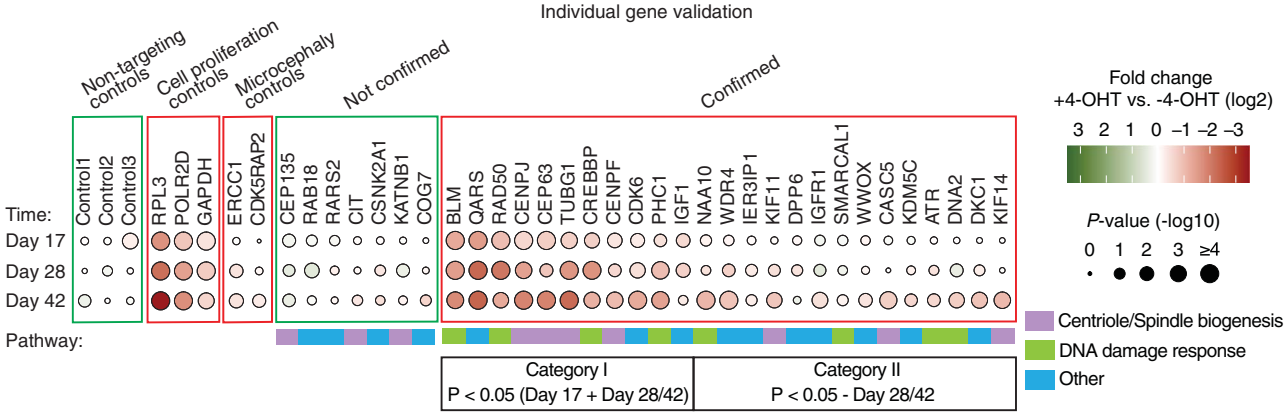

Fig. 3. Independent validation of microcephaly-associated genes identified in CRISPR-LICHT screen. Thirty-two top scoring gRNAs of the CRISPR-LICHT microcephaly screen were tested individually in an independent experimental setup. Cell loss caused by gRNAs was measured by flow cytometry (see fig. S9A for details). Color indicates fold changes (+4-OHT versus −4-OHT, log2) (green: cell-gain; red: cell-loss), and dot size indicates *P* values (−log10). The categories (I and II, see materials and methods) and pathways that candidate genes are associated with are indicated below (centriole and spindle biogenesis: purple; DNA damage response: green; other: cyan) (n = 6 organoids for both −4-OHT and +4-OHT, two differentiation experiments for each time point and gene tested). *P* values are by unpaired two-tailed Student's t test.

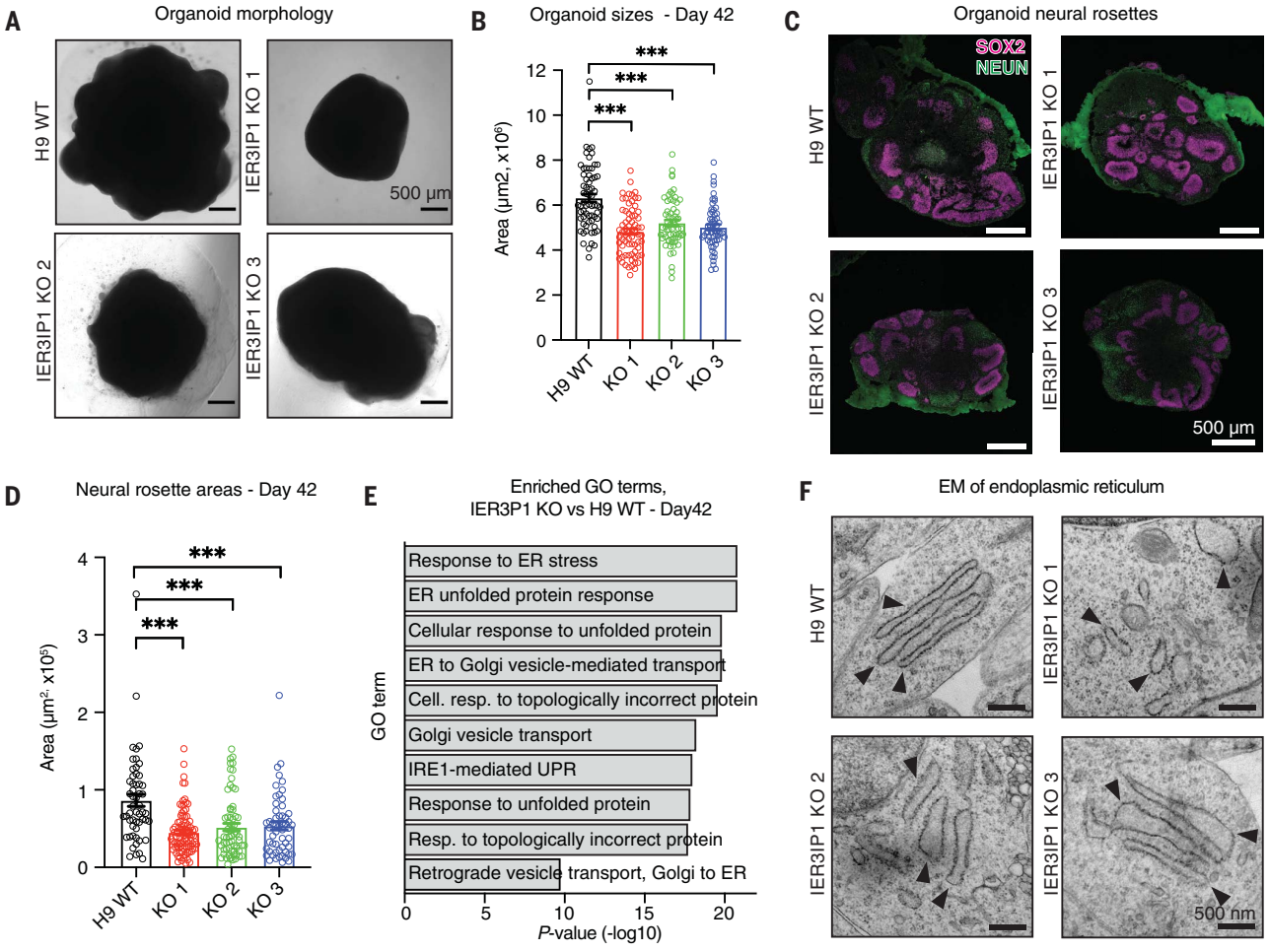

Fig. 4. *IER3IP1* deletion results in a microcephalic phenotype and increased UPR and ER stress. (**A**) Bright-field images of WT and *IER3IP1* KO lines 1 to 3 at day 42. Scale bars, 500 µm. (**B**) Organoid sizes (in square micrometers) at day 42 [*n* = 65 (WT), 70 (KO 1), 62 (KO 2), and 60 (KO 3); eight differentiation experiments]. Data bars represent means ± SEM. ***$P < 10^{-4}$ by ordinary one-way ANOVA using Dunnett's multiple comparison test. (**C**) IHC of WT and *IER3IP1* KO organoids 1 to 3 at day 42. Staining is for SOX2 (magenta) and NEUN (green). Scale bars, 500 µm. (**D**) Neural rosette areas (in square micrometers) of SOX2+ rosettes at day 42 [*n* = 54 (WT), 67 (KO 1), 56 (KO 2), and 91 (KO 3)]. Data bars represent means ± SEM. ***$P < 10^{-4}$ by ordinary one-way ANOVA using Dunnett's multiple comparison test. (**E**) GO terms of up-regulated genes in RNA-seq of *IER3IP1* KO 1 versus WT at day 42. (**F**) EM images of ER structures in neural rosette areas of WT and *IER3IP1* KO organoids 1 to 3. Arrowheads indicate ER structures.

negative controls and cell proliferation positive controls were chosen on the basis of a published design algorithm (*15*) (table S4). The viral library showed equal gRNA and gRNA-LB representation (fig. S7, A and B) and was used to infect inducible eCas9 hESCs. Cells were sorted by flow cytometry for virus integration (fig. S7C), organoids were generated, and eCas9 expression was induced at day 6. Genomic DNA (gDNA) of dTomato and eCas9 positive cells was processed and gRNA, LB, and CB information was sequenced (table S5). Combined gRNA and LB complexity was sufficient to confidently discriminate separate lineages (fig. S7D). Nontargeting control gRNAs and cell proliferation control gRNAs showed normal or depletion distributions, respectively (Fig. 2C and table S6). Three of four gRNAs targeting the microcephaly gene *CDK5RAP2* showed significant depletion, which demonstrated the ability of CRISPR-LICHT to identify moderate LOF-induced cell loss, as observed in microcephaly (*4*). CB introduction eliminated PCR biases and enabled us to distinguish lineages with low cell numbers with high precision (Fig. 2, D and E, and fig. S7E). To determine the effect of dual barcoding, we analyzed our results without taking either the CB information or the LB and CB information into account. This failed to score nontargeting, cell proliferation, and *CDK5RAP2* controls (fig. S8), which indicates that CRISPR-LICHT provides a powerful tool for LOF screening in cerebral organoids.

We ranked the 172 microcephaly candidate genes, and we selected 32 LOE2 or LOE3 genes that showed significant depletion of two or more gRNAs for further analysis (table S7). We performed individual gRNA validations in independent flow cytometry–based mixing experiments (fig. S9A), validating 78% of gRNAs from the CRISPR-LICHT screen (Fig. 3 and table S8). Of the 25 validated genes, most were involved in centriole biogenesis and the DNA damage response—both microcephaly-associated pathways. We followed gRNA effects over time, reasoning that genes involved in general proliferation control would cause cell-loss phenotypes even before the earliest time point analyzed (category I: $P < 0.05$ at day 17 and day 28 or 42), whereas genes that regulate neurogenesis are more likely to have stronger effects during later stages (category II: $P > 0.05$ at day 17 and $P < 0.05$ either at day 28 or day 42).

IER3IP1 is a microcephaly-causing gene regulating the unfolded protein response

To evaluate the potential of our screen for identifying previously unidentified pathways controlling brain proliferation, we concentrated

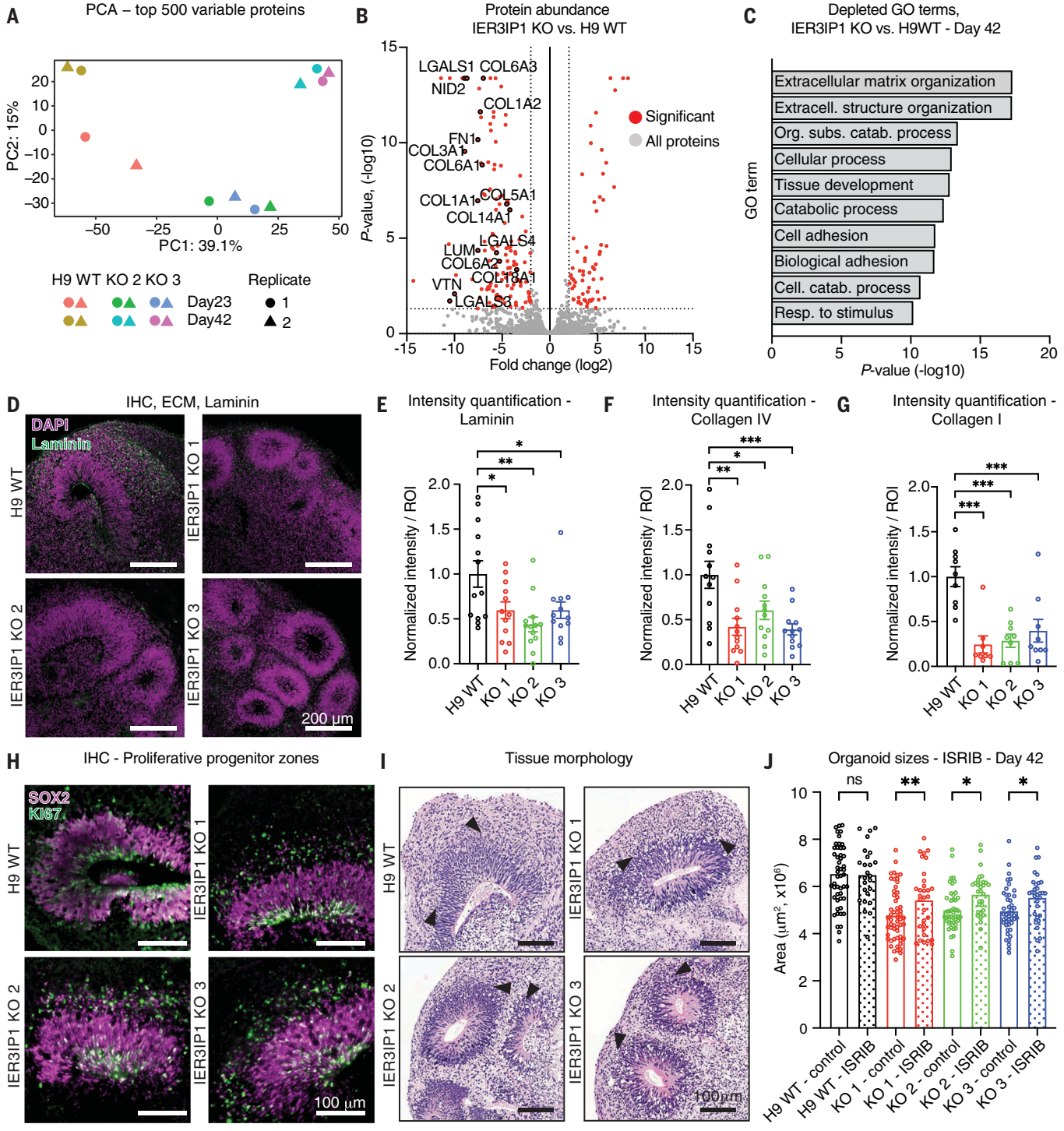

Fig. 5. Loss of ECM proteins in *IER3IP1* KO and partial phenotype rescue using ISRIB. (**A**) Principal components analysis (PCA) plot of mass spectrometry (MS) data of WT and *IER3IP1* KO 2 and 3 organoids at days 23 and 42 ($n = 2$ organoids per time point and cell line). (**B**) Volcano plot of MS data at day 42. Significant proteins are red, and all proteins are gray. (**C**) GO terms of depleted proteins day 42. Org. subs. catab. process, organic substance catabolic process; Cell. catab. process, cellular catabolic process. (**D**) IHC of WT and *IER3IP1* KO organoids 1 to 3 at day 42. Staining is for 4′,6-diamidino-2-phenylindole (DAPI) (magenta) and laminin (green). Scale bars, 200 µm. (**E** to **G**) Intensity quantifications of laminin [$n = 13$ images (WT) and 12 images (KO 1 to 3)] (E), collagen IV ($n = 12$) (F), and collagen I [$n = 9$ (H9 WT and KO 2 and 3) and 8 (KO 1)] (G). Data are from two differentiation experiments for each. Data bars represent means ± SEM. $^{*}P < 0.05$; $^{**}P < 10^{-3}$; and $^{***}P < 10^{-4}$ by ordinary one-way ANOVA using Dunnett's multiple comparison test. (**H**) IHC of WT and *IER3IP1* KO organoids 1 to 3 at day 42. Staining is for SOX2 (magenta) and Ki67 (green). Scale bars, 100 µm. (**I**) H&E staining of WT and *IER3IP1* KO organoids 1 to 3 at day 42. Scale bars, 100 µm. (**J**) Organoid sizes (in square micrometers) of WT and *IER3IP1* KO organoids 1 to 3 ±ISRIB at day 42 [$n = 51$ (WT–control), 25 (H9 WT–ISRIB), 46 (KO 1–control), 31 (KO 1–ISRIB), 45 (KO 2–control), 31 (KO 2–ISRIB), 55 (KO 3–control), 31 (KO 3–ISRIB)]. Data bars represent means ± SEM. $^{**}P = 0.002$; $^{*}P = 0.016$ (KO 2–control versus KO 2–ISRIB); and $^{*}P = 0.02$ (KO 3–control versus KO 3–ISRIB) by unpaired two-tailed Student's t test. ROI, region of interest.

on underexamined category II genes that are predicted to be involved in pathways other than centrosome regulation or the DNA damage response. We selected *IER3IP1* (fig. S9, B and C) (*17*, *18*), which is predicted to contain two intralumenally connected endoplasmic reticulum (ER) transmembrane domains (*19*, *20*). In patients, either one of these domains are homozygously mutated, which presumably leads to nonfunctional proteins (*17*). To study *IER3IP1*, we engineered three independent hESC lines carrying homozygous LOF mutations in *IER3IP1* (fig. S10, A and B). Consistent with patient phenotypes, *IER3IP1* KO organoids were smaller than wild-type (WT) organoids (Fig. 4, A and B, and fig. S10, C and D). This defect was rescued by reexpression of WT *IER3IP1* but not by expression of a mutant version of *IER3IP1* harboring the most common patient mutation, L78P (*21*), which confirms that this patient mutation is causal for the observed microcephaly phenotype (fig. S11). IHC of *IER3IP1* KO organoids revealed that they display smaller neural rosettes than WT organoids, which indicates neural progenitor loss (Fig. 4, C and D). The yeast homolog of *IER3IP1*, *Yos1p*, acts in the secretory pathway to control the exit of secreted proteins from the ER to the Golgi apparatus (*21*, *22*). *IER3IP1* was ubiquitously expressed in cerebral organoids and localized in cells' cytosol in close proximity to but distinct from luminal ER and Golgi markers (fig. S12). Thus, *IER3IP1* likely functions at the ER and its loss may lead to ER dysfunction.

To understand transcriptional changes after *IER3IP1* mutation, we performed RNA-seq over time (fig. S13, A and B). Although WT and *IER3IP1* KO transcriptomes were similar at the pluripotent stage, they diverged in organoids. Gene ontology (GO) enrichment analysis revealed that *IER3IP1* KO organoids were enriched for neural differentiation pathways on day 28 at the expense of cell-division associated pathways (fig. S13, C and D, and tables S9 and S10). GO enrichment analysis at day 42 did not yield significantly depleted pathways nor did we observe any major dorsal-ventral patterning differences between *IER3IP1* KO and WT organoids throughout the organoids' growth, which indicates that *IER3IP1* is not involved in fate control (fig. S13, E and F, and table S11). Up-regulated pathways revealed by GO enrichment analysis in *IER3IP1* KO organoids at day 42 involved ER stress and the unfolded protein response (UPR), along with the secretory pathway and Golgi vesicle transport (Fig. 4E and table S12), which represent a transcriptional response to disturbed ER functionality. To confirm this finding, we performed electron microscopy (EM) on *IER3IP1* KO and WT organoids (Fig. 4F) and observed a significant increase in the width of ER structures but not in their length or area (fig. S14, A to C), which is indicative of increased ER stress (*23*). Temporal gene expression analysis of the top enriched GO term "response to ER stress" (fig. S14D) revealed that both hESCs and day 17 organoids show an up-regulated UPR signature, which failed to be down-regulated in *IER3IP1* KO organoids at day 28 and 42. Additionally, genes associated with the ER-associated protein degradation (ERAD) pathway were selectively up-regulated in *IER3IP1* KO organoids, further indicating imbalanced protein homeostasis in the ER.

Deregulated ECM proteins deposition and tissue integrity defects in *IER3IP1* KO organoids

IER3IP1's ubiquitous expression, the likely function in the ER, and the *Yos1p* secretory phenotype in yeast all point to an intracellular housekeeping function. To understand how *IER3IP1* loss may lead to brain-specific defects, we hypothesized that secreted cargo proteins specifically required for brain development may be affected by deregulated protein homeostasis. To identify misregulated proteins, we performed mass spectrometry and found many ECM proteins to be depleted in *IER3IP1* KO organoids—a result confirmed by GO enrichment analysis—despite being largely unchanged on a transcriptional level (Fig. 5, A to C; figs. S13E and S15; and tables S11, S13, and S14). GO terms for proteins enriched in *IER3IP1* KO organoids suggest a relative increase in neurons (fig. S15F and table S15). IHC for the ECM proteins laminin, collagen IV, and collagen I confirmed the loss of ECM proteins in *IER3IP1* KO organoids, showing significantly reduced signal compared with WT organoids (Fig. 5, D to G, and fig. S16, A and B).

Loss of several ECM proteins in mice causes premature differentiation and neural progenitor loss—similar to defects in *IER3IP1* KO organoids—as well as tissue integrity defects (*24*). To study the tissue integrity in *IER3IP1* KO organoids, we analyzed neural progenitor localization using SOX2, KI67 (Fig. 5H), and PAX6 antibodies (fig. S16, C and D). Proliferative SOX2+KI67+ progenitors were abnormally localized outside the ventricular-like proliferative neural rosettes, which was also evident using PAX6 staining. This suggests the shedding of neural progenitors from neural rosettes. Tissue integrity defects were also observed using hematoxylin and eosin (H&E) staining: *IER3IP1* KO organoids displayed a less-organized rosette architecture, evident by the lower density of nuclei around the ventricle and the uneven basal borders of neural rosettes (Fig. 5I). Our data are consistent with a model in which *IER3IP1* loss leads to reduced ECM deposition, contributing to deregulated rosette integrity and abnormal localization of SOX2+ and PAX6+ neural progenitors, which results in premature neurogenesis, culminating in microcephaly. Thus, a functional ER including an efficient secretory pathway is required for correct brain development by depositing sufficient ECM for tissue integrity and the proliferation of neural progenitors.

Genes involved in the ER-Golgi secretory flux are transcriptionally up-regulated in *IER3IP1* KO organoids; however, this up-regulation is insufficient to prevent microcephaly-related phenotypes. We hypothesized that pharmacological up-regulation of protein translation could increase the levels of mature secreted proteins in *IER3IP1* KO organoids, potentially rescuing microcephaly-related defects. To test this idea, we used integrated stress response inhibitor (ISRIB) (*25*–*27*), a small-molecule drug that promotes eIF2B functionality, thereby restoring protein synthesis and overcoming protein translation inhibition caused by UPR. ISRIB-treated *IER3IP1* KO organoids showed an increase in organoid sizes and neural rosette sizes (Fig. 5J and fig. S17). Thus, modulation of eIF2B functionality by pharmacological intervention is sufficient to rescue the morphological defects that occur in *IER3PI1* KO organoids.

We developed CRISPR-LICHT, a method for LOF screening in human organoids. By combining CRISPR-Cas9 technology with dual barcoding, we overcome the limitations of pooled LOF screening caused by the unequal lineage growth inherent to developing tissues. We used the method to test microcephaly candidate genes: Most top hits were independently validated, which indicates that CRISPR-LICHT data are of sufficient quality to score disease phenotypes, thereby nearly doubling the number of genes that are model-verified to cause microcephaly. Among the 25 genes validated in this study are several with functions not linked to the most extensively analyzed microcephaly pathways, which could expand our view of processes linked to growth control of the human brain. Our cost-effective method can potentially be applied to other organoid systems, allowing the rapid testing of candidate genes for a broad range of human diseases.

REFERENCES AND NOTES

1. D. Jayaraman, B.-I. Bae, C. A. Walsh, *Annu. Rev. Genomics Hum. Genet.* **19**, 177–200 (2018).
2. A. Pinson, T. Namba, W. B. Huttner, *Front. Cell. Neurosci.* **13**, 305 (2019).
3. G. M. Mirzaa, K. J. Millen, A. J. Barkovich, W. B. Dobyns, A. R. Paciorkowski, *Am. J. Med. Genet.* **164A**, 1503–1511 (2014).
4. M. A. Lancaster *et al.*, *Nature* **501**, 373–379 (2013).
5. J. G. Doench, *Nat. Rev. Genet.* **19**, 67–80 (2018).
6. M. A. Lancaster *et al.*, *Nat. Biotechnol.* **35**, 659–666 (2017).
7. M. Jinek *et al.*, *Science* **337**, 816–821 (2012).
8. L. Cong *et al.*, *Science* **339**, 819–823 (2013).
9. I. M. Slaymaker *et al.*, *Science* **351**, 84–88 (2016).
10. T. Wang, J. J. Wei, D. M. Sabatini, E. S. Lander, *Science* **343**, 80–84 (2014).
11. O. Shalem *et al.*, *Science* **343**, 84–87 (2014).

12. M. A. Lodato *et al*., *Science* **350**, 94–98 (2015).
13. H.-E. C. Bhang *et al*., *Nat. Med.* **21**, 440–448 (2015).
14. A. Llorca *et al*., *eLife* **8**, 517–527 (2019).
15. G. Michlits *et al*., *Nat. Methods* **14**, 1191–1197 (2017).
16. D. A. Shagin *et al*., *BMC Genomics* **18**, 440 (2017).
17. I. Valenzuela *et al*., *Eur. J. Med. Genet.* **60**, 517–520 (2017).
18. J. Sun, D. Ren, *Oncotarget* **8**, 56768–56779 (2017).
19. A. Bernsel *et al*., *Proc. Natl. Acad. Sci. U.S.A.* **105**, 7177–7181 (2008).
20. W. H. Yiu, J. W. M. Poon, S. K. W. Tsui, K. P. Fung, M. M. Y. Waye, *Gene* **337**, 37–44 (2004).
21. M. Heidtman, C. Z. Chen, R. N. Collins, C. Barlowe, *Mol. Biol. Cell* **16**, 1673–1683 (2005).
22. M. Heidtman, C. Z. Chen, R. N. Collins, C. Barlowe, *J. Cell Biol.* **163**, 57–69 (2003).
23. C. M. Oslowski, F. Urano, *Methods Enzymol.* **490**, 71–92 (2011).
24. K. R. Long, W. B. Huttner, *Open Biol.* **9**, 180216 (2019).
25. H. H. Rabouw *et al*., *Proc. Natl. Acad. Sci. U.S.A.* **116**, 2097–2102 (2019).
26. C. Sidrauski, A. M. McGeachy, N. T. Ingolia, P. Walter, *eLife* **4**, e05033 (2015).
27. A. M. Paşca *et al*., *Nat. Med.* **25**, 784–791 (2019).

ACKNOWLEDGMENTS

We thank all members of the Knoblich laboratory for technical expertise and feedback. We thank IMP/IMBA biooptics services for expert microscopy and flow cytometry services; M. Novatchkova, T. Burkard from IMP/IMBA Bioinformatics, and D. Malzl (CIBIV) for sequencing analysis; and M. Schutzbier, G. Duernberger, O. Hudecz, and E. Roitinger from the IMP/IMBA/GMI Protein Chemistry Facility for mass spectrometry analysis. We thank A. Sommer, C. Czepe, and the Vienna BioCenter Core Facilities GmbH (VBCF) Next Generation Sequencing unit (www.viennabiocenter.org/facilities) for consultation and sequencing; A. Piszczek and A. Kavirayani, both from the VBCF HistoPathology facility (www.viennabiocenter.org/facilities), for H&E stainings and pathology consultations, respectively; and N. Drexler and the EM Facility of the VBCF for EM consultation, optimization, and imaging. We thank Life Science Editors (lifescienceeditors.com) for editing assistance. We thank A. Jackson (Institute of Genetics & Molecular Medicine, Edinburgh, UK) for microcephaly candidate genes included in the screen and discussions. **Funding:** C.E. received funding from an EMBO postdoctoral fellowship (ALTF 966-2010), D.L. and S.H. are members of the VBC doctoral program, and F.P. is a member of the FWF DK-RNA program. Work in A.v.H.'s laboratory is supported by the Austrian Science Fund (project SFB-F78 P11). Work in J.A.K.'s laboratory is supported by the Austrian Academy of Sciences, the Austrian Federal Ministry of Education, Science and Research, the city of Vienna, the Austrian Science Fund (Special Research Program F78 Stem Cell, F 7803-B, and project SFB-F78 P04), and a European Research Council (ERC) advanced grant under the European Union's Horizon 2020 program (no. 695642). **Author contributions:** C.E., D.L., and J.A.K. designed the study, analyzed data, and wrote the manuscript with input from all authors. C.E. and D.L. performed experiments with help from R.A.W. S.H., F.P., and B.S. performed bioinformatic analysis under the supervision of A.v.H. J.A.B. performed additional bioinformatic analysis. U.E. and J.Z. provided gRNA predictions, reagents, and technical expertise. J.A.K. acquired funding. **Competing interests:** The authors declare no competing interests. **Data and materials availability:** Mass spectrometry data are available via ProteomeXchange with identifier PXD019350. Next generation sequencing data used in this work are available under Gene Expression Omnibus accession no. GSE151384. All H9-based cell lines are subject to a material transfer agreement from WiCell.

SUPPLEMENTARY MATERIALS

science.sciencemag.org/content/370/6519/935/suppl/DC1
Materials and Methods
Figs. S1 to S17
Tables S1 to S15
References (*28–34*)
MDAR Reproducibility Checklist

View/request a protocol for this paper from *Bio-protocol*.

4 March 2020; accepted 10 September 2020
Published online 29 October 2020
10.1126/science.abb5390

IMMUNOLOGY

Fetal mast cells mediate postnatal allergic responses dependent on maternal IgE

Rasha Msallam[1]*, Jozef Balla[2]*, Abhay P. S. Rathore[3], Hassen Kared[1], Benoit Malleret[1,4], Wilfried A. A. Saron[2], Zhaoyuan Liu[5], Jing Wen Hang[4], Charles Antoine Dutertre[1,2], Anis Larbi[1], Jerry K. Y. Chan[6,7,8], Ashley L. St. John[2,3,4,9]†, Florent Ginhoux[1,5,10]†

Mast cells (MCs) are central effector cells in allergic reactions that are often mediated by immunoglobulin E (IgE). Allergies commonly start at an early age, and both MCs and IgE are detectable in fetuses. However, the origin of fetal IgE and whether fetal MCs can degranulate in response to IgE-dependent activation are presently unknown. Here, we show that human and mouse fetal MCs phenotypically mature through pregnancy and can be sensitized by maternal IgE. IgE crossed the placenta, dependent on the fetal neonatal Fc receptor (FcRN), and sensitized fetal MCs for allergen-specific degranulation. Both passive and active prenatal sensitization conferred allergen sensitivity, resulting in postnatal skin and airway inflammation after the first allergen encounter. We report a role for MCs within the developing fetus and demonstrate that fetal MCs may contribute to antigen-specific vertical transmission of allergic disease.

Mast cells (MCs) are innate immune cells present in all vascularized tissues. They reside close to mucosal surfaces, blood vessels, and nerve fibers. Their positioning enables them to act as sentinels, constantly sampling the surrounding microenvironment, and they have the ability to respond rapidly to a wide variety of pathogens, allergens, or tissue-derived danger signals (*1*–*4*). MCs contain large numbers of secretory granules, storing an extensive array of preformed mediators such as histamine, serotonin, proteases (e.g., tryptase and chymase), proteoglycans, and some cytokines (*5*). Additionally, they synthesize prostaglandins, leukotrienes, and cytokines de novo (*6*). Therefore, they can initiate a complex program of inflammation while also regulating the development of adaptive immune responses (*3*, *7*). MCs are required in many animal allergic disease models (*8*, *9*) and contribute to human allergic diseases, as suggested by their activation during acute allergic episodes and the efficacy of MC-stabilizing therapeutics in allergic conditions (*10*, *11*).

Allergic diseases are caused by pathological immune responses to innocuous environmental substances such as plant pollen, pet dander, house dust mites, and various foods (*12*, *13*). On the basis of the route of sensitization and exposure, they can manifest as asthma, allergic rhinitis, atopic dermatitis, food allergy, or anaphylaxis. Allergic diseases affect ~10 to 30% of the general population, and their prevalence has been increasing over time (*14*, *15*). Allergic reactions are primarily mediated by immune mechanisms that promote Th2-polarized immunity, leading to immunoglobulin E (IgE) production that triggers MC activation upon allergen exposure (*16*–*18*). However, MC degranulation can also be triggered by alternate mechanisms, including immune complexes, anaphylatoxins, and through other G protein–coupled receptors such as MrgX2 (*19*–*21*). Sensitization of MCs to antigens occurs when IgE binds to the high-affinity receptor for the Fc region of IgE (FcεRI) present on the cell surface (*2*). Upon subsequent antigen exposure, the IgE-armed MCs rapidly detect antigen and degranulate, with their released products leading to inflammation (*2*).

During embryonic development in mice, MCs together with macrophages appear relatively early in fetal tissues, preceding other immune cell types (*22*, *23*). MCs colonize the developing fetus in two waves, which are distinct both temporally and by the tissue of residence (*22*). The initial wave of yolk sac–derived progenitors with MC potential is detectable between embryonic day 7.5 (E7.5) and E10.5 (*22*). Fetal MCs are thought to influence the development of several organs (*24*–*26*); however, whether they are functional contributors to fetal and neonatal immune and allergic responses through the capture of allergen-specific maternal IgE is presently unknown.

Here, we show that maternal IgE can enter the fetus, dependent on the neonatal Fc receptor for IgG (FcRN), after both passive and active maternal sensitization. IgE is able to prime fetal MCs, which are functional before birth, for allergen detection postpartum. Consequently, the offspring born from mice sensitized before pregnancy develop allergic inflammation upon the first exposure to the allergen. Furthermore, MC-bound IgE is present in human fetal skin, suggesting that a similar mechanism may occur in humans. Our results demonstrate that maternally derived IgE can predispose for allergic disease through fetal MC binding and/or activation in neonatal and early life upon the first exposure to the allergen, suggesting potential therapeutic targets to mitigate neonatal allergies.

Results

Murine fetal MCs are phenotypically mature

Although the earliest progenitors of MCs originate in primitive hematopoiesis during embryonic development (*22*), the time course of their maturation and the acquisition of molecules required for effector functions in allergic inflammation are not yet fully described. To address this, we used flow cytometry to analyze the expression of phenotypic markers on skin-resident MCs of fetuses and newborns (NBs) compared with adult MCs. Cells having an MC phenotype ($CD45^+F4/80^-CD11b^-CD90^-MHCII^-CD117^+CD200R^+$) (Fig. 1A), which constituted ~20% of skin $CD45^+$ cells at E17.5 (fig. S1A), were selected for further phenotypic characterization at various developmental stages. This involved the detection of other MC markers such as CD16/32, CD63, integrin-β7, the granule component heparin, and FcεRI (Fig. 1, B and C, and fig. S1B). FcεRI expression was low but confirmed to be present on fetal MCs and began increasing in NBs (Fig. 1C). Increased maturity of adult MCs compared with fetal MCs was indicated by the greater relative expression of markers that mediate allergic effector functions, such as heparin and FcεRI (Fig. 1, B and C, and fig. S2A). FcεRI expression was confirmed by immunostaining to colocalize with MCs (fig. S2B). Conversely, the MC progenitor- and migration-associated markers integrin-β7 (*27*) and CX3CR1 (*22*) were more highly expressed on fetal MCs, as was c-kit (CD117) (Fig. 1, A and B, and fig. S2A). However, fetal MCs also gradually increased the expression of the maturation marker and granule component heparin (Fig. 1B and fig. S2A), which also could be visualized by toluidine blue staining (fig. S2C), and colocalized with the MC protease MCPT1 (fig. S2D). The relative numbers of MCs that were positive for these and additional markers in E12.5, E14.5, E16.5, NB, and adult skin are provided in

[1]Singapore Immunology Network (SIgN), A*STAR, Singapore 138648, Singapore. [2]Program in Emerging Infectious Diseases, Duke-NUS Medical School, Singapore 169857, Singapore. [3]Department of Pathology, Duke University Medical Center, Durham, NC 27705, USA. [4]Department of Microbiology and Immunology, Yong Loo Lin School of Medicine, National University of Singapore, Singapore 117545, Singapore. [5]Shanghai Institute of Immunology, Shanghai Jiao Tong University School of Medicine, Shanghai 200025, China. [6]Department of Reproductive Medicine, KK Women's and Children's Hospital, Singapore 229899, Singapore. [7]Academic Clinical Program of Obstetrics and Gynaecology, Duke-NUS Medical School, Singapore 229899, Singapore. [8]Experimental Fetal Medicine, Yong Loo Lin School of Medicine, National University of Singapore, Singapore 117597, Singapore. [9]SingHealth Duke-NUS Global Health Institute, Singapore 169857, Singapore. [10]Translational Immunology Institute, SingHealth/Duke-NUS Academic Medical Centre, The Academia, Singapore 169856, Singapore.
*These authors contributed equally to this work.
†Corresponding author. Email: Florent_Ginhoux@immunol.a-star.edu.sg (F.G.); ashley.st.john@duke-nus.edu.sg (A.L.S.)

fig. S2A. Scanning electron microscopy showed that isolated MCs from multiple embryonic stages appeared granulated (Fig. 1D). By immunostaining, we confirmed the presence of MCs loaded with heparin-containing granules in the embryonic skin based on the colocalization of heparin with c-kit and CX3CR1, an early MC marker in embryos (*22*), beginning as early as E12.5, and their density increased with gestational age (Fig. 1E). Together, these data indicate that fetal MCs having low expression for FcεRI and containing heparin to the same or similar degree as adult MCs expand during fetal development, supporting that some fetal MCs might be functionally mature and contain the components required for allergic responses before birth.

Maternal IgE drives antigen-specific degranulation of fetal MCs

We next investigated whether fetal MCs can functionally bind IgE to become sensitized. Although allergen-specific IgE is detectable in human neonates and cord blood (*28*–*31*), intrinsic IgE production was found to be detectable only ~9 months after birth (*32*), suggesting that neonatal IgE is at least partially derived from the mother. Therefore, to experimentally address whether IgE transfers from mother to fetus, we passively sensitized pregnant mice with IgE and verified whether these antibodies were later detectable on fetal MCs. For this, we administered exogenous IgE to the dam at E16.5 and collected the fetal and maternal skin 24 hours later (Fig. 2A). This led to increased binding of IgE to fetal MCs, although to a lesser extent than to maternal MCs (Fig. 2, B and C). The binding of IgE to fetal MCs was also increased after injection of dams with higher doses of IgE (Fig. 2C). Moreover, IgE persisted on the fetal MCs, because it was present to an equal degree on MCs from the skin of NBs compared with E17.5 (Fig. 2C). Immunostaining of E17.5 fetal tissue confirmed IgE binding to skin MCs (counterstained with toluidine blue for MC identification) after injection into dams (Fig. 2D). Fetal MCs could also be identified by toluidine blue staining (Fig. 2E) and by flow cytometry (Fig. 2F and fig. S4) of fetal lung tissue. Flow cytometry indicated the expression of FcεRI on a small proportion of skin and lung MCs, in contrast to monocytes, which did not express FcεRI (Fig. 2G and fig. S4). We also observed an increase in the granulation of fetal lung MCs after IgE injection of dams (Fig. 2H), suggesting an increase in the maturation of MCs in the presence of IgE. Together, these data show that translocation of maternal IgE to the fetus occurs and that maternal IgE can bind to fetal MCs in multiple tissues.

To address whether fetal MCs are functionally capable of degranulation mediated by maternally derived IgE, we collected E17.5

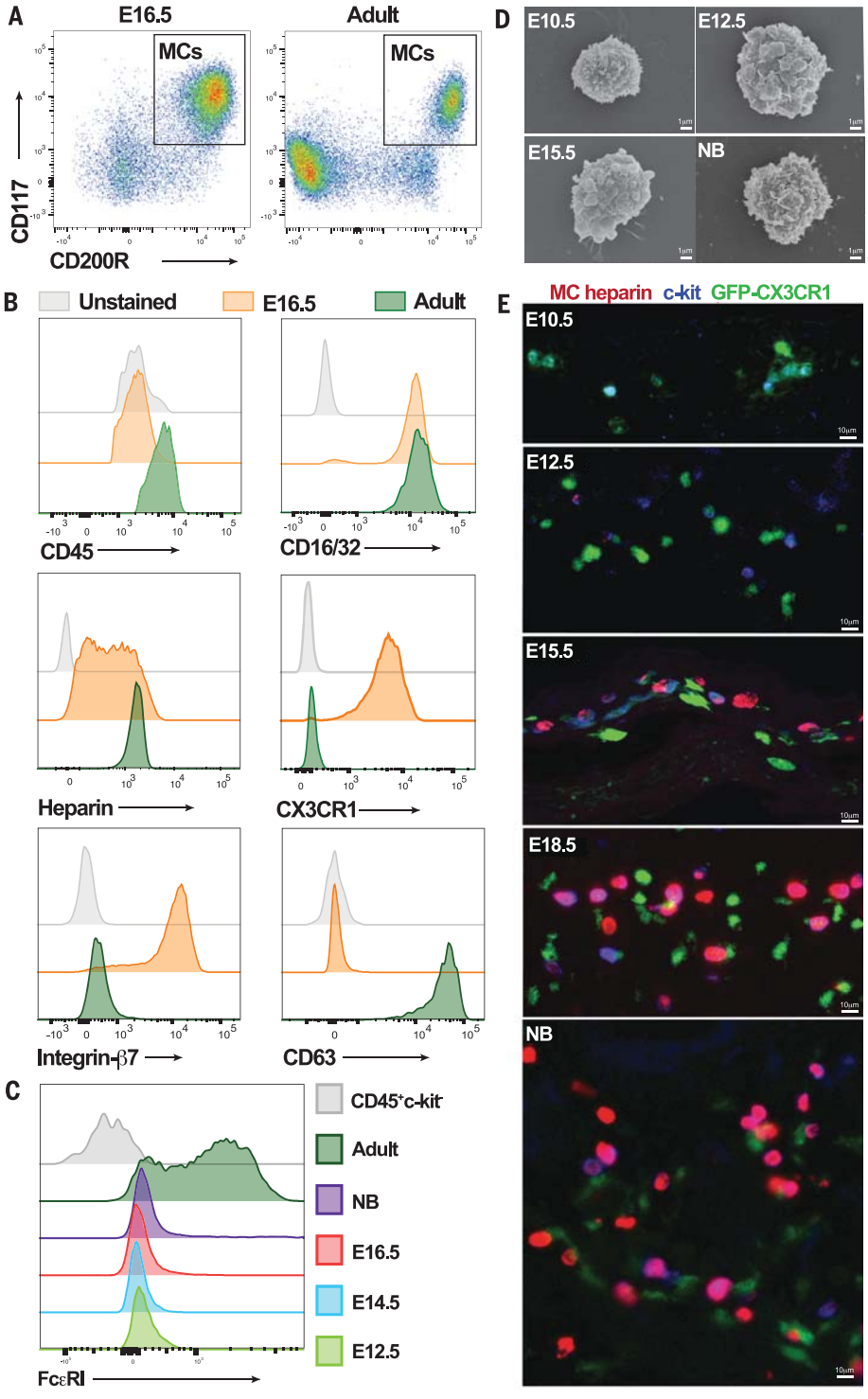

Fig. 1. Mast cells are present in the fetal skin and mature during pregnancy. (**A**) Flow cytometry plots of MCs identified in fetal (E16.5) and adult skin after gating on DAPI$^-$CD45$^+$F4/80$^-$CD11b$^-$CD90$^-$MHCII$^-$ cells. The full gating strategy is shown in fig. S1. (**B**) Histograms showing the expression of various MC phenotypic markers on E16.5 and adult (orange and dark green, respectively) mouse skin MCs. (**C**) Expression of FcεRI on fetal MCs throughout development compared with adult MCs. (**D**) Scanning electron microscope images of sorted mouse fetal and NB MCs. The full gating strategy is shown in fig. S3. Scale bar, 1 μm. (**E**) Immunofluorescence staining for MC markers (c-kit is shown in blue and heparin in red) in CX3CR1^{GFP} mouse skin sections at various time points of fetal development showing gradual increases in their density and granulation. Scale bar, 10 μm.

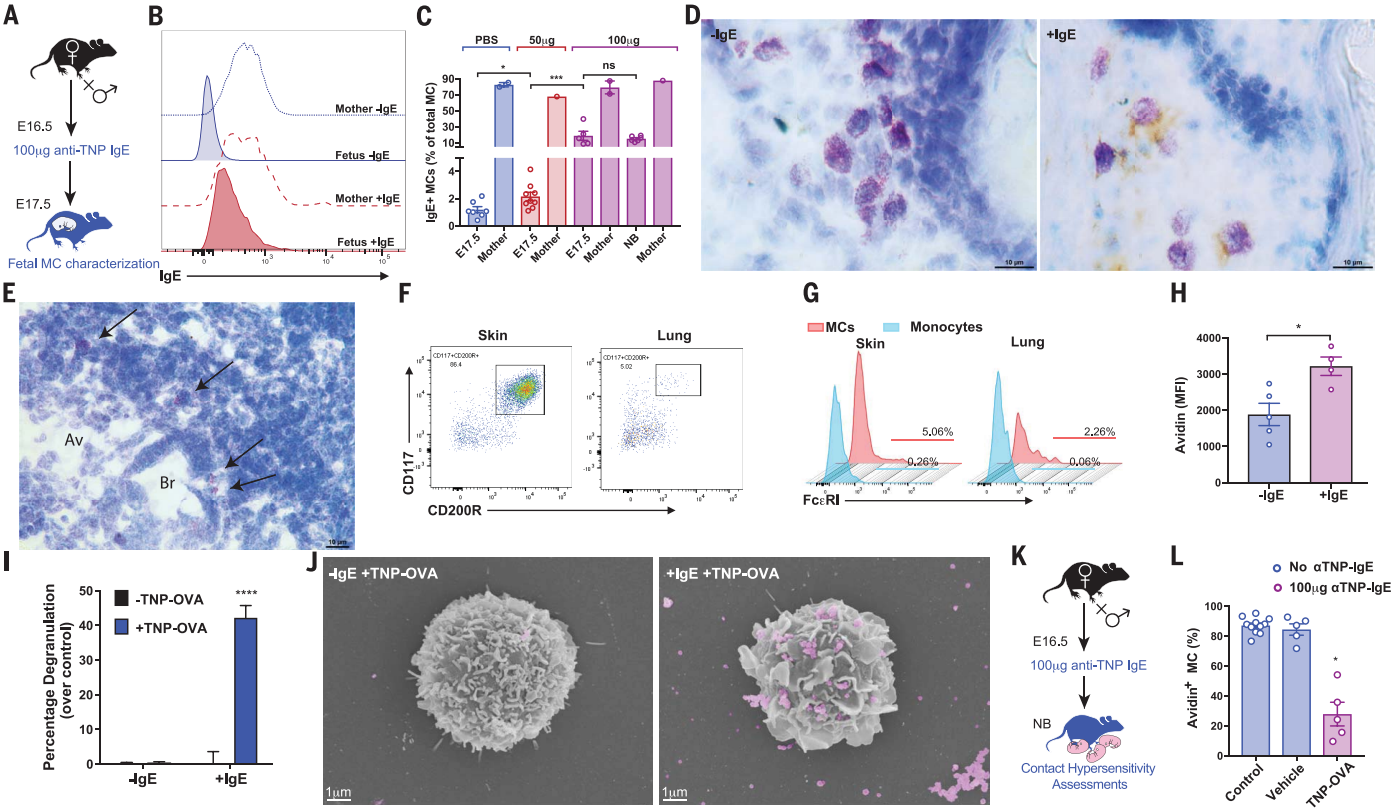

Fig. 2. Maternal IgE binds fetal MCs and induces their maturation and antigen-specific activation. (**A**) Schematic of the experimental design of passive maternal sensitization with TNP-specific IgE at E16.5, followed by fetal skin MC characterization. (**B**) IgE binding to maternal (blue) and fetal (red) MCs by flow cytometry. (**C**) Quantification of the percentage of IgE^+ MCs after intravenous injection of various doses of IgE comparing the percentages in the maternal, fetal, and NB skin. Fetal groups were compared with each other by Student's unpaired *t* test. $*p < 0.05$; $***p < 0.001$; ns, not significant. Data points represent individual animal responses and error bars indicate the mean ± SEM. (**D**) Immunohistochemistry for IgE (brown) in fetal skin sections followed by counterstaining using toluidine blue to visualize granulated MCs (purple). IgE staining could be visually observed on MCs in the fetuses of IgE-injected dams. (**E**) Fetal MCs could also be seen in toluidine blue–stained lung tissue sections. Arrows point to granulated MCs, as indicated by purple staining. Av, alveolar space; Br, bronchiole. (**F**) Identification of MCs in fetal skin and lung tissue at E17.5. The gating strategy for the identification MCs is provided in figs. S1A and S4. (**G**) Histograms represent staining for FcεRI on fetal skin and lung MCs and monocytes (E17.5). (**H**) Mean fluorescence intensity of avidin staining (to indicate heparin content) was determined in lung MCs of NB mice (with and without IgE injection of dams at E16.5), showing increased granulation of fetal MCs in the presence of maternal IgE. Data points represent individual animal responses and error bars indicate the mean ± SEM. (**I**) Antigen-specific degranulation of fetal MCs after maternal sensitization was confirmed by a β-hexosaminidase assay after isolation of fetal MCs from sensitized (IgE^+) and unsensitized (IgE^-) groups by magnetic bead separation and challenge with antigen (TNP-OVA) or control media. $****p < 0.001$. Data indicate the mean ± SEM of technical replicates. (**J**) Electron micrographs of TNP-OVA–exposed MCs isolated from dams with (+IgE) and without (–IgE) IgE injection. Extracellular granules in both images are false-colored pink to aid visualization. Scale bar, 1 μm. (**K**) Schematic of the experimental design of the experiment to assess MC degranulation in antigen-challenged NBs. (**L**) Percentage of granulated MCs ($Avidin^+$) of total MCs in the NB skin 6 hours after paining of TNP-OVA or vehicle. $*p < 0.05$. Data points represent individual animal responses and error bars indicate the mean ± SEM.

fetuses from mothers passively sensitized with either IgE specific for the hapten 2,4,6-trinitrophenyl (TNP) or vehicle on E16.5 (Fig. 2A) and isolated fetal MCs from skin cell suspensions by immunomagnetic positive selection. When antigen-specific activation was induced ex vivo by exposing the MCs to ovalbumin (OVA)–conjugated TNP, only MCs isolated from fetuses of the maternal sensitization group, but not the control groups, showed significant degranulation (Fig. 2, I and J, and fig. S3). Next, to investigate whether the sensitization of fetal MCs with maternally derived IgE can initiate an allergic response in vivo in NBs, we used a neonatal model of contact hypersensitivity in which anti-TNP IgE was administered to dams at E16.5 and NBs were challenged by painting a solution of TNP-OVA onto the dorsal skin (Fig. 2K). The antigen-specific allergic reaction was indicated by MC degranulation in the skin, as measured by flow cytometry. Vehicle-treated NBs developed no allergic reaction in the skin, whereas MC degranulation was detected in the skin of antigen-exposed neonates (Fig. 2L). Because allergic responses were acquired to an experimental antigen, these results indicate the ability of maternal IgE to induce antigen-specific degranulation of fetal MCs and to mediate early postnatal allergic responses at the first encounter with the allergen.

Fetuses born to allergic mothers develop airway hyperreactivity upon their first allergen exposure

We next used an active sensitization model to determine whether maternal allergy can influence postnatal allergic responses of progeny and to investigate the mechanism of maternal IgE transfer to fetal mice. Female mice were sensitized using a protocol that is known to induce a strong type II allergic response similar to that observed in allergic humans (*33*, *34*).

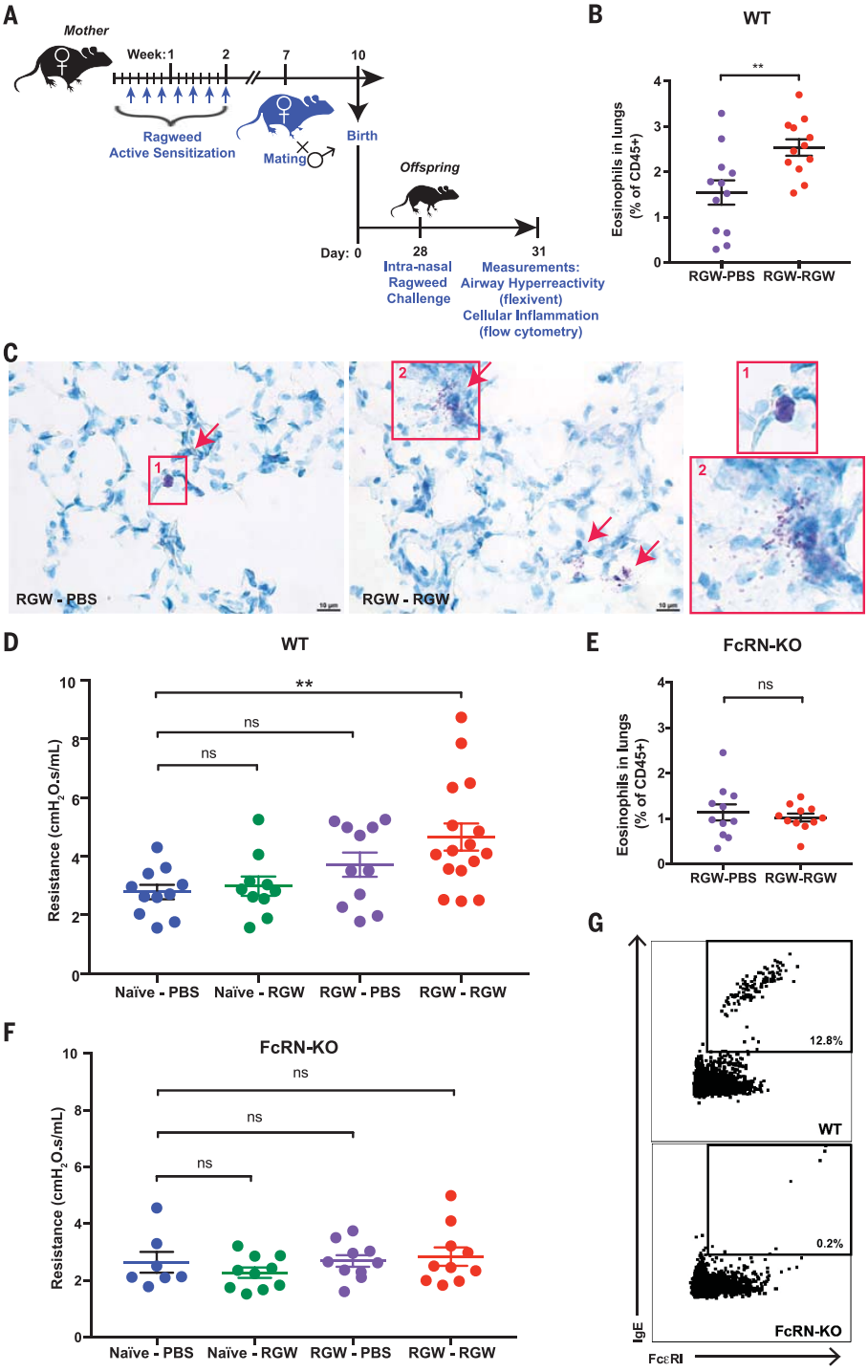

Fig. 3. Antigen-specific enhancement of allergic disease after maternal sensitization is FcRN dependent. (**A**) Schematic of the active sensitization protocol of mice against RGW antigen, followed by mating and measurements of allergic responses in progeny intranasally challenged with RGW or vehicle 4 weeks after birth. (**B**) Significant eosinophilia in the offspring of RGW-sensitized dams that were challenged with RGW (RGW-RGW) compared with littermates challenged with PBS (RGW-PBS). Eosinophils were defined as $CD45^+CD11c^-Ly6g^-SiglecF^+$ cells, with the gating strategy provided in fig. S5A. Data points represent individual animal responses compiled from three independent litters, with the mean ± SEM indicated. $^{**}P < 0.01$. (**C**) Visualization of intact MCs in the lungs of RGW-PBS mice and MC degranulation in the lungs of RGW-RGW mice 6 hours after challenge. Additional representative images are provided in fig. S5C. (**D**) Measurements of airway hyperreactivity in response to escalating doses of inhaled methacholine 72 hours after RGW or vehicle challenge. Offspring born to RGW-sensitized dams that were challenged with RGW (RGW-RGW) showed increased airway hyperreactivity compared with all other groups. The highest methacholine concentration is presented, and the full escalating dose curve is provided in fig. S6A. Data points represent individual animal responses compiled from three independent litters, with the mean ± SEM indicated. $^{**}P < 0.01$. (**E**) Eosinophilia after RGW challenge was not detected in FcRN-KO mice born to RGW-sensitized dams compared with PBS-challenged littermate controls. Data points represent individual animal responses compiled from three independent litters, with the mean ± SEM indicated. (**F**) In FcRN-KO mice, RGW challenge did not influence airway hyperreactivity. Data points represent individual animal responses compiled from three independent litters, with the mean ± SEM indicated. Data were compared by Student's unpaired *t* test for (B) and (E) and by one-way ANOVA with Holm-Sidak posttest for (D) and (F). ns, not significant. (**G**) IgE binding to fetal MCs is FcRN dependent, as determined by flow cytometry. Plots show MCs from the skin of E17.5 WT and FcRN-KO mice fetuses after maternal IgE injection at E16.5. Percentage of $Fc\varepsilon RI^+$ MCs that are IgE^+ is given.

For this, ragweed (*Ambrosia artemisiifolia*) pollen protein extract (RGW) was administered for 2 weeks for active sensitization, followed by 5 weeks without any treatments to allow for any ongoing inflammation to resolve before initiating pregnancy (Fig. 3A). Allergic reactions in the offspring were measured at 4 weeks of age by intranasal RGW allergen challenge and evaluation of their allergic inflammation after 72 hours (Fig. 3A and fig. S5A). We observed a significant and allergen-specific increase in airway eosinophilia (Fig. 3B), which was confirmed by histology (fig. S5B). We also observed that the progeny of RGW-sensitized animals showed MC degranulation in the lungs after RGW challenge (Fig. 3C and fig. S5C). Other immune cell types, including dendritic cells and neutrophils, which are not as strongly associated with acute respiratory allergy, did not significantly differ between the groups (fig. S5, D and E). Functionally, allergic inflammation in the lung is characterized by airway hyperreactivity (*8*, *33*). Therefore, we measured airway hyperreactivity after RGW challenge in response to an inhaled bronchoconstricting stimulus involving intubation and exposure to escalating doses of nebulized β-methylcholine. Bronchoconstriction was reflected in the increase in airway resistance to airflow. Upon allergen

challenge, mice born from RGW-sensitized dams showed significantly higher airway hyperreactivity compared with those born to nonsensitized dams or various controls (Fig. 3D and fig. S6A), suggesting transfer of allergy from mother to the fetus. The control groups included mice born to sensitized or nonsensitized dams that were not challenged with an allergen (Fig. 3D and fig. S6A). Furthermore, mice born from RGW-sensitized dams that were challenged with a nonspecific complex antigen, house dust mite, did not display allergic disease, confirming allergen specificity (fig. S6B). The effect of maternal sensitization was lost in mice aged longer when challenge was done after 6 weeks of age (fig. S6C). These data show that the offspring of allergic mothers can develop airway inflammation in an antigen-specific and time-dependent manner upon the first exposure to an allergen without prior sensitization themselves.

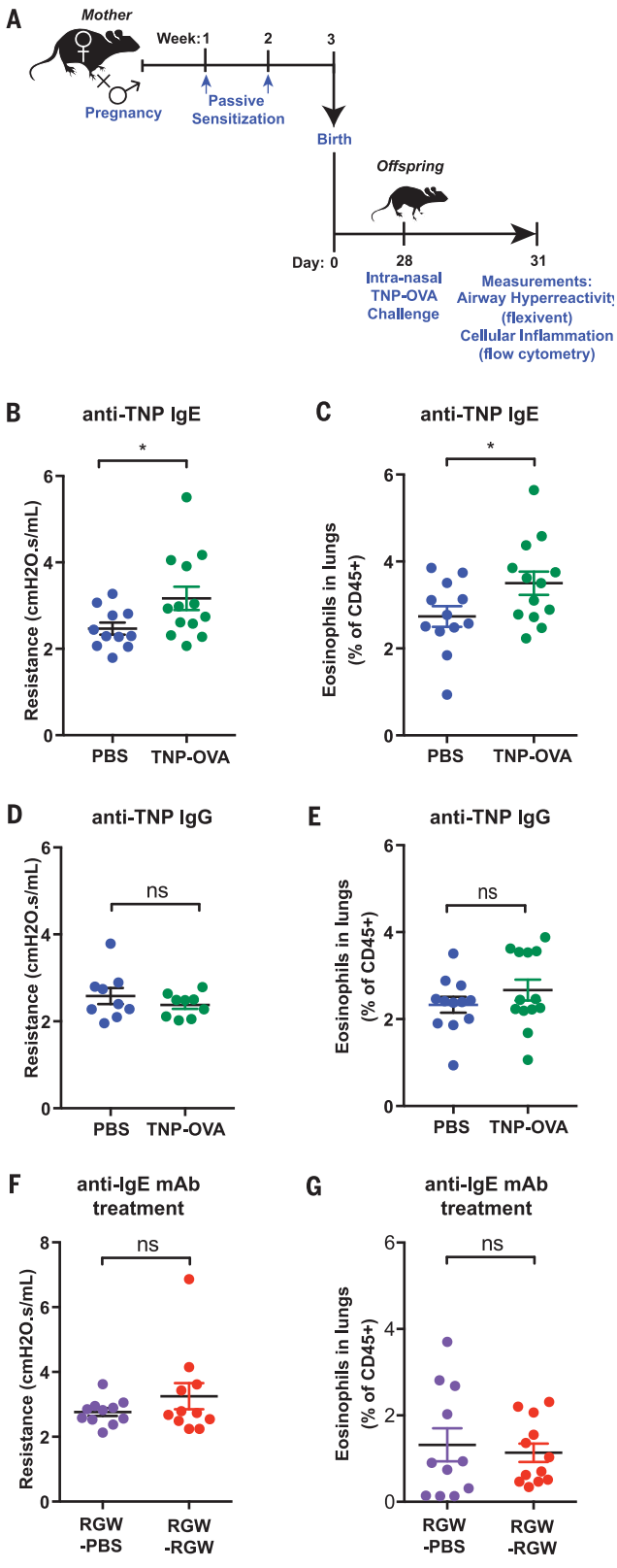

Fig. 4. Maternal IgE can mediate antigen-specific allergic disease. (**A**) Schematic of the passive sensitization model in which TNP-specific IgE or IgG was injected into pregnant mice 8 and 16 days after confirmation of pregnancy, and groups of littermates from three independent litters were challenged intranasally with TNP-OVA or vehicle 4 weeks after birth. Allergic responses in terms of lung eosinophilia were measured 3 days after challenge. (**B**) Airway resistance was significantly elevated 3 days after challenge with the experimental antigen TNP-OVA compared with phosphate-buffered saline (PBS)–challenged littermate controls after passive sensitization of dams with TNP-specific IgE during pregnancy. (**C**) Eosinophilia was observed in the lungs and TNP-OVA–challenged mice compared with PBS-challenged littermate controls. (**D** and **E**) No differences in airway resistance (D) or eosinophil infiltration (E) were observed between littermates given TNP-OVA or PBS challenges after passive sensitization of their mothers with anti-TNP IgG. (**F** and **G**) No differences in airway resistance (F) or eosinophil infiltration (G) were observed between littermates of mice born to females that were actively sensitized to RGW as in Fig. 3A and treated with a monoclonal antibody against IgE at E8.5 during pregnancy. Groups were compared by Student's unpaired *t* test. *$p < 0.05$; ns, not significant. For (B) to (F), data points represent individual animal responses of three litters of progeny, with the mean ± SEM indicated.

Transfer of allergic disease from mother to fetus is FcRN and IgE dependent

To gain a mechanistic understanding of how maternal allergen sensitivity is transferred to offspring in utero, we investigated the role of FcRN in this process. FcRN is expressed by the fetal endothelial cells and syncytiotrophoblast cells of the placenta, where it serves a critical role in regulating antibody transfer from mother to fetus (*35*, *36*). Although FcRN is best characterized for its ability to transfer IgG transplacentally, we hypothesized that it was involved in IgE translocation based on recent in vitro evidence of FcRN-mediated transfer of IgG-IgE complexes (*37*). To test the role of FcRN in IgE translocation into the fetus and, consequently, allergy transfer, we performed the active RGW sensitization experiment in FcRN-deficient mice (Fig. 3A). In contrast to wild-type (WT) mice (Fig. 3B), there was no allergen-specific eosinophilia detected in the progeny of RGW-sensitized FcRN-deficient mice (Fig. 3E), even though adult FcRN-knockout (KO) mice had no defects in IgE production (fig. S7A) and were capable of generating intrinsic allergic responses after sensitization and challenge with antigen (fig. S7B). Furthermore, in the FcRN-deficient progeny of sensitized dams, there was no detectable increase in airway hyperreactivity to inhaled methacholine (Fig. 3F and fig. S7C). To investigate the influence of FcRN on IgE translocation into fetuses, we injected equivalent amounts of IgE into pregnant WT and FcRN-KO mice at E16.5. At E17.5, IgE could be detected by flow cytometry on the fetal skin MCs of WT but not FcRN-KO mice (Fig. 3G), supporting its ability to translocate in an FcRN-dependent manner. These results suggest that the transfer of allergen-specific sensitization from the mother to the offspring is mediated by FcRN.

Because FcRN can mediate both IgG and IgE transfer (*37*), we investigated whether IgE is sufficient to cause postnatal allergic inflammation. We used a passive sensitization model in which pregnant mice were injected with TNP-specific IgE (Fig. 4A). Juvenile mice were challenged 4 weeks after birth with TNP-OVA, and the allergic responses in the lungs were measured 72 hours after challenge and compared with their unchallenged control littermates. Antigen challenge induced significant

airway hyperreactivity (Fig. 4B) and eosinophil influx into the lungs (Fig. 4C), indicative of an IgE-dependent allergic response. Similar to the active sensitization model, these responses were lost in FcRN-KO mice (fig. S8, A and B). The hyperreactivity responses were also dose dependent, with a higher dose of IgE inducing a stronger effect in the progeny compared with littermate controls (fig. S8, C and D). In contrast to IgE, injection of an equivalent amount of anti-TNP IgG was insufficient to induce detectable airway hyperreactivity or inflammation (Fig. 4, D and E). To further support that IgE mediates these allergic responses, we also used a monoclonal blocking antibody against IgE, which is a similar strategy to the anti-IgE human therapeutic omalizumab, an effective treatment for some types of allergic disease (*38*, *39*). Injection of RGW-sensitized pregnant dams with anti-IgE on E8.5 of pregnancy (Fig. 3A) significantly reduced subsequent allergic responses in the progeny so that RGW challenge failed to increase airway resistance (Fig. 4F) or induce eosinophilia (Fig. 4G), supporting the critical role of IgE in this model.

Because IgE transfer could occur in complex with IgG (*37*), we confirmed the presence of IgG-IgE immune complexes in the blood of sensitized dams (fig. S8E). We investigated whether IgE could be observed in fetal endothelial cells of the placenta after injection in pregnant dams. Staining of placental tissues

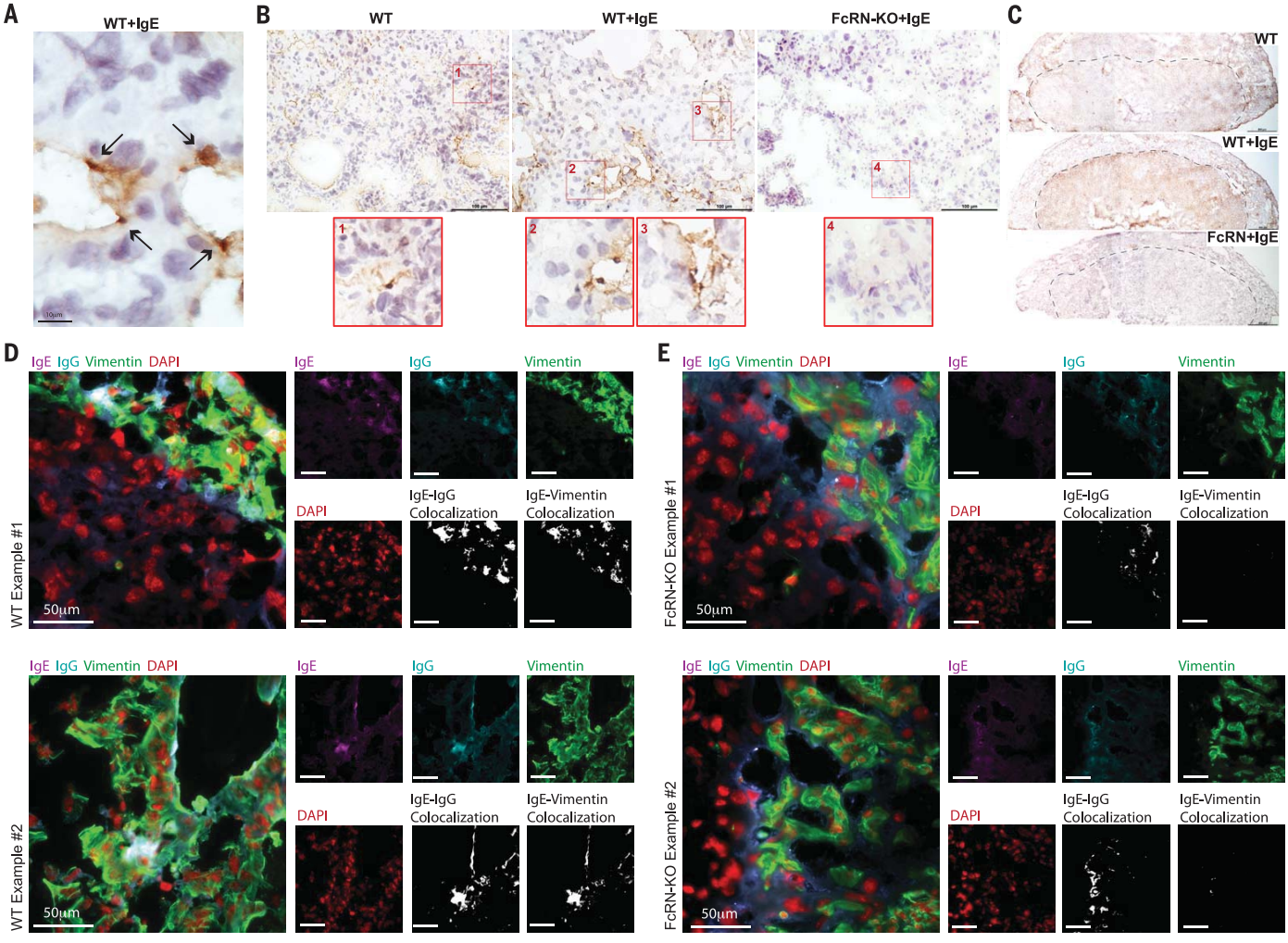

Fig. 5. IgE associates with IgG in fetal endothelial cells of the placenta. (**A**) High-magnification immunohistochemistry image showing IgE-stained endothelial cells in the placenta from E17.5 of mice that received exogenous IgE. The IgE staining was noted in endothelial cells lining the blood vessels (arrow). Scale bar, 10 μm. (**B**) IgE-bound endothelial cells were also observed in naïve (WT) mice, albeit in small numbers. IgE injection (WT+IgE) increased areas of IgE-stained endothelial cells, which was not observed in FcRN-KO mice (FcRNKO+IgE). Scale bar, 100 μm. The red boxed areas are shown at higher resolution below. (**C**) Stitched images depicting IgE staining in entire placentas from WT naïve, WT+IgE, and FcRN-KO+IgE mothers. A dashed line demarcates maternal decidua (above) from the fetal labyrinth (below). IgE staining was largely observed in the fetal labyrinth, which is densely packed with fetal blood vessels. IgE staining in the labyrinth substantially increased when IgE was injected into mothers. IgE staining was not observed in FcRN-KO mice. Scale bar, 500 μm. For (A) to (C), immunohistochemistry was performed using anti-IgE antibody, and dark brown color shows positive signal for IgE staining. Sections were counterstained with hematoxylin to discern the tissue architecture, and the nuclei appear blue. (**D** and **E**) Multicolor immunofluorescent images showing staining of IgE (magenta), IgG (cyan), fetal endothelial vessels (green), and nucleus (red) in the placenta. (D) In WT placenta, colocalization of IgE with IgG (IgE-IgG complexes) and IgE with fetal vessels (uptake of IgE-IgG complexes by fetal endothelial cells) was noted. Scale bar, 50 μm. Images are representative of $n = 3$ animals. (E) Although IgE-IgG complexes were formed in FcRN-KO mice, no colocalization of IgE with fetal vessels was observed. Two representative images from each group are presented as examples 1 and 2. Scale bar, 50 μm. Images are representative of $n = 2$ animals. The data indicate that IgE binding to fetal endothelial cells is dependent on FcRN.

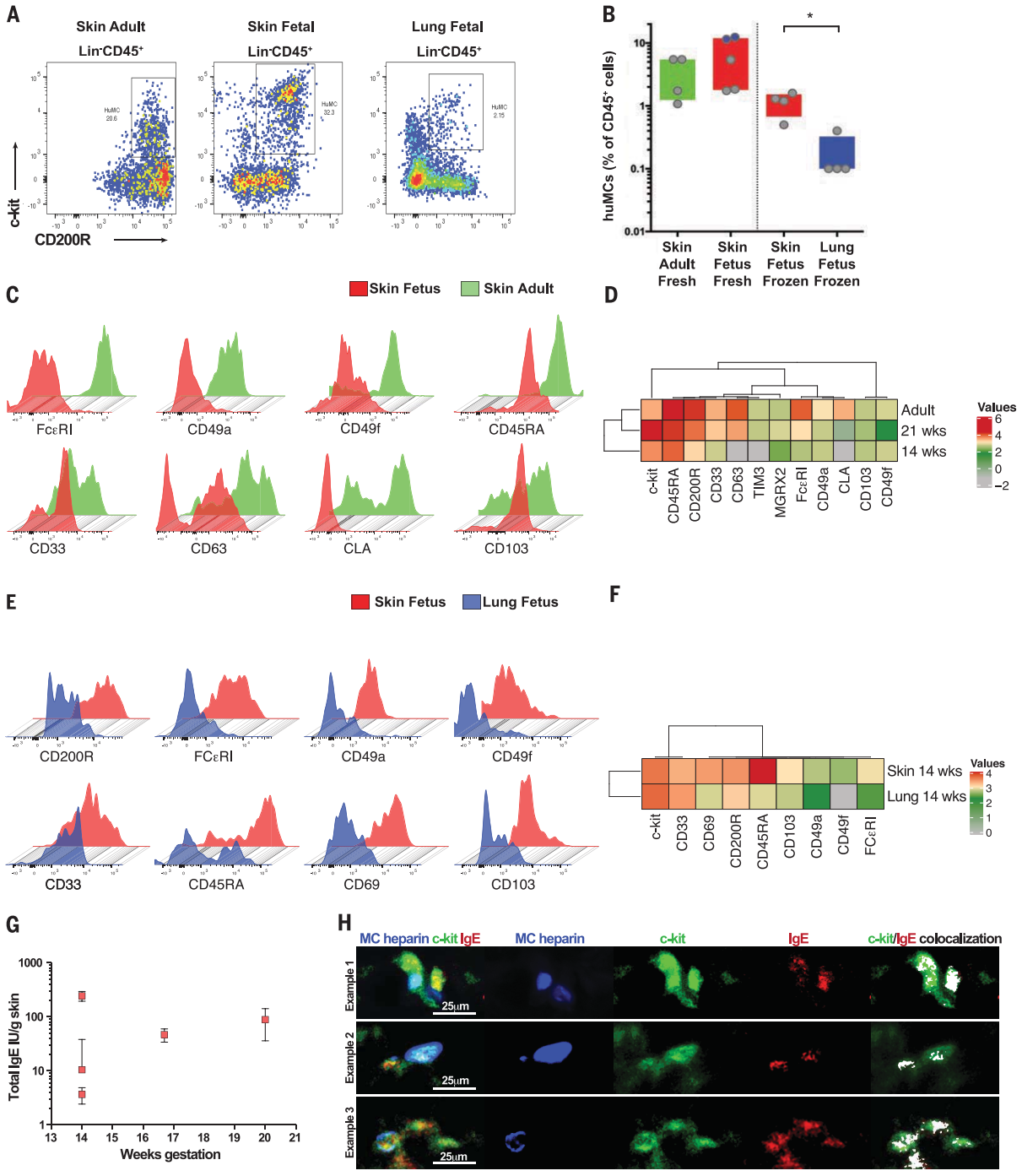

Fig. 6. Human fetal MCs mature in utero, where they also bind IgE. (**A**) Flow cytometry plots depicting the identification of huMCs in adult and human fetal tissues as c-kit$^+$CD200R$^+$ from cells gated on CD45$^+$Lin$^-$ (CD123$^-$CD14$^-$HLA-DR$^-$CD56$^-$CD34$^-$CD127$^-$, as shown in fig. S9, A and B) for skin and lung tissues at 14 weeks of gestation. (**B**) Quantification of huMCs in adult skin and fetal skin and lungs as a percentage of CD45$^+$ cells. huMCs constituted a reduced percentage of CD45$^+$ cells in the lung compared with the skin. $p < 0.05$, determined by Student's unpaired t test. Data points indicate individual donor samples. (**C**) Flow cytometry histograms of expression of various surface markers on huMCs (CD45$^+$CD123$^-$CD14$^-$HLA-DR$^-$CD56$^-$CD34$^-$CD127$^-$c-kit$^+$CD200R$^+$ cells, as defined in fig. S9A). Control gray histograms for comparison of expression levels are adult skin T cells. (**D**) Heatmap of the relative expression of various markers on fetal skin huMCs compared with adult skin huMCs by multicolor flow cytometry. Heatmap presentations in the form of flow cytometry plots are provided in fig. S9B. For (A) and (B), $n = 3$ for 14 weeks of gestation, $n = 2$ for 21 weeks of gestation, and $n = 4$ for adult samples. (**E**) Flow cytometry comparison of the relative expression of various markers of fetal huMCs and lung huMCs at 14 weeks of gestation. (**F**) Heatmap of the relative expression of various markers on fetal skin huMCs compared with paired lung huMCs from the same donors ($n = 4$ for 13 to 15 weeks of gestation) by multicolor flow cytometry, both defined as in fig. S9, A and C. (**G**) Quantification of human IgE in fetal skin. Graph depicts the concentrations in samples from five individual fetuses, with the error bars representing the SEM of technical replicates for each sample. (**H**) Immunofluorescence staining of fetal human skin showing colocalization between MC and IgE (in white), detected by overlapping signals for heparin (blue) and c-kit (green) with IgE (red). Rows are replicates showing representative MCs. Scale bar, 25 μm. An experimental repeat of this panel using an alternate antibody against human IgE is provided in fig. S10.

showed that IgE was detectable in the placenta, associated with cells having endothelial cell morphology (Fig. 5A), and the staining was brighter after maternal IgE injection (Fig. 5, B and C). By contrast, FcRN-KO mice lacked staining for IgE in the placenta (Fig. 5, B and C). We confirmed the lack of IgE association with fetal endothelial cells by confocal microscopy. IgE was detected to be colocalized with IgG within vimentin-positive fetal endothelial cells in WT mice (Fig. 5D). However, in FcRN-KO mice (Fig. 5E), IgG and IgE appeared colocalized but neither showed colocalization with the fetal endothelial cells, further supporting the FcRN-dependent mechanism of IgE transfer by vimentin-expressing placental endothelial cells.

Human fetal MCs are phenotypically mature and IgE bound

We next investigated whether fetal human MCs (huMCs) are phenotypically mature and if, similar to fetal murine MCs, they are associated with maternal IgE. To characterize the phenotype of huMCs from the early second trimester of pregnancy (14 weeks) compared with adult skin huMCs, we used a comprehensive multicolor flow cytometry panel. Skin and lung huMCs were identified in concatenated samples for each time point ($n = 3$ for 14 weeks and $n = 4$ for adult samples) by gating on lineage-negative hematopoietic cells that were positive for the MC marker c-kit, and stem cells were excluded by selecting cells positive for the myeloid lineage marker CD200R ($CD45^+CD123^-CD14^-HLA\text{-}DR^-CD56^-CD34^-CD127^-c\text{-}kit^+CD200R^+$; Fig. 6A and fig. S9, A and B). The percentage of huMCs in adult and fetal skin were comparable, whereas the fetal lung had a lower percentage of huMCs than paired fetal skin from the same donors (Fig. 6B), similar to our murine results. Fetal skin samples showed heterogeneous expression of markers related to huMC functionality, such as FcεRI and CD63, but generally expressed lower levels than adult skin huMCs (Fig. 6C). Other markers were decreased in expression in fetal samples, such as cutaneous lymphocyte associated antigen (CLA) (Fig. 6C), whereas the levels of c-kit were higher in fetal compared with adult huMCs (Fig. 6A). We also used a staining panel designed to characterize the expression of a broad array of markers associated with MCs or tissue residency, including integrin and adhesion molecules. This revealed that MC maturation was also characterized by increasing expression of CD200R, CD45RA, CD33, MGRX2, and Tim-3 (T-cell immunoglobulin and mucin-domain containing-3), as well as integrin family molecules such as CD49a and CD49f (Fig. 6C and fig. S9C). Gradual increases in markers such as FcεRI, CLA, CD63, CD200R, and others from weeks 14 to 21 ($n = 2$) of pregnancy to adult huMCs suggests maturation of huMCs in the skin throughout gestation (Fig. 6D). We also analyzed paired fetal skin and lung tissues from the same donors ($n = 4$) and found that MCs had a similar phenotype in terms of expression of cellular markers (Fig. 6, E and F), although skin MCs had higher expression levels of certain markers associated with maturation such as FcεRI and CD200R in the paired ~14-week samples (Fig. 6, E and F). Together, these results emphasize fetal MC heterogeneity and indicate that by the second trimester, there is a subset of MCs present that is phenotypically mature.

We next sought to confirm whether the other component required for allergic sensitization, IgE, is detectable in human fetal skin and bound to MCs. Quantification of IgE in human fetal skin showed that it was detectable in all samples obtained from various gestational time points (Fig. 6G). Human fetal skin was shown by confocal microscopy to contain both immature and granulated MCs (Fig. 6H). Multiple staining methods showed that IgE colocalized with c-kit staining, supporting that IgE in human fetal skin is MC bound (Fig. 6H and fig. S10). These data indicate that human fetal MCs can be sensitized with IgE in utero.

Concluding remarks

Our results demonstrate that maternal allergy predisposes progeny for allergen-specific disease upon the first antigen exposure postpartum. In humans, allergies frequently start during very early life (*15*, *40*), and allergic symptoms can also apparently develop upon the very first exposure to a triggering antigen (*29*). Maternal but not paternal IgE levels are predictive of infant atopic status (*41*, *42*). Furthermore, the sensitization profile of IgE in maternal blood highly correlates with that of fetal blood (*43*, *44*), as does the ratio of allergen-specific and total IgE in the maternal blood and cord blood (*45*). These studies suggested that neonates can be exposed to factors predisposing for allergic disease even before birth and are consistent with the mechanistic role that we have defined here for maternal IgE in mediating fetal allergic responses in experimental murine models. We also observed that MCs in human fetal skin and lungs are phenotypically mature, and in the skin they appear to be bound to IgE, suggesting that similar allergic responses may occur in humans postpartum.

Increased allergic responses that were allergen nonspecific have been observed in the progeny of atopic mice and were thought to be related to active maternal Th2 inflammation during gestation (*46*, *47*). However, those studies involved acute allergic sensitization or inflammation in the mother during pregnancy and a period of offspring sensitization to the experimental allergen after birth, which our results show may not be necessary for postnatal allergy. Thus, our study adds to a growing literature revealing developmental origins of health and disease (*48*), where prenatal exposure to maternal allergen-specific antibodies can influence subsequent health and, potentially, long-term disease. Indeed, our active sensitization model indicates that allergic responses induced weeks before pregnancy in mothers can mediate antigen-specific and allergic inflammation in the skin and lungs of the progeny even several weeks after birth. Although these responses may be important during the early weeks of life, we noted that the maternally derived allergic responses waned over time and were lost by 6 weeks after birth in the airway challenge model. We also observed a dose dependency on the concentrations of IgE. Subsequent studies will be needed to determine whether this decay in maternally derived allergic disease is due to the half-life of IgE or to the turnover or reduced presence of fetal MCs or other factors, and if fetal exposure to allergen can prolong the maternal influence on allergic responses.

Until recently, the source of fetal IgE was unclear, because it was thought that FcRN mediated only IgG transfer from mother to fetus. A recent study examining IgG abundance in human fetuses showed that antibody transfer occurs earlier than previously thought (*49*), and in mice this FcRN-dependent transcytosis begins shortly after placentation starts (*50*). Our results support in vitro demonstrations that there is an FcRN-dependent mechanism for maternal IgE transcytosis (*37*), because colocalization of IgE with fetal endothelial cells and the effects of active maternal sensitization were both lost in mice lacking FcRN. It has also been shown that the binding of monomeric IgE to FcεRI on MCs can modify many aspects of the MC state, including expansion, survival, migration, and activation (*2*, *51*–*53*). Consistent with this, we observed here that fetal MC maturation is induced by exogenous IgE. Atopic individuals frequently have high circulating levels of total IgE, which are correlated with the severity of allergic disease (*54*–*57*). Because we observed that passive sensitization of pregnant mice with IgE induced MC maturation, this suggests that fetal MC maturation in humans may be heterogeneous and influenced by the varied levels of maternal IgE available to the fetus. Our assessments of fetal huMCs supported that IgE was bound to them, but further studies are needed to assess the correlations between maternal IgE responses and fetal MC phenotypes. In adult humans, allergic disease and positive skin test reactions are correlated with serum IgE levels (*58*), and we also observed correlations between the amounts of IgE bound to fetal skin MCs and the concentrations injected into the dams in the mouse model.

The ratio of IgG to IgE may play a role in whether maternal antibodies are able to sensitize

offspring, because it has been shown in animal models that high levels of maternal IgG can reduce sensitization of offspring to experimental antigens (*59*). In our model, injection of the same concentration of IgG that induced IgE-mediated allergy did not result in detectable allergic responses. Although this does not exclude the potential of maternal IgG to participate in allergic responses in progeny, it suggests that those responses are less likely. This is consistent with the fact that 1000-fold higher concentrations of IgG compared with IgE are needed to induce MC activation (*60*). Although IgG-antigen complexes are able to induce MC degranulation (*61*, *62*), IgG sensitization of MCs in the absence of antigen is also less likely to occur because the affinity of IgG for activating receptors on MCs is greatly increased in the form of immune complexes (*60*). Our results using the anti-IgE monoclonal antibody, which abrogated fetal allergic responses when injected into pregnant dams, further support the specific role of IgE in mediating maternally derived allergic responses. In addition, differing levels of IgE were detected in the human fetal skin samples analyzed here. Further studies are needed to determine whether these levels have any correlation with the mother's allergic status and if antibodies in maternal breast milk, which contains multiple subclasses of antibodies including IgE (*63*, *64*), could also contribute to or modulate allergic sensitization postpartum.

Although MCs have been best described for their contributions to harmful allergic responses, they also contribute to protective immunity against multiple classes of pathogens. Conceivably, as in adults, IgE-mediated activation of fetal MCs could be protective in the context of postpartum exposure to certain pathogens, toxins, and venoms to which mothers have been exposed and against which they have subsequently mounted a protective response. Therefore, transfer of maternal IgE to the fetus may confer transient but potent immunity to various pathogens encountered during the mother's lifetime, mediating crucial protective functions in early life, aside from their implications in harmful allergic responses as shown here. However, it also remains to be understood whether maternal IgE could play a role in sensitizing progeny for intrinsic IgE production, which might either have protective functions in some circumstances of pathogen exposure or, alternatively, exacerbate allergies later in life. Our broadened understanding that fetal MCs are mature and capable of mediating IgE-dependent responses has implications for understanding both fetal health and long-term postnatal immune homeostasis.

REFERENCES AND NOTES

1. S. N. Abraham, A. L. St. John, *Nat. Rev. Immunol.* **10**, 440–452 (2010).
2. S. J. Galli, M. Tsai, *Nat. Med.* **18**, 693–704 (2012).
3. A. L. St. John, S. N. Abraham, *J. Immunol.* **190**, 4458–4463 (2013).
4. M. Enoksson *et al*., *J. Immunol.* **186**, 2523–2528 (2011).
5. S. Wernersson, G. Pejler, *Nat. Rev. Immunol.* **14**, 478–494 (2014).
6. J. A. Boyce, *Immunol. Rev.* **217**, 168–185 (2007).
7. S. J. Galli, S. Nakae, M. Tsai, *Nat. Immunol.* **6**, 135–142 (2005).
8. C. Taube *et al*., *J. Immunol.* **172**, 6398–6406 (2004).
9. E. B. Brandt *et al*., *J. Clin. Invest.* **112**, 1666–1677 (2003).
10. S. C. Beck *et al*., *Front. Immunol.* **10**, 494 (2019).
11. T. Zhang, D. F. Finn, J. W. Barlow, J. J. Walsh, *Eur. J. Pharmacol.* **778**, 158–168 (2016).
12. C. Lupinek *et al*., *Methods* **66**, 106–119 (2014).
13. S. L. Prescott, *Curr. Opin. Allergy Clin. Immunol.* **3**, 125–132 (2003).
14. H. Backman *et al*., *Clin. Exp. Allergy* **47**, 1426–1435 (2017).
15. M. I. Asher *et al*., *Lancet* **368**, 733–743 (2006).
16. M. Barner, M. Mohrs, F. Brombacher, M. Kopf, *Curr. Biol.* **8**, 669–672 (1998).
17. R. S. Geha, H. H. Jabara, S. R. Brodeur, *Nat. Rev. Immunol.* **3**, 721–732 (2003).
18. A. L. St John, W. X. G. Ang, A. P. S. Rathore, S. N. Abraham, *J. Allergy Clin. Immunol.* **141**, 1936–1939.e2 (2018).
19. U. Baumann *et al*., *J. Immunol.* **167**, 1022–1027 (2001).
20. D. L. Sylvestre, J. V. Ravetch, *Immunity* **5**, 387–390 (1996).
21. K. Tatemoto *et al*., *Biochem. Biophys. Res. Commun.* **349**, 1322–1328 (2006).
22. R. Gentek *et al*., *Immunity* **48**, 1160–1171.e5 (2018).
23. F. Ginhoux *et al*., *Science* **330**, 841–845 (2010).
24. J. Liu *et al*., *Sci. Rep.* **5**, 17569 (2015).
25. K. M. Lenz *et al*., *J. Neurosci.* **38**, 8044–8059 (2018).
26. J. N. Lilla, Z. Werb, *Dev. Biol.* **337**, 124–133 (2010).
27. M. F. Gurish *et al*., *J. Exp. Med.* **194**, 1243–1252 (2001).
28. M. C. García-Ara, M. T. Boyano-Martínez, J. M. Díaz-Pena, M. F. Martín-Muñoz, M. Martín-Esteban, *Clin. Exp. Allergy* **34**, 866–870 (2004).
29. S. H. Sicherer *et al*., *J. Allergy Clin. Immunol.* **126**, 1191–1197 (2010).
30. A. J. Sybilski, A. Doboszynska, B. Samolinski, *Eur. J. Med. Res.* **14** (Suppl 4), 233–236 (2009).
31. A. Bahrainwala, S. Hassan, M. Long, J. Kaplan, *Ann. Allergy Asthma Immunol.* **95**, 480–483 (2005).
32. J. O. Lima *et al*., *J. Allergy Clin. Immunol.* **106**, 911–917 (2000).
33. P. W. Hellings *et al*., *Clin. Exp. Allergy* **31**, 782–790 (2001).
34. C. Jin *et al*., *J. Clin. Invest.* **121**, 941–955 (2011).
35. N. E. Simister, C. M. Story, H. L. Chen, J. S. Hunt, *Eur. J. Immunol.* **26**, 1527–1531 (1996).
36. F. Antohe, L. Rădulescu, A. Gafencu, V. Gheție, M. Simionescu, *Hum. Immunol.* **62**, 93–105 (2001).
37. A. Bundhoo *et al*., *Clin. Exp. Allergy* **45**, 1085–1098 (2015).
38. W. Busse *et al*., *J. Allergy Clin. Immunol.* **108**, 184–190 (2001).
39. M. Haak-Frendscho, R. Saban, R. L. Shields, P. M. Jardieu, *Immunology* **94**, 115–121 (1998).
40. R. S. Gupta *et al*., *Pediatrics* **128**, e9–e17 (2011).
41. C. A. Liu *et al*., *J. Allergy Clin. Immunol.* **112**, 899–904 (2003).
42. M. De Amici *et al*., *Immunobiology* **222**, 450–453 (2017).
43. K. Bønnelykke, C. B. Pipper, H. Bisgaard, *J. Allergy Clin. Immunol.* **121**, 646–651 (2008).
44. E. Bertino *et al*., *Pediatr. Allergy Immunol.* **17**, 484–488 (2006).
45. K. Bønnelykke, C. B. Pipper, H. Bisgaard, *J. Allergy Clin. Immunol.* **126**, 657–663 (2010).
46. K. Hamada *et al*., *J. Immunol.* **170**, 1683–1689 (2003).
47. P. K. Richgels, A. Yamani, C. A. Chougnet, I. P. Lewkowich, *J. Allergy Clin. Immunol.* **140**, 1404–1415.e9 (2017).
48. M. Mandy, M. Nyirenda, *Int. Health* **10**, 66–70 (2018).
49. C. Pou *et al*., *Nat. Med.* **25**, 591–596 (2019).
50. A. P. S. Rathore, W. A. A. Saron, T. Lim, N. Jahan, A. L. St John, *Sci. Adv.* **5**, eaav3208 (2019).
51. C. B. Mathias *et al*., *J. Immunol.* **182**, 2416–2424 (2009).
52. K. Asai *et al*., *Immunity* **14**, 791–800 (2001).
53. J. Kalesnikoff *et al*., *Immunity* **14**, 801–811 (2001).
54. S. C. Park *et al*., *Int. J. Pediatr. Otorhinolaryngol.* **86**, 167–171 (2016).
55. Y. L. Tu *et al*., *PLOS ONE* **8**, e80996 (2013).
56. V. Kiiski, O. Karlsson, A. Remitz, S. Reitamo, *Acta Derm. Venereol.* **95**, 943–947 (2015).
57. T. Haselkorn *et al*., *Pediatr. Allergy Immunol.* **21**, 1157–1165 (2010).
58. L. R. Freidhoff, D. A. Meyers, D. G. Marsh, *J. Allergy Clin. Immunol.* **73**, 490–499 (1984).
59. A. Ohsaki *et al*., *J. Exp. Med.* **215**, 91–113 (2018).
60. F. Takizawa, M. Adamczewski, J. P. Kinet, *J. Exp. Med.* **176**, 469–475 (1992).
61. A. Oshiba *et al*., *J. Clin. Invest.* **97**, 1398–1408 (1996).
62. A. Syenina, C. J. Jagaraj, S. A. Aman, A. Sridharan, A. L. St John, *eLife* **4**, e05291 (2015).
63. X. Meng *et al*., *J. Crohns Colitis* **13**, 431–441 (2019).
64. K. Duchén, B. Björkstén, *Pediatr. Allergy Immunol.* **7**, 44–47 (1996).

ACKNOWLEDGMENTS

Funding: This work was supported by SIgN (A*STAR) core funding to F.G. and by Duke-NUS start-up funding and MOE2014-T2-2-123 to A.L.S. J.K.Y.C. and F.G. are supported by Singapore Ministry of Health's National Medical Research Council (NMRC) CIRG/1484/2018. J.K.Y.C. is supported by NMRC CSA (SI)/008/2016. **Author contributions:** R.M. and J.B. performed most experiments and analyzed the data, with additional experiments and data analysis contributed by A.P.S.R., H.K., B.M., W.A.A.S., Z.L., J.W.H., and A.L.S. R.M., J.B., A.L.S., and F.G. interpreted the data. J.B. and A.L.S. wrote the manuscript with additional contributions by R.M. and F.G. J.K.Y.C. provided the fetal tissues. A.L.S. and F.G. conceived, funded, and supervised the project. All authors reviewed the manuscript and contributed to discussions. **Competing interests:** The authors declare no competing interests. **Data and materials availability:** All data needed to evaluate the conclusions of this study are present in the main text and/or the supplementary materials.

SUPPLEMENTARY MATERIALS

science.sciencemag.org/content/370/6519/941/suppl/DC1
Materials and Methods
Figs. S1 to S10
Table S1
References (*65*–*67*)

View/request a protocol for this paper from *Bio-protocol*.

3 November 2019; resubmitted 25 July 2020
Accepted 20 October 2020
Published online 29 October 2020
10.1126/science.aba0864

CORONAVIRUS

Ultrapotent human antibodies protect against SARS-CoV-2 challenge via multiple mechanisms

M. Alejandra Tortorici[1,2]*, Martina Beltramello[3]*, Florian A. Lempp[4], Dora Pinto[3], Ha V. Dang[1], Laura E. Rosen[4], Matthew McCallum[1], John Bowen[1], Andrea Minola[3], Stefano Jaconi[3], Fabrizia Zatta[3], Anna De Marco[3], Barbara Guarino[3], Siro Bianchi[3], Elvin J. Lauron[4], Heather Tucker[4], Jiayi Zhou[4], Alessia Peter[3], Colin Havenar-Daughton[4], Jason A. Wojcechowskyj[4], James Brett Case[5], Rita E. Chen[5], Hannah Kaiser[4], Martin Montiel-Ruiz[4], Marcel Meury[4], Nadine Czudnochowski[4], Roberto Spreafico[4], Josh Dillen[4], Cindy Ng[4], Nicole Sprugasci[3], Katja Culap[3], Fabio Benigni[3], Rana Abdelnabi[6], Shi-Yan Caroline Foo[6], Michael A. Schmid[3], Elisabetta Cameroni[3], Agostino Riva[7], Arianna Gabrieli[7], Massimo Galli[7], Matteo S. Pizzuto[3], Johan Neyts[6], Michael S. Diamond[5], Herbert W. Virgin[4,8,9], Gyorgy Snell[4], Davide Corti[3], Katja Fink[3]†, David Veesler[1]†

Efficient therapeutic options are needed to control the spread of severe acute respiratory syndrome coronavirus 2 (SARS-CoV-2) that has caused more than 922,000 fatalities as of 13 September 2020. We report the isolation and characterization of two ultrapotent SARS-CoV-2 human neutralizing antibodies (S2E12 and S2M11) that protect hamsters against SARS-CoV-2 challenge. Cryo–electron microscopy structures show that S2E12 and S2M11 competitively block angiotensin-converting enzyme 2 (ACE2) attachment and that S2M11 also locks the spike in a closed conformation by recognition of a quaternary epitope spanning two adjacent receptor-binding domains. Antibody cocktails that include S2M11, S2E12, or the previously identified S309 antibody broadly neutralize a panel of circulating SARS-CoV-2 isolates and activate effector functions. Our results pave the way to implement antibody cocktails for prophylaxis or therapy, circumventing or limiting the emergence of viral escape mutants.

Severe acute respiratory syndrome coronavirus 2 (SARS-CoV-2) emerged at the end of 2019 and was sequenced by January 2020 (*1*, *2*). Although the reservoir host responsible for spillover into the human population remains uncertain, SARS-CoV-2 appears to have originated in bats from which closely related viruses and viral sequences have been identified (*1*, *3*). SARS-CoV-2 belongs to the sarbecovirus subgenus and is closely related to SARS-CoV, which was responsible for an epidemic in 2002–2003 that resulted in 8098 cases and 774 fatalities worldwide (*4*, *5*). The lack of preexisting immunity to SARS-CoV-2 due to its divergence from the four circulating endemic coronaviruses, and its high human-to-human transmissibility, have resulted in the ongoing coronavirus disease 2019 (COVID-19) pandemic, which has already caused more than 29 million infections and more than 922,000 fatalities as of mid-September 2020.

SARS-CoV-2 infection is initiated upon attachment of the viral transmembrane spike (S) glycoprotein via a receptor-binding motif (RBM) to angiotensin-converting enzyme 2 (ACE2), leading to membrane fusion and entry into host cells (*6*–*13*). As for all coronaviruses, SARS-CoV-2 S is the main target of neutralizing antibodies (Abs) and a focus of vaccine design and therapeutic targeting efforts (*14*). Although vaccine development programs are fast-tracked (*15*–*20*), large-scale manufacturing and administration to a large enough population for achieving community protection will likely take many months. Prophylactic and/or therapeutic antiviral drugs could address the gap before safe and efficient vaccines become widely available and will continue to have utility in unvaccinated individuals or those who respond poorly to vaccination.

We recently described a monoclonal Ab (mAb), isolated from the memory B cells of a SARS survivor obtained 10 years after recovery, that neutralizes SARS-CoV-2 and SARS-CoV through recognition of the S receptor–binding domain (RBD) but without blocking ACE2 attachment (*21*). An optimized version of this mAb (named S309) is currently under evaluation in phase 2/3 clinical trials. The isolation of many other RBD-targeted neutralizing Abs from COVID-19 convalescent patients (*22*–*28*) and the demonstration that they provide in vivo protection against SARS-CoV-2 challenge in small animals and nonhuman primates (*25*, *29*–*31*) showed that the RBD is the major target of neutralizing Abs upon natural CoV infection. Clinical evaluation of therapeutic Abs directly interfering with ACE2 binding is ongoing (*30*–*34*). mAbs with exceptionally high neutralization potency, along with distinct and complementary mechanisms of action compared to existing mAbs, may enable the formulation of mAb cocktails with enhanced efficacy to control the spread of the virus and prevent resistance. Here, we assessed the possibility of combining two ultrapotent neutralizing Abs that we discovered, namely S2E12 and S2M11, which exploit different mechanisms of action.

Results

Isolation of ultrapotent SARS-CoV-2 neutralizing Abs

To identify highly potent mAbs elicited upon SARS-CoV-2 infection, we sorted memory B cells from two individuals recovering from severe COVID-19 disease, using biotinylated prefusion SARS-CoV-2 S ectodomain trimer as bait. Two mAbs, S2E12 and S2M11, stood out for their high neutralization activity against authentic SARS-CoV-2 virus and two different SARS-CoV-2 S pseudotyped viruses [using either murine leukemia virus (MLV) or vesicular stomatitis virus (VSV) backbones]. In an assay that measures inhibition of authentic SARS-CoV-2 entry (SARS-CoV-2-Nluc (*35*)), we determined half-maximal inhibitory concentrations (IC_{50}) of 3 to 6 ng/ml (20 to 40 pM) (Fig. 1, A and B). We determined IC_{50} values of 1.9 to 2.5 ng/ml for SARS-CoV-2 S-VSV (fig. S1A) and 10.3 to 30.4 ng/ml for SARS-CoV-2 S-MLV (fig. S1B). In an authentic SARS-CoV-2 focus reduction neutralization test that measures inhibition of virus entry and spread (*36*), the IC_{50} values were 1.2 to 6.6 ng/ml (fig. S1C). The exceptional potency of these mAbs was demonstrated further by the concentrations necessary to inhibit 90% of authentic SARS-CoV-2-Nluc viral entry (IC_{90}), which we determined as 26.4 ± 7.8 ng/ml and 12.7 ± 3.1 ng/ml for S2E12 and S2M11, respectively (Fig. 1, A and B). The higher neutralization potency of immunoglobulin G (IgG) compared to Fab observed for each mAb suggested that the distinct binding affinities and/or bivalent binding contribute to potency (Fig. 1, A and B). The S2E12 heavy chain uses VH1-58*01, D2-15*01, and JH3*02 genes, whereas S2M11 derives from VH1-2*02, D3-3*01, and JH4*02 genes. The heavy-chain variable gene nucleotide sequence germline identity is 96.53% for S2M11 and 97.6% for S2E12, showing a low level of somatic hypermutation for these two mAbs.

Both S2E12 and S2M11 bound to the SARS-CoV-2 RBD and prefusion-stabilized S ectodomain trimer (*6*) but not to the SARS-CoV RBD or S (*37*) by enzyme-linked immunosorbent

[1]Department of Biochemistry, University of Washington, Seattle, WA 98195, USA. [2]Institut Pasteur and CNRS UMR 3569, Unité de Virologie Structurale, Paris, France. [3]Humabs BioMed SA, a subsidiary of Vir Biotechnology, Bellinzona, Switzerland. [4]Vir Biotechnology, San Francisco, CA 94158, USA. [5]Departments of Medicine, Molecular Microbiology, Pathology and Immunology, Washington University School of Medicine, St. Louis, MO, USA. [6]Rega Institute for Medical Research, Laboratory of Virology and Chemotherapy, KU Leuven, Belgium. [7]III Division of Infectious Diseases, Luigi Sacco University Hospital, University of Milan, Italy. [8]Washington University School of Medicine, St. Louis, MO, USA. [9]UTSouthwestern Medical Center, Dallas, TX, USA.
*These authors contributed equally to this work.
†Corresponding author. Email: dveesler@uw.edu (D.V.); katja.fink@alumni.ethz.ch (K.F.)

assay (ELISA) (Fig. 1, C to F). Using surface plasmon resonance (SPR) and flow cytometry, we further observed that S2E12 and S2M11 compete for binding to the SARS-CoV-2 RBD or to SARS-CoV-2 S, presented either as a recombinantly expressed prefusion-stabilized S ectodomain trimer or as full-length S expressed at the surface of ExpiCHO cells (fig. S2, A and B). When added first, S2M11 competed in a concentration-dependent manner with the sarbecovirus-neutralizing S309 mAb for binding to SARS-CoV-2 S, whereas it could bind with minimal competition when added after S309 (fig. S2B). Whereas the S2E12 Fab (or IgG) bound to SARS-CoV-2 S and RBD similarly, the binding affinity of the S2M11 Fab (or IgG) for the S trimer was enhanced relative to that of the isolated SARS-CoV-2 RBD (Fig. 1G and fig. S2C). Specifically, S2M11 binding kinetics to SARS-CoV-2 S were biphasic, including a first phase with identical binding kinetics and affinity as measured for binding to the isolated RBD, and a second phase with a much slower off-rate and therefore higher affinity. We observed that binding of S2M11 Fab and IgG to S was increased at pH 5.4, a condition that favors the closed trimer conformation, compared to pH 7.4 (*38*) (Fig. 1G, fig. S2C, and table S1). Conversely, binding of the S2E12 Fab to S was diminished at pH 5.4 (and moderately reduced for S2E12 IgG), possibly due to the increased number of S trimers with closed RBDs (Fig. 1G; fig. S2, A and C; and table S1).

Collectively, these findings indicate that S2E12 and S2M11 target overlapping or partially overlapping SARS-CoV-2 RBD epitopes. The finding that S2M11 preferentially interacts with the S trimer relative to the RBD suggests that this mAb might bind to a quaternary epitope only displayed in the context of a native closed prefusion S. Finally, the enhanced binding of S2E12 to SARS-CoV-2 S in conditions favoring RBD opening (pH 7.4) indicates that this mAb might recognize a cryptic epitope not exposed in the closed S trimer.

S2E12 potently neutralizes SARS-CoV-2 by targeting the RBM

To understand the mechanism of S2E12-mediated potent neutralization of SARS-CoV-2, we characterized a complex between the SARS-CoV-2 S ectodomain trimer and the S2E12 Fab fragment using cryo–electron microscopy (cryo-EM). Three-dimensional (3D) classification of the data showed the presence of S trimers with one, two, or three Fabs bound to open RBDs for which we determined structures at 3.5, 3.3, and 3.3-Å resolution, respectively (Fig. 2, A and B; fig. S3, A to G; and table S2). We subsequently used local refinement to obtain a 3.7-Å map of the region corresponding to the S2E12 variable domains and RBD, which markedly improved local resolution due to conformational dynamics relative to the rest

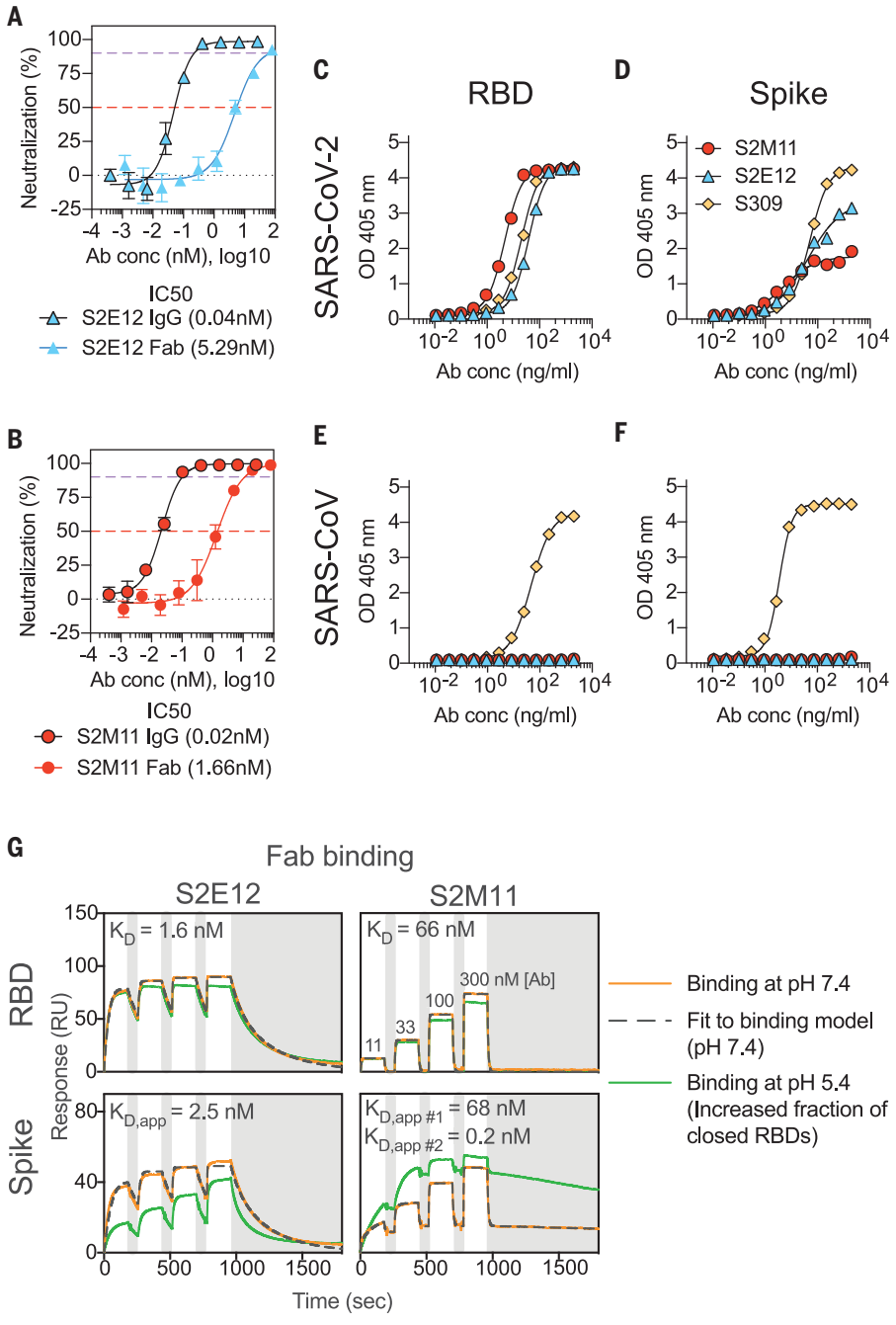

Fig. 1. S2E12 and S2M11 neutralize SARS-CoV-2 ultrapotently by targeting the RBD. (**A** and **B**) Neutralization of authentic SARS-CoV-2 (SARS-CoV-2-Nluc) by S2E12 (A) and S2M11 (B) IgG or Fab. Symbols are means ± SD of triplicates. Dashed lines indicate IC_{50} and IC_{90} values. Average IC_{50} values are indicated in parentheses below the graphs (determined from two independent experiments). (**C** to **F**) ELISA binding of S2M11 (red), S2E12 (blue), or S309 (yellow) mAbs to immobilized SARS-CoV-2 RBD (C), SARS-CoV-2 S (D), SARS-CoV RBD (E), or SARS-CoV S (F). Symbols show means of duplicates. (**G**) SPR analysis of S2E12 and S2M11 Fab binding to the SARS-CoV-2 RBD or S ectodomain trimer. Experiments were carried out at pH 7.4 (orange) and pH 5.4 (green) and were repeated twice with similar results (one experiment is shown). The apparent equilibrium dissociation constants ($K_{D,\ app}$) at pH 7.4 are indicated. White and gray stripes indicate association and dissociation phases, respectively. S2M11 binding to S was fit to two parallel kinetic phases and the resulting $K_{D,\ app\ \#1}$ and $K_{D,\ app\ \#2}$ were interpreted as apparent affinities for open RBDs (tertiary epitope) and closed RBDs (quaternary epitope), respectively. This is supported by the similar binding kinetics and affinity of the faster off-rate phase ($K_{D,\ app\ \#1}$) with that observed for S2M11 binding to the isolated RBD (compare with table S1 for full fit results). Ab conc, mAb concentration.

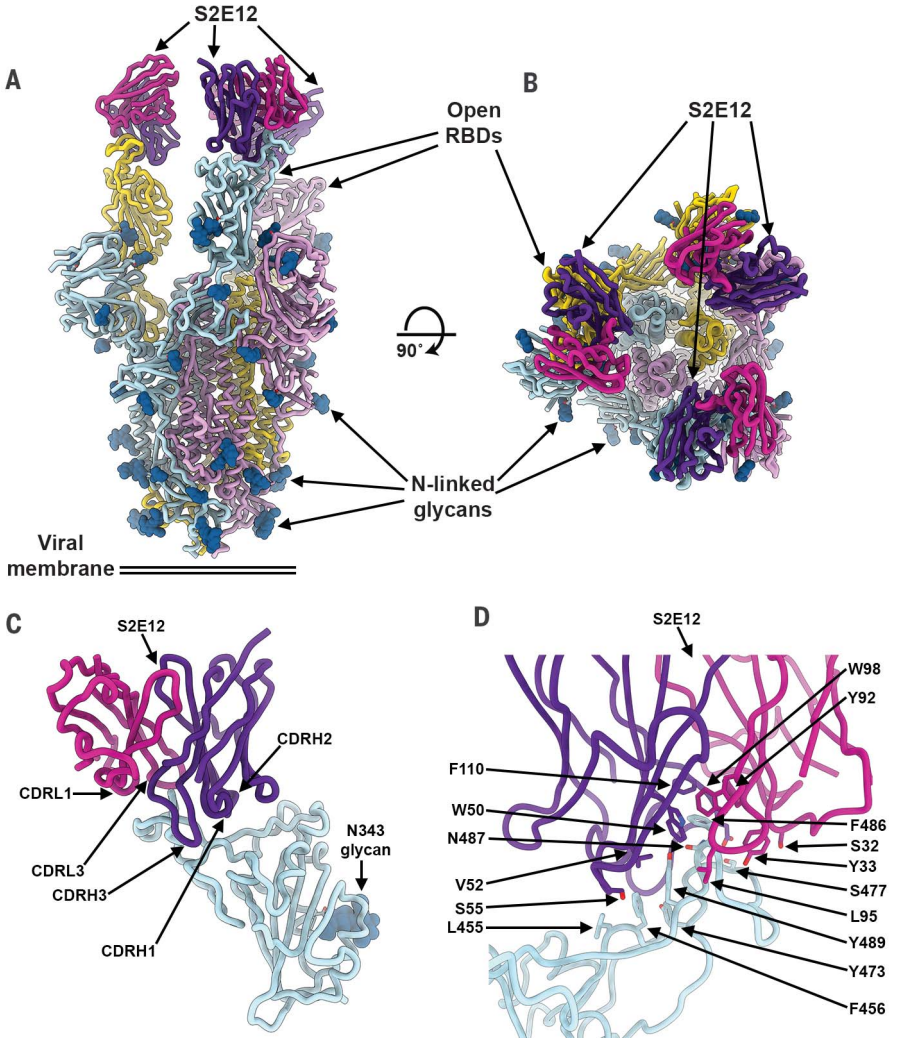

Fig. 2. The S2E12 neutralizing mAb recognizes the SARS-CoV-2 RBM. (**A** and **B**) Cryo-EM structure of the prefusion SARS-CoV-2 S ectodomain trimer with three S2E12 Fab fragments bound to three open RBDs viewed along two orthogonal orientations. (**C**) The S2E12 concave paratope recognizes the convex RBM tip. (**D**) Close-up view showing selected interactions formed between S2E12 and the SARS-CoV-2 RBD. In (A) to (D), each SARS-CoV-2 S protomer is colored distinctly (cyan, pink, and gold), whereas the S2E12 light- and heavy-chain variable domains are colored magenta and purple, respectively. N-linked glycans are rendered as blue spheres in (A) to (C). Abbreviations for the amino acid residues are as follows: E, Glu; F, Phe; I, Ile; L, Leu; N, Asn; Q, Gln; S, Ser; T, Thr; V, Val; W, Trp; and Y, Tyr.

of the S trimer, and used it along with a 1.4-Å crystal structure of the S2E12 Fab to build a model (fig. S3, D to G, and tables S2 and S3).

S2E12 recognizes an RBD epitope overlapping with the RBM (i.e., ACE2 receptor-binding site) that is partially buried at the interface between protomers in the closed S trimer (Fig. 2, A to D, and fig. S4, A and B). As a result, S2E12 can only interact with open RBDs, as is the case for ACE2 as well as for several previously described neutralizing mAbs, including S2H14 (*22*, *25*, *28*). The concave S2E12 paratope recognizes the convex RBM tip through electrostatic and van der Waals interactions (Fig. 2, C and D). Specifically, S2E12 utilizes the heavy-chain complementary-determining regions (CDRs) 1 to 3 and the light-chain CDR1 and CDR3, respectively, accounting for two-thirds and one-third of the paratope buried surface area, to recognize residues 455 to 458 and 473 to 493 of the SARS-CoV-2 RBD (Fig. 2, C and D). Nearly all the S2E12 contacts with the RBD are mediated by germline-encoded residues with only one out of five heavy-chain (G109) and one out of four light-chain (G94) mutated residues contributing to the paratope. The structural data explain that S2E12 binds efficiently to both the RBD and the prefusion S trimer (Fig. 1G) and efficiently neutralizes SARS-CoV-2 (Fig. 1, A and B, and fig. S1, A and C): (i) S2E12 recognizes a tertiary 3D epitope, i.e., an epitope that is fully contained within one S protomer; (ii) ~50% of S trimers naturally harbor one open RBD at the viral surface or in recombinantly expressed S ectodomain trimers as observed by cryo–electron tomography and single-particle cryo-EM, respectively (*6*, *39*); and (iii) S2E12 binding shifts the RBD conformational equilibrium toward open S trimers, as previously described for RBM-targeted mAbs (*22*, *28*, *37*).

S2M11 locks the SARS-CoV-2 S trimer in the closed state through binding to a quaternary epitope

We carried out cryo-EM analysis of S2M11 in complex with SARS-CoV-2 S to elucidate the molecular basis of its preferential recognition of the S trimer compared to the RBD and its mechanism of neutralization. Three-dimensional classification of the cryo-EM data revealed the exclusive presence of S trimers adopting a closed conformation, which allowed us to determine a 2.6-Å structure of SARS-CoV-2 S bound to three S2M11 Fab fragments (Fig. 3, A and B; fig. S5, A to F; and table S2). S2M11 recognizes a quaternary epitope through electrostatic interactions and shape complementarity, comprising distinct regions of two neighboring RBDs within an S trimer (Fig. 3, C and D). Specifically, S2M11 CDRH1, CDRH2, and the heavy-chain framework region 3 (FR3) are docked into the RBM crevice (burying a surface of ~400 Å^2), whereas CDRH3 spans the interface between the RBM and helices 339 to 343 and 367 to 374, as well as residue 436 of an adjacent RBD belonging to the neighboring protomer (i.e., burying a total surface of ~500 Å^2) (Fig. 3, C and F). Although most interactions are mediated by the S2M11 heavy chain, CDRL2 interacts with residues 440 to 441 and CDRL1 forms key contacts with the glycan at position N343, which is rotated ~45° compared to the orientation that it adopts in the S309-bound S structure (*21*), both sets of interactions occurring with the neighboring RBD (quaternary epitope) (Fig. 3, C and F, and fig. S5G). Three out of eight S2M11 heavy-chain residues that are mutated relative to contribute to epitope recognition (Ile^{54}, Thr^{77}, and Phe^{102}), whereas none of the two light-chain mutated residues participate in RBD binding.

The observation that all particle images correspond to closed S trimers when bound to S2M11 contrasts with our previous finding of ~50%/50% of trimers closed or with one RBD open in the absence of bound mAb (*6*) or in complex with S309 (*21*) or S2H13 (*28*), which do not select for any specific RBD conformation. On the basis of these data, we conclude that S2M11 stabilizes the closed conformation of the S trimer by interacting with a composite epitope including two neighboring RBDs (from two distinct protomers) that are close to each

other in the closed state but spread apart upon RBD opening (*6*) (fig. S4, C and D). These results also explain the enhanced S2M11 binding affinity for S compared to the RBD (Fig. 1G), as only the S trimer enables binding to the quaternary epitope, which buries a ~60% greater paratope surface area compared to binding to the isolated RBD (Fig. 3, A to F). We therefore interpret the biphasic binding as S2M11 interacting with a tertiary epitope present in open RBDs (fast off-rate), based on the identical kinetics and affinity measured relative to those of the isolated RBD, and S2M11 recognizing its full quaternary epitope (slow off-rate).

S2M11 and S2E12 inhibit SARS-CoV-2 attachment to ACE2 and trigger Fc-mediated effector functions

The structural data indicate that both S2E12 and S2M11 would compete with ACE2 attachment to the RBD, as they recognize epitopes overlapping with the RBM (Fig. 4, A and B). Moreover, S2M11-induced stabilization of SARS-CoV-2 S in the closed conformational state yields S trimers with masked RBMs that are incompetent for receptor engagement, as previously shown for an engineered S construct covalently stabilized in the closed state (*40*). Hence, both S2E12 and S2M11 blocked binding of SARS-CoV-2 S or RBD to immobilized human recombinant ACE2 measured by biolayer interferometry (Fig. 4, C and D). Additionally, both S2E12 and S2M11 inhibited binding of ACE2 to SARS-CoV-2 S expressed at the surface of Chinese hamster ovary (CHO) cells (Fig. 4E), validating this mechanism of neutralization using full-length native S trimers. The comparable efficiency of S2E12 and S2M11 in blocking S attachment to ACE2 correlates with their similar neutralization potencies.

To further investigate the mechanism of SARS-CoV-2 inhibition by S2E12 and S2M11, we performed a cell-cell fusion assay using VeroE6 cells (which endogenously express ACE2 at their surface) transiently transfected with full-length wild-type SARS-CoV-2 S. Although S2E12 and S2M11 bind and stabilize different conformations of the S protein, both mAbs efficiently blocked syncytia formation (Fig. 4F), which results from S-mediated membrane fusion. The absence of syncytia formation likely is explained by S2E12- or S2M11-mediated disruption of ACE2 binding along with S2M11-induced inhibition of membrane fusion through conformational trapping of SARS-CoV-2 S in the closed state.

Ab-dependent cell cytotoxicity (ADCC) mediated by natural killer cells or Ab-dependent cell phagocytosis (ADCP) mediated by macrophages or monocytes are Fc-mediated effector functions that can contribute to protection by facilitating virus clearance and by supporting immune responses in vivo, independently of direct neutralization (*41*). As a prerequisite for

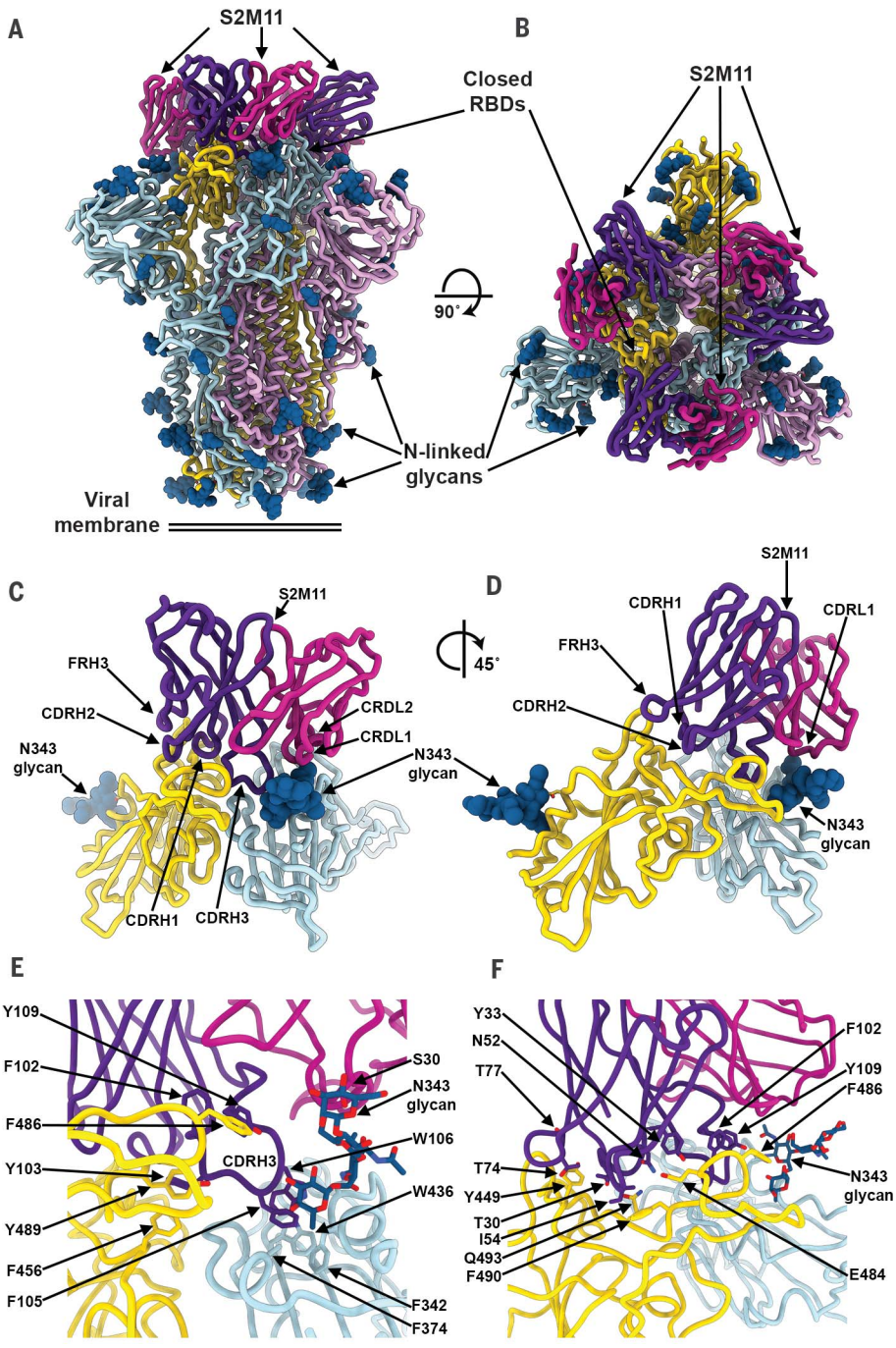

Fig. 3. The S2M11 neutralizing mAb recognizes a quaternary epitope spanning two RBDs and stabilizes S in the closed state. (**A** and **B**) Cryo-EM structure of the prefusion SARS-CoV-2 S ectodomain trimer bound to three S2M11 Fab fragments viewed along two orthogonal orientations. (**C** and **D**) The S2M11 binding pose, which involves a quaternary epitope spanning two neighboring RBDs. (**E** and **F**) Close-up views showing selected interactions formed between S2M11 and the SARS-CoV-2 RBDs. In (A) to (F), each SARS-CoV-2 S protomer is colored distinctly (cyan, pink, and gold), whereas the S2M11 light- and heavy-chain variable domains are colored magenta and purple, respectively. N-linked glycans are rendered as blue spheres in (A) to (D) and as sticks in (E) and (F). FR, framework.

ADCC to occur, we first demonstrated that infected cells express SARS-CoV-2 S on their surface (fig. S6, A and B). Then, to evaluate the ability of S2M11 and S2E12 to leverage ADCC and ADCP, we tested if these mAbs (IgG1 backbone) could induce FcγRIIa and FcγRIIIa-mediated signaling using a luciferase reporter assay. S2M11 promoted efficient, dose-dependent FcγRIIIa-mediated (but not FcγRIIa-mediated) signaling, in particular for the high-affinity

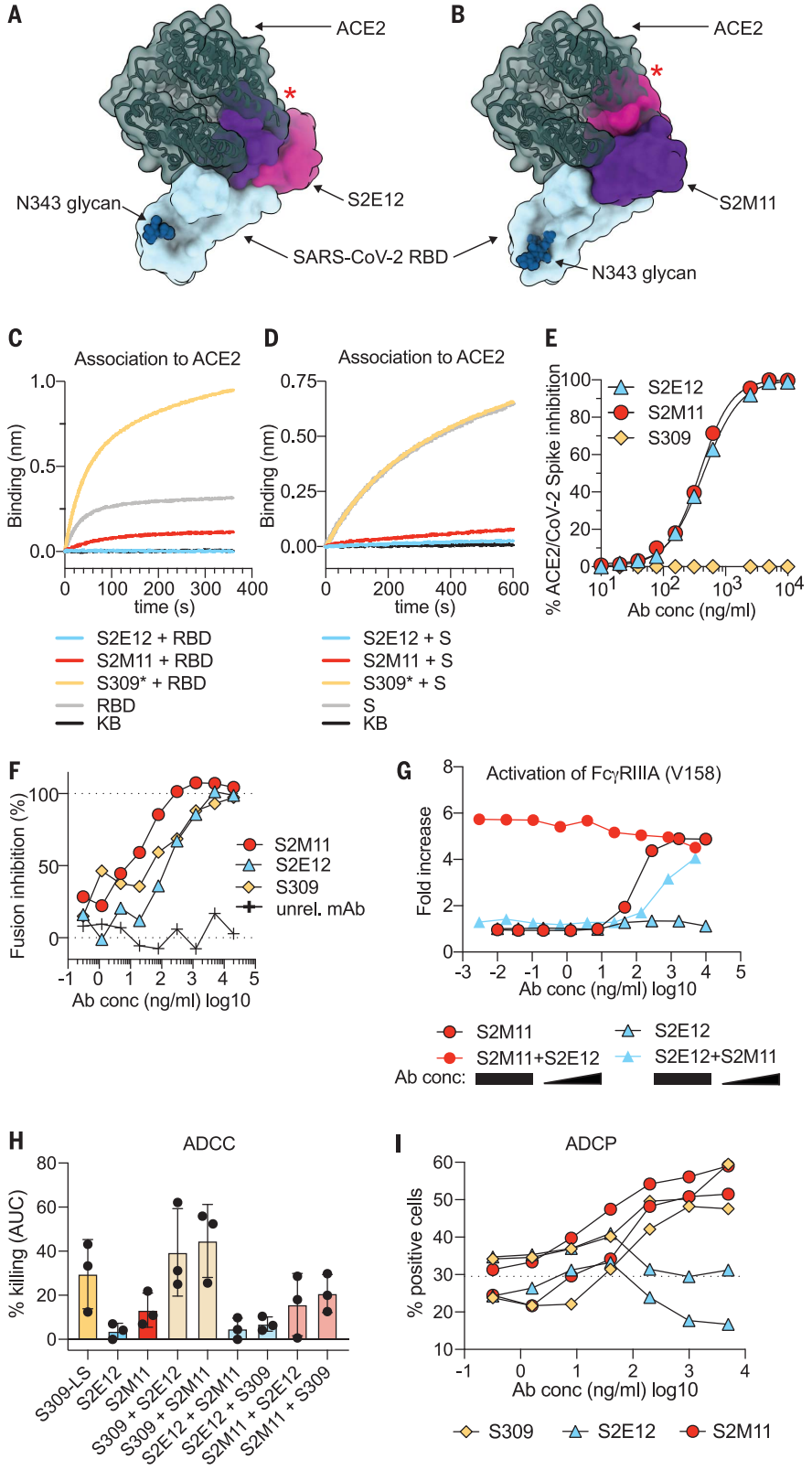

Fig. 4. S2E12 and S2M11 prevent SARS-CoV-2 S attachment to ACE2 and inhibit membrane fusion, and S2M11 triggers effector functions. (**A**) S2E12 (magenta/purple) and ACE2 (dark green) bind overlapping binding sites on the SARS-CoV-2 RBD (blue). (**B**) S2M11 (magenta/purple) and ACE2 (dark green) bind overlapping binding sites on the SARS-CoV-2 RBD (blue). The red stars indicate steric clashes. (**C** and **D**) Binding of the SARS-CoV-2 RBD (C) or S ectodomain trimer (D) alone (gray) or precomplexed with the S2M11 (red), S2E12 (blue), or S309* (yellow) mAbs to the ACE2 ectodomain immobilized at the surface of biosensors analyzed by biolayer interferometry. S309* is an optimized version of the parent S309 mAb (*21*). KB, kinetic buffer (negative control). (**E**) Binding of varying concentrations of S2E12 (blue), S2M11 (red), or S309 (yellow) mAbs to full-length S expressed at the surface of CHO cells in the presence of the ACE2 ectodomain (20 μg/ml) analyzed by flow cytometry (one measurement per condition). (**F**) Cell-cell fusion inhibition assay with Vero E6 cells transfected with SARS-CoV-2 S and incubated with varying concentrations of S2E12 (blue), S2M11 (red), S309 (yellow), or a control mAb. The values are normalized to the percentage of fusion without mAb and to the percentage of fusion of non-transfected cells. (**G**) FcγRIIIa (high-affinity variant V158) signaling induced by individual mAbs or mAb cocktails. For mAb cocktails, the concentration of the constant mAb was 5 μg/ml. The concentration of the diluted mAb is indicated on the *x* axis. (**H**) ADCC using primary NK cells as effectors and SARS-CoV-2 S-expressing CHO cells as targets. The magnitude of NK cell–mediated killing is expressed as the area under the curve (AUC) for each mAb used at concentrations ranging between 0.1 ng/ml and 20 μg/ml. For mAb cocktails, the mAb listed first was kept constant at 5 μg/ml. Each symbol represents one donor; data are combined from two individual experiments. See fig. S6E for curves from a representative donor. (**I**) ADCP using peripheral blood mononuclear cells (PBMCs) as a source of phagocytic cells (monocytes) and PKH67–fluorescently labeled S-expressing CHO cells as target cells. The *y* axis indicates percentage of monocytes double-positive for anti-CD14 (monocyte) marker and PKH67. The dashed line indicates the signal detected in the presence of target and effector cells but without mAb (baseline). Each line indicates the data for one PBMC donor. Symbols are means of duplicates. Data are from one experiment. Ab conc, mAb concentration.

(V158) variant of the Fc receptor, to levels comparable to that of the cross-reactive mAb S309 (Fig. 4G and fig. S6, C and D) (*21*). By contrast, S2E12 triggered FcγRIIa-mediated (but not FcγRIIIa-mediated) signaling, possibly as a result of the distinct orientation of the mAb relative to the membrane of the effector cells in comparison to S2M11 and S309 (Fig. 4G and fig. S6C). Accordingly, S2M11 but not S2E12 showed FcγRIIIa-dependent ADCC activity (Fig. 4H and fig. S6E) and ADCP activity (Fig. 4I). As we observed efficient activation of effector functions when mixing S2M11 with S2E12 or S309 (Fig. 4, G and H, and fig. S6E), we propose that cocktails of these mAbs can leverage additional

protective mechanisms in vivo besides inhibition of viral entry.

Formulation of ultrapotent neutralizing Ab cocktails against SARS-CoV-2

Surveillance efforts have led to the identification of a number of S mutants among circulating SARS-CoV-2 isolates. Several naturally occurring RBD mutations were shown to abrogate interactions with known mAbs and to reduce immune sera binding, raising concerns that viral neutralization escape mutants could emerge or be selected under pressure from mAb-based antiviral treatments (*42*). To investigate if S2E12- and S2M11-mediated neutralization might be affected by SARS-CoV-2 polymorphism, we tested binding of either mAb to 29 S protein variants (corresponding to mutations detected in circulating SARS-CoV-2 isolates) expressed at the surface of Expi CHO cells. The Y449N, E484K/Q, F490L, and S494P RBD variants led to decreased S2M11 binding to S, whereas none of the mutants tested affected interactions with S2E12, although several of them are found in the epitope of this latter mAb (table S4). The impact of these substitutions on S2M11 binding is explained by the structural data showing that the SARS-CoV-2 S Y449 and E484 side chains are hydrogen-bonded to the S2M11 heavy-chain F29 backbone amide and the N52/S55 side chains, respectively, and the F490 and S494 residues are buried at the interface with S2M11. SARS-CoV-2 S-VSV pseudotyped virus entry assays with selected S variants confirmed these results and showed that the Y449N, E484K/Q, F490L/S, and S494P individual substitutions abrogated S2M11-mediated neutralization, whereas the L455F variant reduced neutralization potency by an order of magnitude (fig. S7, A, C, and E). S2E12 neutralized efficiently all variants tested except G476S that showed an order-of-magnitude decreased activity (fig. S7, B, D, and F). In agreement with deep mutational scanning data (*43*), we found that the Y449N variant was impaired in its ability to bind ACE2 (fig. S8), which is expected to reduce viral fitness, likely explaining that this mutation has been reported to date in only one out of 90,287 complete SARS-CoV-2 genome sequences. Although rare, the G476S, E484K/Q, S494P, and F490L/S mutations have been detected in 20, 10 (E to K) or 17 (E to Q), 15, and 5 (F to L) or 8 (F to S) viral isolates, respectively, and in theory could be selected under the selective pressure of S2E12 or S2M11. Overall, 15 SARS-CoV-2 S variants with a single amino acid substitution within the S2M11 epitope were reported, with a prevalence of less than 0.1% as of September 2020 (fig. S7G).

To circumvent the risk of emergence or selection of neutralization escape mutants, we assessed whether S2M11, S2E12, and S309 could be combined in two-component mAb cocktails on the basis of their complementary mechanisms of action. SARS-CoV-2 S-VSV pseudotyped virus entry assays showed that mAb cocktails potently neutralized the Y449N, S494P, and G476S variants and overcame the neutralization escape phenotype observed with single mAbs (fig. S7, H to J). A concentration matrix of S2E12 and S2M11 revealed their additive neutralization effects without antagonism, even though both Abs compete for binding to the RBM (fig. S9, A to C). Moreover, the combination of S309 with S2E12, which do not compete for binding to S, and S309 and S2M11, which partially compete (i.e., for attachment to the closed S trimer), also yielded additive neutralization effects (fig. S9, D to F), suggesting that two- (or three-) component mAb cocktails are a promising therapeutic strategy to prevent the emergence or the selection of viral mutants escaping mAb therapy.

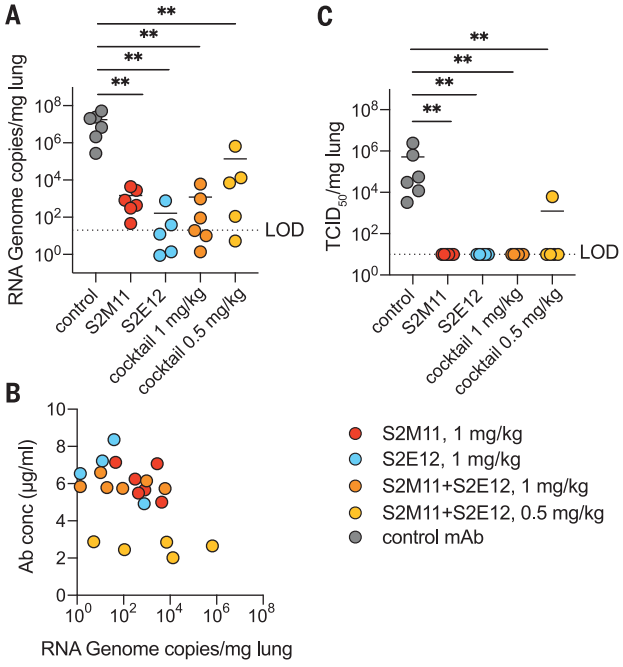

Fig. 5. S2E12, S2M11, or cocktails of the two mAbs provide robust in vivo protection against SARS-CoV-2 challenge. Syrian hamsters were injected with the indicated amount of mAb 48 hours before intranasal challenge with SARS-CoV-2. (**A**) Quantification of viral RNA in the lungs 4 days after infection. (**B**) The concentration of mAbs measured in the serum before infection (day 0) inversely correlates with the viral RNA load in the lung 4 days after infection. (**C**) Quantification of replicating virus in lung homogenates harvested 4 days after infection using a $TCID_{50}$ assay. For mAb cocktails, the total dose of an equimolar mixture of both mAbs is indicated.

S2M11 and S2E12 protect hamsters against SARS-CoV-2 challenge

To evaluate the protective efficacy of S2E12 and S2M11 against SARS-CoV-2 challenge in vivo, we tested either mAb or a cocktail of both mAbs in a Syrian hamster model (*44*). The mAbs were engineered with heavy- and light-chain constant regions from Syrian hamster IgG2 to allow optimal triggering of Fc-dependent effector functions. mAbs were administered by intraperitoneal injection 48 hours before intranasal challenge with 2×10^6 median tissue culture infectious dose ($TCID_{50}$) of SARS-CoV-2. Four days later, lungs were collected for the quantification of viral RNA and infectious virus. Either mAb alone or cocktails with 0.5 mg/kg or 1 mg/kg total mAb decreased the amount of viral RNA detected in the lungs by two to five orders of magnitude compared to hamsters receiving a control mAb (Fig. 5A). The amounts of viral RNA detected at day 4 inversely correlated with serum mAb concentration measured at the time of infection (Spearman's R −0.574, $p = 0.0052$) (Fig. 5B). Prophylactic administration of these mAbs at all doses tested completely abrogated viral replication in the lungs, with the exception of a single animal that received the low-dose cocktail and was partially protected (Fig. 5C). These data show a notable protective efficacy of both mAbs at low doses, individually or as cocktails, in line with their ultrapotent in vitro neutralization.

Discussion

S2M11 and S2E12 were identified among almost 800 screened Abs isolated from 12 individuals who recovered from COVID-19. The ultrapotency and quaternary epitope of S2M11 appear to be rare compared to more canonical RBM-specific neutralizing Abs, as the latter type of mAbs were present in every donor we analyzed. A mAb recognizing the closed S conformation (mAb 2-43) was previously identified, and low-resolution mapping of its binding site suggested that it might interact with a quaternary epitope that appears distinct from that of S2M11 (*45*). Two recent reports describe the identification of a mAb and of a nanobody targeting quaternary epitopes, spanning two neighboring RBDs, which are present in the closed S trimer. Nb6 was identified from a naïve nanobody library, affinity matured and

trimerized to achieve an IC_{50} of 160 pM, however, without the ability to exert effector functions (*46*). C144 was isolated from a COVID-19 convalescent serum sample, uses *VH3-53* and *VL2-14* genes, harbors a 25-residue long CDRH3, and efficiently neutralizes SARS-CoV-2 (*47*). Similar to S2M11, Nb6 (along with its engineered derivatives) and C144 use CDR(H)3 to bridge two neighboring RBDs and stabilize SARS-CoV-2 S in the closed state. A long CDRH3 of 15 or more amino acid residues was a common feature of C144-type mAbs (*47*). Contrary to the C144 25-residue-long CDRH3, S2M11 achieves this bridging with a relatively short CDRH3 of 18 amino acids [IMGT definition (*48*)]. As a result, all three binders inhibit SARS-CoV-2 through interfering with ACE2 attachment to S through direct competition and locking of the S trimer in the closed state. mAbs recognizing viral surface glycoproteins by binding to quaternary epitopes have been identified against Epstein-Bar virus (*49*), dengue virus (*50*–*53*), Zika virus (*54*), Ebola virus (*55*), West Nile virus (*56*), and HIV (*57*) and proved to be exceptionally potent or broad. S2M11, along with Nb6 and C144, therefore defines a distinct class of potent neutralizers of SARS-CoV-2 relative to previously isolated mAbs.

We recently described that the magnitude of Ab responses to SARS-CoV-2 S and nucleoprotein and neutralizing Ab titers correlate with clinical scores (*28*). The SARS-CoV-2 RBD is the main target of potent neutralizing S-specific Abs in COVID-19 patient sera or plasma samples, thereby focusing most of the selective pressure imposed by the humoral immune response on this domain (*23*, *28*). Given that several RBD variants have been found among circulating SARS-CoV-2 isolates, combining RBD-specific mAbs with different binding modes and distinct mechanisms of neutralization could prove essential for successful clinical application. A combination of S2M11 and S2E12 or cocktails of either of these mAbs with S309 yielded additive effects on neutralization potency. Moreover, Ab cocktails comprising S309 and/or S2M11 demonstrated robust activation of ADCC and ADCP, suggesting that combining these mAbs using distinct neutralization mechanisms would trigger these protective mechanisms in vivo. S2E12 and S2M11 (harboring a hamster Fc), individually or formulated as cocktails, conferred significant protection using mAb doses that are, to our knowledge, the lowest reported for human mAbs tested in hamster models. As a result, the mAb cocktails characterized here are expected to take advantage of both ultrapotent neutralization, different mechanisms of action, and Fc-mediated effector functions to protect from a broad spectrum of circulating SARS-CoV-2 isolates and limit the emergence of neutralization escape mutants. We propose that combinations of mAbs leveraging multiple distinct mechanisms of action with additive or synergistic effects could provide additional benefits for clinical application.

REFERENCES AND NOTES

1. P. Zhou *et al*., *Nature* **579**, 270–273 (2020).
2. N. Zhu *et al*., *N. Engl. J. Med.* **382**, 727–733 (2020).
3. H. Zhou *et al*., *Curr. Biol.* **30**, 2196–2203.e3 (2020).
4. C. Drosten *et al*., *N. Engl. J. Med.* **348**, 1967–1976 (2003).
5. T. G. Ksiazek *et al*., *N. Engl. J. Med.* **348**, 1953–1966 (2003).
6. A. C. Walls *et al*., *Cell* **181**, 281–292.e6 (2020).
7. D. Wrapp *et al*., *Science* **367**, 1260–1263 (2020).
8. J. Lan *et al*., *Nature* **581**, 215–220 (2020).
9. J. Shang *et al*., *Nature* **581**, 221–224 (2020).
10. R. Yan *et al*., *Science* **367**, 1444–1448 (2020).
11. M. Hoffmann *et al*., *Cell* **181**, 271–280.e8 (2020).
12. Q. Wang *et al*., *Cell* **181**, 894–904.e9 (2020).
13. M. Letko, A. Marzi, V. Munster, *Nat. Microbiol.* **5**, 562–569 (2020).
14. M. A. Tortorici, D. Veesler, *Adv. Virus Res.* **105**, 93–116 (2019).
15. P. M. Folegatti *et al*., *Lancet* **396**, 467–478 (2020).
16. J. Yu *et al*., *Science* **369**, 806–811 (2020).
17. F. C. Zhu *et al*., *Lancet* **395**, 1845–1854 (2020).
18. L. A. Jackson *et al*., *N. Engl. J. Med.* NEJMoa2022483 (2020).
19. U. Sahin *et al.*, Concurrent human antibody and T_H1 type T-cell responses elicited by a COVID-19 RNA vaccine. *medRxiv* 2020.2007.2017.20140533 [Preprint]. (20 July 2020). https://doi.org/10.1101/2020.07.17.20140533.
20. M. J. Mulligan *et al.*, Phase 1/2 Study to Describe the Safety and Immunogenicity of a COVID-19 RNA Vaccine Candidate (BNT162b1) in Adults 18 to 55 Years of Age: Interim Report. *medRxiv* 2020.2006.2030.20142570 [Preprint]. (1 July 2020). https://doi.org/10.1101/2020.06.30.20142570.
21. D. Pinto *et al*., *Nature* **583**, 290–295 (2020).
22. C. O. Barnes *et al*., *Cell* **182**, 828–842.e16 (2020).
23. D. F. Robbiani *et al*., *Nature* **584**, 437–442 (2020).
24. C. Wang *et al.*, A human monoclonal antibody blocking SARS-CoV-2 infection. *bioRxiv*, 2020.2003.2011.987958 [Preprint]. (12 March 2020). https://doi.org/10.1101/2020.03.11.987958.
25. Y. Wu *et al*., *Science* **368**, 1274–1278 (2020).
26. P. J. M. Brouwer *et al*., *Science* **369**, 643–650 (2020).
27. E. Seydoux *et al.*, Characterization of neutralizing antibodies from a SARS-CoV-2 infected individual. *bioRxiv* 2020.2005.2012.091298 [Preprint]. (12 May 2020). https://doi.org/10.1101/2020.05.12.091298.
28. L. Piccoli *et al*., Mapping neutralizing and immunodominant sites on the SARS-CoV-2 spike receptorbinding domain by structure-guided high-resolution serology. *Cell* 10.1016/j.cell.2020.09.037 (2020).
29. W. B. Alsoussi *et al*., *J. Immunol.* **205**, 915–922 (2020).
30. T. F. Rogers *et al*., *Science* **369**, 956–963 (2020).
31. S. J. Zost *et al*., *Nature* **584**, 443–449 (2020).
32. J. Hansen *et al*., *Science* **369**, 1010–1014 (2020).
33. R. Shi *et al*., *Nature* **584**, 120–124 (2020).
34. B. Ju *et al*., *Nature* **584**, 115–119 (2020).
35. X. Xie *et al*., A nanoluciferase SARS-CoV-2 for rapid neutralization testing and screening of anti-infective drugs for COVID-19. *bioRxiv* 2020.2006.2022.165712 [Preprint]. (23 June 2020). https://doi.org/10.1101/2020.06.22.165712.
36. J. B. Case *et al*., *Cell Host Microbe* **28**, 475–485.e5 (2020).
37. A. C. Walls *et al*., *Cell* **176**, 1026–1039.e15 (2019).
38. T. Zhou *et al*., *bioRxiv* 2020.07.04.187989 (2020).
39. Z. Ke *et al*., *Nature* (2020).
40. M. McCallum, A. C. Walls, J. E. Bowen, D. Corti, D. Veesler, *Nat. Struct. Mol. Biol.* (2020).
41. S. Bournazos, T. T. Wang, J. V. Ravetch, *Microbiol. Spectr.* **4**, 10.1128/microbiolspec.MCHD-0045-2016 (2016).
42. Q. Li *et al*., *Cell* **182**, 1284–1294.e9 (2020).
43. T. N. Starr *et al*., *Cell* **182**, 1295–1310.e20 (2020).
44. R. Boudewijns *et al.*, STAT2 signaling as double-edged sword restricting viral dissemination but driving severe pneumonia in SARS-CoV-2 infected hamsters. *bioRxiv* 2020.2004.2023.056838 [Preprint]. (2 July 2020). https://doi.org/10.1101/2020.04.23.056838.
45. L. Liu *et al*., *Nature* **584**, 450–456 (2020).
46. M. Schoof *et al.*, An ultra-potent synthetic nanobody neutralizes SARS-CoV-2 by locking Spike into an inactive conformation. *bioRxiv* 2020.2008.2008.238469 [Preprint]. (17 August 2020). https://doi.org/10.1101/2020.08.08.238469.
47. C. O. Barnes *et al.*, Structural classification of neutralizing antibodies against the SARS-CoV-2 spike receptor-binding domain suggests vaccine and therapeutic strategies. *bioRxiv* 2020.2008.2030.273920 [Preprint] (30 August 2020). https://doi.org/10.1101/2020.08.30.273920.
48. X. Brochet, M. P. Lefranc, V. Giudicelli, *Nucleic Acids Res.* **36**, W503–W508 (2008).
49. J. Snijder *et al*., *Immunity* **48**, 799–811.e9 (2018).
50. G. Fibriansah, S. M. Lok, *Antiviral Res.* **128**, 7–19 (2016).
51. W. Dejnirattisai *et al*., *Nat. Immunol.* **16**, 170–177 (2015).
52. E. N. Gallichotte *et al*., *PLOS Pathog.* **14**, e1006934 (2018).
53. D. G. Widman *et al*., *Sci. Rep.* **7**, 17169 (2017).
54. F. Long *et al*., *Proc. Natl. Acad. Sci. U.S.A.* **116**, 1591–1596 (2019).
55. B. R. West *et al*., *mBio* **9**, e01674-18 (2018).
56. B. Kaufmann *et al*., *Proc. Natl. Acad. Sci. U.S.A.* **107**, 18950–18955 (2010).
57. E. T. Crooks *et al*., *PLOS Pathog.* **11**, e1004932 (2015).

ACKNOWLEDGMENTS

We are grateful to J. Quispe, Q. Beedle, and Y.-J. Park for assistance with data collection and data analysis. We thank A. Covizzi and M. Schiuma for help with patient sample collection. We thank X. Zhang, E. Maas, C. Dekeyzer, and L. Bervoets for help with the hamster experiments. We also thank I. Hoffman for help with refinement of the S2E12 Fab crystal structure. We acknowledge the Paul Scherrer Institut, Villigen, Switzerland, for provision of synchrotron radiation beamtime at beamline X10SA of the Swiss Light Source and thank V. Olieric for assistance with data collection. We gratefully acknowledge the authors, originating and submitting laboratories of the sequences from GISAID's EpiFlu Database on which this research is based. **Funding:** This study was supported by the National Institute of General Medical Sciences (R01GM120553, D.V.), the National Institute of Allergy and Infectious Diseases (HHSN272201700059C, D.V.), a Pew Biomedical Scholars Award (D.V.), an Investigators in the Pathogenesis of Infectious Disease Award from the Burroughs Wellcome Fund (D.V.), Fast Grants (D.V.), the University of Washington Arnold and Mabel Beckman cryoEM center, the Pasteur Institute (M.A.T.) the KU Leuven/UZ Leuven COVID-19 Fund (J.N.), the Flanders Fonds voor Wetenschappelijk Onderzoek (FWO, G0G4820N, J.N.), and the Bill and Melinda Gates Foundation (INV-006366, J.N). **Author contributions:** M.A.T., H.V.D, L.E.R., F.A.L., C.H.D., M.S.D., G.S, D.C., K.F., and D.V. designed experiments. A.R., A.G., M.G., and F.B. collected donors' samples. M.A.T., H.V.D., M.M.C, J.E.B., N.C., S.J., N.S., K.C., M.M., and C.N. expressed and purified proteins. M.B., D.P., A.M., A.D.M, B.G., S.B., F.Z., M.A.S., E.C., E.L, H.T., A.P., J.W., H.K., M.M.R., J.D., J.B.C, R.E.C., and F.B. isolated and characterized mAbs. H.V.D, L.E.R., M.M., and A.M. carried out binding assays. S.C.F., R.A., and J.N. assessed effects in the hamster model and performed data analysis. M.A.T. collected cryo-EM data. M.A.T. and D.V processed the cryo-EM data and built the models. N.C., C.N., and G.S. carried out the crystallographic work. R.A, S.-Y.C.F, and J.N. conducted and supervised hamster experiments. M.A.T., M.B., D.P., H.V.D., L.E.R., M.M., F.A.L., R.S., C.H.D., M.S.P., G.S, D.C., K.F., and D.V. analyzed the data. K.F. and D.V. wrote the manuscript with input from all authors. G.S., M.S.D., H.W.V., D.C., K.F., and D.V. supervised the project. M.S.D. and D.V. acquired funding for this project. **Competing interests:** All authors except M.A.T, H.V.D, M.M.C., J.E.B. , J.B.C., R.E.C., R.A., SY.C.F., A.R., A.G., M.G., J.N., M.S.D., and D.V. are employees of Vir Biotechnology Inc. and may hold shares in Vir Biotechnology Inc. M.S.D. is a consultant for Inbios, Vir Biotechnology, NGM Biopharmaceuticals, and on the Scientific Advisory Boards of Moderna and Immunome. D.V. is a consultant for Vir Biotechnology. The Diamond laboratory has received unrelated funding support in sponsored research agreements from Moderna and Emergent BioSolutions. The Veesler, Diamond and Neyts laboratories have received sponsored research agreements from Vir Biotechnology Inc. H.W.V. is a founder of PierianDx and Casma Therapeutics. Neither company provided funding for this work or is performing related work. D.C. is currently listed as an inventor on patent applications that disclose subject matter described in this manuscript. **Data and materials availability:** The cryo-EM maps and atomic coordinates have been deposited to the Electron Microscopy Data Bank (EMDB) and Protein Data Bank (PDB) with accession numbers EMD-22668 and PDB 7K4N (S2E12-bound SARS-CoV-2 S), EMD-22660 and PDB 7K45 (RBD/S2E12 local refinement), and EMD-22659 and PDB 7K43 (S2M11-bound SARS-CoV-2 S). The crystal structure of the S2E12 Fab was deposited to the PDB with accession number PDB 7K3Q. Materials generated in this study will be made available on request, but we may require a completed materials transfer agreement signed with Vir Biotechnology. This work is licensed under a Creative Commons Attribution 4.0 International (CC BY 4.0) license, which permits unrestricted use, distribution, and reproduction in any medium, provided the original work is properly cited. To view a copy of this license, visit https://creativecommons.org/licenses/by/4.0/. This license does not apply to figures/photos/artwork or other

content included in the article that is credited to a third party; obtain authorization from the rights holder before using such material.

SUPPLEMENTARY MATERIALS
science.sciencemag.org/content/370/6519/950/suppl/DC1

Materials and Methods
Figs. S1 to S9
Tables S1 to S4
References (*58*–*83*)
MDAR Reproducibility Checklist

View/request a protocol for this paper from *Bio-protocol*.

14 August 2020; accepted 21 September 2020
Published online 24 September 2020
10.1126/science.abe3354

REPORT

SURFACE SCIENCE

Control of long-distance motion of single molecules on a surface

Donato Civita[1], Marek Kolmer[2]*, Grant J. Simpson[1], An-Ping Li[2], Stefan Hecht[3,4,5], Leonhard Grill[1]†

Spatial control over molecular movement is typically limited because motion at the atomic scale follows stochastic processes. We used scanning tunneling microscopy to bring single molecules into a stable orientation of high translational mobility where they moved along precisely defined tracks. Single dibromoterfluorene molecules moved over large distances of 150 nanometers with extremely high spatial precision of 0.1 angstrom across a silver (111) surface. The electrostatic nature of the effect enabled the selective application of repulsive and attractive forces to send or receive single molecules. The high control allows us to precisely move an individual and specific molecular entity between two separate probes, opening avenues for velocity measurements and thus energy dissipation studies of single molecules in real time during diffusion and collision.

Thermally induced diffusion of atoms and molecules on a surface is typically a random process consisting of uncorrelated hops on the atomic surface lattice (*1*); this was first observed with the field-ion microscope (*2*). Thermal motion of molecules across surfaces occurs mainly via hopping to adjacent lattice sites (*3*, *4*), but larger displacements were also predicted (*5*). Indeed, molecules showed mean-squared displacements of four lattice constants over the surface, a value that is increased to seven when the molecule–surface interaction is reduced (*6*).

In the absence of thermal motion, a scanning tunneling microscope (STM) tip can be used to induce molecular displacement. Single molecules can be moved controllably over a surface, typically hopping from one lattice site to the next (*7*, *8*). Longer distances, beyond the manipulation pathway, have been achieved with sexiphenyl molecules on Ag(111), where the molecules were initially dragged with the STM tip over the surface and then continued to move further after the tip was retracted, albeit with deflections from their original propagation path (*9*). Recently, CF_2 species (fragments after CF_3 dissociation) were found to move linearly on a corrugated Cu(110) surface before they collided with other species to form new products (*10*). The fragments were propelled up to ~5 nm, driven by excess energy from bond dissociation in a manner similar to "hot" adatoms, which translate even further after dissociative chemisorption (*11*).

We show how individual molecules can be moved controllably over large distances (150 nm) on a surface along an atomically precise track. We studied dibromoterfluorene (DBTF) molecules (Fig. 1A) on Ag(111) by STM under ultrahigh vacuum and at low temperatures (below 7 K) (supplementary materials and methods). The molecule, originally designed for growth of molecular wires on metal surfaces (*12*, *13*), has terminal Br substituents. Moreover, three geminal dimethyl side groups lift the aromatic fluorene units and lower its diffusion barrier, as reported for other species (*6*). Isolated molecules consist of three lobes that reflect the dimethylfluorene groups and two smaller protrusions at the termini indicative of the Br substituents (Fig. 1B).

The orientation of a molecule on a surface can affect its diffusion properties, at least on corrugated surfaces (*14*, *15*). To test this effect on the flat Ag(111) surface, we rotated single molecules by STM manipulation (Fig. 1C, arrow). Unexpectedly, the molecule exhibits a sharp increase in mobility when oriented exactly along the atomically close-packed [1$\bar{1}$0] direction (fig. S1) and appears as a smooth stripe in the subsequent image of the same area (Fig. 1D). The stripe does not exhibit a terminus, but runs across the entire STM image. When the adjacent region is scanned

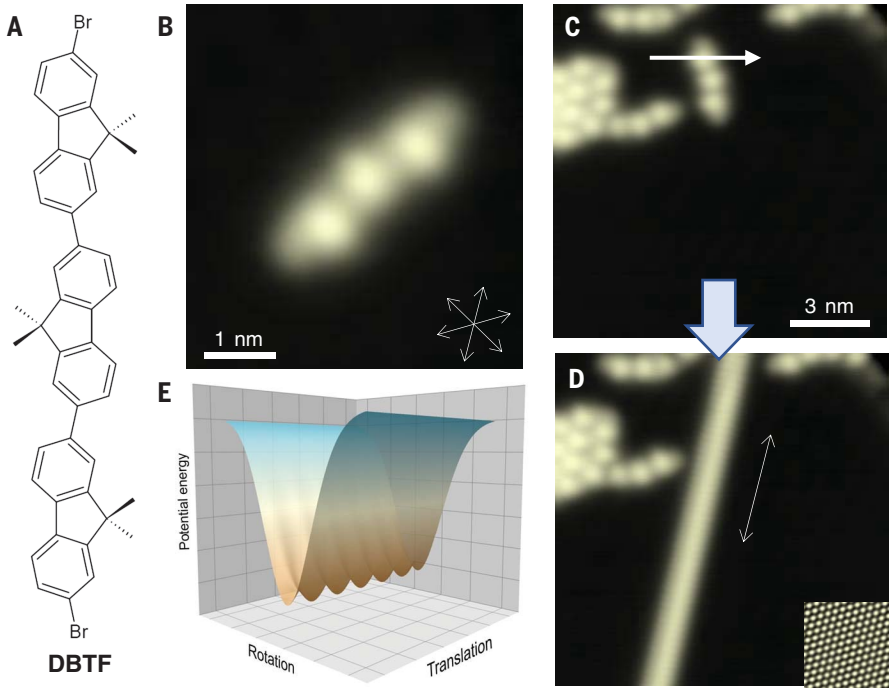

Fig. 1. Mobile DBTF molecules on Ag(111). (**A**) Chemical structure of DBTF. (**B**) STM image (0.6 V, 300 pA) of a single DBTF molecule on Ag(111). (**C** and **D**) STM images (0.6 V, 300 pA) before and after lateral manipulation [indicated by the arrow in (C)], which caused the appearance of a stripe. These stripes typically appeared smooth but can, with use of a good tip, show an internal structure, reflecting the surface periodicity (fig. S4). Close-packed directions of the Ag(111) substrate [indicated by arrows in (B) and (D)] were determined from an STM image (0.1 V, 500 nA) of the surface with atomic resolution [inset of (D)]. (**E**) Scheme of the potential energy surface for a molecule oriented in the [1$\bar{1}$0] direction with a shallow corrugation for translation along the high-mobility direction and higher barriers for rotation out of this orientation.

[1]Department of Physical Chemistry, University of Graz, Heinrichstrasse 28, 8010 Graz, Austria. [2]Center for Nanophase Materials Sciences, Oak Ridge National Laboratory, Oak Ridge, TN 37831, USA. [3]Department of Chemistry and IRIS Adlershof, Humboldt-Universität zu Berlin, Brook-Taylor-Str. 2, 12489 Berlin, Germany. [4]DWI -Leibniz Institute for Interactive Materials, Forckenbeckstr. 50, 52074 Aachen, Germany. [5]Institute of Technical and Macromolecular Chemistry, RWTH Aachen University, Worringer Weg 2, 52074 Aachen, Germany.
*Present address: Ames Laboratory, U.S. Department of Energy, Ames, IA 50011, USA.
†Corresponding author. Email: leonhard.grill@uni-graz.at

(i.e., above or below the area in Fig. 1D), the stripe continues on precisely the same line.

We assign these stripes to molecules that follow the STM tip during scanning. They are highly mobile in one direction but spatially confined to one atomic row in the other direction. Accordingly, they reflect molecules that are always under the tip whenever the tip crosses this row (fig. S2), which causes the bright appearance in the image. These stripes always remain in the same position on the surface, independent of the scan direction (fig. S3). The molecules translate easily in this state and do not rotate back to their stable orientation, indicating a substantial barrier for rotation compared with an extremely low barrier for one-dimensional translation (Fig. 1E).

One-dimensional diffusion of molecules has been observed on corrugated surfaces with anisotropic diffusion barriers, for instance, the (110) surfaces of face-centered cubic (fcc) metals (*6*, *16*), or "walking" molecules guided by thiol linkers to move along one line (*3*). The directional motion of the linker-free DBTF on the flat Ag(111) surface is notable because, in general, diffusion barriers are very low and approximately isotropic on fcc (111) surfaces (*17*). The linear shape of DBTF is likely important, but a simple comparison with terfluorene (TF) molecules (the Br-free analog) showed that the Br substituents also affect the molecular motion. Although TF showed the same stripe formation, it could spontaneously change direction (fig. S5), in contrast to DBTF, which never did. Hence, the Br atoms keep the molecules on track, likely because their interaction with the surface substantially contributes to the barrier for molecular rotation (Fig. 1E).

The mobile molecule (Fig. 1D) was attracted by the tip (for details about the stripe formation, see fig. S6). To test this attraction, a mobile molecule was placed in a clean surface area and then (remotely) pulled over the surface by placing the tip laterally very far away (on exactly the same $[1\bar{1}0]$ atomic row). In this experiment, a large, clean terrace was chosen, and two areas (I and II) separated by 150 nm were selected (Fig. 2A). These areas were initially devoid of single molecules and stripes but contained molecular islands as references. Then, area I was imaged alone and a stripe was created in that area by STM manipulation, as confirmed by subsequent imaging (Fig. 2B). The $[1\bar{1}0]$ atomic row underneath the stripe was identified (Fig. 2B), and its location was transferred to the overview image (Fig. 2A).

In the next step, the bias voltage was switched off and the STM tip was vertically retracted far from the surface (~200 nm). The tip was moved laterally in a large loop out of the image area (indicated by external arrows around Fig. 2A) to avoid dragging of the molecule. Because of the

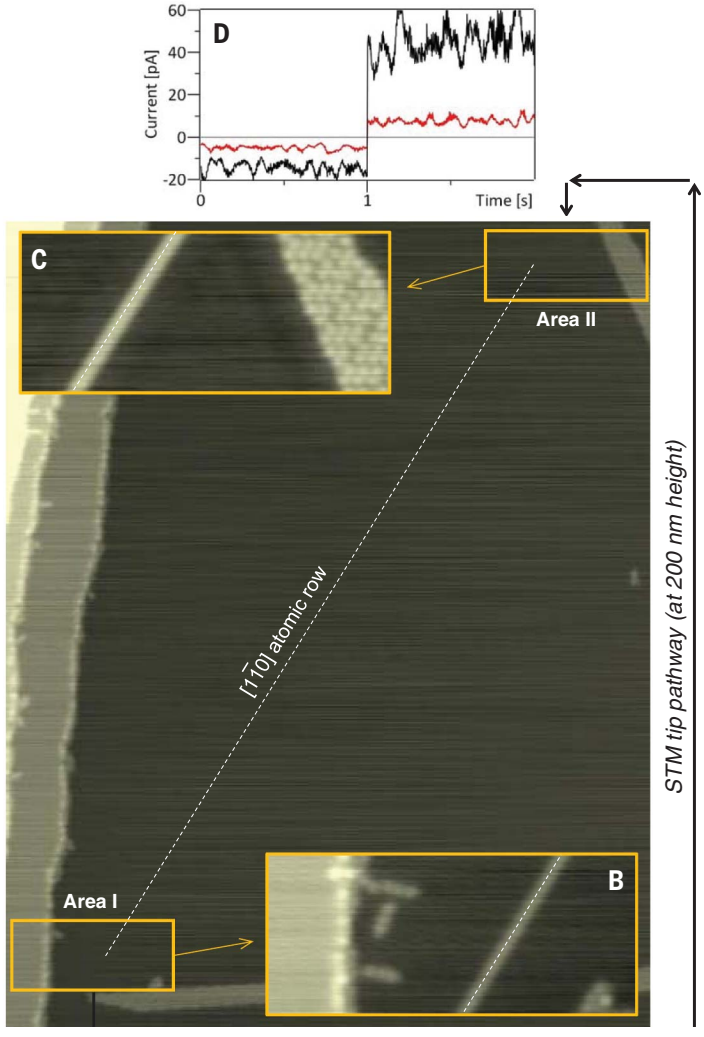

Fig. 2. Long-distance displacement of single molecules. (**A**) STM image (0.6 V, 300 pA, 116 nm by 147 nm) of a large Ag(111) terrace. (**B** and **C**) Areas I and II, at a distance of 150 nm, were scanned before (B) and after (C) moving the STM tip along the indicated pathway. Dashed lines indicate one and the same atomic row in the $[1\bar{1}0]$ direction. (**D**) Current as a function of time (fig. S7), taken (at fixed tip height) directly after tip reapproach in area II. The bias voltage was changed from −1 V to +0.6 V at *t* of 1 s, which led to attraction and thus pulling of the molecule across the terrace (the red curve shows the same experiment, but without a molecule).

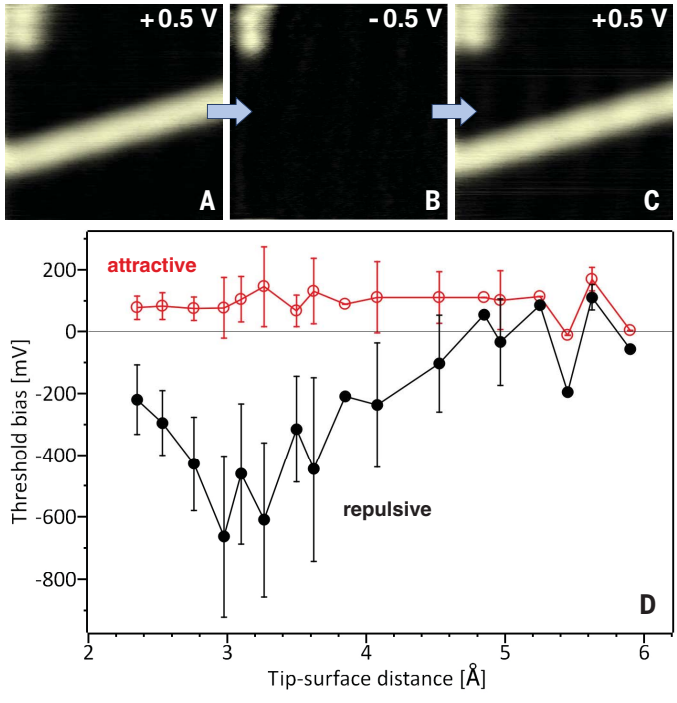

Fig. 3. Attraction and repulsion. (**A** to **C**) STM images (9.2 nm by 9.2 nm, 10 pA) of the same surface area (see stable molecule at the top left as reference) scanned consecutively at different bias voltages (as indicated). The stripe was visible at +0.5 V but disappeared at −0.5 V and reappeared if the bias was restored. (**D**) Threshold bias voltages for attraction (open circles) and repulsion (solid circles) as a function of the tip–sample distance.

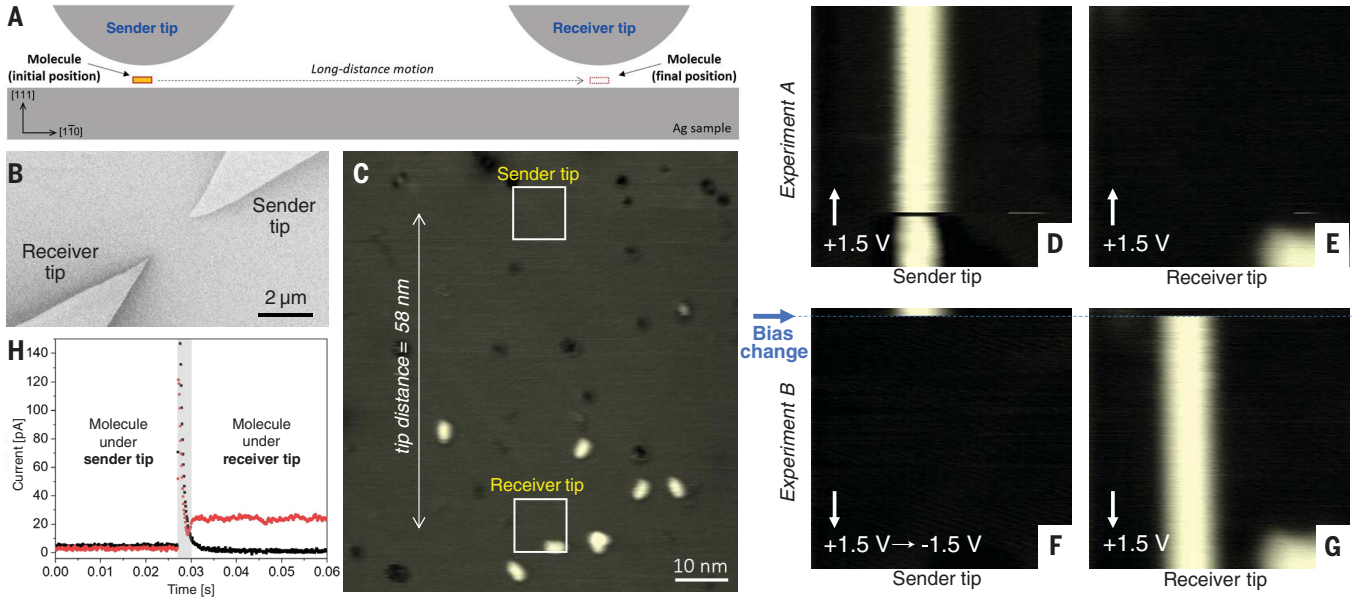

Fig. 4. Sender–receiver experiments with single molecules. (**A**) Scheme of the two-probe experiment where the sender tip was first attractive and later repulsive (sending mode), while the receiver tip was always in the attractive mode. (**B**) Scanning electron microscope (SEM) image of the tips above the surface. The increased surface contamination (compared with the single-tip experiments) was caused by the SEM, which was required for tip positioning. Defect-free surface areas were chosen for the sender–receiver experiments to ensure unperturbed molecular mobility. (**C**) STM image (0.6 V, 3 pA) with indicated 10 nm by 10 nm areas, at a distance of 58 nm, that were scanned simultaneously by the two tips. (**D** to **G**) Two experiments (named A and B) where the two tips remained in the areas marked in (C). The slow scan direction is indicated by white arrows. During experiment B the bias of the sender tip was changed from +1.5 V to −1.5 V (indicated by a blue arrow) to induce molecular motion; all other bias voltages were constant. (**H**) Tunneling currents as a function of time (*t* of 0 s is arbitrary), measured simultaneously with both tips, the sender tip (black) and receiver tip (red). After the transition period (gray-shaded area), which was affected by the bias change of the sender tip (fig. S13), successful transfer registered as a modified signal.

vertical retraction to large tip heights at zero bias (i.e., in the absence of electrostatic forces), the molecule remained in the same position in area I during this entire loop motion [it would have been found at the next step edge if it moved spontaneously without the STM tip (fig. S8)].

Finally, the tip was made to reapproach the surface in area II, and the tip was placed over the [1$\bar{1}$0] atomic row that had been identified before (Fig. 2, dashed line). The arrival of the very same molecule (imaged before in area I) could then be recorded in real time by following the tunneling current, which showed an abrupt step when the bias was changed (at time *t* of 1 s) from −1 V to +0.6 V (Fig. 2D). In addition to the changed direction of current (caused by the inverted bias polarity), the modulus of the current was greater after 1 s, revealing that the molecule had indeed arrived underneath the tip (Fig. 2D). The same experiment in the absence of a molecule lacked this effect (red curve in Fig. 2D). Hence, the tip pulled the molecule as soon as a suitable bias voltage was chosen.

Subsequent imaging of area II confirmed this process, as it showed the characteristic stripe (Fig. 2C), which had been absent. Most notably, the stripe appeared precisely on the [1$\bar{1}$0] atomic row that was identified in Fig. 2B. Hence, the stripe in Fig. 2C is the spatial extension of the previously created stripe (Fig. 2B), so the very same molecule was remotely pulled over a distance of 150 nm over the surface. We assign this unexpectedly large range to the very high mobility of the molecule along the high-symmetry direction of the surface. The process can be reproduced multiple times in succession for the same molecule (fig. S9), as well as for other mobile molecules in all three possible orientations (fig. S1C).

In addition to these attractive forces that pull single molecules toward the tip, repulsive interactions can also occur, depending on the bias voltage polarity. Thus far, we have presented results for positive bias voltages, but if an area with a stripe is scanned first at positive and then at negative bias voltages, the stripe disappears completely and the image becomes featureless (Fig. 3, A and B). The stripe reappears at exactly the same position in a subsequent image taken again at positive polarity (Fig. 3C). This effect could also be visualized within the same image by changing the voltage during scanning (fig. S10).

Hence, the stripe is present or absent depending on the bias voltage, as the mobile molecule is either attracted or repelled by the STM tip (Fig. 3D). This effect is electrostatic in origin. It is most likely caused by a positive charge at the molecule–surface interface (*18*) and thus, depending on the bias polarity, attractive or repulsive interactions with the electric field in the STM junction (a detailed discussion is provided in the supplementary materials and methods; fig. S11). From these measurements, it was not possible to deduce in which of the two possible directions (along one atomic row, i.e., left or right in Fig. 3B) the molecule was repelled. By taking advantage of step edges in the vicinity to "detect" the molecules after repulsion, we found that the molecules could indeed move in both (opposite) directions (fig. S12). Moreover, these experiments showed that the molecule was not simply located near the tip but was instead repelled rather far away on the surface.

As shown in Fig. 2, molecular motion could be induced over large distances with an extremely high lateral precision of about 0.1 Å (i.e., the lateral resolution of the STM). We studied whether a sender–receiver experiment could be realized with a single molecule, in which the molecule is transferred between two tips of a multiprobe STM (Fig. 4A) with two separate scanners measuring on the same Ag(111) surface independently. First, the two sharp tips were brought close together (Fig. 4B), and the same scan area was consecutively imaged by each tip to identify their relative

positions. Then, two small areas on this large overview image (Fig. 4C) were selected for independent imaging by each tip (sender and receiver). Notably, the tips, which were placed ~60 nm apart, scanned the indicated areas simultaneously without mutual interaction (imaging was not affected by the presence of the other tip).

A mobile molecule was introduced on demand using STM manipulation (as in Fig. 1, C and D) in the scanning area of the sender tip only (no mobile molecules present at receiver tip). Care was taken to ensure that, when extrapolated, the molecular stripe would extend from the sender tip area to the receiver (for later detection). As soon as this was achieved, we performed the two-probe experiment in two parts. In experiment A, the two tips simultaneously scanned their areas at bias voltages of +1.5 V (thus both in the regimen of attractive forces that trap the molecule underneath the tip). Accordingly, the sender tip imaged the characteristic stripe of the mobile molecule (Fig. 4D) while the receiver tip scanned only the Ag(111) surface (Fig. 4E, blank image).

In experiment B, the two areas were imaged again, initially with the same settings, but after a few lines were scanned, the bias voltage polarity of the sender tip was inverted (Fig. 4, F and G, dashed line) and the receiver tip continued with the same settings. That is, the sender tip was switched into the repulsion mode and the receiver tip remained attractive. Accordingly, the molecular stripe disappeared in the image of the sender tip (Fig. 4F) but appeared in the same moment (i.e., scanning line) in the image of the receiver tip (Fig. 4G). Hence, a single molecule was sent from one tip to another over a distance of 49 nm. The one-dimensionality of the molecular translation allowed detection of the molecule exactly underneath the receiver tip, as planned. This experiment was reproducible, although the molecule sometimes traveled in the opposite direction from the sender tip.

To gain insight into the temporal progress of the molecule transfer, we fixed the (lateral and vertical) positions of both tips at appropriate locations and measured the tunneling current as a function of time. The sending or receiving of the molecule led to a decrease or an increase in the two current signals, respectively (Fig. 4H). The time resolution was limited by our setup, and the upper limit for the time from sender to receiver tip was 2.3 ± 0.5 ms (fig. S13). Considering our one-probe experiment (Fig. 2) with a time period of <2 ms for a 150-nm translation (fig. S7), the molecule most likely took less than 2 ms to move 49 nm between two tips. Thus, we estimate a lower velocity limit of an individual molecule of 25 μm/s. The real velocity was likely much greater but probably not as high as those measured indirectly for molecular ensembles at room temperature, which were driven either thermally (*15*, *19*) or by excess energy from chemical reactions (*11*).

Our results reveal how single molecules, which appear to move easily in one dimension, can be tracked by scanning probe microscopy. Likely improvements in STM time resolution using faster electronic control should enable measurement of the absolute velocity of various molecules on different surfaces and enable direct correlation of molecular motion with chemical and structural properties. Such experiments should allow determination of momentum and kinetic energy, in addition to the precise spatial location, and thus pave the way toward measurement of energy dissipation during diffusion or after collision of single molecules with other adsorbates. Moreover, the experiment permits transfer of specific molecular entities and information encoded therein between precisely defined locations.

REFERENCES AND NOTES

1. Z. Zhang, M. G. Lagally, *Science* **276**, 377–383 (1997).
2. G. Ehrlich, F. G. Hudda, *J. Chem. Phys.* **44**, 1039–1049 (1966).
3. K.-Y. Kwon *et al.*, *Phys. Rev. Lett.* **95**, 166101 (2005).
4. J. A. Miwa *et al.*, *J. Am. Chem. Soc.* **128**, 3164–3165 (2006).
5. K. D. Dobbs, D. J. Doren, *J. Chem. Phys.* **97**, 3722–3735 (1992).
6. M. Schunack *et al.*, *Phys. Rev. Lett.* **88**, 156102 (2002).
7. L. Bartels, G. Meyer, K.-H. Rieder, *Phys. Rev. Lett.* **79**, 697–700 (1997).
8. L. Grill *et al.*, *Nat. Nanotechnol.* **2**, 95–98 (2007).
9. S.-W. Hla, K.-F. Braun, B. Wassermann, K.-H. Rieder, *Phys. Rev. Lett.* **93**, 208302 (2004).
10. K. Anggara, L. Leung, M. J. Timm, Z. Hu, J. C. Polanyi, *Faraday Discuss.* **214**, 89–103 (2019).
11. H. Brune, J. Wintterlin, R. J. Behm, G. Ertl, *Phys. Rev. Lett.* **68**, 624–626 (1992).
12. L. Lafferentz *et al.*, *Science* **323**, 1193–1197 (2009).
13. A. Saywell, J. Schwarz, S. Hecht, L. Grill, *Angew. Chem. Int. Ed.* **51**, 5096–5100 (2012).
14. R. Otero *et al.*, *Nat. Mater.* **3**, 779–782 (2004).
15. P. Rotter *et al.*, *Nat. Mater.* **15**, 397–400 (2016).
16. J. Weckesser, J. V. Barth, K. Kern, *J. Chem. Phys.* **110**, 5351–5354 (1999).
17. M. Ternes, C. P. Lutz, C. F. Hirjibehedin, F. J. Giessibl, A. J. Heinrich, *Science* **319**, 1066–1069 (2008).
18. P. S. Bagus, V. Staemmler, C. Wöll, *Phys. Rev. Lett.* **89**, 096104 (2002).
19. A. Tamtögl *et al.*, *Nat. Commun.* **11**, 278 (2020).

ACKNOWLEDGMENTS

We thank P. Jacobson for helpful discussions and careful reading of the manuscript, as well as J. Burns and J. Poplawsky for assistance during tip preparation for the two-probe experiments and J. Schwarz for help with molecular synthesis. **Funding:** Financial support from the "Doc Academy NanoGraz" at the University of Graz, and the European Commission via the MEMO project (FET open project no. 766864) is gratefully acknowledged. Two-probe STM experiments were conducted at the Center for Nanophase Materials Sciences, which is a DOE Office of Science User Facility. **Author contributions:** D.C. performed the experiments. D.C., G.J.S., and L.G. analyzed the data. Two-probe experiments and analysis were performed together with M.K. and A.-P.L. S.H. designed the molecules. L.G. wrote the manuscript with feedback from all authors. **Competing interests:** Authors declare no competing interests. **Data and materials availability:** All data needed to evaluate the conclusions in the paper are available in the main text or the supplementary materials.

SUPPLEMENTARY MATERIALS

science.sciencemag.org/content/370/6519/957/suppl/DC1
Materials and Methods
Figs. S1 to S13
References (*20*–*34*)

29 May 2020; accepted 27 August 2020
10.1126/science.abd0696

MATERIALS SCIENCE

Artificial multimodal receptors based on ion relaxation dynamics

Insang You[1,2,3], David G. Mackanic[2], Naoji Matsuhisa[2], Jiheong Kang[2], Jimin Kwon[3], Levent Beker[2]*, Jaewan Mun[2], Wonjeong Suh[1], Tae Yeong Kim[1], Jeffrey B.-H. Tok[2], Zhenan Bao[2]†, Unyong Jeong[1]†

Human skin has different types of tactile receptors that can distinguish various mechanical stimuli from temperature. We present a deformable artificial multimodal ionic receptor that can differentiate thermal and mechanical information without signal interference. Two variables are derived from the analysis of the ion relaxation dynamics: the charge relaxation time as a strain-insensitive intrinsic variable to measure absolute temperature and the normalized capacitance as a temperature-insensitive extrinsic variable to measure strain. The artificial receptor with a simple electrode-electrolyte-electrode structure simultaneously detects temperature and strain by measuring the variables at only two measurement frequencies. The human skin–like multimodal receptor array, called multimodal ion-electronic skin (IE^M-skin), provides real-time force directions and strain profiles in various tactile motions (shear, pinch, spread, torsion, and so on).

The receptors of the somatosensory system of human skin are composed of ion conductors, and their operation is based on ion dynamics. A large number of thermoreceptors and mechanoreceptors are spatially distributed in the dermis (*1*); hence, the spatial profiles of strain and temperature on the skin can be perceived distinctively (Fig. 1A). The viscoelastic deformability of the ionic receptors (*2*) maintains stable electrical signals under large shear strains. Furthermore, formation of wrinkles is a way to visualize three-dimensional (3D) deformations of the skin by various stimulation (press, shear, pinch, torsion, and combinations thereof) (*3*). For instance, wrinkles are seen in compressed regions of skin while the regions of the other side are stretched (Fig. 1B) (*4*). Temperature sensing is important in tactility and monitoring physiological changes of the body (*5*). Because 3D deformations create complex stress fields, real-time acquisition of the spatial profiles of contact and strain is essential to understanding the perception of the skin sensory system.

Electronic skin (e-skin) that imitates human somatosensory functions is expected to play a key role as an alternative to biological skin or as a sensing and actuation interface in virtual reality (*6*). It has shown potential applicability to haptic devices (*7*), wearable health care sensors (*8*–*10*), prostheses (*11*), artificial skin for robots (*12*), and implantable medical devices (*13*). Despite the notable advances, manufacturing a multistimuli responsive e-skin is still a challenge. Previous studies attempted to integrate different types of sensors (*14*, *15*); however, they are structurally complex. Although multimodality in a single sensing unit is desirable, signal interference reduces the measurement accuracy and requires calibration whenever the conditions of use change (*16*, *17*). Because an intrinsic material property is not dependent on the sensor dimension, it has been used to distinguish temperature from the extrinsic values like resistance or capacitance (*18*, *19*). Attempts have been made to decouple temperature and deformation using intrinsic variables like thermoelectric (*20*) and pyroelectric voltage (*21*); however, there has been no stretchable e-skin that can decouple temperature and strain in a single unit.

We explore the ion relaxation dynamics of a deformable ion conductor and fabricate an artificial multimodal ionic receptor (AMI receptor). In a non-Faradaic ion conductor, migration and polarization of ions take place under an applied alternative current (ac) field. The electrical properties of ion conductors are dependent on the measurement frequency (*22*–*24*). The ion migration or polarization dominates at low or high frequencies, respectively (Fig. 1C). The bulk resistance (ion resistance; $R = d/\sigma A$) and the bulk capacitance (geometric capacitance; $C = \epsilon A/d$) depend on ion conductivity (σ), the dielectric constant (ϵ), and geometric factors [area (A) and thickness (d)]. The electrical behavior of an ion conductor can be interpreted by the equivalent circuit model. A Bode plot of an ion conductor is composed of three distinct regions depending on ac frequency (supplementary text, section S1; and fig. S1): the diagonal line in the low-frequency region (dominated by the electric double layer), the flat line in the middle-frequency region (dominated by ion migration), and the diagonal line in the high-frequency region (dominated by molecular polarization) (*25*, *26*). R and C can be approximated by the real impedance in the flat region ($R \approx Z_{re}$) and by the imaginary impedance in the diagonal region ($C \approx 1/\omega Z_{im}$), respectively, where ω is angular frequency.

The discharging process takes place in a RC parallel circuit in a certain time scale called the charge relaxation time ($\tau = \epsilon/\sigma = RC$) (*27*) [different from the conductivity relaxation (*28*)]. The charge relaxation frequency (τ^{-1}) is the cutoff frequency between the flat line and the high-frequency diagonal line in a Bode plot. Figure 1D shows the change of Bode plot under mechanical stretching. The entire impedance plot shifts down because the impedance from R and C decreases with stretching. However, τ^{-1}, consisting of the intrinsic variables (σ, ϵ), does not change with stretching because the dimensional parameters cancel each other. Figure 1E shows the change in the Bode plot under heating. R moves down by heating, and τ^{-1} shifts to a higher frequency. The downshift in the flat region is much larger than the downshift in the diagonal region because of the higher temperature sensitivity of ion conductivity than of the dielectric constant. Figure 1F states the principle of thermo-mechanical decoupling. The relaxation time can be used as a strain-insensitive intrinsic variable for detecting temperature without geometrical information of the sensor. The capacitance can be used as a temperature-insensitive extrinsic variable for sensing the strain. The temperature effect in the capacitance can be removed through normalization to a reference capacitance (C_o) at the measured temperature. These two variables (τ and C/C_o) provide complete thermomechanical decoupling and allow simultaneous monitoring of mechanical and thermal stimulations.

An ion conductor, 1-ethyl-3-methylimidazolium bis(trifluoromethylsulfonyl)imide (EMIM TFSI), was spin-coated (5 μm in thickness) on a stretchable composite electrode film made with Ag nanowires and a thermoplastic block copolymer, polystyrene-*block*-poly(ethylene butylene)-*block*-polystyrene (SEBS) (*29*). By stacking the two multilayers, the ion conductor layer was sandwiched between the two electrodes (materials and methods, and fig. S2). The multilayers had good adhesion owing to the conformal contact between the thin viscoelastic layers. Bode plots of the ion conductors with various ion concentrations (1 to 50 wt %) were measured at 20°C (Fig. 2A). The resistance decreased markedly with increasing ion concentration owing to the reduced viscosity and increased mobile ions. Three parameters were considered in choosing a proper ion conductor: (i) Low ion concentration is favored to obtain a high temperature sensitivity because of the high activation energy (fig. S3). (ii) Both R and C should be measurable at accessible frequencies (10^2 to 10^6 Hz). (iii) Large R assures a large impedance

[1]Department of Materials Science and Engineering, Pohang University of Science and Technology (POSTECH), Pohang 37673, Republic of Korea. [2]Department of Chemical Engineering, Stanford University, Stanford, CA 94305-5025, USA. [3]Department of Chemical Engineering, Pohang University of Science and Technology (POSTECH), Pohang 37673, Republic of Korea.
*Present address: Department of Mechanical Engineering, Koç University, Istanbul 34450, Turkey.
†Corresponding author. Email: zbao@stanford.edu (Z.B.); ujeong@postech.ac.kr (U.J.)

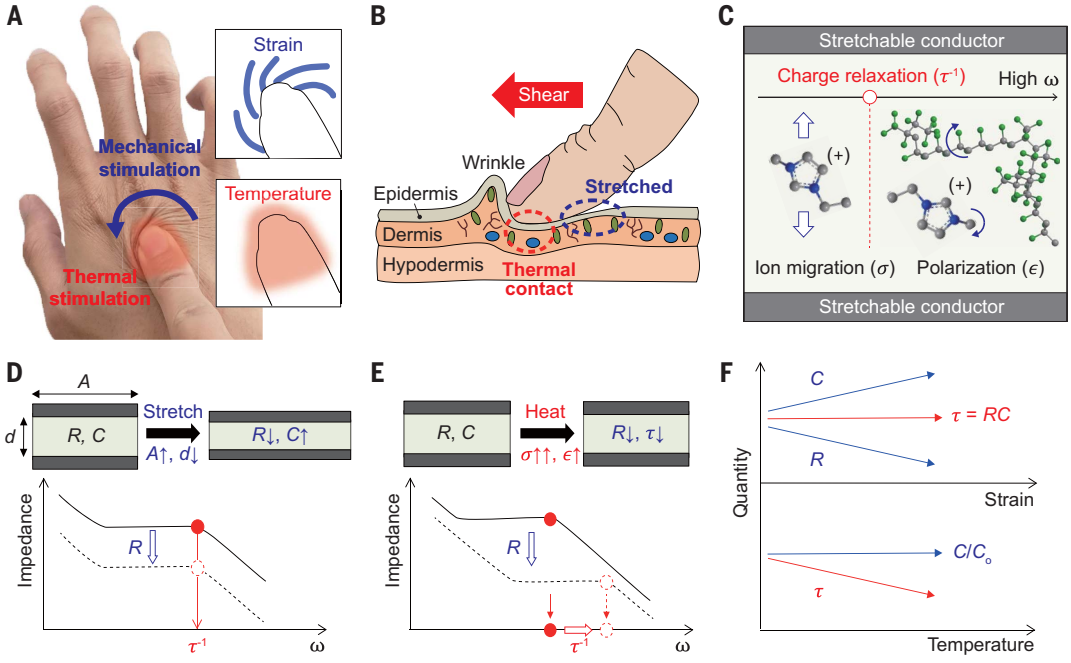

Fig. 1. Concepts for the AMI receptor. (**A**) Conceptual strain and temperature profiles on real skin when the mechanical thermal stimuli are applied simultaneously. (**B**) Scheme of real skin containing thermoreceptors and mechanoreceptors for recognizing tensile strain and temperature distinctively. The dashed red and blue circles indicate the region that changed temperature by contact with an external object and the region stretched by shear force respectively. (**C**) Frequency-dependent observable behaviors of the ion conductor to the alternative electric field. (**D**) Schematic Bode plot showing a parallel downshift by stretching, changing the resistance (*R*) but maintaining the charge relaxation frequency (τ^{-1}). The solid red circle and dashed circle represent cutoff frequency point on the Bode plot before and after applying stimulation, respectively. (**E**) Schematic Bode plot showing a decrease of *R* and an increase of τ^{-1} by heating. The conductivity (σ) increases more than the dielectric constant (ϵ). (**F**) Conceptual plots of the strain-insensitive intrinsic variable (τ or τ^{-1}) (top) and the temperature-insensitive extrinsic variable (C/C_o) (bottom). *R* and *C* are susceptible to strain, and τ decreases by heating.

difference from the stretchable electrode so that less noise is incurred during deformation. We chose the 5 wt % ion concentration condition for the AMI receptor (indicated by a dark blue line in Fig. 2A). Because the resistance of the stretchable electrode (10^2 ohm) was less than 1% of *R* (fig. S4), it was negligible in the electrical characterization.

We set the target temperature sensing around body temperature (20° to 50°C). Figure 2B presents Bode plots of the ion conductor (5 wt %) at various temperatures. The shaded regions indicate the possible frequency ranges at which *R* could be directly measured (the region containing flat lines, colored blue) and *C* could be obtained (the region containing flat lines, colored blue). For the AMI receptor, *R* and *C* were measured at 200 Hz (ω_1) and 5×10^5 Hz (ω_2). ω_1 and ω_2 denote frequency, instead of angular frequency (e.g., $\omega 1 = \omega/2\pi$) This simple impedance analysis at two fixed frequencies is advantageous for real-time monitoring. The validity of this concept was verified by comparing with the values obtained by the conventional Nyquist fitting process (supplementary text, section S2; and fig. S5). In the ion conductors with high ion concentrations (≥5 wt %), the frequency for measuring *C* was out of the accessible range (>10^6 Hz) (fig. S6). Figure 2C shows the temperature dependence of σ and ϵ. σ was about 100 times more sensitive than the relative ϵ. This large sensitivity difference is because σ follows the Arrhenius behavior with a high activation energy, whereas the change of ϵ is rarely affected by temperature variation (*30*). The linear σ behavior in Arrhenius plot implies that the impedance of the sensor was governed by the ion impedance; thus, the contact impedance and the electrode impedance were negligible.

Figure 2D shows the use of ln(τ) as the strain-insensitive variable to detect temperature. All of the plots measured at different strains (ε = 0, 30, 50%) fell into a master curve, indicating that τ was not affected by the dimensional changes (fig. S7). The fitted governing equation had an excellent reliability (coefficient of determination (R^2) = 0.99999) with the measured data at ε = 0% (fig. S8). The temperature sensitivity was 10.4% per °C (supplementary text, section S3), and the average measurement error at ε = 50% was only 0.29°C (table S1). The AMI receptor showed identical temperature measurements during 5000 strain cycles at ε = 30% and had no thermal hysteresis under repeated temperature cycles (fig. S8). The temperature accuracy under mechanical deformation is superior to the stretchable thermistors (fig. S9 and table S2) (*16*–*19*, *31*–*35*). Temperature sensing by τ does not require a calibration process; thus, it can be used with any surface curvature and topology. When ln(*R*) was used for temperature measurements, it caused a large measurement error (+2.6°C) under stretching (ε = 50%) because it is an extrinsic variable (fig. S10).

The capacitance is affected by both temperature and strain. We normalized *C* with C_o to remove the temperature effect of the dielectric constant. C_o is a capacitance measured at the frequency of ω_2 in the nonstrained state at the corresponding temperature. It can be obtained from a fitting curve between C_o and ln(τ) (fig. S11). Figure 2E shows strain sensing using C/C_o as a temperature-insensitive extrinsic variable. All the plots of C/C_o versus uniaxial strain at various temperatures fell into a master curve; thus, the strain could be calculated from a curve-fitting equation. The response of C/C_o to stretching was reproducible during repeated stretching cycles at different strains (Fig. 2F and fig. S11).

We confirmed real-time multimodal sensing with several tests. First, we attached the AMI receptor onto the skin above the jugular vein and monitored body temperature (*36*) before and after drinking alcohol (Fig. 2G). Temperature was measured under normal and stretched states by moving the neck. The measured temperature increased from 36.13° to 36.94°C after drinking and then decreased to 36.35°C after 12 hours, which matched well with temperature measured by an infrared (IR) thermometer, whereas the measured temperature under normal and stretched states showed a small difference (~0.12°C) (fig. S12). Additionally, we attached the AMI receptor on the wrist and measured both strain and temperature while the wrist was repeatedly bent and the environmental temperature was varied (fig. S13 and movie S1). The measured strain tracked the bending motions and the

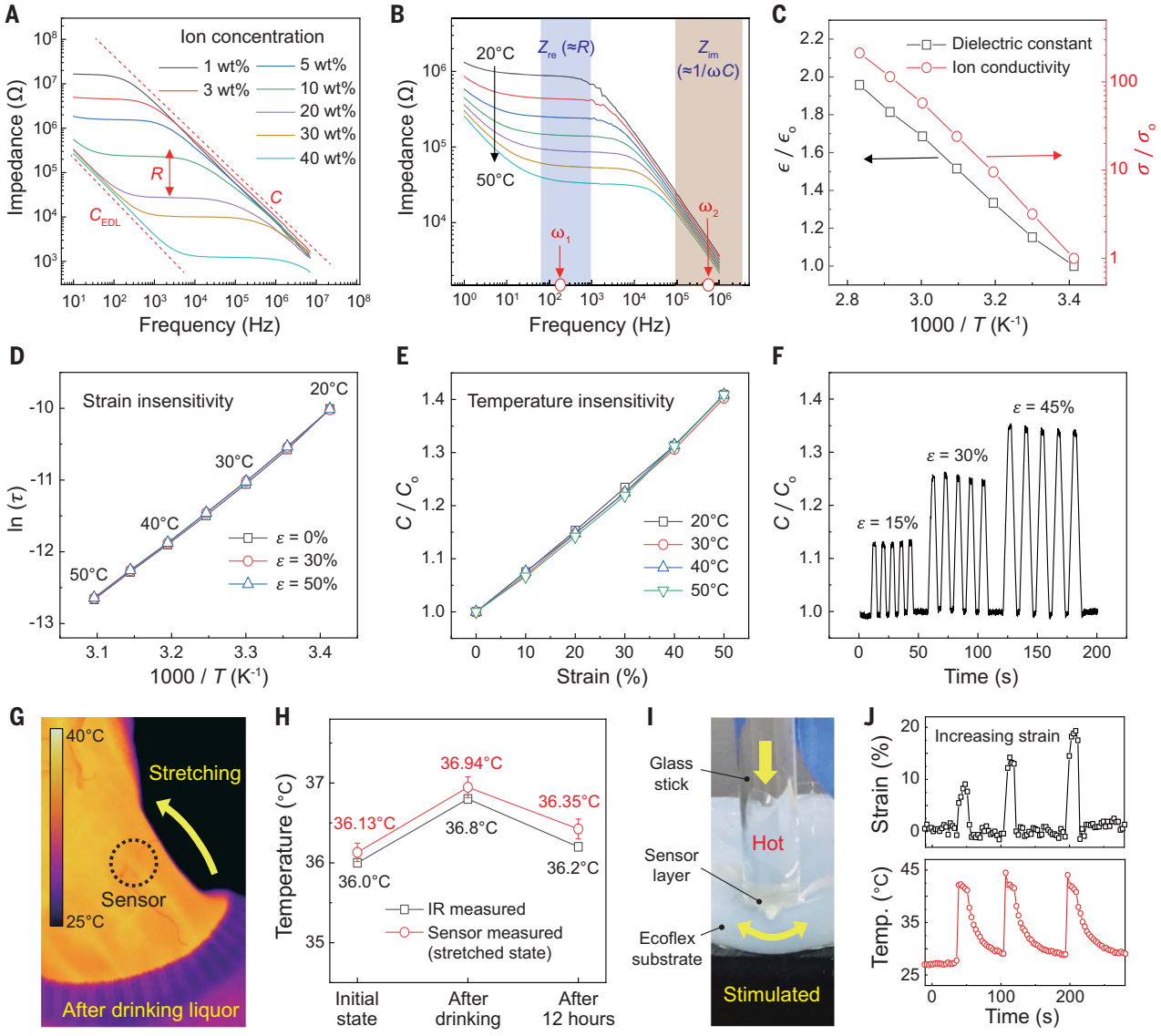

Fig. 2. Characteristics of the AMI receptor and its responses to heating and stretching. (**A**) Bode plots obtained from ion conductors with different ion concentrations at 20°C. (**B**) Bode plots from an ion conductor (5 wt % ion concentration) at various temperatures. The circles with red outlines indicate the frequencies at which R (ω_1) and C/C_o (ω_2) were measured. (**C**) Responses of the normalized dielectric constant and the normalized conductivity to temperature change. (**D**) Changes of ln(τ) with respect to T^{-1} (T, temperature) at three tensile strains (ε). ln(τ) is insensitive to strains. (**E**) Changes in C/C_o as a function of tensile strains at different temperatures. C/C_o is insensitive to temperature. (**F**) Response of C/C_o during repeated stretching cycles at different tensile strains. (**G** and **H**) IR camera image of an AMI receptor sensor attached to the skin (G) and measured temperature changes before and after drinking alcohol in the stretched state (H). (**I** and **J**) Camera image showing the stretched AMI receptor sensor on an elastomer substrate when pressed by a hot glass stick (I) and the corresponding changes of strain and temperature (J).

measured temperature followed the environmental temperature history, without signal interference, indicating that the AMI receptor is thermomechanically decoupled completely during real-time monitoring.

To check the thermomechanical decoupling upon contact (pressure), a hot (45°C) glass stick was pressed repeatedly on the AMI receptor, which was placed on a thick, soft elastomer substrate (Fig. 2H). The applied force was varied (0.4, 0.8, and 1.2 N), and the corresponding strain of the sensor was measured (8.6, 13.9, and 19.1%). The measured temperature showed the same profiles despite the different degrees of deformation. When pressed by a cold glass stick repeatedly with a fixed force (1.2 N), the measured strain did not change, but the measured temperature increased gradually (fig. S14).

We fabricated the multimodal ion-electronic skin (IE^M-skin) with 10-by-10 AMI receptor arrays and placed it on a dummy hand (Fig. 3, A and B). The ion conductor film was sandwiched between patterned electrodes. We emulated the mechanical behavior of thin skin to realize 3D deformations by inserting a low-friction interface between the IE^M-skin and the bottom elastomer substrate. The interface was made by rubbing silica powder (or baby powder) on the bottom substrate. The edges of the IE^M-skin and the bottom substrate were bonded with a silicon adhesive. The contact point was recognized by the temperature profile in the IE^M-skin. When a shear stress was applied to the IE^M-skin, the front of the contact point created wrinkles and the rear of the contact point was stretched (Fig. 3C).

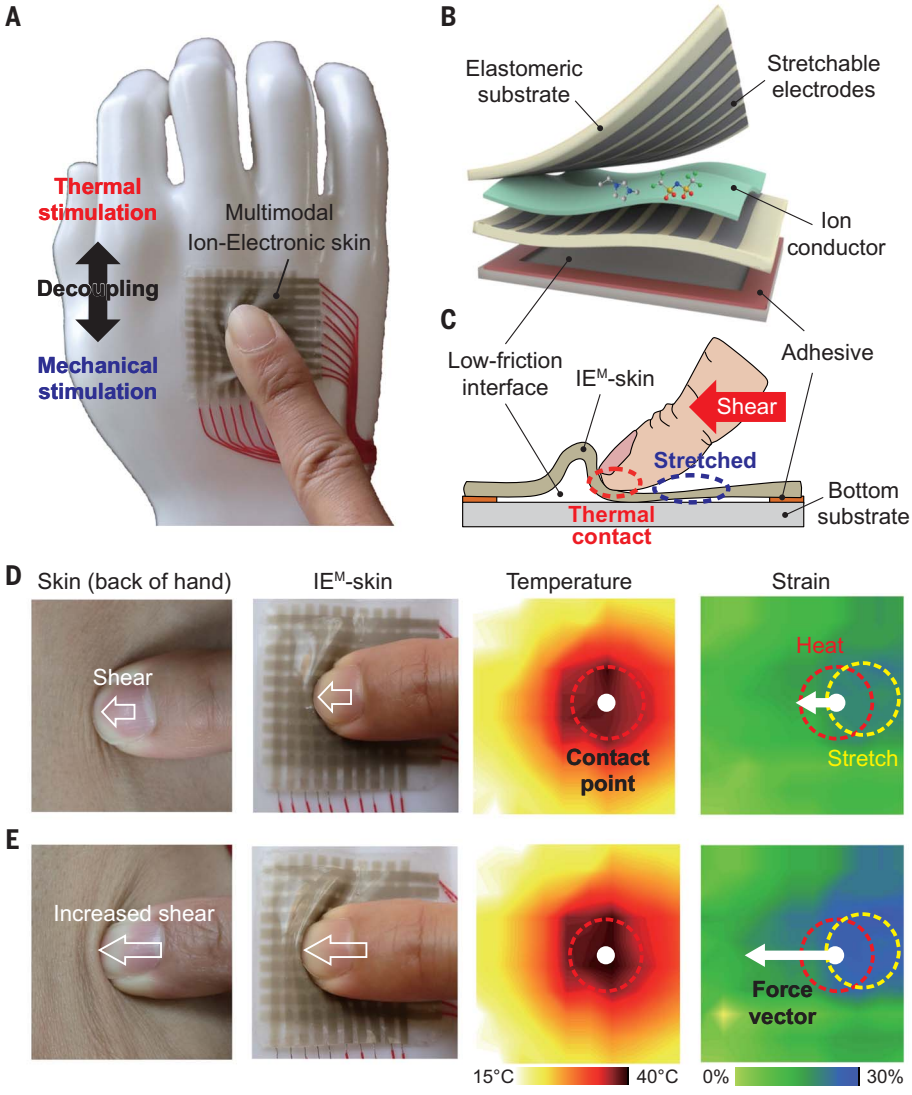

Fig. 3. Structure of IE^{M}-skin and the response to unidirectional shear force. (**A**) Camera image of the IE^{M}-skin attached to a dummy hand. (**B**) Structure of the IE^{M}-skin. A pixelated matrix of the AMI receptors is placed on a low-friction layer, and the edges are adhered to a bottom elastomer substrate. (**C**) Response of the IE^{M}-skin to a shear force. It forms the wrinkles in the front of the force contact point, and it is stretched at the rear. (**D** and **E**) Responses of the IE^{M}-skin under a weak (D) and strong (E) unidirectional shear applied with the forefinger. Camera images of real skin on the back of a hand and the IE^{M}-skin are shown, as well as the corresponding profiles of temperature and strain. The white arrows in the camera images and the white dots in the temperature profiles represent the shear direction and the contact point, respectively. The red and yellow dashed circles and the solid white arrows indicate the heated region, strained region, and the force vector, respectively.

The 2D temperature and strain profiles were obtained from the collected strain dataset of τ and C/C_o in the pixelated AMI receptors. The temperature profile was obtained without any assumption about the type of deformation because τ is not affected by dimensional changes. For the 2D strain profile, each strain value of the AMI receptor was approximated to the strain under uniaxial deformation by applying the measured C/C_o to the governing equation acquired by the uniaxial strain test. This method is feasible, regardless of whether the deformation is uniaxial or biaxial, because the calculated strain reflects the area change in the small region of the AMI receptor. Figure 3D shows a series of images (real skin, IE^{M}-skin, 2D temperature profile, and 2D strain profile) from when a directional shear was applied with a forefinger. The arrows in the camera images present the shear direction and wrinkles that were observed in the IE^{M}-skin similarly to those in biological skin. The contact region was identified as the highest-temperature region in the temperature profile (indicated by a red dashed circle with a white dot marking the center). Projection of the contact region in the strain profile shows that the stretched region is located behind the contact region in the shear direction. As the shear force increased, the strain profile became prominent in the stretched region, whereas the temperature profile did not show any noticeable change (Fig. 3E). Because the compression strain was released by the 3D wrinkle formation (fig. S15), the shear direction was determined as extending from the stretched region to the contact region (indicated by the white arrow). In this way, any unidirectional shear could be recognized by the force vector (fig. S16). When normal force (pressure) was applied on the IE^{M}-skin, the centers of the heated region and the strained region overlapped (fig. S17). Note that the temperature of the IE^{M}-skin in this study changes according to the environmental temperature; thus, it may not be possible to detect contact with an object that has the same temperature as the environment. This situation can be avoided by embedding a heater in the substrate of the IE^{M}-skin to keep a constant substrate temperature (e.g., body temperature). When an object with a temperature lower or higher than the substrate temperature comes in contact with IE^{M}-skin, the temperature perturbation changes the relaxation times of the contacted AMI receptors, allowing the IE^{M}-skin to detect the object until the object temperature reaches the substrate temperature by heat flux through the interface.

We extended the shear analysis to various multiple shearing motions (pinch, spread, tweak, shear, and touch) (Fig. 4A). For each motion, the corresponding temperature and strain profile of the IE^{M}-skin are displayed. The spread motion had opposite shear directions on the same line, and the strain was distributed in between the contact regions. The tweak motion showed the opposite shear directions next to each other. When shear was combined with touch, the shear direction and the touch were both detected. This recognition of the additional contact on the fully stretched region implies that the temperature sensing would play an important role in the perception of touch in real skin. In the shear-based motions, the number of the contact regions is the same or larger than the number of the stretched regions.

Torsion can generate more complex strain fields and wrinkles (fig. S18). Figure 4B presents a counterclockwise torsion and the corresponding strain analysis. The contact region from the temperature profile was projected in the strain profile. Multiple strain regions were seen (labeled 1, 2, and 3). The largest (region 1) and smallest (region 3) strain regions were formed at the front and the rear of the torsion angle, respectively. The strain field at the bottom of Fig. 4B presents the vector analysis of the torsional shear force. The thin yellow arrows

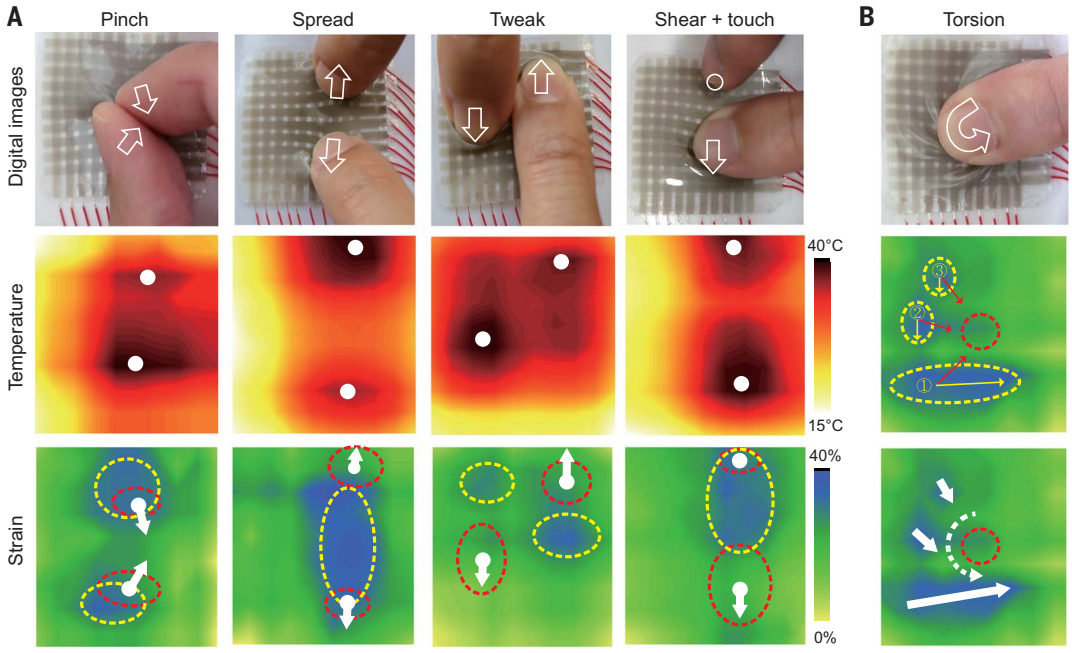

Fig. 4. Complex strain fields under multiple stress and torsion. (**A**) Camera images of the IE^{M}-skin under stimulations involving multiple stresses (pinch, spread, tweak, and shear and touch). The corresponding temperature and strain profiles are shown together. In the strain profiles, the contact region (white dots), strained region (yellow dashed circles), heated region (red dashed circles), and the force vector (solid white arrows) are shown. (**B**) Camera image of the IE^{M}-skin under torsion. The strain profiles display the vector analysis. The numbers 1, 2, and 3 indicate different strain regions. The thin yellow arrows, thin red arrows, and thick white arrows represent the local strain directions, the shear directions from the strained region to the contact point, and the local torsion vectors, respectively.

represent the local strain directions. They were combined with the thin red arrows, which indicate the shear directions from the center of the strain region to the contact point. The local torsion vectors (indicated by thick white arrows) were anticipated by the vector sum between the local strain and the local shear. The local torsion vectors describe the torsion direction and the relative magnitudes along the torsion angle.

On the basis of ion relaxation dynamics, we propose two independent variables for measuring strain and temperature simultaneously from a single sensor unit. The charge relaxation time (τ) is an intrinsic variable for measuring temperature independent of dimensional changes, whereas the normalized capacitance (C/C_o) is an extrinsic variable that is sensitive to dimensional changes (strain). We realized skin-like real-time multimodal detection by analyzing the strain field and temperature field under various tactile motions (shear, pinch, spread, torsion, and so on). The concept can be extended to sensing other stimulations that cause changes in σ or ϵ. For instance, chemical stimulation can be detected using τ without signal interference by mechanical deformation (fig. S19) (*37*).

REFERENCES AND NOTES

1. R. S. Johansson, A. B. Vallbo, *J. Physiol.* **286**, 283–300 (1979).
2. F. H. Silver, J. W. Freeman, D. DeVore, *Skin Res. Technol.* **7**, 18–23 (2001).
3. K. Efimenko *et al.*, *Nat. Mater.* **4**, 293–297 (2005).
4. B. Delhaye, A. Barrea, B. B. Edin, P. Lefèvre, J.-L. Thonnard, *J. R. Soc. Interface* **13**, 20150874 (2016).
5. W. Jänig, in *Handbook of Clinical Neurology*, A. A. Romanovsky, Ed. (Elsevier, 2018) vol. 156, chap. 2, pp. 47–56.
6. T. Someya, M. Amagai, *Nat. Biotechnol.* **37**, 382–388 (2019).
7. J. Ge *et al.*, *Nat. Commun.* **10**, 4405 (2019).
8. J. Kim, A. S. Campbell, B. E.-F. de Ávila, J. Wang, *Nat. Biotechnol.* **37**, 389–406 (2019).
9. I. You *et al.*, *Adv. Mater.* **28**, 6359–6364 (2016).
10. H. U. Chung *et al.*, *Science* **363**, eaau0780 (2019).
11. L. E. Osborn *et al.*, *Sci. Robot.* **3**, eaat3818 (2018).
12. G. Cheng *et al.*, *Proc. IEEE* **107**, 2034–2051 (2019).
13. Y. Liu *et al.*, *Nat. Biomed. Eng.* **3**, 58–68 (2019).
14. Q. Hua *et al.*, *Nat. Commun.* **9**, 244 (2018).
15. D. H. Ho *et al.*, *Adv. Mater.* **28**, 2601–2608 (2016).
16. H. Ota *et al.*, *Nat. Commun.* **5**, 5032 (2014).
17. T. Q. Trung, S. Ramasundaram, B. U. Hwang, N. E. Lee, *Adv. Mater.* **28**, 502–509 (2016).
18. R. C. Webb *et al.*, *Nat. Mater.* **12**, 938–944 (2013).
19. T. Q. Trung *et al.*, *ACS Appl. Mater. Interfaces* **11**, 2317–2327 (2019).
20. F. Zhang, Y. Zang, D. Huang, C. A. Di, D. Zhu, *Nat. Commun.* **6**, 8356 (2015).
21. N. T. Tien *et al.*, *Adv. Mater.* **26**, 796–804 (2014).
22. R. Gerhardt, *J. Phys. Chem. Solids* **55**, 1491–1506 (1994).
23. X.-Z. R. Yuan, C. Song, H. Wang, J. Zhang, *Electrochemical Impedance Spectroscopy in PEM Fuel Cells: Fundamentals and Applications* (Springer, 2009) pp. 139–192.
24. A. K. Jonscher, *J. Phys. D* **32**, R57–R70 (1999).
25. B.-A. Mei, O. Munteshari, J. Lau, B. Dunn, L. Pilon, *J. Phys. Chem. C* **122**, 194–206 (2017).
26. C. Gainaru *et al.*, *J. Phys. Chem. B* **120**, 11074–11083 (2016).
27. H. A. Haus, J. R. Melcher, in *Electromagnetic Fields and Energy* (Massachusetts Institute of Technology: MIT OpenCourseWare), chap. 7.7; http://ocw.mit.edu [accessed 11 December 2019).
28. K. Seeger, *Semiconductor Physics* (Springer, 2013).
29. I. You, M. Kong, U. Jeong, *Acc. Chem. Res.* **52**, 63–72 (2019).
30. Y. Shim, H. J. Kim, *J. Phys. Chem. B* **117**, 11743–11752 (2013).
31. J. Wu *et al.*, *ACS Appl. Mater. Interfaces* **10**, 19097–19105 (2018).
32. G. A. Salvatore *et al.*, *Adv. Funct. Mater.* **27**, 1702390 (2017).
33. C. Yan, J. Wang, P. S. Lee, *ACS Nano* **9**, 2130–2137 (2015).
34. Y. Chen, B. Lu, Y. Chen, X. Feng, *Sci. Rep.* **5**, 11505 (2015).
35. C. Zhu *et al.*, *Nat. Electron.* **1**, 183–190 (2018).
36. H. Ao, J. K. Moon, H. Tanimoto, Y. Sakanashi, H. Terasaki, *Resuscitation* **45**, 111–118 (2000).
37. M. L. Jin *et al.*, *Adv. Mater.* **30**, e1706851 (2018).

ACKNOWLEDGMENTS

Funding: This work was supported by the Center for Advanced Soft-Electronics funded by the Ministry of Education, Science and Technology as a "Global Frontier Project" (CASE-2015M3A6A5072945); a National Research Foundation of Korea (NRF) grant funded by the Korean government (MSIT) (no. NRF-2020R1A2C3012738); and the Technology Innovation Program (10077533, Development of robotic manipulation algorithm for grasping/assembling with the machine learning using visual and tactile sensing information) funded by the Ministry of Trade, Industry, and Energy (MOTIE, Korea). D.G.M. acknowledges support from the U.S. National Science Foundation Graduate Research Fellowship Program under grant no. DGE-114747. **Author contributions:** I.Y., Z.B., and U.J. conceived the concept and designed the experiments. I.Y., D.G.M., N.M., J.Ka., and Z.B. designed the stretchable ion conducting polymer. I.Y., N.M., J.M., and U.J. designed the stretchable electrode. I.Y. and D.G.M. characterized the electrical properties of the ion conductor. I.Y., L.B., and J.Kw. analyzed impedance spectroscopy data with equivalent circuit modeling. I.Y., W.S., and T.Y.K. fabricated the AMI receptor and IE^{M}-skin, then measured the strain and temperature profiles. I.Y., J.B.-H.T., Z.B., and U.J. co-wrote the paper. **Competing interests:** The authors declare that they have no conflict of interest. **Data and materials availability:** All data are available in the main text or the supplementary materials.

SUPPLEMENTARY MATERIALS

science.sciencemag.org/content/370/6519/961/suppl/DC1
Materials and Methods
Supplementary Text
Figs. S1 to S19
Tables S1 and S2
References
Movie S1

10 December 2019; accepted 24 September 2020
10.1126/science.aba5132

MATERIALS SCIENCE

Nanomesh pressure sensor for monitoring finger manipulation without sensory interference

Sunghoon Lee[1], Sae Franklin[2], Faezeh Arab Hassani[1]*, Tomoyuki Yokota[1], Md Osman Goni Nayeem[1], Yan Wang[1], Raz Leib[3], Gordon Cheng[2], David W. Franklin[3], Takao Someya[1,4]†

Monitoring of finger manipulation without disturbing the inherent functionalities is critical to understand the sense of natural touch. However, worn or attached sensors affect the natural feeling of the skin. We developed nanomesh pressure sensors that can monitor finger pressure without detectable effects on human sensation. The effect of the sensor on human sensation was quantitatively investigated, and the sensor-applied finger exhibits comparable grip forces with those of the bare finger, even though the attachment of a 2-micrometer-thick polymeric film results in a 14% increase in the grip force after adjusting for friction. Simultaneously, the sensor exhibits an extreme mechanical durability against cyclic shearing and friction greater than hundreds of kilopascals.

Precise measurement of finger manipulation is critical to understand and reproduce the sense of natural touch for applications in prosthetic hands (*1*, *2*), human-machine interaction (*3*, *4*), clinical restoration of hand function (*5*, *6*), and digital archiving of a craftsman's skills (*7*, *8*). Advances in examining the sense of touch have come from optical-based estimation of finger forces based on nail color (*9*, *10*), force sensor–integrated objects (*11*), and instrumented gloves (*12*–*16*). An application of soft and flexible sensors to the fingertip enabled direct measurement of the force between the finger and other objects (*17*–*19*); the mechanical properties of the sensors decreased physical interferences that would arise from the mechanical mismatch between the skin and sensors. Furthermore, use of elastomeric substrates (*20*, *21*) and/or a reduction in sensor thickness (*22*, *23*) has substantially improved the conformability of sensors to the skin and enabled more accurate monitoring of finger touch. Recently, ultrathin (a few micrometers) sensors have been demonstrated, which reduce the loss in sensation (*24*–*26*). However, the challenge is to monitor finger touch without losing any touch sensation (*27*). Covering the human finger with any object, even a superthin layer, causes substantial degradation of natural touch, affecting the sensory information and distorting the inherent control (*28*–*30*).

[1]Department of Electrical Engineering and Information Systems, School of Engineering, The University of Tokyo, 7-3-1 Hongo, Bunkyo-ku, Tokyo 113-8656, Japan. [2]Institute for Cognitive Systems, Department of Electrical and Computer Engineering, Technical University of Munich, Karlstraße 45/II, 80333 München, Germany. [3]Neuromuscular Diagnostics, Department of Sport and Health Sciences, Technical University of Munich, Georg-Brauchle-Ring 60/62, 80992 München, Germany. [4]Institute for Advanced Study, Technical University of Munich, Lichtenbergstrasse 2a, 85748 Garching, Germany.
*Present address: Department of Electrical and Electronic Engineering, University of Bristol, Bristol, UK.
†Corresponding author. Email: someya@ee.t.u-tokyo.ac.jp

We monitor force using sensors directly attached to the highly sensitive fingertip. To minimize sensory interference, we developed ultrathin nanomesh sensors composed of compliant nanoporous structures. Figure 1, A and B, shows an optical image of a pressure sensor on a fingertip and the cross-sectional scanning electron microscopic (SEM) image of the sensor formed on polyimide film, respectively. The nanomesh sensor consists of the following four layers: (i) a polyurethane nanomesh–embedded passivation layer, (ii) a top Au nanomesh electrode layer, (iii) a parylene-coated polyurethane nanomesh intermediate layer, and (iv) a bottom Au nanomesh electrode layer. The four layers are laminated in sequence onto objects, such as skin, without other substrates.

The bottom and top Au nanomesh layers are prepared by using electrospun polyvinyl alcohol (PVA) nanofibers as a sacrificial supporting layer (*31*). The intermediate and passivation layers are made of polyurethane nanofibers that have a diameter in the range of 200 to 400 nm. In the case of the intermediate layer, an additional 200-nm-thick parylene layer is deposited around polyurethane nanofibers. An air gap between the bottom Au electrode layer and the intermediate layer is formed, as shown in Fig. 1B. To ensure mechanical durability while keeping the sensor thin, a passivation layer of polyurethane nanofibers attached with dissolved PVA nanofibers is introduced. The thickness of the intermediate and the passivation layers are ~10.5 and 2.5 μm, respectively. The detailed structure is described in the materials and methods (see also fig. S1).

Layers can be bonded to each other after dissolution of the PVA nanofibers by water mist (fig. S2). When high pressure or shear force is applied, the layers do not detach from each other, maintaining the sensor structure and its functionalities (fig. S3). The top Au nanomesh layer shows a stable conductivity, even though it is formed on a porous and rough nanofiber surface (fig. S4). Therefore, the pressure applied to sensors can be monitored by the capacitance change between the bottom and top Au nanomesh electrodes, because of the deformation of the parylene-coated polyurethane nanomesh intermediate layer. In addition, the pressure sensitivity of the sensor is mainly determined by the mechanical properties of the intermediate layer. The parylene-coated polyurethane intermediate layer was selected for this sensor because it exhibits higher sensitivity compared with a sensor using the polyurethane-only intermediate layer (figs. S5 and S6).

Figure 2A shows the capacitance change of the sensor using the 200-nm parylene-coated polyurethane intermediate layer. The sensitivity (slope of the capacitance change–pressure curve) is 0.141 kPa^{-1} in the low-pressure range (<1 kPa) and 0.010 kPa^{-1} in the high-pressure range (>10 kPa). In addition to the nanomesh intermediate layer, the number of PVA nanofibers used to form the top Au nanomesh layer also affected the sensitivity of the sensor (figs. S7 and S8). When the number of PVA nanofibers was small (with an electrospinning time of 10 min), the sensitivity was 0.028 kPa^{-1}. By contrast, when the number of PVA nanofibers was large (with an electrospinning time of 50 min), the sensitivity decreased to 0.0014 kPa^{-1}. SEM observations showed that the porous structure of the intermediate layer was maintained after the smaller number of PVA nanofibers were dissolved on the surface of intermediate layer (fig. S8B). However, when the number of PVA nanofibers was large, the dissolved PVA filled the pores on the surface of the intermediate layer (fig. S8D). Therefore, to maintain the nanoporous structure of the intermediate layer, a small number of PVA nanofibers was used.

Nanomesh sensors maintained their functionality after repeated cyclic pressing. As shown in Fig. 2B and fig. S9, the change in the performance of the sensor was negligibly small, with a less than 0.15% decrease over 1000 cycles of pressing at 19.6 kPa (capacitance change of 0.658 on the first cycle and 0.659 on the 1000th cycle). In addition, the top Au nanomesh electrode maintained the conductivity without a considerable degradation during the repeated cyclic pressing.

To check the applied pressure dependence of the response time, three pressure levels (0.98, 4.9, and 19.6 kPa) were repeatedly applied for 2 s and released for 2 s while measuring the change in the sensor capacitance (fig. S10). As shown in Fig. 2, C and D, the sensor showed similar response times for each pressure, in which all showed a response time between 190 and 220 ms for the maximum capacitance change of 80%.

Furthermore, nanomesh sensors exhibited durability against friction. The functionality

of the sensors could be maintained even when the sensor surface was rubbed with a vertical pressure of more than 100 kPa. To evaluate the mechanical durability of the sensor against friction, experiments were carried out by repeatedly rubbing the surface of the sensor with a spherical polyurethane ball of 3-mm diameter (fig. S11). The friction force was controlled by an external load weight. When the surface of the sensor was rubbed 300 times with a 50-g weight, the change in electrical characteristics was negligibly small (relative capacitance of 0.997 after 300 cycles) (Fig. 3A). In addition, the nanomesh sensor still exhibited pressure sensitivity after the high friction was applied, for which the sensitivities were 0.077 kPa^{-1} (before friction) and 0.070 kPa^{-1} (after friction) with a change of less than 9.7% (Fig. 3B).

Figure 3, C to E, shows a dynamic change in capacitance during the cyclic friction application. During the rubbing of the nanomesh sensor surface with the polyurethane ball, pressure was applied to the sensor, resulting in an increase in the capacitance. In each cycle, the polyurethane ball passed through the sensor surface twice (forward and backward), resulting in two peaks for each cycle. Figure 3C shows all 300 cycles, and the peak amplitude was 6.63 pF for the first cycle and 6.34 pF for the 300th cycle. Although the amplitude was changed by 4.6%, the pressure due to the friction could be detected with minimal performance change of the pressure sensor properties (Fig. 3, D and E).

The durability of the nanomesh sensors was achieved by the introduction of the thin polyurethane nanomesh–embedded passivation layer. For comparison, a sensor comprising only three layers (top electrode layer, intermediate layer, and bottom Au electrode layer) without the polyurethane nanomesh–embedded passivation layer was prepared. Both sensors were rubbed 10 times by using different load weights between 10 and 100 g (fig. S12, A and B). The nanomesh sensor with the passivation layer showed a sufficiently small change in electrical properties regardless of the weight, such that the change in the sensor capacitance remained less than 4.1% compared with the initial sensor capacitance (fig. S12C). In the case of the sensor without the polyurethane nanomesh–embedded passivation layer, it showed a huge degradation in the sensor performance. The initial capacitance value (capacitance without pressing) was reduced by 79.7% when the surface was rubbed with a weight of 70 g or greater.

The functionality of the top Au nanomesh electrode was evaluated after the application of friction. The conductance of the nanomesh electrode, with and without the passivation layer, was measured after rubbing 10 times with the various friction loads (fig. S12D). For the sensor with the polyurethane nanomesh–

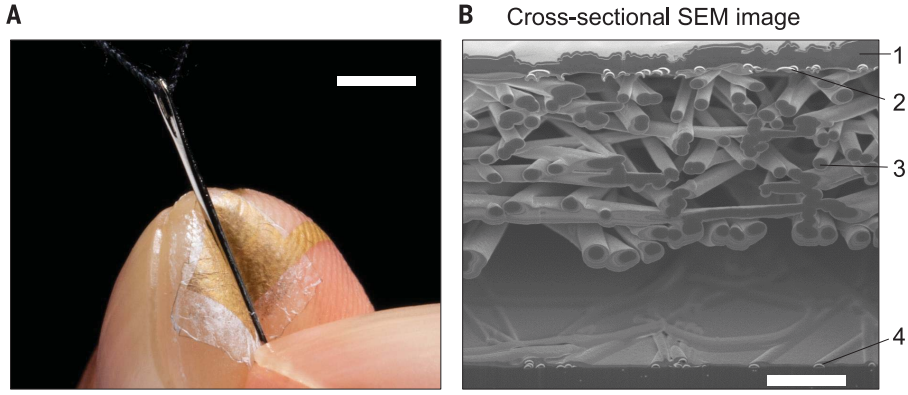

Fig. 1. Structure of the nanomesh pressure sensor. (**A**) Nanomesh pressure sensor attached to an index finger. Scale bar, 5 mm. (**B**) Cross-sectional SEM image of the nanomesh sensor laminated on polyimide film at a tilt angle of 52°. The sensor consists of four layers: a polyurethane nanomesh–embedded passivation layer (1), a top Au nanomesh electrode layer (2), a parylene-coated polyurethane nanomesh intermediate layer with an air gap (3), and a bottom Au nanomesh electrode layer (4). The surface of the sensor is covered by a protective layer during the SEM observation. Scale bar, 5 μm.

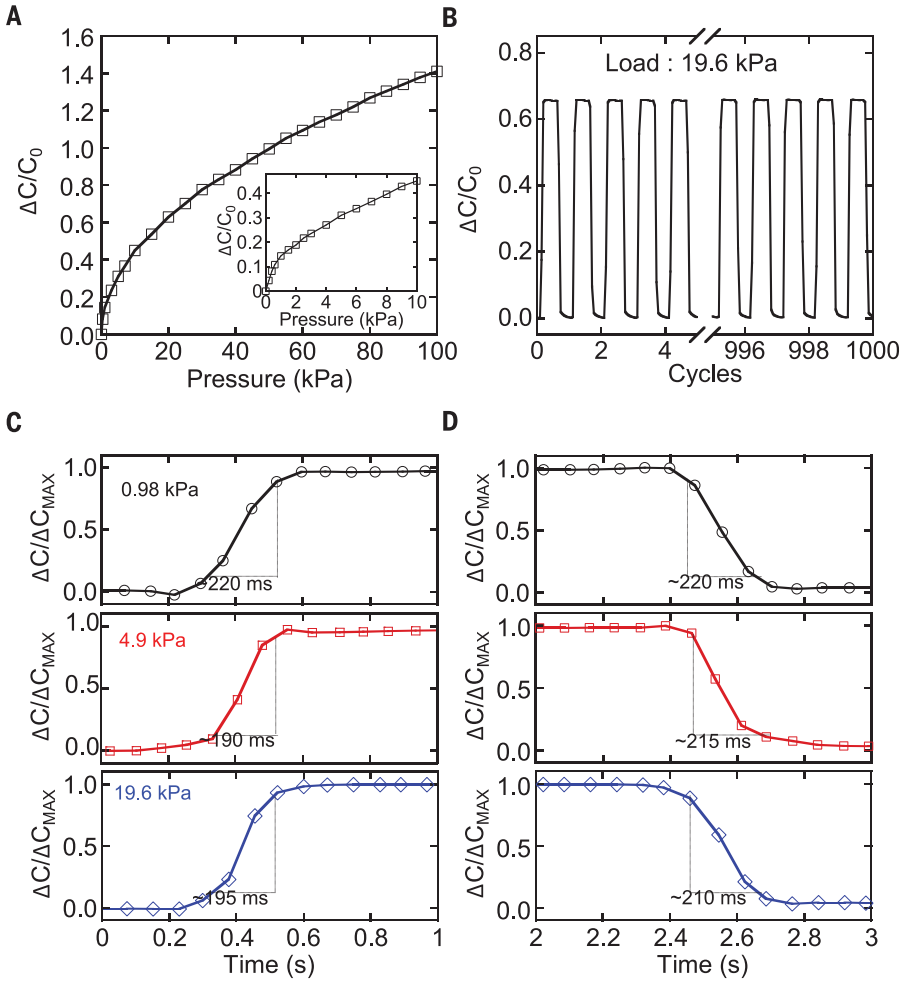

Fig. 2. Electrical characterization of nanomesh pressure sensor. (**A**) Relative capacitance change ($\Delta C/C_0$) as a function of pressure applied to sensor. The inset represents the pressure ranging from 0 to 10 kPa. (**B**) Pressure sensitivity of the nanomesh sensor during 1000 cyclic pressure applications. (**C** and **D**) Response time of the nanomesh sensor when pressing (C) and releasing (D) with three pressure levels (0.98, 4.9, and 19.6 kPa). The capacitance change is normalized by a maximum capacitance change (ΔC_{MAX}) at each pressure application.

embedded passivation layer, the conductance was slightly decreased from 0.0137 to 0.0119 S after the 100-g friction test. This conductance was sufficiently high to measure the capacitance of the sensor. However, in the case of the nanomesh electrode without the passivation layer, the conductance gradually decreased as the weight increased from 10 to 60 g and became less than 1.05×10^{-4} S after rubbing with the weight of 70 g. The SEM observations of the Au nanomesh surface showed that the Au nanomesh layer was partially delaminated when there was no passivation layer (fig. S13). The delaminated area increased with the increase in the friction weight, which was consistent with the change of conductivity.

To scientifically demonstrate the minimal effect of nanomesh sensors on human sensation, we conducted an object-grasping experiment. If the nanomesh material affects the sensory feedback from the finger, then participants will produce a larger grip force for the same load force (*27*, *30*). Eighteen participants grasped and lifted an instrumented object (four different masses) under seven different conditions: bare finger, three thicknesses of nanomesh material, and three thicknesses of parylene film (Fig. 4A). For each material condition and mass, participants produced 10 trials wherein they grasped the object with their thumb and index finger, lifted it, and held for 5 s. For objects with larger masses, the grip force increased (Fig. 4B). These grip forces were similar between the bare finger (red line) and all three nanomesh material thicknesses (blue lines) but were larger for the parylene film conditions (green lines). The same trend in the data can be seen for individual participants (Fig. 4, C and D). After a significant main effect of surface material ($F_{6,371}$ = 2.15, P = 0.04), mass ($F_{1,371}$ = 1425.37, P < 0.001), and their interaction ($F_{6,371}$ = 3.43, P = 0.0026) on the grip force values, post hoc tests were used to examine differences in the surface material. There were no significant differences between the bare finger and any of the nanomesh materials (all P = 1.0), whereas all three parylene film thicknesses exhibited larger grip forces than either the bare finger (all P < 0.001) or the nanomesh materials (all P < 0.001).

During object lifting, grip force increases both with decreasing sensory feedback and decreasing friction between the fingers and the object (*32*). The friction coefficient for each condition was measured by a slip ratio experiment (*27*) (see materials and methods). There was a main effect of surface material on the friction coefficient by using a general linear model ($F_{6,100}$ = 4.94, P < 0.001; Fig. 4E). To remove any potential friction effect, we subtracted the minimum grip force necessary based on the grasp friction coefficient and expressed the amount of grip force exceeding this level as a function of the material thickness (Fig. 4, F and G). There was a significant main effect of surface material ($F_{6,371}$ = 4.5, P < 0.001) and mass ($F_{1,371}$ = 86.42, P < 0.001) but no interaction ($F_{6,371}$ = 1.08, P = 0.375) on adjusted grip force. After this adjustment, post hoc tests demonstrated that application of the nanomesh material has no effect on the grip force across all conditions compared with the bare finger (all comparisons P = 1.0). Even though the parylene film is thinner, the friction-adjusted grip force was increased compared with the bare finger (all comparisons P < 0.01), with a mean (±SEM) increase in friction-adjusted grip force of 13.8 ± 3.3%. Therefore, application of the nanomesh material was not found to interfere with the sensorimotor processing of object grasping, whereas materials of similar thickness (parylene) do affect this processing.

The nanomesh material can be used to measure grasping force with the sensors directly attached to the index finger. To avoid the effect of skin capacitance, we added a shielding layer and an Au nanomesh shield electrode layer (figs. S14 and S15). We compared the capacitance change in the nanomesh sensor with forces measured by a commercial (Nano 25, ATI) force sensor (fig. S16). While pressing on the force sensor with the nanomesh-attached finger, we simultaneously measured the capacitance change in nanomesh sensor

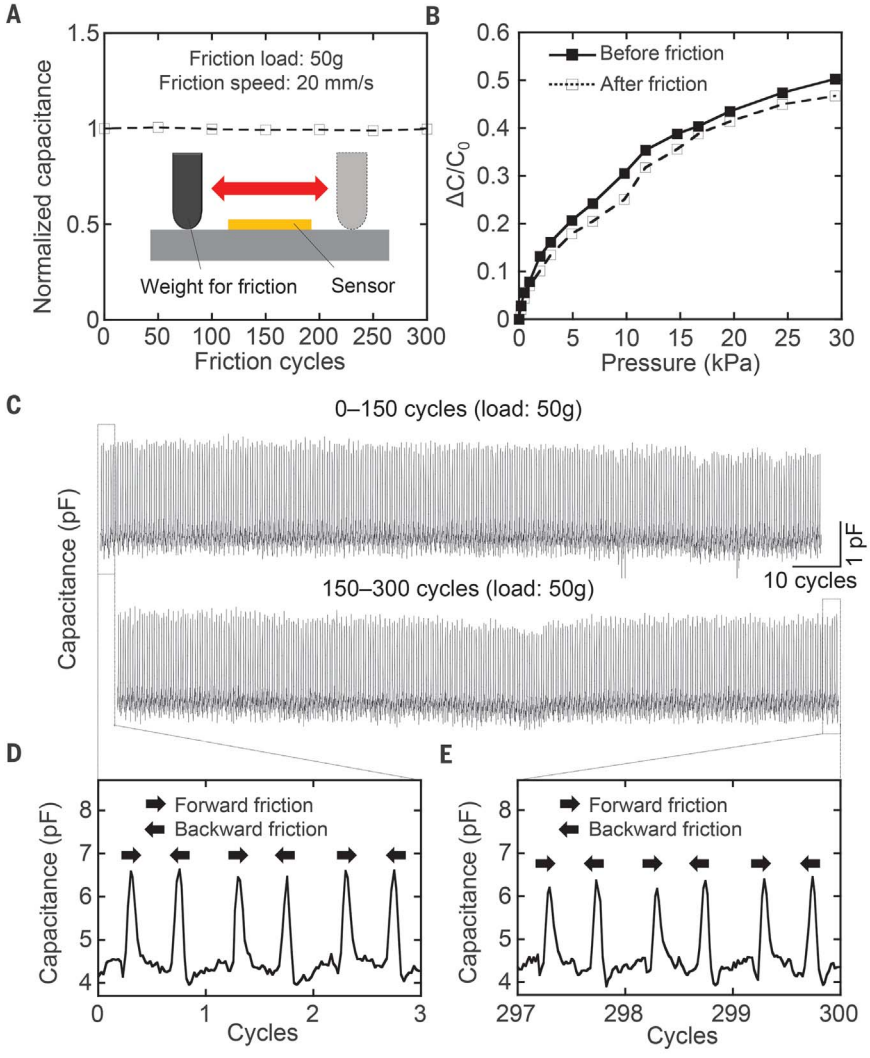

Fig. 3. Durability of the nanomesh sensor against friction. (**A**) Normalized capacitance of the device after the application of friction. The capacitance (initial capacitance without pressing) is normalized by the capacitance before application of friction. The sensor surface is rubbed by a spherical polyurethane ball with a weight of 50 g with a friction speed of 20 mm/s. The red arrow represents the direction of friction (forward and backward friction) for each cycle. (**B**) Pressure sensitivity before the friction test and after 300 cyclic frictions. (**C** to **E**) Dynamic capacitance change during cyclic friction applications.

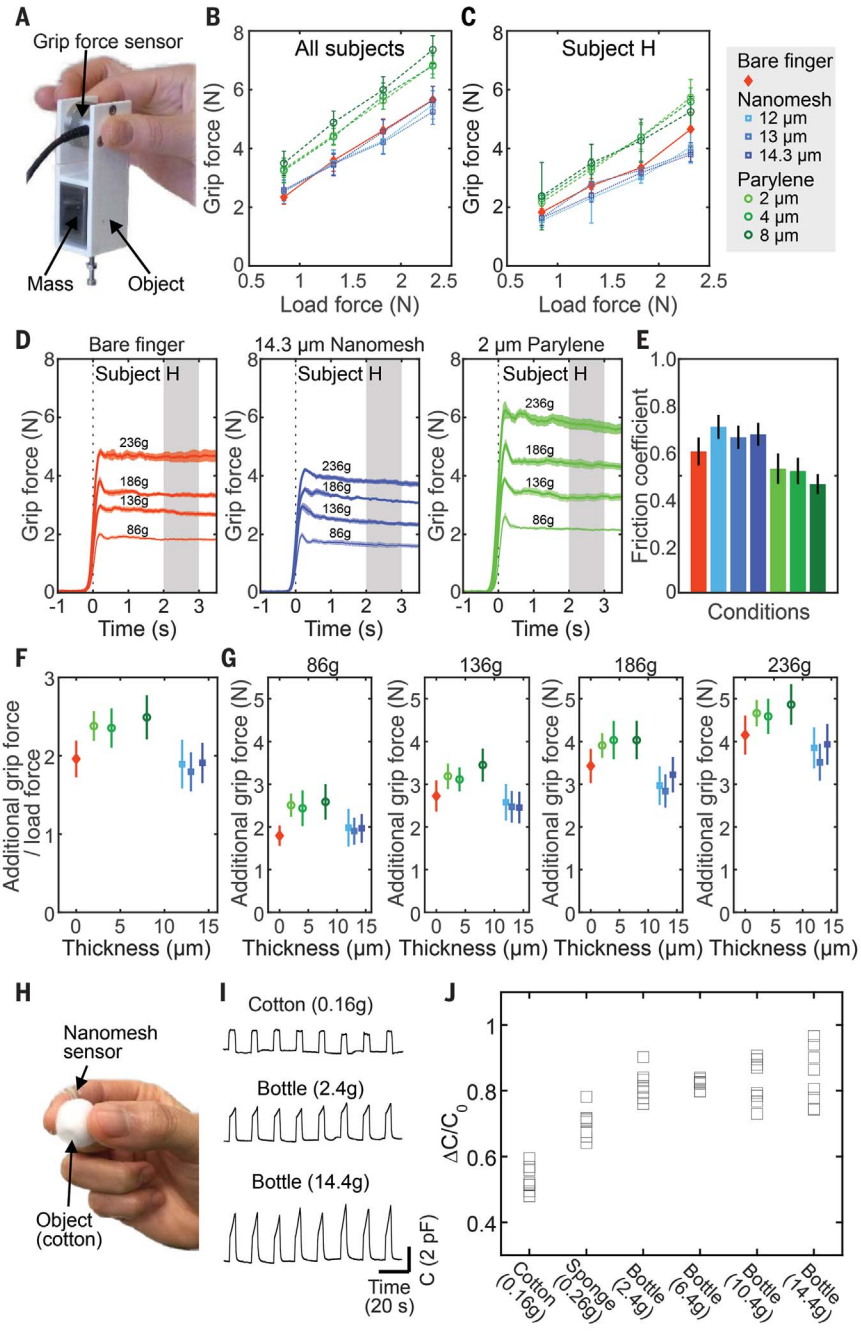

Fig. 4. The effects on human sensation caused by sensor attachment and force monitoring using the nanomesh sensor attached on finger. (**A**) Participants with seven different surface conditions on the index finger lift an object with four different masses that measures grip force. (**B**) Grip force (mean ± SEM) scaled with the load force across all participants. Nanomesh material on the index finger (blue) did not affect this relation compared with the bare finger (red). (**C**) Same relation shown for a single participant. (**D**) Grip force as a function of time (from object liftoff) for the different object masses for a single participant with bare finger, 14.3-μm nanomesh, and 2-μm parylene conditions. The shaded region indicates SEM. The gray-shaded area shows the time over which the grip force was measured for analysis. (**E**) Estimated friction coefficient between the finger and the object under the seven different surface conditions (color indicates condition). (**F**) Friction-adjusted additional grip force (exerted grip force minus minimum grip force, according to object friction) divided by load force plotted as a function of surface material thickness. Despite increased thickness, all nanomesh materials show similar adjusted grip force to the bare finger. (**G**) Additional grip force as a function of material thickness, as shown for each object mass separately. (**H**) A participant grasps a natural object (e.g., cotton ball) while the nanomesh sensor measures the grip force. (**I**) Capacitance as a function of time as the participant grasps different objects (cotton ball and small plastic bottles). (**J**) Nanomesh sensor measurement of grip force for six different natural objects. Each square indicates the peak value of one lift.

and the force change in the force sensor. The test consisted of repetitive cycles in which the force was applied for 5 s and released for 5 s, and the applied finger force gradually increased between repetitions. The nanomesh sensor exhibited the capacitance change in a similar fashion to the various finger forces, demonstrating the ability to measure finger force by using the nanomesh sensor. To show this capability in daily activities, we measured the precision grip while lifting an object. Objects, including a cotton ball, a cubic sponge, and bottles of different weights, were repeatedly lifted for 3 s and released for 12 s. Using the repeated capacitance changes for each object, we show an increase in the grip force, as measured by the nanomesh sensor, due to different shape or weights of objects (Fig. 4, H to J, and fig. S17), although there are trial-by-trial variations owing to feedforward planning (*33*) and motor noise (*34*).

We have demonstrated the monitoring of finger force without detectable effects on human sensation. The nanomesh sensors exhibit mechanical durability against shearing and friction while the ultrathin compliant structure preserves human sensitivity. Simultaneous achievement of imperceptible operation and superior durability opens the possibility of pressure monitoring in applications that require precise and continuous monitoring of motions in natural states. To improve the accuracy of estimated force, an increased number of pressure sensors and acquisition of a spatial pressure distribution will be needed. The development of stretchable and/or water-

resistive pressure sensors would further enhance the stability of sensors and enable a long-term pressure monitoring of finger and other biological objects. (figs. S18 and S19).

REFERENCES AND NOTES

1. A. Chortos, J. Liu, Z. Bao, *Nat. Mater.* **15**, 937–950 (2016).
2. H. Zhao, K. O'Brien, S. Li, R. F. Shepherd, *Sci. Robot.* **1**, eaai7529 (2016).
3. T. Yamada *et al*., *Nat. Nanotechnol.* **6**, 296–301 (2011).
4. C. Wang *et al*., *Nat. Mater.* **12**, 899–904 (2013).
5. G. J. Snoek, M. J. IJzerman, F. A. C. G. in 't Groen, T. S. Stoffers, G. Zilvold, *Spinal Cord* **38**, 244–249 (2000).
6. F. J. Valero-Cuevas, *J. Biomech.* **38**, 673–684 (2005).
7. N. Jowett, V. LeBlanc, G. Xeroulis, H. MacRae, A. Dubrowski, *Am. J. Surg.* **193**, 237–242 (2007).
8. A. Erol, G. Bebis, M. Nicolescu, R. D. Boyle, X. Twombly, *Comput. Vis. Image Underst.* **108**, 52–73 (2007).
9. S. A. Mascaro, H. H. Asada, *IEEE Trans. Robot. Autom.* **17**, 698–708 (2001).
10. Y. Sun, J. M. Hollerbach, S. A. Mascaro, *IEEE Trans. Biomed. Eng.* **55**, 2363–2371 (2008).
11. A. Naceri *et al*., *J. Neurophysiol.* **117**, 2025–2036 (2017).
12. M. Santello, M. Flanders, J. F. Soechting, *J. Neurosci.* **18**, 10105–10115 (1998).
13. L. Dipietro, A. M. Sabatini, P. Dario, *IEEE Trans. Syst. Man Cybern. C* **38**, 461–482 (2008).
14. J. Lee *et al*., *Adv. Mater.* **27**, 2433–2439 (2015).
15. S. Sundaram *et al*., *Nature* **569**, 698–702 (2019).
16. E. Battaglia *et al*., *IEEE Trans. Haptics* **9**, 121–133 (2016).
17. S. Gong *et al*., *Nat. Commun.* **5**, 3132 (2014).
18. A. P. Gerratt, H. O. Michaud, S. P. Lacour, *Adv. Funct. Mater.* **25**, 2287–2295 (2015).
19. Y. Gao *et al*., *Adv. Mater.* **29**, 1701985 (2017).
20. C. Dagdeviren *et al*., *Nat. Commun.* **5**, 4496 (2014).
21. Y. Cao *et al*., *Small* **14**, e1703902 (2018).
22. S. Lee *et al*., *Nat. Nanotechnol.* **11**, 472–478 (2016).
23. D. H. Kim *et al*., *Science* **333**, 838–843 (2011).
24. M. Kaltenbrunner *et al*., *Nature* **499**, 458–463 (2013).
25. Y. Tetsu *et al*., *Appl. Phys. Express* **10**, 087201 (2017).
26. M. Kondo *et al*., *Sci. Adv.* **6**, eaay6094 (2020).
27. G. Westling, R. S. Johansson, *Exp. Brain Res.* **53**, 277–284 (1984).
28. C. K. Bensel, *Ergonomics* **36**, 687–696 (1993).
29. A. Kopka, J. M. Crawford, I. J. Broome, *Acta Anaesthesiol. Scand.* **49**, 459–462 (2005).
30. S. Bilaloglu *et al*., *J. Neurophysiol.* **115**, 1122–1131 (2016).
31. A. Miyamoto *et al*., *Nat. Nanotechnol.* **12**, 907–913 (2017).
32. R. S. Johansson, J. R. Flanagan, *Nat. Rev. Neurosci.* **10**, 345–359 (2009).
33. R. J. van Beers, *Neuron* **63**, 406–417 (2009).
34. A. A. Faisal, L. P. J. Selen, D. M. Wolpert, *Nat. Rev. Neurosci.* **9**, 292–303 (2008).

ACKNOWLEDGMENTS

We thank T. Sakurai, Y. Ukiya, T. Mori, M. Sudama, S. Nagai, and M. Mori of the University of Tokyo (Japan) for the technical support and fruitful discussions. We also thank F. Bergner, K. Stadler, and S. Stenner of the Technical University of Munich (Germany) for technical support with the experimental device. **Funding:** This work was supported by the Japan Science and Technology (JST) ACCEL (grant number JPMJMI17F1), Japan Society for the Promotion of Science (JSPS) KAKENHI (grant number 17H06149), and the Technische Universität München – Institute for Advanced Study, funded by the German Excellence Initiative (and the European Union Seventh Framework Programme under grant agreement n° 291763). **Author contributions:** S.L., F.A.H., M.O.G.N., and Y.W. fabricated the nanomesh devices. S.L., F.A.H., M.O.G.N., Y.W., T.Y., and T.S. contributed the electric and mechanical characterizations and analysis of the nanomesh devices. S.F., R.L., G.C., and D.W.F. contributed to the evaluation of the effect on human sensation caused by sensor attachment. S.L., S.F., R.L., and D.W.F. performed the calibration and measurement of natural objects. S.L., S.F., F.A.H., D.W.F., and T.S. wrote the manuscript. T.S. supervised this project. **Competing interests:** The authors declare no competing interests. **Data and materials availability:** All data supporting the findings of this study are included within either the paper or the supplementary materials.

SUPPLEMENTARY MATERIALS

science.sciencemag.org/content/370/6519/966/suppl/DC1
Materials and Methods
Figs. S1 to S19
References (*35*–*40*)

24 May 2020; accepted 15 October 2020
10.1126/science.abc9735

STELLAR ASTROPHYSICS

An extremely metal-deficient globular cluster in the Andromeda Galaxy

Søren S. Larsen[1]*, Aaron J. Romanowsky[2,3], Jean P. Brodie[3,4], Asher Wasserman[3]

Globular clusters (GCs) are dense, gravitationally bound systems of thousands to millions of stars. They are preferentially associated with the oldest components of galaxies, so measurements of their composition can constrain the build-up of chemical elements in galaxies during the early Universe. We report a massive GC in the Andromeda Galaxy (M31), RBC EXT8, that is extremely depleted in heavy elements. Its iron abundance is about 1/800 that of the Sun and about one-third that of the most iron-poor GCs previously known. It is also strongly depleted in magnesium. These measurements challenge the notion of a metallicity floor for GCs and theoretical expectations that massive GCs could not have formed at such low metallicities.

Globular clusters (GCs) are roughly spherical agglomerations of thousands to millions of stars, bound by their mutual gravity; their central densities can exceed 10^6 solar masses per cubic parsec ($M_\odot$ pc^{-3}) (*1*). GCs formed early in the history of the Universe and therefore record the early stages of galaxy formation and evolution. The nearest neighboring spiral galaxy, the Andromeda Galaxy, also known as Messier 31 (M31), has a system of GCs that align spatially and kinematically with stars in the outer parts of the galaxy. The GCs in the outer parts of M31 appear to belong to at least two kinematically distinct subsystems that were accreted separately (*2*).

The GC systems in most galaxies are dominated by clusters with low abundances of elements heavier than hydrogen and helium ("metals"), relative to the composition of the Sun. However, there appears to be a deficit of GCs at the very lowest metal abundances ("metallicities") (*3*). The most metal-poor GCs in the Milky Way have iron abundances of [Fe/H] ≈ −2.5 (*4*), where square brackets denote the abundance ratios of the elements, relative to the solar photospheric composition, on a logarithmic scale. The number of iron atoms per hydrogen atom in the most metal-poor GCs is thus about 1/300 that in the Sun. The notion of a metallicity floor for GCs at [Fe/H] = −2.5 is supported by observations of GCs in several external galaxies (*5*), and various explanations have been suggested. The correlation between mass and metallicity for galaxies in the early Universe might set a minimum metallicity for formation of GCs that are sufficiently massive to survive until the present day, or the formation of massive GCs could be suppressed at low metallicities owing to inefficient gas cooling (*3*, *5*–*7*). A metallicity floor for GCs would thus have implications for cluster and star formation and for the build-up of metals in galaxies during the early Universe.

Because the metallicity distributions of both GCs and individual stars decline steeply toward low metallicities and are poorly constrained, it remains unclear how statistically significant the proposed metallicity floor is. In M31, three clusters with metallicities that may fall in the range −2.8 < [Fe/H] < −2.5 are known (*8*), but the uncertainties are large (0.3 to 0.4 dex) and the metallicities may lie well above the floor. Similarly, three GCs in the Sombrero Galaxy may have metallicities below [Fe/H] = −2.5 (*9*), but the uncertainties on the spectroscopic measurements are large and the red colors of these clusters suggest higher metallicities.

We investigate the globular cluster RBC EXT8 (hereafter EXT8) in M31, located at right ascension $00^h53^m14^s.53$, declination +41°33′24″.5 (J2000 equinox) according to the Revised Bologna Catalogue (*10*). Kinematic analysis (*2*) has shown that EXT8 belongs to the smoothly distributed component of the M31 halo and lies at a projected distance of 27 kpc from the galaxy center. Figure 1 shows a color-magnitude diagram for GCs in M31 (*11*). With an apparent magnitude in the *g*-band of g = 15.87, EXT8 is among the brighter GCs in M31. Its integrated light color with respect to the *u*-band ($u - g$ = 1.11) is less red than most of the other GCs, suggesting a low metallicity. Previous low-resolution spectroscopy yielded an age ≥8 billion years and [Fe/H] between −2.8 and −2.0 (*12*, *13*).

We obtained a spectrum of the integrated light of EXT8 with the High-Resolution Echelle Spectrometer (HIRES) (*14*) on the Keck I telescope on 25 October 2019. Given EXT8's brightness and compact size, a total integration time of 2400 s was sufficient to obtain a signal-to-noise ratio of about 200 per Å near the Mg I triplet at 5170 Å. We used a slit width of 1.15″, which gave a nominal spectral resolving power $R \equiv \lambda/\Delta\lambda \approx 37000$, where λ is the wavelength and Δλ the width of a spectral resolution element. The observations covered a spectral range of 3840 to 8060 Å.

Figure 2 shows the H β lines in the spectra of EXT8 and Messier 15 (M15) for comparison, the latter being one of the most metal-poor GCs in the Milky Way (*15*). The spectrum of M15 was obtained with the Ultraviolet and Visual Echelle Spectrograph (UVES) on the Very Large Telescope and has a spectral resolving power similar to that of the EXT8 spectrum (*16*). M15's velocity dispersion (σ = 12.9 ± 0.3 km s^{-1}) is similar to that of EXT8 (σ = 13.3 ± 0.8 km s^{-1}), allowing direct comparison. Absorption in the H β line becomes stronger at younger ages and can be used as an age indicator in the spectra of GCs (*17*). Although the blue color of EXT8 could, in principle, be caused by a younger age, Fig. 2 shows no discernible difference in the strengths or shapes of the H β lines in the two spectra, indicating that EXT8 is similarly old, so must be a metal-poor GC.

Figure 3 shows two metallicity-sensitive features. Figure 3A shows the Fe I feature near 4957 Å (actually a blend of several Fe I lines, of which the two strongest are marked), which is much weaker in the spectrum of EXT8 than in M15. Figure 3B shows two of the three lines of the Mg I triplet (Fraunhofer's *b* feature) at 5167 and 5173 Å. The third line, at 5184 Å, falls in the gap between the two detectors of UVES but is included in the HIRES spectrum. The Mg I lines, as well as other lines visible in this region of the spectra, are much weaker in the EXT8 spectrum.

To quantify these results, we analyzed the EXT8 spectrum using a spectral fitting technique used in previous studies of extragalactic GCs (*16*, *18*). Figure 3 shows the best-fitting model spectrum for M15 (*16*), with an iron abundance of [Fe/H] = −2.39 ± 0.02. This model spectrum is based on a color-magnitude diagram (CMD) of M15 (*19*). We do not have spatially resolved data to empirically build a CMD for EXT8, so we substituted it with stellar models (*20*) with a metal fraction chosen to self-consistently match that derived from the spectral modeling. We found an iron abundance of [Fe/H] = −2.91 ± 0.04 for EXT8 from model fitting of the wavelength range 4400 to 6200 Å (*19*). These model spectra are also shown in Fig. 3. We tested the assumptions required for the input CMD and found that they do not substantially affect this measurement (*19*). We conclude that EXT8 is about 0.5 dex more metal-poor than the value of [Fe/H] = −2.39 found for M15. The metallicity of EXT8 lies well below the metallicity floor suggested by previous studies.

At the signal-to-noise ratio of our EXT8 spectrum, most spectral features are weak

[1]Department of Astrophysics/Institute of Mathematics, Astrophysics and Particle Physics, Radboud University, 6500 GL Nijmegen, Netherlands. [2]Department of Physics and Astronomy, San José State University, San Jose, CA 95192, USA. [3]University of California Observatories, University of California, Santa Cruz, CA 95064, USA. [4]Centre for Astrophysics and Supercomputing, Swinburne University of Technology, Hawthorn, VIC 3122, Australia.
*Corresponding author. Email: s.larsen@astro.ru.nl

because of the low metallicity. Nevertheless, our model fitting yielded abundances for several additional elements. From the Mg I *b* lines, we found a low magnesium abundance of [Mg/Fe] = −0.35 ± 0.05. Magnesium is thus even more strongly depleted than iron, relative to the Sun. The other Mg lines that are typically measured in integrated-light GC spectra are very weak (*19*) but are generally consistent with the low magnesium abundance inferred from the *b* lines: [Mg/Fe] = $-0.16^{+0.27}_{-0.58}$ (using Mg I 4571 Å), [Mg/Fe] = $-0.96^{+0.65}_{-\infty}$ (Mg I 4703 Å), and [Mg/Fe] = −0.35 ± 0.25 (Mg I 5528 Å). The consistency between the magnesium abundances measured from the *b* triplet and from the weaker lines is supported by prior analysis of M15, where the weaker lines yielded [Mg/Fe] = +0.18 ± 0.06 (*16*). From our model fitting of M15, we find an almost identical abundance of [Mg/Fe] = +0.17 ± 0.02 (using the two Mg *b* lines included in the UVES spectrum). Magnesium is among the elements thought to be produced via the α process of nucleosynthesis (*21*). For other α elements, we find average abundance ratios of [Si/Fe] = +0.65 ± 0.31, [Ca/Fe] = +0.35 ± 0.07, and [Ti/Fe] = +0.19 ± 0.06 for EXT8 (*19*). Relative to iron, these elements are thus on average enhanced by roughly a factor of 2 compared to the composition of the solar photosphere.

The enhanced abundances of silicon, calcium, and titanium are typical for metal-poor, old populations, which is usually attributed to enrichment of α elements dominated by core-collapse supernovae (*22*). However, the very low magnesium abundance is not easily explained within this framework. It may be related to the phenomenon of multiple stellar populations in GCs, of which the outer halo cluster NGC 2419 is one of the most extreme cases in the Milky Way (*23*, *24*). In NGC 2419, some individual stars have magnesium abundances as low as [Mg/Fe] = −1, although more typical values for the Mg-depleted stars in NGC 2419 (which constitute about 40% of the stars in this cluster) are [Mg/Fe] ≈ −0.5. The distribution of [Mg/Fe] values within EXT8 is not constrained by our measurements, but the [Mg/Fe] value measured from the integrated light can be reproduced if the cluster contains two populations with [Mg/Fe] ≈ −1.0 and [Mg/Fe] ≈ +0.3 that each account for about half of the stars (*19*). In this case, a larger difference between two populations is required in EXT8 than in NGC 2419.

Further evidence for multiple populations in EXT8 comes from the abundance of sodium. From the Na I resonance doublet at 5890, 5896 Å (Fraunhofer's *D* feature), we find sodium to be enhanced relative to scaled-solar composition, [Na/Fe] = +0.23 ± 0.07, as is commonly observed in GCs (*25*). However, the *D* lines may be contaminated by absorption from interstellar gas along the line of sight toward EXT8. Other Na I lines that are immune to this effect are very weak in the spectrum of EXT8, but from the doublet at 5683, 5688 Å, we measure [Na/Fe] = $+0.26^{+0.32}_{-\infty}$, which is consistent with the value inferred from the *D* lines.

In NGC 2419, the Mg-poor stars are also enriched in K, reaching [K/Fe] ≈ +1.5 (*23*, *24*). For EXT8 we measure [K/Fe] = +0.67 ± 0.15,

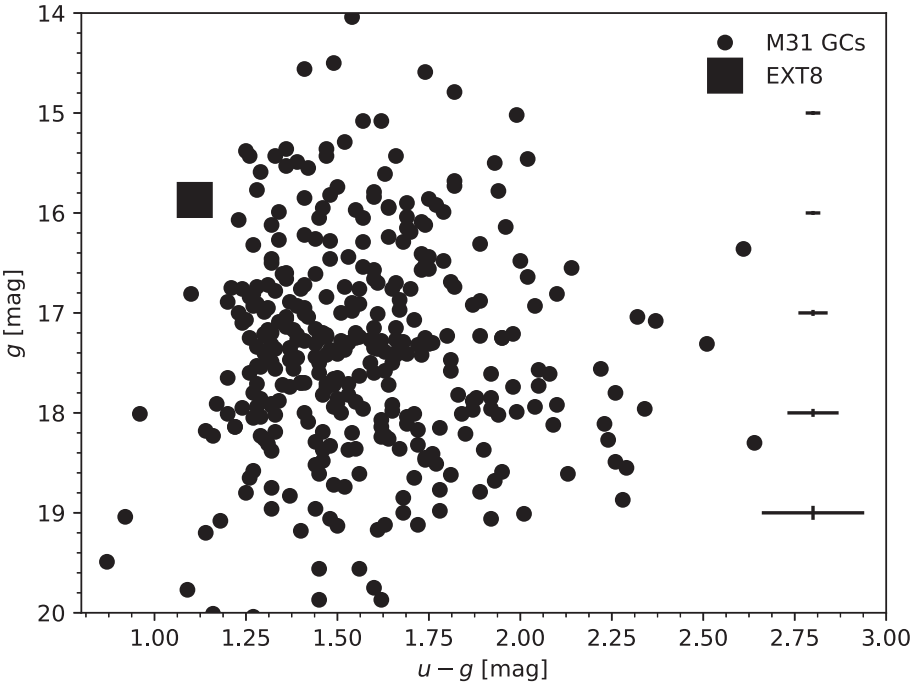

Fig. 1. Color-magnitude diagram for globular clusters in M31 (*11*). No correction for dust reddening has been applied. EXT8 is marked with a large square and has one of the bluest *u* − *g* colors among the GCs in M31. Typical 1σ error bars are shown on the right.

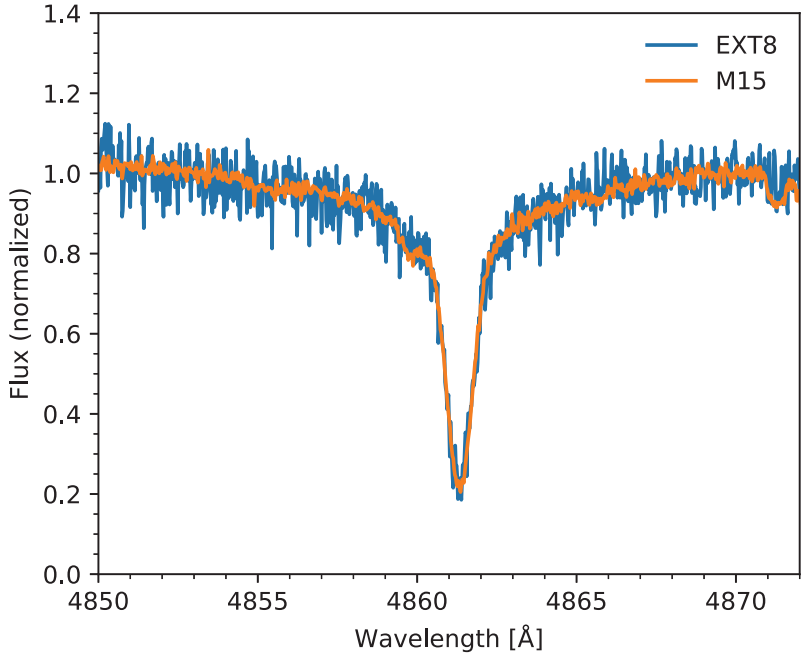

Fig. 2. Comparison of the H β lines in the spectra of EXT8 (blue) and Messier 15 (orange). The very similar H β line profiles in the two spectra indicate similar, old ages for the two clusters.

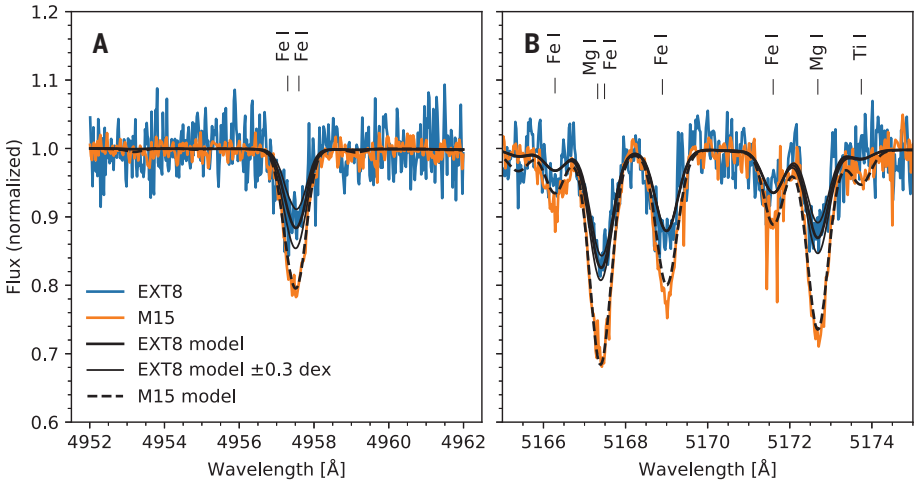

Fig. 3. Iron and magnesium features in the spectra of EXT8 (blue) and Messier 15 (orange). The best-fitting models are shown with thick black lines (for EXT8) and dashed black lines (for M15). Models for EXT8 in which the abundances have been varied by ±0.3 dex for iron (**A**) and magnesium (**B**) are shown with thinner lines.

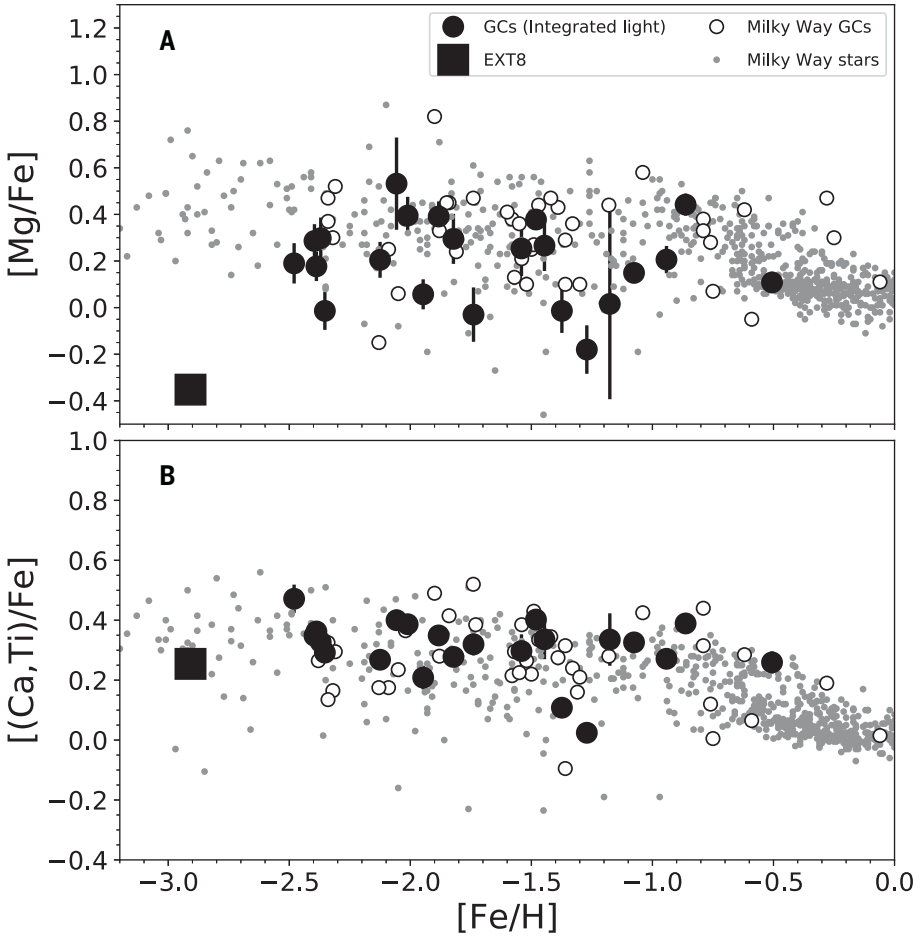

Fig. 4. Abundance measurements for EXT8 and other Galactic and extragalactic GCs. (**A**) [Mg/Fe] as a function of [Fe/H]. (**B**) The average of [Ca/Fe] and [Ti/Fe]. The large square shows our measurements for EXT8, and the filled circles show integrated-light measurements for GCs in the NGC 147, NGC 6822, Fornax, and WLM dwarf galaxies, M33, and the Milky Way (*16*, *18*). Data for resolved Milky Way GCs are shown with open circles (*30*) and data for field stars (*31*) with small gray dots. Error bars indicate the 1σ uncertainties.

but this value may require correction downward by about 0.3 dex to account for our assumption of local thermodynamic equilibrium in the spectral modeling (*26*). This would then make the [K/Fe] ratio in EXT8 similar to that observed in metal-poor halo stars in the Milky Way and in M15 (*27*). Hence, we find no evidence of a K-enriched population in EXT8.

From the model fitting, we also determined the velocity broadening of the observed spectrum. The line-of-sight velocity dispersion, corrected for instrumental broadening, is $\sigma = 13.3 \pm 0.8$ km s^{-1}. The half-light radius of EXT8 is 2.8 pc, leading to an estimated dynamical mass of $M_{dyn} = (1.14 \pm 0.16) \times 10^6\ M_\odot$ (*19*). For an absolute magnitude in the *V*-band of $M_V = -9.28$ (*28*), the corresponding mass-to-light ratio in solar units is $M_{dyn}/L_V = 2.6 M_\odot/L_{\odot,V}$, where L_V and $L_{\odot,V}$ are the luminosities of EXT8 and the Sun in the *V*-band. EXT8 thus extends the trend for metal-poor GCs to have high *M/L* values (*29*). A lower *M/L* would be expected for a younger age, so the measured value is consistent with EXT8 being an old, metal-poor system.

Figure 4 shows a comparison of EXT8 with previous integrated-light spectroscopy of Galactic and extragalactic GCs (*16*, *18*), along with literature data for individual stars in Galactic GCs and individual stars (*30*, *31*). EXT8 is an outlier in a [Mg/Fe] versus [Fe/H] plot (Fig. 4A), being more metal-poor than other GCs and more magnesium-poor than individual stars with similarly low iron abundances. The GCs have a larger spread in [Mg/Fe] than the individual stars, with scatter toward lower magnesium abundances. This has previously been interpreted as a signature of multiple populations (*32*, *33*). When excluding magnesium, Fig. 4B shows that EXT8 has an [α/Fe] ratio (here defined as the average of [Ca/Fe] and [Ti/Fe]) that overlaps with those seen in individual metal-poor stars and in other GCs.

Within the standard paradigm of hierarchical galaxy assembly, metal-poor GCs are expected to have formed in the early Universe in low-mass galaxies that merged to form larger galaxies (*6*, *7*, *34*). The correlation between the mass and metallicity of galaxies therefore imprints a maximum mass for a GC that could form with a given metallicity. At [Fe/H] = −2.9, the maximum mass is expected to be about $10^5\ M_\odot$ (*6*, *7*). The existence of a possible remnant of a disrupted GC in the Milky Way with [Fe/H] = −2.7 and an estimated mass below $10^5\ M_\odot$ (*35*) is consistent with this notion. However, we expect clusters as massive and metal-poor as EXT8 to be extremely rare. In a simulation containing 10,553 GCs with masses greater than $10^5\ M_\odot$, only three (~0.03%) had [Fe/H] < −2.5

and masses above $10^6\,M_\odot$ (*36*), where we have converted the total metal fractions (*36*) to [Fe/H] values (*19*). If half of the 400 to 500 GCs in M31 (*10*) have masses greater than $10^5\,M_\odot$, this would correspond to a probability of 6 to 7% of finding a single GC as massive and metal-poor as EXT8.

REFERENCES AND NOTES

1. H. Baumgardt, M. Hilker, *Mon. Not. R. Astron. Soc.* **478**, 1520–1557 (2018).
2. D. Mackey *et al*., *Nature* **574**, 69–71 (2019).
3. B. W. Carney, J. B. Laird, D. W. Latham, L. A. Aguilar, *Astron. J.* **112**, 668 (1996).
4. J. D. Simpson, *Mon. Not. R. Astron. Soc.* **477**, 4565–4576 (2018).
5. M. A. Beasley *et al*., *Mon. Not. R. Astron. Soc.* **487**, 1986–1993 (2019).
6. N. Choksi, O. Y. Gnedin, H. Li, *Mon. Not. R. Astron. Soc.* **480**, 2343–2356 (2018).
7. J. M. D. Kruijssen, *Mon. Not. R. Astron. Soc.* **486**, L20–L25 (2019).
8. N. Caldwell, R. Schiavon, H. Morrison, J. A. Rose, P. Harding, *Astron. J.* **141**, 61 (2011).
9. A. Alves-Brito *et al*., *Mon. Not. R. Astron. Soc.* **417**, 1823–1838 (2011).
10. S. Galleti, L. Federici, M. Bellazzini, F. F. Pecci, S. Macrina, *Astron. Astrophys.* **416**, 917–924 (2004).
11. M. B. Peacock *et al*., *Mon. Not. R. Astron. Soc.* **402**, 803–818 (2010).
12. Z. Fan *et al*., *Res. Astron. Astrophys.* **11**, 1298–1310 (2011).
13. B. Chen *et al*., *Astron. J.* **152**, 45 (2016).
14. S. S. Vogt *et al*., *Proc. SPIE* **2198**, 362 (1994).
15. W. E. Harris, *Astron. J.* **112**, 1487 (1996).
16. S. S. Larsen, J. P. Brodie, J. Strader, *Astron. Astrophys.* **601**, A96 (2017).
17. G. Worthey, *Astrophys. J. Suppl. Ser.* **95**, 107 (1994).
18. S. S. Larsen, J. P. Brodie, A. Wasserman, J. Strader, *Astron. Astrophys.* **613**, A56 (2018).
19. See supplementary materials.
20. J. Choi *et al*., *Astrophys. J.* **823**, 102 (2016).
21. E. Burbidge, G. Burbidge, W. Fowler, F. Hoyle, *Rev. Mod. Phys.* **29**, 547–650 (1957).
22. B. M. Tinsley, *Astrophys. J.* **229**, 1046 (1979).
23. J. G. Cohen, E. N. Kirby, *Astrophys. J.* **760**, 86 (2012).
24. A. Mucciarelli *et al*., *Mon. Not. R. Astron. Soc.* **426**, 2889–2900 (2012).
25. E. Carretta *et al*., *Astron. Astrophys.* **505**, 117–138 (2009).
26. Y. Takeda, G. Zhao, Y.-Q. Chen, H.-M. Qiu, M. Takada-Hidai, *Publ. Astron. Soc. Jpn.* **54**, 275–284 (2002).
27. Y. Takeda *et al*., *Publ. Astron. Soc. Jpn.* **61**, 563–576 (2009).
28. A. P. Huxor *et al*., *Mon. Not. R. Astron. Soc.* **442**, 2165–2187 (2014).
29. J. Strader, N. Caldwell, A. C. Seth, *Astron. J.* **142**, 8 (2011).
30. B. J. Pritzl, K. A. Venn, M. Irwin, *Astron. J.* **130**, 2140–2165 (2005).
31. K. A. Venn *et al*., *Astron. J.* **128**, 1177–1195 (2004).
32. J. E. Colucci, R. A. Bernstein, S. Cameron, A. McWilliam, J. G. Cohen, *Astrophys. J.* **704**, 385–414 (2009).
33. C. M. Sakari, M. Shetrone, K. Venn, A. McWilliam, A. Dotter, *Mon. Not. R. Astron. Soc.* **434**, 358–386 (2013).
34. W. E. Harris *et al*., *Astrophys. J.* **636**, 90–114 (2006).
35. Z. Wan *et al*., *Nature* **583**, 768–770 (2020).
36. C. Usher *et al*., *Mon. Not. R. Astron. Soc.* **480**, 3279–3301 (2018).
37. S. Larsen, ISPy3: Integrated-light Spectroscopy for Python3. Zenodo (2020); https://doi.org/10.5281/zenodo.4036092.
38. S. S. Larsen, *Astron. Astrophys. Suppl. Ser.* **139**, 393–415 (1999).
39. S. S. Larsen, BAOLab 0.94.1g, Version 0.94.1g, Zenodo (2020); https://doi.org/10.5281/zenodo.4036106.

ACKNOWLEDGMENTS

We thank M. Gieles and E. Starkenburg for helpful discussions and comments on the manuscript and D. VandenBerg for valuable advice on the selection of isochrones. Comments from the anonymous referees helped improve the presentation. The data were obtained at the W. M. Keck Observatory, which is operated as a scientific partnership among the California Institute of Technology, the University of California and the National Aeronautics and Space Administration. The Observatory was made possible by the generous financial support of the W. M. Keck Foundation. The authors wish to recognize and acknowledge the very significant cultural role and reverence that the summit of Maunakea has always had within the indigenous Hawaiian community. We are most fortunate to have the opportunity to conduct observations from this mountain. **Funding:** A.J.R. was supported by National Science Foundation grant AST-1616710, and as a Research Corporation for Science Advancement Cottrell Scholar. J.P.B. acknowledges support from HST grant HST-GO-15078. A.J.R. and S.S.L. were supported in part by the National Science Foundation under grant no. NSF PHY-1748958. **Author contributions:** J.P.B. secured the observing time for this project. All authors contributed to the planning of the observations, and the inclusion of EXT8 as a target was suggested by A.J.R.. A.W. conducted the observations. S.S.L. carried out the data reduction and analysis and drafted the paper. All authors assisted in the interpretation of the results and writing of the paper. **Competing interests:** None declared. **Data and materials availability:** The average measured abundances are listed in table S2, and individual measurements are in tables S3 to S9. The raw observations of EXT8 and Hodge III are available in the W. M. Keck Observatory Archive at http://koa.ipac.caltech.edu, EXT8 under program ID U177Hr, Semester 2019B, and Hodge III under program ID U040Hr, Semester 2015B, P.I. Brodie. The UVES observations of M15 are available in the ESO archive at http://archive.eso.org, program ID 095.B-0677(A), P. I. Larsen. The CFHT MegaCam images of EXT8 are available in the CFHT data archive at www.cadc-ccda.hia-iha.nrc-cnrc.gc.ca/en/cfht, proposal ID 16BC25, product IDs 2011389p, 2011390p, and 2011391p. The spectral analysis was carried out with the ISPy3 code https://github.com/soerenslarsen/ISPy3 (*37*), and the King model fitting was done with the Baolab code (*38*), available at https://github.com/soerenslarsen/baolab and Zenodo (*39*).

SUPPLEMENTARY MATERIALS

science.sciencemag.org/content/370/6519/970/suppl/DC1
Materials and Methods
Supplementary Text
Figs. S1 to S3
Tables S1 to S10
References (*40*–*58*)

7 February 2020; accepted 30 September 2020
Published online 15 October 2020
10.1126/science.abb1970

ANTIFUNGAL DISCOVERY

A marine microbiome antifungal targets urgent-threat drug-resistant fungi

Fan Zhang[1]*, Miao Zhao[2]*, Doug R. Braun[1], Spencer S. Ericksen[3], Jeff S. Piotrowski[4], Justin Nelson[4], Jian Peng[5], Gene E. Ananiev[3], Shaurya Chanana[1], Kenneth Barns[1], Jen Fossen[2], Hiram Sanchez[2], Marc G. Chevrette[6,7,8], Ilia A. Guzei[9], Changgui Zhao[1], Le Guo[1], Weiping Tang[1], Cameron R. Currie[6,7], Scott R. Rajski[1], Anjon Audhya[10], David R. Andes[2]†, Tim S. Bugni[1]†

New antifungal drugs are urgently needed to address the emergence and transcontinental spread of fungal infectious diseases, such as pandrug-resistant *Candida auris*. Leveraging the microbiomes of marine animals and cutting-edge metabolomics and genomic tools, we identified encouraging lead antifungal molecules with in vivo efficacy. The most promising lead, turbinmicin, displays potent in vitro and mouse-model efficacy toward multiple-drug–resistant fungal pathogens, exhibits a wide safety index, and functions through a fungal-specific mode of action, targeting Sec14 of the vesicular trafficking pathway. The efficacy, safety, and mode of action distinct from other antifungal drugs make turbinmicin a highly promising antifungal drug lead to help address devastating global fungal pathogens such as *C. auris*.

Infectious fungal diseases are among the deadliest threats to global human health. Worldwide, nearly 2 million people die each year from fungal infections, and the death toll continues to rise with increasing at-risk immunocompromised populations (*1*, *2*). Poor outcomes are exacerbated further with the emergence of pathogens that are resistant to first-line antifungal drugs (*3*–*5*). Most recently, the pandrug-resistant "killer fungus," *C. auris*, has emerged and is spreading in health care facilities worldwide, prompting an urgent-threat alert from the Centers for Disease Control and Prevention (CDC) (*6*, *7*).

To address the global threat of multidrug-resistant (MDR) pathogens, new antifungal agents are urgently needed. Today, only three antifungal drug classes are available for clinical use. The development of new antifungals has been hampered, in part, by the evolutionary history fungi and animals share, limiting treatment options to drugs because of limited efficacy and/or toxic side effects. Most antifungal agents, as with other antimicrobial leads, originate from a natural product source, including two of the three available antifungal classes (*8*, *9*). However, conventional screening strategies have been seriously challenged by the high frequency of rediscovering known molecules. More recently, however, natural product–based screening has enjoyed a renaissance driven by development of screening approaches and sources of natural products (*10*–*13*).

To identify antifungal candidates, we implemented a discovery platform that leverages liquid chromatography–mass spectrometry (LC-MS)–based metabolomics, genomics, and antimicrobial activity screening of metabolomic arrays from bacterial isolates from the microbiome of marine animals (*10*, *11*). Here, we describe the discovery and early development of a promising antifungal, turbinmicin, from a sea squirt microbiome constituent, *Micromonospora* sp. The compound exhibits in vitro and in vivo broad-spectrum activity against emerging MDR human fungal pathogens, including *C. auris*. Turbinmicin's safety profile and highly selective mechanism of action (MOA) against *C. auris* and *Aspergillus fumigatus* support development of the compound for clinical use while also unveiling an exploitable fungal target.

Chemical diversity is critical to discovery programs (*11*, *14*). To generate a diversity library, we did LC-MS profiling on 1482 actinobacteria from marine invertebrates collected in the Florida Keys between 2012 and 2016. We then applied strain prioritization by metabolomics using HCAPCA (hierarchical cluster analysis principal components analysis), an LC-MS–based metabolomics tool that we recently published (supplementary materials) (*15*). Data resulting from HCAPCA enabled us to prioritize 174 chemically diverse strains. As shown in the PCA scores plot (Fig. 1C), strain WMMC-415 separated from the group, indicating chemical variance. The PCA loadings plot (Fig. 1D) showed a number of compounds that contributed to the variance, including turbinmicin. After fermentations, a two-step orthogonal chromatographic approach was employed to array molecules into 174 96-well plates (supplementary materials) (*12*, *16*, *17*). We assessed the in vitro activity of these metabolomic arrays against *Candida albicans* by high-throughput screening. One hit from a *Micromonospora* sp. was prioritized on the basis of potency, MS, and nuclear magnetic resonance (see supplementary materials). This led to the discovery of the antifungal agent that we named turbinmicin (Fig. 1). Turbinmicin belongs to a small group of highly oxidized type II polyketides. Although representatives such as actinomadurone, lysolipin, and xantholipin display an array of biological activities, none have been thoroughly evaluated for MOA, but changes in structure affect the spectrum of activity (*18*–*23*).

We used high-purity turbinmicin for expanded, clinically relevant in vitro antifungal screens and in vivo evaluation for both efficacy and safety through determination of a maximum tolerated dose (MTD) in a mouse model. To assess the spectrum of activity for turbinmicin, we analyzed its activity against a collection of 39 clinical isolates using microbroth methods from the Clinical Laboratory Standards Institute (CLSI M27 and M38). Clinical isolates in this group included MDR pathogens representing each of the defined resistance mechanisms to available antifungal classes for common fungal pathogens (*C. albicans*, *C. auris*, *Candida glabrata*, *Candida tropicalis*, *A. fumigatus*, *Fusarium* spp., *Scedosporium* spp., and *Rhizopus* spp.) (Fig. 2A and table S2) (*24*, *25*). As examples, the collection includes panresistant *C. auris* [strain B11211, turbinmicin minimum inhibitory concentration (MIC) 0.25 μg/mL, fluconazole MIC >256 μg/mL, amphotericin B MIC 2 μg/mL, and micafungin MIC 4 μg/mL], echinocandin- and triazole-resistant *C. glabrata*, and triazole-resistant *A. fumigatus*. The turbinmicin MICs ranged from 0.03 to 0.5 μg/mL across most genera, with the exception of the *zygomycetes*, which required concentrations of 4 to 8 μg/mL for growth inhibition. Turbinmicin exhibited similar activity against isolates resistant to available antifungal classes, indicating a lack of cross-resistance and, potentially, a distinct MOA. We selected the panresistant isolate of *C. auris* for further pharmacodynamic characterization of the activity of various turbinmicin concentrations over time. Fungicidal activity was observed at concentrations exceeding the MIC, with the highest concentrations exhibiting a reduction of more than 2-log in organism burden at 4 hours (Fig. 2B).

Preliminary safety was established by using a human red blood cell (RBC) hemolysis assay as well as MTD determinations by using a mouse model. Turbinmicin concentrations exceeding the MIC by 1000-fold did not exhibit

[1]Pharmaceutical Sciences Division, University of Wisconsin–Madison, Madison, WI, USA. [2]Department of Medicine, University of Wisconsin–Madison, Madison, WI, USA. [3]Small Molecule Screening Facility, University of Wisconsin Carbone Cancer Center, Madison, WI, USA. [4]Yumanity Therapeutics, Cambridge, MA, USA. [5]Department of Computer Science, University of Illinois at Urbana–Champaign, Urbana, IL, USA. [6]Department of Genetics, University of Wisconsin–Madison, Madison, WI, USA. [7]Department of Bacteriology, University of Wisconsin–Madison, Madison, WI, USA. [8]Wisconsin Institute for Discovery and Department of Plant Pathology, University of Wisconsin–Madison, Madison, WI, USA. [9]Department of Chemistry, University of Wisconsin–Madison, Madison, WI, USA. [10]Department of Biomolecular Chemistry, School of Medicine and Public Health, University of Wisconsin–Madison, Madison, WI, USA.
*These authors contributed equally to this work.
†Corresponding author. Email: tim.bugni@wisc.edu (T.S.B.); dra@medicine.wisc.edu (D.R.A.)

RBC toxicity, suggesting a wide therapeutic window for this compound (Fig. 2C). To identify the MTD, mice were administered single turbinmicin doses beginning at 1 mg/kg and increasing twofold. Mice showed no evidence of toxicity at dose levels as high as 256 mg/kg. We next explored in vivo efficacy using the U.S. Food and Drug Administration (FDA) standard fungal model for invasive candidiasis. This neutropenic mouse model involves *Candida* injection into the bloodstream and assessment of treatment response by viable fungal burden in the kidney (*26*, *27*). Mice injected with a panresistant strain of *C. auris* (strain B11211) received five doses of turbinmicin, increasing by twofold and administered every 6 hours (0.25 to 4 mg/kg every 6 hours) over a 24-hour treatment period. We observed dose-dependent efficacy over the concentration range and a 3.6 $\log_{10}$ reduction in organism burden at the highest dose level compared with vehicle-treated control mice (Fig. 2D). There were no signs of toxicity observed over the dose range for any of the mice. Standard-of-care therapy with a humanized regimen of the echinocandin micafungin produced an outcome similar to that of untreated controls, as expected for the MDR organism (*28*, *29*). Notably, the antifungal activity displayed by turbinmicin in these models has correlated well with efficacy in these infection models; in fact, decreases in fungal burden (<1 $\log_{10}$) much lower than those observed in this work have been linked to efficacy in humans (*28*, *30*).

To further assess the clinical utility of turbinmicin, we also evaluated its efficacy toward a filamentous fungal pathogen using triazole-resistant *A. fumigatus* (strain F11628, CYP51 G138C mutation, posaconazole MIC 8 μg/mL and turbinmicin MIC 0.03 μg/mL) (table S2). This pathogen is particularly difficult to treat with currently available antifungals and leads to a high mortality rate (>50%). For the in vivo model, we selected a neutropenic and corticosteroid immunosuppressed mouse model of invasive pulmonary aspergillosis that assesses treatment response by quantitative polymerase chain reaction (PCR) measurement of lung fungal burden (*31*). *A. fumigatus*–infected mice were administered turbinmicin every 6 hours over a 4-day treatment period. We empirically chose a lower dose range (0.25 to 1 mg/kg) of turbinmicin for these studies given the lower MIC observed for *A. fumigatus* when compared with *C. auris*. Turbinmicin similarly produced dose-dependent reductions in fungal burden with a 1.5 $\log_{10}$ drop in *Aspergillus* in the lungs of mice treated with 1 mg/kg every 6 hours (Fig. 2E). All mice appeared healthy after the 16 turbinmicin administrations over the 4-day treatment period. Treatment with a clinically recommended triazole (posaconazole), using doses approximating exposures in humans, was ineffective, consistent with the known azole resistance (*32*, *33*).

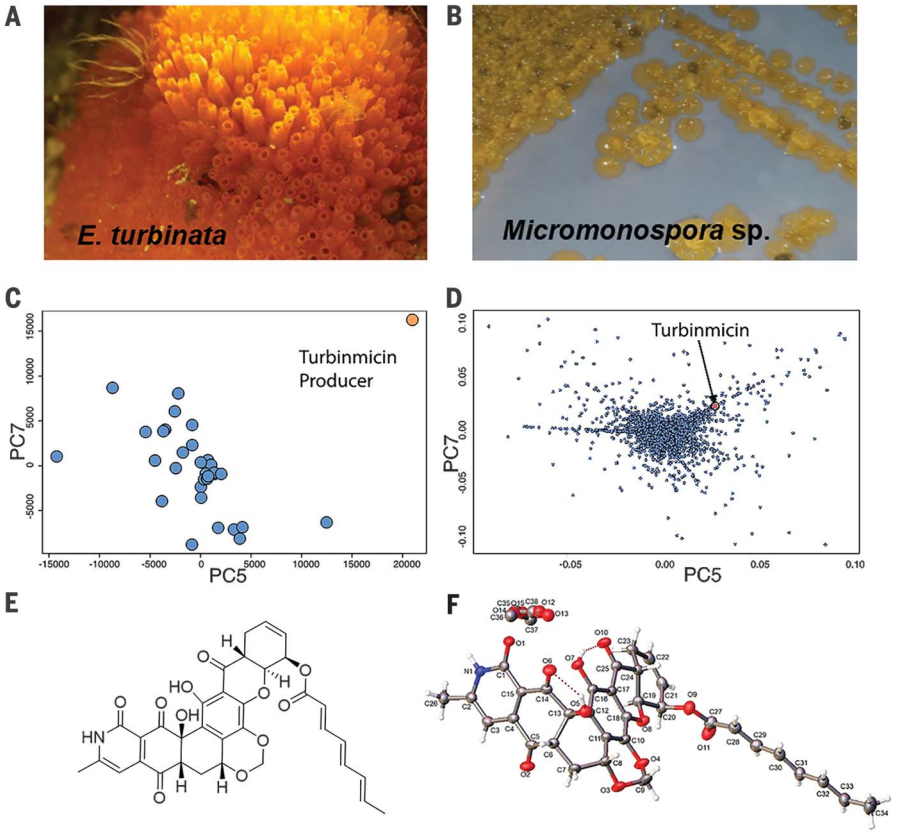

Fig. 1. Turbinmicin discovery from marine microbiome using MDR drug discovery platform. (**A**) Turbinmicin-producing strain was isolated from the ascidian *Ecteinascidia turbinata*. (**B**) Turbinmicin-producing bacterium *Micromonospora* sp. WMMC-415. (**C** and **D**) WMMC-415 was prioritized on the basis of its chemical diversity after HCAPCA processing of a 174-strain library. PCA scores plot (C) revealed WMMC-415's chemical diversity, and the PCA loadings plot (D) showed a number of diverse metabolites produced by WMMC-415, including turbinmicin; for the purposes of clarity, data in (C) and (D) are from a 30-member subpool of the 174-strain library. (**E**) Structure of turbinmicin. (**F**) X-ray ORTEP drawing of turbinmicin shown with 50% probability ellipsoids depicting its absolute configuration.

MOA inquiries for turbinmicin began with our application of *Saccharomyces cerevisiae* DNA-barcoded knockout and knockdown libraries. For essential genes, we used the Decreased Abundance by mRNA Perturbation (DAmP) knockdown library (~1000 knockdowns), in which all essential genes were effectively knocked down through a modification of the 5′ untranslated region that destabilizes corresponding mRNA transcripts (*34*). In parallel, we evaluated the effect of turbinmicin in the diagnostic DNA-barcoded knockout library (310 knockouts) of nonessential gene mutants (*35*). After exposure to turbinmicin (1 to 5 μg/mL), genomic DNAs were extracted and their barcodes amplified by using multiplexed PCR; amplified sequences were determined by Illumina sequencing (*36*–*38*). Chemical-genetic profiles at each concentration revealed DAmP mutants that were most sensitive to turbinmicin. *SEC14* was the most notable, as reflected by the most pronounced negative chemical-genetic interactions at three of five tested concentrations (Fig. 3A). Sec14p, encoded by *SEC14*, is a phosphatidylinositol–phosphatidylcholine transfer protein required for correct trans-Golgi network dynamics. Sec14p is a validated fungal target, and no approved antifungal agents target Sec14p (*39*–*41*).

The relevance of Sec14p as one of if not the dominant target of turbinmicin was supported by the nonessential knockout library. *ERV14*, *GUP1*, and *BST1* deletion mutants showed concentration-dependent hypersensitivities to turbinmicin (Fig. 3B), and all encode proteins involved with vesicle-mediated trafficking. Using the most sensitive nonessential deletion mutants (CG score ≤ −1.5), we then built a genetic interaction network using TransposeNET, an algorithm that imputes network nodes using sparse data from diagnostic gene sets (*42*). The resulting network revealed *SEC14* as

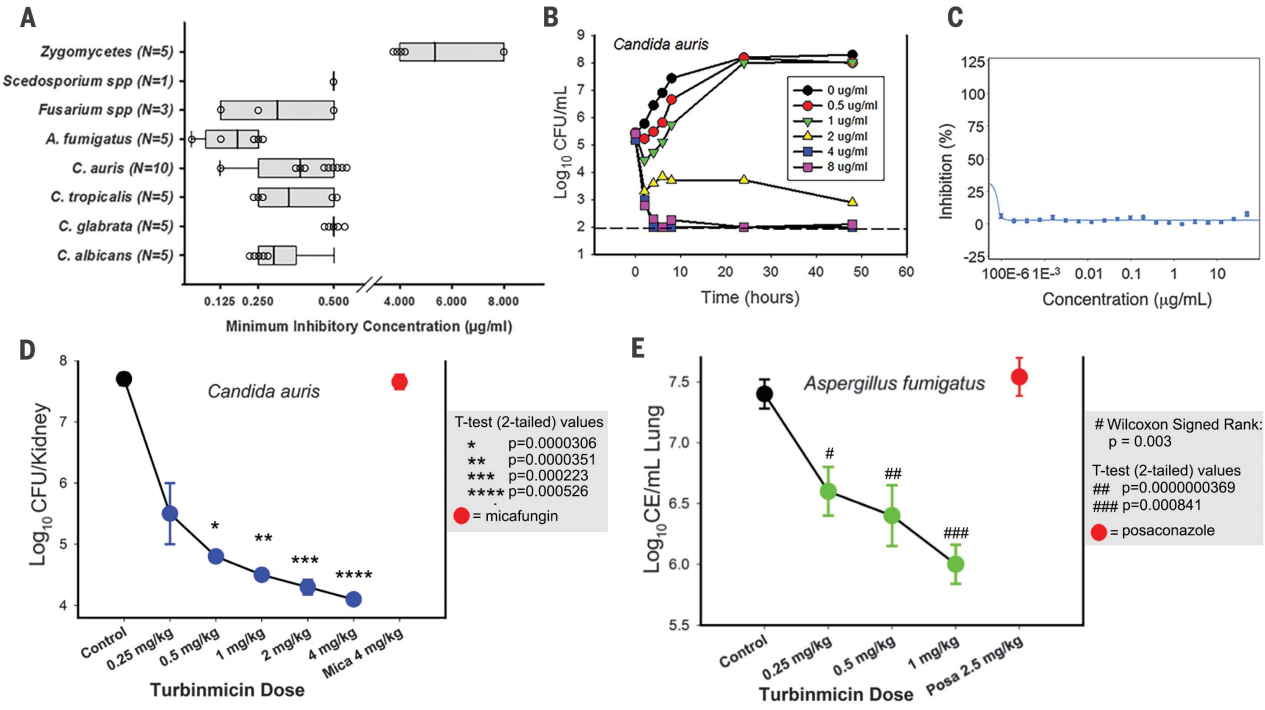

Fig. 2. Turbinmicin displays potent in vitro and in vivo efficacy against multiple MDR fungal pathogens and mammalian safety. (**A**) In vitro activity of turbinmicin against 39 fungal isolates. (**B**) Time-kill curves for turbinmicin against *C. auris* B11211. Kill curves are generated from data collected at 0, 2, 4, 6, 8, 24, and 48 hours after subjection to turbinmicin at concentrations spanning 1 to 16 times the MIC. CFU, colony-forming units. (**C**) Toxicity of turbinmicin on erythrocytes was performed by hemolysis assay. No hemolytic activity was detected for turbinmicin at all test concentrations. (**D**) Multidose in vivo experiments with turbinmicin against *C. auris* B11211 by using a neutropenic, mouse, disseminated candidiasis model (3 mice per dose). The multidose experiments invoked the administration of turbinmicin at doses of 0.25, 0.5, 1, 2, or 4 mg/kg at 6-hour intervals (over a 24-hour period) by intraperitoneal (IP). Mica, micafungin. (**E**) In vivo multidose experiments with turbinmicin against *A. fumigatus* F11628 by using a pneumonia model (3 mice per dose). Multidose experiments invoked the administration at doses of 0.25, 0.5, or 1 mg/kg at 6-hour intervals (over a 4-day period) by IP. CE, conidial equivalents; Posa, posaconazole. Statistics handling for both (D) and (E) used paired *t* test for normally distributed data and Wilcoxon signed-rank for non-normal data; *P* values for each data point are indicated in each panel (shaded box).

a central "hidden" node within this network (Fig. 3C), unifying the DAmP and diagnostic nonessential chemical-genetic data and further supporting Sec14p as the putative target of turbinmicin. Time-kill studies using *C. albicans* mutants from a haploinsufficiency library provided further support for Sec14p as turbinmicin's principal target (*43*). *C. albicans* deletion mutants in the orthologs of *SEC14*, *DOP1*, *BET5*, *SUN13*, and *SEC31* (Fig. 3D) all displayed hypersensitivity relative to wild-type *C. albicans*, consistent with turbinmicin's ability to impair vesicle-mediated transport (*43*).

To further test the hypothesis that turbinmicin impairs vesicle-mediated trafficking by inhibiting Sec14p, we directly examined membrane trafficking through the secretory and endocytic pathways of *S. cerevisiae* using the model cargo protein GFP (green fluorescent protein)–Snc1 (*44*). During exponential growth, GFP-Snc1 accumulates largely on the plasma membrane of nascent buds, with more modest localization to Golgi and endosomal membranes. However, in the presence of turbinmicin, GFP-Snc1 no longer concentrated within buds and instead remained entirely associated with the Golgi and endosomes (Fig. 3E and fig. S23). By contrast, cell polarity was not noticeably affected (fig. S23). Again, these data are consistent with previous studies showing that Sec14p inactivation localizes Snc1 to the Golgi and endosomes (*44*–*46*).

Finally, docking of turbinmicin into the phospholipid binding pocket of Sec14p produced a predominant binding mode with turbinmicin's heptacyclic ring system overlapping the co-crystallized ligand positions of picolinamide (6F0E) and β-octylglucoside (1AUA) (*39*) and turbinmicin's polyene tail extending into a hydrophobic cleft left vacant by the co-crystallized ligands (fig. S24). This observation was consistent with experimental findings in which cleavage of the turbinmicin side chain (through hydrolysis) reduced antifungal activity (see supplementary materials). These in silico studies, as with chemical genomics, haploinsufficiency, and membrane trafficking analyses, implicate Sec14p as the principal fungal liability exploited by turbinmicin and is foundational to its MOA.

The current and predicted impact of emerging antimicrobial resistance is a public health crisis underscored by recent reports from the World Health Organization and the CDC (*7*, *47*). For the first time, the CDC has classified the fungal pathogen *C. auris* as a highest-priority urgent risk (*7*). A major developmental challenge for antifungal agents is the establishment of their safety in humans and ability to evade or forestall resistance mechanisms. For instance, the echinocandins, despite their efficacy and generally excellent safety profiles, are inherently prone to resistance mechanisms associated with cryptococcal organisms; this susceptibility represents a major limitation and underscores the need for improved approaches. Both amphotericin and the azoles are characterized and limited by toxicity issues. The azoles, by virtue of their affinity for specific CYP450 enzymes, are particularly limited by toxicities stemming from drug–drug interactions. Studies to map turbinmicin's potential for toxicity are warranted, but the results of mouse models are thus far promising. Our data implicate Sec14p as the primary antifungal

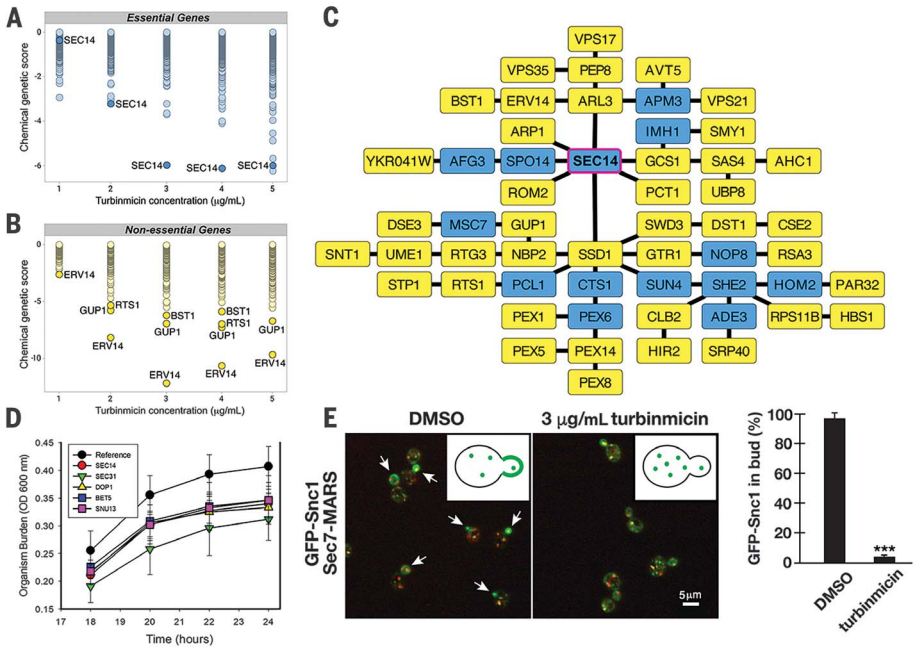

Fig. 3. MOA hypothesis of turbinmicin. Dose-wise chemical-genetic profiles of turbinmicin against the *S. cerevisiae* DAmP essential gene pool (**A**) and the diagnostic nonessential gene pool (**B**). Mean negative chemical-genetic interactions are represented in green [n = 6 except for 2 μg/mL turbinmicin in (C), in which n = 5]. (**C**) Resulting TransposeNET genetic interaction network built by using sensitive, nonessential gene mutants. Input genes are represented by yellow nodes, and "hidden" nodes are represented in blue. *SEC14* was a hidden node and highlighted with a magenta border. (**D**) Time-kill curve for turbinmicin against wild type and *C. albicans* mutants. Mutant *C. albicans* SEC14 H1 5C10, DOP1 H1 27E12, BET5 H1 5C5, SUN13 H1 4B5, SEC31 H1(PGA63) 29A6, and SEC31 H1(PGA63) 51H11 were used in this study. OD, optical density. (**E**) Representative images of GFP-Snc1 localization (green) relative to Golgi membranes (red) in the presence and absence of 3 μg/mL turbinmicin (five biological replicates each and at least 100 cells examined per condition; ***P < 0.001 based on a t test; error bars are SEM). Spectroscopy with pure turbinmicin (3 μg/mL) revealed fluorescence properties distinct and noninterfering with respect to those of the GFP and MARS (mRFPmars). Arrows highlight the distribution of GFP-Snc1 in buds in the absence of turbinmicin (also shown in the graphic). Scale bar, 5 μm. DMSO, dimethyl sulfoxide.

target of turbinmicin; potential off-target effects appear to be limited and devoid of downstream toxicities. Careful attention to monitoring for adverse effects with more prolonged treatments similar to those required for management of fungal disease in patients (typically 2 to 6 weeks), as well as studies in additional animal species, will be needed before further development toward human administration.

Our results illustrate that animal microbiomes harbor bacterial diversity readily translating to chemical diversity in the form of biosynthetic gene clusters (BGCs) that encode previously untested natural product scaffolds. Such scaffolds may use MOAs against microbial pathogens distinct from current drugs. Turbinmicin, with its highly functionalized polycyclic core and lipophilic side chain, appears to constitute one such scaffold. The BGC class associated with turbinmicin is rare (supplementary materials and figs. S21 and S22). The therapeutic potential of turbinmicin demonstrates the continued importance of microbial sources as beacons of discovery, especially given what we now know about evolutionarily selected microbiomes and ecosystems as well as the use of cutting-edge dereplication approaches. The promising in vitro and in vivo activity against urgent fungal pathogens, mammalian safety, and exploitation of Sec14p as a target argue for further preclinical development of turbinmicin as an antifungal lead.

REFERENCES AND NOTES

1. G. D. Brown *et al.*, *Sci. Transl. Med.* **4**, 165rv13 (2012).
2. P. G. Pappas *et al.*, *Clin. Infect. Dis.* **50**, 1101–1111 (2010).
3. A. H. Fairlamb, N. A. Gow, K. R. Matthews, A. P. Waters, *Nat. Microbiol.* **1**, 16092 (2016).
4. J. W. van der Linden, M. C. Arendrup, W. J. Melchers, P. E. Verweij, *Emerg. Infect. Dis.* **22**, 158–159 (2016).
5. D. S. Perlin, *Clin. Infect. Dis.* **61**, S612–S617 (2015).
6. J. F. Meis, A. Voss, *N. Engl. J. Med.* **380**, 890–891 (2019).
7. CDC, "Antibiotic resistance threats in the United States, 2019" (U.S. Department of Health and Human Services, 2019).
8. J. Clardy, M. A. Fischbach, C. R. Currie, *Curr. Biol.* **19**, R437–R441 (2009).
9. D. J. Newman, G. M. Cragg, *J. Nat. Prod.* **83**, 770–803 (2020).
10. S. Chanana *et al.*, *Metabolites* **7**, 34 (2017).
11. Y. Hou *et al.*, *Anal. Chem.* **84**, 4277–4283 (2012).
12. D. C. Earl *et al.*, *Nat. Commun.* **9**, 39 (2018).
13. M. G. Chevrette *et al.*, *Nat. Commun.* **10**, 516 (2019).
14. A. Hernandez, L. T. Nguyen, R. Dhakal, B. T. Murphy, *Nat. Prod. Rep.* (2020).
15. S. Chanana, C. S. Thomas, F. Zhang, S. R. Rajski, T. S. Bugni, *Metabolites* **10**, 297 (2020).
16. F. Zhang *et al.*, *Org. Lett.* **20**, 5529–5532 (2018).
17. N. Adnani, C. R. Michel, T. S. Bugni, *J. Nat. Prod.* **75**, 802–806 (2012).
18. T. Bunyapaiboonsri *et al.*, *Tetrahedron* **72**, 775–778 (2016).
19. T. Bunyapaiboonsri *et al.*, *Tetrahedron Lett.* **58**, 3223–3225 (2017).
20. F. Annang *et al.*, *J. Nat. Prod.* **81**, 1687–1691 (2018).
21. W. Zhang *et al.*, *Chem. Biol.* **19**, 422–432 (2012).
22. P. Lopez *et al.*, *Gene* **461**, 5–14 (2010).
23. M. Chu *et al.*, *J. Nat. Prod.* **60**, 525–528 (1997).
24. Clinical Laboratory Standards Institute, "Reference method for broth microdilution antifungal susceptibility testing of yeasts" (Approved standard M27-A3, Clinical Laboratory Standards Institute, ed. 3, 2007).
25. Clinical Laboratory Standards Institute, "Reference method for broth dilution antifungal susceptibility testing of filamentous fungi" (Approved standard M38, Clinical Laboratory Standards Institute, 2017).
26. M. Zhao *et al.*, *Antimicrob. Agents Chemother.* **62**, e02542–e17 (2018).
27. A. J. Lepak, D. R. Andes, "Animal models to evaluate anti-infective pharmacodynamics" in *Antibiotic Pharmacodynamics*, J. Rotschafer, D. Andes, K. Rodvold, Eds. (Humana Press, 2016), pp. 59–87.
28. D. Andes *et al.*, *Antimicrob. Agents Chemother.* **55**, 2113–2121 (2011).
29. A. J. Lepak, M. Zhao, E. L. Berkow, S. R. Lockhart, D. R. Andes, *Antimicrob. Agents Chemother.* **61**, e00791-17 (2017).
30. A. J. Lepak, K. Marchillo, J. Vanhecker, D. R. Andes, *Antimicrob. Agents Chemother.* **57**, 6284–6289 (2013).
31. M. Zhao *et al.*, *Antimicrob. Agents Chemother.* **63**, e02372-18–8 (2019).
32. D. Andes, A. Pascual, O. Marchetti, *Antimicrob. Agents Chemother.* **53**, 24–34 (2009).
33. A. J. Lepak, K. Marchillo, J. Vanhecker, D. R. Andes, *Antimicrob. Agents Chemother.* **57**, 579–585 (2013).
34. Z. Yan *et al.*, *Nat. Methods* **5**, 719–725 (2008).
35. J. S. Piotrowski *et al.*, *Nat. Chem. Biol.* **13**, 982–993 (2017).
36. M. Costanzo *et al.*, *Science* **353**, aaf1420 (2016).
37. J. Nelson *et al.*, *Bioinformatics* **34**, 1251–1252 (2018).
38. S. W. Simpkins *et al.*, *PLOS Comput. Biol.* **14**, e1006532 (2018).
39. V. Pries *et al.*, *Cell Chem. Biol.* **25**, 279–290.e7 (2018).
40. I. Filipuzzi *et al.*, *PLOS Genet.* **12**, e1006374 (2016).
41. A. H. Nile *et al.*, *Nat. Chem. Biol.* **10**, 76–84 (2014).
42. V. Khurana *et al.*, *Cell Syst.* **4**, 157–170.e14 (2017).
43. D. Xu *et al.*, *PLOS Pathog.* **3**, e92 (2007).
44. J. G. D'Arcangelo, K. R. Stahmer, E. A. Miller, *Biochim. Biophys. Acta* **1833**, 2464–2472 (2013).
45. A. J. Curwin, G. D. Fairn, C. R. McMaster, *J. Biol. Chem.* **284**, 7364–7375 (2009).
46. C. M. McDonold, J. C. Fromme, *Dev. Cell* **30**, 759–767 (2014).
47. World Health Organization (WHO). "Antimicrobial resistance-global report on surveillance" (WHO, 2014).

ACKNOWLEDGMENTS

This work is dedicated to the spirit and legacy of Prof. Robert M. Williams (February 1953 to May 2020). We thank the Analytical Instrumentation Center and the Medicinal Chemistry Center within the School of Pharmacy, University of Wisconsin–Madison for instrumentation as well as the National Magnetic Resonance Facility at Madison (NMRFAM). We also thank D. DeMaria (Sea Samples, Summerland Key, Florida, USA) for the collection of marine invertebrate specimens. **Funding:** This work was supported by funding from the University of Wisconsin–Madison School of Pharmacy and the Graduate School at the University of Wisconsin, NIH (grants U19 AI109673 and U19 AI142720 to T.S.B., C.R.C., and D.R.A.), NIGMS (grant R35 GM134865 to A.A. and grant R01 GM104192 to T.S.B.), and NIAID (grant R01 AI073289 to D.R.A.). This study made use of the National Magnetic Resonance Facility at Madison, which is supported by the NIH (grant P41GM103399) (NIGMS) (old number: P41RR002301). Equipment was purchased with funds from the University of Wisconsin-Madison, the NIH (P41GM103399, S10RR02781, S10RR08438, S10RR023438, S10RR025062, S10RR029220), the NSF (DMB-8415048,

OIA-9977486, BIR-9214394), and the USDA. **Author contributions:** Consistent with CRediT taxonomy, the roles of contributing authors are as follows: Conceptualization: T.S.B., D.R.A., C.R.C., and W.T.; methodology: F.Z., M.Z., D.R.B., J.S.P., J.N., J.P., G.E.A., S.C., K.B., I.A.G., C.Z., and L.G.; software: S.C., J.P., T.S.B., S.S.E., and J.S.P.; validation: I.A.G., F.Z., M.Z., D.R.B., A.A., D.R.A., and M.G.C.; formal analysis: F.Z., M.Z., S.S.E., J.S.P., J.N., G.E.A., J.F., A.A., and M.G.C.; investigation: F.Z., M.Z., S.S.E., C.Z., H.S., L.G., and A.A.; resources: D.R.B., S.S.E., G.E.A., S.C., K.B., H.S., and I.A.G.; data curation: F.Z., M.Z., G.E.A., W.T., C.R.C., S.R.R., A.A., D.R.A., and T.S.B.; writing—original draft: F.Z., S.R.R., M.Z., T.S.B., and D.R.A.; writing—review and editing: F.Z., J.F., H.S., J.S.P., C.R.C., S.R.R., A.A., D.R.A., and T.S.B.; visualization: T.S.B., D.R.A., C.R.C., and A.A.; supervision: T.S.B., D.R.A., C.R.C., and W.T.; project administration: D.R.A., T.S.B., and W.T.; and funding acquisition: D.R.A., C.R.C., T.S.B., and A.A. **Competing interests:** F.Z., D.R.B., T.S.B., M.Z., and D.R.A. are inventors on patent application no. PCT/US19/68786 filed through the Wisconsin Alumni Research Foundation (WARF), which covers turbinmicin and related compositions and uses thereof as antifungal agents with activity against MDR fungal infections. The remaining authors declare no competing interests. **Data and materials availability:** All data are available in the main text and/or supplementary materials. Materials are subject to standard Uniform Biological Materials Transfer Agreement. Crystallographic data for turbinmicin have been deposited with the Cambridge Crystallographic Data Centre (deposition number CCDC 1556369).

SUPPLEMENTARY MATERIALS

science.sciencemag.org/content/370/6519/974/suppl/DC1
Materials and Methods
Figs. S1 to S27
Tables S1 to S3
References (*48*–*76*)
Data Files S1 to S3
MDAR Reproducibility Checklist

View/request a protocol for this paper from *Bio-protocol*.

23 July 2020; accepted 5 October 2020
10.1126/science.abd6919

WATER PHASES

Experimental observation of the liquid-liquid transition in bulk supercooled water under pressure

Kyung Hwan Kim[1,2]*, Katrin Amann-Winkel[1]*, Nicolas Giovambattista[3,4], Alexander Späh[1], Fivos Perakis[1], Harshad Pathak[1], Marjorie Ladd Parada[1], Cheolhee Yang[2], Daniel Mariedahl[1], Tobias Eklund[1], Thomas. J. Lane[5,6], Seonju You[2], Sangmin Jeong[2], Matthew Weston[1], Jae Hyuk Lee[7], Intae Eom[7], Minseok Kim[7], Jaeku Park[7], Sae Hwan Chun[7], Peter H. Poole[8], Anders Nilsson[1]†

We prepared bulk samples of supercooled liquid water under pressure by isochoric heating of high-density amorphous ice to temperatures of 205 ± 10 kelvin, using an infrared femtosecond laser. Because the sample density is preserved during the ultrafast heating, we could estimate an initial internal pressure of 2.5 to 3.5 kilobar in the high-density liquid phase. After heating, the sample expanded rapidly, and we captured the resulting decompression process with femtosecond x-ray laser pulses at different pump-probe delay times. A discontinuous structural change occurred in which low-density liquid domains appeared and grew on time scales between 20 nanoseconds to 3 microseconds, whereas crystallization occurs on time scales of 3 to 50 microseconds. The dynamics of the two processes being separated by more than one order of magnitude provides support for a liquid-liquid transition in bulk supercooled water.

The discovery of the apparent divergence of isothermal compressibility (*1*) and heat capacity (C_P) (*2*) as water is supercooled has inspired many theoretical scenarios to explain the origin of this anomalous behavior (*3*–*5*). One popular hypothesis proposes the existence of a liquid-liquid transition (LLT) in supercooled water between high-density liquid (HDL) and low-density liquid (LDL), terminating at a liquid-liquid critical point (LLCP) at positive pressures (*3*, *6*). The anomalous behavior of water in this hypothesis is attributed to fluctuations emanating from the LLCP. Recently, the structure of supercooled water was found to change continuously upon cooling at 1 bar down to 227 K (*7*, *8*), indicating one-phase behavior without an LLT at ambient pressure. Therefore, the experimental results imply that if the LLT indeed exists, the associated LLCP must be located at pressure (P) > 1 bar (*3*). Rapid ice formation in conditions at which the LLT has been proposed has restricted studies of pure bulk water to computer simulations, with some models exhibiting an LLT and others not (*6*, *9*–*16*). Although measurements on amorphous ice and ultraviscous supercooled water at temperatures in the range of 115 to 150 K (*17*–*19*) are consistent with a LLT, it has been argued that these observations are not related to real liquid states (*20*–*22*) and cannot be directly connected to the two proposed liquid phases at higher temperatures.

An LLT has previously been detected in phosphorus, where the structure factor in x-ray scattering showed a discontinuous change with varying pressure (*23*). Also, in interfacial ice, a nonequilibrium phase transition was observed as a discontinuous change and coexistence of peaks in diffraction experiments (*24*). On the basis of neutron-scattering experiments of water, it has been proposed that distinct HDL and LDL phases may be identified by their well-defined peak positions in the structure factor (*25*). In particular, the position of the first peak in the O–O scattering is strongly sensitive to the existence of tetrahedral structures (LDL) or interstitial molecules between the first and second shells (HDL) (*25*–*27*). Hence, the most direct way to detect an LLT in supercooled water may be to follow the liquid structure with x-ray or neutron scattering and observe whether the scattering peaks undergo a discontinuous change like in phosphorus and interfacial ice, but with positions as predicted from the neutron-scattering results for water. The challenge is to conduct such an experiment at different pressures and on a time scale short enough so that the LLT may be observed before ice crystallization occurs.

Recent experimental approaches have allowed access to deeply supercooled water under conditions in which ice crystallization is rapid—for example, fast cooling of micrometer-sized droplets and ultrafast probing with an x-ray laser (*7*, *8*) as well as nanosecond heating of thin ice films into the liquid state (*28*). However, these studies have been limited to atmospheric pressure (1 bar) rather than the high-pressure conditions of the proposed LLT. In order to avoid crystallization, and given that the presence of ions has a similar effect as that of pressure on water, another recent approach has been to use highly concentrated supercooled aqueous solutions, which gives results indicating the existence of an LLT (*29*). However, it is unclear whether these results can be connected to an LLT in pure bulk supercooled water under conditions in which fast ice crystallization occurs.

We used a new compression-decompression procedure carried out on ultrafast time scales, where the initial pressure increase was imposed by laser-pulse–induced heating. When the time scale of the laser-induced energy release is much shorter than the time for sound to travel through the sample [valid with heating time scales of <0.1 ns for a >0.1-μm-thick water film (*30*)], the heating is isochoric, and the pressure inside the sample increases considerably. After the ultrafast laser pulse ends, the sample expands rapidly as the internal pressure decreases toward that of the surroundings. However, if the liquid dynamics are fast enough to relax the sample on a time scale shorter than the time for expansion, quasi-equilibrium behavior will be observed during the decompression process. We probed the system with x-ray scattering at different time delays during the decompression and observed a sudden change in the structure factor, which is indicative of a discontinuous LLT. We also detected ice crystallization occurring at longer time scales, confirming that the LLT is metastable and distinct from the liquid-ice transition.

We mounted high-density amorphous (HDA) ice samples in a cryostat inside a vacuum chamber to allow for pump-probe measurements in a transmission geometry, using infrared and x-ray lasers (Fig. 1A). Our samples were prepared ex situ under pressure and quenched-recovered at 78 K, at which the temperature was low enough to kinetically arrest the sample. The chosen samples in the measurement had a thickness of either 35 to 55 μm or 15 to 25 μm. They were then pumped by a 100-fs, 2-μm-wavelength infrared (IR) pulse, which excited a combination of O–H stretch and H–O–H bending modes that rapidly decayed into heat (*31*), and increased the temperature on a time scale of ≈20 ps (*32*). Excitations of the electron system may also be possible because our laser fluence (6.5 J/cm^2) was above the threshold known for nonlinear optical breakdown (*33*, *34*). However, no noticeable higher order behavior was observed in our experimental data, indicating that there is not a prominent contribution from a nonlinear process (*35*).

[1]Department of Physics, AlbaNova University Center, Stockholm University, SE-10691 Stockholm, Sweden. [2]Department of Chemistry, Pohang University of Science and Technology (POSTECH), Pohang 37673, Republic of Korea. [3]Department of Physics, Brooklyn College of the City University of New York, Brooklyn, NY 11210, USA. [4]Ph.D. Programs in Chemistry and Physics, The Graduate Center of the City University of New York, New York, NY 10016, USA. [5]SLAC National Accelerator Laboratory, 2575 Sand Hill Road, Menlo Park, CA 94025, USA. [6]Deutsches Elektronen-Synchrotron (DESY), Notkestrasse 85, 22607 Hamburg, Germany. [7]Pohang Accelerator Laboratory, Pohang, Gyeongbuk 37673, Republic of Korea. [8]Department of Physics, St. Francis Xavier University, Antigonish, NS B2G 2W5, Canada.
*These authors equally contributed to this work.
†Corresponding author. Email: andersn@fysik.su.se

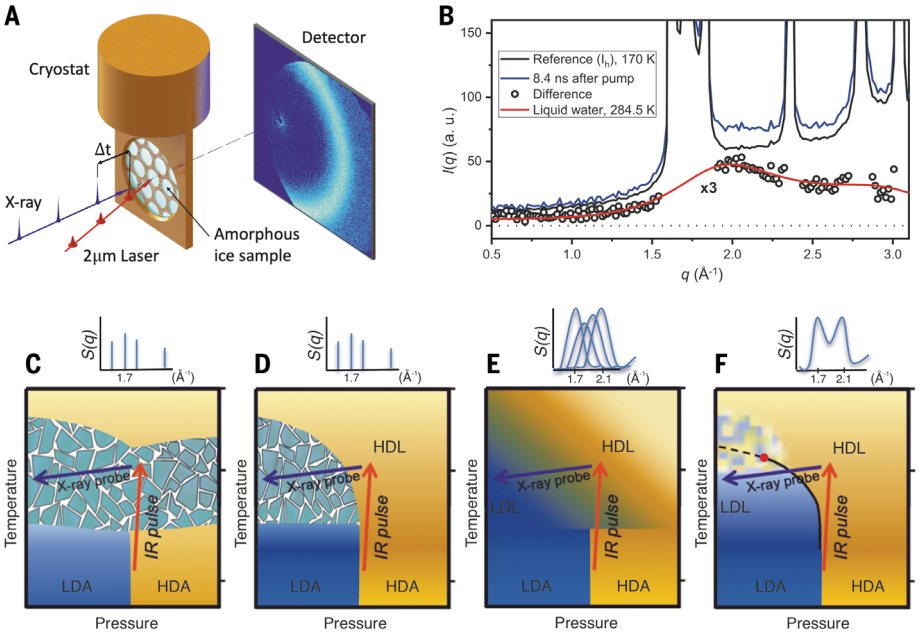

Fig. 1. Experimental set-up and different possible outcomes of the experiment. (**A**) Schematic of the experimental setup, with a sample holder containing a Cu-grid where amorphous ice samples are mounted, pump-probe scheme with IR and x-ray laser pulses, and a 2D detector for x-ray scattering measurements. (**B**) Laser-induced melting of ice I_h from a 170 K base temperature. The difference between the 8.4-ns delay and the unpumped sample omits regions where intense Bragg peaks lie. The difference data are compared with previously measured water scattering at 284.5 K (*41*). The difference is multiplied by a factor of 3 for clarity. (**C** to **F**) Four different hypotheses for the potential scenarios during the pump-probe experiment. At low temperatures, the equilibrium phase boundary between LDA and HDA is depicted. The original pressure of HDA is estimated from its preparation by pressure annealing and assuming constant sample density (*35*). The small sketches on top of the figures illustrate the evolution of the structure factor $S(q)$ probed with x-ray pulses along the blue arrow in the phase diagram. (C) HDA crystallizes immediately after exposure to the IR pump pulse (red arrow), resulting in Bragg-reflections in $S(q)$. (D) HDA transforms into supercooled water, followed by crystallization, resulting in Bragg peaks but at longer delay times. (E) Transformation into supercooled water, followed by a continuous transition from HDL to LDL, during which the first diffraction maximum in $S(q)$ is expected to shift continuously to lower-momentum transfers q. (F) $S(q)$ develops a second maximum at q = 1.7 Å^{-1} as LDL forms, which coexists with the maximum at q = 2.1 Å^{-1} associated with HDL, which is consistent with a first-order phase transition between HDL and LDL as proposed by the LLT scenario.

A 2-μm IR pulse can superheat ice and partially melt it within 10 ns (*36*), and such partial melting was achieved with the current setup for a 100-μm-thick hexagonal ice (I_h) sample (Fig. 1B) (*35*). When we applied equivalent heating to our HDA samples (<55 μm thick), the temperature increased from 115 to ~205 ± 10 K, as estimated from temperature-induced shifts in the Bragg reflections after crystallization occurred (*35*). We could estimate the pressure of the sample immediately after the IR was applied by using existing experimental data for liquid water. The density of HDA is known to be in the range of 1.13 to 1.16 ± 0.02 g/cm^3 (*37*), and isochoric heating maintained the density initially after the IR pump. From pressure-dependent measurements of density and temperature of supercooled water (*38*, *39*), we derived that the pressure after the IR pulse was between 2.5 and 3.5 kbar.

After the IR pulse was applied, spontaneous decompression began, during which the temperature remained approximately constant until cooling through heat conduction became essential after ~100 μs (*35*). This isothermal decompression carried the sample downward in pressure, and we probed the samples with intense <50-fs hard x-ray pulses of 9.7 keV at various time delays (8.4 ns to 1 ms) with respect to the IR pulse. Scattering patterns were recorded from individual x-ray shots on a large two-dimensional (2D) detector. For each time delay, 20 images were summed together, for which each image was measured with an x-ray shot taken at a fresh sample position.

In Fig. 1, C to F, we show predictions for the structure factor $S(q)$ as a function of momentum transfer q during decompression in four hypothetical scenarios: (i) Shown in Fig. 1C, direct crystallization to the high-pressure phase ice IX or I_h occurred immediately after the IR pulse was applied, because these are the underlying stable crystal phases. (ii) Shown in Fig. 1D, we assumed that only a single liquid phase existed that first appeared and then directly transformed into ice I_h or stacking disordered ice (I_{sd}) as the liquid decompressed (*10*). (iii) Shown in Fig. 1E, a continuous crossover from HDL to LDL occurred during decompression before crystallization (*4*). (iv) Shown in Fig. 1F, there was a discontinuous LLT from HDL to LDL before crystallization (*3*).

In cases (i) and (ii), we expected to see Bragg peaks in $S(q)$ caused by crystallization before any indication of the LDL structure. In case (iii), the first peak of $S(q)$ would shift smoothly with q upon decompression, similar to variations observed with pressure for 300 K water (*40*) or with temperature for 1 bar water (*8*, *41*). Last, in case (iv), for which there would be a discontinuous LLT involving distinct macroscopic phases, the HDL peak in $S(q)$ would remain at fixed q, and a new peak would appear and remain fixed at a different q (that of LDL) during decompression (*18*, *42*), similar to the previously observed LLT in phosporous (*23*).

The x-ray scattering intensity of the 35- to 55-μm-thick HDA samples is shown in Fig. 2A at various time delays after the IR pulse. The peak position before the IR pulse was at q = 2.15 Å^{-1}, which is consistent with recent studies of HDA (*18*, *27*). At 8.4 ns after the IR pulse was applied, the samples had undergone heating, and we observed that the peak position remained constant and near to that of liquid water at 300 K and pressures of 2 to 3 kbar (*40*). After 16.8 ns, a shoulder appeared at q = 1.7 Å^{-1}—a similar q position to that of LDA and LDL (*25*, *27*). This peak grew in intensity as decompression continued, up to a time delay of 3 μs. At longer time delays (3 μs to 1 ms), we observed the development of Bragg peaks corresponding to I_{sd} that increased over time. At the final time delay measured (1 ms), all samples had converted into ice.

Selected time delays of thinner samples (15 to 25 μm thickness) where the amount of HDL conversion to LDL was enhanced in comparison with the thicker ones are shown in Fig. 2B. After 1 μs, there is almost a 1:1 ratio of the two components. This enhancement was consistent with thinner samples having a more uniform heating than that of thicker samples, where the IR light is absorbed more at the front than at the back surface, leading to a larger temperature gradient (*35*). The two observed interconverting phases have q positions near HDL and LDL, as previously estimated from the extrapolation of temperature- and pressure-dependent neutron-scattering data of water at higher temperatures (*25*).

The scenarios in Fig. 1, D to F, can be applicable only if the sample after the IR pulse

was a liquid, rather than an amorphous solid, and remained liquid during the decompression process. Much evidence supports this interpretation. Immediately after the IR pulse, the sample was driven to a point in the phase diagram lying above the homogeneous ice nucleation temperature (T_H), conditions that are consistent with relatively fast liquid-like diffusion. In this region, water has been observed as a metastable liquid on a time scale of minutes before transforming to high-pressure crystalline ice phases (*43*). We observed no Bragg peaks corresponding to such crystalline ice phases at any delay times up to 1 ms, which is consistent with the sample being in a metastable liquid state above T_H.

To understand the immediate appearance of liquid-like diffusion after the IR-pulse heating of HDA, we used molecular dynamic simulations of the ST2 water model. There was a temperature offset of 25 K, meaning that the experimental temperature of 205 K corresponds to ~230 K in ST2 water (*35*). The mean-square displacement (MSD) of ST2 molecules are shown in Fig. 3A as function of time after rapid heating (at 3000 K/ns) of HDA. Starting at 80 K, HDA was heated to one of three different final temperatures in the range from 200 to 250 K and was then held constant. If there were a delay for the sample to enter the liquid state, the MSD would be initially constant and then increase linearly after the delay.

In our simulations, we saw that the MSD immediately increased linearly with time, as expected for a diffusing liquid. From these results, we can state that within 20 ps, after fast heating from HDA, a liquid state was obtained. This process was much faster than the partial melting of ice I_h by our IR pulse, which took ~10 ns (Fig. 1B). However, crystal melting, a transition between phases with qualitatively different structures, is an activated process that requires crossing a free-energy barrier. Our experimental HDA samples were held for 0.5 to 5 hours at 115 K, near the glass transition temperature of HDA (*18*, *37*), so before heating, they were already in an ultraviscous liquid state. The samples encountered no free-energy barrier on heating from 115 to 205 K, which is consistent with HDA and HDL being structurally closely related, and as a result, the

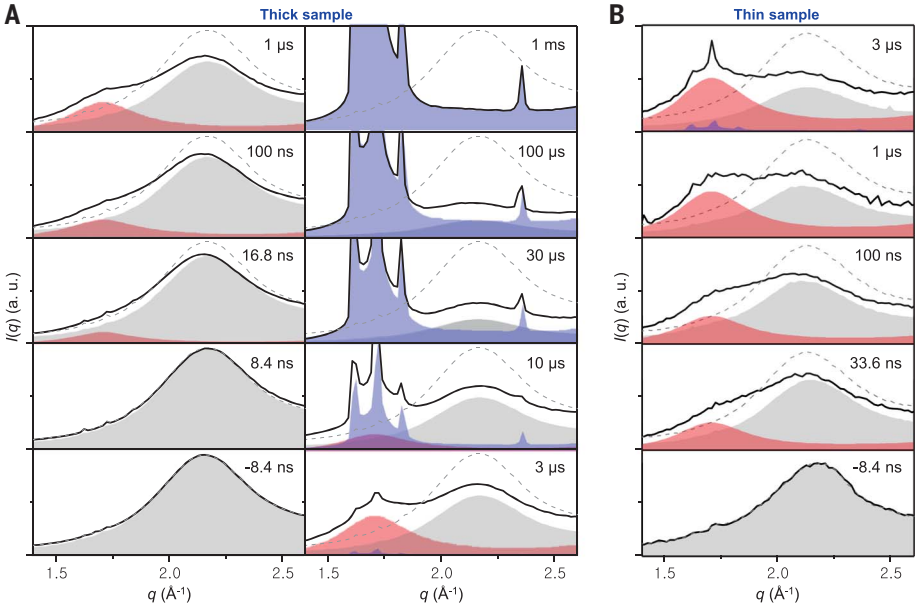

Fig. 2. Wde-angle x-ray scattering following the LLT from HDL to LDL. (**A**) Experimental x-ray scattering intensities, $I(q)$, of HDA samples of thickness 35 to 55 μm measured before (gray dashed line) and after (black solid line) the laser excitation. Data obtained at IR pump/x-ray probe delay times of −8.4 ns to 1 ms are shown. The contributions from HDL, LDL, and crystalline ice are indicated as gray, red, and blue shaded areas, respectively. (**B**) $I(q)$ curves of thinner HDA samples (15 to 25 μm thickness) after the laser excitation.

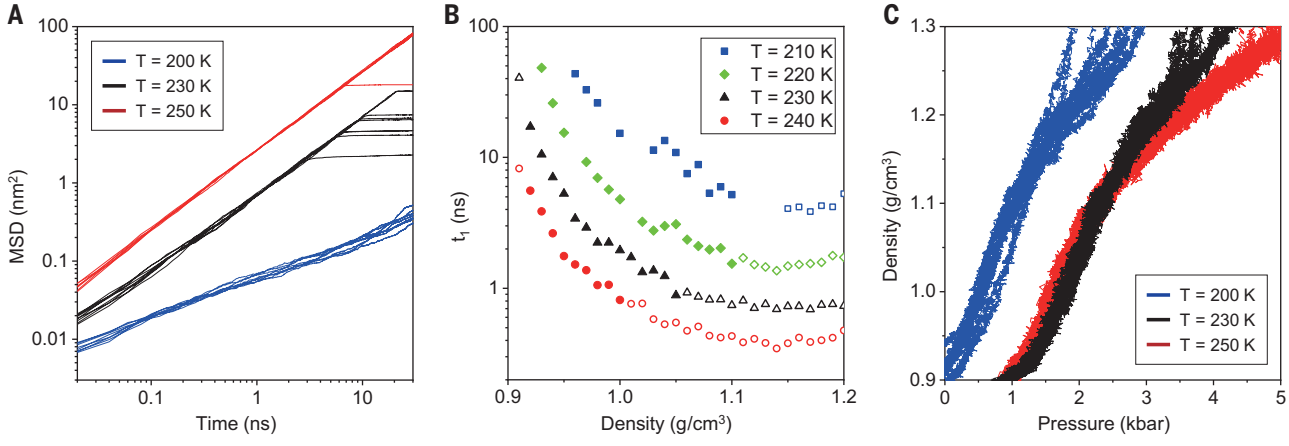

Fig. 3. Molecular dynamics simulation. (**A**) MSD of water molecules as a function of time during annealing of ultrafast heated HDA at T = 200 (blue), 230 (black), and 250 K (red) and at density 1.30 g/cm^3. At T = 230 K, all trajectories crystallize to a high-pressure ice form after t_x = 3 to 20 ns, and hence, the corresponding MSD(t) becomes constant at $t > t_x$. Some trajectories crystallize at T = 250 K as well, but no crystallization occurs at T = 200 K (within 30 ns). (**B**) Relaxation time, t_1, of liquid water as a function of density for several isotherms at 210 (blue), 220 (green), 230 (black), and 240 K (red). We computed t_1 using $t_1 = (1\ \text{nm}^2)/(6D)$, where D is the diffusion coefficient. Open symbols correspond to homogenous liquid systems that are either pure HDL or pure LDL, and solid symbols correspond to systems that have phase-separated into a mixture of coexisting HDL and LDL regions. (**C**) Density as a function of pressure during the decompression of ultrafast heated HDA at T = 200 (blue), 230 (black), and 250 K (red). The decompression rate is 3 kbar/ns.

onset of fast diffusion was immediate (*44*), as confirmed by our simulations when heated from the amorphous state starting from either 80 K or 115 K.

The diffusion coefficient D for liquid water at 205 K and 3 kbar can be interpolated from experimental data (*45*), from which we obtained $D = 2 \times 10^{-11}$ m^2/s. To convert D to a characteristic time for liquid-like diffusion, we define $t_1 = (1\ \text{nm}^2)/6D$, where t_1 is the average time required for the MSD to reach 1 nm^2, which is equivalent to diffusion of over three times the diameter of a water molecule. We found that immediately after the IR pulse, t_1 was 8 ns. For the ST2 model, when the system had a temperature in the range from 220 to 240 K and a density of 1.2 g/cm^3, the time t_1 was between 0.5 and 2 ns (Fig. 3B), which is consistent with the time scale found experimentally and confirms the temperature offset of ST2 water. Even after our shortest delay time (8.4 ns), the sample produced by the IR pulse had ample time to access the liquid state of HDL.

The time scale for liquid-like relaxation in the low-density regions that formed in our samples during decompression could be estimated in several ways. Previous measurements in thin layers of LDL water at 1 bar and 205 K found $D = 2 \times 10^{-13}$ m^2/s (*28*), corresponding to t_1 = 800 ns, a factor of about 100 times longer than the HDL formed after the IR pulse. Consistent with this factor, for ST2 water, we found that t_1 increased by a factor of ~50 as the system converted from pure HDL to pure LDL (Fig. 3B). Also, experimental crystallization times on the order of milliseconds were observed for an LDL liquid at 160 K obtained after fast decompression of high-pressure crystalline ice VIII (*46*) and could be modeled by using liquid-like diffusion. At 205 K, we observed crystallization on a time scale of 10 μs, indicating an LDL state with much greater molecular mobility than at 160 K. Furthermore, at $T > 200$ K, the density varied almost instantaneously in the ST2 model during fast decompression (Fig. 3C), which is in agreement with our observation that the transformation rate in the experiment was limited only by the speed of sound in the sample (*35*).

Both experiments and simulations indicated that a liquid-like equilibrium was established at 205 K in LDL within a time that is a factor of 50 to 100 times longer than for HDL. Because liquid-like equilibrium was established in HDL at 205 K within several nanoseconds, we can access equilibrium LDL within a few hundred nanoseconds. On this basis, the distinct high- and low-density phases observed on a submicrosecond time scale (Fig. 2) can be interpreted as quasi-equilibrated liquid phases. There is no immediate conversion to ice upon heating the sample, nor a continuous liquid-state conversion, as would be expected from the scenarios depicted in Fig. 1, C to E. The formation of crystalline ice would occur on time scales more than one order of magnitude longer than the conversion to LDL. It follows that our experimental data can only be quantitatively fit with the scenario shown in Fig. 1F (*35*), which shows the same discontinuous behavior in the x-ray scattering intensity as in the LLT of phosphorus (*23*).

To better characterize the progression of the LLT, we used scattering differences from the 35- to 55-μm-thick samples to estimate the fractional population of each phase in the sample as a function of the time delay (Fig. 4A) (*35*). We observed a small fraction of LDL at 16.8 ns that reached a maximum of ~40% of the total scattering intensity at 3 μs that was accompanied by a corresponding decrease in the HDL fraction. At 3 μs, crystalline ice appeared and became dominant at later times. The shape of the LDL scattering peak was not consistent with any substantial contributions of small nanocrystals of I_{sd} when LDL first appeared (*35*). The formation of crystalline ice occurred on a time scale more than one order of magnitude longer than the conversion of HDL to LDL, demonstrating that the LLT, although a metastable phase transition, was a distinct process from the liquid-to-ice transition.

Because of the dynamic nature of the decompression process, we expected that the conversion of HDL to LDL occurred in the region of the phase diagram between the equilibrium HDL-LDL coexistence line and the metastability limit (or spinodal) of the HDL phase. In this region, the transition should manifest itself at short times as localized LDL fluctuations, followed by nucleation and growth of LDL domains as the decompression proceeds (*47*). Small LDL fluctuations were evident in Fig. 4B, which shows the small-angle x-ray scattering (SAXS) intensity in the range from 0.1 to 0.3 Å^{-1} as a function of the time delay. There was a SAXS enhancement at short times peaking between 50 and 100 ns. The estimated correlation length, obtained by fitting the SAXS curves, peaks at 10 to 20 Å in the same time interval (*35*).

LDL fluctuations of this size appearing within the HDL phase would result in some contribution of scattering between atom pairs being in both LDL and HDL and would cause interference in the scattering process and affect the LDL peak position in q-space. Such interference has been observed in the conversion of unannealed HDA (uHDA), in contrast to expanded HDA (eHDA) (*18*). At early time delays, we observed such a shift (*35*), indicating that interference did arise from small LDL regions, which is consistent with the SAXS information.

At time delays longer than 100 ns, the interference was almost gone, and the SAXS enhancement was no longer visible, suggesting that the LDL domains grew to macroscopic size, and the contribution of atom pairs across the interface became negligible. Although the complete conversion of the sample to LDL was preempted by ice crystallization, for our thin samples, the HDL:LDL ratio reached 1:1 at 1 μs before any ice appeared (Fig. 2B). Nucleation and growth of LDL domains within HDL was

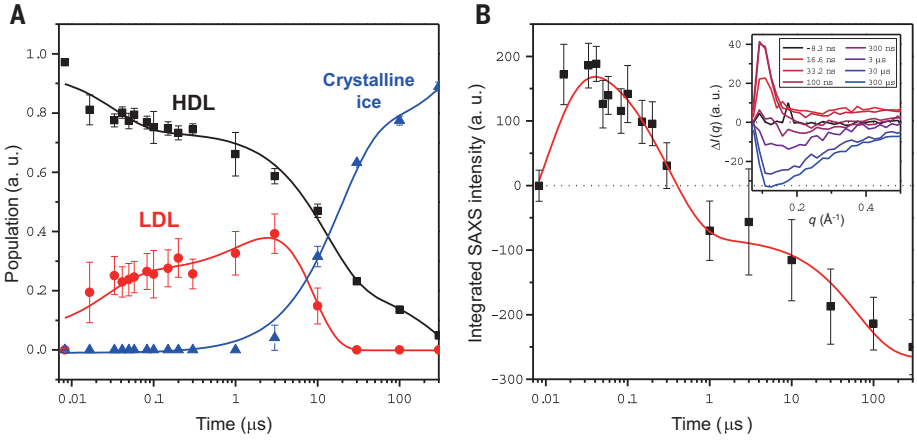

Fig. 4. Time-dependent population changes and SAXS intensity. (**A**) Time-dependent population changes of HDL (black squares), LDL (red circles), and crystalline ice (blue triangles). The solid black, red, and blue lines are shown to guide the eye. The error bar at each data point indicates the standard error determined from 20 independent measurements. (**B**) Time-dependent integrated SAXS intensity from q = 0.1 to 0.3 Å^{-1}. The solid red line is shown to guide the eye. (Inset) The difference between the unpumped and pumped scattering curves at various time delays in the SAXS region. After 1 μs, the samples became more homogeneous than the unpumped sample, resulting in a negative SAXS difference.

only consistent with a discontinuous first-order LLT and would not be observed in a continuous transformation of a spatially homogenous system from high to low density.

Our results reveal structural changes in liquid water at 205 K consistent with crossing a discontinuous LLT between HDL and LDL phases occurring at a pressure between ambient and 3.5 kbar. Although some uncertainty exists in our estimate of the temperature (195 to 215 K) at which the decompression process occurs in our experiments, our results show that an LLT occurred in the high-temperature region of the "no-man's land" (pressures and temperatures at which usually only crystallization occurs), and well above the temperature range of the amorphous ice phases, as confirmed by partially melting of hexagonal ice by using our IR heating procedure. Furthermore, the time scale we observed for the LLT (nanoseconds to microseconds) is consistent with a previous experimental estimate, based on extrapolations from 10 ms at 174 K to nanoseconds and microseconds at 220 K by using temperature-dependent kinetic measurements analyzed with an Arrhenius expression (*42*).

It has been observed that at 1 bar, crystallization occurs on a 10- to 100-μs time scale at ~8 K below T_H (*8*). Considering that we observed that ice crystallization from the LDL phase occurred on the same time scale, we expect that the HDL spinodal of the LLT (at ≈205 K) is a few degrees below T_H and follows closely the homogeneous ice nucleation line (*43*). A more narrow range of 1.5 to 2 kbar for the HDL spinodal is consistent with a recent LLT study that used a water-rich ideal solution that prevented crystallization (*48*).

Our observation of an LLT during isothermal decompression at positive pressure, combined with water at 1 bar changing continuously on cooling, implies the existence of an LLCP at positive pressures (*7*, *8*). We expect that the procedure presented here could provide more details about the nature of the LLT and help refine the location of the LLCP. The latter could be identified from critical fluctuations observed through SAXS intensity enhancements at lower q than in the present study, thus allowing detection of a diverging correlation length (*6*).

REFERENCES AND NOTES

1. R. J. Speedy, C. A. Angell, *J. Chem. Phys.* **65**, 851–858 (1976).
2. C. A. Angell, W. J. Sichina, M. Oguni, *J. Phys. Chem.* **86**, 998–1002 (1982).
3. P. H. Poole, F. Sciortino, U. Essmann, H. E. Stanley, *Nature* **360**, 324–328 (1992).
4. S. Sastry, P. G. Debenedetti, F. Sciortino, H. E. Stanley, *Phys. Rev. E Stat. Phys. Plasmas Fluids Relat. Interdiscip. Topics* **53**, 6144–6154 (1996).
5. R. J. Speedy, *J. Phys. Chem.* **86**, 982–991 (1982).
6. P. G. Debenedetti, F. Sciortino, G. H. Zerze, *Science* **369**, 289–292 (2020).
7. K. H. Kim *et al.*, *Science* **358**, 1589–1593 (2017).
8. J. A. Sellberg *et al.*, *Nature* **510**, 381–384 (2014).
9. T. A. Kesselring, G. Franzese, S. V. Buldyrev, H. J. Herrmann, H. E. Stanley, *Sci. Rep.* **2**, 474 (2012).
10. D. T. Limmer, D. Chandler, *J. Chem. Phys.* **138**, 214504 (2013).
11. E. B. Moore, V. Molinero, *Nature* **479**, 506–508 (2011).
12. J. C. Palmer *et al.*, *Nature* **510**, 385–388 (2014).
13. F. Smallenburg, F. Sciortino, *Phys. Rev. Lett.* **115**, 015701 (2015).
14. S. D. Overduin, G. N. Patey, *J. Chem. Phys.* **138**, 184502 (2013).
15. R. S. Singh, J. W. Biddle, P. G. Debenedetti, M. A. Anisimov, *J. Chem. Phys.* **144**, 144504 (2016).
16. J. C. Palmer *et al.*, *J. Chem. Phys.* **148**, 137101 (2018).
17. O. Mishima, Y. Suzuki, *Nature* **419**, 599–603 (2002).
18. F. Perakis *et al.*, *Proc. Natl. Acad. Sci. U.S.A.* **114**, 8193–8198 (2017).
19. K. Winkel, E. Mayer, T. Loerting, *J. Phys. Chem. B* **115**, 14141–14148 (2011).
20. C. A. Tulk, J. J. Molaison, A. R. Makhluf, C. E. Manning, D. D. Klug, *Nature* **569**, 542–545 (2019).
21. J. S. Tse *et al.*, *Nature* **400**, 647–649 (1999).
22. J. J. Shephard, C. G. Salzmann, *J. Phys. Chem. Lett.* **7**, 2281–2285 (2016).
23. Y. Katayama *et al.*, *Nature* **403**, 170–173 (2000).
24. D. S. Yang, A. H. Zewail, *Proc. Natl. Acad. Sci. U.S.A.* **106**, 4122–4126 (2009).
25. A. K. Soper, M. A. Ricci, *Phys. Rev. Lett.* **84**, 2881–2884 (2000).
26. J. L. Finney, A. Hallbrucker, I. Kohl, A. K. Soper, D. T. Bowron, *Phys. Rev. Lett.* **88**, 225503 (2002).
27. D. Mariedahl *et al.*, *J. Phys. Chem. B* **122**, 7616–7624 (2018).
28. Y. Xu, N. G. Petrik, R. S. Smith, B. D. Kay, G. A. Kimmel, *Proc. Natl. Acad. Sci. U.S.A.* **113**, 14921–14925 (2016).
29. S. Woutersen, B. Ensing, M. Hilbers, Z. Zhao, C. A. Angell, *Science* **359**, 1127–1131 (2018).
30. K. S. Kjær *et al.*, *Phys. Chem. Chem. Phys.* **15**, 15003–15016 (2013).
31. K. Ramasesha, L. De Marco, A. Mandal, A. Tokmakoff, *Nat. Chem.* **5**, 935–940 (2013).
32. H. Iglev, M. Schmeisser, K. Simeonidis, A. Thaller, A. Laubereau, *Nature* **439**, 183–186 (2006).
33. N. Linz, S. Freidank, X. X. Liang, A. Vogel, *Phys. Rev. B* **94**, 024113 (2016).
34. J. Savolainen, F. Uhlig, S. Ahmed, P. Hamm, P. Jungwirth, *Nat. Chem.* **6**, 697–701 (2014).
35. Materials and methods are available as supplementary materials.
36. S. Fanetti *et al.*, *J. Phys. Chem. Lett.* **10**, 4517–4522 (2019).
37. K. Amann-Winkel *et al.*, *Proc. Natl. Acad. Sci. U.S.A.* **110**, 17720–17725 (2013).
38. O. Mishima, *J. Chem. Phys.* **133**, 144503 (2010).
39. V. Holten, M. A. Anisimov, *Sci. Rep.* **2**, 713 (2012).
40. L. B. Skinner *et al.*, *J. Chem. Phys.* **144**, 134504 (2016).
41. L. B. Skinner, C. J. Benmore, J. C. Neuefeind, J. B. Parise, *J. Chem. Phys.* **141**, 214507 (2014).
42. C. Lin, J. S. Smith, X. Liu, J. S. Tse, W. Yang, *Phys. Rev. Lett.* **121**, 225703 (2018).
43. H. Kanno, R. J. Speedy, C. A. Angell, *Science* **189**, 880–881 (1975).
44. P. G. Debenedetti, F. H. Stillinger, *Nature* **410**, 259–267 (2001).
45. F. X. Prielmeier, E. W. Lang, R. J. Speedy, H. D. Lüdemann, *Ber. Bunsenges. Phys. Chem* **92**, 1111–1117 (1988).
46. C. Lin, J. S. Smith, S. V. Sinogeikin, G. Shen, *Proc. Natl. Acad. Sci. U.S.A.* **115**, 2010–2015 (2018).
47. K. Takae, H. Tanaka, *Proc. Natl. Acad. Sci. U.S.A.* **117**, 4471–4479 (2020).
48. Z. Zhao, C. A. Angell, *Angew. Chem. Int. Ed.* **55**, 2474–2477 (2016).

ACKNOWLEDGMENTS

Funding: This work has been supported by a European Research Council Advanced Grant under project 667205 and the Swedish National Research Council. K.A.-W. acknowledges funding by the Ragnar Söderbergs Stiftelse. T.J.L. was supported by by U.S. Department of Energy contract DE-AC02-76SF00515. This work is also supported by the National Research Foundation of Korea (NRF) grant funded by the Korea government (MSIT) (2019R1C1C1006643). The experiments were performed at beamline XSS of PAL-XFEL (proposals 2018-1st-XSS-009, 2018-2nd-XSS-006, and 2019-1st-XSS-008) funded by the Korea government (MSIT). P.H.P. is supported by the Natural Sciences and Engineering and Research Council (Canada). The simulations were supported by ACENET and Compute Canada. **Author contributions:** A.N. designed and supervised the study. K.A.-W. designed sample preparation. K.A.-W and A.S designed sample holder. K.A.-W., D.M., T.E., A.S., and M.L.P. prepared ice samples. K.H.K., K.A.-W., A.N., A.S., F.P., H.P., and M. W. designed experimental setup, chamber, and laser geometry. K.H.K., K.A.-W., A.N., A.S., F.P., H.P., M.L.P., C.Y., D.M., T.E., T.J.L, S.Y., S.J., J.H.L., I.E., M.K., J.P., and S.H.C. performed the x-ray experiments. N.G. and P.H.P. performed the computer simulations. K.H.K., A.S., C.Y., S.Y., and S.J. analyzed the data. A.N., K.H.K., K.A.-W., A.S., H.P., M.L.P., P.H.P., N.G., and T.J.L. wrote the manuscript. **Competing interests:** The authors declare no competing interests. **Data materials availability:** All data necessary for evaluating the conclusions of the study are included in the supplementary materials.

SUPPLEMENTARY MATERIALS

science.sciencemag.org/content/370/6519/978/suppl/DC1
Materials and Methods
Supplementary Text
Figs. S1 to S17
Tables S1 and S2
References (*49*–*79*)

27 March 2020; resubmitted 11 August 2020
Accepted 6 October 2020
10.1126/science.abb9385

GEOPHYSICS

Oceanic plateau of the Hawaiian mantle plume head subducted to the uppermost lower mantle

Songqiao Shawn Wei[1]*, Peter M. Shearer[2], Carolina Lithgow-Bertelloni[3], Lars Stixrude[3], Dongdong Tian[1]

The Hawaiian-Emperor seamount chain that includes the Hawaiian volcanoes was created by the Hawaiian mantle plume. Although the mantle plume hypothesis predicts an oceanic plateau produced by massive decompression melting during the initiation stage of the Hawaiian hot spot, the fate of this plateau is unclear. We discovered a megameter-scale portion of thickened oceanic crust in the uppermost lower mantle west of the Sea of Okhotsk by stacking seismic waveforms of *SS* precursors. We propose that this thick crust represents a major part of the oceanic plateau that was created by the Hawaiian plume head ~100 million years ago and subducted 20 million to 30 million years ago. Our discovery provides temporal and spatial clues of the early history of the Hawaiian plume for future plate reconstructions.

Earthquakes and volcanism at plate boundaries are well explained with the theory of plate tectonics, but explaining intraplate hot spot volcanoes requires the mantle plume hypothesis (*1*, *2*). This hypothesis posits deep-rooted and relatively fixed plumes of hot material upwelling through the mantle from the deep Earth and accounts for the age-progressive surface expression known as the Hawaiian-Emperor seamount chain. As the Pacific Plate moves northwest (*3*, *4*), the newest volcanoes are found in Hawaii to the southeast, and the oldest seamounts are near the Kamchatka-Aleutian trench junction in the northwest. The ~47 million year (Ma) bend of the seamount chain is usually attributed to a change in the Pacific Plate motion (*5*). The history of the Hawaiian-Emperor seamount chain is critical for understanding Earth's interior evolution and plate tectonics. In the classical view, a mantle plume consists of a large head (>2000 km across) and a thin tail (~200 km wide) (*6*). The plume head generates a large igneous province (LIP), such as the Ontong-Java oceanic plateau or the Deccan Traps. The plume tail creates an age-progressive intraplate volcanic chain. Several efforts have been made to associate ancient LIPs to hot spot volcanoes (*7*). For instance, the Deccan Traps are considered to result from the head of the Reunion mantle plume surfacing more than 68 Ma ago (*8*). However, because of the debatable early history of the Hawaiian-Emperor seamount chain, the fate of the Hawaiian mantle plume head and resulting oceanic plateau is unknown.

According to a variety of plate reconstructions (*3*, *4*), the Hawaiian-Emperor seamount chain entered the Kamchatka subduction zone. One proposal places this event as the cause of the cusp between the Kurile-Kamchatka and the Aleutian-Alaska trenches (*9*). The subduction of the seamounts generates arc lavas with geochemical signatures similar to oceanic island basalts on the Kamchatka Peninsula (*10*). The oldest surface portion of the Hawaiian-Emperor chain, the Meiji Guyot (older than 81 Ma) and Detroit Seamount (76 to 81 Ma) (*11*) are about to subduct into the Kamchatka Trench (Fig. 1). But whether the older parts of the seamount chain, particularly the plume head, also subducted into the deep mantle or stayed on Earth's surface is debated (*12*–*14*). The fate of the Hawaiian plume head is critical to the origin of the mantle plume, which provides a temporal constraint on the longevity and persistence of chemical characteristics of Earth's deep mantle. Furthermore, the subduction of the expected oceanic plateau caused by the Hawaiian plume head may have changed plate motions. Niu *et al.* (*12*) proposed that the collision of this oceanic plateau with the Kamchatka Trench was responsible for the Pacific Plate reorientation that resulted in the 47-Ma bend in the Hawaiian-Emperor chain.

More importantly, the fate of this oceanic plateau is critical for understanding the role of oceanic plateaus in building continental lithosphere and in mantle convection. Owing to their excess crustal thickness and volume, oceanic plateaus are thought to be more difficult to subduct than individual seamounts (*15*). Because the Yakutat terrane southeast of Alaska is the only oceanic plateau that is currently undergoing subduction (*16*), whether oceanic plateaus were commonly subducted in the past is unclear. By analyzing ophiolitic basalts in Kamchatka, Portnyagin *et al.* (*14*) proposed that the Hawaiian plume head, or at least part of it, was accreted to the forearc of Kamchatka. This mechanism provides an important way to grow continental crust (*7*). In contrast, a seismic study of compressional-to-shear (*P*-to-*S*) waves converted at seismic discontinuities (receiver functions) in South

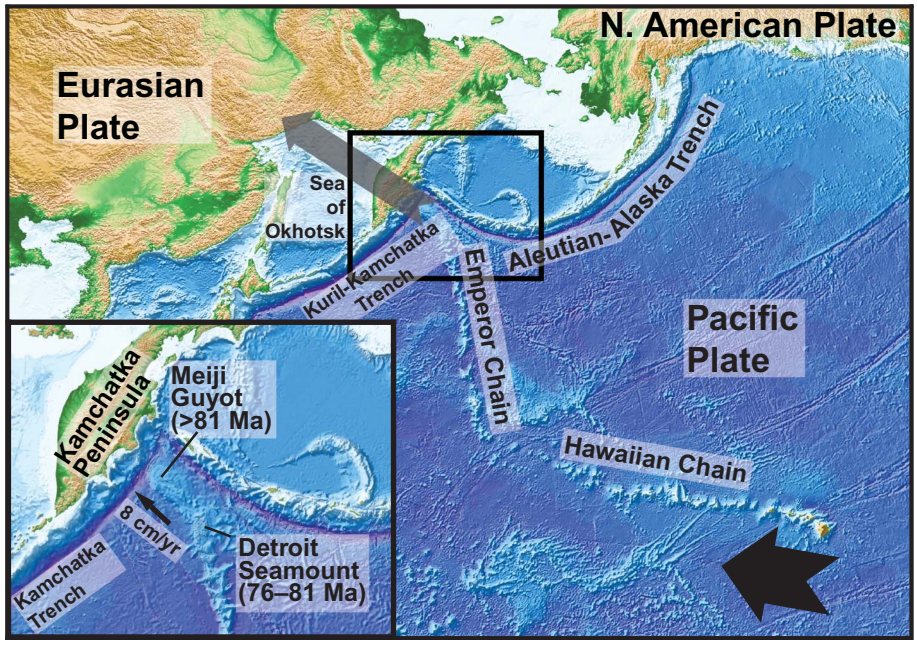

Fig. 1. Topographic-bathymetric map (*43*) of the northern Pacific Ocean and Northeast Asia. The bold black arrow indicates the current motion of the Pacific Plate at Hawaii relative to the Hawaiian plume, whereas the gray arrow represents the approximate trajectory of the Hawaiian-Emperor seamount chain into the Kamchatka subduction zone based on plate reconstructions (*3*, *4*). Inset shows the Kamchatka region where the oldest seamounts (Meiji Guyot and Detroit Seamount) of the Hawaiian-Emperor chain are about to subduct into the Kamchatka Trench at a speed of 8 cm/year.

[1]Department of Earth and Environmental Sciences, Michigan State University, East Lansing, MI 48824, USA. [2]Cecil H. and Ida M. Green Institute of Geophysics and Planetary Physics, Scripps Institution of Oceanography, University of California, San Diego, La Jolla, CA 92093, USA. [3]Department of Earth, Planetary, and Space Sciences, University of California, Los Angeles, CA 90095, USA.
*Corresponding author. Email: swei@msu.edu

America suggests that an oceanic plateau with a thickness of at least 13 to 19 km has subducted to ~100 km depth and is responsible for the Pampean flat slab (*17*). Geodynamic models also show that oceanic plateaus can subduct into the upper mantle, resulting in slowdown of subduction (*18*), formation of a flat slab (*19*), surface topography elevation (*20*), and dynamic uplift (*21*). In comparison with the subduction of normal oceanic crust of 6- to 7-km thickness, the input of thick oceanic plateaus might also change, at least locally, mantle composition and dynamics.

Although mantle plume conduits have been successfully imaged using seismic tomography with dense datasets (*22*), oceanic plateaus potentially subducted into the lower mantle have a 20- to 40-km crustal thickness that is smaller than the resolution in most tomographic studies. Owing to a lack of data, the tomography resolution in northeastern Siberia is particularly low in both global (*23*) and regional (*24*) images. Seismic reflected waves are more sensitive to sharp boundaries and provide a more effective tool to detect small-scale compositional heterogeneities in the deep mantle. Many seismic reflectors in the lower mantle have been imaged globally and attributed to segments of subducted crust (*25*–*27*). But ancient oceanic plateaus have not been detected in the lower mantle, in part because of the limited data coverage in regions where they are expected.

We stacked *SS* precursors (*SdS*) from 45 years of global seismic data to detect seismic reflectors in the lower mantle (*28*). The *SdS* seismic phase is the underside *S* wave reflection off the *d*-km discontinuity, which arrives before the surface-reflected *SS* phase (fig. S1A). Because *SS* precursors sample the midpoints between earthquakes and seismic stations, they provide good data coverage for remote regions and are widely used to image seismic discontinuities in the upper and mid-mantle (*29*). Besides the major seismic discontinuities extending globally, previous observations detected many smaller-scale reflectors using *SS* or *PP* precursors (*26*, *30*).

We focus on a seismic reflector observed at ~810 km depth west of the Sea of Okhotsk, which was previously detected by limited data of *PP* precursors (*30*). The reflector has a width on the order of 1000 km and a depth varying from 780 to 820 km across (Fig. 2). When compared with global tomography models (*23*), the 810-km reflector appears to coincide with the Kamchatka slab, which is the ancient Pacific Plate subducted along the Kamchatka Trench (Fig. 3B). Given the limited resolution of tomography models, determining whether the reflector is at or above the slab surface (top interface) is challenging. The exact shape of this 810-km reflector is unclear because of the wide Fresnel zone (~1000 km across) and the low horizontal resolution of *SS* precursors. Additionally, determining the absolute reflector depth and topography relies on the seismic velocity in the upper mantle. With different three-dimensional (3D) mantle velocity models, the average depth of the 810-km reflector varies from 780 to 830 km depending on the choice of model, and its topography also changes from flat to elevated in the center by 30 km (figs. S2 and S3). The seismic signal *S810S* corresponding to the 810-km reflector has an apparent amplitude as strong as that of the *S660S* signal for the 660-km discontinuity. The absolute amplitude of *S810S* is influenced by incoherent stacking and seismic attenuation effects that are difficult to constrain (*28*). Therefore, we conclude that this megameter-scale reflector marks an *S*-wave impedance (product of density and *S*-wave velocity) increase at 780 to 820 km depths on the same order of magnitude of the impedance increase across the 660-km discontinuity.

In certain regions, we observe an azimuthal dependence of *S810S* in which the signal is only

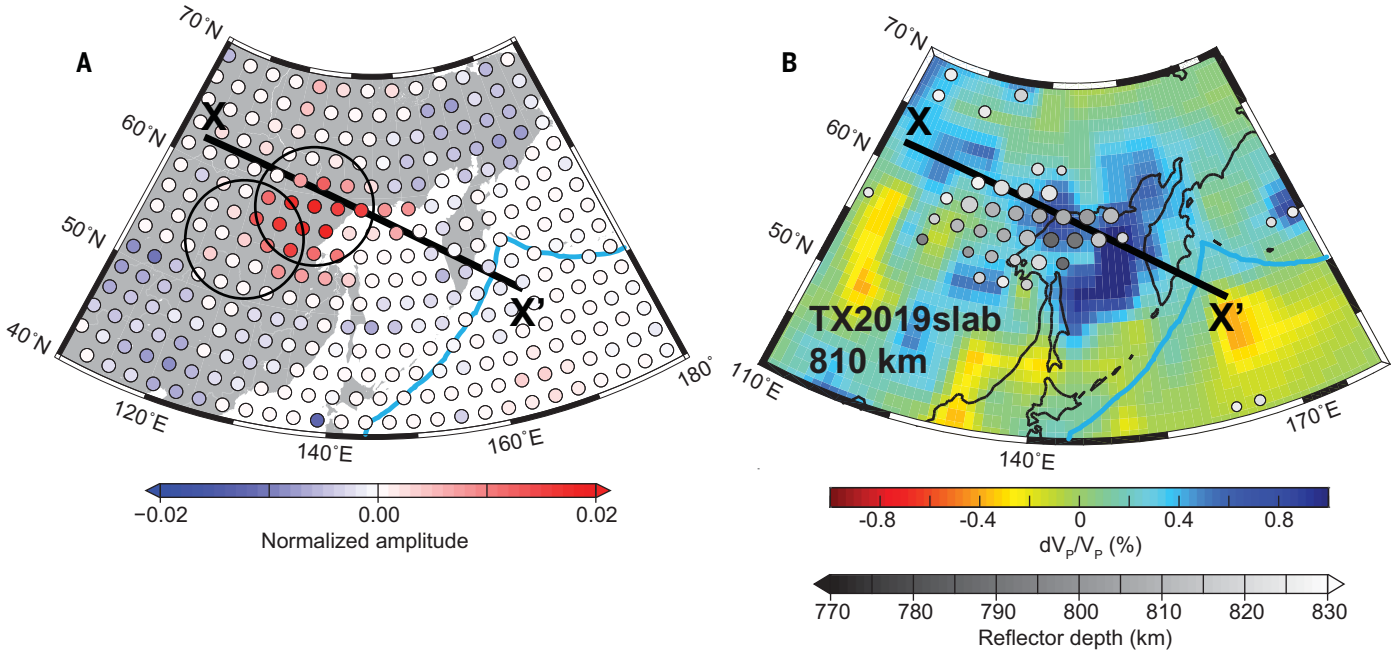

Fig. 2. Maps of the 810-km reflector compared with velocity tomography. (**A**) Map of amplitudes (above the 95% confidence level) of stacked *SS* precursor waveforms at 810 km depth in the Siberia-Okhotsk-Kamchatka region. The *SS* precursor amplitude is normalized to the *SS* amplitude in the same cap. Red circles show the high amplitude of *S810S*, indicating the 810-km reflector. *SS* precursors are stacked in overlapping bouncepoint caps of 5° radius and 2° spacing. The two large circles outline the actual area of caps, which are represented by small solid circles at their centers that are color-coded by amplitude. The lateral resolution of our data is ~1000 km, which is comparable to the size of each cap and the Fresnel zone width. The black line indicates the cross section X-X′ in Fig. 3. The blue curves illustrate convergent plate boundaries (*44*). (**B**) Depth of the 810-km reflector in caps superimposed on the TX2019slab *P*-wave tomography model (*23*) at 810 km depth. dV_P/V_P, fractional *P*-wave velocity perturbation. The reflector depth is shown by the grayscale in caps where it is detected. Circle sizes are scaled to indicate the depth uncertainty, such that larger circles have lower uncertainties. In caps where the 810-km reflector is less evident owing to low amplitude, its depth has larger uncertainties. Caps with depth uncertainties greater than 10 km are omitted.

detectable along certain azimuths (fig. S4A). This dependence raises the question of whether the *S810S* signal is caused by near-source or near-receiver structures rather than a reflector beneath the midpoints (*31*). However, tests of this possibility confirm the existence of the 810-km reflector west of the Sea of Okhotsk, partly because our observation results from thousands of seismograms with a variety of focal mechanisms (*28*). Although 3D heterogeneity near sources or receivers may contaminate the *S810S* signals with *PPPS* and *PPPPS* signals from the radial component, the energy contribution should be negligible because the similar *PS* and *PPS* waves are too weak to detect on the transverse component (fig. S5E). The azimuthal dependence may also suggest azimuthal anisotropy and small-scale heterogeneity that are difficult to determine conclusively given our limited data and resolution. Nevertheless, tests of possible scattering artifacts generated by distant 3D structures indicate that only a near-midpoint reflector is a plausible explanation for the *S810S* observations (*28*).

The 810-km reflector is surprising because it requires large and rapid increases in density and *S*-wave velocity. The surface of a flat and cold slab is a natural candidate to explain the reflector. Synthetic waveform modeling shows that either a moderately fast–velocity slab underneath a sub-660 low-velocity zone (LVZ) or a high-velocity slab is required to generate an *S810S* signal similar to our observation (fig. S6). By taking uncertainties of the *S810S* amplitude into account, conservative estimates lead to a 2% velocity reduction for the sub-660 LVZ or a 4% velocity increase within 5 km across the slab surface. However, neither the LVZ nor the ultra-high-velocity anomaly appears in any seismic tomography model, and we cannot explain either with thermal variations. In addition, the coherence of the *S810S* observations suggests that the 810-km reflector is nearly flat with a dip angle smaller than 2° within a megameter-wide area (figs. S7 and S8). Such a smooth and flat slab, although often a feature in conceptual models, is unlikely to be a realistic geometry in the mantle. For reference, the Pampean flat slab extends only ~300 km laterally at a depth of ~100 km before dipping into the deep Earth (*17*). Therefore, a simple slab model that is purely controlled by temperature cannot explain our observation.

This flat 810-km reflector could alternatively be caused by a pressure-dominated mineral phase transition. We used a thermodynamic simulation package called HeFESTo (*32*, *33*) to calculate density and *S*-wave velocity profiles of mantle minerals for a variety of bulk compositions along various 1D thermal profiles (*28*). The mantle composition can be represented by pyrolite, a synthetic rock with the chemical composition of the upper mantle that reaches equilibrium. On the other hand, the mantle is hypothesized as a mechanical mixture of two end-members of mantle differentiation, basalt and harzburgite, that never reaches equilibrium (*34*). With an identical bulk chemical composition, an equilibrium assemblage (pyrolite) and a mechanical mixture of basalt and harzburgite have different phase assemblages and therefore different mineralogical compositions and seismic velocities (*34*). A pyrolitic or harzburgite composition can produce a 660-km discontinuity corresponding to the olivine transition (ringwoodite to bridgmanite and ferropericlase) but with no obvious signal at ~810 km depth (fig. S9). In contrast, a basaltic composition can produce a strong *S810S* signal corresponding to the garnet transition (majorite to bridgmanite) but a small *S660S* signal. If the mantle is a mechanical mixture of basalt and harzburgite, we expect to observe the olivine transition at ~660 km depth because of harzburgite, and the garnet transition at ~810 km depth because of the basaltic component. The predicted *S810S* signal is much weaker than the observation even if the basalt fraction (f) is 30%, which is much higher than the 18% fraction suggested for the entire mantle (*34*). Therefore, an equilibrium assemblage of pyrolitic composition or a mechanical mixture of basalt and harzburgite cannot explain the observed *S810S* signal.

A more realistic model is represented by a flat slab at 800 to 950 km depth with a basaltic

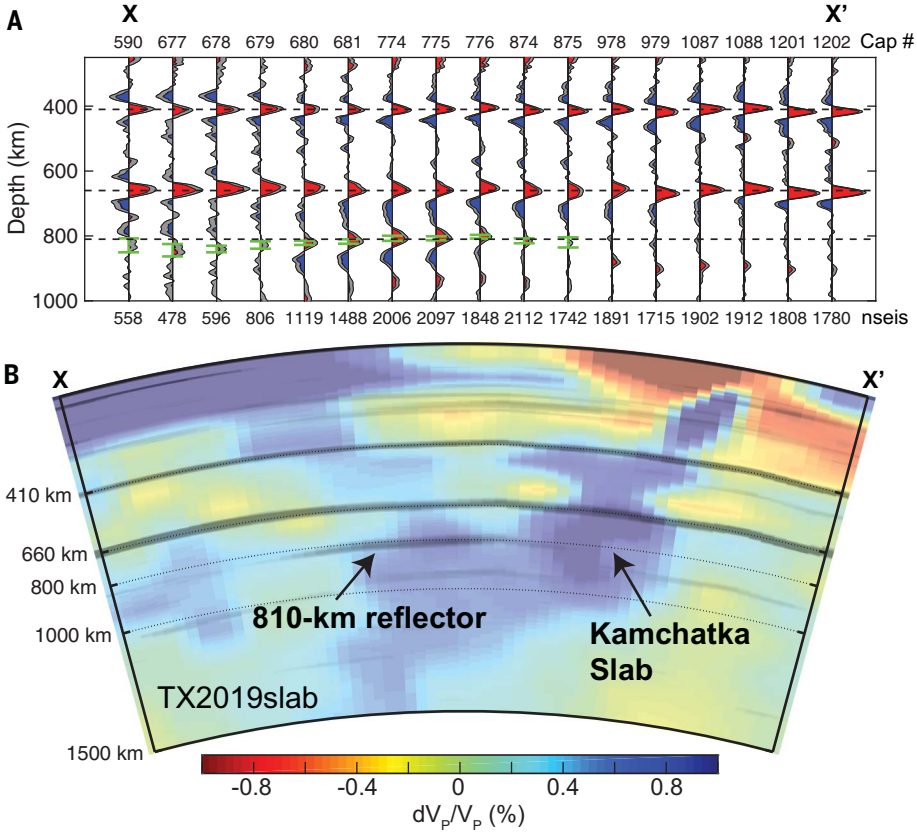

Fig. 3. Cross section of apparent discontinuities and reflectors along the cross section shown in Fig. 2A. (**A**) Stacked *SS* precursors observed in overlapping caps of 5° radius and 2° spacing. All seismograms are converted to the depth domain, stacked, and then corrected for 3D velocity heterogeneity using the TX2019slab *S*-wave velocity model (*23*). Red and blue indicate robust positive and negative signals above the 95% confidence levels, respectively, whereas gray shows the stack uncertainty (2σ). Black dashed lines show depths of 410, 660, and 810 km. The cap indices (Cap #) are shown along the top, and the numbers of seismograms (nseis) stacked in those caps are shown along the bottom. A strong peak appears at ~810 km depth in certain caps. Green error bars indicate the depth of the 810-km reflector in each cap where it is detected. Weak positive signals at greater depths are artifacts resulting from interfering seismic phases (topside reflections off the 410- and 660-km discontinuities, that is, *Ss410s* and *Ss660s*, respectively) rather than *SS* precursors. Similar cross sections with different depth corrections based on other *S*-wave tomography models are shown in fig. S2. (**B**) Apparent discontinuities and reflectors (dark stripes) from *SS* precursor stacks superimposed on the TX2019slab *P*-wave tomography model (*23*). All positive signals shown in (A) are interpolated and shown as dark stripes, whereas all negative signals are omitted. Similar cross sections superimposed on other *P*-wave tomography models are shown in fig. S3.

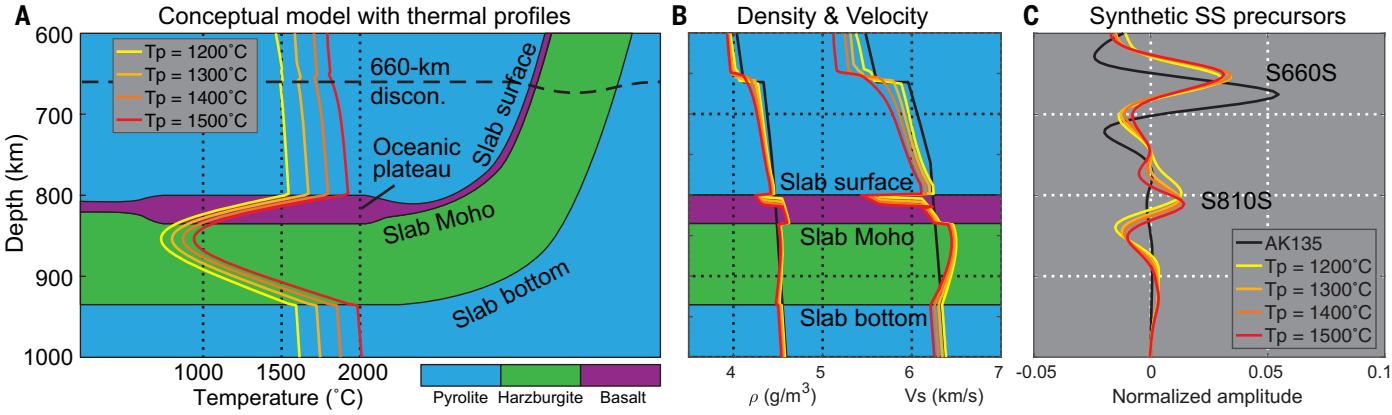

Fig. 4. The garnet transition in an oceanic plateau in the lower mantle can explain the observed *S810S* signal. (**A**) A conceptual model of the Kamchatka slab subducted into the lower mantle. Blue, green, and purple colors represent pyrolitic, harzburgite, and basaltic compositions, respectively. The oceanic plateau has a crustal thickness of 35 km, whereas the other parts of the oceanic crust are 6 km thick. Yellow to red curves show the thermal profiles across the flat slab with a variety of potential temperatures (T_P). (**B**) Density (ρ) and *S*-wave velocity (V_S) profiles corresponding to the thermal profiles in (A). Black curves indicate the AK135 reference model (*45*). The density profiles of the slab crust cross that of the reference model at 800 to 830 km depths owing to the majorite-bridgmanite transition, indicating that the oceanic crust is neutrally buoyant along all thermal profiles. (**C**) Synthetic *SS* precursor waveforms corresponding to the density and velocity profiles in (B). The *S810S* signal is strong enough to be observed along all thermal profiles. Note that we do not try to fit the exact waveform because of the large uncertainties of thermodynamic parameters of minerals and the *S810S* amplitude.

crust overriding on a depleted (harzburgite) slab mantle in the pyrolitic ambient mantle (*35*). Although seismic impedance decreases from the ambient mantle to the slab crust, it increases from the crust to the slab depleted mantle. More importantly, majorite garnet in the slab crust may transform to bridgmanite near 810 km depth, producing a sharp increase in seismic impedance (*28*). The impedance changes in a model with a normal crustal thickness of 6 km are not resolvable by long-period *SS* precursors with the vertical resolution of 30 to 50 km in the uppermost lower mantle (fig. S10A). In contrast, we obtain a strong *S810S* signal if we assume an oceanic plateau with a 35-km-thick crust, which is comparable to the crust of the Ontong-Java Plateau (*36*). This *S810S* signal results from the combination of all impedance changes from the slab surface to Moho (Fig. 4). If the oceanic plateau is 20 km thick, the *S810S* signal is still detectable, but with a weaker amplitude (fig. S10B). Furthermore, the density profile of the slab crust crosses that of the ambient mantle owing to the majorite-bridgmanite transition, suggesting that the slab crust, regardless of its thickness, is neutrally buoyant at the depths of 800 to 835 km. We cannot assess whether the slab crust has been detached from the downgoing slab mantle, as suggested by geodynamic models (*37*), because a model with an orphan slab crust can also produce a detectable *S810S* signal (fig. S10C). Nevertheless, the thick crust of the subducted oceanic plateau, roughly as wide as the Ontong-Java Plateau, probably has been floating in the mantle at 800 to 835 km depth since it reached these depths as a result of the neutral buoyancy. This explains the large dimension of the flat slab at a nearly constant depth in the uppermost lower mantle. The possible topographic changes of the 810-km reflector may be caused by thermal and thickness variations of the oceanic plateau.

By comparing with seismic tomographic models and exploring all possible geodynamic and mineralogical explanations, we conclude that the 810-km reflector we observed most likely indicates a megameter-scale thickened crust subducted to the lower mantle. Because this thick crust is on the trajectory of the Hawaiian-Emperor seamount chain (Fig. 1), we propose that it is a major portion of the oceanic plateau associated with the head of the Hawaiian mantle plume. Because oceanic plateaus are small compared with the volume of global oceanic crust, the subduction of these plateaus will not bias our estimate of the mantle bulk composition. However, this process can lead to localized enrichment of basalt in the mantle and can locally alter the slab buoyancy, slowing down subduction (*18*) and contributing to the flattening of slabs above the 660-km discontinuity. If we assume a constant subduction rate of 75 mm/year and a slab dip angle of 50° above the flat part (*38*), this oceanic plateau subducted into the Kamchatka Trench ~20 to 30 Ma ago. The subduction of the oceanic plateau is apparently much younger than the bend of the Hawaiian-Emperor seamount chain and therefore not related to the change in the Pacific Plate motion ~47 Ma ago (*5*). Previous studies suggest that the collision between the Ontong Java Plateau and the northern Australian Plate margin 6 Ma ago caused a series of plate tectonics events, including the counterclockwise rotation of the Pacific Plate (*39*). The subduction of this Hawaiian plume oceanic plateau temporally coincides with a kink of the Hawaiian-Emperor chain east of Midway Island. However, the causality is unclear, partially because the East Pacific Rise collided with the North American Plate around the same time. On the other hand, the subduction of the Pampean flat slab ~10 Ma ago did not cause any drastic plate reorganization. Further studies with more observations are needed to examine the relationship between oceanic plateau subduction and plate reorganization.

Plate reconstruction models using different mantle reference frames with moving hot spot frames suggest that the Hawaiian hot spot moved from the Izanagi Plate to the Pacific Plate ~100 Ma ago if the hot spot existed earlier (*3*, *4*, *40*, *41*). If the Hawaiian plume head surfaced on the Izanagi Plate, the oceanic plateau would have been subducted into the Aleutian Trench toward the North Pole more than 70 Ma ago, which is inconsistent with our observation. Therefore, we believe that the oceanic plateau associated with the Hawaiian plume head was formed on the Pacific Plate no earlier than 106 Ma ago. This estimate is consistent with the 93-to 120-Ma-old ophiolitic basalts in Kamchatka that were produced by the Hawaiian plume and accreted to the Kamchatka forearc much later (*14*). Given the available plate reconstruction models (*3*, *4*, *40*, *41*), we hypothesize that the Hawaiian plume head surfaced ~100 Ma ago to create a megameter-scale oceanic plateau at the Izanagi-Pacific Ridge (fig. S11). As the mid-ocean ridge spread, the oceanic plateau broke into two parts, and

the Izanagi part moved northward and subducted into the ancient Aleutian Trench ~72 Ma ago. On the other hand, before the Pacific part of the oceanic plateau subducted into the Kamchatka Trench, its eastern margin might also have encountered the Aleutian Trench and a possible subduction zone between the Kula and Kronos Plates (*42*). There are discrepancies between the plate reconstruction models and our inferences regarding the subduction time and the present position of the Pacific part of the oceanic plateau. This direct comparison is challenging because the detailed history of this plateau highly depends on the initial location and migration rate of the Izanagi-Pacific Ridge. However, our observations provide critical constraints for future plate reconstructions.

REFERENCES AND NOTES

1. J. T. Wilson, *Can. J. Phys.* **41**, 863–870 (1963).
2. W. J. Morgan, *Nature* **230**, 42–43 (1971).
3. K. J. Matthews *et al*., *Global Planet. Change* **146**, 226–250 (2016).
4. T. H. Torsvik *et al*., *Geochem. Geophys. Geosyst.* **20**, 3659–3689 (2019).
5. T. H. Torsvik *et al*., *Nat. Commun.* **8**, 15660 (2017).
6. I. H. Campbell, R. W. Griffiths, *Earth Planet. Sci. Lett.* **99**, 79–93 (1990).
7. S. E. Bryan, L. Ferrari, *Geol. Soc. Am. Bull.* **125**, 1053–1078 (2013).
8. P. Glišović, A. M. Forte, *Science* **355**, 613–616 (2017).
9. P. R. Vogt, *Nature* **241**, 189–191 (1973).
10. G. P. Avdeiko, D. P. Savelyev, A. A. Palueva, S. V. Popruzhenko, in *Volcanism and Subduction: The Kamchatka Region*, J. Eichelberger, E. Gordeev, P. Izbekov, M. Kasahara, J. Lees, Eds. (Geophysical Monograph Series, American Geophysical Union, 2007), pp. 37–55.
11. R. A. Duncan, R. A. Keller, *Geochem. Geophys. Geosyst.* **5**, Q08L03 (2004).
12. Y. L. Niu, M. J. O'Hara, J. A. Pearce, *J. Petrol.* **44**, 851–866 (2003).
13. B. Steinberger, C. Gaina, *Geology* **35**, 407–410 (2007).
14. M. Portnyagin, D. Savelyev, K. Hoernle, F. Hauff, D. Garbe-Schonberg, *Geology* **36**, 903–906 (2008).
15. M. Cloos, *Geol. Soc. Am. Bull.* **105**, 715–737 (1993).
16. G. Rossi, G. A. Abers, S. Rondenay, D. H. Christensen, *J. Geophys. Res. Solid Earth* **111**, B09311 (2006).
17. C. R. Gans *et al*., *Geophys. J. Int.* **186**, 45–58 (2011).
18. P.-A. Arrial, M. I. Billen, *Earth Planet. Sci. Lett.* **363**, 34–43 (2013).
19. J. van Hunen, A. P. van den Berg, N. J. Vlaar, *Tectonophysics* **352**, 317–333 (2002).
20. L. Liu *et al*., *Nat. Geosci.* **3**, 353–357 (2010).
21. F. M. Dávila, C. Lithgow-Bertelloni, *Earth Planet. Sci. Lett.* **425**, 34–43 (2015).
22. S. W. French, B. Romanowicz, *Nature* **525**, 95–99 (2015).
23. C. Lu, S. P. Grand, H. Y. Lai, E. J. Garnero, *J. Geophys. Res. Solid Earth* **124**, 11549–11567 (2019).
24. J. M. Lees *et al*., in *Volcanism and Subduction: The Kamchatka Region*, J. Eichelberger, E. Gordeev, P. Izbekov, M. Kasahara, J. Lees, Eds. (Geophysical Monograph Series, American Geophysical Union, 2007), pp. 65–75.
25. H. Kawakatsu, F. L. Niu, *Nature* **371**, 301–305 (1994).
26. L. Waszek, N. C. Schmerr, M. D. Ballmer, *Nat. Commun.* **9**, 385 (2018).
27. R. Maguire, J. Ritsema, S. Goes, *Geophys. Res. Lett.* **45**, 8913–8922 (2018).
28. Materials and methods are available as supplementary materials.
29. P. M. Shearer, *Geophys. J. Int.* **115**, 878–904 (1993).
30. N. Schmerr, C. Thomas, *Earth Planet. Sci. Lett.* **311**, 101–111 (2011).
31. Z. Zheng, B. Romanowicz, *Geophys. J. Int.* **191**, 1361–1373 (2012).
32. L. Stixrude, C. Lithgow-Bertelloni, *Geophys. J. Int.* **184**, 1180–1213 (2011).
33. L. Stixrude, C. Lithgow-Bertelloni, *Geophys. J. Int.* **162**, 610–632 (2005).
34. W. B. Xu, C. Lithgow-Bertelloni, L. Stixrude, J. Ritsema, *Earth Planet. Sci. Lett.* **275**, 70–79 (2008).
35. L. Stixrude, C. Lithgow-Bertelloni, *Annu. Rev. Earth Planet. Sci.* **40**, 569–595 (2012).
36. W. P. Richardson, E. A. Okal, S. Van der Lee, *Phys. Earth Planet. Inter.* **118**, 29–51 (2000).
37. P. E. van Keken, S. Karato, D. A. Yuen, *Geophys. Res. Lett.* **23**, 1821–1824 (1996).
38. E. M. Syracuse, G. A. Abers, *Geochem. Geophys. Geosyst.* **7**, Q05017 (2006).
39. P. Wessel, L. W. Kroenke, *J. Geophys. Res. Solid Earth* **105**, 28255–28277 (2000).
40. R. D. Müller *et al*., *Annu. Rev. Earth Planet. Sci.* **44**, 107–138 (2016).
41. P. V. Doubrovine, B. Steinberger, T. H. Torsvik, *J. Geophys. Res. Solid Earth* **117**, B09101 (2012).
42. M. Domeier *et al*., *Sci. Adv.* **3**, eaao2303 (2017).
43. W. H. F. Smith, D. T. Sandwell, *Science* **277**, 1956–1962 (1997).
44. P. Bird, *Geochem. Geophys. Geosyst.* **4**, 1027 (2003).
45. B. L. N. Kennett, E. R. Engdahl, R. Buland, *Geophys. J. Int.* **122**, 108–124 (1995).
46. R. D. Müller *et al*., *Geochem. Geophys. Geosyst.* **19**, 2243–2261 (2018).
47. National Research Institute for Earth Science and Disaster Resilience, F-net dataset (2019); https://doi.org/10.17598/nied.0005.

ACKNOWLEDGMENTS

We thank L. Colli, S. Dorfman, M. J. Krawczynski, R. Maguire, A. McNamara, W. Panero, J. Wu, and X. Yue for constructive discussions and Y. Liu for valuable help using GPlates (*46*). Three anonymous reviewers provided helpful comments to improve the manuscript. We thank the 2019 Interior of the Earth Gordon Research Conference for providing opportunities of interdisciplinary collaboration. We also appreciate the free access to GPlates for plate reconstructions. Seismic data analysis was supported in part through computational resources and services provided by the Institute for Cyber-Enabled Research at Michigan State University. **Funding:** This work was made possible by NSF grants OCE-1842989 to S.S.W., EAR-1620251 to P.M.S., EAR-1900633 to C.L.-B., and EAR-1853388 to L.S. S.S.W. and D.T. were also supported by the MSU Geological Sciences Endowment. C.L.-B. was further supported by the Louis B. and Martha B. Slichter Endowment for Geosciences. **Author contributions:** S.S.W., with the help of P.M.S. and D.T., analyzed the seismic data. C.L.-B. and L.S. conducted the thermodynamic simulations of mantle minerals. D.T. downloaded and maintained the seismic database. S.S.W. took the lead in writing the manuscript, and all authors discussed the results and edited the manuscript. **Competing interests:** The authors declare no competing interests. **Data and materials availability:** We use 1987–2018 data from the following seismic networks (abbreviations defined at www.fdsn.org/networks/): AC, AE, AF, AI, AK, AT, AU, AV, BE, BL, BX, C1, CB, CD, CH, C,CM, CN, CT, CU, CZ, DK, DR, DW, EI, G, GB, GE, GT, HL, HT, IC, II, IP, IU, JP, KN, KO, KP, KR, KS,KZ, LX, MC, MI, MM, MS, MX, MY, NA, ND, NJ, NO, NR, NU, OE, OV, PL, PM, PR, PS, RM, RV, S, SV,TA, TM, TR, TT, TW, UK, US, VE, WI, and WM. All raw seismic data are available at the Data Management Center of Incorporated Research Institutions for Seismology (http://ds.iris.edu/ds/nodes/dmc/). We also use 1995–2018 F-net data from Japan's National Research Institute for Earth Science and Disaster Resilience (*47*). The thermodynamic simulation package HeFESTo (*32*, *33*) is available at https://github.com/stixrude/HeFESToRepository, and Table_270914 in this GitHub repository includes all parameters used for the thermodynamic simulations. GPlates is available at www.gplates.org.

SUPPLEMENTARY MATERIALS

science.sciencemag.org/content/370/6519/983/suppl/DC1
Materials and Methods
Figs. S1 to S12
References (*48*–*63*)
Movie S1

27 May 2020; accepted 8 October 2020
10.1126/science.abd0312

DEVELOPMENTAL BIOLOGY

Tissue topography steers migrating *Drosophila* border cells

Wei Dai[1]*†, Xiaoran Guo[1]*, Yuansheng Cao[2], James A. Mondo[1], Joseph P. Campanale[1], Brandon J. Montell[3], Haley Burrous[1], Sebastian Streichan[4], Nir Gov[5], Wouter-Jan Rappel[2], Denise J. Montell[1]‡

Moving cells can sense and respond to physical features of the microenvironment; however, in vivo, the significance of tissue topography is mostly unknown. Here, we used *Drosophila* border cells, an established model for in vivo cell migration, to study how chemical and physical information influences path selection. Although chemical cues were thought to be sufficient, live imaging, genetics, modeling, and simulations show that microtopography is also important. Chemoattractants promote predominantly posterior movement, whereas tissue architecture presents orthogonal information, a path of least resistance concentrated near the center of the egg chamber. E-cadherin supplies a permissive haptotactic cue. Our results provide insight into how cells integrate and prioritize topographical, adhesive, and chemoattractant cues to choose one path among many.

Cell migrations are essential in development, homeostasis, and disease. Although chemoattractants and repellents have been extensively studied (*1*–*3*), physical features of the microenvironment may be equally important. Here, we used *Drosophila* border cells as a model and uncovered a role for tissue topography in directional cell migration in vivo. Border cells are 6 to 10 follicle cells that migrate ~150 μm over 3 to 6 hours within ovarian egg chambers, which are composed of 15 nurse cells and one oocyte encased within ~850 follicle cells (*4*–*6*) (Fig. 1A and movie S1).

The oocyte secretes chemoattractants that activate receptor tyrosine kinases (RTKs) (*7*–*10*). The platelet-derived growth factor/vascular endothelial growth factor (PDGF/VEGF)–related factor 1 (PVF1) activates its receptor, PVR (*8*). The ligands Spitz (Spi), Keren (Krn), and Gurken (Grk) activate the *Drosophila* epidermal growth factor receptor (EGFR) (*7*). Border cells lacking expression or activity of both RTKs fail to reach the oocyte (*8*), and ectopic PVF1, Spi, or Krn is sufficient to reroute them (*9*, *10*). Similarly, lymphocyte homing, axon pathfinding, and migration of the zebrafish lateral line (*11*), neural crest (*12*), and primordial germ cells (*13*) have been attributed primarily to chemoattraction and/or repulsion. Although substrate stiffness has been studied (*14*–*17*), other physical features such as tissue topography remain relatively unexplored.

[1]Department of Molecular, Cellular, and Developmental Biology, University of California, Santa Barbara, CA 93106, USA. [2]Department of Physics, University of California, San Diego, CA 92093, USA. [3]Independent researcher. [4]Department of Physics, University of California, Santa Barbara, CA 93106, USA. [5]Department of Chemical Physics, Weizmann Institute of Science, Rehovot, Israel.
*These authors contributed equally to this work.
†Present address: Cardiovascular Medicine Division, Brigham and Women's Hospital, Harvard Medical School, Boston, MA 02115, USA.
‡Corresponding author. Email: dmontell@ucsb.edu

By reconstructing egg chambers in three dimensions (3D), we noticed two orthogonal components to border cell pathway selection. Border cells migrate from anterior to posterior, the obvious path in a typical lateral view (Fig. 1A and fig. S1A). In addition, they follow a central path (Fig. 1B; fig. S1, B and C; and movie S1) despite encountering ~40 lateral alternatives (Fig. 1B and movie S2).

To address whether the extracellular RTK ligands are present in gradients that might explain both posterior and medial guidance, we used CRISPR to epitope-tag endogenous PVF1, Spi, and Krn (see the materials and methods) [Grk directs dorsal movement only as the cells near the oocyte (*4*)]. Extracellular hemagglutinin (HA)–tagged Krn (Fig. 1C) accumulated in an anterior (low) to posterior (high) gradient; however, its concentration was not higher medially than laterally (Fig. 1, D and E, and fig. S2, A and B). Intracellular, but not extracellular, HA-tagged PVF1 was detectable (fig. S2, C and D). Tagged Spi was undetectable.

Because we could not detect all ligands, we addressed their contributions by expressing dominant-negative receptors (PVR^{DN} and $EGFR^{DN}$), which impedes posterior migration (*8*) (Fig. 1F and fig. S3, A and B). Mediolateral defects were rare, occurring in <10% of egg chambers (Fig. 1F). RNA interference (RNAi) caused similar effects (fig. S3C). Therefore, some other factor(s) must guide the cells medially.

Live imaging of egg chambers with ectopic PVF1 provided further evidence for independent attraction to the egg chamber center (Fig. 1, G and H, and fig. S4). Border cells frequently protruded toward the ligand-expressing cells but remained on the central path (fig. S4, B and C). In other cases (Fig. 1H), border cells migrated along a patch of PVF1-expressing follicle cells, lingered, and then left the clone and returned to the egg chamber center, ignoring more direct routes to the oocyte. PVF1 expression in all anterior follicle cells produced similar results (fig. S4D). Thus, even in the presence of ectopic chemoattractant, border cells preferred the egg chamber center, again suggesting that another signal steers them medially.

Of all the migration-defective mutants analyzed, only nurse cell knockdown of E-cadherin exhibited marked mediolateral defects (*18*) (Fig. 2, A and B), causing border cells to move between follicle cells and nurse cells (fig. S5 and movie S3).

How does nurse cell E-cadherin contribute to central path selection? We detected no significant difference in E-cadherin concentration (fig. S6) or dynamics (fig. S7) on central versus side paths, and E-cadherin knockdown did not significantly alter the HA-Krn distribution (fig. S8). Additionally, follicle cells normally express more E-cadherin than nurse cells do (fig. S9A). However, follicle cell RNAi caused no defect (fig. S9B), and E-cadherin overexpression in follicle cells did not affect pathfinding (fig. S9, C to E). Moreover, asymmetric E-cadherin overexpression on nurse cells caused no medial guidance defect (Fig. 2, C and D). Therefore, although the presence of E-cadherin is required, E-cadherin concentration differences are insufficient to steer border cells.

We observed that border cells pulled on wild-type nurse cell membranes as they migrated (Fig. 2E, movie S4, and fig. S10). By contrast, border cells protruding between E-cadherin–negative cells did not deflect their membranes (Fig. 2, F to H, and movie S4), suggesting that border cells could not get traction. This likely accounts for their inability to take the central path. We conclude that E-cadherin supplies a permissive traction cue. This mechanical function amplifies RTK signaling and shapes forward protrusions, as previously described (*18*); however, something other than differential adhesion must normally steer border cells to the central path.

Because neither chemoattractant nor adhesive cues fully accounted for medial pathfinding, we reconstructed egg chambers in 3D and characterized central versus side migration paths. The nurse cell–oocyte complex is a syncytium packed within the follicular epithelium (fig. S11 and movie S5) (*19*). A feature of the central path is that it is where three or more nurse cells come together (lines in Fig. 3A and fig. S12). Side paths are largely composed of two nurse cell interfaces (lines in Fig. 3B, planes in Fig. 3C, and movie S6). The junctures with three or more nurse cells are enriched near the center (Fig. 3D).

We considered the influences that this geometry would likely have on border cells squeezing between nurse cells (see the supplementary text, sections ST1 and ST2). Because of the energy cost of unzipping nurse cell-to-nurse cell adhesions, protrusion into regions where multiple nurse cells meet should be more favorable (Fig. 3E). This geometry

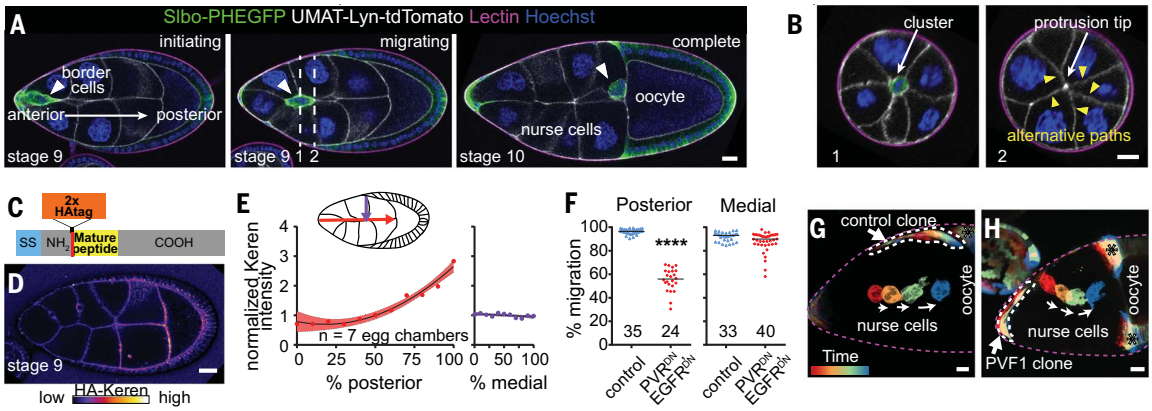

Fig. 1. Medial migration is not primarily controlled by chemoattraction. (**A**) Lateral views of egg chambers showing border cell migration between nurse cells to the oocyte. Dashed lines in (A) indicate cross-sections shown in (**B**). (**C**) HA-tagged endogenous Keren schematic. (**D**) Anti-HA–stained living egg chamber. (**E**) HA-Keren quantification. Dots indicate locations on the path. (**F**) Quantification of border cell position. Each dot indicates one cluster. ****$P < 0.0001$ (Mann-Whitney test). (**G** and **H**) Rainbow views of border cell migration in control or with ectopic UAS-PVF1. Scale bars, 20 μm.

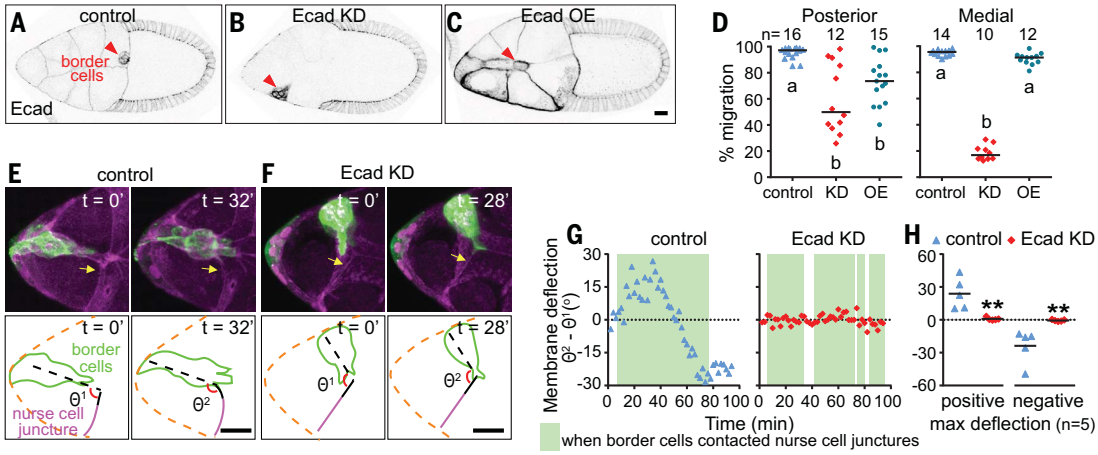

Fig. 2. E-cadherin, a permissive medial traction cue. (**A** to **C**) Images of control, nurse cell E-cadherin knockdown (KD), or mosaic nurse cell overexpression (OE). (**D**) Quantification of migration. Letters a and b designate significantly different groups. $P < 0.01$ (Kruskal-Wallis test). (**E** and **F**) Still images from movies showing border cells pulling on nurse cell junctures in a control egg chamber (E) and the absence of deflection in a E-cadherin–knockdown egg chamber (F). (**G**) Traces of nurse cell membrane deflections. (**H**) Quantification of maximum deflections. **$P < 0.01$ (Mann-Whitney test). Scale bars, 20 μm.

argument predicts larger spaces where more nurse cells meet (fig. S13, A to D), which we confirmed by measuring extracellular spaces using fluorescent dextran (Fig. 3, F and G). As predicted, germline E-cadherin knockdown opened larger spaces (fig. S13, E to G), confirming that E-cadherin normally seals nurse cells together. The free space should be most relevant at the scale of protrusions, which then steer the cluster. In vitro, migrating cells have been shown to choose channels that accommodate the nucleus (*20*); here, we show that in vivo, even smaller spaces can guide cells.

To test the prediction that crevices where more cells meet present a lower energy barrier for protrusion, we examined 3D movies. Junctures with three or more nurse cells lined the center path, and forward-directed protrusions always extended between multiple nurse cells. Moreover, when cells encountered two paths each composed of junctures of three or more nurse cells, the cluster extended two protrusions (fig. S14A). Eventually, the protrusion between the greater number of nurse cells always won.

When cells probed side paths, protrusions into three-nurse-cell junctures were more frequent (Fig. 3H and fig. S14B), even though two-nurse-cell interfaces offer vastly greater surface area (Fig. 3, A and C). We conclude that crevices where multiple nurse cells meet create an energetically favorable path, and tissue topography, specifically junctures between three or more nurse cells, normally promotes central pathway selection.

To test whether the combination of an anteroposterior chemoattractant gradient and a bias toward multiple-cell junctures is in principle sufficient to explain border cell behavior, we developed a dynamic model that describes the trajectory of border cells moving within a realistic egg chamber (Fig. 4A). We modeled the border cell cluster as a particle that moves stochastically in an effective potential $U(\vec{r})$ (ST3) that incorporates two independent guidance terms: $\alpha D(\vec{r})$, the energy cost for the cluster to move between N nurse cells, and $\beta S(\vec{r})$, the anteroposterior chemoattractant gradient. Simulating normal border cell migration conditions replicated normal trajectories (Fig. 4A and movie S7). Eliminating the chemoattractant caused posterior migration defects but little deviation from the central path (Fig. 4, A and B), consistent with our experimental results (Fig. 1F). By contrast, eliminating the preference for junctures with three or more nurse cells randomized mediolateral path selection without posterior migration defects. Eliminating both terms produced numerous mediolateral and anteroposterior defects (Fig. 4, A and B, and fig. S15).

To further test the influence of geometry on guidance, we analyzed egg chambers with atypical geometries. In mutants that disrupt early germ cell divisions (*21*), we found some 31-nurse-cell egg chambers (fig. S16) with a central two-nurse-cell interface (Fig. 4C). In each instance, the border cells selected the junctures with three or more nurse cells even when off-center (Fig. 4C). Simulating migration using the 31-nurse-cell geometry and the same parameters as for wild-type produced the same result (Fig. 4, D and E).

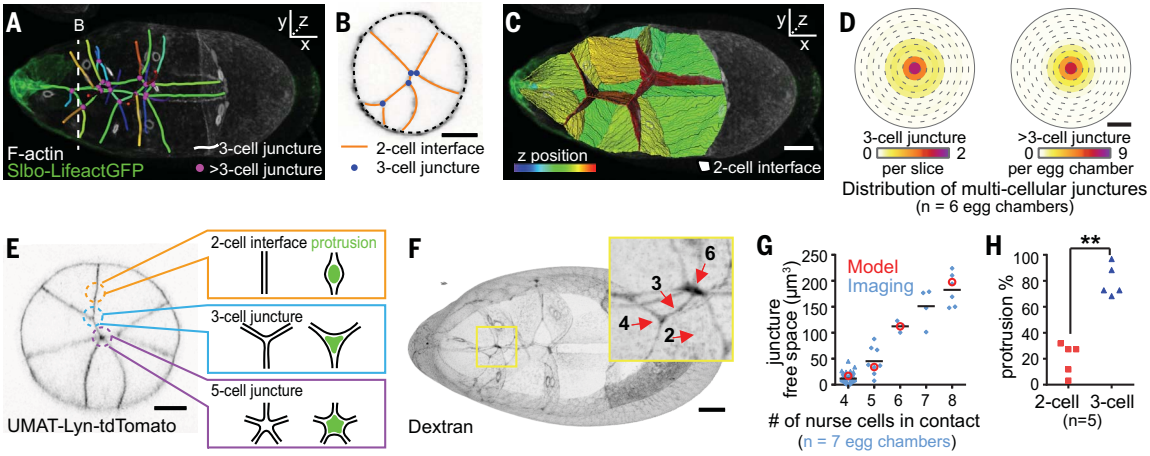

Fig. 3. Centrally enriched multiple-cell junctures. (**A** to **C**) Three-dimensional reconstructions of nurse cell contacts. Dashed line in (A) indicates cross-section in (B). (**D**) Heatmap showing distributions of three- (left) or more-than-three- (right) cell junctures as a function of mediolateral position. (**E**) Schematic representation of protrusion into nurse cell junctures. (**F**) Extracellular spaces filled with fluorescent dextran in wild-type. (**G**) Quantification of the extracellular juncture volume. Values from the 3D model (red) (see the supplementary text, section ST1) and the experimental data (blue). (**H**) Percentage side protrusions extending to two-cell or three-cell junctures as a fraction of total side protrusions. $^{**}P < 0.01$ (paired *t* test). Scale bars, 20 μm.

Fig. 4. Multiple-cell junctures steer cells. (**A**) Representative simulated trajectories through the wild-type geometry shown in Fig. 3A. (**B**) Quantification of 99 simulations. (**C**) Cross-sections showing border cell and nurse cell positions relative to the egg chamber center. (**D**) Representative simulated trajectory. (**E**) Comparison of the distance from the border cell centroid to the egg chamber center versus the nearest three-cell juncture. $^{***}P < 0.001$ (paired *t* test). Scale bars, 20 μm.

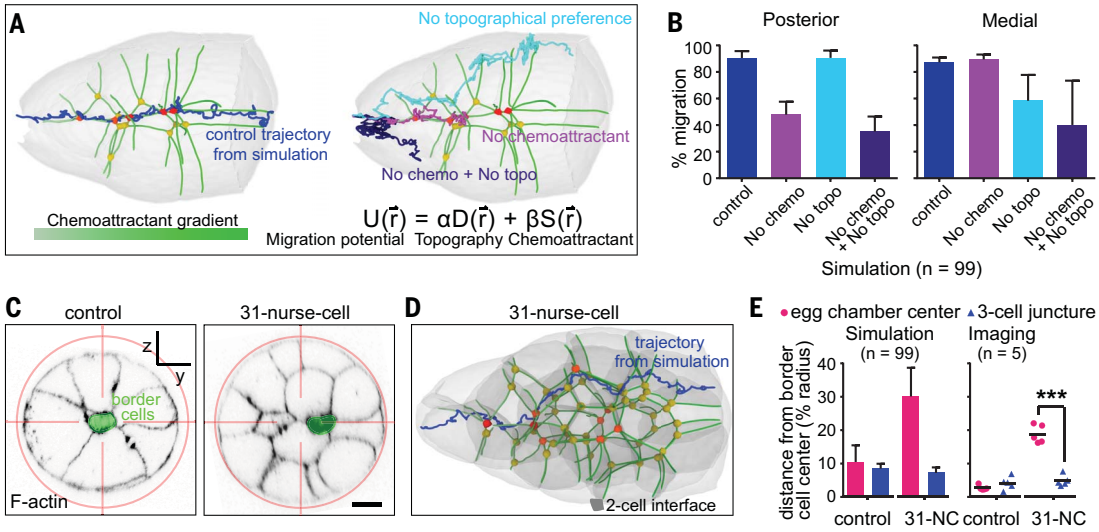

We also simulated migration in egg chambers lacking nurse cell E-cadherin. The model predicted and experiments confirmed that border cells zigzag along grooves between two nurse cells and the follicular epithelium (fig. S17 and movie S8), where there is more free space (fig. S13, F and G).

We then reexamined the 10% of PVR^{DN}, $EGFR^{DN}$ egg chambers in which border cells were off-center (Fig. 1F). The border cells again moved to sites where multiple nurse cells met (fig. S18), supporting the finding that multiple-cell junctures are energetically favorable even when off-center. Simulations recapitulated the result (figs. S18C and S15B). Many other features of the central path proved inconsequential (figs. S19 to S21).

We measured and manipulated chemical, adhesive, and topographical cues and elucidated their relative contributions to the selection of one migration path among many. RTK signaling normally attracts border cells posteriorly toward the highest ligand concentration. We previously showed that E-cadherin amplifies small differences in chemoattractant concentration between the front and back of the cluster to ensure robust posterior migration (*18*). Here, we show that nurse cell E-cadherin provides traction, but differential adhesion does not steer the cells medially.

For medial path selection, the organization of the nurse cells is an instructive cue, though we cannot exclude that additional factors such as unknown attractants or repellents might also contribute. At the junctures where multiple nurse cells meet, they do not quite touch because of geometry, leaving tiny openings where protrusions need not break as many adhesion bonds between nurse cells. The concentration of multiple-cell junctures near the egg chamber center provides an energetically favorable medial path.

We gained further insight into how the cells integrate and prioritize the chemical and geometric cues. Normally, the chemoattractants primarily guide the cells posteriorly and multicellular junctures steer them centrally. Near the end of migration, as border cells approach the oocyte, junctures with more than three nurse cells are absent (Fig. 3A), weakening the central bias of topographical information. Moreover, chemoattractant levels are highest, and the dorsally enriched ligand Gurken is present (*10*). The border cells typically squeeze between two nurse cells to move dorsally (fig. S22, A and B, and movie S9). Adding Grk into the model and simulation accurately predicted this dorsal turn (fig. S22, C and D, and movie S10). Like the effect of ectopic PVF1, this result shows that when the ligand

concentration is high enough, the chemical cue can dominate, allowing cells to move through suboptimal physical space. Similarly, when E-cadherin–mediated traction is unavailable on nurse cells, border cells migrate on follicle cells, choosing grooves where multiple cells meet. This work thus elucidates how border cells integrate and prioritize chemical, adhesive, and physical features of their in vivo microenvironment to choose a path.

REFERENCES AND NOTES

1. D. Cai, D. J. Montell, *Curr. Opin. Cell Biol.* **30**, 91–98 (2014).
2. Y. Artemenko, T. J. Lampert, P. N. Devreotes, *Cell. Mol. Life Sci.* **71**, 3711–3747 (2014).
3. K. F. Swaney, C.-H. Huang, P. N. Devreotes, *Annu. Rev. Biophys.* **39**, 265–289 (2010).
4. D. J. Montell, W. H. Yoon, M. Starz-Gaiano, *Nat. Rev. Mol. Cell Biol.* **13**, 631–645 (2012).
5. E. Scarpa, R. Mayor, *J. Cell Biol.* **212**, 143–155 (2016).
6. P. Friedl, D. Gilmour, *Nat. Rev. Mol. Cell Biol.* **10**, 445–457 (2009).
7. P. Duchek, P. Rørth, *Science* **291**, 131–133 (2001).
8. P. Duchek, K. Somogyi, G. Jékely, S. Beccari, P. Rørth, *Cell* **107**, 17–26 (2001).
9. J. A. McDonald, E. M. Pinheiro, D. J. Montell, *Development* **130**, 3469–3478 (2003).
10. J. A. McDonald, E. M. Pinheiro, L. Kadlec, T. Schupbach, D. J. Montell, *Dev. Biol.* **296**, 94–103 (2006).
11. J. Bussmann, E. Raz, *EMBO J.* **34**, 1309–1318 (2015).
12. R. Mayor, E. Theveneau, *Development* **140**, 2247–2251 (2013).
13. B. E. Richardson, R. Lehmann, *Nat. Rev. Mol. Cell Biol.* **11**, 37–49 (2010).
14. M. R. Ng, A. Besser, G. Danuser, J. S. Brugge, *J. Cell Biol.* **199**, 545–563 (2012).
15. G. Aranjuez, A. Burtscher, K. Sawant, P. Majumder, J. A. McDonald, *Mol. Biol. Cell* **27**, 1898–1910 (2016).
16. E. H. Barriga, K. Franze, G. Charras, R. Mayor, *Nature* **554**, 523–527 (2018).
17. M. R. Zanotelli *et al*., *Nat. Commun.* **10**, 4185 (2019).
18. D. Cai *et al*., *Cell* **157**, 1146–1159 (2014).
19. J. I. Alsous, P. Villoutreix, N. Stoop, S. Y. Shvartsman, J. Dunkel, *Nat. Phys.* **14**, 1016–1021 (2018).
20. J. Renkawitz *et al*., *Nature* **568**, 546–550 (2019).
21. N. R. Matias, J. Mathieu, J.-R. Huynh, *PLOS Genet.* **11**, e1004653 (2015).

ACKNOWLEDGMENTS

We thank B. Cheng, S. Dhar, Y. Li, M. A. Pastor, and R. Wu for technical assistance. **Funding:** This work was supported by NIH grant GM46425 to D.J.M., NSF grant PHY-1707637 to W.-J.R., and ACS grant PF-17-024-01-CSM to J.P.C. We thank the Developmental Studies Hybridoma Bank for providing antibodies and H. Sung, H. J. Rene, the Bloomington *Drosophila* Stock Center, and the Vienna *Drosophila* Resource Center for providing fly stocks. We acknowledge the use of the NRI-MCDB Microscopy Facility and the Imaris computer workstation supported by the Office of the Director, NIH, under award no. S10OD010610. N.S.G. is the incumbent of the Lee and William Abramowitz Professorial Chair of Biophysics and this research was supported by the Israel Science Foundation (grant no. 1459/17). **Author contributions:** W.D., X.G., J.A.M., J.P.C., and D.J.M. designed experiments. W.D., X.G., J.A.M., J.P.C., and H.B. performed experiments. Y.C., W.-J.R., and N.G. performed modeling. B.J.M. produced graphical illustrations and animations. S.S. assisted with light sheet imaging and data analysis. W.D., X.G., Y.C., J.A.M., J.P.C., N.G., W.-J.R., and D.J.M. prepared the manuscript. **Competing interests:** The authors declare no competing interests. **Data and materials availability:** All data are available in the manuscript or the supplementary materials. Materials are available upon request.

SUPPLEMENTARY MATERIALS

science.sciencemag.org/content/370/6519/987/suppl/DC1
Materials and Methods
Supplementary Text
Figs. S1 to S23
Tables S1 to S11
References (*22*–*28*)
Movies S1 to S10

View/request a protocol for this paper from *Bio-protocol*.

15 September 2019; resubmitted 11 May 2020
Accepted 28 September 2020
10.1126/science.aaz4741

ZIKA VIRUS

Enhanced Zika virus susceptibility of globally invasive *Aedes aegypti* populations

Fabien Aubry[1], Stéphanie Dabo[1], Caroline Manet[2], Igor Filipović[3], Noah H. Rose[4,5], Elliott F. Miot[1,6], Daria Martynow[1], Artem Baidaliuk[1,6], Sarah H. Merkling[1], Laura B. Dickson[1], Anna B. Crist[1], Victor O. Anyango[1], Claudia M. Romero-Vivas[7], Anubis Vega-Rúa[8], Isabelle Dusfour[9], Davy Jiolle[10,11], Christophe Paupy[10,11], Martin N. Mayanja[12], Julius J. Lutwama[12], Alain Kohl[13], Veasna Duong[14], Alongkot Ponlawat[15], Massamba Sylla[16], Jewelna Akorli[17], Sampson Otoo[17], Joel Lutomiah[18], Rosemary Sang[18], John-Paul Mutebi[19], Van-Mai Cao-Lormeau[20], Richard G. Jarman[21], Cheikh T. Diagne[22], Oumar Faye[22], Ousmane Faye[22], Amadou A. Sall[22], Carolyn S. McBride[4,5], Xavier Montagutelli[2], Gordana Rašić[3], Louis Lambrechts[1]*

The drivers and patterns of zoonotic virus emergence in the human population are poorly understood. The mosquito *Aedes aegypti* is a major arbovirus vector native to Africa that invaded most of the world's tropical belt over the past four centuries, after the evolution of a "domestic" form that specialized in biting humans and breeding in water storage containers. Here, we show that human specialization and subsequent spread of *A. aegypti* out of Africa were accompanied by an increase in its intrinsic ability to acquire and transmit the emerging human pathogen Zika virus. Thus, the recent evolution and global expansion of *A. aegypti* promoted arbovirus emergence not solely through increased vector–host contact but also as a result of enhanced vector susceptibility.

The mosquito *Aedes aegypti* is found throughout the tropics and subtropics, and its range has been predicted to further expand with climate change (*1*). *A. aegypti* consists of two subspecies originally described on the basis of morphological and ecological differences (*2*) and subsequently supported by modern population genetics (*3*). The globally invasive subspecies *A. aegypti aegypti* (*Aaa*) thrives in urban environments of Asia and the Americas, where it oviposits in artificial containers and preferentially bites humans. The African subspecies *A. aegypti formosus* (*Aaf*) inhabits both urban and forest habitats of sub-Saharan Africa and bites a variety of vertebrate animals (*4*, *5*). Coexistence of the two subspecies as genetically distinct entities has been documented only along the coast of Kenya, whereas in some locations of Senegal and Angola *A. aegypti* populations consist of a genetic blend of *Aaa* and *Aaf* (*3*, *6*, *7*).

The human-specialist *Aaa* is thought to have evolved from generalist ancestors in western Africa ~5000 to 10,000 years ago (*6*, *8*). "Domestication" allowed the global expansion of *Aaa* during the slave-trading period (17th to 19th centuries), and this expansion in turn fueled the first global pandemics of yellow fever and dengue (*9*). Today, *A. aegypti* is the main global vector of arboviruses, including not only dengue virus (DENV) and yellow fever virus (YFV) but also newly emerging arboviruses such as Zika virus (ZIKV) and chikungunya virus (*10*). The high efficiency of *Aaa* as an arbovirus vector is generally attributed to its strong preference for humans and proclivity to lay eggs in human-made containers (*9*).

Despite ample evidence for variation in flavivirus susceptibility within and between *A. aegypti* populations (*11*), surprisingly little attention has been paid to the consequences of *A. aegypti*'s domestication and global expansion out of Africa for its innate ability to acquire arbovirus infections and subsequently become infectious. A few studies in the 1970s and 1980s, motivated by the historical absence of yellow fever in Asia, ruled out the hypothesis that Asian populations of *A. aegypti* were inefficiently infected by YFV; however, the researchers noticed that *Aaf* populations were generally less susceptible to YFV than their *Aaa* counterparts (*12*, *13*). A similar conclusion was made for DENV susceptibility (*14*), but experimental variations in virus titers of the artificial blood meals in these early studies did not allow a formal worldwide comparison.

Here, we investigated the worldwide variation of *A. aegypti* susceptibility to ZIKV infection using a panel of 14 laboratory colonies recently established (2 to 16 laboratory generations) from field-collected specimens (table S1). ZIKV is a flavivirus (family *Flaviviridae*) first isolated from a sentinel monkey in Uganda in 1947 (*15*) and mainly transmitted among humans by *A. aegypti*. The first reported human epidemic of ZIKV occurred in 2007 on the Pacific island of Yap, Micronesia (*16*). Subsequent larger ZIKV outbreaks were recorded in French Polynesia and other Pacific islands during 2013 and 2014 (*17*). In 2015, ZIKV was detected in Brazil, from where it rapidly spread across the Americas and the Caribbean, causing hundreds of thousands of human cases (*18*). The factors underlying the explosiveness and magnitude of ZIKV emergence in the Pacific and the Americas are still poorly understood. Reciprocally, the lack of major human epidemics of ZIKV in regions with seemingly favorable conditions, such as Africa or continental Asia, remains largely unexplained to date (*18*).

To compare ZIKV susceptibility between our *A. aegypti* colonies, we generated empirical dose-response curves based on a standardized membrane feeding assay (fig. S1A). Dose-response curves account for the strong dose dependency of infection success (*19*, *20*) and provide an absolute measure of susceptibility, which can be summarized by the virus dose infecting 50% of blood-fed mosquitoes [50% oral infectious dose (OID_{50})]. Multiple blood meals are known to enhance systemic virus dissemination in ZIKV-infected *A. aegypti*, but they do not affect initial infection prevalence (*21*); therefore, a single infectious blood meal is adequate to obtain relevant OID_{50} estimates. Because ZIKV susceptibility is also influenced by the virus strain (*20*, *22*), we used a panel of seven wild-type ZIKV strains encompassing the current viral genetic diversity (table S2).

We first measured ZIKV susceptibility in a worldwide panel of eight *A. aegypti* colonies (table S1) originating from Africa (Cameroon, Uganda, Gabon), the Americas (Colombia, Guadeloupe, French Guiana), and Asia (Thailand, Cambodia). We individually scored the infection status of 3113 female *A. aegypti* after

[1]Insect-Virus Interactions Unit, Institut Pasteur, UMR2000, CNRS, Paris, France. [2]Mouse Genetics Laboratory, Institut Pasteur, Paris, France. [3]Mosquito Control Laboratory, QIMR Berghofer Medical Research Institute, Brisbane, Queensland, Australia. [4]Department of Ecology & Evolutionary Biology, Princeton University, Princeton, NJ, USA. [5]Princeton Neuroscience Institute, Princeton University, Princeton, NJ, USA. [6]Collège Doctoral, Sorbonne Université, Paris, France. [7]Laboratorio de Enfermedades Tropicales, Departamento de Medicina, Fundación Universidad del Norte, Barranquilla, Colombia. [8]Institut Pasteur of Guadeloupe, Laboratory of Vector Control Research, Transmission Reservoir and Pathogens Diversity Unit, Morne Jolivière, Guadeloupe, France. [9]Vector Control and Adaptation, Institut Pasteur de la Guyane, Vectopole Amazonien Emile Abonnenc, Cayenne, French Guiana, France. [10]MIVEGEC, Montpellier University, IRD, CNRS, Montpellier, France. [11]Centre Interdisciplinaire de Recherches Médicales de Franceville, Franceville, Gabon. [12]Department of Arbovirology, Uganda Virus Research Institute, Entebbe, Uganda. [13]MRC-University of Glasgow Centre for Virus Research, Glasgow, UK. [14]Virology Unit, Institut Pasteur in Cambodia, Phnom Penh, Cambodia. [15]Department of Entomology, Armed Forces Research Institute of Medical Sciences, Bangkok, Thailand. [16]Unité d'Entomologie, de Bactériologie, de Virologie, Département de Biologie Animale, Faculté des Sciences et Techniques, Université Cheikh Anta Diop, Dakar, Senegal. [17]Department of Parasitology, Noguchi Memorial Institute for Medical Research, University of Ghana, Accra, Ghana. [18]Arbovirus/Viral Hemorrhagic Fevers Laboratory, Center for Virus Research, Kenya Medical Research Institute, Nairobi, Kenya. [19]Centers for Disease Control and Prevention, Fort Collins, CO, USA. [20]Institut Louis Malardé, Papeete, Tahiti, French Polynesia. [21]Viral Diseases Branch, Walter Reed Army Institute of Research, Silver Spring, MD, USA. [22]Institut Pasteur Dakar, Arbovirus and Viral Hemorrhagic Fevers Unit, Dakar, Senegal.
*Corresponding author. Email: louis.lambrechts@pasteur.fr

oral exposure to three different infectious doses of six ZIKV strains. The infection status depended on a three-way interaction between infectious dose, ZIKV strain, and mosquito population (multivariate logistic regression, $P = 0.0238$), indicating that the dose-response curves differed significantly among virus-population pairs (Fig. 1A). When mosquito populations were nested within their continent of origin (Asia, Africa, Americas) in the statistical model, there was a strong effect of the continent ($P < 0.0001$), which was mainly driven by the significantly lower ZIKV susceptibility of the three African mosquito populations. Across the ZIKV strains, the OID_{50}

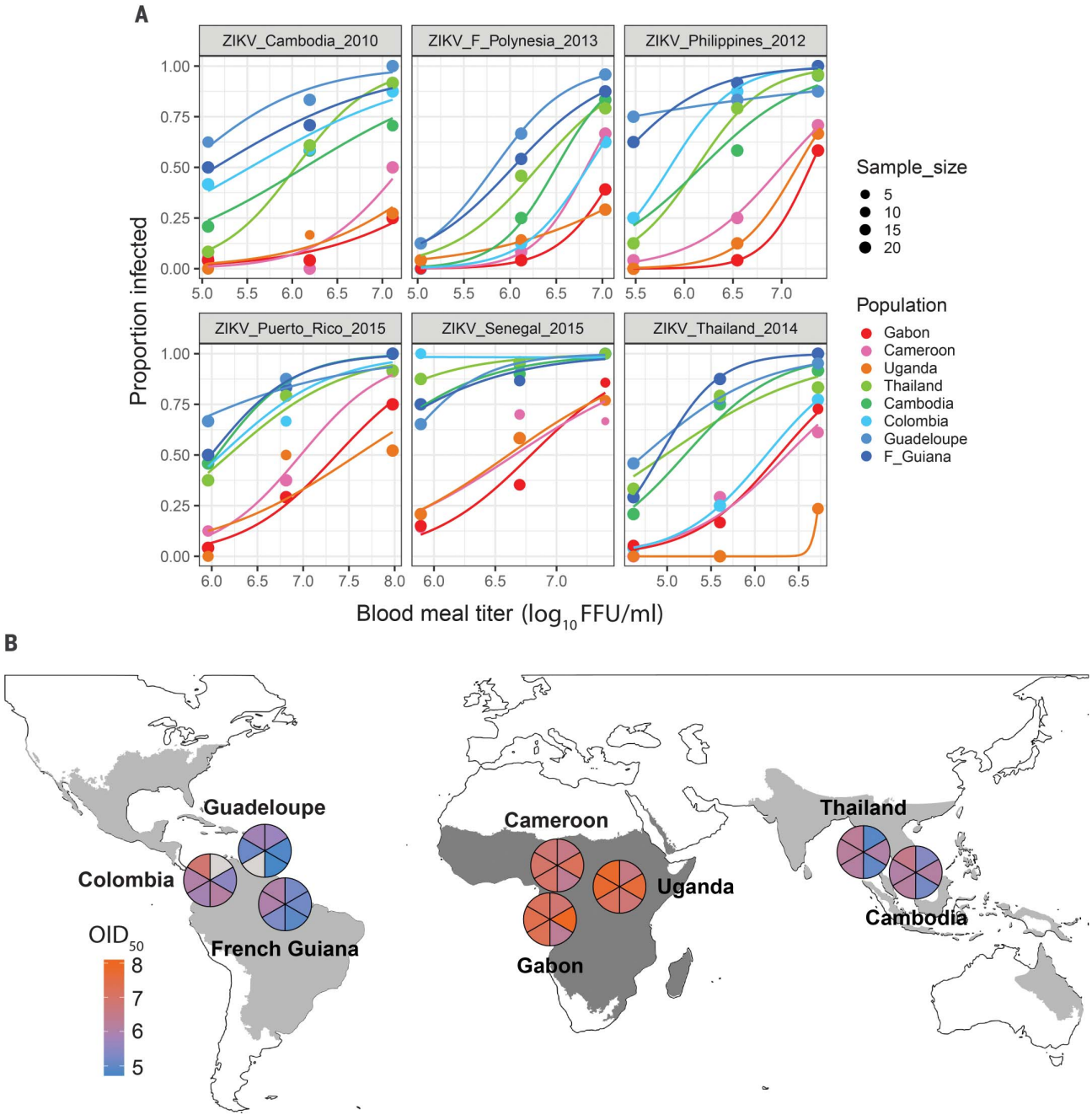

Fig. 1. Native populations of *A. aegypti* in Africa are less susceptible to ZIKV than globally invasive populations outside Africa. (**A**) Dose-response curves of eight field-derived *A. aegypti* colonies challenged by six low-passage ZIKV strains. The proportions of ZIKV-infected mosquitoes 7 days post–oral challenge are shown as a function of the blood meal titers in log_{10}-transformed FFU per milliliter. Each box represents a different ZIKV strain, as labeled at the top. The logistic regression lines are color-coded for the different mosquito populations. (**B**) Geographical origins of the eight *A. aegypti* colonies and their estimated OID_{50} values (expressed in log_{10}-transformed FFU per milliliter) for the six low-passage ZIKV strains tested in (A). The pie charts show the six OID_{50} values estimated from the dose-response curves shown in (A) (clockwise from the top: ZIKV_Senegal_2015, ZIKV_Cambodia_2010, ZIKV_Thailand_2014, ZIKV_Philippines_2012, ZIKV_Puerto_Rico_2015, and ZIKV_F_Polynesia_2013) and represented on a color scale (except for the undetermined OID_{50} values, which are shown in gray). The gray background indicates the approximate distribution of *A. aegypti* (*43*). The light gray represents the globally invasive subspecies *Aaa*, whereas the dark gray represents the African subspecies *Aaf*.

estimates (table S3) ranged from 6.3 to 8.1 $\log_{10}$ focus-forming units (FFU)/ml for the three African populations and from 4.7 to 6.8 $\log_{10}$ FFU/ml for the five non-African populations (Fig. 1B). We confirmed that variation in ZIKV susceptibility did not simply reflect differences in colonization history between the mosquito populations. We analyzed the OID_{50} estimates as a function of the average number of generations spent in the laboratory and found no statistical support for an effect of the number of generations [analysis of variance (ANOVA), $P = 0.8236$] or an interaction effect between the ZIKV strain and the generation (ANOVA, $P = 0.8618$).

The three African colonies of our worldwide panel were significantly less susceptible to ZIKV infection than their non-African counterparts; however, they did not represent the full extent of *A. aegypti* genetic diversity in the ancestral range of the species (*6*). These three colonies came from places expected to harbor relatively pure *Aaf* populations, whereas other African populations from the Sahelian region show signatures of mixed ancestry with globally invasive *Aaa* (*7*, *8*). To expand our assessment of African *A. aegypti* populations, we examined a panel of six additional mosquito colonies (table S1) originating from Senegal (NGO, KED), Ghana (KUM), Uganda (ENT), and Kenya (KAK, RAB) (*7*). We measured the ZIKV susceptibility of these colonies in our standardized membrane feeding assay, and the colonies from Gabon and Guadeloupe of our worldwide panel were included as references (Fig. 2A). The six African colonies differed significantly in their dose-response to the ZIKV_Cambodia_2010 strain (multivariate logistic regression excluding reference colonies, $P < 0.0001$; $n = 271$) but not to the ZIKV_Senegal_2011 strain ($P = 0.0587$; $n = 363$). The OID_{50} estimates (table S3) ranged from 6.3 (NGO) to 7.9 (KED) $\log_{10}$ FFU/ml for the ZIKV_Cambodia_2010 strain and from 4.9 (NGO) to 6.2 (KED) $\log_{10}$ FFU/ml for the

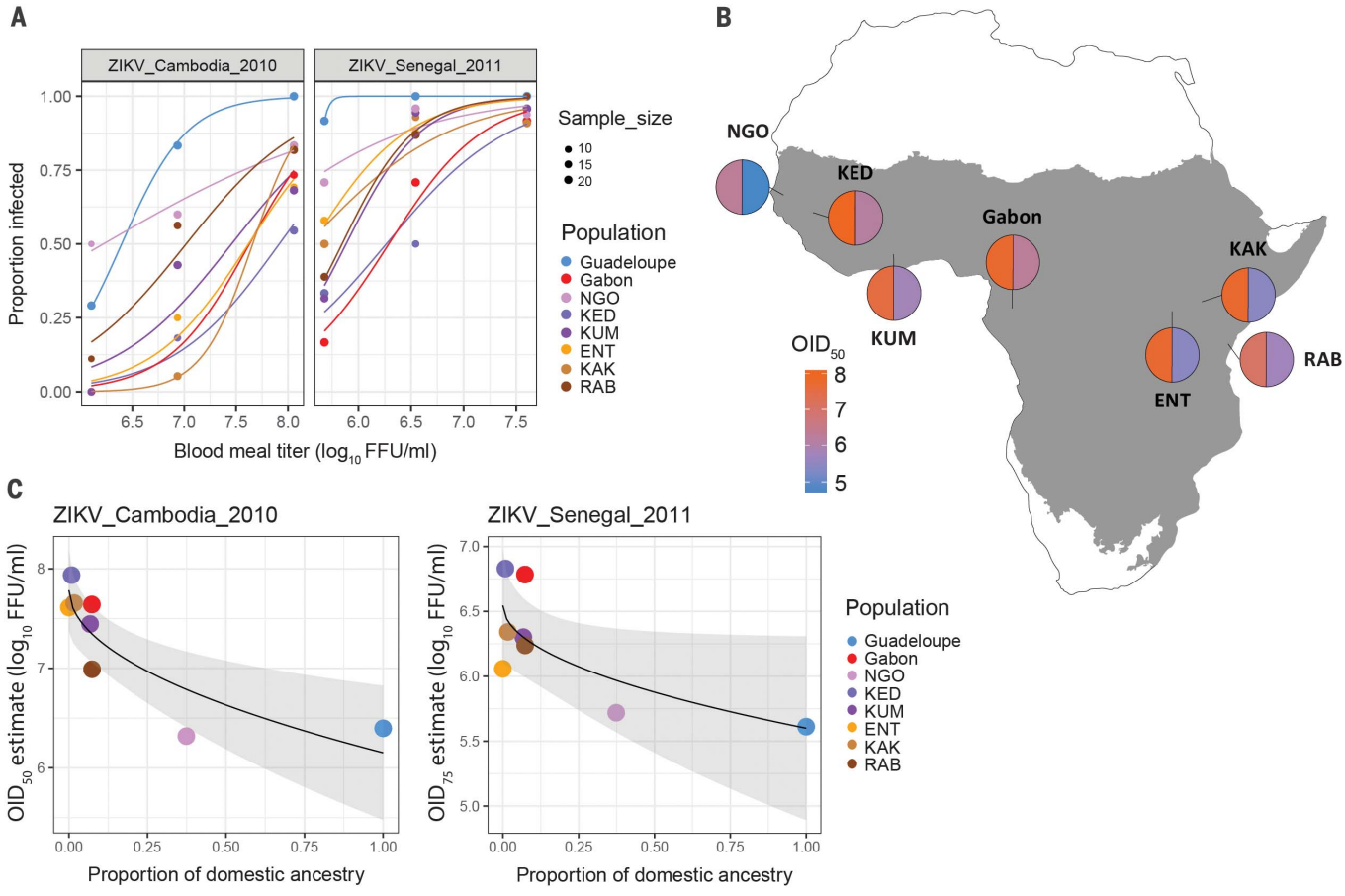

Fig. 2. ZIKV susceptibility among African populations of *A. aegypti* correlates positively with their proportion of domestic genetic ancestry. (**A**) Dose-response curves of eight field-derived *A. aegypti* colonies challenged by two low-passage ZIKV strains. The colonies from Gabon and Guadeloupe are the same as in the worldwide panel shown in Fig. 1 and served as resistant and susceptible references, respectively. The other six colonies were derived from a panel of African populations sampled in a separate study (*7*) and abbreviated as follows: NGO, Ngoye, Senegal; KED, Kédougou, Senegal; KUM, Kumasi, Ghana; ENT, Entebbe, Uganda; KAK, Kakamega, Kenya; RAB, Rabai, Kenya. The proportions of ZIKV-infected mosquitoes 7 days post–oral challenge are shown as a function of the blood meal titers in $\log_{10}$-transformed FFU per milliliter. Each box represents a different ZIKV strain, as labeled at the top. The logistic regression lines are color-coded for the different mosquito populations. (**B**) Geographical origins of the seven African *A. aegypti* colonies and their estimated OID_{50} values, expressed in $\log_{10}$-transformed FFU per milliliter, for the two low-passage ZIKV strains tested in (A). The pie charts show the OID_{50} values estimated from the dose–response curves (left, ZIKV_Cambodia_2010; right, ZIKV_Senegal 2011) and represented on a color scale. The gray shading indicates the approximate distribution of *A. aegypti* (*43*). (**C**) Relationship between ZIKV susceptibility of the colonies and the average proportion of domestic genetic ancestry of their wild-caught founders, inferred by ADMIXTURE analyses (*7*). Note that ZIKV susceptibility is represented by OID_{50} estimates for ZIKV_Cambodia_2010 and by OID_{75} estimates for ZIKV_Senegal_2011 because of the higher overall infectiousness of the latter strain. Each box represents a different ZIKV strain, as labeled at the top. The black lines represent the square root regression results for the ZIKV_Cambodia_2010 strain ($R^2 = 0.761$; $P = 0.0047$) and the ZIKV_Senegal_2011 strain ($R^2 = 0.519$; $P = 0.0437$). The best-fit regression function was obtained by comparing R^2 values between various regression models.

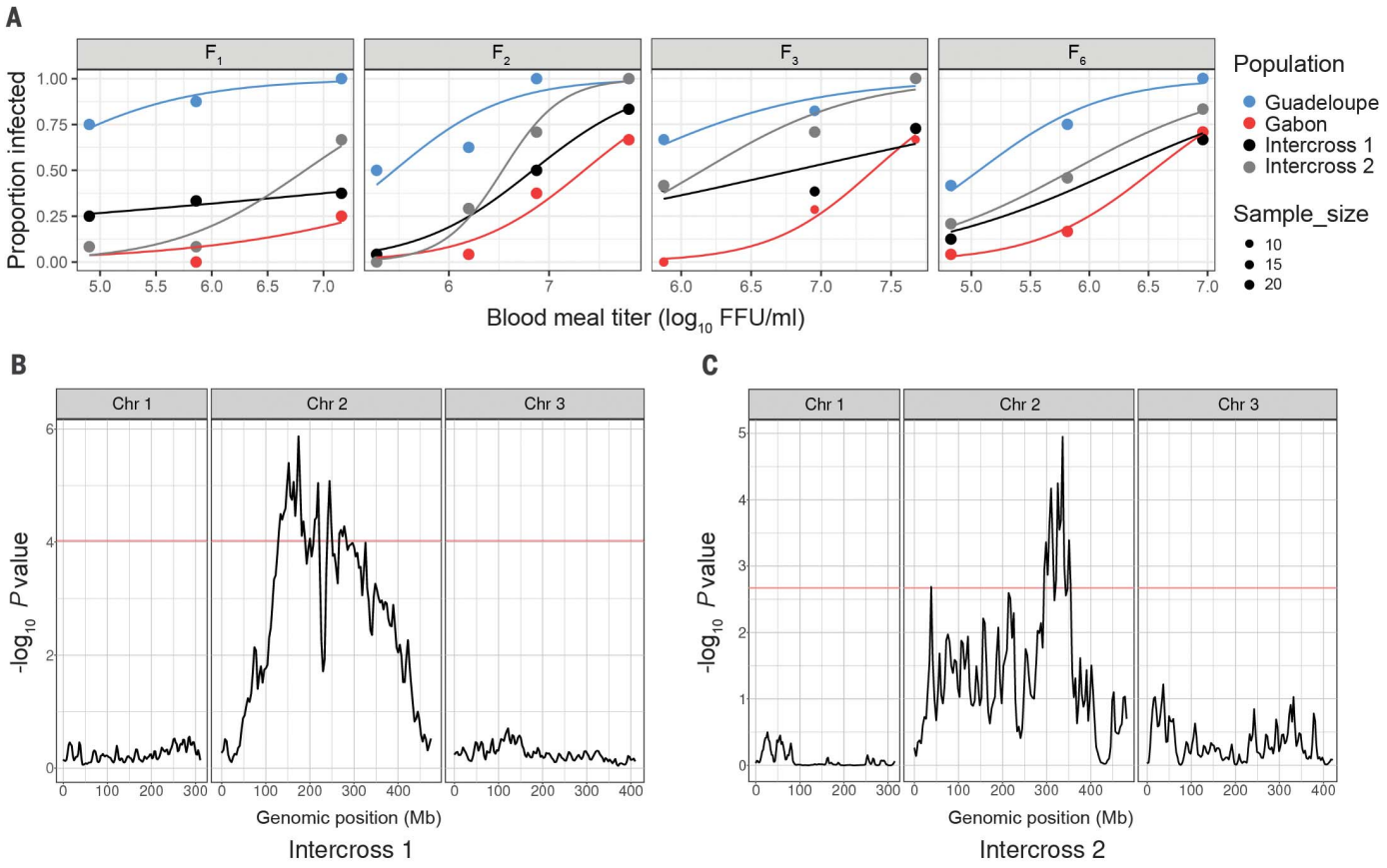

Fig. 3. Genetic analysis of intercrossed African and non-African mosquitoes identifies genomic regions underlying ZIKV susceptibility. (**A**) Dose-response curves of the parental colonies and the F_1, F_2, F_3, and F_6 generations of intercross 1 (Guadeloupe males × Gabon females) and intercross 2 (Gabon males × Guadeloupe females) orally challenged with the ZIKV_Cambodia_2010 strain. The percentage of ZIKV-infected mosquitoes 7 days post–oral challenge is shown as a function of the blood meal titers in $\log_{10}$-transformed FFU per milliliter. Each box represents a different intercross generation, as labeled at the top, and the lines represent the logistic regression results. (**B** and **C**) QTL mapping results obtained for the F_4 generation of intercross 1 (B) and intercross 2 (C). The statistical significance of the genotype-phenotype association, averaged by 5-Mb moving windows, is shown along the three chromosomes. The horizontal red lines indicate the 0.1% (B) and 5% (C) genome-wide FDR thresholds, calculated with the Benjamini-Hochberg method implemented in QTLseqr (*44*).

ZIKV_Senegal_2011 strain (Fig. 2B). There was no evidence for an effect of the laboratory generation (ANOVA, $P = 0.7399$) or an interaction effect between the ZIKV strain and the laboratory generation (ANOVA, $P = 0.9236$) on the OID_{50} estimates. Although the ZIKV_Senegal_2011 strain was more infectious overall, we noticed that for both virus strains the most and least susceptible African colonies were the same (NGO and KED, respectively). These two colonies are expected to differ genetically according to the recent study that analyzed the whole-genome sequences of their wild progenitors (*7*). In that study, ADMIXTURE analysis identified three genomic clusters (East Africa, Central/West Africa, and globally invasive domestic ancestry components) and detected a variable level of domestic ancestry in several African *A. aegypti* populations. For instance, the average proportion of domestic ancestry in the wild progenitors was 37.4% for NGO and 0.86% for KED (*7*). We thus analyzed ZIKV susceptibility as a function of the level of domestic ancestry and found that they were positively associated (Fig. 2C), both for the ZIKV_Cambodia_2010 strain (square root regression, $P = 0.0047$; $R^2 = 0.761$) and for the ZIKV_Senegal_2011 strain (square root regression, $P = 0.0437$; $R^2 = 0.519$). When we omitted the pure *Aaa* reference population from Guadeloupe, the relationship was still significant for the ZIKV_Cambodia_2010 strain (linear regression, $P = 0.0047$; $R^2 = 0.824$) but no longer for the ZIKV_Senegal_2011 strain (linear regression, $P = 0.1189$; $R^2 = 0.414$). These results provide further evidence for the higher ZIKV susceptibility of the domestic subspecies *Aaa* relative to the African subspecies *Aaf*.

To investigate the genetic basis of *A. aegypti* worldwide variation in ZIKV susceptibility, we intercrossed the colony from Guadeloupe (susceptible parent; 100% *Aaa*) with the colony from Gabon (resistant parent; 7.3% *Aaa*) to perform quantitative trait locus (QTL) mapping by bulk segregant analysis (fig. S2). In two reciprocal intercrosses, F_1 hybrids displayed a level of susceptibility to the ZIKV_Cambodia_2010 strain that was intermediate but closer to the resistant parent (Fig. 3A), suggesting that resistant alleles were partially dominant. The level of ZIKV susceptibility remained intermediate during the next five generations of both intercrosses (Fig. 3A). After three generations of recombination, we genotyped phenotypic pools of the F_4 progeny based on their ZIKV-resistant (uninfected) or ZIKV-susceptible (infected) phenotype (two replicate pools of 48 individuals per phenotype). We used a total of ~230,000 single-nucleotide polymorphisms identified on a genome-wide scale by restriction site–associated DNA sequencing to detect deviations in allele frequencies between ZIKV-resistant and ZIKV-susceptible pools. In the first intercross (Guadeloupe males × Gabon females), we detected a cluster of five highly significant QTLs associated with infection status [false discovery rate (FDR) < 0.001] located between 128.3 and 282.7 Mb on

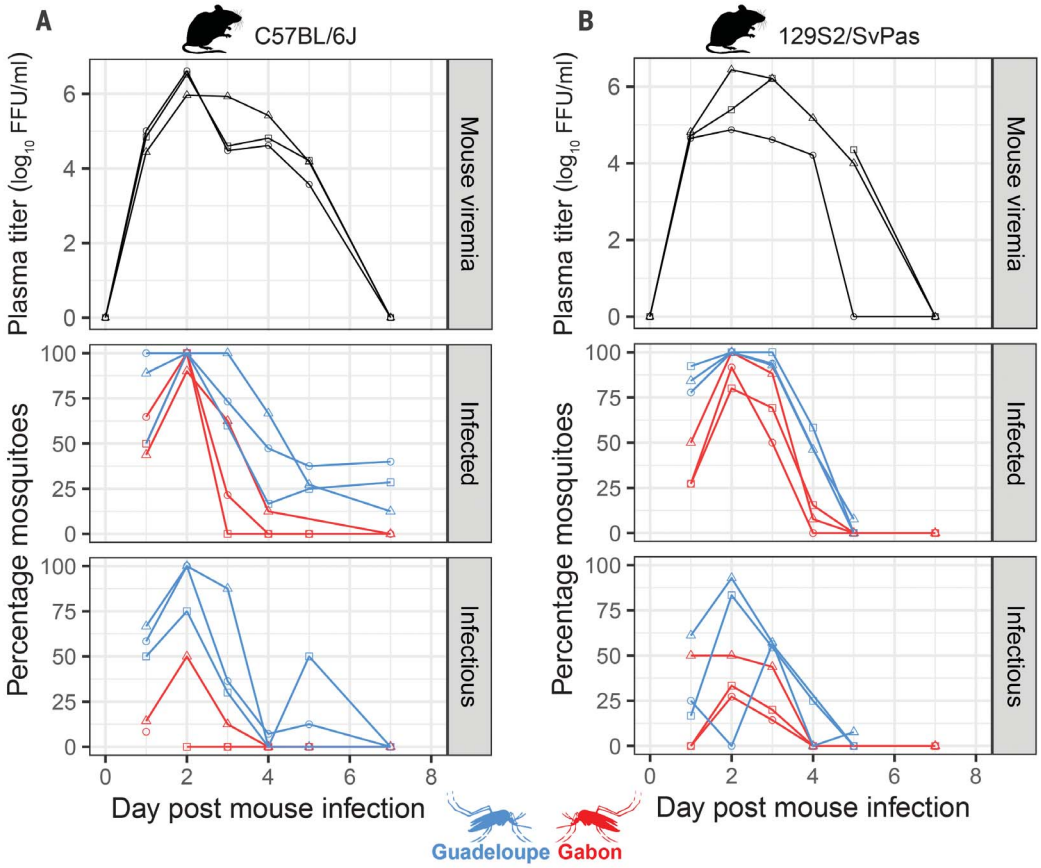

Fig. 4. African mosquitoes have less potential than non-African mosquitoes to acquire and transmit ZIKV from a viremic host. Mouse-to-mosquito transmission of ZIKV was evaluated in immunocompromised (*Ifnar1*$^{-/-}$) C57BL/6J (**A**) and 129S2/SvPas (**B**) mouse strains. The graphs show the time course of mouse plasma viremia (infectious titers expressed in log_{10}-transformed FFU per milliliter) (top graph), mosquito infection (percentage of ZIKV-infected mosquitoes 14 days post–blood meal) (middle graph), and mosquito infectiousness (percentage of mosquitoes with ZIKV-positive saliva 14 days post–blood meal) (bottom graph) during the mouse viremic period. In all panels, each line represents one of three replicate mice, identified by different symbols. In the middle and bottom graphs, each data point represents a group of 2 to 20 (median, 11) mosquitoes. The blue and red colors represent mosquitoes from Guadeloupe and Gabon, respectively.

chromosome 2 (Fig. 3B; table S4). In the second intercross (Gabon males × Guadeloupe females), we also detected four QTLs associated with infection status, albeit with lower statistical support (FDR < 0.05), between 37.0 and 344.8 Mb on chromosome 2 (Fig. 3C; table S4). For both intercrosses, there was a complete lack of genotype-phenotype association signal on chromosomes 1 and 3 (Fig. 3, B and C). The strongest QTL signals on chromosome 2 were distinct between the two intercrosses, which could reflect incomplete detection power and/or causative variants that are not fixed differences between the parental populations (*23*). Earlier genetic mapping studies of DENV susceptibility in *A. aegypti* also yielded different QTL sets in separate crosses, including QTLs located at different positions of chromosome 2 (*24*, *25*). Analyses of ancestry differences confirmed that in both intercrosses the significant QTL corresponded to an enrichment of the resistant parental genome in the resistant progeny (fig. S3). Although our QTL mapping approach had a relatively low resolution due to the limited number of unique recombination events captured in only three generations, it provided clear evidence that the difference in ZIKV susceptibility between the Gabon and Guadeloupe colonies is governed by one or more genetic loci on chromosome 2.

Finally, we evaluated the impact of the observed difference in ZIKV susceptibility between *Aaa* and *Aaf* on transmission potential in a mouse model of ZIKV infection. Artificial infectious blood meals are a convenient proxy, but they do not necessarily recapitulate the complexity of a blood meal taken on a live host, which potentially contains host factors and viral antigens that may influence virus acquisition by mosquitoes (*26*–*28*). In addition, infection probability is only one component of the virus transmission process, which also requires systemic dissemination and viral release in mosquito saliva (*11*). To address the limitations of artificial blood meals, we compared the cumulative amount of virus transmission between the Gabon and Guadeloupe colonies when mosquitoes acquired infection from a live host. Groups of mosquitoes from both colonies were allowed to simultaneously blood feed on the same ZIKV-infected mice (fig. S1B). After intraperitoneal injection of the ZIKV_Cambodia_2010 strain, immunocompromised mice (*Ifnar1*$^{-/-}$) from two genetic backgrounds (C57BL/6J and 129S2/SvPas) developed viremia that peaked 2 to 3 days after infection and was detectable in plasma for about 1 week (Fig. 4). Across the mouse viremic period, the proportions of infected (ZIKV-positive body) and infectious (ZIKV-positive saliva) mosquitoes roughly followed the kinetics of plasma viremia but were substantially lower for Gabon than for Guadeloupe mosquitoes (Fig. 4). Accounting for differences between replicate mice, the infection rate was significantly lower (multivariate logistic regression, $P < 0.0392$) for the Gabon mosquitoes at all time points, with the exception of day 2 post–mouse infection in the C57BL/6J strain ($P = 0.0898$) and day 5 post–mouse infection in the 129S2/SvPas strain ($P = 0.2976$). Likewise, the proportion of infectious mosquitoes was significantly lower ($P < 0.0176$) for the Gabon colony on days 2 and 3 post–mouse infection in both mouse strains, as well as on days 1 and 5 post–mouse infection ($P < 0.0305$) in the C57BL/6J strain. Therefore, the large difference in ZIKV susceptibility previously observed with artificial infectious blood meals translated into a substantially lower potential to transmit ZIKV of *Aaf* relative to *Aaa*.

Together, our results indicate that domestication of *A. aegypti* about 5000 to 10,000 years ago (*6*, *8*) was accompanied by an increase in its innate ability to acquire and transmit ZIKV. Today, some African populations of *A. aegypti*, such as NGO in western Senegal, display morphological, behavioral, and genetic features typical of *Aaa* populations outside Africa (*7*), as does their ZIKV susceptibility. This is consistent with an earlier study in Senegal that

reported a cline in the relative abundance of *Aaa* and *Aaf* (based on morphological features) that correlated with variation in DENV susceptibility (*29*). Whether the differential ZIKV susceptibility between *Aaa* and *Aaf* extends to other flaviviruses than ZIKV remains to be ascertained. Experimental infections of the *A. aegypti* colonies from our worldwide panel with YFV (fig. S4) and DENV (fig. S5) showed a similar pattern as for ZIKV. These data are consistent with a higher genetic resistance of *Aaf* against flaviviruses in general; however, without a broader panel of YFV and DENV strains, we cannot rule out the existence of strain-specific interactions (*30*). It is unlikely that the increased ZIKV susceptibility of the globally invasive *Aaa* subspecies was driven by relaxed natural selection, because arboviruses apparently do not represent a meaningful selective force on mosquito populations (*31*). Moreover, ZIKV usually circulates in sylvatic cycles that involve other mosquito species than *A. aegypti* (*32*), reducing opportunities for natural selection to act. We speculate that increased susceptibility was a by-product of adaptation to the domestic lifestyle due to genetic drift and/or genetic linkage between domestic genes and susceptibility genes, but this remains to be tested. This hypothesis is supported by the overlap between the most significant ZIKV susceptibility QTL spanning from 128 to 189 Mb on chromosome 2 and a previously identified genomic hotspot for human specialization between 133 and 168 Mb on the same chromosome (*7*). For example, the human-preferring NGO population showed higher levels of genetic differentiation from animal-preferring populations and elevated levels of domestic ancestry in this genomic region (up to 50% versus the 37.4% genome-wide average).

Regardless of the underlying evolutionary mechanism, the marked difference in ZIKV susceptibility between *Aaa* and *Aaf* may help to explain one puzzling aspect of Zika epidemiology. Although ZIKV was first isolated in Uganda and is known to be present across most of Africa, it has yet to cause large-scale human outbreaks on that continent (*33*, *34*). Arbovirus emergence is primarily driven by urbanization, globalization, and the failure of prevention measures, and the risk is further modulated by region-specific factors such as the immune and genetic background of human populations (*35*, *36*). The low seroprevalence of neutralizing antibodies against ZIKV typically observed in Africa (*37*–*39*) makes it unlikely that herd immunity is the main factor preventing ZIKV outbreaks. Our findings suggest that instead the lower transmission potential of *Aaf* could have hindered ZIKV emergence on the African continent. This explanation is consistent with the few examples of ZIKV circulation in human populations of Africa and points to opportunities for experimental confirmation with additional mosquito samples. ZIKV was detected in Gabon in 2007, but the vector was presumably another mosquito species, *Aedes albopictus* (*40*). ZIKV circulated during 2016 and 2017 in Angola (*41*), but a recent study found that an *A. aegypti* population from Luanda, Angola, consisted of a genetic mixture of *Aaa* and *Aaf* (*6*). Possibly, a similar situation could have facilitated the large ZIKV outbreak that occurred in Cape Verde during 2015 and 2016 (*42*), according to the untested assumption that the local *A. aegypti* population there harbors a large proportion of domestic ancestry, similar to the nearby populations of western Senegal. We conclude that the evolution of human specialization and subsequent spread of *A. aegypti* out of Africa may have promoted arbovirus emergence not solely through increased vector–host contact but also as a result of enhanced vector permissiveness.

REFERENCES AND NOTES

1. M. U. G. Kraemer *et al.*, *Nat. Microbiol.* **4**, 854–863 (2019).
2. P. F. Mattingly, *Ann. Trop. Med. Parasitol.* **51**, 392–408 (1957).
3. A. Gloria-Soria *et al.*, *Mol. Ecol.* **25**, 5377–5395 (2016).
4. J. E. Brown *et al.*, *Proc. R. Soc. B* **278**, 2446–2454 (2011).
5. C. S. McBride, *Curr. Biol.* **26**, R41–R46 (2016).
6. P. Kotsakiozi *et al.*, *Ecol. Evol.* **8**, 7835–7848 (2018).
7. N. H. Rose *et al.*, *Curr. Biol.* **30**, 3570–3579.e6 (2020).
8. J. E. Crawford *et al.*, *BMC Biol.* **15**, 16 (2017).
9. O. J. Brady, S. I. Hay, *Annu. Rev. Entomol.* **65**, 191–208 (2020).
10. S. C. Weaver, C. Charlier, N. Vasilakis, M. Lecuit, *Annu. Rev. Med.* **69**, 395–408 (2018).
11. W. C. Black 4th *et al.*, *Arch. Med. Res.* **33**, 379–388 (2002).
12. T. H. Aitken, W. G. Downs, R. E. Shope, *Am. J. Trop. Med. Hyg.* **26**, 985–989 (1977).
13. W. J. Tabachnick *et al.*, *Am. J. Trop. Med. Hyg.* **34**, 1219–1224 (1985).
14. D. J. Gubler, S. Nalim, R. Tan, H. Saipan, J. Sulianti Saroso, *Am. J. Trop. Med. Hyg.* **28**, 1045–1052 (1979).
15. G. W. Dick, S. F. Kitchen, A. J. Haddow, *Trans. R. Soc. Trop. Med. Hyg.* **46**, 509–520 (1952).
16. M. R. Duffy *et al.*, *N. Engl. J. Med.* **360**, 2536–2543 (2009).
17. D. Musso, E. J. Nilles, V. M. Cao-Lormeau, *Clin. Microbiol. Infect.* **20**, O595–O596 (2014).
18. D. Musso, A. I. Ko, D. Baud, *N. Engl. J. Med.* **381**, 1444–1457 (2019).
19. A. T. Ciota *et al.*, *Emerg. Infect. Dis.* **23**, 1110–1117 (2017).
20. C. M. Roundy *et al.*, *Emerg. Infect. Dis.* **23**, 625–632 (2017).
21. P. M. Armstrong *et al.*, *Nat. Microbiol.* **5**, 239–247 (2020).
22. E. Calvez *et al.*, *Emerg. Microbes Infect.* **7**, 159 (2018).
23. H. Bastide, J. D. Lange, J. B. Lack, A. Yassin, J. E. Pool, *Genetics* **204**, 1307–1319 (2016).
24. C. F. Bosio, R. E. Fulton, M. L. Salasek, B. J. Beaty, W. C. Black 4th, *Genetics* **156**, 687–698 (2000).
25. C. Gomez-Machorro, K. E. Bennett, M. del Lourdes Munoz, W. C. Black 4th, *Insect Mol. Biol.* **13**, 637–648 (2004).
26. Y. Liu *et al.*, *Nature* **545**, 482–486 (2017).
27. M. N. Nguyet *et al.*, *Proc. Natl. Acad. Sci. U.S.A.* **110**, 9072–9077 (2013).
28. Y. Zhu *et al.*, *Nat. Microbiol.* **4**, 2405–2415 (2019).
29. M. Sylla, C. Bosio, L. Urdaneta-Marquez, M. Ndiaye, W. C. Black 4th, *PLOS Negl. Trop. Dis.* **3**, e408 (2009).
30. L. B. Dickson, I. Sanchez-Vargas, M. Sylla, K. Fleming, W. C. Black 4th, *PLOS Negl. Trop. Dis.* **8**, e3153 (2014).
31. L. Lambrechts, M. C. Saleh, *Cell Host Microbe* **26**, 309–313 (2019).
32. G. Gutiérrez-Bugallo *et al.*, *Nat. Ecol. Evol.* **3**, 561–569 (2019).
33. A. G. Buchwald, M. H. Hayden, S. K. Dadzie, S. H. Paull, E. J. Carlton, *Acta Trop.* **209**, 105468 (2020).
34. D. Weetman *et al.*, *Int. J. Environ. Res. Public Health* **15**, 220 (2018).
35. H. Ketkar, D. Herman, P. Wang, *Viruses* **11**, 150 (2019).
36. A. Wilder-Smith *et al.*, *Lancet Infect. Dis.* **17**, e101–e106 (2017).
37. J. T. Kayiwa *et al.*, *J. Gen. Virol.* **99**, 1248–1252 (2018).
38. A. C. Willcox *et al.*, *Am. J. Trop. Med. Hyg.* **99**, 756–763 (2018).
39. B. Kisuya, M. M. Masika, E. Bahizire, J. O. Oyugi, *Trans. R. Soc. Trop. Med. Hyg.* **113**, 735–739 (2019).
40. G. Grard *et al.*, *PLOS Negl. Trop. Dis.* **8**, e2681 (2014).
41. S. C. Hill *et al.*, *Lancet Infect. Dis.* **19**, 1138–1147 (2019).
42. O. Faye *et al.*, *Emerg. Infect. Dis.* **26**, 1084–1090 (2020).
43. M. U. Kraemer *et al.*, *eLife* **4**, e08347 (2015).
44. B. N. Mansfeld, R. Grumet, *Plant Genome* **11**, 180006 (2018).
45. F. Aubry *et al.*, Enhanced Zika virus susceptibility of globally invasive *Aedes aegypti* populations, Zenodo (2020); https://doi.org/10.5281/zenodo.3981206.

ACKNOWLEDGMENTS

We thank C. Lallemand for assistance with mosquito rearing and the Institut Pasteur animal facility staff for the breeding of *Ifnar1*$^{-/-}$ mice. We thank the volunteers and the ICAReB staff for the human blood supply. We are grateful to A.-B. Failloux for sharing the YFV strain. **Funding:** This work was primarily funded by the European Union's Horizon 2020 research and innovation programme under ZikaPLAN grant agreement no. 734584 (to L.L.). This work was also supported by Agence Nationale de la Recherche (grants ANR-16-CE35-0004-01, ANR-17-ERC2-0016-01, and ANR-18-CE35-0003-01 to L.L.), the French Government's Investissement d'Avenir program Laboratoire d'Excellence Integrative Biology of Emerging Infectious Diseases (grant ANR-10-LABX-62-IBEID to L.L. and X.M.), the Inception program (Investissement d'Avenir grant ANR-16-CONV-0005 to L.L.), the City of Paris Emergence(s) program in Biomedical Research (to L.L.), the QIMR Berghofer Medical Research Institute (Seed Funding Grant to G.R.), the Programme Opérationnel FEDER-Guadeloupe-Conseil Régional 2014-2020 (grant 2015-FED-192 to A.V.-R.), the European Union's Horizon 2020 research and innovation programme under ZIKALLIANCE grant agreement no. 734548 (to A.V.-R.), the U.S. National Institutes of Health (grant NIDCD R00-DC012069 to C.S.M.), a Helen Hay Whitney Postdoctoral Fellowship (to N.H.R.), the UK Medical Research Council (grant MC_UU_12014/8 to A.K.), and the CDC (J.-P.M.). C.S.M. is a New York Stem Cell Foundation—Robertson Investigator. The funders had no role in study design, data collection and interpretation, or the decision to submit the work for publication. **Author contributions:** F.A. and L.L. designed and coordinated the study. F.A., S.D., C.M., E.F.M., D.M., A.B., S.H.M., L.B.D., A.B.C., and V.O.A. performed the mosquito experiments. I.F. and G.R. generated and analyzed the RAD-seq data and performed the QTL mapping. N.H.R. performed the admixture analyses. N.H.R., C.M.R.-V., A.V.-R., I.D., D.J., C.P., M.N.M., J.J.L., A.K., V.D., A.P., M.S., J.A., S.O., J.L., R.S., J.-P.M., and C.S.M. performed field collections to initiate mosquito colonies. V.-M.C.-L., R.G.J., C.T.D., Oum.F., Ous.F., and A.A.S. obtained the virus isolates and organized their transfer. N.H.R. and C.S.M. coordinated the collection and the maintenance of the African mosquito panel. F.A., C.M., X.M., and L.L. designed and implemented the mouse-to-mosquito transmission assay. F.A. and L.L. wrote and revised the manuscript with input from all other authors. **Competing interests:** The authors declare no competing interests. **Data and materials availability:** Raw sequencing data were deposited to the SRA repository under accession number PRJNA640190. All other raw data are available at Zenodo (*45*). Sharing some of the materials is subject to material transfer agreements with Institut Louis Malardé, Institut Pasteur Dakar, Princeton University, Universidad del Norte, the Walter Reed Army Institute of Research, and the World Reference Center for Emerging Viruses and Arboviruses.

SUPPLEMENTARY MATERIALS

science.sciencemag.org/content/370/6519/991/suppl/DC1
Materials and Methods
Figs. S1 to S5
Tables S1 to S4
References (*46*–*63*)
MDAR Reproducibility Checklist

View/request a protocol for this paper from *Bio-protocol*.

16 June 2020; accepted 16 September 2020
10.1126/science.abd3663

Announcement of the 3rd International Forum for Outstanding Scholars of Nanchang University

WE go deep into the spirit of inspection from President Xi who come and meet NCU twice;
WE won and carry forward the glory of the National Technology Invention Awards 1st prize;
Nanchang University is awaiting your join and ambitious contributions in Jiangxi!

The 3rd International Outstanding Scholars Forum of Nanchang University will be launched on December 18, 2020. The forum aims to build a platform for exchanges and cooperation among outstanding scholars at home and abroad, promote interdisciplinary communications and academic innovation, enhance mutual cooperation and trust, deepen the comprehensive understanding of Nanchang University, motivate high-level talents to come to Jiangxi and make contributions, and jointly promote "Double First-Class" construction of Nanchang University. We sincerely welcome all global talent to join us at NCU.

FORUM SCHEDULE

Registration deadline: December 4, 2020 (Tentative)
Time: December 18-19, 2020
Forum registration and specific agenda will be sent to the invitees in an invitation letter.

QUALIFICATIONS

1.Devoted to higher education in China, support the leadership of the CPC, abide by the law, with professional ethics and rigorous academic attitude.
2.Outstanding scholars who have obtained a doctorate and have research experiences in overseas top universities, institutes or R&D bases, have achieved remarkable achievements; or domestic outstanding scholars who have obtained a doctorate with outstanding academic performance and great academic potential.

APPLICATION

1. Eligible scholars are supposed to log in to register:
The portal: https://zpjob.acabridge.cn/frontend/frm/?f_id=116
2. Registered applicants will be reviewed and those who have passed the review will receive e-invitation letters.
3. The invited scholars should fill out the receipt within two weeks after receiving the invitation letter and confirm whether to participate.

FORUM RECRUITMENT DISCIPLINES

Faculty of Humanities:
Chinese Language and Literature, Foreign Language and Literature, Journalism and Communication.
Faculty of Social Science:
Law, Applied Economics, Theoretical Economics, Sociology, Politics, Management Science and Engineering, Tourism Management, Exhibition Economy and Management, Hotel Management, Marxist Theory
Faculty of Science and Engineering (Division I) :
Luminescent Materials and Devices, Ferroelectric Materials and Chemistry, Space Science and Technology, Energy Materials and Devices, Ultra-high Temperature Materials and Equipment, Information Materials and Devices, Rare Earth Materials, Basic Mathematics, Computational Mathematics, Condensed Matter Physics, Plasma Physics, Optics, Synthesis and Catalysis, Intelligent Manufacturing Engineering, Mechanical Engineering, Material Shaping and Control, Information and Communication Engineering, Computer Science and Technology, Electrical Engineering, Intelligent Technology and Big Data, Software Engineering, Cyber Security, etc.
Faculty of Science and Engineering (Division II):
Food Science and Engineering, Biology, Botany, Ecology, Aquaculture, Environmental Science and Engineering, Chemical Engineering and Technology, Process Equipment and Control Engineering, Resource Cycle Science and Engineering, Mechanics
Faculty of Medicine:
Basic Medicine, Clinical Medicine, Pharmacy, Nursing, Public Health and Preventive Medicine, etc.

SUPPORT POLICY

Jiangxi Provincial Government Support Package:
Priority to the application of the "Double Thousand Plan" talent project and the "Jinggang Scholar" talent project of Jiangxi Province. If selected, certain project funding and talent subsidies will be given.
Nanchang Municipal Government Support Package:
One-time living allowance of 50,000 yuan for employment, settlement, renting, etc. and a house purchase subsidy of 100,000 yuan per person for full-time doctoral students; 1,000 yuan Settlement rewards per person for the first relocation of household registration to Nanchang (including collective household registration), .
Nanchang University Support Package:
Salary negotiable for each person and sufficient funding for scientific research; the school also provides a talent temporary apartment, as well as job opportunity for spouse, in case which is not available a one-time living allowance will be provided; One-stop high-quality education resources from elementary school to high school for children; high-quality medical security services from the school's affiliated hospitals.

OTHER INSTRUCTIONS

1. The forum will be organized according to the requirements for COVID-19 prevention and control and the application situation. Due to the pandemic, the forum will finally be held offline & online.
2. In principle scholars already in China should participate onsite, and scholars still abroad can participate online; domestic round-trip transportation (most 5000 yuan/person), board and lodging expenses will be borne by the school.
3. The invited scholars must prepare academic reports in advance.

CONTACT

Contact: Mr. Yang, Mr. Chen
Tel: +86-791-83969074
Email: rscrsk@ncu.edu.cn
Address: No. 999 Xuefu Avenue, Honggutan New District, Nanchang, Jiangxi Province

ADVERTISEMENT

Internet+ 2020·SCUT

我敢闯 我会创

Dare to Differ, Dare to Win

"建行杯"第六届中国国际互联网+大学生创新创业大赛

The 6th China International College Students' "Internet+" Innovation and Entrepreneurship Competition

Innovation and entrepreneurship is a global trend and the lingua franca of the youth worldwide. Faced with the great opportunities and challenges of the information age, young people around the world, as the mainstay of innovation and entrepreneurship, have been endeavoring to enhance people-to-people exchanges and cooperation in technology and humanities, join hands to build an "Internet+" platform of innovation and entrepreneurship to boost global economic development, and create a community of shared future for humanity.

In May 2015, for the purpose of promoting innovation and entrepreneurship in the field of higher education, the first China College Students' "Internet+" Innovation and Entrepreneurship Competition was officially launched. After being successfully held for five consecutive years, it is now the world's largest innovation and entrepreneurship competition for university students and graduates. In 2019, the event drew 4.57 million participants (1.09 million teams) from 4,093 colleges and universities in 124 countries and regions. Over a thousand professionals from China and abroad were invited to judge the competition and mentor the participants. Among these professionals were investors, entrepreneurs, start-up incubator mentors, as well as experts in innovation and entrepreneurship education.

During the past five years, a great many college students stood out on the stage of the "Internet+" Competition, and have grown into a major force in innovation and entrepreneurship. A large number of extraordinary projects raced to emerge, covering a wide range of areas that reflected the latest achievements of a new round of technological revolution, such as unmanned helicopter systems, micro-satellites, advanced materials, big data, cloud computing, and artificial intelligence. These projects, through the competition, earned wider market visibility, gained higher valuation, and obtained investment more quickly. In 2019, 284 entry projects were introduced in the investment and financing event of the competition, which facilitated 406 intentions of investment that worth more than 1.7 billion yuan.

ADVERTISEMENT

Among the best of these teams is "Youmi Technology" from South China University of Technology. In 2015, it won the second place at the first "Internet+" Competition with its leading intelligent digital marketing technology. Today, Youmi Technology Co., Ltd., an enterprise founded by the team, has been listed as one of the "Top 100 Internet Companies in China". Since the start of the competition, more and more Chinese college students have devoted themselves to entrepreneurship. Statistics show that 741,000 college students started their own businesses in 2019, with an increase of 9% compared to 2018.

Since the International Track was set up as part of the competition in 2017, the numbers of international universities, projects and students participating in the event have been increasing year by year. In 2020, the 6th "Internet+" Competition adds the word "international" to its name for the first time. It has attracted more than 6 million entrants from China and abroad. There are 3,291 international projects developed by teams from 1,158 universities outside China, among which many are from the world's best-known universities, such as University of Oxford, University of Cambridge, Harvard University, Stanford University, and Massachusetts Institute of Technology. College students in China are presenting an international business card of the "Internet+" Competition to their peers across the globe.

South China University of Technology (SCUT), which is the host of this year's competition, is a comprehensive, research-intensive university located in Guangzhou, the third largest city in China. In 2020, it was ranked within the world's top 200 universities by the Academic Ranking of World Universities. SCUT has a long tradition of and rich experience in fostering abilities of innovation and the spirit of entrepreneurship among students. In 1999, it was the first university in China to promote the goal of "innovation, creation, and entrepreneurship" in student training. Through a series of reforms, it has established a comprehensive education system for innovation and entrepreneurship. Focusing on emerging engineering fields, it aims to cultivate talents that will shape the future with capabilities of "learning, thinking, and acting". Up till now, there are nearly 100 listed companies founded or led by alumni of SCUT, which is therefore known as the "cradle of entrepreneurs".

The finals of the 6th China International College Students' "Internet+" Innovation and Entrepreneurship Competition will be held at SCUT's campus at the Guangzhou Higher Education Mega Center from November 17 to 21, 2020. The finals will proceed in both on-site and online venues, enabling students from different countries and regions to compete in the same arena. We expect young people from all over the world to join us in this event where creativity converges, aspirations emerge, and cooperative awareness develops. As young talents compete, communicate, and cooperate in this arena, they will set an example of innovation and entrepreneurship for the youth worldwide in this new era.

Welcome to join us!
Email: info@pilcchina.org

ADVERTISEMENT

ScienceCareers online @sciencecareers.org

Massachusetts Institute of Technology

Assistant Professors
Department of Biological Engineering

The Ragon Institute, together with the Department of Biological Engineering at the Massachusetts Institute of Technology (MIT), in Cambridge, MA is seeking outstanding scientists for tenured or tenure-track faculty positions to start July 1, 2021 or on a mutually agreed date thereafter. The Institute is located at the heart of the MGH, MIT and Harvard communities in Kendall Square with state-of-the-art research facilities. The Ragon Institute was officially established in February 2009 as a joint institute involving faculty from Massachusetts General Hospital (MGH), MIT, and Harvard University. The MIT Department of Biological Engineering at MIT has a long established presence as a leader in the field especially in the areas of immune engineering and infectious diseases.

The missions of the Ragon Institute and MIT BE are highly complementary: The Ragon Institute's ultimate goal is to harness the immune system to prevent and cure human diseases. MIT BE aims to lead the discipline of biological engineering, fusing engineering with modern molecular-to-'omic biology to measure, model, manipulate, and make biological systems for powerful new biological technologies. Candidates for this joint position may have research interests broadly at the interface of these two missions relating to immunology, immunotherapy, and infectious disease. Examples of particular areas of interest for joint appointment at the Ragon Institute and MIT BE include: systems biology, computational modeling, or machine learning approaches to studying host-pathogen interactions or the immune system; imaging technologies for macro- to nano-scale structural biology; engineering approaches toward the understanding or therapeutic modulation of innate or adaptive immunity.

The search is for candidate(s) to be hired at the assistant professor level; however, under special circumstances, a senior faculty appointment with tenure is possible, commensurate with experience. Applicants must have a Ph.D. and/or M.D. or equivalent degree in Biology and related fields (Biochemistry, Microbiology, etc.), Computer Science, or Engineering (Biological, Mechanical, Chemical, etc.) by the start of employment, and have a track record of exceptional achievement in basic or translational research and the potential to develop an outstanding independent research program that supports the Institute's ultimate goal of harnessing the immune system to prevent and cure human diseases.

MIT faculty duties include teaching at the undergraduate and/or graduate levels, research, and supervision of student research. The successful candidates will be provided with a generous start-up package to complement outstanding laboratory and office space, as well as access to state-of-the-art core facilities including advanced flow cytometry, microscopy, BSL-3 facilities and an extensive clinical specimen repository. The successful candidates will be expected to build and maintain an internationally recognized, extramurally funded research program complemented by substantial support from Institute funds. The candidates should possess the ability to work collaboratively with other scientists, in addition to the scholarly qualities required to mentor doctoral students from graduate programs at MIT.

Interested candidates should submit application materials electronically at https://school-of-engineering-faculty-search.mit.edu/mit-ragon. Each application must include: a curriculum vitae; the names and addresses of three or more references; a strategic statement of research interests; and a statement of teaching interests. In addition, candidates should provide a statement regarding their views on diversity, inclusion, and belonging, including past and current contributions as well as their vision and plans for the future in these areas. It is the responsibility of the candidate to arrange for reference letters to be uploaded at https://faculty-searches.mit.edu/letters/. Please address questions to the search committee chair, Dr. Darrell Irvine (djirvine@mit.edu). Responses received by December 1, 2020 will be given priority.

With MIT's strong commitment to diversity in engineering and science education and research, we especially encourage those who will contribute to our diversity and outreach efforts to apply.

MIT is an equal employment opportunity employer.

http://web.mit.edu

ASSISTANT / ASSOCIATE PROFESSOR
Pharmaceutics

WAYNE STATE UNIVERSITY

The Department of Pharmaceutical Sciences, Eugene Applebaum College of Pharmacy and Health Sciences, invites applications for a 12-month tenure-track Assistant or Associate Professor position. Applicants are to have an earned PhD in the pharmaceutical sciences or in a related discipline, or an MD or equivalent degree. Scientists with a record of high impact research in pharmaceutics at the chemical biology interface in areas drug discovery, delivery and development, metabolic disease, neurosciences and oncology will receive preference. The finalist will have or develop a vigorous externally funded research program and teach effectively in our PhD, MS and PharmD programs. We offer an uncommonly collegial academic culture, competitive start-up and compensation packages, generous benefits, premiere laboratory facilities and extensive research support. Submit applications via **http://jobs.wayne.edu** under Department H1822-Pharmaceutical Sciences posting **#044919**. Further details are available from Dr. Timothy Stemmler **tstemmle@med.wayne.edu** or **(313) 577-5712**.

Wayne State University is a Carnegie Highest Research Activity (R1) institution and a premier, public, urban research university in midtown Detroit where students from all backgrounds enjoy a rich, high quality education. The College is in one of the most dynamic communities leading city revitalization. The metropolitan area offers a cosmopolitan environment with rich cultural offerings, strong schools and outstanding affordable housing in the beautiful Great Lakes region. Our deep-rooted commitments to excellence, collaboration, integrity, diversity and inclusion give students exceptional preparation for success in a global society. We encourage applications from all underrepresented groups including women and people of color.

Wayne State is an affirmative action/equal opportunity employer. All qualified applicants will receive consideration without regard to race, color, religion, sex, national origin, age, disability, veteran status, or any other characteristic protected by law. Application review will begin in late **November, 2020**. The positions will remain open until filled.

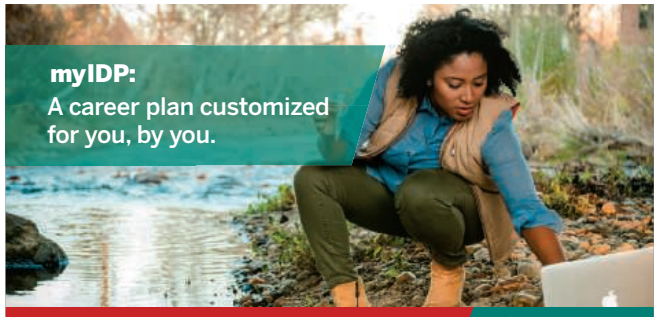

For your career in science, there's only one Science

Features in myIDP include:

- Exercises to help you examine your skills, interests, and values.
- A list of 20 scientific career paths with a prediction of which ones best fit your skills and interests.

myIDP

Visit the website and start planning today!
myIDP.sciencecareers.org

ScienceCareers AAAS In partnership with:

FASEB · University of Massachusetts Medical School UMASS · UCSF University of California San Francisco · UIC · Burroughs Wellcome Fund

GROUP LEADERS

Centers of Research Excellence
Ohio State University Comprehensive Cancer Center
Pelotonia Institute for Immuno-Oncology

The Ohio State University Comprehensive Cancer Center – Arthur G. James Cancer Hospital and Richard J. Solove Research Institute (OSUCCC – James) is seeking candidates for the position of **Group Leader** in the Pelotonia Institute for Immuno-Oncology (PIIO). This is an excellent opportunity for a proven leader and innovator with an active and established research program to join the PIIO's executive team in accelerating the pace for discovery and translation in immuno-oncology (IO).

The PIIO is a comprehensive bench-to-bedside research initiative focused on developing life-saving cancer immunotherapy breakthroughs at all levels – from prevention to treatment to survivorship. Established by a pledge of more than $100 million from Pelotonia (**pelotonia.org**) and the OSUCCC - James, the PIIO represents Ohio State University's commitment to grow the exciting area of immuno-oncology. Led by founding director and renowned immunologist **Zihai Li, MD, PhD**, the PIIO builds upon a rich portfolio of active investigator-initiated IO clinical trials being conducted at the OSUCCC – James. Its external advisory board is comprised of multiple world leaders in the field of IO including Drs. Lisa Butterfield, Lieping Chen, Carl June, Miriam Merad, Robert Schreiber, and Cassian Yee (**cancer.osu.edu/PIIO**). The Institute's initiatives include recruiting outstanding researchers; developing first-in-class, first-in-man IO agents; training the next generation of IO scientists; and fostering high-impact and holistic partnerships.

The successful candidate will serve as a senior member of the PIIO's leadership team, directing one of the Institute's four interconnected **Centers of Research Excellence:**

- **Cancer Immuno-Genomics:** a program conducted in partnership with Nationwide Children's Hospital which involves understanding the relationship between cancer genomics and immune evasion and includes epigenetics, neo-antigen vaccine, epitope prediction, TCR repertoire analysis, HLA typing, and CRISPR screening;
- **Cell Therapy:** where immune cells are collected from a patient's blood, engineered, and returned to that patient to target and eradicate cancer and includes adoptive cell therapy with T cells and natural killer cells;
- **Systems Immuno-Oncology:** which seeks a better understanding of cellular systems to create more efficient and effective immunological tools to fight cancer and includes immune regulation, microbiome, NK and T cell biology, and tumor microenvironment;
- **Translational Immuno-Oncology:** an area that focuses on transforming immuno-oncology discoveries into new or improved cancer treatments applicable at patient bedsides. This team works with the Drug Development Institute at the OSUCCC – James on developing new drug therapies.

The successful candidate – while maintaining an independent research program and obtaining extramural funding – will recruit, retain, and further develop strong investigators committed to advancing their Center of Research Excellence; set the strategic vision for growing its Center's research initiatives; and develop and enhance collaborative partnerships both internally and externally. The Group Leader will work closely with leaders of the PIIO's **Immuno-Informatics (Data Science) Group**, where big data and quantitative science are used to improve immuno-oncology research and includes machine learning, neo-antigen discovery, spatial statistics, etc.; and **Immune Monitoring and Discovery Platform**, which is backed by a new facility with technology that allows scientists to get a 360-degree view—down to the single-cell level—of what happens in the immune system during treatment with immuno-oncology agents.

Candidates will have access to state-of-the-art laboratory spaces; cutting-edge core research facilities (Spectrum Flow Cytometry, Time-of-Flight Mass Cytometry, Multiplex Histology, Single Cell Technology, GMP Facility for Cell Therapy, Antibody Engineering Facility, Immuno-Informatics and more); a competitive salary commensurate with experience, and ample start-up funding.

Applicants must hold advanced degrees such as a MD, DVM, PharmD, PhD, or MD/PhD. The ideal candidate will have a national and international reputation in their field and significant independent research experience with both historical and current federal funding of research projects as a Principal Investigator. The successful candidate is expected to maintain an extramurally funded research program, perform collaborative research with others, participate in graduate and medical education, and must be board-certified and meet medical licensure requirements in Ohio for those also pursuing a clinical position. The successful candidate will become faculty at the rank of either Associate Professor or Full Professor. The Ohio State University is an EOE/AA/M/F/D/V employer.

To Apply: Send cover letter, Curriculum Vitae, 2-3 page description of current and future research interests, and contact information for three references to the office of the director of the PIIO, Zihai Li, MD, PhD, via Tamra Brooks at **tamra.brooks@osumc.edu**.

Baylor College of Medicine

FACULTY POSITION IN PHARMACOLOGY AND CHEMICAL BIOLOGY

Baylor College of Medicine (BCM) is recognized as one of the nation's premier academic health science centers and is known for excellence in education, research, and healthcare and community service. Located in the Texas Medical Center, BCM offers a highly interactive environment and a strong infrastructure for research. The Department of Pharmacology and Chemical Biology is focused on using small molecules and biologics to understand and modify disease-relevant cellular processes. The Department invites applications from outstanding scientists for a tenure track position at the **Assistant, Associate or Full Professor** rank.

The successful candidate will possess or develop an independent, funded research program in drug discovery, chemical biology, protein design and engineering or other areas broadly relevant to pharmacology. The candidate will supervise graduate students and postdoctoral fellows and contribute to the educational programs in the Department and College. Candidates should have a Ph.D. and/or M.D. degree and postdoctoral experience as well as a strong record of research accomplishments. Competitive compensation and a generous start up package will be provided.

Applicants should submit a curriculum vitae, summary of research accomplishments, statement of research interests, and the names of three references as a single PDF to **pharmacology@bcm.edu**. Review of applications will begin in **December 2020**, and continue until the position is filled. Diversity among BCM's students, trainees, faculty and staff is a prerequisite to accomplishing BCM's institutional mission, and to maintaining the highest standards in training for healthcare providers and biomedical scientists, scientific innovation, and patient-centered care.

BCM is committed to ensuring equal opportunity for all qualified persons without taking into account race, color, national origin, creed, sex, sexual orientation, ancestry, age, veteran status or disability unrelated to job requirements.

ScienceCareers online @sciencecareers.org

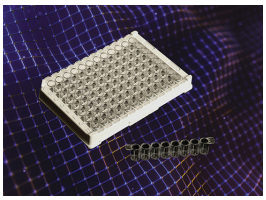

Optimized Microplates for Affinity Binding Assays

Porvair Sciences' medium- and high-bind Krystal microplates set a new standard for uniform and reproducible capture of a wide range of biomolecules ready for affinity binding assays such as ELISAs. Manufactured from high-quality crystal polystyrene, these new automation-ready plates are available in a choice of ANSI/SLAS standard (96-well and breakable 8-well-strip) formats. Offering working volumes up to 320 µL, the plates incorporate a flat bottom to ensure superb assay detection every time. Designed for hydrophobic passive adsorption of lipid-rich large biomolecules and antigens, including viral antigens, medium-bind Krystal plates offer a binding capacity of approximately 100 ng immunoglobulin G (IgG)/cm²–200 ng IgG/cm². Krystal high-bind plates are optimized for passive adsorption of proteins with different grades of hydrophilicity. Offering a binding capacity of 400 ng IgG/cm²–500 ng IgG/cm², the high-bind plates are ideal for immunoassay of glycoproteins and serum samples.

Porvair Sciences
For info: 800-552-3696
www.microplates.com/krystal-medium-and-high-bind

T-Cell Activation Assay Kit

The Agilent Seahorse XF T-cell activation assay offers you improved insight into early T-cell activation dynamics with the ability to test modulators in real time. Our new turnkey solution, the Seahorse XF Hu T-Cell Activation Assay Kit, provides you with validated reagents for consistent results; streamlined workflows with ready-to-use, PDL-coated XF microplates; and a convenient data-analysis tool for profiling maximum response and area under curve. By measuring the increase in glycolysis as proton efflux rate, Agilent Seahorse technology provides an early kinetic window to interrogate T-cell activation.

Agilent
For info: 800-227-9770
www.agilent.com

Antibody Panels for Immune Checkpoints

Discover our range of hand-picked antibody panels to key immuno-oncology targets, which are designed to save you time and provide you with easy access to the best selection of clones on the market. Each panel contains a selection of monoclonal antibodies that detect the same protein, increasing your chances of finding a compatible clone for your assay with just one purchase. We eliminate the need for prescreening by narrowing our catalog to the most suitable immunohistochemistry (IHC)-optimized clones and packaging them in an easily accessible kit so you can determine the best antibody for your IHC research assay needs.

abcam
For info: 888-772-2226
www.abcam.com

Customized CAR-T Constructs

AMS Biotechnology announces a custom chimeric antigen receptor T-cell (CAR-T) service. Drawing upon our expertise in monoclonal antibody development (rabbit and mouse), we can help you design, plan, and execute your CAR-T study, whether you are in the preclinical, clinical, or proof-of-concept stage. We can start with a target molecule (Phase I) or antibody (Phase II). Then we construct the single-chain variable fragment (ScFv), transfer it into a CAR lentivector of your choice, make lentiviruses, and transduce activated human (or mouse) T-cells. After the CAR-T cells proliferate, cytotoxicity is measured in a real-time assay, CAR expression is analyzed, and cytokine production is quantified.

AMS Biotechnology
For info: 617-945-5033
www.amsbio.com/custom-car-t-development

Fluorescent-Labeled Recombinant Proteins

R&D Systems fluorescent-labeled proteins are designed to simplify detection of a specific chimeric antigen receptor (CAR) on CAR-T cells. Our fluorescent-labeled recombinant proteins are amine-labeled and rigorously tested to ensure consistent labeling of each lot. The proteins are manufactured with controlled procedures to ensure a consistent fluorescein to protein (F/P) ratio, and quality-control tested by flow cytometry to evaluate equivalent staining. Using fluorescent-labeled proteins, target cells expressing the corresponding CAR can be directly stained and detected by flow cytometry. This method of evaluating CAR expression is highly specific, reduces processing time, and eliminates background staining that may occur by indirect detection of the CAR using an epitope-tagged target antigen and a fluorophore-labeled secondary antibody.

R&D Systems
For info: 800-343-7475
www.rndsystems.com

FFPE and Liquid Biopsy Reference Standards

Horizon Discovery Group has added two new sample formats to its cell-based OncoSpan reference standards for use in the development and validation of workflows for cancer diagnostic assays. Horizon's OncoSpan range now includes formalin-fixed, paraffin-embedded (FFPE) and cell-free DNA (cfDNA) formats for mimicking solid tumors and liquid biopsy samples, respectively, in addition to its well-established genomic DNA format. Its cfDNA format offers one of the largest number of variants and genes—over 380 and 152 respectively—of any characterized reference standard, to help standardize liquid biopsy testing. These cell line–derived reference standards closely mimic patient samples and offer an unlimited, reproducible resource to ensure consistency during the establishment and validation of diagnostic assays. All three formats are delivered with batch-specific NGS data, orthogonally validated by droplet digital PCR, to allow researchers to further validate their analysis pipeline.

Horizon Discovery Group
For info: 800-235-9880
horizondiscovery.com

Electronically submit your new product description or product literature information! Go to www.sciencemag.org/about/new-products-section for more information.

Newly offered instrumentation, apparatus, and laboratory materials of interest to researchers in all disciplines in academic, industrial, and governmental organizations are featured in this space. Emphasis is given to purpose, chief characteristics, and availability of products and materials. Endorsement by *Science* or AAAS of any products or materials mentioned is not implied. Additional information may be obtained from the manufacturer or supplier.